



FACULTEIT LANDBOUWKUNDIGE EN
TOEGEPASTE BIOLOGISCHE
WETENSCHAPPEN



Academiejaar 2002-2003

**COMPUTATIONAL FLUID DYNAMICS OF SETTLING TANKS:
DEVELOPMENT OF EXPERIMENTS AND
RHEOLOGICAL, SETTLING, AND SCRAPER SUBMODELS**

**NUMERIEKE STROMINGSMECHANICA VAN BEZINKTANKS:
ONTWIKKELING VAN EXPERIMENTEN EN SUBMODELLEN
VOOR REOLOGIE, SLIBBEZINKING EN SLIBVERWIJDERING**

door

ir. Bob DE CLERCQ

*Thesis submitted in fulfillment of the requirements
for the degree of Doctor (Ph.D) in Applied Biological Sciences*

*Proefschrift voorgedragen tot het bekomen van de graad
van Doctor in de Toegepaste Biologische Wetenschappen*

op gezag van

Rector: **Prof. Dr. A. De Leenheer**

Decaan:

Prof. Dr. ir. H. VAN LANGENHOVE

Promotor:

Prof. Dr. ir. P. VANROLLEGHEM

**COMPUTATIONAL FLUID DYNAMICS OF SETTLING TANKS:
DEVELOPMENT OF EXPERIMENTS AND
RHEOLOGICAL, SETTLING AND SCRAPER SUBMODELS**

by

ir. Bob DE CLERCQ

PhD Review Committee

Prof. P. Krebs (TU Dresden, Germany)

Prof. J. McCorquodale (University of New Orleans, USA)

Prof. P. Van Der Meeren (UGent)

Prof. P. Vanrolleghem (UGent)

Prof. J. Vierendeels (UGent)

Examination Committee

Prof. J. Viaene (chair)

Dr. ir. D. Kinnear (UGent)

Prof. J. Pieters (secretary)

20.6.2003

The author and the promoter give the authorization to consult and to copy parts of this work for personal use only. Any other use is limited by the Laws of Copyright. Permission to reproduce any material contained in this work should be obtained from the author.

De auteur en de promotor geven de toelating dit doctoraatswerk voor consultatie beschikbaar te stellen, en delen ervan te kopiëren voor persoonlijk gebruik. Elk ander gebruik valt onder de beperkingen van het auteursrecht, in het bijzonder met betrekking tot de verplichting uitdrukkelijk de bron te vermelden bij het aanhalen van de resultaten van dit werk.

De promotor:

De auteur:

Prof. Dr. ir. Peter Vanrolleghem

ir. Bob De Clercq

The research reported in this dissertation was conducted at the Department of Applied Mathematics, Biometrics and Process Control (BIOMATH) of Ghent University. It was made possible by the Fund for Scientific Research - Flanders (Belgium) (F.W.O.) and the Ghent University Fund (B.O.F.). The author is a F.W.O. Research Assistant.

Het onderzoek beschreven in deze thesis werd verricht aan de Vakgroep Toegepaste Wiskunde, Biometrie en Procesregeling (BIOMATH) van de Universiteit Gent. Het werd verder mogelijk gemaakt door het Fonds voor Wetenschappelijk Onderzoek - Vlaanderen (F.W.O.) en het Bijzonder Onderzoeksfonds (B.O.F.) van de Universiteit Gent. De auteur is een F.W.O. Aspirant.

Woord vooraf

Een doctoraat... het heeft me veel moeite gekost, maar het loonde zeker de moeite. In 1996 zochten Henk en ik een thesisonderwerp in het laatste jaar bio-ingenieur en belandden in de vakgroep Toegepaste Wiskunde, Biometrie en Procesregeling. Peter Vanrolleghem was er destijds doctor-assistent en bouwde een onderzoeksgroep uit rond modellering en procescontrole. Als eerste thesisstudenten op de vakgroep, die trouwens een slechte naam had wegens een *teveel* aan wiskunde (tja, bio-ingenieurs houden blijkbaar niet van wiskunde-gerwante vakken), vonden we het er blijkbaar wel leuk zodat we nog wat langer bleven. Henk ging voor een doctoraat, en zelf opteerde ik voor een project. Na een jaartje ging ik dan wel, met wat meer ervaring, op de arbeidsmarkt naar een job zoeken. Het is er nooit van gekomen... Peter stuurde me naar een KVIV studiedag in Antwerpen i.v.m. numerieke stromingsmechanica. Ik was zo enthousiast over de "kleurrijke" en "bewegende" beeldjes van vloeistofstromingen in reactoren dat ik Peter vroeg of hieromtrent geen doctoraat mogelijk was. En zo zijn we dan aan de slag gegaan in 1998 met een beurs van het Fonds voor Wetenschappelijk Onderzoek (FWO).

Het eerste jaar was een jaar van leren aangezien niemand van de vakgroep kaas had gegeten van het onderwerp. En er was geen geld voorhanden om software aan te kopen of experimenten uit te voeren. Concreet gezegd, er moest een project geschreven worden om geld in het laatje te brengen. Het project werd aanvaard door het FWO, maar de experimenten bleven uit, evenals de simulaties. Ik begon te twijfelen of dit doctoraat wel een goede keuze was voor mezelf. Na vele diepe, en ook humoristische, gesprekken met Martijn begon ik te solliciteren zoals (blijkbaar) vele doctoraatstudenten tegenwoordig doen. Het was zo motiverend dat zelfs ook Martijn begon te solliciteren. Eén klein detail, Martijn ging voor Aquafin werken, en ik bleef. Peter wist namelijk dat ik graag eens naar het buitenland wou trekken en kwam met het voorstel af om naar Australië te gaan voor 10 maanden. Ik tekende uiteraard onmiddellijk... In deze context wil ik zeker het FWO bedanken voor de geboden kans en vooral de financiële steun. Het was niet enkel een persoonlijke verrijking; ik heb er leren zelfstandig werken wat zeker niet altijd even evident is. Tevens heb ik de mogelijkheid gehad om er een netwerk van beroepsmensen uit te bouwen waar ik achteraf, en ook nu nog, op kan steunen. Ook verschillende meettechnieken heb ik er geleerd en uitgeprobeerd. Maar niet het minste, ik heb er enorm genoten van het goede en warme weer! Mijn dank gaat ook uit naar Rogier, Lisa en haar ouders voor de goede opvang aldaar. *In this respect, I owe many thanks to Paul Lant for the work opportunity and support at the Advanced Wastewater Management Centre (Brisbane). My gratitude also goes to Matthew for his friendship and professional support in Brisbane and during his three months stay in Belgium. I expect, and I am pretty sure about it, that the Duvels gave him memories to enjoy for a long time.*

In Australië hervond ik mezelf, vond ik inspiratie en het enthousiasme om het doctoraat af te werken (goede zet van Peter!). Zeker naar het einde toe werd het doctoraat meer belastend: simulaties leveren niet altijd de gewenste resultaten, en dat merk je maar al te goed wanneer je met modelvalidaties begint.

Ondanks de laatste loodjes heb ik het doctoraat met veel plezier beëindigd, en wil ik zeker Peter danken voor de geboden kansen om naar cursussen en internationale conferenties te gaan en zo je kennis en persoonlijkheid te verruimen. Ook de mensen van Biomath, de meer populaire naam van de vakgroep, wil ik bedanken voor de leuke op de georganiseerde fuiven, weekends en verjaardagsdrinks.

Een kleine "spin-off" van mij doctoraat is Ellen die ik heb leren kennen aan de vakgroep. Haar wil ik dan ook bedanken voor de liefde, vreugde en de steun die ze heeft gegeven. Uiteraard mogen mijn ouders niet vergeten worden die me altijd de kans en motivatie hebben (mee)gegeven om verder te studeren. Aan hen wil ik dan ook dit doctoraat opdragen. Bedankt.

Gent, juni 2003
Bob De Clercq

Contents

1 Introduction.....	1
1.1 Functions of the secondary settling tank.....	2
1.2 Factors influencing the capacity and performance of secondary settling tanks.....	5
1.2.1 Biological influences.....	5
1.2.2 Physical and chemical influences.....	7
1.2.3 Hydraulic influences.....	9
1.3 Other solids separation techniques.....	11
1.4 Design of settling tanks.....	12
1.4.1 Surface and solids loading rates.....	12
1.4.2 Types of settling tanks.....	14
1.4.3 Solids removal mechanisms.....	16
1.4.4 Inlet structure.....	17
1.4.5 Weir placement and loading rates.....	18
1.5 Dissertation goals.....	19
1.6 Outline of the dissertation.....	21
1.7 Conclusions.....	22
2 Mathematical Modelling of Settling Tanks.....	25
2.1 Introduction.....	25
2.2 Basics of flow modelling.....	28
2.2.1 The Navier-Stokes equations.....	29
2.2.2 Introduction to turbulence modelling.....	32
2.2.3 Solids transport modelling.....	39
2.2.4 Boundary and operational conditions.....	53
2.3 Conclusions.....	59
3 Numerical Computation of Flows.....	61
3.1 Discretisation of PDEs.....	62
3.1.1 Discretisation techniques.....	63
3.1.2 Discretisation schemes.....	69
3.2 Solution of discretised equations.....	75
3.2.1 Integration methods for systems of ordinary differential equations.....	75
3.2.2 Iterative methods for the solution of algebraic systems.....	78
3.2.3 Solution algorithms for pressure-velocity coupling.....	84
3.3 Numerical techniques used in Fluent.....	88
3.4 Conclusions.....	89
4 Experimental Techniques for Model Calibration and Validation.....	91
4.1 Settling velocity.....	92
4.2 Residence time distribution.....	95
4.2.1 Tracer selection.....	95
4.2.2 Tracer preparation, introduction, sampling and analysis.....	97
4.2.3 Mathematical analysis of RTDs.....	101
4.3 Solids concentration.....	102
4.3.1 <i>Ex situ</i> solids concentration measurements.....	103
4.3.2 <i>In situ</i> solids concentration measurements.....	104

4.4 Liquid velocity.....	106
4.4.1 Lab-scale velocity measurement techniques.....	106
4.4.2 Full-scale velocity measurement techniques.....	107
4.4.3 Acoustic Doppler velocity meters.....	109
4.5 Particle size distribution.....	119
4.5.1 Particle sizing techniques.....	120
4.5.2 <i>In situ</i> versus <i>ex situ</i> sizing techniques.....	126
4.5.3 The focused beam reflectance method revisited.....	127
4.6 Rheology.....	138
4.6.1 Tube rheometers.....	138
4.6.2 Rotational rheometers.....	139
4.7 Conclusions.....	140
5 Case Study: Oxley Creek WWTP.....	143
5.1 Plant layout and settling tank description.....	143
5.2 Modelling the settling tank.....	148
5.2.1 Settling velocity of zeolite-composite sludge.....	148
5.2.2 Mechanistic description of the settling tank: contributing mathematical equations.....	152
5.2.3 Some remarks on meshing.....	157
5.2.4 Modelling the inlet structure.....	159
5.2.5 Steady-state and dynamic simulations.....	162
5.2.6 Mesh dependency of the flow field.....	166
5.2.7 Hydrodynamic phenomena in circular settling tanks.....	172
5.2.8 Adjusting bulk density for zeolite.....	176
5.2.9 Modelling the scraper mechanism.....	178
5.3 Model Validation.....	184
5.3.1 Validation of solids concentration profiles.....	184
5.3.2 Validation of hydraulics.....	189
5.4 Conclusions.....	196
6 Particle Sizing in Secondary Settling Tanks	199
6.1 Experimental layout.....	199
6.2 Results and discussion.....	200
6.2.1 <i>In situ</i> steady-state PSD profiling.....	200
6.2.2 <i>In situ</i> dynamic PSD profiling.....	203
6.3 Implications to settling tank modelling.....	204
6.4 Conclusions.....	206
7 Sludge Rheology in Secondary Settling Tanks	207
7.1 On the complexity of sludge rheology.....	207
7.1.1 Properties affecting the experimental layout.....	207
7.1.2 Thixotropy or rheomalaxis?	212
7.1.3 Modelling of rheomalaxis.....	214
7.2 Considerations about yield stress.....	218
7.2.1 Theoretical background.....	218
7.2.2 Calibration of the rheological model.....	220
7.2.3 Effect of rheology on settling tank performance.....	227
7.3 Implications to settling tank modelling.....	234
7.4 Conclusions.....	236

8 Conclusions and Perspectives	239
8.1 Particle size distributions (PSD).....	240
8.2 Sludge rheology.....	241
8.3 Development of a CFD model.....	244
8.3.1 Modelling of the scraper.....	244
8.3.2 Model validation.....	246
8.4 General conclusions.....	247
Appendix A: Introduction to Tensor Notation	249
Appendix B: Spectral Analysis of ADCP Data	251
B.1 Introduction.....	251
B.2 Program in S-Plus.....	251
Appendix C: Calculation of Bulk and Solids Density	255
C.1 Governing formula.....	255
C.2 Calculation of dry solids density.....	256
C.3 Bulk density affected by multiple components.....	257
Appendix D: User-Defined Functions used in Fluent	259
D.1 Solids transport in settling tanks.....	259
D.2 Solids and tracer transport in settling tanks.....	267
Appendix E: Calculation of the Scraper's Force	273
E.1 Needed information about the scraper.....	274
E.2 Calculation of the scraper's radial velocity.....	275
E.3 Application: Scraper at Oxley WWTP.....	278
Appendix F: Sludge Flow on Sloped Flat Floors	281
F.1 Momentum balance of the flow system.....	281
F.2 Computed velocity profiles.....	282
References	285
List of Abbreviations and Symbols	307
Summary	313
Samenvatting	317
Curriculum Vitae	321

1

Introduction

Liquid and solid wastes are inevitably produced in populated areas. If untreated wastewater accumulates in the environment, the decomposition of its organic compounds can lead to the depletion of dissolved oxygen and the production of malodorous gases. In addition, municipal wastewater contains numerous pathogenic microorganisms and may contain toxic compounds. Nutrients that stimulate the growth of aquatic plants are also present; algal blooms associated with eutrophication causes fish kills due to the lack of oxygen and/or the production of toxics.

The collection of stormwater and drainage dates from ancient times, and the collection of wastewater began in the early 1800s. The systematic treatment of wastewater followed in the late 1800s and early 1900s (Tchobanoglous & Burton, 1991) and consists of physical, chemical and biological process units. Grouping of these process units results in the *primary*, *secondary* and *tertiary treatments*. In primary treatment, only physical operations such as screening and solids sedimentation are used to remove the floating and settleable solids in the wastewater. In secondary treatment, biological and physical processes degrade the organic matter. In the tertiary wastewater treatment, additional processes are included in the plant's layout to remove other constituents, such as nitrogen and phosphorus, as they are not significantly reduced by secondary treatment.

The key process of a typical WasteWater Treatment Plant (WWTP) is the *activated sludge system* (Figure 1.1), which is recognised as the most widely used way to purify the wastewater (Tchobanoglous & Burton, 1991). It consists of two main process units, i.e. a biological reactor and a settling tank. In the former process, microorganisms degrade, and grow on, the organic compounds present in the wastewater. In wastewater technology the amount of waste is usually expressed in terms of five-day Biological Oxygen Demand (BOD_5) and Chemical Oxygen Demand (COD). The former variable corresponds to the amount of dissolved oxygen used in five days by microorganisms in the biochemical oxidation of organic matter. Due to several disadvantages of the BOD_5 test (see Tchobanoglous & Burton, 1991), COD is used as a complementary and alternative measure of the amount of organic matter in the wastewater. The COD represents the oxygen equivalent of the organic matter that can be oxidised by means of a strong chemical oxidising agent in an acidic medium. Both variables, BOD_5 and COD, are widely applied.

To degrade the waste, the biomass may be supplied with oxygen by an aeration system. This diffused or mechanical aeration also keeps the microorganisms in suspension. If nitrogen and phosphorus also must be removed, additional units without oxygen supply can be placed in a specific configuration with the aeration tanks. In these tanks separate mixers thoroughly suspend the microorganisms. Hence, the system consists of a sequence of interconnected

aerobic, anoxic and anaerobic biological reactors. To complete the activated sludge system, produced biomass has to be separated from the clean water. For this, sedimentation is usually applied and takes place in the settling tank. In order to maintain the desired biomass concentration in the biological reactor a large portion of the settled solids is returned or recycled (the so-called *Return Activated Sludge RAS*); the part wasted corresponds to the produced biomass. The degree of recirculation depends on the mode of operation.

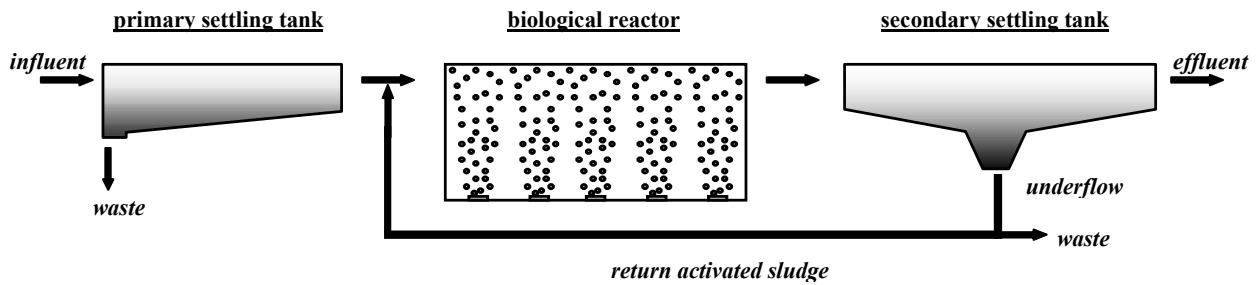


Figure 1.1 Layout of a typical activated sludge system

From Figure 1.1, sedimentation is applied before and after the biological reactor. The primary settling tank removes the particulates present in the incoming flow or influent. The organic (biomass) fraction however, produced in the biological reactor, is separated in the secondary settling tank.

The removal of solids is very important due to its association to large amounts of COD and nutrients (Ekama *et al.*, 1997). Wanner (1994) determined the washout of solids to represent 50-80% of the effluent BOD. One gram of sludge dry matter may further contribute 0.07 g of nitrogen and 0.02 g of phosphorus to the effluent (Gujer *et al.*, 1995). In this respect, Tiehm *et al.* (1999) reported 45-90% of COD and 35-80% of phosphorus associated with solids in raw sewage and primary effluent (i.e. the outflow of the primary settling tank). However, for secondary effluents particulate COD drops to 14-45% but the particulate phosphorus increases to 55-80%. These figures clearly indicate that solids separation is crucial for the overall treatment performance. Poor effluent quality due to settling problems has been reported at 20 to 50% of wastewater treatment plants in many countries (Piirtola *et al.*, 1999). Efficient activated sludge treatment therefore requires efficient settling tanks.

1.1 Functions of the secondary settling tank

Settling tanks receive an influx of solids from the biological unit process. The internal quiescent flows allow the solids to settle in the reactor; as a result, a thickened solids blanket forms. In addition to this vertical settling flux, the underflow rate creates a second vertical flux (see Figure 1.1). Clear supernatant is discharged as effluent.

The settling tank fulfils three major functions in the activated sludge system: (i) a thickener to produce a continuous underflow of highly concentrated sludge for return to the biological reactor, (ii) a clarifier to produce a clear effluent and (iii) a storage tank to store sludge during peak flows. Should the settling tank fail in one of these functions, excess Suspended

Solids (SS) are carried over the effluent weirs and escape with the effluent. Besides delivering an effluent of poor quality, excessive loss of solids (several hundreds of mg/l) could also affect the behaviour of the biological process by an uncontrolled decrease in biomass concentration. The resulting low sludge age, also termed solids retention time, can lead to a decrease in nitrogen removal if the nitrifying microorganism concentration decreases significantly.

The thickening capacity of the secondary settling tank is governed by the tank's geometry, prevailing flow rates, settleability and compactability of the sludge, and the solids concentration in the biological reactor. When thickening fails, the treatment capacity will obviously decrease because less biomass is recycled to the biological unit. To quantify sludge thickening, different measures are used in practice. In this respect, many theories and designs of secondary settling tanks are based on the solids settling velocity and the Sludge Volume Index SVI (Ekama *et al.*, 1997). The latter is the volume in millilitres occupied by one gram of solids after settling for 30 minutes (Dick & Vesilind, 1969). However, many variants (Lee *et al.*, 1983; Bye & Dold, 1998) of the standard definition of SVI have been applied in design rules. Depending on the design procedure, the required surface area and depth can be calculated to satisfy the thickening function of the secondary settling tank for selected values of solids settleability and reactor concentration.

Closely related to the thickening function is the storage of solids in the settling tank. During wet weather events solids are washed out of the biological reactor due to increased flow rates. To cope with this inflow into the settling tank two completely different design and operating philosophies are maintained. The first approach copes with the solids inventory shift by considering extra tank volume during the design. This additional volume is necessary because the solids blanket in the settling tank rises toward the free surface, i.e. if the settling and underflow fluxes cannot compensate the influx of solids. An advantage of having a permanent solids blanket may be the filtering of small flocs when the water flows through it; however, this only happens when filaments link the flocs in an immobile structure (Fuchs & Staudinger, 1999). Since this concept implies vertical flows, it may only occur in vertical flow settling tanks (see Section 1.4.2). Alternatively, no storage volume may be accommodated for the extra solids entering the settling tank (Ekama *et al.*, 1997; Parker *et al.*, 2001). In this case, the incoming solids flux is kept below the sum of the settling and underflow fluxes; hence, a solids blanket rise does even not occur under peak flow conditions. In practice, this approach is achieved by maintaining low solids concentrations in the biological reactor by using large tank volumes, or by applying step feed. In the latter control strategy the inlet of fresh wastewater is temporarily moved toward the outlet of the biological reactor. Because return sludge is stored in the part before the inlet, the solids flux to the settling tank is reduced and subsequently also the mass of solids to be stored in the settling tank (Andrews *et al.*, 1976; Thompson *et al.*, 1989; Sorour *et al.*, 1994).

According to Ekama *et al.* (1997), the clarification function of the settling tank is equally important as thickening. Literature contains numerous studies about thickening and its control (e.g. Keinath *et al.*, 1977; Dixon, 1985; Wahlberg, 1997), whereas clarification failure control is rarely mentioned (e.g. Keinath & Laquidara, 1982). Flocculants have not been considered here, but can be used for control as well (see Section 1.2.2). Obviously,

clarification is closely related to thickening; without thickening the solids would washout and appear in the effluent. However, to achieve a proper clarification very good solids separation should prevail; for instance, to obtain an effluent solids concentration of less than 10 mg/l at a reactor concentration of 3.5 g/l more than 99.7% of the solids entering the settling tank needs to be separated, stored and recycled to the biological reactor. Failure to achieve the required solids removal as a result of poor clarification can result in non-compliance with regulatory effluent quality standards, although the settling tank works perfectly as a thickener and the biological reactor shows the desired removal efficiency for organic matter. The causes of clarification failure can be manifold. To quickly isolate and resolve the problem, Parker *et al.* (1999) proposed the Structured Diagnostic Approach (SDA). This technique includes the DSS/FSS test (Wahlberg *et al.*, 1995; Kinnear, 2000), which allows a differentiation between flocculation and/or hydraulic causes for the failure. The DSS/FSS test consists of three parts, i.e. (i) the Effluent Suspended Solids (ESS) test, (ii) the Dispersed Suspended Solids (DSS) test, and (iii) the Flocculated Suspended Solids (FSS) test. The DSS are defined as the SS remaining in the supernatant after 30 minutes of settling; the measuring technique was originally developed by Parker *et al.* (1970). On the other hand, the FSS are the suspended solids that remain in the supernatant after 30 minutes of settling preceded by 30 minutes of flocculation. Whereas the DSS test quantifies the state of flocculation at the moment and location of sampling, the FSS test attempts to simulate the optimum degree to which the sample can be flocculated. Together with the Effluent Suspended Solids (ESS) one can investigate the clarification failure and locate the problem. Table 1.1 gives the possible combinations between DSS and FSS at high ESS, and the conclusions that can be drawn.

Table 1.1 Analysis of clarification failure (at high ESS) by DSS/FSS testing (Wahlberg *et al.*, 1995)

DSS	FSS	cause
high	high	biological flocculation
high	low	physical flocculation
low	high	impossible
low	low	hydraulics

The DSS and/or FSS testing have proven useful in a number of applications including the following: (i) determining the effect of aeration tank turbulence level on the effluent non-settleable solids (Parker *et al.*, 1970; Das *et al.*, 1993), (ii) assessing flocculation and floc breakup phenomena in conveyance channels (Parker *et al.*, 1970; Parker & Stenquist, 1986; Das *et al.*, 1993), (iii) determining the benefits of flocculation in minimising ESS in activated sludge plants (Wahlberg *et al.*, 1994), and (iv) assessing alternative flocculator centre well designs (Kinnear *et al.*, 1998).

From the previous, it is obvious that the storage and thickening of sludge in the settling tank cannot be considered independent of the biological reactor; both units form a dynamic system. Hence, many factors influence the settling tank capacity and solids removal efficiency. They can be generally classified as hydraulic, physical and biological factors.

1.2 Factors influencing the capacity and performance of secondary settling tanks

The previous sections described the settling tank complexities. Not only is its (thickening) capacity and (removal efficiency or) performance related to the biological reactor, also many internal processes play a role that are of biological, physical and chemical origin. However, a clear distinction is difficult to make.

1.2.1 Biological influences

Microorganisms resident in the activated sludge process interact with each other and their environment. In this respect, single bacteria simply follow the flow and are washed out of the system before they can multiply. Instead, flocs increase their residence time in the system by sedimentation in the settling tank.

It has been suggested that at low substrate concentrations the filamentous bacteria grow faster than floc forming bacteria due to their higher surface-to-volume ratio, while the floc forming bacteria have higher growth rates at high substrate concentrations. Hence, the filamentous bacteria clearly have a competitive advantage at low substrate concentrations. This principle is known as the kinetic selection theory (Chudoba *et al.*, 1973). As a result, at low substrate concentrations, floc-forming bacteria are washed out of the biological unit; their residence time in the system is lower than the inverse of the specific growth rate. This can have detrimental effects on the effluent quality due to non-settling solids in the settling tank; a good balance between filamentous and floc-forming bacteria is essential for strong and well-settling flocs (Sezgin *et al.*, 1978).

Bioflocculation was found to increase the rate of substrate transport to the cells in permeable flocs compared to dispersed cells (Logan & Hunt, 1988). In this way, the microorganisms are able to survive in the substrate-diluted biological reactor. Unfortunately, not all flocs grow in such a way that good settling properties are obtained. Tomlinson (1976) found that 52% of the treatment plants in the UK showed a serious loss of solids in the final effluent.

Some six different classes of solids sedimentation problems can be identified (Wanner, 1994; EPA, 1987). They are summarised in Table 1.2.

Table 1.2 Classification of solids separation problems (Wanner, 1994; EPA, 1987)

Type	Description
dispersed growth	no floc formation
pinpoint floc	besides good settling flocs, a lot of small un-settleable flocs are present
filamentous bulking	abundance of filamentous bacteria
rising sludge	denitrification in the secondary settling tank releases nitrogen gas that causes sludge to rise
viscous bulking	overproduction of exocellular slime
foam and scum	accumulation of biomass at the surface caused by non-degradable detergents or by specific filamentous bacteria

How and why these floc types arise is not completely known; different cause-effect relations exist though. Sludge with good settling characteristics originates from a properly working biological reactor in terms of carbon, nitrogen and phosphorous removal. In this respect, it is known that toxics result in deflocculation (Galil *et al.*, 1998; Bott *et al.*, 2000). To prevent oxidations of crucial proteins and DNA by toxics, the microorganisms have an intracellular pool of easily oxidisable molecules. These redox-controlling molecules act in a sacrificial manner by scavenging the harmful electrophilic toxics to avoid macromolecular oxidation. However, this defence system results in an efflux of potassium leading to deflocculation (Bott *et al.*, 2000). The resulting smaller flocs settle slower and are more prone to hydraulic currents, increasing the probability of solids washout in the settling tank. In an extensive study in 1993, Li & Ganczarzyk assessed the influence of treatment plant operating conditions on the particle size distribution and dispersion of the activated sludge particles (Barbusinski & Koscielniak, 1995). They concluded that the organic loading rate, i.e. the amount of BOD₅ or COD available per unit of solids mass and time, and the availability of the dissolved oxygen per unit of organic loading rate were the two most significant factors influencing the size distribution of the sludge flocs.

Concerning the organic loading rate, Barbusinski & Koscielniak (1995) observed sizes that increased with the loading rate. On the other hand, Echeverría *et al.* (1992) indicated that as long as the organic loading rate stays within the range 0.25-0.6 g BOD₅/g SS.day the sludge is characterised by low SVIs. A pulse-wise addition of substrate may lead to well-settling solids as well (Beun *et al.*, 1999).

Echeverría *et al.* (1992) also observed that low oxygen concentrations have a detrimental effect on the SVI, i.e. bulking occurred. This is caused by an excessive growth of filamentous bacteria and the formation of porous flocs (Wilén & Balmér, 1999). In this respect, Starkey & Karr (1984) observed that nine months of dissolved oxygen concentrations below 1 mg/l in the aeration tanks resulted in increased effluent turbidities. However, an increase in oxygen concentration to 3 mg/l restored the effluent quality in a couple of days. According to Wilén & Balmér (1999), shutting down the aeration for a period between one and four hours did not affect the settling properties of the sludge; the turbidity significantly increased during the anaerobic period and decreased during the aerobic period. Shorter alternating conditions, however, progressively damaged the flocs and the deflocculated state persisted (Wilén *et al.*, 2000).

Wilén *et al.* (2000) summarised several deflocculation mechanisms. The mechanisms are understood to some extent, but their relative significance is not well known. Extracellular Polymeric Substances (EPS) help to sustain the floc structure (e.g. Goodwin & Forster, 1985). However, under anaerobic conditions the EPS is hydrolysed and the flocs fall apart (Wilén *et al.*, 2000). Starkey & Karr (1984) further related deflocculation to an inhibition of EPS production and the eucaryote population (protozoa and rotifers). Also the amount of polysaccharides correlates well to flocculation (Wahlberg *et al.*, 1992). It is generally affected by organic macromolecules as well (Narkis & Rebhun, 1997). In this respect, DNA released by cell lysis has been observed to enhance flocculation (Vallom & McLoughlin, 1984).

So far, only changes in floc structure have been discussed. The settleability, however, can also alter by means of variation in cell density. In this respect, Schuler *et al.* (2001) observed a significant increase in floc density when cells stored polyphosphates. Hence, it is clear that

the operation of the activated sludge system again has an influence; increased cell density may improve the settling tank's capacity.

Finally, nitrogen gas can be produced by denitrification when the mixed liquor entering the settling tank still contains nitrate-nitrogen concentrations greater than $6-8 \text{ g NO}_3^- \text{-N/m}^3$ (Henze *et al.*, 1993; Kim *et al.*, 1994; Siegrist & Gujer, 1994; Siegrist *et al.*, 1995). These nitrogen gas bubbles attach to the flocs, increasing their buoyancy. As a result, the rising sludge forms a scum layer and deteriorates effluent quality (Figure 1.2). When rising sludge is avoided, however, a considerable amount of nitrogen can be removed in the clarifier. Full-scale experiments performed by Koch *et al.* (1999) showed that denitrification in the investigated settling tank accounted for 37% of the total nitrogen removal by denitrification. This corresponded to 19% of the total inlet nitrogen. Although the largest portion of denitrification occurred in the inlet channel to the tank, it definitely opens perspectives to improve the plant's performance by optimising the biological processes in the secondary settling tank.



Figure 1.2 Example of rising sludge (left) as compared to normal settleable sludge (right)

1.2.2 Physical and chemical influences

It is clear that biological processes have a significant influence on the settleability of solids. Physical and chemical influences also occur. These factors are all related to floc aggregation and floc breakup, i.e. flocculation and deflocculation.

Flocculation consists of two discrete steps, i.e. transport and attachment of particles. Before particles can collide they first have to be transported in order to approach each other; this is achieved by local variations in fluid/particle velocities. Depending on the transport mechanism three types of flocculation exist:

- *Perikinetic flocculation*, i.e. aggregation by the random thermal Brownian motion of particles
- *Orthokinetic flocculation*, i.e. aggregation by imposed velocity gradients due to mixing
- *Differential sedimentation*, i.e. aggregation by differences in settling velocities

Following transport, collision and attachment must occur as well. In this respect, the rate of successful collisions depends on the collision efficiency, defining the percentage of collisions leading to attachment. Many effects influence this efficiency, such as electrostatic forces, structural effects (e.g. fractal properties) and hydrodynamic interactions (e.g. Kusters, 1991;

Spicer, 1997). The last-mentioned influence on the collision efficiency, i.e. the hydrodynamic interactions, determines how particles approach each other. As particles collide, fluid must flow out of the space between them. This motion of fluid causes the particles to rotate relative to one another, such that they deviate from a linear path. This curvilinear approach, as opposed to the traditional rectilinear approach, lowers the collision efficiency. It greatly depends on the floc structure such as porosity and permeability. In this respect, the fractal properties of flocs become important and indicate that their large-scale structure recurs at progressively smaller scales. Logan & Wilkinson (1991), Logan & Kilps (1995), Veerapaneni & Wiesner (1996), Guan *et al.* (1998), Thill *et al.* (1998) and Lee *et al.* (2000) provide additional detail.

With the rectilinear approach, Han & Lawler (1992) found that differential sedimentation was the dominant mechanism for flocculation only when one particle is significantly larger than the other. Perikinetic flocculation only occurred when both particles are very small. Orthokinetic flocculation, on the other hand, was the most dominant mechanism. However, when considering the curvilinear approach, orthokinetic flocculation was far less important.

In the original work of Smoluchowski (1917) mixing, i.e. shear, was recognised as an important factor for both flocculation and deflocculation. Three decades later, Camp & Stein (1943) extended the theory of Smoluchowski with an expression for the local shear rate or velocity gradient. They introduced the fluid's volume-averaged root-mean-square velocity gradient \mathcal{G} as

$$\mathcal{G} = \left(\frac{\varepsilon}{\nu} \right)^{\frac{1}{2}} \quad (1.1)$$

Here, the velocity gradient is defined as function of the local rate of energy dissipation ε and the kinematic fluid viscosity ν . The authors moved from the local scale to the global scale by using the volume-averaged energy dissipation. Although the parameter is widely used in sanitary engineering (Parker *et al.*, 1970, 1972; Das *et al.*, 1993; Wahlberg *et al.*, 1994; Spicer & Pratsinis, 1996; Spicer *et al.*, 1998; Biggs, 2000), many criticisms on its use are found in literature (e.g. Cleasby, 1984; Clark, 1985; DuCoste & Clark, 1998). Equation 1.1 only seems to be valid for particles smaller than the smallest turbulent length scales, i.e. the so-called *Kolmogorov microscale*. At the latter scale, viscous forces predominantly dissipate turbulent energy.

Not only the shear rate in the settling tank should be considered; also the shearing from the aeration system may affect the particle size distribution in the settling tank and, as a result, its performance. This is demonstrated in Figure 1.3. For five different treatment plants with fine bubble aeration it was observed that an increase in turbulence intensity resulted in more floc breakup and an increase in ESS (Parker *et al.*, 1992).

If the settling tank does not perform well in terms of clarification and thickening, one still has the option of dosing additives to improve the settling characteristics on the short-term. If the additions are of mineral origin, these weighteners increase the net particle density by their own weight (Rasmussen *et al.*, 1996; Bidault *et al.*, 1997; Dymaczewski *et al.*, 1997; Clauss *et al.*, 1998; Piirtola *et al.*, 1999; Vanderhasselt *et al.*, 1999b). For that reason it is

called ballasted settling. Other additions, like organic polymers, simply result in larger flocs by enhancing flocculation. Hence, these flocculants also increase the settling velocity (Vanderhasselt *et al.*, 1999a).

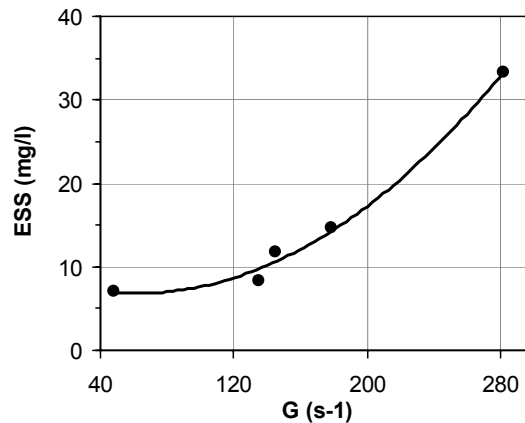


Figure 1.3 The effect of G on effluent suspended solids for fine bubble aerated plants (redrawn from Parker *et al.*, 1992)

1.2.3 Hydraulic influences

It is clear from Section 1.2.2 that the flow field in the settling tank determines the orthokinetic aggregation and breakup of flocs. Obviously, it will affect the settling and resuspension of solids in the tank as well (Takamatsu *et al.*, 1974). In this respect, Baud & Hager (2000) observed tornado vortices in the corners of rectangular settling tanks. They were capable of scouring the top of the solids blanket and significantly reduce the solids removal efficiency. The hydraulics of secondary settling tanks therefore have a large influence on the efficiency of the WWTP.

The first theory about the efficiency of settling tanks was developed by Hazen (1904) for individual particle settling in a uniform flow. Anderson (1945) discovered that the flow is far from uniform because of density stratification. The solids-loaded influent has a higher density than the ambient water and, hence, plunges as a density jet to the bottom of the tank; this is the so-called *density current* (Figure 1.4). As a result, a secondary counter-current is induced at the surface; even a three- or four-layered structure in the flow field can be experimentally observed (Larsen, 1977; Bretscher *et al.*, 1992; van Marle & Kranenburg, 1994). The density current is characterised by high velocities and appears in the vicinity of the solids blanket (Kinnear & Deines, 2001). Therefore, settled solids may resuspend with increasing flow rates and can be transported to the effluent weirs; consequently, the effluent quality deteriorates. However, van Marle & Kranenburg (1994) indicated that density currents also might be favourable for secondary clarification. The layered flow pattern in the settling tank may result in high solids removal efficiencies, since it tends to reduce short circuiting. If short circuiting is prevented, the hydraulic detention time in the layered flow (with alternating flow directions) will equal that of uniform flow. The latter is beneficial for the settling tank performance (Hazen, 1904). Krebs *et al.* (1999) came to similar conclusions; however, when strong density effects prevail, as is usually the case in

secondary settling tanks, increased tank depths are recommended. In addition, experiments of Konicek & Burdych (1988) show flocculation in the density current, being beneficial for the solids removal efficiency.

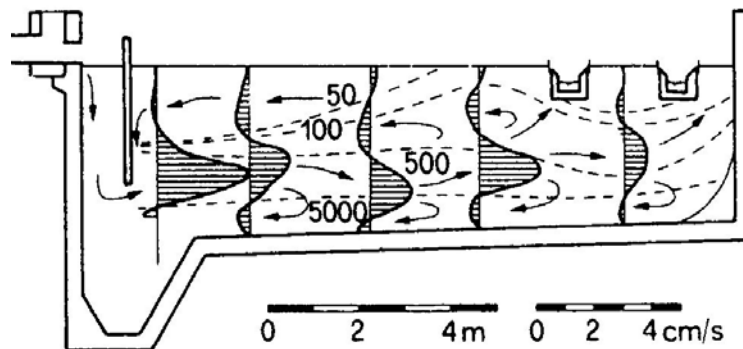


Figure 1.4 Example of flow pattern in a secondary settling tank (---: equal solids concentration in mg/l) (Bretscher *et al.*, 1992)

Density currents as described above originate from the solids present in the flow. However, the density difference between the incoming and ambient mixture may also result from differences in temperature (e.g. McCorquodale & Zhou, 1993). Ekama *et al.* (1997) compared various energy inputs and showed that surface cooling and wind can be dominant factors affecting the overall hydrodynamics in secondary settling tanks. According to full-scale observations of Wells & LaLiberte (1998), differences of only 1°C between surface and bottom temperature seemed enough to induce a density current. McCorquodale in 1987 (Zhou *et al.*, 1992) and Taebi-Harandy & Schroeder (2000) even mentioned temperature differences of only 0.2°C. Wells & LaLiberte (1998) suggested that vertical mixing induced by surface cooling was able to keep the particles in suspension by the resulting convective currents.

To reduce the deteriorating effect of the density current on the effluent quality, influences of both the size of aperture and the vertical location of the inlet structure have been investigated (Fischerström *et al.*, 1967; Larsen, 1977; Krebs, 1991b; Krebs *et al.*, 1995). Also the depth (Bretscher *et al.*, 1992) and radius of inlet baffles (Zhou & McCorquodale, 1992c) deserved attention in literature. All these structural modifications focus on minimising the total inlet energy flux, including a potential energy component due to buoyancy and a kinetic component (Krebs *et al.*, 1995). This minimum energy flux occurs when both the potential and kinetic energy are equal. Hence, it is clear that energy dissipation is of paramount importance. As a result, angle bars near the inlet (Krebs *et al.*, 1995) or the installation of porous walls (Krebs *et al.*, 1992; Baumer *et al.*, 1996) in the settling tank are found to prevent strong density currents.

1.3 Other solids separation techniques

In Section 1.1 it was shown that the conventional activated sludge system is restricted to fairly low biomass concentrations in the biological reactor because of the gravitational separation limitation in the settling tank. As a consequence, the required reactor volumes are large and the biological conversion rates are low.

Sedimentation is the most widely used solids separation technique in wastewater treatment, although attention is growing for alternatives. Wastewater sometimes contains low-density particles that slowly settle or even float. Hence, problems arise when the effluent quality legislation becomes more stringent. The removal of coliform bacteria and viruses will become more important as well. The increasing land costs form another incentive to look for new technologies that occupy less space (Davies *et al.*, 1998). Two technologies becoming a future threat for the existence of settling tanks are dissolved air flotation and membrane filtration. Both are discussed shortly.

Dissolved Air Flotation (DAF) is a clarification process in which flocs are floated by sparging air in the suspension; the buoyancy of the bioflocs increases due to attached air bubbles (Edzwald, 1995; Kiuru, 2001). At the free surface the biomass is skimmed. There exist many advantages of DAF over gravity settling. The most important ones are listed below (Matsui *et al.*, 1998; Schofield, 2001):

- better removal of low-density flocs such as algae and flocs produced during coagulation
- high hydraulic loadings, which result in smaller tanks compared to sedimentation
- positive control of separation process
- relatively robust to hydraulic and quality variations in raw water
- clarified water has a consistently high chemical and bacteriological quality

The main drawbacks, however, are the electrical power requirements, and the necessary separate flocculator and DAF cell.

The second concurrent technology that may become important in the future is the membrane filtration technique. Early interest in membrane use arose because of the high land costs in Japan (Davies *et al.*, 1998). The membrane modules can be directly integrated in the biological reactor, and they thus replace the secondary settling tanks (Engelhardt *et al.*, 1998; Günder & Krauth, 1998). In addition, the membrane module is also able to combine further tertiary treatment that is normally achieved by additional process units such as sand filtration or disinfection. In this respect, Herath *et al.* (1998) showed that membranes may be even capable at removing viruses.

With biomass concentrations that can be 3-5x higher than conventional activated sludge processes, the reactor volumes can be significantly reduced (Günder & Krauth, 1998).

Similar to the DAF technology this technique demands a large power input. However, Davies *et al.* (1998) indicated that the technology is certainly competitive with the smaller activated sludge units. It is expected that the cost of membranes will reduce in the near future. The cost of power will therefore determine its economical feasibility for larger process units.

1.4 Design of settling tanks

From Section 1.1 it was understood that settling tanks have three functions. Whether they are fulfilled or not, depends on both the operation and the design of the tank. In Europe, it seems that designs strive to good thickening capacities, whereas the US designs focus more on effluent quality, i.e. high clarification efficiency (Krebs, 1999). Previous sections already dealt with the settling characteristics of the activated sludge, hence, they will not be repeated here. Nevertheless, they are very important in the design of settling tanks. The determination of settling velocities is, unfortunately, not common practice. On the other hand, the SVI is traditionally determined due to its ease of measurement. Consequently, many researchers have looked for relationships between the settling velocity and the SVI (Daigger & Roper, 1985; Ekama & Marais, 1986; Yuen, 2002) that can be subsequently used for design.

Designing settling tanks involves many factors. Tchobanoglous & Burton (1991) summarised them as follows:

- settling characteristics as related to the thickening requirements for proper plant operation
- surface and solids loading rates
- tank types
- solids removal mechanisms
- inlet design
- weir placement and loading rates
- sidewater depth
- flow distribution between different process units
- scum removal

Whereas the first factor has already been discussed, only the next five factors will be dealt with below. They are considered as being the most important ones, although *all* factors should be focused upon when designing a settling tank. However, a complete discussion is beyond the scope of this introductory chapter. Therefore, for the other issues, the reader is referred to Tchobanoglous & Burton (1991) and Ekama *et al.* (1997).

1.4.1 Surface and solids loading rates

For the design of settling tanks it is essential to have information about the hydraulic and solids loads. To define these process variables, let us consider the schematic representation of a settling tank in Figure 1.5. All flow rates are denoted by Q , whereas solids concentrations are expressed as X ; the (free) surface area is denoted by A .

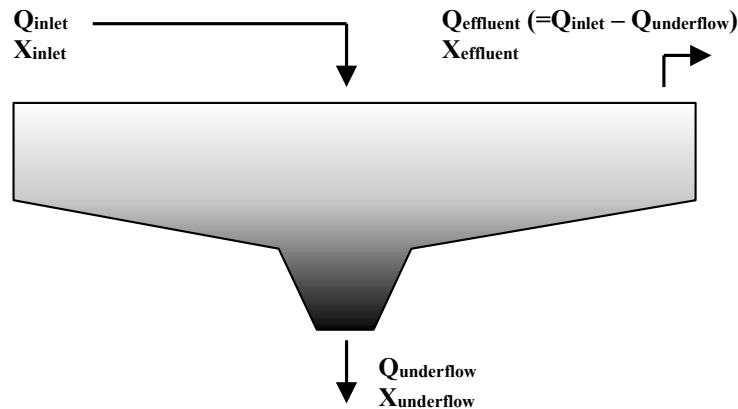


Figure 1.5 Hydraulic and mass flows over the settling tank

From the figure it is clear that the feed or inlet flow is divided into (i) the underflow, which creates a downward water velocity ($v_{dw} = Q_{underflow}/A$) at the bottom of the tank, and (ii) the effluent flow, which creates an upward velocity ($v_{up} = Q_{effluent}/A$) at the top of the tank. This upward water velocity is called the *Surface Overflow Rate* (SOR). In order to achieve satisfactory removal efficiencies, the SOR must be appreciably lower than the local settling velocity of the flocs. The SOR was recognised as early as 1904 (Hazen, 1904) as a decisive design value for the removal of solids particles that do not undergo any change in size, shape, and density while settling. Camp (1946) showed that the settling velocity of solids could be related to the SOR only under laminar flow conditions. In this respect, Camp (1952) discussed different non-ideal situations that occur in reality, and affect the idealised solids removal as predicted by Hazen.

Because of the large amount of solids that may be lost in the effluent if design criteria are exceeded, the SOR should always be based on peak flow conditions, i.e. wet weather flows and peak wet weather flows. During the past two decades, SOR was assumed to be the most important parameter affecting the ESS (Ekama *et al.*, 1997). This was based on the reasoning that more particles become part of the ESS when the SOR increases. In contrast to this, full-scale operational data have been reported that show no relationship between ESS and SOR (Figure 1.6, top). On the other hand, Parker *et al.* (2001) observed a gradual increase of ESS with SOR; however, the design return activated sludge capacity was a constraining factor in this study. Because it was set for a lower design SOR, the solids blanket rose with increasing SOR. It was believed that if the constraint had been removed, the ESS versus SOR relationship would have been horizontal as in Figure 1.6 (top). Hence, as long as the settling tank is well-designed and good sludge settling properties occur, the SOR will not influence effluent quality.

Equally important for the design of secondary settling tanks is the Solids Loading Rate (SLR) to define the capacity of the tank. This operational parameter is simply calculated as the total solids flux applied divided by the surface area of the tank. Although each tank is characterised by a limiting SLR because of its design, its capacity is also determined by the biology of the sludge and its thickening qualities. In contrast to SOR, SLR seems to be related to the ESS (Figure 1.6, bottom). In this case, an overall increase of ESS with SLR can be observed. However, the ESS does not show any dependency on the SLR for most individual settling tanks. According to Parker *et al.* (2001), this is due to internal tank hydraulics.

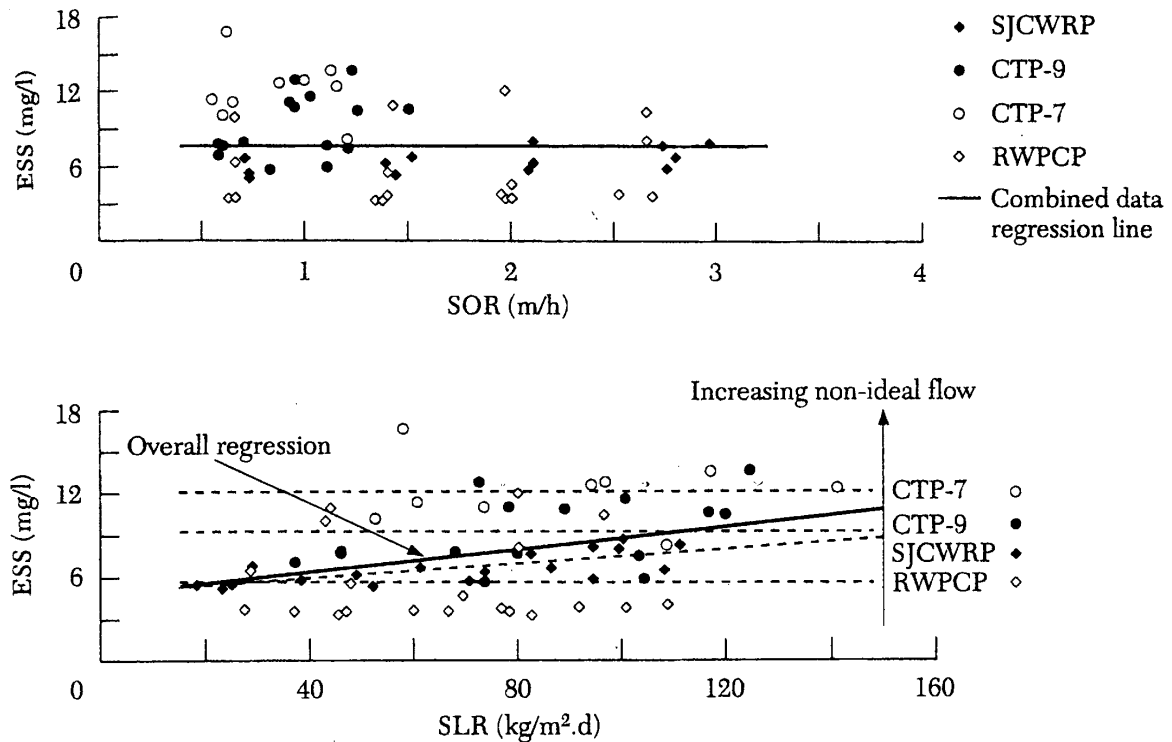


Figure 1.6 Effluent suspended solids concentration plotted against surface overflow rate (top) and solids loading rate (bottom) for two circular (CTP-7 and CTP-9) and two rectangular (SJCWRP and RWPCP) secondary settling tanks (Wahlberg *et al.*, 1994)

1.4.2 Types of settling tanks

Three types of secondary settling tanks can be found in practice, i.e. circular, rectangular and vertical flow configurations. Although square tanks are used on occasion, they are not as efficient in solids removal as circular and rectangular tanks. Solids accumulate in the corners of the square tanks and are swept over the weirs by the movement of the solids collector mechanism (Tchobanoglous & Burton, 1991).

When circular (Figure 1.7) and rectangular (Figure 1.8) settling tanks are properly designed, they show the same removal efficiency and capacity (Parker *et al.*, 2001). The design of circular tanks is however preferable for a number of constructional and operational costs. Firstly, the investment costs for large-volume circular tanks are lower than for rectangular tanks. It is only when large combined units of rectangular settling tanks are being built that construction costs are more or less the same (Kalbskopf, 1970; Parker *et al.*, 2001). Circular tanks also offer the advantage of allowing solids removal at the bottom by scraper blades, which is cheaper and safer to operate and with a longer life than chain conveyers (Kalbskopf, 1970).

If the horizontal dimension of the settling tank is relatively small compared to the water depth (ratio of horizontal to vertical distance less than 2), the flow can be assumed to be predominantly vertical (Ekama *et al.*, 1997). Therefore, this type of tank is called the *vertical flow settling tank* (Figure 1.9). With such tank geometry and positioning the inlet structure in the solids blanket results in a fluidisation of the sludge. The solids blanket then acts like a floc filter that even removes very fine particles (Fuchs & Staudinger, 1999).

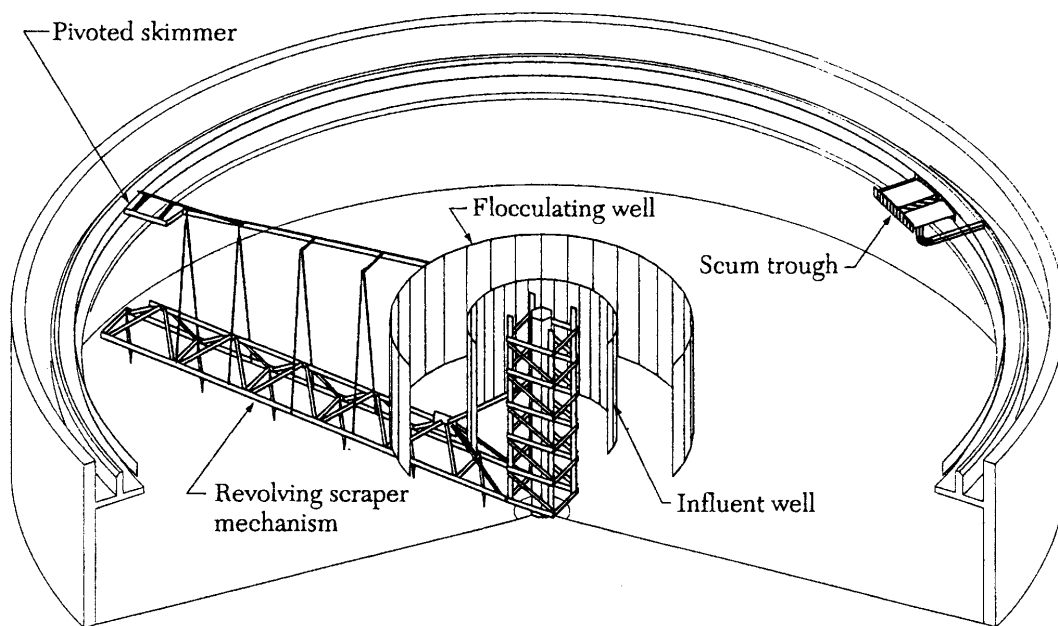


Figure 1.7 Circular settling tank with scraper mechanism and flocculator (Ekama *et al.*, 1997)

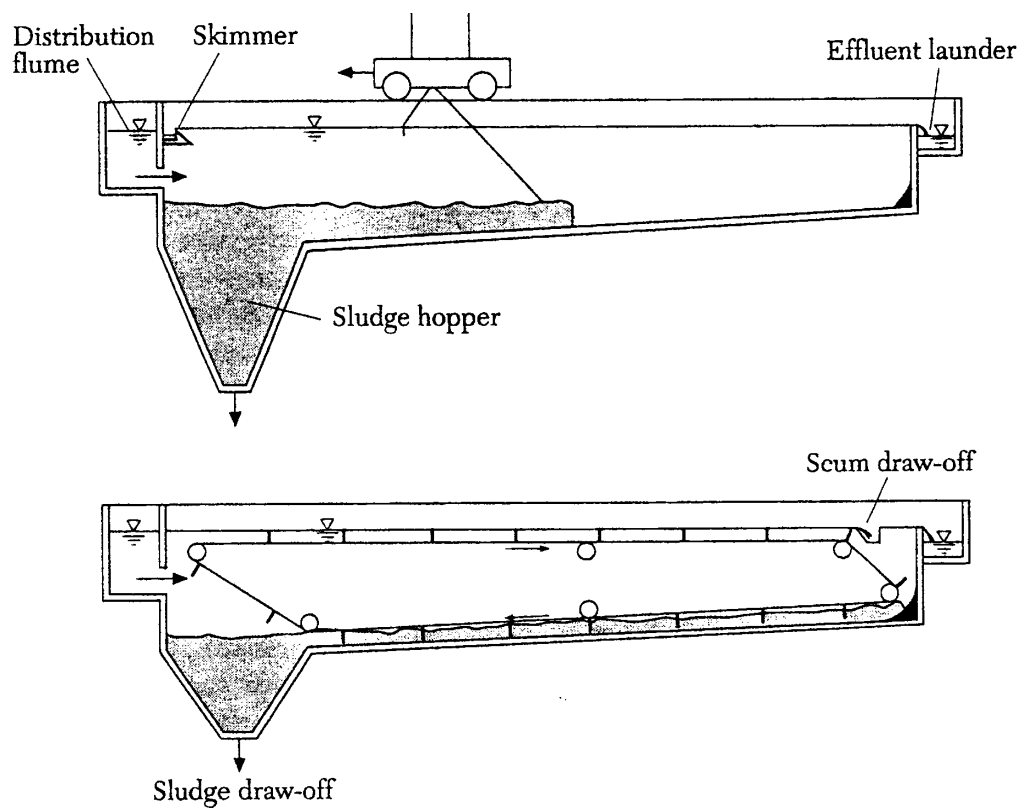


Figure 1.8 Rectangular settling tank with different solids removal mechanisms: travelling-bridge (top) and chain-and-flight (bottom) type collectors (Ekama *et al.*, 1997)

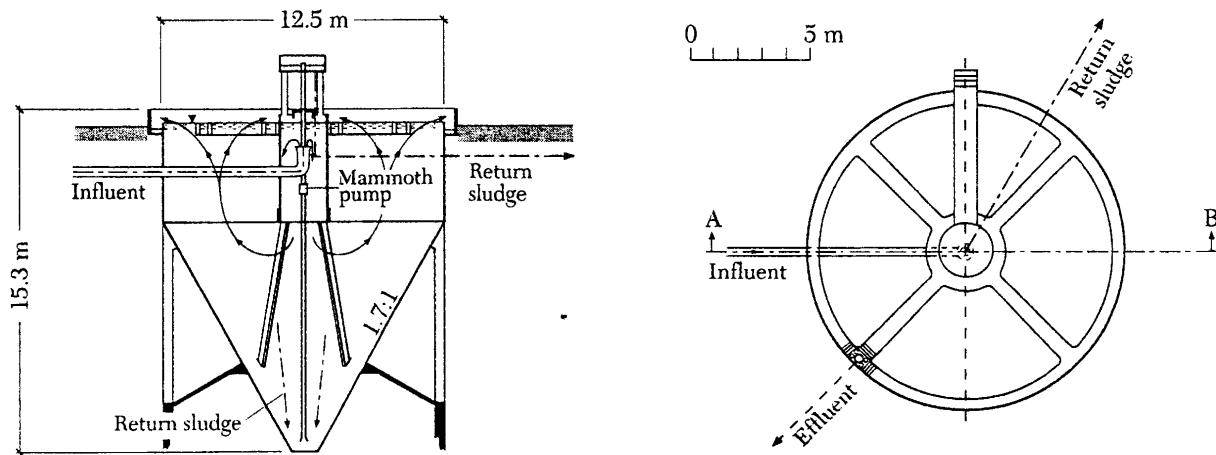


Figure 1.9 Vertical flow settling tank (Dortmund type): side view (left), and plan view (right) (Ekama *et al.*, 1997)

The performance of conventional settling tanks may be improved by the installation of tubes or parallel plates to establish laminar flow. As a result, these tanks have a very small settling distance; the solids settled in the tubes or on the plates slide out due to gravitation. The major drawback of these systems is the tendency to clog because of biofouling.

If limited land area is available, tray or multiple-storey settling tanks may be an option (Tchobanoglous & Burton, 1991; Yuki, 1991; Stamou *et al.*, 2000). With this type of settling tanks, two tanks are built on top of each other to save space. Although they can be operated in parallel, Camp (1952) even suggested to use them in series.

The last type of settling tanks to be mentioned is of the intrachannel type. These have typically been designed to improve the performance of the oxidation ditch activated sludge process. The devices permit liquid and solids separation and sludge return to occur within the aeration channel. The mixed liquor to be separated flows into the settling tank at the stern, with minimal velocity and energy to promote an even distribution of flow across the width of the settling tank. Traditionally, the effluent is collected at the end of the tank by weirs. Sludge hoppers are located along the bottom length and width of the settling tank; each hopper contains a removal pipe extending into the aeration channel. A head differential caused by the higher channel flow velocity beneath the settling tank creates a flow through the removal pipes; hence, the sludge is in the settling tank only for a short time, and solids thickening hardly occurs. This system of solids removal performs as well as conventional settling tanks. The major advantages are the reduction in land area requirements, reduced operating requirements, elimination of sludge recycle systems, and reduced capital costs.

1.4.3 Solids removal mechanisms

The solids removal mechanism is directly related to the type of settling tank. According to Günthert (1984), this device has two functions: (i) collection of settled and thickened sludge, and (ii) solids transportation from the point of settling to the hopper from where the thickened sludge is returned to the biological process unit. Additionally, short solids retention times, small disturbance in solids settling, and a quick conveyance at a maximum

solids concentration are desired. The type of removal mechanism depends more or less on the type of settling tank.

Two different sludge collector systems are commonly used in rectangular settling tanks: (i) traveling-bridge and (ii) chain-and-flight type collectors (Figure 1.8). For the travelling bridge type the mechanism with mounted scrapers travels up and down the tank on wheels or on rails supported on the sidewalls. The chain-and-flight consists of a pair of looped conveyor chains, at which solids removal blades from wood or fibreglass are mounted. Hence, the solids are scraped from the bottom and transported to the hopper.

The circular settling tank can be equipped with two kinds of mechanisms: (i) those that scrape or plough the solids to the centre hopper, and (ii) those that remove the solids directly from the bottom by means of suction. With the suction mechanism it can be expected that solids blanket levels are lower as compared to scrapers (Parker *et al.*, 2001). These rapid solids removal mechanisms are especially popular in the USA. The design engineer of the 1960s accepted both low concentrated sludge and high recycle rates returning fresh sludge to improve the activated sludge efficiency (Albertson, 1991; Albertson & Okey, 1992). Further, to avoid deterioration of the effluent quality, US designs only allow a blanket at peak loads. This is the opposite of European practice (Parker *et al.*, 2001). Whereas the suction devices are more common in the USA, the scraper is extensively used in European settling tanks (Albertson & Okey, 1992).

How the scraper works, is still under debate. Two theories are commonly accepted. Firstly, the scraper is considered from a mechanical perspective, i.e. it pushes the solids to the hopper (Warden, 1981; Günthert, 1984; Billmeier, 1988; Albertson, 1991; Albertson & Okey, 1992; Albertson, 1994; Narayanan *et al.*, 2000). Secondly, the scrapers are not truly conveying the solids, but are merely resuspending it (Murk, 1969; Boyle, 1980; Kinnear & Deines, 2001). During a specialised European COST meeting on secondary settling tanks (COST Action 624, 14-15 November 2002, Prague), the mechanism of the scraper action was recognised as one of the issues still to be solved.

1.4.4 Inlet structure

As mentioned in Section 1.2.3, density currents prevail in both rectangular and circular settling tanks. In the inlet region, ambient water is entrained, which enforces the current. To reduce the detrimental effect of these currents the inlet region of the tank is of crucial importance (Ekama *et al.*, 1997).

Section 1.2.3 also highlighted the fact that the existence of the density current is strongly related to the ratio of the potential and the kinetic energy. In common inlet structures the potential energy is usually higher than the kinetic energy; this is due to the higher bulk density of the incoming suspension. To decrease this potential energy, the inlet should be positioned close to the bottom. As a result, resuspension of solids may occur however (Parker *et al.*, 1996). The size of the aperture, on the other hand, needs to be optimised with respect to both potential and kinetic energy. Indeed, a smaller aperture decreases the potential energy but the kinetic energy will increase progressively (Krebs *et al.*, 1995).

As soon as the sludge is released in the settling tank, it spreads over the cross-section of the tank. To what extent this occurs, depends on the magnitude of the density current. The energy dissipation is a crucial element in this flow spreading as it is related to the decay of

the density current (Krebs *et al.*, 1995). Again, the design of the inlet structure largely influences this energy dissipation. Energy dissipation is therefore induced by baffling the inlet and introducing the liquid tangentially (Ekama *et al.*, 1997). Describing all different types of energy dissipators is beyond the scope of this dissertation, but for more information the reader is referred to Larsen (1977), Krebs (1991a, b), Krebs *et al.* (1995) and Tekippe (2002).

The energy-dissipating inlet structure is also necessary to use the complete volume of the flocculator well since, otherwise, solids stratification would occur (Parker *et al.*, 2001). According to Parker *et al.* (1996), floc breakup is typical for aeration basins and mixed liquor transfer systems, but a subsequent flocculation step would always reduce the supernatant suspended solids (Das *et al.*, 1993). According to Parker & Stenquist (1986), average ESS concentrations of 10 mg/l can be obtained in well-designed activated sludge systems. To this end, a flocculator well is constructed in the inlet region of the settling tank. Flocculator wells were initially equipped with mixers to induce G levels of 30 to 70 s^{-1} ; these levels were found by Parker *et al.* (1970) to be optimal in lab-scale flocculation tests. However, it was observed that without mixers, and at a G less than 5 s^{-1} , the same effluent quality could be obtained (Parker & Stenquist, 1986). From modelling exercises, Zhou & McCorquodale (1992c) concluded that a too large flocculator well resulted in a recirculation of fluid from the main settling tank into the well which, thereby, strengthened the density current. A too small well on the other hand would lead to increased density currents too (Merrill *et al.*, 1992). An optimal diameter was found to be 20-35% of the tank diameter (Merrill *et al.*, 1992; Vitasovic *et al.*, 1997; Kinnear *et al.*, 1998).

1.4.5 Weir placement and loading rates

At the outlet of the settling tank the clear water flows over weirs. In the past, the weirs were usually located at the end wall. These single launders, however, were not well positioned with respect to the detrimental effect of density currents. After traversing the main tank's volume the current encounters the end wall where it is redirected upwards towards the launder (Kawamura & Lang, 1986). Consequently, suspended solids from the inlet or eroded from the solids blanket arrive in the effluent. Already in 1945, Anderson observed this and came up with a solution. By placing the launders inboard from the wall, the density current would reach the free surface without affecting the effluent quality. The inboard launders also allowed the use of double-sided weirs; therefore, lower weir loading rates (typically expressed as flow rate per unit length of weir) are possible. The weir configuration usually has to satisfy criteria for maximum weir loading. According to Ekama *et al.* (1997), designers are nowadays more concerned about the impact of the weir configuration and placement on the settling tank performance; they found that, except for extreme conditions, the weir loading rate itself has little effect on the effluent quality (see also Kawamura & Lang, 1986). Whereas the inboard launders are located at 60-80% of the tank radius, inset double-sided weirs are only 1-2 m from the wall (Figure 1.10, left). However, these designs are less optimal because the outer weir produces less clear effluent than the inner one. This is due to higher velocities between the wall and outer weir (Ekama *et al.*, 1997).

Alternatively, when single weirs at the end wall are considered, baffles can be used to redirect the density current into the tank and away from the effluent weirs (Stukenberg *et al.*, 1983; Ekama *et al.*, 1997). An example of such baffle is shown in Figure 1.10 (right).

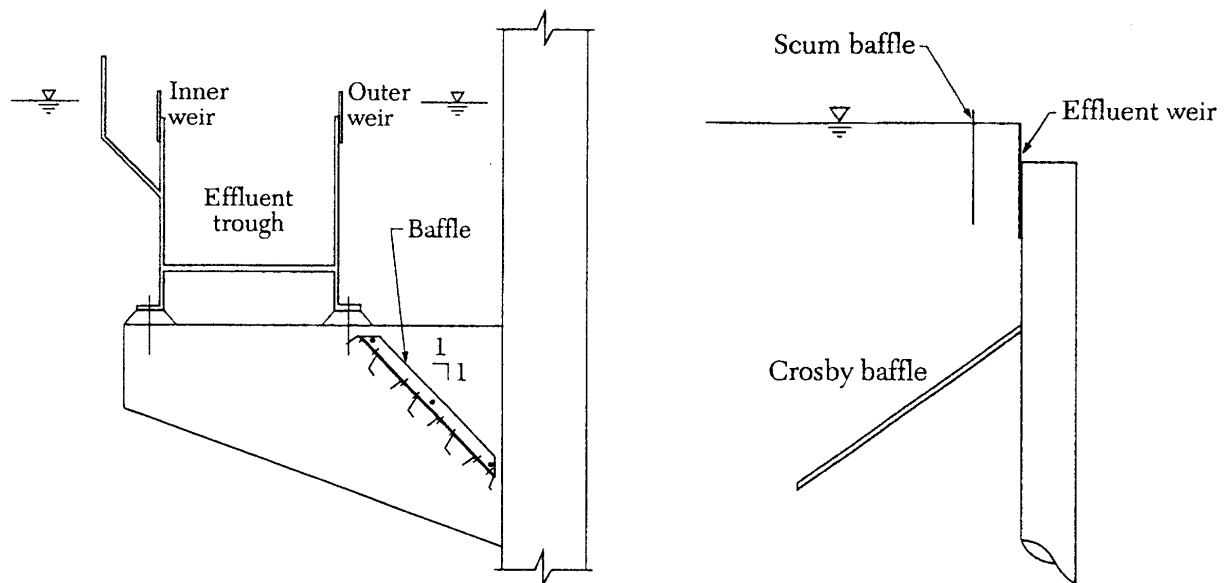


Figure 1.10 Examples of weirs: inset double-sided weirs (left), and single weir with Crosby baffle (right) (Ekama *et al.*, 1997)

1.5 Dissertation goals

From the previous sections, many factors clearly affect the capacity and performance of the settling tank. To account for them, present-day designs are typically oversizing the settling tanks. In that way, designers hope to cope with undesired and unpredictable system disturbances. These may be of hydraulic, biological or physico-chemical origin.

In this respect, modelling the impact of these disturbances on the system can provide considerable information to be used for design. Overdesigning settling tanks is thus reduced to a more plausible extent. Unfortunately, modelling the internal flow and solids concentration fields are nowadays only used for retrofitting and system analysis. In the Netherlands, however, settling tank design rules were reconsidered in 2002 by means of Computational Fluid Dynamics (CFD) models (STOWa, 2002a, b). With this approach overdesign is avoided somewhat by investigating each settling tank individually.

In this respect, the SediFloc project was started in 2000. It is a joint project of BIOMATH (Department of Applied Mathematics, Biometrics and Process Control) and PAINT (Particle and Interfacial Technology Group) at the Faculty of Agricultural and Applied Biological Sciences (Ghent University). SediFloc is an acronym merging "SEDimentation" and "FLOCculation". The ultimate goal of the project is to adequately model flocculation and deflocculation in the final settling tank, and accounting for all its hydraulic and physico-chemical influences. As a result, better predictions of effluent quality should be possible. An overview of the outline of the project is given in Figure 1.11.

In order to study the influence of different environmental conditions on (de)flocculation, sludge first has to be standardised. With this in mind, sludge is grown in a Sequencing Batch Reactor (SBR) that is extensively monitored (Lee & Vanrolleghem, 2003). Sludge stability is checked by means of molecular techniques and nutrient removal performance (Govoreanu *et al.*, 2002). This standardised sludge is subsequently applied to a flocculator of five litres. In there, several environmental conditions can be imposed. Online measurements consist of, *inter alia*, particle size distributions to reflect the state of flocculation/deflocculation. After every experiment practically relevant variables such as the settling velocity and SVI are monitored. This large amount of data is not only used to increase our understanding of the (de)flocculation process, but it also feeds a Population Balance Model (PBM) which aims at describing its dynamics (Nopens *et al.*, 2002; Nopens & Vanrolleghem, 2003). Ultimately, the PBM needs to be incorporated in a numerical model predicting the flow and solids concentration fields in the settling tank. The PBM in this CFD model is believed to better predict the effluent quality. The CFD model therefore synthesises the knowledge of two dissertations in preparation, i.e.

- Quantification of Activated Sludge Flocculation/Deflocculation Dynamics (by R. Govoreanu),
- Modelling Physico-Chemical Influences on the Activated Sludge Flocculation Process: a Population Balance Approach (by I. Nopens).

As a spin-off of the project, data from the CFD model is utilised to calibrate and validate a one-dimensional model of the settling tank. Starting point for this approach is the assumption that a fully calibrated and validated CFD model (relatively) accurately represents reality. Hence, CFD simulations are regarded as numerical experiments, i.e. they reproduce results that can be equivalent to those coming from real experiments but at much lower expense and in larger quantity. Different strategies for settling tank operation can be easily tested without expensive field experiments. Knowledge from these exercises may be subsequently utilised for one-dimensional model calibration and validation. Indeed, this virtual experimental design finally results in an experiment giving the most information necessary to calibrate the one-dimensional model.

The above makes clear that CFD is a tool with many potentials. Firstly, CFD may be used for optimising settling tank design and retrofitting to improve effluent quality and underflow solids concentration. Secondly, it may increase our understanding of internal (physical and biological) processes and their interactions. This knowledge can again be used for process optimisation. The last potential concerns the cost-effectiveness of a validated CFD model; simulation results can be seen as numerical experiments and (partly) replace expensive field experiments.

This dissertation focuses on the modelling aspects of the project and aims at the correct prediction of the flow and solids concentration fields in the settling tank by means of CFD. However, the modelling of flocculation and deflocculation itself is *not* considered in this work. Further, the development of new numerical techniques to solve the set of model equations is not aimed at either. Instead, research is performed on the model structure and its phenomenological submodels. In this respect, submodels for rheology, solids settling and

the solids removal mechanism are investigated on their predictive power. Experimental work on full-scale installations has been conducted to validate the model and to increase our understanding of internal processes.

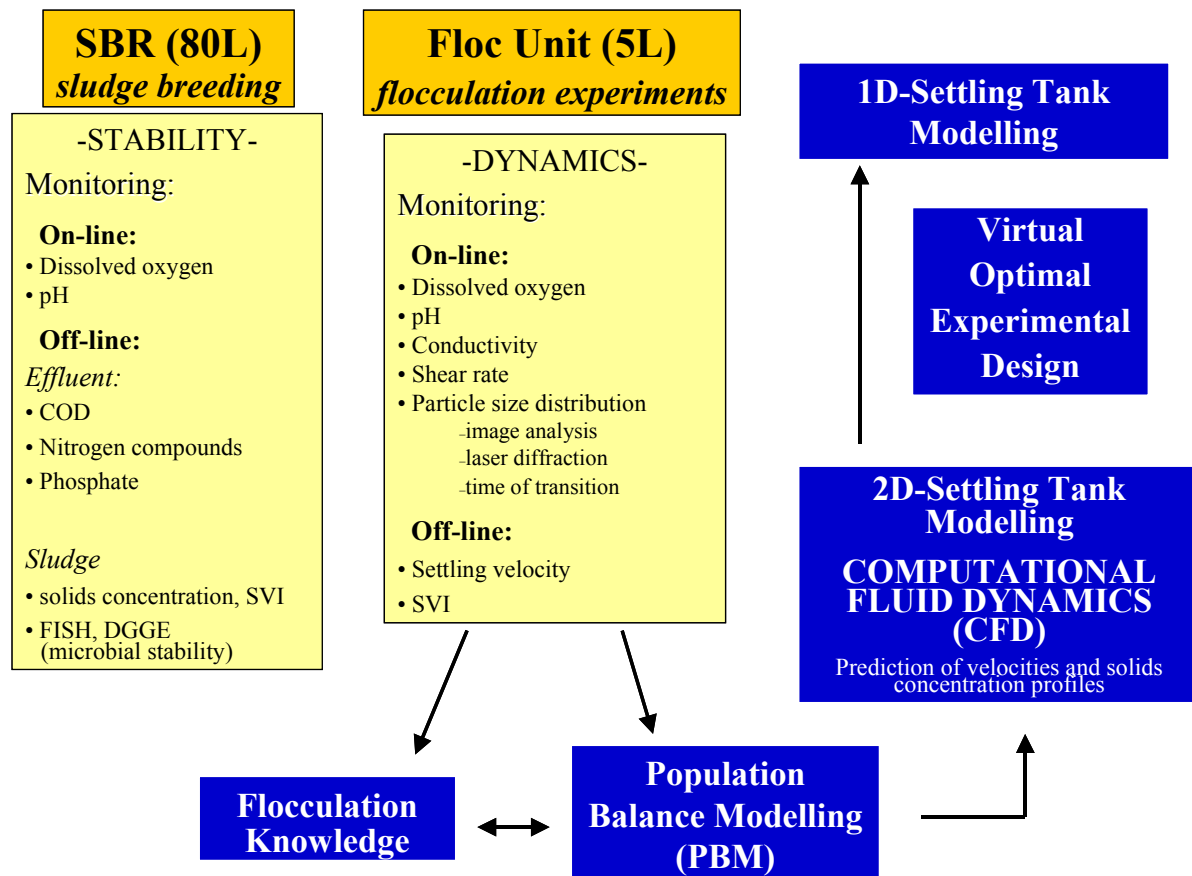


Figure 1.11 Overview of the SediFloc project

1.6 Outline of the dissertation

Whereas this chapter focused on a general introduction to wastewater treatment and the settling tank as process unit, Chapter 2 discusses the modelling principles of hydraulic and solids transport in settling tanks. Although it principally describes the tank in two and/or three dimensions, simple models will be briefly mentioned as well. The complexity of the former models increases further by including phenomena such as turbulence. Because turbulence has a significant influence on flow behaviour, it cannot be neglected in the model. Of course, the complete model can only be solved when the initial hydraulic and solids fields are known; also the conditions at the boundaries of the tank should be defined.

Although the settling tank behaviour is described by a model, the governing model equations still need to be solved. In this respect, *computational fluid dynamics* is a science that is completely dedicated to the mathematics behind the equations and its interpretations. Due to its complexity, only an introductory chapter is included in this dissertation. This PhD definitely does not aim at developing code to solve the governing equations; only commercial

software is used. However, a certain background knowledge on the equations and mathematical algorithms is needed to appropriately interpret the results. Chapter 3 will therefore deal with some general computational issues.

To calibrate and validate a model, experiments are indispensable. Data about solids settling velocities and rheology are typically determined off-line. To confront the model with reality, however, it is preferable to collect data *in situ*. Depending on the model, information such as liquid and/or particle velocities, particle size distributions and solids concentrations are needed. This is not always self-evident as instruments mostly are invasive and may alter the measurement conditions. Hence, care should be taken with the interpretation of data. In this respect, Chapter 4 gives an extensive overview of measurement techniques used for this purpose with their advantages and disadvantages. Where possible, data from this research will be used for illustration.

Chapter 5 deals with the simulation results of a case study, in which a secondary settling tank at Oxley Creek WWTP (Oxley, Australia) is considered. The modelling procedure followed is discussed step by step. Data about sedimentation has been collected. To validate the model, calculated solids concentration profiles are compared with measured profiles. The predicted flow field, on the other hand, is studied by means of a simplified flow-pattern test. With this technique the fate of an inert tracer in the tank is followed up; hence, it gives an idea about the flow field. Note that all validations have been conducted under non-steady conditions due to the diurnally changing influent conditions of the treatment plant.

As mentioned before, flocculation is very important for the tank's performance. For that reason, particle size distributions have been measured *in situ*. Both the measurements and the need to model particle size distributions are discussed in Chapter 6.

For proper calculation of the tank capacity, the sludge rheology may be important in terms of solids transport at the bottom of the tank. An incorrectly modelled solids transport may result in elevated solids blankets and deteriorating effluent quality. In this respect, Chapter 7 discusses rheological experiments performed with a sensitive rotational rheometer. Based on three municipal WWTP sludges, a rheological model is proposed that especially accounts for sludge rheology at low shear. Time dependent rheological behaviour was studied as well. The model obtained in this research was confronted with widely used models in literature in terms of predicted solids concentration and flow fields.

Finally, the results of all experiments and simulations are summarised in a separate chapter. Also the perspectives for further research are discussed.

1.7 Conclusions

As demonstrated in this chapter, the settling tank clearly plays an important role in the treatment of wastewater. It does not only produce a clear effluent that can be discharged into the river, but it also functions as a solids thickener and a storage tank for solids during

wet weather peak flows. However, to what extent these functions are fulfilled depends on many factors. Firstly, the biological factor can be mentioned. Depending on the growth or cultivation conditions in the activated sludge system, sludge with specific properties is obtained. For instance, too many filamentous bacteria may result in bulking, i.e. the bioflocs hinder each other in their settling and have a reduced density. As a result, the effluent quality deteriorates. Secondly, physical and chemical influences may also alter the settling tank operation. These factors are linked to the flocculation of sludge and the hydraulic pattern in the settling tank. Large and dense flocs obviously settle faster and increase the removal efficiency of the tank. Further, solids sedimentation can interact with internal flows; too high liquid velocities may scour solids from the solids blanket interface, wash them out and, hence, they arrive in the receiving river with all the associated detrimental effects.

To minimise the adverse effects on the removal performance, many systems have been proposed in literature. Retrofitting and new settling tank designs try to cope with the static and dynamic system disturbances. In this respect, STOWa in the Netherlands applied Computational Fluid Dynamics (CFD) modelling to account for hydraulic influences on the solids removal. This approach incorporates the two-dimensional and/or three-dimensional geometry of the settling tank. By modelling the internal (physical and/or biological) processes it increases our system understanding. If it is well validated, the CFD model calculations may be even regarded as numerical experiments that can replace the costly field experiments. However, for now this is only possible for very simple flows; settling tanks still demand a lot of research.

This dissertation has to be seen as an effort to optimise CFD models for settling tanks by developing submodels for, e.g., rheology and scraper mechanism. In this respect, the next chapter will introduce modelling techniques for settling tanks, with special emphasis on CFD.

2 Mathematical Modelling of Settling Tanks

2.1 Introduction

This chapter reviews the basics of settling tank modelling. Settling tank models are tools used to represent the physical, chemical and biological processes in the real system. Engineers mostly consider mathematical and physical models. The latter models are scale models where the real process is mimicked on a small scale; however, true similarity cannot be achieved because some scale-effects occur in settling tanks (Ekama *et al.*, 1997).

The simplest mathematical models consist of mathematical relations between known inputs and outputs. These statistical and empirical models are sometimes called *black box* because they provide little insight into the process physics. This type of models is therefore restricted in use within the boundaries of calibration. In their most complex form, however, mathematical models can describe the important processes occurring in the system by solving the partial-differential equations of continuity, momentum, energy, transport of dispersed solids and biological reactions; in addition, realistic boundary conditions must be provided. For that reason, these Computational Fluid Dynamics (CFD) models can be called *deterministic* or *glass box* models. They reveal the role of fundamental laws on the process performance. Because of their origin deterministic models can be applied beyond their range of validity, albeit with caution. Further, there is an alternative class of models (so-called *opaque* or *grey*) that are based on simplifications of physical laws, e.g. flux theory, plug flow and advection-dispersion models.

Mathematical models also can be classified by their spatial resolution. There are simple models that do not consider any spatial variability of certain state variables; i.e. an identical state is assumed for every point in space. Besides these simple zero-dimensional (0D) models, there also exist very complex three-dimensional (3D) models that account for the state variability in space. In addition, models can simulate steady-state or unsteady conditions in the system.

Since the overflow rate concept was introduced by Hazen (1904), conceptual models were utilised for the design of settling tanks. However, the traditional model of Hazen is only applicable to primary settling tanks because the settling rate is assumed to be dependent on

only the particle size. This condition is more likely to be fulfilled in primary than secondary settling tanks. More recently, Krebs *et al.* (2000) introduced a conceptual model for secondary settling tanks, which is based on a linear solids concentration profile in the solids blanket. Contrary to this model, the classical flux theory of Kynch (1952) returns a hindered solids settling velocity. The theory however only provides an underflow solids concentration. The previously very simple models do not include any real spatial orientation. Many models used to describe, for instance, trickling filters and aeration basins in wastewater treatment have simple hydraulic models but rather sophisticated biological reaction models like the IAWQ Activated Sludge Models, ASM (e.g. Henze *et al.*, 1987). In this respect, the behaviour of inhomogeneously mixed systems can be predicted with the use of, for instance, the tanks-in-series approach (Levenspiel, 1970; Froment & Bischoff, 1990). Here, the system's response to disturbances is described by a series of Completely Stirred Tank Reactors or CSTRs. On every CSTR the conservation law is applied. However, the method is not restricted to a series, but every imaginable connection between CSTRs can be used such as backflows and recycles. Although the entire model can become rather complex, the internal model structure does not necessarily reflect the system's spatial structure.

On the contrary, if the tanks-in-series model has the same structure as the spatial discretisation of the system, one-, two- or three-dimensional models are possible. In this respect, common (dynamic) 1D settling tank models are based on the above-mentioned flux theory. It is assumed that settling tanks show uniform profiles of horizontal velocity and that horizontal gradients in concentration are negligible. Consequently, only the processes in the vertical direction are modelled. The resulting idealised settling column is spatially discretised in a number of layers, which are each considered CSTRs (Figure 2.1). Between the different layers i and $i+1$ solid fluxes of advective and gravitational origin exist. The last-mentioned flux corresponds to the sedimentation of particles.

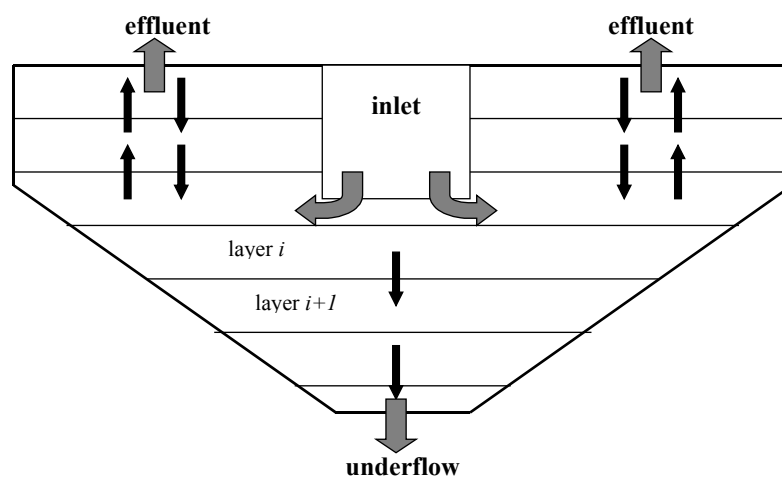


Figure 2.1 1D model approach of a settling tank

Instead of using a limited number of CSTR layers for settling tank modelling, the 1D advection-dispersion equation can be solved numerically; this partial differential equation reads (Ekama *et al.*, 1997)

$$\frac{\partial X}{\partial t} + u \frac{\partial X}{\partial y} + \frac{\partial v_s X}{\partial y} - D_c \frac{\partial^2 X}{\partial y^2} = 0$$

where X is the solids concentration, y the vertical coordinate, u the bulk liquid velocity and v_s the settling velocity of solids. To account for non-ideal flow behaviour, dispersion is introduced into the model by the dispersion coefficient D_c (e.g. Watts *et al.*, 1996). According to Ekama *et al.* (1997), the 1D models have proved adequate for coupling with the activated sludge models because they give a reasonable approximation of the solids balance and of the solids shift from the aeration tank to the secondary settling tank where it is partly stored during wet-weather loading (e.g. Manning *et al.*, 1999). Moreover, the application of such models does not require excessive computer capacity. For that reason, they are popular in the field of model-based process control (e.g. Vanderhasselt *et al.*, 1997). In a real plant there are many factors influencing the performance and the capacity of the settling tank; many boundary and flow conditions cannot be reflected in the 1D model. There are four categories of unconsidered influences,

- *geometry*, e.g. shape of the basin, inlet and outlet arrangements, and baffles
- *flow*, e.g. density effects causing non-uniform velocity profiles. This may result in short-circuits from the inlet to the outlet, resuspension of settled flocs and turbulence
- *solids removal mechanism*, which results in many unsteady effects
- *environmental*, e.g. wind shear, air and inlet water temperature

The prediction of the settling tank performance is therefore a matter of calibration. Due to the above-mentioned influences it is highly questionable whether 1D models will ever be able to predict the dynamics of effluent quality. Also, different internal structures, e.g. baffles, cannot be investigated by means of these models. Hence, more advanced models are needed.

2D and 3D models have the potential to describe the internal flow pattern and the appropriate solids and solutes transport phenomena. Their application is mainly related to the evaluation of internal structural changes, e.g. baffles, on the settling tank efficiency. This fundamental modelling also gives insight in the process physics. Since they are based on fundamental conservation laws, 2D and 3D models can in principle be employed outside their range of calibration. However, care has to be taken. A disadvantage of the models is that their use is computationally very demanding and, therefore, they still cannot be used for control purposes. Instead, they reveal the internal flow pattern of the system; this information can be used to generate the proper model structure that requires less computation time. These simpler models typically consist of CSTRs (Londong *et al.*, 1998; Alex *et al.*, 1999 and 2002). When large time periods are considered in the simulation exercise, it is essential to account for the shift in solids inventory between the biological reactor and the settling tank. In this respect, Merrill *et al.* (1992) and Ji *et al.* (1996) combined a 2D model for the settling tank with the CSTR approach for the aeration tank. The model coupled the hydrodynamic and solids transport equations in the settling tank together with the biological and physical processes in the reactor.

To conclude, Krebs (1995) and Ekama *et al.* (1997) described the advantages and disadvantages of the different types of models. Here, an updated summary is given in Table 2.1.

Table 2.1 Overview of the capacities of the different models

purpose	conceptual	flux model	1D layer model	1D advection-dispersion model	2D and 3D model
dimensioning	+	0	p	p	0
operation ¹⁾	-	+/0	+/p	p	p
effluent ¹⁾	-	-/-	0/-	0/-	p
recycle ¹⁾	0	+/0	+/0	+/+	+
solids blanket ¹⁾	0	-/-	+/0	+/p	+
flocculation	-	-	-	-	p
combination with ASM	-	-	+	p	p
control	-	+	+	p	0
design (inlet, outlet)	-	-	-	-	+
process understanding	-	0	0	+	+
ready for applicability	+	+	+	0	0
computer capacity	+	+	+	0	0

+ positive, 0 neutral, - negative, p development potential

¹⁾ two grades are distinguished for stationary/dynamic cases

In this dissertation CFD is applied to a secondary settling tank. More background information about the modelling of flows is given in the next section. Due to its significant impact on the flow field, turbulence will be considered as well. Because the settling tank aims at a gravitational separation of solids from the liquid, transport of solids deserves more attention. To conclude this chapter, an overview of different boundary conditions as applied in literature will be given.

2.2 Basics of flow modelling

The mathematical history of fluid dynamics begins with Leonhard Euler who was invited by Frederik the Great to Potsdam in 1741. According to a popular story, one of his tasks was to engineer a water fountain. As a true theorist, he began by trying to understand the laws of motion of fluids. In 1755 he wrote Newton's law for a fluid, which in modern tensor notation reads (for the case of constant density ρ):

$$\frac{\partial u_i}{\partial t} + u_j \frac{\partial u_i}{\partial x_j} = -\frac{1}{\rho} \frac{\partial p}{\partial x_i}$$

where u_i is the instantaneous velocity component in the direction x_i , and p is the instantaneous total pressure. An introduction to tensor notation can be found in Appendix A. In fact, trying to build a fountain on the basis of this so-called *Euler equation* was bound to fail. The equation predicts, for a given pressure gradient, velocities that are much higher than those observed. One missing idea was that of viscous dissipation, which is due to the

friction of one parcel of fluid against neighbouring ones. The appropriate term was added to the Euler equation by Navier in 1827 and by Stokes in 1845. The result is known as the *Navier-Stokes equation*:

$$\frac{\partial u_i}{\partial t} + u_j \frac{\partial u_i}{\partial x_j} = -\frac{1}{\rho} \frac{\partial p}{\partial x_i} + \frac{\partial}{\partial x_j} \left[\nu \left(\frac{\partial u_i}{\partial x_j} + \frac{\partial u_j}{\partial x_i} \right) \right]$$

where ν is the kinematic viscosity. This pioneering work indicated the start of a whole new branch of science, and a lot of knowledge about fluid dynamics has been gained in the mean time.

The hydrodynamic state of a local fluid parcel can be completely described by three basic relations; they are considered here to be the three laws of conservation, i.e.

- *conservation of mass*, i.e. continuity
- *conservation of momentum*, i.e. Newton's second law
- *conservation of energy*, i.e. the first law of thermodynamics

Temperature variations may make a difference in full-scale settling tank operation. In this dissertation however, no interest is shown in temperature variations; hence, the energy equation is omitted in further discussions. Therefore, the only two unknown variables that must be obtained from these basic equations are the velocity and pressure. The conservation equations, however, also need the density and the dynamic viscosity as fluid and transport properties respectively.

Finally, to solve the set of partial differential equations, velocity and pressure have to be known at every point of the flow boundary. These are the so-called *boundary conditions*.

The preceding considerations apply to a fluid of assumed homogeneous composition, i.e. diffusion and chemical reactions are not considered. Complex systems such as settling tanks where the behaviour of components in the fluid are to be modelled, must therefore consider at least two extra basic relations, i.e.

- *conservation of species*
- *laws of chemical reaction*

Additionally, knowledge about the diffusion coefficient, chemical constants and reaction rates has to be provided.

2.2.1 The Navier-Stokes equations

A rigorous derivation of the conservation equations is beyond the scope of this dissertation; the reader is referred to the work of e.g. White (1991) and Hirsch (1997). Although many simplifications can be made, the conservation laws are given in their extended form; i.e. density gradients make application of the differential operator on the bulk density necessary. Multiphase flows and chemical reactions are not considered.

Firstly, the continuity equation is given as follows

$$\underbrace{\frac{\partial \rho}{\partial t}}_{\text{rate of change}} + \underbrace{\frac{\partial \rho u_i}{\partial x_i}}_{\text{advective transport}} = 0 \quad (2.1)$$

Secondly, the momentum equation is written as

$$\underbrace{\frac{\partial \rho u_i}{\partial t}}_{\text{rate of change}} + \underbrace{\frac{\partial \rho u_i u_j}{\partial x_j}}_{\text{advective transport}} = \underbrace{\frac{\partial \sigma_{ij}}{\partial x_j}}_{\text{stress}} + \underbrace{g_i \rho}_{\text{gravitational force}} \quad (2.2)$$

where g is the vector acceleration of gravity, and σ_{ij} is the total stress tensor due to internal forces. Because the equation conserves momentum, both body and surface forces applied on the considered fluid parcel have to be accounted for. The body forces are those which apply to the entire mass of the fluid element. Such forces are usually applied externally such as gravity here. On the other hand, surface forces are applied by internal stresses σ_{ij} on the sides of the fluid element. Then, the total surface force vector F_{surface} is written as the divergence of σ_{ij} ,

$$F_{\text{surface}} = \frac{\partial \sigma_{ij}}{\partial x_j}$$

where the divergence of σ_{ij} is to be interpreted in the tensor sense, so that the result is a vector (see Appendix A).

The total stress exerted on a surface actually consists of two parts, i.e. pressure and viscous stress τ_{ij} .

$$\sigma_{ij} = -p\delta_{ij} + \tau_{ij}$$

The Kronecker-delta δ_{ij} (see Appendix A) enables the pressure force p to act only normal to a surface. Further, the viscous stress is dependent on the strain rate $\dot{\gamma}_{ij}$. The latter is the three-dimensional analogy of the frequently used shear rate or velocity gradient. The strain rate tensor is defined as

$$\dot{\gamma}_{ij} = \frac{\partial u_i}{\partial x_j} + \frac{\partial u_j}{\partial x_i}$$

The simplest assumption for the variation of viscous stress with strain rate is a linear law, which applies to Newtonian fluids (see Section 2.2.3.2). The constant proportionality factor is the dynamic viscosity μ . These simple considerations about viscosity were first made by Stokes in 1845, and are applicable to all gases and most common fluids. The total stress tensor can thus be written as

$$\sigma_{ij} = -p\delta_{ij} + \mu \left(\dot{\gamma}_{ij} - \frac{2}{3} \frac{\partial u_i}{\partial x_j} \delta_{ij} \right) \quad (2.3)$$

Here, the second term of the right-hand side of Equation 2.3 describes the deformation and dilatation of a fluid parcel respectively. The Kronecker-delta in this term is needed to make the expression also applicable to normal stresses, i.e. when $i = j$.

Substituting body and surface forces in the momentum conservation equation finally results in the full Navier-Stokes equations (Equations 2.1 and 2.2).

However, straightforward attempts to solve the Navier-Stokes equations are still very non-realistic. To demonstrate the problem, the water velocity in the Nile is calculated. The river's altitude drops hundreds of meters in about a thousand kilometres. The typical angle of inclination is about 10^{-4} rad, and the typical river depth is approximately 10 meters. Equating the gravity force and the viscous force, the steady velocity is found to be of the order of 10^7 cm/s instead of the observed 10^2 cm/s. Some issue is clearly overlooked; the estimate even contradicts simple energy conservation arguments. When converting all potential energy to kinetic energy, a velocity of 10^4 cm/s is estimated. This is still off the mark by two orders of magnitude. The solution to this discrepancy was suggested by Reynolds who stressed the importance of the dimensionless ratio of the non-linear advection term to the viscous term in the Navier-Stokes equations. With a velocity u on a, still to define, spatial scale l , the non-linear term in Equation 2.2 is estimated as u^2/l ; the viscous term is about $\nu u/l^2$. The ratio of the two is known as the Reynolds number Re ,

$$Re = \frac{ul}{\nu}$$

Hence, the magnitude of Re measures how large the non-linearity is compared to the effect of the viscous dissipation in a particular fluid flow. For $Re \ll 1$, the non-linearity can be neglected. Unfortunately, in many natural circumstances Re is very large. Reynolds understood that for $Re \gg 1$ there is no stable stationary solution for the equation of motion. The solutions are strongly affected by the non-linearities, and the actual flow pattern is complicated and vortical. Such flows are called *turbulent*.

Modern concepts about high-Reynolds-number turbulence started with the insights of Richardson in 1922. Richardson proposed a concept of the creation of turbulence by large-scale forcing (at a scale l_0), setting up a cascade of energy transfers to smaller and smaller scales by the non-linearities of fluid motion, until the energy dissipates at small scales η by viscosity, turning into heat (Figure 2.2). This smallest scale is the Kolmogorov scale. Finally, based on these insights Kolmogorov conveyed an analytical turbulence theory in 1941; a comprehensive review can be found in Frisch (1998).

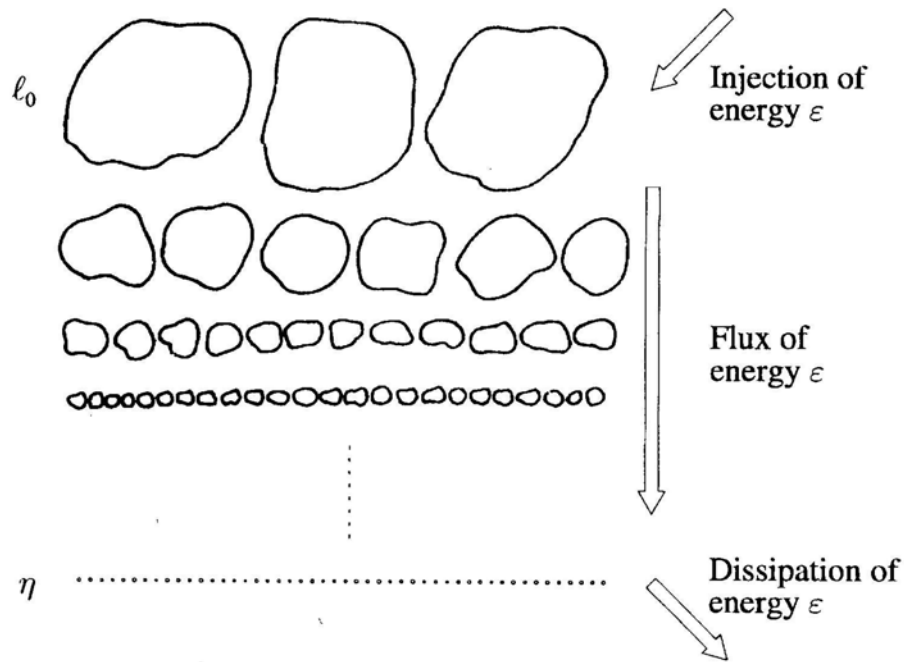


Figure 2.2 Energy cascade from large-scale to small-scale eddies (Frisch, 1998)

2.2.2 Introduction to turbulence modelling

This section will discuss turbulence in hydrodynamics. Turbulence is very difficult to define precisely. However, its characteristics can be summarised as follows (Tennekes & Lumley, 1972):

- *Irregularity*: the first characteristic of turbulence is the randomness of all turbulent flows. One therefore relies on statistical techniques to describe these phenomena.
- *Diffusivity*: the diffusivity of turbulence, which causes rapid mixing and increased rates of momentum, heat, and mass transfer is another important feature of turbulence.
- *Large Reynolds numbers*: it results in instabilities for laminar flows. The randomness of viscous diffusion and the non-linearity of the inertial term make the Navier-Stokes equations nearly intractable.
- *Three-dimensional vorticity fluctuations*: the random rotational or vorticity fluctuations that characterise turbulence cannot maintain themselves if the velocity fluctuations were two-dimensional, since an important vorticity-maintenance mechanism known as vortex stretching is absent in two-dimensional flows.
- *Dissipation*: viscous shear stresses perform deformation work which increases the internal energy of the fluid at the expense of kinetic energy of the turbulence. Hence, turbulence needs a continuous supply of energy to make up for these viscous losses.
- *Continuum*: turbulence is a continuum phenomenon, governed by the equations of fluid mechanics. Even the smallest scales occurring in a turbulent flow are far larger than any molecular length scale.
- *Turbulent flows are flows*: turbulence is not a feature of fluids, but of fluid flows. Most of the dynamics are the same in all fluids, whether they are liquids or gases, as long as the Reynolds number is large enough.

Visualisations are very illuminating but fail to describe turbulence in a quantitative way. The Navier-Stokes equations inherently incorporate turbulence. To solve the flow field the equations are discretised (see Chapter 3) and solved on a computer. Such Direct Numerical Simulation (DNS) of turbulence is a recent field of computational fluid dynamics. White (1991) illustrates the limitations of computational turbulence by considering a simple turbulent pipe flow. The prediction of the fine details of such a turbulent flow at, for instance, $Re = 10^7$, would require 10^{22} numerical operations. Even if the required mesh would fit on this virtual computer with a common speed of 2 ns per operation (2 GHz processor), the computation still would take 160000 years. Even the future supercomputer Cray X1 (expected in 2010) with a speed of 10^{-6} ns per operation, i.e. a 10^6 GHz microprocessor, still would need 4 months for this extremely simple flow. Therefore, many empirical modelling approaches have been presented throughout time. They will be discussed next.

2.2.2.1 Reynolds-averaged Navier-Stokes equations

Despite the increasing available computational power, it is clear that the previously mentioned DNS is still very computationally demanding. However, for proper modelling of the hydrodynamics the equations can be averaged out in time, over the turbulent fluctuations (Figure 2.3). This leads to the so-called *Reynolds-averaged Navier-Stokes equations* (Bradshaw, 1978; White, 1991; Hirsch, 1997), which require empirical or at least semi-empirical information on the turbulence structure and its relation to the averaged flow.

The turbulent averaging process is introduced in order to obtain the laws of motion for the "mean", time-averaged, turbulent quantities. This time-averaging is defined in such a way that it removes the influence of the turbulent fluctuations while not destroying the time dependence associated with other time-dependent phenomena with time scales distinct from those of turbulence. Thus, following the original idea of Reynolds in 1895, it is assumed that any variable f is resolved into a mean value \bar{f} plus a fluctuating value f' , where

$$\bar{f} = \frac{1}{T} \int_{t_0}^{t_0+T} f dt$$

where the averaging period T is large compared to the relevant period of the fluctuations. This averaging procedure can now be applied to fluctuations in velocity and pressure, i.e.

$$u_i = \bar{u}_i + u_i'$$

$$p = \bar{p} + p'$$

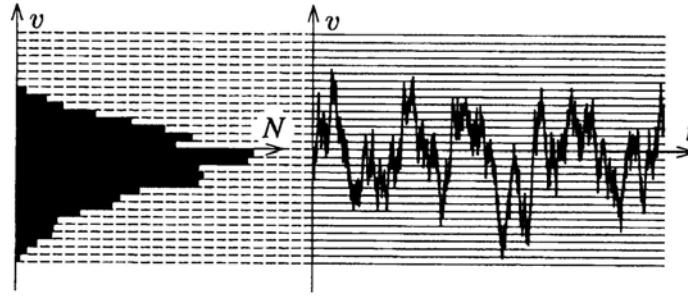


Figure 2.3 The probabilistic nature of turbulent velocity (Frisch, 1998)

Substituting these relations into the continuity equation reveals that exactly the same equation is retained, except that now averaged flow variables are used. In case of the momentum equations, however, an additional stress term appears. Consequently, the total viscous stress is written as

$$\sigma_{ij} = \underbrace{\mu \left(\dot{\gamma}_{ij} - \frac{2}{3} \frac{\partial u_i}{\partial x_i} \delta_{ij} \right)}_{\text{laminar}} - \underbrace{\overline{\rho u_i' u_j'}}_{\text{turbulent}}.$$

As is shown, the stress can be decomposed in a (Newtonian) laminar-viscous stress and an additional apparent turbulent-stress tensor. However, the relation between the latter so-called *Reynolds stresses* and the mean flow quantities is unknown. The application of the Reynolds-averaged equations therefore requires the introduction of some modelling of these unknown relations, based on theoretical considerations but coupled with empirical expressions. To conclude, the Reynolds-averaged equations are given below. For convenience, the bar indicating the averaged quantities $\overline{\rho}$, $\overline{u_i}$ and \overline{p} are left out.

$$\frac{\partial \rho}{\partial t} + \frac{\partial \rho u_i}{\partial x_i} = 0$$

$$\frac{\partial \rho u_i}{\partial t} + \frac{\partial \rho u_i u_j}{\partial x_j} = -\frac{\partial p}{\partial x_i} + \frac{\partial}{\partial x_j} \left[\mu \left(\dot{\gamma}_{ij} - \frac{2}{3} \frac{\partial u_i}{\partial x_i} \delta_{ij} \right) - \overline{\rho u_i' u_j'} \right] + g_i \rho$$

2.2.2.2 The eddy-viscosity concept

The concept of eddy viscosity has become perhaps the most frequently used tool in the modelling of turbulent flows.

Boussinesq's eddy viscosity concept proposed in 1877 assumes that, in analogy to the viscous stresses in laminar flows, the Reynolds stresses are proportional to the mean-velocity gradients. For general flow considerations, this concept may be expressed as (Hirsch, 1998)

$$-\overline{\rho u_i' u_j'} = \mu_\tau \left(\dot{\gamma}_{ij} - \frac{2}{3} \frac{\partial u_i}{\partial x_i} \delta_{ij} \right) - \frac{2}{3} \rho k \delta_{ij}$$

where k is the turbulent kinetic energy, and μ_t is the turbulent or eddy viscosity. Whereas the dynamic viscosity μ is a fluid property, the eddy viscosity strongly depends on the state of turbulence. The introduction of the above equation does not introduce the desired turbulence model, but only provides a framework for constructing such a model (see Section 2.2.2.3).

For complex flows, more than one Reynolds stress is of significance. Hence, different eddy viscosities are sometimes introduced for the turbulent momentum transport in different directions; for instance, in large water bodies the eddy viscosity is often described differently for the horizontal and vertical transport. However, the eddy viscosity concept has proved successful in many practical calculations and is still the basis of most turbulence models in use today (Rodi, 1984).

2.2.2.3 Classification of turbulence models

Turbulence models were developed that do not use turbulent viscosities but employ differential transport equations for the Reynolds stress $\overline{\rho u_i' u_j'}$. One possible way of classification would be according to whether the models use the eddy-viscosity concept. However, there are such large differences between the simplest and the most advanced eddy-viscosity models that a finer subdivision is needed. Comprehensive reviews on turbulence models can be found in Rodi & Spalding (1970), Bradshaw (1978), Rodi (1984) and Hirsch (1998). The majority of the model classification presented in this section is based on the review of Rodi (1984).

The use of a constant eddy viscosity tuned to suit the flow problem has indeed little to do with turbulence modelling; it does not account for changes in local turbulence structure, hence in general it cannot correctly describe the details of the mean flow field. The first model to determine the distribution of the eddy viscosity over the flow field was suggested by Prandtl in 1925 and is known as the Prandtl mixing-length hypothesis. He related the eddy viscosity to a mixing length l_m and the mean fluctuating velocity u . In order to calculate the eddy viscosity, Prandtl postulated

$$\nu_t = \frac{\mu_t}{\rho} = l_m^2 \left| \frac{\partial u}{\partial x} \right|.$$

Due to its frequent use in literature, the eddy viscosity as introduced here, i.e. ν_t , will be used throughout the remainder of this chapter. The main issue with this kind of model is the difficulty to specify the length scale for complex flows. Both models, i.e. a constant eddy viscosity and the mixing length hypothesis, implicitly assume that the turbulence is dissipated where it is generated, which means that there is no transport of turbulence (or of quantities characterising it) in the flow field. In cases where the local state of turbulence is significantly influenced by the turbulence generation somewhere else in the flow (or by the generation at previous times: history effects), the simplest models neglecting turbulence transport are inadequate. The example of grid turbulence aptly demonstrates this issue: the turbulence is generated by the wakes directly behind the grid and is then transported

downstream by the mean motion. The simplest models would yield zero turbulence, i.e. a zero eddy viscosity, because the mean velocity is uniform in the downstream region.

In order to account for the transport of turbulence, models have been developed that employ transport equations for quantities characterising turbulence; e.g. a typical velocity scale that describes the turbulent velocity fluctuations. Similar to the conservation equations they contain terms representing both advective transport by the mean motion and diffusive transport by the turbulent motion (also the rate of change in unsteady flows). Some models only use a transport equation for a velocity scale to characterise the velocity fluctuations. In this respect, the physically most meaningful scale is \sqrt{k} . When this scale is used in the eddy-viscosity relation, the so-called *Kolmogorov-Prandtl expression* is obtained:

$$v_t = c_\mu' \sqrt{k} l$$

where c_μ' and l are an empirical constant and length scale respectively. The latter was determined for several types of free jets by Rodi & Spalding (1970), and can be extrapolated to different configurations of inlet slots. Kolmogorov and Prandtl also suggested to determine the distribution of k by solving a transport equation for this quantity. Such an equation can be derived in exact form from the Navier-Stokes equations. To complete the turbulence model the length scale l is still needed. In most models, l is determined from simple empirical relations similar to those for the above-mentioned mixing length l_m . However, l is not easier to describe than the latter; both are dependent on the type of flow.

These one-equation models account for advective and diffusive transport of the turbulent-velocity scale and are therefore superior to the mixing-length hypothesis when this kind of transport is important. The application of one-equation models is mainly restricted to shear layers (i.e. a flow characterised by velocity gradients) due to the ease of determining the length scale. Yet, for most shear layers the simpler mixing-length model works equally well. Different algebraic formulae to calculate the length scale have been proposed, but they have been tested insufficiently; they are also rather complex and computationally demanding (Rodi, 1984). Therefore, two-equation models that also determine the length scale from a transport equation have gained popularity.

With two-equation models, besides the energy also the length scale is transported. The eddies generated, for instance, by a grid are convected downstream so that their size at any location depends very much on their initial size. Other processes influencing the length scale are dissipation and vortex stretching that alter the eddy sizes.

A length-scale equation does not need a length scale itself as dependent variable; any combination of the form $z = k^n l^n$ will suffice because k is known from solving the k -equation (Rodi, 1984). In fact, most equations do not use l as a variable. Experience with various equations has shown that $z = \varepsilon \propto k^{3/2} l^1$ does not require a near-wall correction term because the diffusion of the length scale appears to be well described by ε (Rodi, 1984). Other formulations of the length scale are less effective and require a correction term for the near-wall turbulence damping. The ε -equation therefore has become more popular than the other length-scale equations. Because the k - ε model is widely used, the equations of the complete model are presented below (Rodi, 1984; Hirsch, 1998). Also the eddy viscosity as used in the Navier-Stokes equations is given.

$$v_t = c_\mu \frac{k^2}{\varepsilon} \quad (2.4)$$

$$\underbrace{\frac{\partial \rho k}{\partial t}}_{\text{rate of change}} + \underbrace{\frac{\partial \rho k u_j}{\partial x_j}}_{\text{advective transport}} = \underbrace{\frac{\partial}{\partial x_j} \left[\rho \left(v + \frac{v_t}{\sigma_k} \right) \frac{\partial k}{\partial x_j} \right]}_{\text{diffusive transport}} + \underbrace{\rho v_t \left(\frac{\partial u_j}{\partial x_j} + \frac{\partial u_j}{\partial x_j} \right) \frac{\partial u_j}{\partial x_j}}_{\text{production by shear, } P_s} + \underbrace{\beta g_j \frac{v_t}{\sigma_s} \frac{\partial \rho \phi}{\partial x_j}}_{\text{buoyant production/dissipation, } P_b} - \underbrace{\rho \varepsilon}_{\text{dissipation}}$$

$$\underbrace{\frac{\partial \rho \varepsilon}{\partial t}}_{\text{rate of change}} + \underbrace{\frac{\partial \rho \varepsilon u_j}{\partial x_j}}_{\text{advective transport}} = \underbrace{\frac{\partial}{\partial x_j} \left[\rho \left(v + \frac{v_t}{\sigma_\varepsilon} \right) \frac{\partial \varepsilon}{\partial x_j} \right]}_{\text{diffusive transport}} + \underbrace{c_{1\varepsilon} \frac{\varepsilon}{k} (P_s + P_b) (1 - c_{3\varepsilon} Ri)}_{\text{generation - destruction}} - \underbrace{\rho c_{2\varepsilon} \frac{\varepsilon^2}{k}}_{\text{generation - destruction}}$$

where

$$Ri = \frac{g \frac{\partial \rho}{\partial x}}{\rho \left(\frac{\partial v}{\partial x} \right)^2}$$

is the Richardson number which is the ratio of gravity to inertial forces and characterises the importance of buoyancy effects; v is the velocity component perpendicular to gravitational acceleration, ϕ is the solids mass fraction, β is an empirical constant, and σ_s is the Schmidt number. The latter constant expresses diffusive mass transport due to turbulence. Similarly, σ_k and σ_ε express turbulent diffusive transport of the scalars k and ε respectively. The values of the empirical constants (Table 2.2) are based on extensive examination of free turbulence, but they can also be used for wall flows (Rodi, 1984). However, care should be taken for these wall flows because the local flow field is no longer turbulent. Launder & Spalding (1974) therefore proposed to use the low-Reynolds k - ε turbulence model, and make c_μ and $c_{2\varepsilon}$ dependent on the local turbulent Reynolds number. For axisymmetric jets, the parameters should be made dependent on the local shear. On the other hand, the surface damping of turbulence can be taken into account as well. According to Celik & Rodi (1988) turbulent eddies impinging on the free water surface are suppressed. This causes a reduction in both the length scale of the turbulent eddy (in particular the vertical extent) and the damping of the vertical velocity fluctuations. For that reason, these authors proposed to make c_μ dependent on a kind of surface damping function and the ratio of production to dissipation of turbulent kinetic energy. This function can also account for the damping of the vertical fluctuations by the solids bed. The results showed values of 0.05 near the bed and 0.01 at the free surface, whereas a value of 0.09 for c_μ in the standard k - ε turbulence model is used.

Table 2.2 Recommended typical values of the constants in the k - ε turbulence model (Rodi, 1984; Hirsch, 1998)

c_μ [-]	$c_{1\varepsilon}$ [-]	$c_{2\varepsilon}$ [-]	$c_{3\varepsilon}$ [-]	σ_ε [-]	σ_k [-]
0.09	1.44	1.93	0.8	1.3	1.0

A complete mathematical deduction of the k - ε turbulence model can be found in Mohammadi & Pironneau (1994). The standard k - ε model is based on the assumption that the eddy viscosity is the same for all Reynolds stresses, i.e. an isotropic eddy viscosity is assumed. The calculation of simple thin shear layers is not influenced by this assumption because only the shear stress is important in these flows. In recirculating flows the normal stress and the shear stress terms in the momentum equations are of the same order and are often small compared to the inertial and pressure gradient terms, hence the assumption of isotropy is of little importance (Rodi, 1984). However, for certain flows this assumption is too crude, for instance, it does not produce the turbulence-driven secondary motions in square ducts.

Many modifications to the standard k - ε model have been proposed in literature to more accurately model turbulence in non-trivial flow systems such as flows along curved surfaces, with rotation or flows that separate from the wall. To deal with such issues, the *non-linear* (Pattijn, 1999) and *RNG based k - ε model* (Jones *et al.*, 1999) are some of the new tools available to the turbulence modeller. To allow an anisotropic eddy viscosity, the individual Reynolds stresses can be calculated by the so-called *Reynolds-stress models* and the computationally less expensive *algebraic-stress models* (Bradshaw, 1978; Rodi, 1984; Hirsch, 1998).

The current computer speed is sufficient to solve the time-dependent Navier-Stokes equations for the large-scale motion. The small-scale turbulence than cannot be resolved with the chosen numerical mesh on which the conservation equations are discretised (see Chapter 3), must then be approximated by a model. This kind of modelling approach is called *subgrid-scale modelling* or *large-eddy simulation*. The small-scale details of the model are much less influential for the overall flow behaviour than the turbulence models for the Reynolds-averaged Navier-Stokes equations. This is because the main contribution to the turbulent transport stems from the large-scale motion that can be resolved within the numerical mesh.

A discussion of all these models is beyond the scope of this dissertation. It is clear that many turbulence models are available to the modeller. The next section will give a short literature overview of different turbulence models used for settling tank modelling.

2.2.2.4 Turbulence models used for settling tank modelling

Many approaches to include turbulence in settling tank modelling are proposed during the last two decades. They vary from very rudimentary assumptions about the eddy viscosity to the advanced RNG-based k - ε models.

Krebs *et al.* (1995) and Deidinger *et al.* (1998) modelled turbulence by the simple constant eddy viscosity approach. Imam *et al.* (1983) adopted an algebraic relation to calculate this eddy viscosity. The best agreement between the physical and numerical model was obtained by a linear relation considering both the submerged depth of the inlet baffle and the velocity below it. In this study the inlet region was not taken into account in the computational domain. Imam *et al.* (1983) admitted that a turbulence model more advanced than these algebraic relations would improve the predictions of the unsteady transport. Further, in order to account for buoyancy, McCorquodale *et al.* (1991) and Samstag *et al.* (1992) calculated the eddy viscosity as an algebraic function of the local Richardson number.

The k - ε model has become widely applied for modelling turbulence in settling tanks. Theoretically, the traditional high-Reynolds k - ε model is restricted to locally isotropic and highly turbulent flows. Notwithstanding that low velocities prevail in the solids blanket, this model is generally applied because the Reynolds number of the settling tank is still high due to its large system dimensions and the fairly low viscosity of the suspension (Schamber & Larock, 1981; Lyn & Rodi, 1990; Zhou & McCorquodale, 1992b; Ekama *et al.*, 1997). Due to the possible low *local* Reynolds numbers however, low-Reynolds k - ε models are becoming more popular (Winkler, 2001). Below, only high-Reynolds k - ε turbulence models are discussed.

In many cases, buoyancy is simply omitted from the k - ε turbulence models (e.g. Schamber & Larock, 1981; Stamou *et al.*, 1989; Adams & Rodi, 1990; Zhou & McCorquodale, 1992a,b,c; Narayanan *et al.*, 2001). Simonin *et al.* (1989) discussed to what extent the k - ε model including the effect of density differences correctly models stably stratified flows. It was assumed that the error in the turbulence model and the (in)accuracy of the numerical methods legitimate the omission of the density effect on turbulence. Zhou & McCorquodale (1992a,b) and McCorquodale & Zhou (1993) also omitted the buoyancy correction terms in the k - ε model as a first approximation; their motivation was based on the conclusions of Devantier & Larock (1986). These researchers found that no solutions could be obtained for k and ε for any initially specified velocity, nor solids concentration field. The cause was the stable stratification in the settling tank, i.e. buoyancy was so large that it overwhelmed the shear production and drove k and ε towards negative values. Of course, such values are impossible. Therefore, as a first approximation they omitted the correction terms from the turbulence model.

However, many other researchers opted to take buoyancy into consideration, e.g. Devantier & Larock (1986), Szalai *et al.* (1994), Krebs *et al.* (1996), Vitasovic *et al.* (1997), Lakehal *et al.* (1999), Stamou *et al.* (2000) and Armbruster *et al.* (2001). In this respect, Lakehal *et al.* (1999) investigated the impact of the empirical constant $c_{3\varepsilon}$ that is associated with the buoyancy source term. Their sensitivity analysis revealed that both the velocity and solids concentration profile are very dependent on it. Hence, more experimental data are required to elucidate the issue of buoyancy.

Applications of the RNG-based k - ε model can be found in Lainé *et al.* (1999) and Tyack & Fenner (1999). However, its use remains limited because of a lack of validation studies. More experience and better validation make the standard k - ε model superior to others, at least in popularity. It is clear that incorporation of the buoyancy term in the turbulence model demands for a description of temperature and/or solids concentration because both affect the bulk density. In this dissertation, temperature variations in the settling tank are not considered, hence only solids transport will be discussed below.

2.2.3 Solids transport modelling

Many approaches exist for multiphase modelling. Firstly, the Lagrangian multiphase technique may be mentioned, which calculates the trajectories of the dispersed phase entities. However, the Lagrangian model does not effectively model flows in which particles are undefinably suspended in the continuum, as occurs in suspensions within closed systems such

as stirred tanks, mixing vessels, or fluidised beds. These systems should be treated using the Eulerian multiphase approach as described below.

Further, the Lagrangian model should not be applied whenever the particle volume fraction exceeds 10-12%. Note that the mass loading of the dispersed phase may greatly exceed 10-12%; even problems with mass flows equal to or exceeding the one of the continuous phase can be solved. A second limitation of the Lagrangian approach is the restriction on the number of particles considered. Too many particles, as this is the case for full-scale sedimentation tanks, ask for too large computation times. Hence, the Eulerian model is preferred.

In literature many classifications of multiphase models can be found. Here, the one proposed by Webb & Rowe (1986) is used.

In the Eulerian *multiphase model* the momentum and continuity equations for each phase are written. When dealing with a polydisperse medium, a rigorous treatment of the particle velocities demands a momentum equation for every particle size class. Due to the computational effort, it is obvious that not many size classes can be considered. Moreover, the interfacial boundaries between particles and liquid are mostly problematic to describe. To adequately describe the interactions between the phases at the different interfaces a proper volume averaging is needed to avoid solving the multiphase problem with the interface relations of mass and momentum as boundary conditions. More information on this topic can be found in e.g. Soo (1990), Jackson (1997) and Pedras & de Lemos (1999). Because of the previous issues, one momentum equation is often used for all particle sizes resulting in only one particle velocity. Still, different continuity equations may describe the dispersion and possible interactions between the particle size classes.

A simpler way to model multiphase flows is by means of the *drift-flux* or *drift-velocity model* (Wallis, 1969). Here, most of the troublesome interfacial relationships in the multiphase model are eliminated by applying only one momentum equation for the complete mixture. The relative velocity between the phases and particle size classes is specified through constitutive relations. The basic reasoning of this modelling approach stems from the observation that the Navier-Stokes equations describe the motion of air, despite the fact that air is a mixture of nitrogen and oxygen (van den Akker, 1986).

The drift-flux model can be further simplified to the *homogeneous model* by considering the particles as having the same velocity as the fluid. This has again as consequence that one momentum equation is used for both the continuum and the dispersed phase.

For modelling solids transport in secondary settling tanks a drift-flux-like model is generally adopted. Next to the momentum equation for the mixture, particle transport is described by an extra transport equation. This scalar transport equation originates from ordinary mass conservation. When different particle size classes are considered, separate equations are used for each class. Incorporation of external forces, e.g. gravitation, on the particles is no considerable issue as long as the force can be written in terms of velocities and mass fluxes. Because this type of modelling approach will be used in the dissertation, the transport equation is given below.

$$\frac{\partial \rho \phi}{\partial t} + \frac{\partial}{\partial x_i} \rho \phi (u_i + u_{s,i}) = \frac{\partial}{\partial x_i} \left(\frac{v + v_t}{\sigma_s} \frac{\partial \rho \phi}{\partial x_i} \right) \quad (2.5)$$

where $\mathbf{u}_s = (0, -v_s, 0)$ is the settling velocity vector of solids in a Cartesian coordinate system.

Similar to the averaging of the Navier-Stokes equations, averaging of Equation 2.5 results in an additional term which expresses turbulent mass transport. In direct analogy to the turbulent momentum transport, this turbulent mass transport is often assumed to be related to the gradient of the transported quantity, i.e.

$$-\overline{u_i \rho \phi} = \Gamma \frac{\partial \rho \phi}{\partial x_i}$$

where Γ is the turbulent mass diffusivity. Like the eddy viscosity, Γ is not a fluid property but depends on the state of turbulence. In fact, the analogy between mass and momentum transport suggests that Γ is related to v_t by

$$\Gamma = \frac{v_t}{\sigma_s}.$$

However, the Schmidt number σ_s is also used to express mass diffusivity in laminar flow conditions as can be seen in the former solids transport equation (Equation 2.5). Rodi (1984) mentioned that experiments have shown a rather invariant Schmidt number within one flow and between different flows. Therefore, many models apply a constant Schmidt number. It should be mentioned however that buoyancy and streamline (i.e. lines across which there is no mass flow) curvature affect the value of σ_s .

From a literature review it is clear that the Schmidt number varies between 0.5 and 1, and depends on both the particle size and stratification (Celik & Rodi, 1988; Krebs, 1995; Ekama *et al.*, 1997). Stamou *et al.* (1989) investigated the sensitivity of the residence time distributions (see Chapter 4) and the solids removal efficiency on the value of the Schmidt number; an almost negligible effect was observed. Based on their results, Mazzolani *et al.* (1998) adopted a value of 1. This value for the Schmidt number was also accepted as being appropriate by Larock *et al.* (1983) and Lyn *et al.* (1992), although their choice was determined by the presence of small particles and the low concentrations used. Instead, many other researchers applied 0.7 as a mean value to be used for the entire flow field (Adams & Rodi, 1990; Szalai *et al.*, 1994; Krebs, 1996; Lakehal *et al.*, 1999). Because stratification dampens turbulence, it seems obvious to adopt two different Schmidt numbers, i.e. one for the solids blanket and one for the supernatant. In this respect, Zhou & McCorquodale (1992a, b) used values of 0.5 and 1 for the bottom sludge layers and supernatant respectively. It is to be noted that these values were only valid for vertical solids transport. Since stratification does not occur horizontally a Schmidt number of 1 was retained by the researchers. The different Schmidt numbers were essential to fit the simulated velocity data to the experimentally obtained data. Finally, Samstag *et al.* (1992) related the Schmidt number to the boundary and the interior of the flow field; values of respectively 0.9 and 0.5 were used.

For secondary settling tanks it is clear from Equation 2.5 that sedimentation is an important mass flux in the solids conservation equation. Proper modelling of this flux is therefore crucial for the prediction of effluent quality and sludge blanket behaviour. Moreover, the properties of the biological flocs do not only determine the sedimentation or settling rate; they also alter the rheology of the suspension. As a result, a different laminar momentum transfer between neighbouring fluid parcels is obtained. Due to the importance of sedimentation and rheology, their modelling will be thoroughly discussed in the next two sections.

2.2.3.1 Modelling of solids settling

At the end of the 19th century, theories about how a settling tank actually works had already been developed, but no experimental evidence was forthcoming. Only in 1889, Seddon demonstrated experimentally that gravitation was the driving force acting differently on each class of particle sizes. He further showed the importance of differential settling. Much of the theory of gravitational sedimentation has been based on the later work of Coe & Clevenger (1916), and Kynch (1952). The former authors first defined the existence of four settling zones during batch settling. The following zones were recognised, (i) clear supernatant, (ii) initial-concentration zone, (iii) graded-concentration zone, and (iv) sediment (Figure 2.4). As the initial slurry starts to settle a sharp interface is typically observed; clear supernatant is observed on top of a zone characterised by the initial solids concentration. Due to this settling particles meet the bottom where they reside. Here, compression by the accumulating solids presses the water from between the particles. The sediment and the initial-concentration zone are separated by a transition zone with a graded concentration.

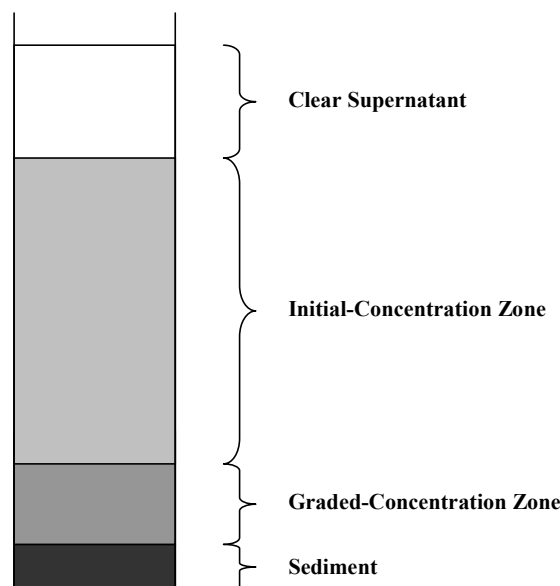


Figure 2.4 Four settling zones as observed during batch settling

In their analysis, Coe & Clevenger (1916) assumed the settling velocity to be constant in the initial-concentration zone. Kynch (1952) continued the work of Coe & Clevenger (1916) and expected that a first-order partial differential equation would describe the entire sedimentation process in the vertical direction y , i.e.

$$\frac{\partial X}{\partial t} + \frac{\partial(v_s X)}{\partial y} = 0$$

where X is again the solids concentration, y the vertical coordinate, and v_s the settling velocity of solids. Kynch's equation was based on, (i) the continuity balance in the vertical direction, and (ii) the settling velocity being solely dependent on the local solids concentration. This velocity is independent of the particle size distribution since all particles are hydrodynamically linked to each other; i.e. they settle as a whole and hinder each other in their movements. According to Fischerström *et al.* (1967), this phenomenon of so-called *hindered settling* occurs at sludge volumes above 100 ml/l. Buscall *et al.* (1987) stated that the critical volume fraction can be anywhere between 0.05 and 0.3 for spherical particles; in the case of highly irregular particle shapes it can be as low as 0.01. In the last decades, many models have been proposed to describe this hindered settling. In literature, models for low and highly concentrated suspensions are distinguished.

In his derivations, Kynch (1952) neglected the momentum equation for the solids. Hence, the compression zone could not be described accurately; only the interface could be predicted. The cause of this inconsistency was the Kynch assumption that the settling is function solely of solids concentration. However, Michaels & Bolger (1962) and Kos (1978) showed that it was dependent on the concentration gradient as well. In this respect, Tiller (1981) extended Kynch's work by properly describing the rise of the suspension-sediment interface by means of the momentum equation for the solids. Tiller's procedure, however, is very complicated. It involves trial and error selection of a set of characteristic lines such that the integrated amount of solids crossing the suspension-sediment interface, plus the amount remaining in suspension, equals the amount originally present in the suspension. Fitch (1983) came to a simpler geometric construction using additional relationships present in Kynch's theory.

Fitch (1979, 1993) showed that the general differential equation, which defines the force balance on the particles, can be utilised in the derivation of most thickening theories presented in literature. To obtain solutions for this equation, typically, various terms are neglected and/or various assumptions are made concerning the constitutive relations (Fitch, 1979; Font, 1988). Mostly, the assumptions concern the definitions of the liquid pressure gradient and the solids stress; the latter is related to pressures originating from particle contact. The liquid pressure gradient can be calculated assuming a Darcian flow through the sediment (Michaels & Bolger, 1962; Cacossa & Vaccari, 1994). Darcy's law formulates the pressure gradient as

$$\frac{\partial p}{\partial y} = k_r v_s$$

where k_r is the resistivity. Whereas the Michaels & Bolger model assumes that both resistivity and solids stress depend on the solids concentration, the Kos model (Kos, 1978)

makes both variables also function of the pressure gradient. In this respect, the flow does not behave in a Darcian way anymore. Although the Kos model is more generally valid, Cacossa & Vaccari (1994) used the Michaels & Bolger model and were able to calibrate it to settling experiments. On the other hand, Zheng & Bagley (1998, 1999) suggested that the mentioned stress is a function of both the local concentration and the rate of change in concentration. With their model, the authors were able to describe hindered settling and compression with the same set of parameters. They also mentioned that the newly introduced parameters are related to solids properties, and not to the operating conditions. Recently, Kinnear (2002) continued this issue of compression modelling by including fundamental solids properties.

The settling tank performance and capacity are clearly affected by the sludge's ability to settle and compact. For that reason, an extended literature was made on the modelling of both hindered and single-particle (discrete) solids settling. A review is given in the next two sections. Finally, a short literature review is given about the use of settling models in CFD.

Discrete settling

The single-particle or discrete settling velocity is mostly expressed as a function of particle characteristics, e.g. porosity, shape factor (ξ), equivalent diameter (D), longest dimension (L) or longest dimension perpendicular to the settling direction (L_p). Amongst many models in literature, Li & Ganczarczyk (1987) proposed the following expressions for the discrete settling velocity $v_{s,d}$:

$$v_{s,d} = a + bL$$

$$v_{s,d} = aL^n$$

The correlation coefficients were high and relatively close to each other, i.e. 0.90 and 0.88. The authors also noted that the non-linear model better describes the relationship for very small particles since it predicts zero velocity when L approaches zero. Hoffmann *et al.* (1999) found a similar expression as the power model of Li & Ganczarczyk (1987), but the variable used is the equivalent diameter. Besides the above relations, Ganczarczyk (1994) discussed a series of expressions for settling. It turned out that

$$v_{s,d} = \frac{a}{\xi} + bD$$

resulted in the highest correlation coefficients (0.95). The two-dimensional shape factor ξ was defined as

$$\xi = \frac{4\pi \text{ surface}}{\text{perimeter}}$$

and could be fitted to the data of Ganczarczyk (1994) with a correlation of 0.95 as

$$\xi = a \left(\frac{1}{L} \right)^n .$$

Finally, Dyer & Manning (1999) mentioned an interesting relation that incorporates the floc fractal dimension D_f ,

$$v_{s,d} = D_f^{D_f - 1}.$$

This fractal dimension describes and is related to the fractal properties of the floc, i.e. the floc shows a specific structure that recurs at progressively smaller scales. Whereas, for instance, a solid sphere has three dimensions, a fractal object generally has a non-integer dimension that is less than three.

Hindered settling

Firstly, suspensions characterised by low solids fractions ($\ll 1$) can be described by Einstein's formula for settling velocities (Kynch, 1952), i.e.

$$v_s = v_{s,d} \left(1 - a \frac{X}{\rho_s} \right)$$

where $v_{s,d}$ is the settling velocity of a single particle in an unbounded flow; ρ_s is the solids density, and a is a lumping factor incorporating particle shape, particle arrangement, etc... Batchelor (1972) continued Einsteins work and obtained a value of 6.55 for a . This was valid for a homogeneous solution of identically small rigid and spherical particles where the ratio particle radius to interparticle distance is larger or equal than 8. A regular arrangement of the particles was assumed.

Another model was presented by Richardson & Zaki (1954), which is widely applied within the field of computational sciences (e.g. Martin *et al.*, 1995). They proposed the following empirical formula,

$$v_s = v_{s,d} \left(1 - \frac{X}{\rho_s} \right)^n$$

According to Lavelle & Thacker (1978), n ranges between 4 and 9. An extension of the model towards polydisperse suspensions was given by Bürger *et al.* (2000).

Further, particle porosity is important to consider because of reduced drag forces. In this respect, Smith (1998) proposed a new theoretical model that is based on permeation of fluid through the particle matrix. With his approach the author was able to describe the increased settling velocities at very low solids fractions (~ 0.01). The settling velocity might indeed reach values of 1.5x the single particle settling velocity due to transitory formations of particles.

In literature many models are based on the previously mentioned settling velocity models (e.g. Head *et al.*, 1997; Höfler *et al.*, 1999). To indirectly include the effect of flocculation on hindered settling, Malcherek (1994) used the following relation for settling velocity,

$$v_s = aX^b \frac{1+cG}{1+dG^2}$$

where a , b , c and d are fitted parameters; and G is the average velocity gradient. It is this velocity gradient that indicates the degree of flocculation.

Secondly, at higher solids concentrations other settling velocity functions can be used. The most important ones are reviewed in Table 2.3. Although Grijspeerdt *et al.* (1995) identified the function of Takács *et al.* (1991) to be the best, the function of Vesilind (1968) is most frequently used (Ekama *et al.*, 1997; Bye & Dold, 1998). Furthermore, the Takács function can be approximated by the Vesilind function for solids concentrations prevailing in the solids blanket (Watts *et al.*, 1996). The obvious advantage of the Takács model is the description of the settling behaviour in both the hindered and clear-supernatant zone; discrete settling prevails in the latter zone.

Table 2.3 Velocity functions for hindered settling

settling velocity	reference
$v_s = v_0 e^{-r_h X}$	Vesilind (1968)
$v_s = v_0 \left[e^{-r_h(X-X_0)} - e^{-r_p(X-X_0)} \right]$	Takács <i>et al.</i> (1991)
$v_s = a \frac{(1-bX)^4}{X}$	Cho <i>et al.</i> (1993)
$v_s = a \frac{e^{-nX}}{X}$	Cho <i>et al.</i> (1993)

v_0 : maximum settling velocity at zero solids concentration

r_h : parameter characteristic for the hindered settling zone

r_p : characteristic settling parameter at low solids concentrations

X_0 : solids concentration below which no settling occurs

a , b : empirical constants

A comparison between six different settling functions was made by Cho *et al.* (1993); however, the Takács function was not considered. It seemed that the exponential model of Cho *et al.* (1993) is superior to the power function of the same authors. On the other hand, Vanderhasselt & Vanrolleghem (2000) compared the exponential function of Cho *et al.* (1993) with the Vesilind and Takács functions. It turned out that the Cho function was better performing in describing entire batch settling curves, whereas the Vesilind function was more efficient in describing the relationship between v_s and X .

Solids settling in CFD models: state-of-the-art

Much research has been done on primary settling tanks where the solids concentration is limited and discrete settling prevails. In this respect, Brouckaert & Buckley (1999) only investigated the flow field without considering particles. Instead, Imam *et al.* (1983) and Larock *et al.* (1983) applied a fixed settling velocity. Because different particle sizes are present in the suspension an averaged velocity was used. More advanced is the work of Lyn *et*

al. (1992) that accounts for flocculation; six different size classes with their respective velocities were considered. Instead, De Cock *et al.* (1999) used 15 size classes. Floc breakup was only included heuristically, i.e. it is assumed that the collision efficiency approaches zero for a maximum floc size.

With respect to secondary settling tanks, both discrete and hindered settling need to be considered. Whereas Steindl *et al.* (1998) only modelled the discrete settling above the solids blanket, Krebs *et al.* (1995) focused on hindered settling. However, most CFD research is devoted to the modelling of both settling regimes. In this respect, the Takács settling velocity function is widely used (e.g. McCorquodale & Zhou, 1993; Vitasovic *et al.*, 1997; Lakehal *et al.*, 1999; Stamou *et al.*, 2000; Armbruster *et al.*, 2001; Narayanan *et al.*, 2001). Although the Takács function intrinsically covers both the discrete and hindered settling, Mazzolani *et al.* (1998) employed a linear combination of the relations describing the latter settling regimes. Recently, solids compression models have also been implemented (STOWa, 2002a,b).

2.2.3.2 Modelling of sludge viscosity

According to Frankel & Acrivos (1967), viscosity primarily arises from the flow within the narrow gaps separating the various flocs from one another. Hence, viscosity is believed to originate from the colloidal properties of solids more than from the molecular properties of the suspension (Sanin, 2002). In flocculated systems, in addition to the solids concentration, the particle size distribution and the quantity of water immobilised as interstitial and vicinal water are important in determining viscosity. Firstly, Dabak & Yucel (1987) demonstrated the major influence of particle size distribution on viscosity. They only considered the mean diameter of the distribution, hence, no rigorous relation could be drawn between viscosity and particle size distribution, although a strong influence was observed. Instead, for identical concentrations, Bhattacharya *et al.* (1992) clearly observed higher viscosities for smaller particles; they did not consider biological sludges but flour suspensions though. Secondly, vicinal water always exists on the surface of flocs, but its quantity is determined by the physical and chemical properties of the surface. Interstitial water, on the other hand, is trapped inside the flocs because of flocculation. In this respect, Li & Ganczarczyk (1990) took into account bound water and mentioned effective porosities of 84%. Without bound water, porosity accounted for up to 99%. Nevertheless, flows through biological flocs hardly exist (Li & Yuan, 2002); hence, small contributions to viscosity can be expected.

From the previous it is clear that not only the solids concentration determines the viscosity, but many other factors have to be considered (Jeffrey & Acrivos, 1976). Besides the solids concentration, Sanin (2002) investigated different influences like pH, conductivity and extracellular polymers. It was found that they all impact viscosity. Also temperature has a major influence and can be described with an exponential model (Manoliadis & Bishop, 1984; Battistoni *et al.*, 1993; Battistoni, 1997; Balmforth & Craster, 2002).

Due to the macroscopic particulate structure sufficient stress has to be applied to make the suspension flow (e.g. Coussot *et al.*, 1996); this threshold stress is called the *yield stress*. This phenomenon is most likely to appear in sludges with high solids concentrations (Dentel, 1997). However, the real existence of yield stress has been the subject of numerous

discussions. It seems to depend on the mechanical history of the sample (Buscall *et al.*, 1987). Further, Campbell & Cresciolo (1982) questioned the usefulness of the numerical value of the calculated yield stress. Actually, the value largely depends on the method to determine this yield stress and the sensitivity of the rheometer. In fact, Barnes & Walters (1985) showed that the yield stress only defines *what cannot be measured*. With constant stress rheometers a very high viscosity was demonstrated at extremely low shear rates, and a transition exists between the high and low shear rates that are applied in the measurement (Figure 2.5, left). But under common conditions of observation, there generally occurs an abrupt change in behaviour around a given shear stress value that is called the yield stress (Figure 2.5, right). Below this critical stress the fluid is deformed in an essentially elastic manner. Above this critical value the fluid flows (Coussot *et al.*, 1996).

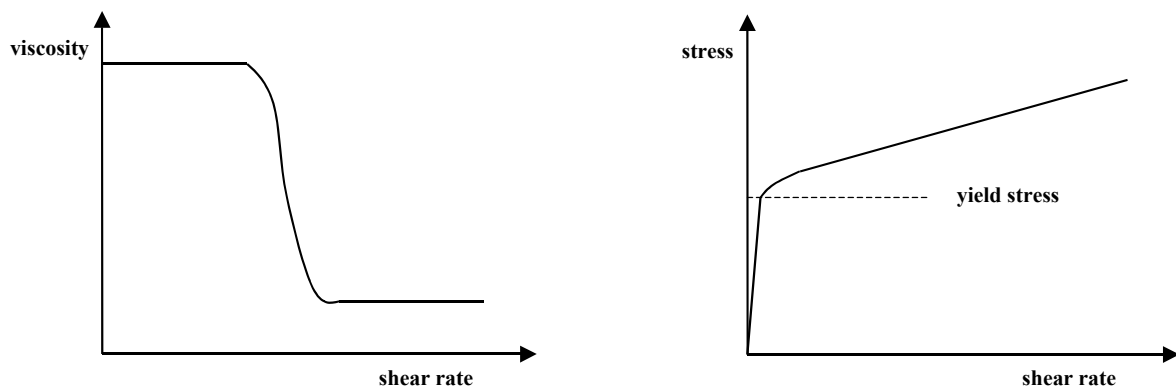


Figure 2.5 The mythology of yield stress: viscosity-shear rate (left), and shear rate-shear stress relation (right) (Barnes & Walters, 1985)

The next section will deal with rheological modelling. Many models have been extensively used in literature, and will be reviewed here. In general, history effects are not mentioned explicitly for sludge systems but have been considered in other research fields. These will be discussed as well. For applications the reader is referred to Chapter 7.

Water is one of the many examples of fluids that acts as a so-called *Newtonian fluid*, i.e. its viscosity is independent of the applied shear rate. In general, the shear stress (τ) can be written as,

$$\tau = \mu \dot{\gamma}$$

where μ and $\dot{\gamma}$ refer to the dynamic viscosity and shear rate respectively. Unfortunately, particulate suspensions rarely behave as Newtonian fluids and can show complex flow phenomena. Therefore, they are called *non-Newtonian fluids*. From a physical-mathematical derivation Levy & Sanchez-Palencia (1983) concluded that these altered fluid mechanics are due to the action of the bulk flow on the particulate microstructure. In literature, many fundamental viscosity models based on lubrication theory have been proposed for concentrated suspensions; they calculate the energy dissipated in the neighbourhood of the small gaps between the particles. The results are then extrapolated over the entire suspension such that the need to calculate the entire flow field around the particles is

avoided (Jeffrey & Acrivos, 1976). Examples can be found in Frankel & Acrivos (1967), Barthés-Biesel & Acrivos (1973), and Coussot *et al.* (1996). Based on such fundamental models, Brenner (1974) emphasised that viscosity greatly depends on particle size and shape. Frankel & Acrivos (1967) also mentioned the importance of particle size distributions in order to obtain successful rheological models. Their impact has been experimentally observed by Campbell & Crescuolo (1982) and Dabak & Yuçel (1987).

Although such fundamental models provide insight in the physics of the process, they are not practical. Numerical simulations of multiphase flows are already very computationally demanding, let alone if the particle size distributions have to be simulated as well. For that reason, it is generally acknowledged that the complexity of the model used in non-Newtonian fluid mechanics has to be inversely proportional to the complexity of the flow problem (Crochet, 1983). Hence, the models employed must be relatively simple. Shear data for various natural or industrial slurries, like biological sludges, have often been well presented with the help of simple models. A classification of non-Newtonian fluids may, for instance, be based on whether or not the relationship between shear stress and shear rate is dependent on time. This will be discussed in the two sections below.

Time-independent non-Newtonian fluids

For time-independent non-Newtonian fluids some possible relationships between shear stress and shear rate are given in Table 2.4. The different flow behaviours are graphically shown in Figure 2.6.

Table 2.4 Some shear stress-shear rate relationships

fluid	relationship stress-shear rate
Newtonian	$\tau = \mu\dot{\gamma}$
Shear - thinning ($n < 1$) (pseudoplastic)	$\tau = K\dot{\gamma}^n$
Shear - thickening ($n > 1$) (dilatant)	
Herschel - Bulkley ($0 < n < \infty$)	$\begin{cases} \tau = \tau_0 + K\dot{\gamma}^n & \tau \geq \tau_0 \\ \dot{\gamma} = 0 & \tau < \tau_0 \end{cases}$
Bingham plastic ($n = 1$)	

In the table, four non-Newtonian fluids are compared to the Newtonian type. The category which closely resembles Newtonian flow is that of the Bingham plastics. The difference is that fluid movement is not initiated until a certain minimum shear stress is overcome, i.e. the previously mentioned yield stress. In 1960 already, Behn already classified sewage sludges as Bingham fluids. Sozanski *et al.* (1997) also applied this type of model for thickened sludge. Others employed both Bingham and pseudoplastic models (Battistoni, 1997; Lotito *et al.*, 1997), while Manoliadis & Bishop (1984) only applied the pseudoplastic model. Different models have been compared by Sanin (2002) and for his type of sludge the pseudoplastic model appeared to fit the best.

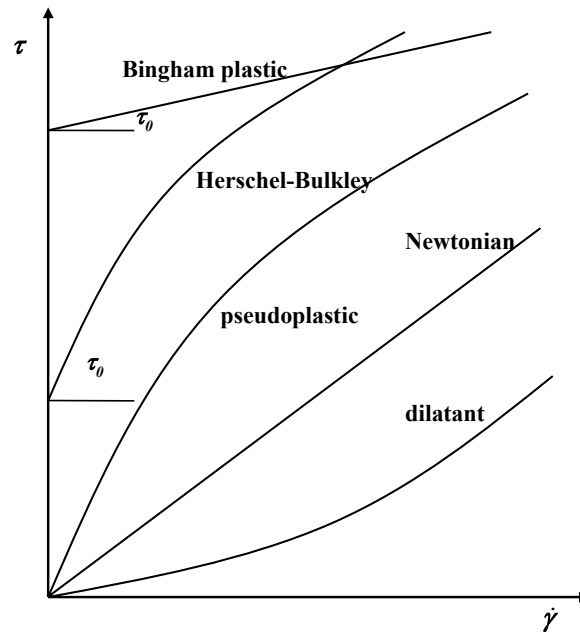


Figure 2.6 Newtonian and non-Newtonian flow behaviours

Another class of non-Newtonian fluids, the dilatant fluids, exhibit a behaviour which is opposite to that of the pseudoplastic fluids (Figure 2.6). According to Behn (1960), this flow type does not appear in wastewater treatment. A pseudoplastic flow with yield stress is called a *Herschel-Bulkley fluid*. In this respect, Monteiro (1997) performed a comparison between this and the Bingham model; a better fit with the Herschel-Bulkley model was obtained.

Although all mentioned models have been successfully fitted to rheological data, the appropriate model largely depends on the sludge properties, for instance, a yield stress is only observed at high solids concentrations. Other parameters such as the specific floc surface have been investigated as well (Dymaczewski *et al.*, 1997), but the solids concentration appears to be the most important variable related to viscosity in a quantitative and easy (practical) way.

Concerning Bingham flow, a power model has been proposed to relate the yield stress to solids concentration. According to Buscall *et al.* (1987), Dabak & Yucel (1987), Battistoni (1997) and Dymaczewski *et al.* (1997), such model is valid for both inorganic and organic particulate suspensions. In literature, exponential models can be found too (Battistoni *et al.*, 1993; Battistoni, 1997; Sozanski *et al.*, 1997). Instead, Bokil (1972) applied the exponential model to the fluid consistency index K . Power and exponential models are also widely used to model the apparent viscosity, i.e. $\tau/\dot{\gamma}$ (Battistoni *et al.*, 1993; Battistoni, 1997; Fitzpatrick *et al.*, 2002). Battistoni (1997) even correlated the apparent viscosity to operational process parameters, such as loading rate. Besides a power model, Lotito *et al.* (1997) mentioned an alternative relation for the yield stress and the fluid consistency index. Depending on the type of sludge a polynomial of second order fitted better than the previous models.

The same authors also applied their power and quadratic model to sludges exhibiting pseudoplastic flow behaviour. For this type of rheology, exponential relations have been used by Sanin (2002).

Concentration dependencies of parameters of the Herschel-Bulkley model are rare in literature. In this respect, Slatter (1997) suggested a relation between solids concentration and the different model parameters, i.e.

$$\tau_0 = a \frac{X^3}{X_m - X}$$

$$K = \mu_{water} \left(1 - \frac{X}{X_m} \right)^{-m}$$

$$n = b_1 X^2 + b_2 X + 1$$

where a , b_1 , b_2 , X_m are empirical parameters.

Time-dependent non-Newtonian fluids

Most sludges are rheologically characterised by time-dependent thinning, i.e. at a constant shear rate, the viscosity decreases in time. Time-dependent thinning is an often overlooked issue, which can be reversible (thixotropy) or irreversible (rheomalaxis or rheodestruction). Time-dependent thickening or rheopectic fluids are not considered here because thickened sludge does not show this flow behaviour. The time-variant viscosity is a consequence of a rearrangement of the floc structure (Buscall *et al.*, 1987). The extent of this structural breakdown depends on both the magnitude of the shear rate and the exposure time of the sludge. Actually, the stress required to destroy the sludge's structure may be divided in three components (Holdsworth, 1993; Dentel, 1997); (i) the stress required to disrupt the large-scale floc network, (ii) the force to overcome viscous stresses, and (iii) the stress needed to break interparticle bonds.

From the above, it becomes clear that the shear history is very important to describe the rheological behaviour of sludges.

The above-mentioned gradual attrition of the structure obviously causes the viscosity to decrease in time; the result is a non-linear stress-shear rate behaviour. Time-dependent thinning can be easily detected by investigating the occurrence of hysteresis in the rheogram (Figure 2.7); in this experiment the shear rate is successively increased and decreased over a certain range of shear rates. From Figure 2.7 the viscosity clearly decreases with increasing shear rate. Sometimes the viscosity might even decrease to 10^{-3} or 10^{-4} of the zero-shear-rate viscosity (Bird, 1976). Further, it is observed that the rheograms of respectively increasing and decreasing shear rates are conceptually the same, i.e. the structure reforms in the same way as it disintegrated. However, the stress-shear rate relation is not identical for the two cases. The area enclosed by this hysteresis loop defines the magnitude of the time-dependent thinning (Battistoni *et al.*, 1993; Steffe, 1996). According to Battistoni (1997), the latter shows a power model with solids concentration as independent variable. In another publication though (Battistoni *et al.*, 1993), the same authors apply an exponential model.

Most experience about time-dependent rheological behaviour originates from food sciences. An overview of the different models can be found in Steffe (1996) and Bhattacharya (1999).

Although appropriate, they will not be discussed here for the sake of clarity; the reader is referred to Chapter 7 where more information about this issue is provided.

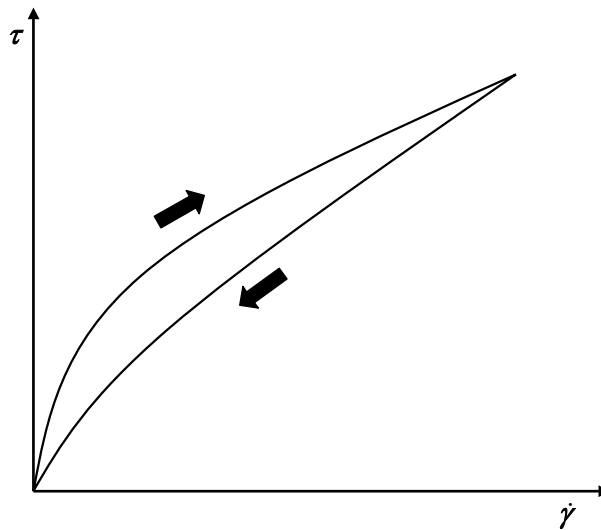


Figure 2.7 Typical "up-down" rheogram illustrating hysteresis

Sludge viscosity in CFD models: state-of-the-art

In the past, the rheological behaviour of sludge was not included in settling tank CFD models. At that time, CFD work was mainly focused on primary settling tanks, in which buoyancy does not dampen turbulence considerably. As a consequence, the eddy viscosity is much larger than the sludge viscosity. Therefore, much CFD work simply excludes the latter viscosity from the momentum equations. Examples can be found in, for instance, Stamou *et al.* (1989), Adams & Rodi (1990), Krebs *et al.* (1995) and Vitasovic *et al.* (1997). On the other hand, Krebs *et al.* (1995) assumed the eddy viscosity in a secondary settling tank to be 100 times the sludge viscosity. The authors based their assumption on the work of Imam *et al.* (1983). Whereas Krebs *et al.* (1995) and Deininger *et al.* (1998) applied a constant eddy viscosity, Imam *et al.* (1983) used a simple algebraic equation involving the depth of the inlet baffle and the velocity under this baffle.

Nowadays, the $k-\varepsilon$ turbulence model is widely accepted to compute the eddy viscosity for settling tanks. Due to turbulence damping by buoyancy in the solids blanket (see Section 2.2.2.4), the eddy viscosity becomes equal to and/or smaller than the sludge viscosity; hence, the sludge viscosity cannot be excluded anymore from the model. As a result, modelling flows in the solids blanket demands the inclusion of some appropriate rheological model for sludge viscosity. In general, a Bingham model is used. However, Dahl (1993), and subsequently applied by Lakehal *et al.* (1999) and Armbruster *et al.* (2001), modified the yield stress to fit the simulated velocity profiles to the observations. As will be discussed in Chapter 7, this modified yield stress is believed to be too large and physically unrealistic.

2.2.4 Boundary and operational conditions

Before any simulation can be performed the system has to be defined by both operational and boundary conditions. The former covers turbulence, sedimentation and rheology phenomena in the settling tank discussed in the previous sections. To complete the mathematical description of the model, boundary conditions for all unknown dependent variables are required as well. These unknown dependent variables are the velocity components, the pressure, the kinetic energy associated with the turbulent motion of the flow, the turbulent energy dissipation rate and the solids concentration. The different imposed boundary conditions are discussed below.

2.2.4.1 Rigid walls

Turbulent flows are significantly affected by the presence of walls. Obviously, the mean velocity field is influenced by the no-slip condition that has to be satisfied at the wall. However, the turbulence is also altered by the presence of walls in other ways. Very close to the wall, viscous damping reduces the tangential fluctuations, whereas the wall reduces the normal fluctuations. Further away from the wall, however, the mean velocity field is largely determined by the turbulent core flow.

Numerous experiments have shown that the near-wall region can be subdivided into three layers (White, 1991). In the innermost layer, the so-called *viscous sublayer* or *inner layer*, the flow is almost laminar, and the molecular viscosity plays a dominant role in momentum and mass transfer. In the outer layer, on the other hand, turbulence plays a major role. At the top-end of this layer the velocity equals the free-stream fluid velocity u_e . Finally, there is an overlap layer where both types of shear are important, i.e. molecular viscosity and turbulence are equally effective. These three layers are visualised in Figure 2.8. Typically, the boundary layer is studied in terms of dimensionless wall distances, i.e. $y^+ \equiv \rho u_\tau y / \mu$. Here, u_τ is the wall-friction velocity, being equal to $(\tau_w / \rho)^{1/2}$, and τ_w is the wall shear stress.

Traditionally, there are two ways to model this near-wall region. Firstly, the turbulence models may be modified to enable the viscosity-affected region, i.e. the viscous sublayer and overlap region, to be resolved with the mesh all the way to the wall. Of course, this approach demands considerable computational power. The second approach does not resolve the viscosity-affected inner region. Instead, semi-empirical formulas, so-called *wall functions*, are used to bridge or link this region between the wall and the fully-turbulent region. The use of these functions obviates the need to modify the turbulence models to account for the presence of the wall. By means of them, the mean fluid velocity is calculated in the first computational cell next to the wall. Because a coarser mesh can be retained near the wall, it is clear that the necessary computational power is smaller.

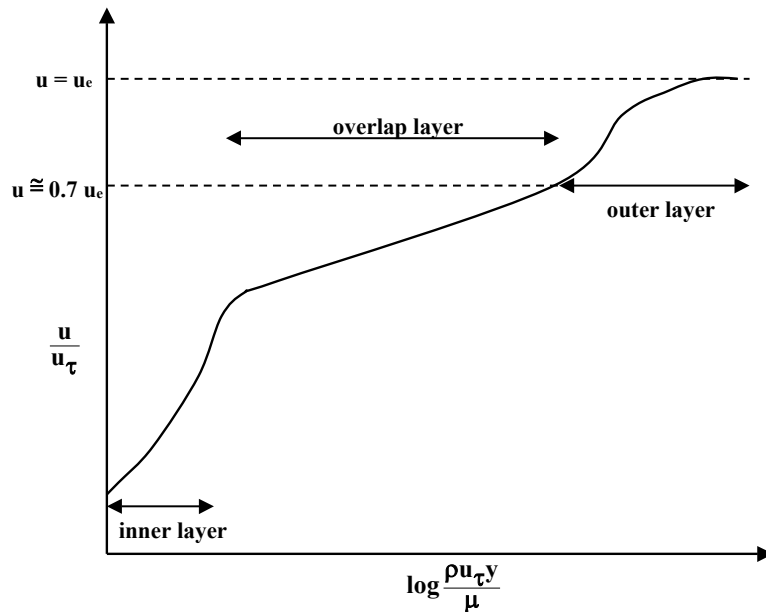


Figure 2.8 Plot of the velocity profile in the boundary layer

Here, the standard wall function of Launder & Spalding (1974) will be discussed. Strictly, this semi-empirical function is only valid for smooth walls. If biofouling is present, the surface roughness would obviously increase and the standard wall function has to be adapted for this roughness. For algae-covered surfaces, Schultz (2000) discussed increases of approximately 120% for the friction coefficient compared to the one of a smooth wall. However, Adams & Rodi (1990) pointed out that for real settling tanks the walls can be considered as being smooth due the prevailing low velocities and the correspondingly large viscous layer. Consequently, the standard wall function is accepted in literature (Adams & Rodi, 1990; Zhou & McCorquodale, 1992c; Krebs *et al.*, 1995; Mazzolani *et al.*, 1998; Armbruster *et al.*, 2001) and is used in this work as well. This wall function for the mean velocity reads (White, 1991)

$$\frac{u}{u_\tau} = \frac{1}{\kappa} \ln(Ey^+) \quad (2.6)$$

where, as defined before,

$$u_\tau \equiv \left(\frac{\tau_w}{\rho} \right)^{\frac{1}{2}}$$

$$y^+ \equiv \frac{\rho y u_\tau}{\mu}$$

and

κ = von Kármán constant, i.e. 0.41 [-]

E = empirical roughness parameter, i.e. 9.81 (for hydraulically smooth walls) [-]

u = mean velocity of the fluid in the computational cell next to the wall

y = distance from the first computational cell to the wall

The logarithmic law for mean velocity is known to be valid for y^+ larger than 30. However, when the mesh is such that y^+ is smaller than this value, the following velocity profile is applied:

$$\frac{u}{u_\tau} = y^+.$$

In literature, modifications of the standard wall function also occur. In this respect, Lakehal *et al.* (1999) altered the formulae to account for the buoyancy production source in the near-wall production of k . On the other hand, Samstag *et al.* (1992) assumed a partial-slip boundary with normal velocities set to zero. It should be noted that this was required to compensate for the failure of the Richardson-number-dependent eddy viscosity. In this way, the velocity distribution near the solid boundary was more properly represented.

Concerning the boundary condition for the solids concentration at the walls, a zero normal flux is taken (Stamou *et al.*, 1989; Ekama *et al.*, 1997; Mazzolani *et al.*, 1998; Lakehal *et al.*, 1999). Like walls, deflectors and baffles are modelled as reflecting boundaries (Imam *et al.*, 1983; Stamou *et al.*, 2000), i.e.

$$\frac{\partial X}{\partial n} = 0$$

where n is the direction perpendicular to the boundary. Instead, Devantier & Larock (1986) allowed a certain fraction of solids to resuspend by the local turbulence.

Identically to the solids concentration, the software used (Fluent 6, Fluent Inc., UK) by default applies a zero normal gradient for the turbulence kinetic energy. Instead, the energy dissipation at the wall-adjacent cells is by default calculated as

$$\varepsilon = \frac{c_\mu^{\frac{3}{4}} k^{\frac{3}{2}}}{\kappa y}. \quad (2.7)$$

On the contrary, Rodi (1984), Celik & Rodi (1988), Adams & Rodi (1990) and Zhou & McCorquodale (1992a) used the following boundary conditions for turbulence properties at the wall

$$k = \frac{u_\tau^2}{c_\mu^{\frac{1}{2}}} \quad \text{and} \quad \varepsilon = \frac{u_\tau^3}{\kappa y}. \quad (2.8)$$

The boundary conditions in Equation 2.8 are computed from a negligible advective and diffusive transport of Reynolds stresses near the wall. The energy dissipation rate as described by Equation 2.7 is based on the latter boundary condition.

2.2.4.2 Bottom boundary and solids removal mechanism

The velocity normal to the bottom is either zero (Stamou *et al.*, 1989; Ekama *et al.*, 1997) or there is an imposed (vertical) withdrawal velocity equal to the underflow flow rate divided by the total bottom surface (Krebs *et al.*, 1996; Ekama *et al.*, 1997; Stamou *et al.*, 2000).

The velocity distribution parallel to the bottom floor is generally described by means of the standard wall function as described in the previous section (Samstag *et al.*, 1992; Krebs *et al.*, 1996; Ekama *et al.*, 1997). To account for the operation of the scraper, a fixed vertical velocity can be imposed as mentioned before. The sludge is then continuously removed over the entire floor area. Another solution is to apply a fixed velocity in the wall-adjacent cells, thus parallel to the floor; this might be either radial (Krebs *et al.*, 1995) or tangential (Szalai *et al.*, 1994). On the other hand, Deininger *et al.* (1998) applied a frictionless tank bottom to model the scraper. Of course, the best results are obtained by including the geometry of the scraper in a 3D model of the settling tank (Botsch, 1990; Winkler *et al.*, 1999). However, this demands for considerable computational power. If a sludge hopper is modelled, a fixed velocity perpendicular to the boundary is specified (Lakehal *et al.*, 1999; Richardson *et al.*, 2000; Stamou *et al.*, 2000; Armbruster *et al.*, 2001).

Concerning the boundary condition for the solids concentration, a zero gradient normal to the bottom floor is accepted in many cases (Stamou *et al.*, 1989; Krebs *et al.*, 1996). The floor can also act as an absorbing boundary where particles may not be resuspended from (Stamou *et al.*, 1989; Mazzolani *et al.*, 1998).

A completely different approach to model the floor can be found in, for instance, Larock *et al.* (1983), Zhou & McCorquodale (1992a) and McCorquodale & Zhou (1993). Here, the floor and the solids blanket were excluded from the computational domain. The solids concentration at the bed boundary was obtained by a mass balance around it. Based on the work of Takamatsu *et al.* (1974) they were able to empirically include solids resuspension. However, this approach is not mass conservative (Ekama *et al.*, 1997).

2.2.4.3 Free Surface

The rigid-lid approximation assumes that there is negligible change in water surface elevation. It is obvious that this approximation simplifies the solution by eliminating the difficulty of calculating the water surface position. Further, the free surface is considered as a symmetry plane. Hence, the normal velocity component is zero. Also, the normal gradients of horizontal velocity and turbulence kinetic energy are zero. These assumptions are generally applied in literature, e.g. Zhou & McCorquodale (1992c), Szalai *et al.* (1994), Krebs *et al.* (1996), Mazzolani *et al.* (1998), Stamou *et al.* (2000) and Armbruster *et al.* (2001).

For the turbulence energy dissipation a symmetry plane was accepted by Devantier & Larock (1986). However, because the free surface reduces the turbulent length scale, the following empirical boundary condition is much used (Celik & Rodi, 1988; Zhou & McCorquodale, 1992b,c; McCorquodale & Zhou, 1993), i.e.

$$\varepsilon = \frac{k^{\frac{3}{2}}}{0.43H}$$

where H is the water depth. This empirical relation replaces the reflective surface boundary condition, which yields unrealistically small energy dissipations due to the low velocity gradients near the surface (Ekama *et al.*, 1997).

For the solids concentrations, no net transport occurs across the surface boundary, thus

$$\frac{v_t}{\sigma_s} \frac{\partial X}{\partial y} + v_s X = 0$$

as proposed by Imam *et al.* (1983) and Celik & Rodi (1988) can be used. The formula results from the solids transport equation in open channel flows which is assumed to be completely developed, i.e. a zero gradient parallel to the free surface exists. As a first approximation, it can be applied in settling tanks as well. Examples of its use can be found in Devantier & Larock (1986), Stamou *et al.* (1989), Zhou & McCorquodale (1992b,c) and McCorquodale & Zhou (1993).

2.2.4.4 Inlet boundary

Most numerical models impose a uniform solids concentration, and velocity across the inlet boundary and perpendicular to it (e.g. Zhou & McCorquodale, 1992c; McCorquodale & Zhou, 1993; Ekama *et al.*, 1997; Steindl *et al.*, 1998; Stamou *et al.*, 2000; Armbruster *et al.*, 2001). Instead, Samstag *et al.* (1992) applied a measured velocity distribution below the flocculator wall. Consequently, they did not model the inlet structure.

Concerning the turbulence properties at the inlet, constant profiles for the turbulence kinetic energy and the energy dissipation are typically adopted. For the turbulence kinetic energy, different approaches can be found in literature. Firstly, this energy can be written in terms of the inlet velocity u_{inlet} , i.e.

$$k_{inlet} = \alpha u_{inlet}^2$$

where α is an empirical constant. In many cases, a value of 0.2 is accepted for this parameter (Celik *et al.*, 1987; Zhou & McCorquodale, 1992a,b; McCorquodale & Zhou, 1993; Ekama *et al.*, 1997). Instead, Adams & Rodi (1990) applied a value of 0.03; their choice was based on measurements. Another approach can be found in Lakehal *et al.* (1999) who used the following relation

$$k_{inlet} = 1.5(T_u u_{inlet})^2,$$

where T_u is the turbulence intensity that is given by

$$T_u = \frac{\sqrt{u'^2}}{u_{inlet}}$$

Here, u' is the fluctuation of the velocity parallel to the boundary. A value of 0.224 is adopted for the turbulence intensity leading to a ratio of k_{inlet}/u_{inlet} that is between the values suggested by Lyn *et al.* (1992) and Ekama *et al.* (1997). The former authors used a value of 0.075 for α . Lastly, instead of the inlet kinetic energy, the turbulence intensity can be specified at the inlet. According to literature, the turbulent intensity might vary between 7 and 30 % (Lyn & Rodi, 1990; Lyn *et al.*, 1992; Szalai *et al.*, 1994; Lakehal *et al.*, 1999).

Noteworthy, Adams & Rodi (1990) showed that the exact values of the turbulence kinetic energy and energy dissipation at the inlet are rather unimportant for the mean flow and the eddy viscosity as long as the eddy viscosity at the inlet is greater than about 10x the kinematic viscosity. For that reason, Wang & Falconer (1998) applied zero values for the turbulence kinetic energy and energy dissipation at the inlet.

Besides zero values, some common formulae for the inlet energy dissipation rate can be found in literature. Zhou & McCorquodale (1992b,c), McCorquodale & Zhou (1993) and Ekama *et al.* (1997) described the inlet turbulence dissipation rate as

$$\varepsilon_{inlet} = \frac{c_\mu^3 k_{inlet}^3}{l_m}$$

with the mixing length l_m taken as

$$l_m = c_\mu (0.5 L_{inlet})$$

where L_{inlet} is the width of the inlet slot, and c_μ is the turbulence parameter as defined in Table 2.4. Instead, Adams & Rodi (1990) applied a slightly higher energy dissipation, i.e. the experimentally obtained constant was slightly larger. A different definition of mixing length was used by Lakehal *et al.* (1999). The following relation was proposed:

$$l_m = \kappa l_u$$

where the turbulent length scale l_u was estimated to be 0.5x the distance from inlet aperture to inlet baffle, which is somewhat higher than recommended in Ekama *et al.* (1997). However, Lakehal *et al.* (1999) noted that their simulations were not sensitive to any variation of l_u .

2.2.4.5 Outlet boundary

At the outlet the values of all variables are simply extrapolated from computed near-outlet values, which is similar to a zero-gradient-type condition (Lyn *et al.*, 1992). This approach was also adopted by many other researchers such as Zhou & McCorquodale (1992b), Szalai *et al.* (1994), Krebs *et al.* (1995), Mazzolani *et al.* (1998) and Stamou *et al.* (2000). Obviously, the

additional conditions that overall continuity and the solids mass balance have to be always satisfied, need to be fulfilled.

When dealing with circular settling tanks the radial velocity requires compensation for the increasing flow cross section (Lakehal *et al.*, 1999; Armbruster *et al.*, 2001). Further, instead of applying a zero gradient for all variables, the normal derivatives of velocity (Samstag *et al.*, 1992; Zhou & McCorquodale, 1992a), turbulence (Schamber & Larock, 1981; Krebs *et al.*, 1996) or solids concentration (Krebs *et al.*, 1996) can be set to zero. Here, it is assumed that the outlet flow is perpendicular to the boundary.

Despite all the variation in outlet boundary conditions, Lyn *et al.* (1992) noted that the boundary conditions do not have a large impact on the mean flow field; they only have a local effect, i.e. near the outlet structure itself.

2.3 Conclusions

As presented in this chapter settling tanks can be modelled in different ways; each is characterised by its own application possibilities and restrictions. In this respect, a distinction can be made according to the spatial dimension that is modelled, i.e. 0D, 1D, 2D or 3D. Here, the technique of computational fluid dynamics was highlighted because it is the topic of this dissertation. In CFD studies, the settling tank is modelled in 2D and/or 3D. The method is able to illuminate the internal hydraulics of the system. To this end, not only the Navier-Stokes equations are needed, but also turbulence and solids transport have to be modelled. For the latter, a drift-flux-like model is mostly applied in literature as described in Section 2.2.3. It was also recognised that knowledge about the behaviour of the suspension is crucial, i.e. information about the sedimentation and rheological properties of the sludge have to be included in the solids and momentum transport models respectively. Besides these operational parameters, no model can be solved without knowledge of the boundary conditions of the system. A literature review on this topic was also covered in the last section of the chapter.

Finally, to solve the large set of partial differential equations, together with the constitutive relations for sedimentation and rheology, a spatial discretisation of the settling tank is necessary. This will be briefly discussed in the next chapter. Also the numerical algorithms to solve the equations will be dealt with.

3 Numerical Computation of Flows

Whereas Chapter 2 deals with the modelling of settling tanks, this chapter focuses on the numerical techniques to solve the resulting set of Partial Differential Equations (PDEs).

Several steps are involved in the computational approach leading from an initial mathematical model to a final numerical solution. The first step, discussed in Chapter 2, is the selection of the level of approximation to the physical problem considered, depending on the required numerical accuracy and the available computational power. The second step is the choice of the discretisation method of the mathematical formulation and involves two components, i.e. the space discretisation and the equation discretisation. The space discretisation consists of setting up a mesh or grid, which replaces the continuous space by a finite number of points. At these points the numerical values of the variables are determined by solving a set of algebraic equations replacing the PDEs. This transformation of equations is the equation discretisation step mentioned. It is obvious that the accuracy of a numerical approximation depends on the size of the mesh, i.e. the better the discretised space approaches the continuous space, the better the approximation of the numerical scheme is. In other words, the error of a numerical simulation evolves to zero when the mesh size tends to zero, and its speed will be characterised by the order of the numerical discretisation of the equations.

As mentioned, once a mesh is defined the equations can be discretised, leading to the transformation of the differential or integral equations to discrete algebraic operations involving the values of the unknowns at the mesh points. The basis of all numerical methods consists of this transformation of the physical equations into an algebraic, linear or non-linear, system of equations. For time-dependent problems an intermediate step is obtained, i.e. a system of Ordinary Differential Equations (ODEs) in time which, through a time-integration scheme (e.g. Euler, Runge-Kutta), will ultimately lead to an algebraic system for the unknowns at a given time level.

When dealing with time-dependent problems, there is obviously no alternative to the use of the time-dependent mathematical model whereby also a time accuracy is required. However, with stationary problems an alternative exists, and the user can decide to work with a time-independent formulation, or apply a time-dependent model, and follow the numerical solution in time until steady state is reached. This last method is often called *time marching* or *pseudo-unsteady*, since the time accuracy is not required in order to reach the steady state in the smallest number of time steps. In this case the numerical schemes are taken from the family of methods for the solution of systems of ODEs in time.

For the discretisation of the time derivative two families of methods can be distinguished, i.e. the explicit and the implicit methods. In explicit methods the unknown variables at the new time in the discretised time derivatives only depend on the flow variables in the advection, diffusion and source terms at the previous times. This therefore leads to a solution with a minimal number of arithmetic operations at each time step. However, this advantage is counterbalanced by the fact that stability and convergence conditions impose severe restrictions on the maximum allowable time step. It therefore leads to the necessity of a large number of small time steps in order to reach the steady-state solution.

In implicit methods, however, unknown variables at the new time not only arise in the time derivatives but also in the other terms of the considered equation. Although a system of implicit equations may pose some computational problems, the discretised equations fortunately result in a rather simple system to resolve. This allows simple algorithms for the solution of the system at each time step, although the number of operations required will be higher when compared with explicit methods. This is compensated by the fact that many implicit methods have, at least for linear problems, no limitation on the time step, and hence, overall, a smaller number of iterations will be needed to reach steady state.

Two families of methods for solving algebraic systems may be distinguished: direct and iterative methods. The former can be defined as leading to the solution of a linear system in one step, while the latter will require many iterative steps. Obviously, for non-linear problems all approaches will necessarily be iterative. Convergence of these iterative schemes is an issue in many cases. Convergence acceleration schemes linked with iterative methods therefore have been developed and have led to important improvements in convergence rates. In this respect, pre-conditioning and multi-grid methods are mentioned.

Finally, all the above steps can strongly interact with each other. The solution techniques for the algebraic system may be largely influenced by the type of discretisation as well as by the flow characteristics. The commercial software used, Fluent (Fluent Inc., UK), gives the user the opportunity to choose from a number of numerical schemes. It was therefore opted to include a chapter that provides a short overview introducing the reader into this large and complicated field of computational fluid dynamics, and provide the background for the selection of methods used in this dissertation. The introductory text below is based on reference works such as Anderson *et al.* (2003), Colella & Puckett (1994), Hirsch (1997, 1998), Lomax *et al.* (2001) and Versteeg & Malalasekera (1995). It is emphasised, however, that this dissertation did not aim for the development of new numerical techniques.

3.1 Discretisation of PDEs

This section will present the three most important techniques to discretise PDEs, i.e. the finite difference method, the finite element method and the finite volume method. Each of these techniques discretises the governing equations in a specific way; however, the discretisation schemes utilised for both time and space can be generalised. Only the way the schemes are obtained differs for each discretisation method. In this section, the properties of discretisation schemes are dealt with as well.

3.1.1 Discretisation techniques

This section discusses the three discretisation techniques available to the modeller, i.e. the Finite Difference Method (FDM), the Finite Element Method (FEM), and the Finite Volume Method (FVM). Whereas the FDM discretises the derivatives of the PDEs by Taylor expansions, the more general FEM approximates the unknown variables by linear combinations of simple functions. Although generally considered as being similar to the former two techniques, the FVM directly discretises the conservation law in space. Due to its wide application (it is also utilised in Fluent) and importance, the FVM is discussed separately.

3.1.1.1 The finite difference method

As will be shown below, the finite difference method is based on the properties of Taylor expansions and on the straightforward application of the definition of derivatives. It is one of the simplest methods to apply, particularly on uniform meshes, but it requires a high degree of mesh regularity. The mesh must be set up in a structured way, whereby the mesh points, in an n -dimensional space, are located at the intersections of n families of rectilinear or curved lines. These curves appear as a form of numerical coordinate lines and each point must lie on only one line of each family.

The idea of the FDM is actually quite simple since it corresponds to an estimation of a derivative by the ratio of two differences according to the definition of the derivative. For a function $f(x)$, e.g. velocity, the derivative at point x is defined by

$$\frac{\partial f(x)}{\partial x} = \lim_{\Delta x \rightarrow 0} \frac{f(x + \Delta x) - f(x)}{\Delta x}$$

If Δx is small, the expression on the right-hand side is an approximation to the exact value of the spatial derivative. For any finite value of Δx an error (the *truncation error*) is introduced which goes to zero for Δx tending to zero. The power of Δx with which this error tends to zero is called *the order of the difference approximation*, and can be obtained from the Taylor series development of $f(x+\Delta x)$ around point x . Developing $f(x+\Delta x)$, one obtains

$$f(x + \Delta x) = f(x) + \Delta x \frac{\partial f(x)}{\partial x} + \frac{\Delta x^2}{2} \frac{\partial^2 f(x)}{\partial x^2} + \dots$$

and therefore,

$$\frac{f(x + \Delta x) - f(x)}{\Delta x} = \frac{\partial f(x)}{\partial x} + \underbrace{\frac{\Delta x}{2} \frac{\partial^2 f(x)}{\partial x^2}}_{O(\Delta x)} + \dots$$

This approximation for the derivative is said to be first order in Δx , indicating that the truncation error $O(\Delta x)$ goes to zero like the first power in Δx .

A very large number of finite difference approximations can be obtained for the derivatives of functions. Here, some simple examples are given.

Let us consider a one-dimensional space, the x -axis, where the space discretisation has been performed such that the continuum is replaced by N discrete mesh points x_i , $i=1, 2, \dots, N$ (Figure 3.1). The values of the function $f(x)$ at the points x_i are indicated by f_i , i.e. $f_i=f(x_i)$. Further, the spacing between the discrete points is considered constant and equal to Δx .

The following approximate finite difference approximations can be defined for the first derivative,

$$\left(\frac{\partial f}{\partial x}\right)_{x=x_i} = \frac{f_{i+1} - f_i}{\Delta x} + \mathcal{O}(\Delta x) \quad (3.1)$$

$$\left(\frac{\partial f}{\partial x}\right)_{x=x_i} = \frac{f_i - f_{i-1}}{\Delta x} + \mathcal{O}(\Delta x) \quad (3.2)$$

With respect to the point $x=x_i$, Equation 3.1 is called a *forward difference*, while Equation 3.2 is a *backward difference*; both are first-order approximations of the derivative. A second-order approximation is obtained from the *central difference*, i.e.

$$\left(\frac{\partial f}{\partial x}\right)_{x=x_i} = \frac{f_{i+1} - f_{i-1}}{2\Delta x} + \mathcal{O}(\Delta x^2) \quad (3.3)$$

which can be easily verified by a Taylor expansion. The three approximations are represented geometrically in Figure 3.1. For more information the reader is referred to the specialised literature mentioned at the beginning of this chapter.

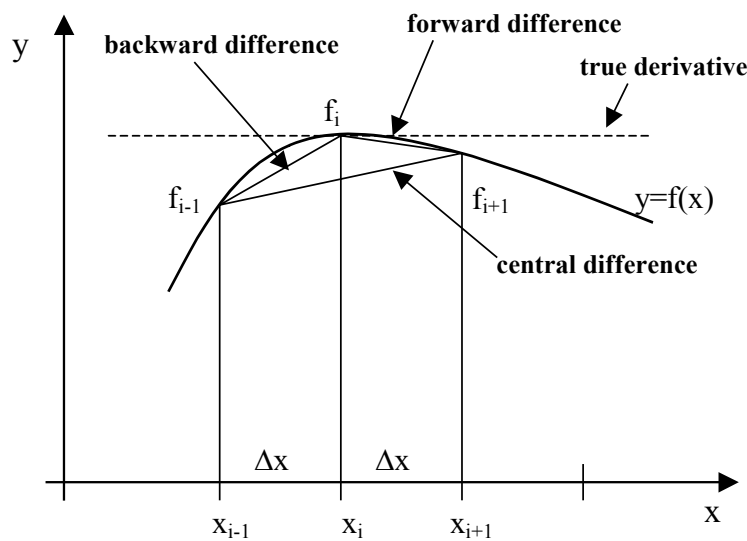


Figure 3.1 Geometric interpretation of difference formulae for first-order derivatives

3.1.1.2 *The finite element method*

The finite element method originates from the field of structural analysis. The concept of *elements* can be traced back to the techniques used in stress calculations, whereby a structure is subdivided into small substructures of various shapes and re-assembled after each *element* had been analysed. It became clear that the method could also be used for continuous field problems. From then on, the finite element method was used as a general approximation method for the numerical solution of physical problems described by field equations in continuous media, like the Navier-Stokes equations. Actually, many schemes of the finite difference type can be seen as special cases of the finite element method. Fundamentally, the finite element method is based on functional analysis.

The basic steps in the finite element approximation differ from the corresponding ones in a finite difference method essentially by the generality of their formulation. In order to set up a finite difference discretisation scheme, one must

- define a space discretisation by which the mesh points are distributed along families of non-intersecting lines;
- develop the unknown functions as a Taylor series expansion around the values of the grid; and
- replace the differential equations by finite difference approximations of the derivatives.

The finite element method defines for each of these three steps a more general formulation, as will become clear from the following.

The space discretisation

The space domain can be discretised by subdivision of the continuum into elements of arbitrary shape and size. Since any polygonal structure may be reduced to triangular and quadrilateral elements the latter are the basis for the space subdivision. The only restriction is that the elements may not overlap and have to cover the complete computational domain. An example of such a space discretisation is given in Figure 3.2.

Within each element a certain number of points are defined, which can be positioned along the straight or curved sides or inside the element. These *nodes* will be the points where the numerical value of the unknown functions, and eventually their derivatives, will have to be determined. The total number of unknowns at the nodes, function values and eventually their derivatives are called the *degrees of freedom* of the numerical problem.

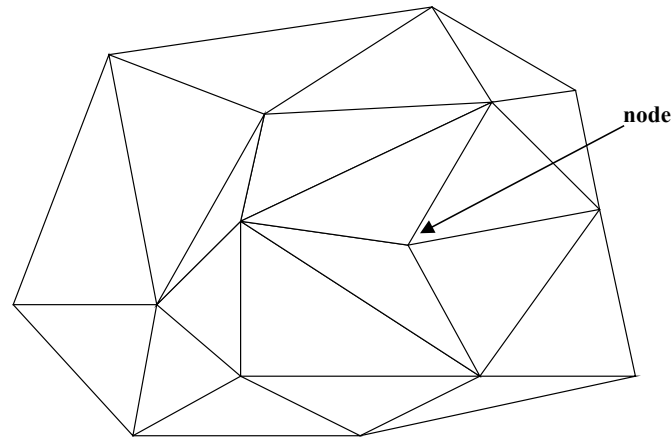


Figure 3.2 Example of finite element subdivision of a domain

Interpolation functions

The field variables are approximated at the nodes by linear combinations of known *basis* functions B (also called *shape*, *interpolation* or *trial* functions). If \tilde{f} is an approximate solution of $f(x)$ one can write a series expansion of the form

$$\tilde{f}(x) = \sum_I f_I B_I(x) \quad (3.4)$$

where the summation extends over all nodes I . Hence, one interpolation function is attached to each nodal value. These function $B_I(x)$ can be quite general, with varying degrees of continuity at the inter-element boundaries.

Two kinds of interpolation functions are possible. Firstly, there are methods that define the interpolation functions on the whole domain, such as trigonometric functions leading to Fourier series. These functions are used in so-called *collocation* and *spectral methods*. In standard finite element methods, however, the interpolation functions are chosen to be locally defined polynomials within each element, being zero outside the considered element. The coefficients f_I of the expansion (Equation 3.4) are the unknown nodal values of the dependent variables f and have to be estimated.

Equation discretisation - integral formulation

To approximate the coefficients f_I in Equation 3.4 the integral formulation of the physical problem, equivalent to the field equations, is required. The most popular technique to obtain this integral formulation is the *method of the weighted residuals*.

In order to illustrate the principles of this approach, consider the following arbitrary two-dimensional equation

$$\frac{\partial^2}{\partial x^2}(kf) + \frac{\partial^2}{\partial y^2}(kf) = a,$$

written as $L(f)=a$, where L represents the differential operator applied to the variable f . If $\tilde{f}(x, y)$ is an approximation to the solution f , the quantity R , called the *residual*,

$$\begin{aligned} R(\tilde{f}) &= L(\tilde{f}) - L(f) \\ &= \left[\frac{\partial^2}{\partial x^2} (k\tilde{f}) + \frac{\partial^2}{\partial y^2} (k\tilde{f}) \right] - a \end{aligned}$$

is different from zero, otherwise \tilde{f} would be the analytical solution. Any solution algorithm will converge if it drives $R(\tilde{f})$ towards zero, although this value will never be reached in a finite number of operations. Hence, the residual appears as a measure of the accuracy or of the error of the approximation \tilde{f} . Since this error cannot be made to vanish simultaneously in all points of the discretised domain Ω , a best solution can be extracted by requiring that some weighted average of the residuals over the domain should be identically zero, i.e.

$$\int_{\Omega} WR(\tilde{f}) d\Omega = 0 \quad (3.5)$$

where $W(x,y)$ is some weighting function with appropriate properties; hence the name *method of weighted residuals*. Equation 3.5 can be rewritten as

$$\int_{\Omega} W \left[\frac{\partial^2}{\partial x^2} (k\tilde{f}) + \frac{\partial^2}{\partial y^2} (k\tilde{f}) \right] d\Omega = \int_{\Omega} a W d\Omega.$$

Reformulating and discretising this equation leads to an algebraic equation applicable to every node of the computational domain. Hence, for the entire domain, a set of I algebraic equations is obtained. The solution returns the wanted nodal values. For the most widely applied method, i.e. the *Galerkin method*, the weighting functions are simply taken equal to the interpolation functions $B_I(x,y)$.

3.1.1.3 The finite volume method

The finite volume method directly discretises the integral formulation of the conservation equations in the physical space. It is noted, however, that it can be considered as a finite difference method applied to the differential form of the conservation laws, written in arbitrary coordinates, or as a variant of the finite element method. Nevertheless, due to its importance and wide range of applications, it will be separately presented here. The technique is further utilised in the Fluent software and, thus, applied in this dissertation as well.

From Chapter 2 it is known that the flow equations, i.e. the Navier-Stokes equations, are the expression of conservation laws. Their general form for a scalar quantity ϕ (per unit volume), with volume sources Q , is given by

$$\frac{\partial}{\partial t} \int_{\Omega} \phi d\Omega + \oint_S \mathbf{F} \cdot d\mathbf{S} = \int_{\Omega} Q d\Omega \tag{3.6}$$

Again, the volume of the discretised domain is denoted by Ω and its enclosed surface by S . \mathbf{F} and $d\mathbf{S}$ are the respective flux and surface vectors for a certain element. The latter vector is always pointed outwards the considered element volume (Figure 3.3). The essential of Equation 3.6 lies in the presence of the surface integral and the fact that the time variation of ϕ inside the volume only depends on the surface values of the fluxes. Hence, for an arbitrary subdivision of the volume Ω into, say, three subvolumes Ω_1 , Ω_2 and Ω_3 one can write the conservation law for each subvolume and recover the global conservation law by adding up the three subvolume conservation laws. Referring to Figure 3.3, Equation 3.6 for each subvolume becomes

$$\begin{aligned} \frac{\partial}{\partial t} \int_{\Omega_1} \phi d\Omega + \oint_{ABCA} \mathbf{F} \cdot d\mathbf{S} &= \int_{\Omega_1} Q d\Omega \\ \frac{\partial}{\partial t} \int_{\Omega_2} \phi d\Omega + \oint_{DEBD} \mathbf{F} \cdot d\mathbf{S} &= \int_{\Omega_2} Q d\Omega \\ \frac{\partial}{\partial t} \int_{\Omega_3} \phi d\Omega + \oint_{AEDA} \mathbf{F} \cdot d\mathbf{S} &= \int_{\Omega_3} Q d\Omega \end{aligned}$$

When summing the surface integrals the contributions of the integral lines ADB and DE always appear twice but with opposite signs, and will cancel each other.

Equation 3.6 is the general formulation of the finite volume method, and the user has to define how to estimate the volume and cell face areas, and how to approximate the fluxes at the faces of the control volume.

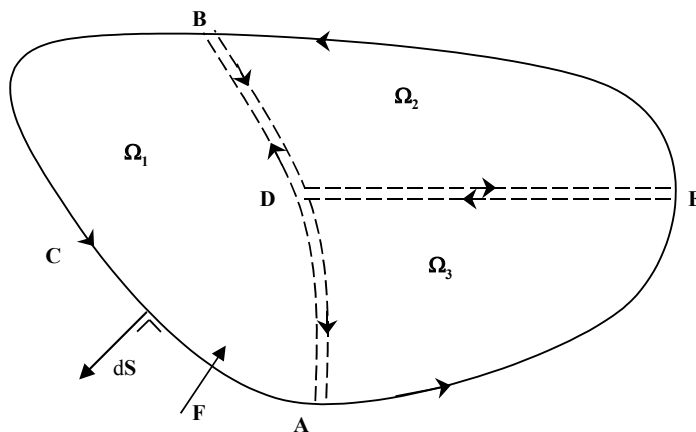


Figure 3.3 Discretisation of the volume Ω into subvolumes

The finite volume method clearly takes full advantage of an arbitrary mesh, where a large number of options are open for the definition of the control volume around which the conservation laws are expressed. Modifying the shape and location of the control volumes associated with a given mesh point, as well as varying the rules and accuracy for the evaluation of the fluxes through the control surface, gives considerable flexibility to the finite volume method. In addition, by the direct discretisation of the integral form of the conservation laws, and consequently a proper numerical treatment of the fluxes, one can ensure that the basic quantities mass, momentum and energy will also remain conserved at the discrete level. This is a most fundamental property for numerical schemes.

3.1.2 Discretisation schemes

Above, the three different discretisation concepts were introduced. Although the methods to obtain the final discretised equations differ in approach, they all use similar discretisation schemes for derivatives. Because many different schemes are used in practice and a selection had to be made in this study as well, the most popular ones will be introduced below.

3.1.2.1 The central difference scheme

In flow problems diffusion and advection are the physical processes to consider. Because the diffusion process affects the distribution of the transported quantity along its gradients in all directions, it is clear that any discretisation scheme should account for this property. Hence, a central difference scheme, similar to Equation 3.3 but for second-order derivatives, is used in practice. Advection, however, only influences the distribution of the transported quantity in the flow direction. Therefore, central difference schemes are doomed to fail. This can be easily demonstrated with the following simple advection of a variable f :

$$\frac{\partial f}{\partial t} + u \frac{\partial f}{\partial x} = 0$$

with u the advection velocity. When forward difference and central difference schemes are applied to the time derivative and advection term respectively, one obtains

$$f_i^{n+1} = f_i^n - \frac{\sigma}{2}(f_{i+1}^n - f_{i-1}^n) \quad \text{with } \sigma = \frac{u\Delta t}{\Delta x}$$

where n indicates the time level and i the node number. The scheme clearly depends on the parameter σ , called the *Courant number*. It can be shown that any value of σ results in increasing errors when solving the equation in time; the scheme is therefore *unstable*. The same test can also be performed for the backward difference scheme in space. In discretised form it is written as

$$f_i^{n+1} = f_i^n - \sigma(f_i^n - f_{i-1}^n)$$

In this case, for certain values of σ the numerical solution follows the exact solution, although with poor accuracy. As a result, the scheme is *conditionally stable*.

These elementary examples show that an analysis of the discretisation schemes is essential to obtain correct solutions. Three basic requirements should be fulfilled for a discretisation scheme to be characterised as a good scheme. The scheme should be

- *consistent*, i.e. the discretised equations should tend to the differential equations to which they are related when Δt and Δx tend to zero (relates the differential equations to its discretised equations),
- *stable*, i.e. the scheme should not allow errors to grow in time indefinitely (relates the computed solution to the exact solution of the discretised equations),
- *convergent*, i.e. the numerical solution should approach the exact solution of the differential equation at any time and point in the computational domain when Δt and Δx tend to zero (relates the computed solution to the exact solution of the differential equation).

For advection-diffusion problems, however, it appears that diffusion can stabilise the solution when applying a central difference scheme to both advection and diffusion terms. The final stability depends on the relative strengths of advection and diffusion in the governing equation. The advection-diffusion equation is as follows (D_c is the diffusion coefficient):

$$\frac{\partial f}{\partial t} + u \frac{\partial f}{\partial x} = D_c \frac{\partial^2 f}{\partial x^2}. \quad (3.7)$$

This leads us to the property of *boundedness*, which states that in the absence of sources the internal node values of the property f should be bounded by its boundary values. For instance, in a steady-state heat conduction problem without sources and with boundary temperatures of 500°C and 200°C all interior values of temperature should be less than 500°C and higher than 200°C. Another requirement for boundedness is that all coefficients of the discretised equations should have the same sign (usually all positive). Physically, this implies that an increase in the variable f at one node should result in an increase in f at neighbouring nodes. If the discretisation scheme does not satisfy the boundedness requirement it is possible that the solution does not converge at all or, if it does, that it contains *wiggles*. This is demonstrated in Figure 3.4 for an advection-diffusion problem in a one-dimensional domain. In order to maintain all coefficients of the discretised equations positive, an appropriate diffusive flux is necessary. As a rule, the ratio of the advection and diffusion fluxes, i.e. the Peclet number Pe , should be smaller than two, or

$$Pe = \frac{u\Delta x}{D_c} < 2$$

In Figure 3.4 the Pe number equals 5, which explains the wiggles in the numerical solution. For a specified flow problem, the Peclet number might clearly pose some stringent upper limits to the mesh size.

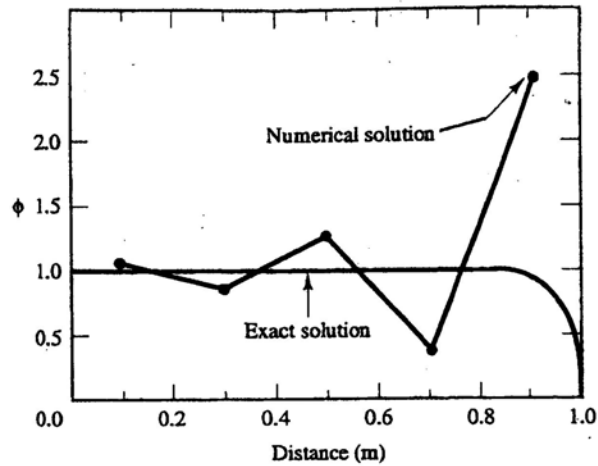


Figure 3.4 Example of wiggles for an advection-diffusion problem in a one-dimensional domain ($Pe = 5$) (Versteeg & Malalasekera, 1995)

To summarise, the application of the central difference scheme for the advection and diffusion terms clearly poses some problems. Firstly, the Peclet number should be lower than two in order to have a stable and second-order accurate scheme. Secondly, the central difference scheme accounts for influences from all directions to calculate the advective flux. Thus the scheme does not recognise the flow direction.

Due to these limitations, central differencing obviously is not a suitable discretisation scheme for general purpose flow problems. Other schemes with more favourable properties have therefore been looked for. Below, the upwind, hybrid, power-law, QUICK and HPLA schemes are shortly discussed. Most of them are implemented in Fluent.

3.1.2.2 The upwind differencing scheme

As mentioned in section 3.1.2.1, one of the major inadequacies of the central differencing scheme is its inability to identify the flow direction. In a strongly advective flow this approach is unsuitable because the computed variable receives as much influence from the upstream as from the downstream nodes. Clearly, the flow properties are transported downstream; the advective gradient should thus be written as

$$\left(\frac{\partial f}{\partial x}\right)_{x=x_i} = \frac{f_i - f_{i-1}}{\Delta x}.$$

This is the downward, or upwind, difference scheme as presented by Equation 3.2. When utilising consistent expressions to calculate fluxes through cell faces, the upwind differencing scheme conserves the transported properties. Further, all coefficients of the discretised equation are positive, resulting in the absence of wiggles in the solution. Although a stable scheme is obtained, the upwind differencing scheme is only first-order accurate on the basis of the Taylor series truncation error.

Because of its simplicity, this scheme has been widely applied in early CFD calculations. Additionally, it can be easily extended to multi-dimensional flow problems. Its major drawback, however, is the production of erroneous results when the flow is not aligned with

the mesh lines. In such problems, the upwind differencing scheme causes the distributions of transported properties to become smeared; the resulting error has a diffusion-like appearance and is referred to as *false* or *numerical diffusion*. To illustrate the effect of numerical diffusion, consider the transport of a scalar property ϕ using upwind differencing in a domain where the flow is at an angle to a Cartesian mesh. In Figure 3.5 (top) a domain is identified with $u = v = 2$ m/s everywhere so that the velocity field is uniform and parallel to the diagonal (solid line) across the mesh. The boundary conditions for ϕ are zero at the south and east boundaries, and 100 at the north and west boundaries. Clearly, the correct solution is known; as the flow is parallel to the solid diagonal the value of ϕ at all nodes above the diagonal should be 100 and below the diagonal it should be zero. Since there is no physical diffusion the exact solution exhibits a step change of ϕ from 100 to zero when the diagonal $X-X$ crosses the solid diagonal.

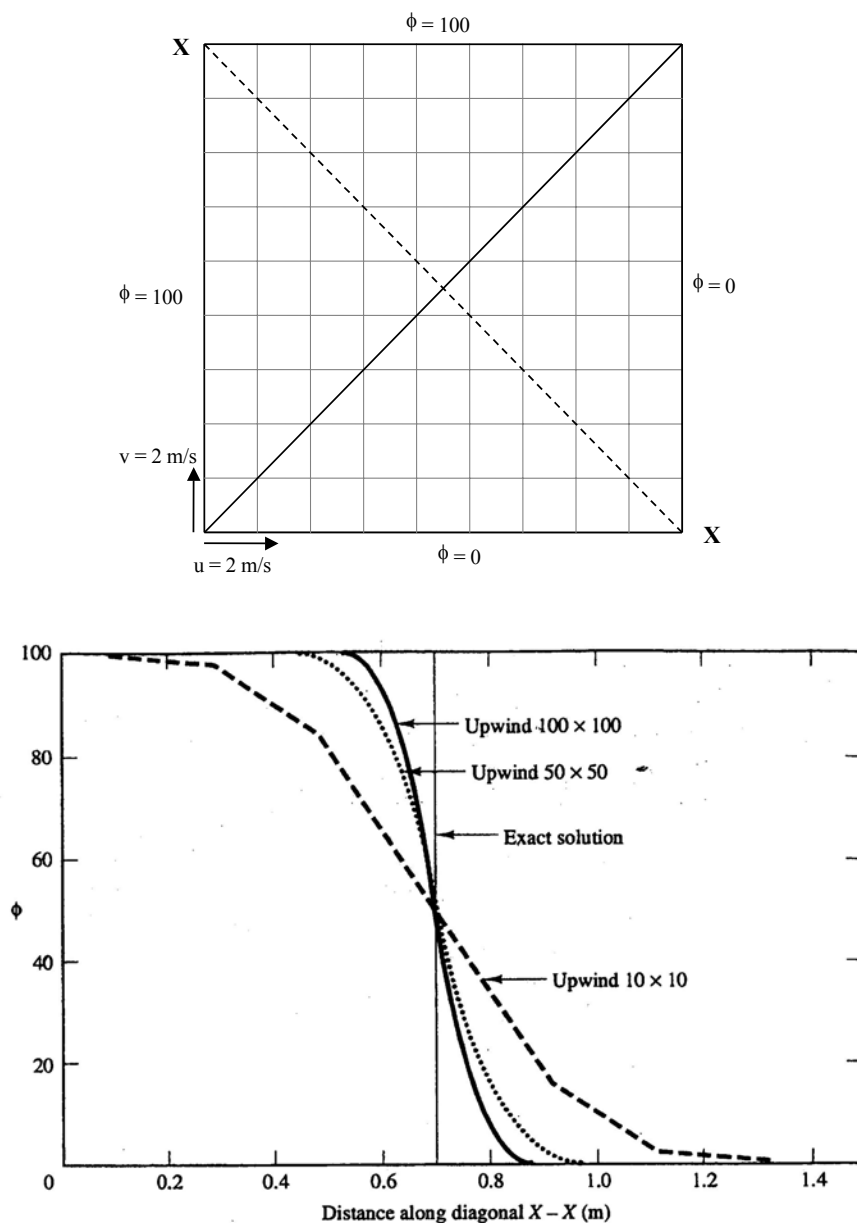


Figure 3.5 Example of numerical diffusion: flow domain considered (top), and numerical solution (bottom) (Versteeg & Malalasekera, 1995)

The calculated results for different mesh resolutions are shown in Figure 3.5 (bottom) together with the exact solution. The numerical results show badly smeared profiles. Here, mesh refinement overcomes the problem of numerical diffusion and gives more accurate results. In practical flow calculations however, this mesh refinement would be computationally too expensive. Therefore, more accurate numerical schemes have to be introduced.

3.1.2.3 *The hybrid differencing scheme*

The hybrid differencing scheme of Spalding (1972) is based on a combination of central and upwind differencing schemes. The hybrid differencing scheme therefore exploits the favourable properties of both schemes. It switches to the upwind differencing when the central difference procedure produces inaccurate results at high Peclet numbers. Hence, at $Pe < 2$ the central difference scheme which is second-order accurate is employed, and the upwind scheme which is only first-order accurate but accounts for the correct advective flow direction, is employed for large Peclet numbers, i.e. $Pe \geq 2$. This highly stable scheme has positive coefficients in the discretised equations, hence, it is unconditionally bounded. The major disadvantage is that the accuracy in terms of Taylor series truncation error is only first-order.

Finally, the hybrid differencing scheme can be easily extended to multi-dimensional flow problems.

3.1.2.4 *The power-law scheme*

The power-law scheme of Patankar (1980) is a more accurate approximation to the one-dimensional exact solution of the advection-diffusion equation and produces better results than the hybrid scheme. In this scheme diffusion is set to zero when the Peclet number exceeds 10. If $0 < Pe < 10$, the flux is evaluated by using a polynomial expression.

Properties of the power-law differencing scheme are similar to those of the hybrid scheme. However, the power-law scheme is more accurate for one-dimensional problems since it attempts to represent the exact solution more closely. The scheme is widely applied for the discretisation of settling tank flow equations (Imam *et al.*, 1983; Zhou & McCorquodale, 1992b, Zhou *et al.*, 1992; McCorquodale & Zhou, 1993).

3.1.2.5 *The QUICK scheme*

The use of upwind quantities ensures that the schemes are very stable and include the transport direction of the flow, but the first-order accuracy makes them prone to numerical diffusion errors. The central difference scheme, however, has second-order accuracy but proved to be unstable. As a result, more accurate higher-order schemes, which preserve upwinding for stability and sensitivity to flow direction, are needed.

The Quadratic Upstream Interpolation for Convective Kinetics (QUICK) scheme of Leonard (1979) is based on a quadratic interpolation for cell face values. In terms of the Taylor series the truncation error is third order on a uniform mesh, and therefore it minimises numerical diffusion errors. The advective flux calculation is based on one downstream and two upstream nodal values. Because not all coefficients in the discretised equations are positive, the QUICK scheme is conditionally stable. This manifests itself as small over- and undershoots in the solution of some problems including those with large gradients of f leading to non-physical behaviour, e.g. negative turbulence properties k and ε , in extreme cases (Figure 3.6). To overcome this problem, many alternatives have been presented in literature by reformulating the scheme to alleviate the stability problem. The new generation of QUICK schemes successfully eliminates this over- or undershooting. In this respect, the alternative scheme as proposed by Leonard & Mokhtari (1990) is implemented in Fluent and applied in this dissertation as well.

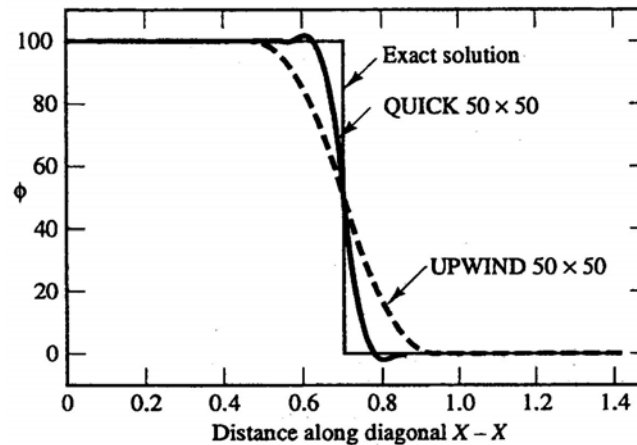


Figure 3.6 Comparison of QUICK and upwind schemes for the 2D test case considered in Figure 3.5 (top) (Versteeg & Malalasekera, 1995)

3.1.2.6 The HPLA scheme

The Hybrid Linear/Parabolic Approximation (HPLA) scheme is based on both the upwind and (traditional) QUICK schemes (Zhu, 1991). As a result, the HPLA scheme combines the unconditional stability of the upwind scheme and the third-order accuracy of the QUICK scheme without numerical diffusion. Similar to the new generation of QUICK schemes, the HPLA scheme is able to resolve steep gradients. The scheme is widely applied in the field of settling tank modelling (e.g. Szalai *et al.*, 1994; Lakehal *et al.*, 1999; Armbruster *et al.*, 2001).

3.1.2.7 The skew upwind schemes

Although the skew upwind schemes minimise numerical diffusion, they also experience over- and undershooting (Zhou *et al.*, 1993). The two major differences between QUICK and skew schemes are: (i) the QUICK scheme principally distinguishes upstream from downstream nodes based on the direction of the velocity at the faces of the control volume, while the

skew scheme defines the upstream nodes along the streamline through a face of the control volume; (ii) the QUICK schemes use higher-order interpolations in the defined upstream directions to obtain the face values, whereas the skew method utilises a linear interpolation. However, advanced interpolation schemes are in use and avoid the occurrence of over- and undershooting (e.g. Zhou *et al.*, 1993).

3.2 Solution of discretised equations

Till this stage the phenomenological equations are discretised in space. If time-independent flow problems are considered, an algebraic system of linear or non-linear equations is obtained. Space discretisation of time-dependent flow problems, however, results in ordinary differential equations. Although developed for time-dependent problems, they can also be utilised as a time-marching method for time-independent flows. Firstly, the discretisation of ordinary differential equations is discussed. To end this section, some methods to solve a system of algebraic equations are mentioned.

3.2.1 Integration methods for systems of ordinary differential equations

Many methods are available for the solution of a system of ordinary differential equations obtained from the semi-discretisation techniques, whereby the space operators $H(f)$ (including the source terms) are discretised separately from the time differential, i.e.

$$\frac{df}{dt} = H(f)$$

This solution method leads to a system of time-dependent ordinary differential equations. In the broad range of available techniques there are explicit and implicit methods. They will be both treated below. Because H may be non-linear in f , specific techniques such as linearisation and predictor-corrector schemes are discussed as well.

3.2.1.1 Multi-step methods

The multi-step integration methods are based on the Taylor expansion of the time derivative, i.e.

$$f^{n+1} = f^n + \Delta t \frac{\partial f^n}{\partial t} + \frac{1}{2} \Delta t^2 \frac{\partial^2 f^n}{\partial t^2} + \frac{1}{6} \Delta t^3 \frac{\partial^3 f^n}{\partial t^3} + \frac{1}{24} \Delta t^4 \frac{\partial^4 f^n}{\partial t^4} + \dots$$

For m -order accuracy the expansion is rewritten as

$$f^{n+1} \approx f^n + \Delta t \frac{\partial}{\partial t} \left\{ f^n + \frac{1}{2} \Delta t \frac{\partial}{\partial t} \left[f^n + \frac{1}{3} \Delta t \frac{\partial}{\partial t} \left(\dots \left(f^n + \frac{1}{m} \Delta t \frac{\partial f^n}{\partial t} \right) \right) \right] \right\}$$

Based on this grouping of terms, a multi-step scheme with m stages may be constructed as

$$\begin{aligned}
 f^{n+\frac{1}{m}} &= f^n + \frac{\Delta t}{m} \frac{\partial f^n}{\partial t} \\
 f^{n+\frac{1}{m-1}} &= f^n + \frac{\Delta t}{m-1} \frac{\partial f^{n+\frac{1}{m}}}{\partial t} \\
 &\vdots \\
 f^{n+\frac{1}{3}} &= f^n + \frac{\Delta t}{3} \frac{\partial f^{n+\frac{1}{4}}}{\partial t} \\
 f^{n+\frac{1}{2}} &= f^n + \frac{\Delta t}{2} \frac{\partial f^{n+\frac{1}{3}}}{\partial t} \\
 f^{n+1} &= f^n + \Delta t \frac{\partial f^{n+\frac{1}{2}}}{\partial t}
 \end{aligned} \tag{3.8}$$

The resulting time-stepping method is similar to the known Runge-Kutta method, but is not identical. The last step of a m -stage Runge-Kutta scheme is a linear combination of all the previous steps. For instance, the last step of the widely used fourth-order Runge-Kutta is written as

$$f^{n+1} = f^n + \Delta t \left(\frac{1}{6} \frac{\partial f^n}{\partial t} + \frac{2}{3} \frac{\partial f^{n+\frac{1}{4}}}{\partial t} + \frac{2}{3} \frac{\partial f^{n+\frac{1}{3}}}{\partial t} + \frac{1}{6} \frac{\partial f^{n+\frac{1}{2}}}{\partial t} \right)$$

The Runge-Kutta method exhibits fourth-order accuracy, even when the spatial operator (or $\partial f/\partial t$) is non-linear in f . The normal multi-step method is only fourth-order accurate for linear relations. The accuracy is reduced to second-order for non-linear situations. Compared to the Runge-Kutta scheme, the simplification of Equation 3.8 has some major advantages for computer implementation. After every time stage the intermediate results do not have to be stored, in contrast with Runge-Kutta, resulting in a significant computer memory reduction when dealing with multi-dimensional flow systems. Notwithstanding, McCorquodale *et al.* (1991) and Samstag *et al.* (1992) applied a fifth-order Runge-Kutta variant to solve the ordinary differential equations obtained after spatial discretisation of the transport equations for the hydrodynamic modelling of secondary settling tanks.

3.2.1.2 Predictor-corrector schemes

Whereas multi-step schemes employ numerical evaluations at intermediate time stages, the predictor-corrector approach takes place at the same time level. This scheme will be introduced as an explicit and approximate method to treat non-linearities of implicit multi-step methods. Indeed, methods for the solution of algebraic systems (see Section 3.2.2.1) cannot deal with non-linearities.

Consider the following general implicit scheme,

$$(1 + \zeta)f^{n+1} - (1 + 2\zeta)f^n = \Delta t [\theta H^{n+1} + (1 - \theta)H^n] - \zeta f^{n-1} \quad (3.9)$$

where θ and ζ are parameters of the numerical scheme. In this respect, this dissertation applies a second-order backward differentiation for the time differentiation as implemented in Fluent. The method used is characterised by θ and ζ being equal to 1 and 0.5 respectively. Clearly, $H^{n+1} = H(f^{n+1})$ has to be evaluated in some way because f^{n+1} is unknown. One may consider an iterative approach, whereby a first estimate \tilde{f}^{n+1} of f^{n+1} is obtained, for instance, by an explicit scheme. This is the so-called *predictor step*. Subsequently, Equation 3.9 is written as

$$(1 + \zeta)\tilde{f}^{n+1} - (1 + 2\zeta)f^n = \Delta t [\theta \tilde{H}^{n+1} + (1 - \theta)H^n] - \zeta f^{n-1} \quad (3.10)$$

and solved for $f^{n+1} = \tilde{f}^{n+1}$. The latter step is called a *corrector step*. Although demonstrated for two steps, the approach can be pursued at the same time level by repeating Equation 3.10 until some form of convergence between two consecutive estimations of \tilde{f}^{n+1} is achieved.

3.2.1.3 Linearisation methods

Another approach to treat non-linearities, which has the advantage of maintaining the fully implicit character of the scheme, is obtained from a local linearisation of the non-linear terms. Hence,

$$H^{n+1} = H^n + \frac{\partial H}{\partial f}(f^{n+1} - f^n) + \mathcal{O}(\Delta t^2)$$

where $\partial H/\partial f$ is the Jacobian of the operator H with respect to the variable f . This linearised operator is subsequently utilised in, for instance, the multi-step methods. Fluent too applies the Jacobian to treat non-linear terms in the governing equations.

3.2.1.4 Alternating direction implicit methods

For an arbitrary mesh, with higher-order discretisations, the implicit multi-step schemes applied to multi-dimensional flow problems result in implicit matrix systems (see Section 3.2.2.1) being no longer, for instance, tridiagonal or pentadiagonal. The implicit matrix will have a more complicated structure, hence the set of algebraic equations will be more difficult to solve as well.

The principle of the Alternating Direction Implicit (ADI) method is to separate the multi-dimensional operator into one-dimensional components. The principle of operator splitting can be easily introduced by means of the two-dimensional diffusion equation, i.e.

$$\frac{\partial f}{\partial t} = k \left(\frac{\partial^2 f}{\partial x^2} + \frac{\partial^2 f}{\partial y^2} \right).$$

Discretised in space with a five-point finite difference scheme, one obtains

$$\frac{df_{ij}}{dt} = \frac{k}{\Delta x^2} \underbrace{(f_{i+1,j} - 2f_{ij} + f_{i-1,j})}_{S_x} + \frac{k}{\Delta y^2} \underbrace{(f_{i,j+1} - 2f_{ij} + f_{i,j-1})}_{S_y}.$$

In matrix notation,

$$\begin{aligned} \frac{dU}{dt} &= SU \\ &= (S_x + S_y)U \end{aligned}$$

represents the set of discretised equations for all nodal points considered. Next, the time discretisation scheme can be split into two (or three, for three-dimensional problems) successive steps, each one involving only the implicit operations originating from a single coordinate, i.e. S_x and S_y . The estimate obtained from the first step is subsequently introduced in the second step. This latter step finally results in the wanted f at the next time level. Although the ADI technique may destabilise the numerical scheme, it definitely shows potential. With respect to settling tank modelling, Imam *et al.* (1983) applied a two-step ADI scheme.

3.2.2 Iterative methods for the solution of algebraic systems

Algebraic systems of equations are obtained either as a result of the application of implicit time-integration schemes to time-dependent formulations (as shown in Section 3.2.1) or from space discretisations of steady-state formulations.

Two large families of methods are available for the solution of a linear algebraic system, i.e. the direct and the iterative methods. Direct methods are based on a finite number of arithmetic operations leading to the exact solution of a linear algebraic system. Iterative techniques, on the other hand, are based on a succession of approximate solutions, leading to the exact solution after an infinite number of steps. These so-called *relaxation methods* determine the solution by starting with an estimate and improving it, iteratively. As the iterations improve the solution, the result is said to *relax* to the true solution. In practice, the number of arithmetic operations of a direct method can be very high, and often larger than the total number of operations in an iterative sequence limited to a finite level of convergence as a consequence of the finite arithmetic (number of digits) of the computer. Since fluid mechanical problems mostly require fine meshes in order to obtain sufficient resolution, direct methods are rarely applied.

The basis of iterative methods is to perform a small number of operations on the matrix elements of the algebraic system in an iterative way, with the aim of approaching the exact solution, within a pre-set level of accuracy, in a finite and, hopefully, small number of

iterations. A large number of methods are available with different rates of convergence and complexity. The classical relaxation methods of Jacobi and Gauss-Seidel, including their variants known as block-relaxation, are the simplest to implement. In this respect, they are widely used (also in Fluent). Another family of iterative techniques are the ADI methods as described in Section 3.2.1.4 which, when optimised, have excellent convergence properties. They are, however, difficult to optimise for general configurations. High rates of convergence can also be obtained with pre-conditioning techniques. The most efficient method, but also the most difficult to program, is the multi-grid method, which appears to be the most efficient of all iterative techniques.

The following sections will introduce these numerical methods; only the basics are aimed at, and it is definitely not the intention to give a complete overview. Interested readers are referred to literature for more in-depth discussions on the numerical techniques.

3.2.2.1 Basic iterative methods

The classical example on which the iterative techniques are introduced and evaluated is Poisson's equation on a uniform mesh. Hence, let us consider the Poisson equation

$$\frac{\partial^2 f}{\partial x^2} + \frac{\partial^2 f}{\partial y^2} = a \quad (3.11)$$

with

$$\begin{aligned} 0 &\leq x \leq L \\ 0 &\leq y \leq L \\ f &= g \text{ on the boundary of the rectangle} \end{aligned} \quad (3.12)$$

and discretised with a second-order, five-point scheme as follows (Figure 3.7)

$$(f_{i+1,j} - 2f_{ij} + f_{i-1,j}) + (f_{i,j+1} - 2f_{ij} + f_{i,j-1}) = a_{ij} \Delta x^2 \quad i, j = 0, 1, \dots, M \quad (3.13)$$

with $\Delta x = \Delta y = L/M$.

If the vector U is set up with the f_{ij} classified *line by line*, that is (with the superscript T indicating the transpose),

$$U^T = (f_{11}, f_{21}, \dots, f_{M-1,1}; f_{12}, f_{22}, \dots, f_{M-1,2}; \dots; f_{1j}, f_{2j}, \dots, f_{ij}, \dots, f_{M-1,j}; \dots, f_{M-1,M-1}).$$

The matrix S shown in Equation 3.14 is conveniently written in block form by introducing the $(M-1) \times (M-1)$ tridiagonal matrix $T(1, -4, 1)$ and the unit $(M-1) \times (M-1)$ matrix I . Hence,

$$S = \begin{pmatrix} T & I & & & \\ I & T & I & & \\ & I & T & I & \\ & & & \ddots & \\ & & & & I & T \end{pmatrix}$$

where S now has $M-1$ lines and columns, each element being itself a $(M-1) \times (M-1)$ matrix. This corresponds to a grouping of all the f_{ij} of the same line into a subvector h_j ,

$$h_j^T = (f_{1j}, \dots, f_{ij}, \dots, f_{M-1,j})$$

$$U^T = (h_1^T, \dots, h_j^T, \dots, h_{M-1}^T)$$

In order to relate the notation in Equation 3.14 to the classical notations of linear algebra, one considers the vector U , with elements f_I , $I = 1, \dots, N = (M-1)^2$, where $N = (M-1)^2$ is the total number of non-boundary mesh points. Hence, Equation 3.14 can be rewritten as

$$\sum_{J=1}^N s_{IJ} f_J = -c_I \quad I = 1, 2, \dots, N \quad (3.15)$$

where the coefficients s_{IJ} represents the space discretisation.

Point Jacobi method

In order to solve for the f_{ij} (or f_I) unknowns in Equation 3.13 one could define an initial approximation of the vector U and attempt to correct this approximation by solving Equation 3.13 sequentially, sweeping through the mesh, point by point, starting at $i = j = 1$, following the mesh line by line or column by column. If f_{ij}^n (or f_I^n) indicates the approximation after n iterations, the corrected approximation f_{ij}^{n+1} (or f_I^{n+1}) can be obtained as

$$f_{ij}^{n+1} = \frac{1}{4} (f_{i+1,j}^n + f_{i-1,j}^n + f_{i,j-1}^n + f_{i,j+1}^n) + \frac{1}{4} c_{ij} \quad \text{for } i, j \neq 0, M$$

Note that this equation is only valid for nodes not being influenced by the boundary. Similar equations can be deduced for boundary-affected nodes. Following the general formulation of system 3.15 the point Jacobi method is defined by the algorithm

$$f_I^{n+1} = \frac{1}{s_{II}} \left(-c_I - \sum_{\substack{J=1 \\ J \neq I}}^N s_{IJ} f_J^n \right) \quad (3.16)$$

The general formulation is best represented in matrix form by decomposing S into a sum of three matrices containing the main diagonal D , the upper triangular part F and the lower triangular part E , i.e.

$$S = D + E + F.$$

Equation 3.16 may thus be written as

$$DU^{n+1} = -C^n - (E + F)U^n \quad (3.17)$$

defining the iterative point Jacobi procedure for system 3.15. With the introduction of the residual R^n at iteration n :

$$R^n \equiv R(U^n) = SU^n + C^n = (D + E + F)U^n + C^n$$

Equation 3.17 can be rewritten, after subtraction of DU^n on both sides,

$$D\Delta U^n = -R^n \quad (3.18)$$

where

$$\Delta U^n = U^{n+1} - U^n$$

The matrix D in Equation 3.18 is called the *convergence* or *conditioning matrix* and makes the system easily solvable. The residual is an important quantity, since it is a measure of the error at a given iteration number n . Obviously, the iterative method will have to generate a sequence of decreasing values of ΔU^n and R^n when the number of iterations increases, because the converged solution should correspond to a vanishing residual.

Point Gauss-Seidel method

In Figure 3.8 (left) one observes that the points $(i, j-1)$ and $(i-1, j)$ have already been updated at iteration $n+1$ when f_{ij} is calculated. One therefore is tempted to use these new values in the estimation of f_{ij}^{n+1} as soon as they have been calculated. A higher convergence rate may be expected because the influence of a perturbation on f^n is transmitted more rapidly. With the Jacobi method a perturbation of $f_{i-1,j}^{n+1}$ will be felt on f_{ij} only after the whole mesh is swept, since it will occur for the first time at the next iteration through the equation for $f_{i,j}^{n+2}$. With the Gauss-Seidel method this influence already appears at the current iteration, because f_{ij}^{n+1} is immediately affected by $f_{i-1,j}^{n+1}$ (see Figure 3.8, right).

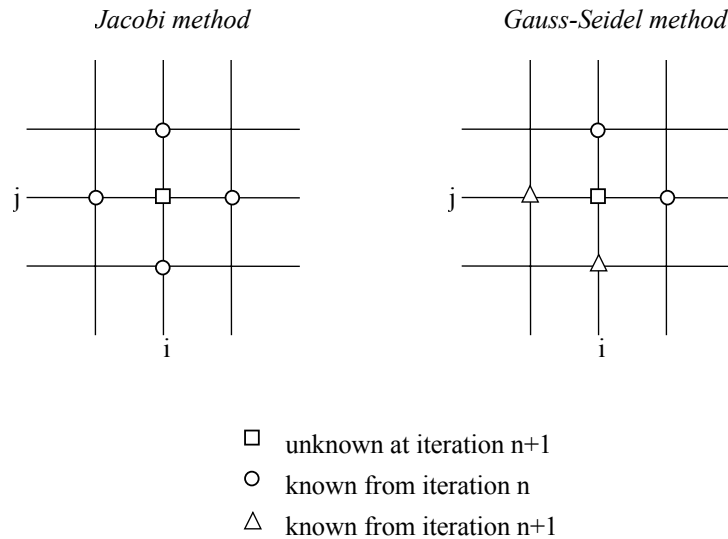


Figure 3.8 Principle of point Jacobi (left) and point Gauss-Seidel (right) methods

3.2.2.2 Over-relaxation methods

One could also be tempted to increase the convergence rate of the relaxation method by "propagating" the corrections $\Delta U^n = U^{n+1} - U^n$ faster through the mesh. This idea is the basis of the over-relaxation method.

If \tilde{U}^{n+1} is the value obtained from the iterative scheme, the value U^{n+1} introduced at the next iteration level is defined by

$$U^{n+1} = \varphi \tilde{U}^{n+1} + (1 - \varphi)U^n$$

where φ is the over-relaxation coefficient. When appropriately optimised for the convergence rate a considerable gain may be achieved.

3.2.2.3 Pre-conditioning techniques

Similar to Equation 3.18 all iterative schemes can be put under the residual form

$$P\Delta U^n = -R^n$$

where P , equalling D for the point Jacobi method, is again the convergence matrix. This way of notation emphasises a clear connection between the behaviour of iterative schemes with the iteration number n and that of time-dependent formulations where n is a time-step index. Indeed, if one views n in this way, the following general iterative scheme may be considered (ϖ is an optimisation parameter of the technique, and Q represents the source terms):

$$P \frac{\Delta U^n}{\zeta} = -\omega(SU^n + Q^n) \equiv -\omega R^n \quad (3.19)$$

as the explicit Euler integration, with time step ζ , of the differential system

$$P \frac{dU}{dt} = -\omega(SU + Q)$$

where one is only interested in the steady state. The operator P may be chosen in such a way that Equation 3.19 is easily solvable.

3.2.2.4 Multi-grid method

The multi-grid method is the most efficient and general iterative technique known today. The technique has its origin in the properties of the conventional iterative methods. From the previous sections it is clear that every time the mesh is swept by the iterative method, the residual is reduced. The high-frequency errors are already reduced after a few iterations; the low-frequency errors are the slowest to be damped and take many iterations. As a consequence, an iterative method with such properties acts as a smoother of the error in such a way that after one or more iteration sweeps through the mesh the error behaviour is sufficiently smooth to be adequately represented on a coarser mesh.

The basic idea of multi-grid methods is as follows:

- Apply one or more sweeps of an iterative method with good smoothing properties for higher-frequency components.
- Transfer the problem to a coarser mesh, where an approximation of the correction ΔU is obtained at a reduced computational cost, since there are fewer mesh points.
- Transfer the corrections obtained to the fine grid in order to generate a new approximation of the solution.

Hence, it is clear that error smoothing on the fine mesh is the essential property of multi-grid methods.

3.2.3 Solution algorithms for pressure-velocity coupling

To model the transport of a scalar, the velocity field needs to be resolved by considering the continuity equation (Equation 2.1), the momentum equations (Equation 2.2) and the formulation of the related stress term (Equation 2.3). However, the solution of this set of equations poses two problems. Firstly, the advective terms in the momentum equations are non-linear. Secondly, to resolve the flow field, the pressure needs to be computed. It appears in the momentum equations, but there is evidently no (transport or other) equation for pressure when considering incompressible fluids. It is noted that for compressible flows an equation of state $p = p(\rho, T)$ exists relating pressure to the local density and temperature. How to deal with the pressure terms for incompressible fluids will be discussed below.

3.2.3.1 Staggered mesh

The solution procedures for the transport of a scalar, as presented in Section 3.1.2, will be utilised to solve the momentum equations as well. However, the solution procedure is not that straightforward due to problems associated with the pressure source terms that need special treatment. As mentioned before, the solution of every flow problem always starts with the discretisation of the flow domain and of the relevant transport equations. Additionally, one needs to decide where to store the velocities. It seems logical to define them at the same locations as the scalar variables such as pressure, temperature, etc. If the velocities and pressures are both defined at the nodes of an ordinary control volume, however, a highly non-uniform pressure field can act like a uniform field in the discretised momentum equations. Figure 3.9 (left) demonstrates this for a simple two-dimensional situation, where a uniform mesh is utilised for simplicity. The neighbouring nodes of the central node P are denoted as N , E , S and W respectively. Further, consider a highly irregular "checker-board" pressure field with values as shown in Figure 3.9 (right).

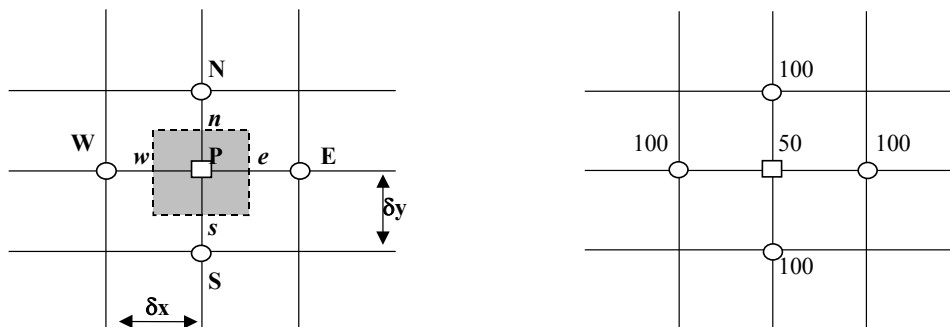


Figure 3.9 Concept of control volume on uniform mesh (left), and example of "checker-board" pressure field (right)

If the pressures at the sides of the control volume, in " e " and " w ", are obtained by linear interpolation the pressure gradient $\partial p / \partial x$ in P is given by

$$\frac{\partial p}{\partial x} = \frac{p_e - p_w}{\delta x} = \frac{\left(\frac{p_E - p_P}{2}\right) - \left(\frac{p_P - p_W}{2}\right)}{\delta x} = \frac{p_E - p_W}{2\delta x} \quad (3.20)$$

The pressure gradient $\partial p / \partial y$ can be written in a similar way. Clearly, the pressure at the central node P does not appear. The velocity in this node is therefore not influenced by the local pressure and *vice versa*; velocity and pressure are thus decoupled. Substituting the appropriate values from the "checker-board" pressure field in Figure 3.9 (right) into Equation 3.20 one finds that all discretised gradients are zero at all the nodal points even though the pressure field exhibits spatial oscillations in both directions.

Obviously, the pressure influence is not properly represented in the discretised momentum equations if the velocities are defined at the scalar grid nodes. A remedy for this problem is the use of a *staggered mesh* for the velocity components. The idea is to evaluate the scalar variables, such as pressure, density, temperature, etc., at ordinary nodal points P , whereas velocity is defined at the half mesh points or at the cell faces in a finite volume

interpretation, i.e. in the points n , e , s and w . If, for instance, the velocity is evaluated in point w the discretisation of the local pressure gradient now becomes

$$\frac{\partial p}{\partial x} = \frac{p_p - p_w}{\delta x} \quad (3.21)$$

and the points w and p for velocity and pressure respectively are coupled. If one considers the "checker-board" pressure field again, substitution of the nodal pressure values into Equation 3.21 now yields non-zero pressure gradient terms. The staggering of the velocity avoids the unrealistic behaviour of the discretised momentum equation for spatially oscillating pressures like the "checker-board" field. A further advantage of the staggered mesh is the generation of velocities at exactly the locations where they are required for the scalar transport, i.e. advection and diffusion, computations. Hence, no interpolation is needed to calculate velocities at the cell faces.

3.2.3.2 The SIMPLE, SIMPLER, SIMPLEC and PISO algorithms

Both problems associated with the non-linearities in the equation set and the pressure-velocity linkage can be resolved by adopting an iterative strategy as the SIMPLE algorithm. The acronym stands for Semi-Implicit Method for Pressure-Linked Equations. In this algorithm the advective fluxes per unit of mass F through cell faces are evaluated from estimated velocity components \tilde{u} . To solve the momentum equations also an estimated pressure field \tilde{p} is used. However, the estimated velocity field does not satisfy the continuity equation. Corrections for both pressure and velocity therefore need to be introduced. The corrections p^c and u^c are written as

$$\begin{aligned} u &= \tilde{u} + u^c \\ p &= \tilde{p} + p^c \end{aligned}$$

Subtracting the momentum equations with the estimated and correct fields yields the momentum equation as function of the corrections p^c and u^c . For the u^c -velocity one obtains (see Figure 3.9 (left))

$$a_w u_w^c = \sum a_{nb} u_{nb}^c + (p_p^c - p_w^c) A_w + b_w \quad (3.22)$$

where the subscript nb refers to the neighbouring points, A_w is the cell face area of the control volume around point w , and b_w is related to the momentum source. At this point an approximation is introduced: all terms on the right-hand side of Equation 3.22, except the pressure term, are dropped to simplify the equation. Omission of these terms is the main approximation of the SIMPLE algorithm. One obtains

$$u_w^c = (p_p^c - p_w^c) \frac{A_w}{a_w} \quad (3.23)$$

Hence, the correction applied to the u -velocity is given by

$$u_w = \tilde{u}_w + (p_p^c - p_w^c) \frac{A_w}{a_w}$$

A similar equation may be set up for the v -momentum equation.

To solve the pressure and velocity field, the velocity corrections (Equation 3.23) are therefore substituted in the continuity equation, which results in a Poisson equation for the pressure corrections; the latter needs to be solved iteratively. The thus obtained pressure corrections are subsequently re-utilised in Equation 3.23 to get a new correction for velocity. As the algorithm proceeds the aim is to progressively improve the estimated fields. The process is iterated until convergence of the velocity and pressure fields occurs.

However, the pressure correction equation is susceptible to divergence unless some under-relaxation is used during the iterative process. The principle is identical to over-relaxation (see Section 3.2.2.2), except that the relaxation coefficient is now between zero and one.

Several variants exist to this SIMPLE algorithm; frequently used algorithms are SIMPLER and SIMPLEC. In Fluent, all three algorithms are implemented and can be chosen by the user. The SIMPLER (SIMPLE Revised) algorithm of Patankar & Spalding (1972) and Patankar (1980) is an improved version of SIMPLE. Instead of using a pressure correction equation, the discretised continuity equation is used to derive a discretised equation for pressure. Hence, an intermediate pressure is obtained directly without the use of corrections. The velocities however are still calculated by means of the velocity corrections (Equation 3.23). Because SIMPLER more effectively calculates the pressure field than SIMPLE, it has significant advantages when solving the momentum equations. Although the number of calculations involved in the SIMPLER algorithm is about 30% larger than that for SIMPLE, the fast convergence rate reportedly reduces the computation time by 30-50%.

The SIMPLEC (SIMPLE-Consistent) algorithm of Van Doormaal & Raithby (1984) follows the same steps as the SIMPLE algorithm, with the difference that the momentum equations are manipulated in such a way that the SIMPLEC velocity correction equations omit terms that are less significant than those omitted in SIMPLE.

The very efficient and fast pressure-velocity calculation procedure PISO, which stands for Pressure Implicit with Splitting of Operators, was proposed by Issa (1986). PISO involves the same steps as SIMPLE but includes an extra corrector step. The SIMPLE method returns a pressure correction, which is subsequently used in Equation 3.22, thus without omitting terms in the discretised momentum equations, to result in a new pressure correction. Although this method implies more computational effort, it may reduce the simulation time considerably.

SIMPLEC and PISO are as efficient as SIMPLER in certain flow types but it cannot be stated that they are better. Their relative performance depends on flow conditions, the degree of coupling between the momentum equations and scalar equations, the amount of under-relaxation used, etc.

With respect to settling tank modelling, the SIMPLE algorithm has been frequently used to solve the unsteady and incompressible RANS equations (Zhou & McCorquodale, 1992a,b,c). Instead, Stamou *et al.* (1989), Adams & Rodi (1990) and Szalai *et al.* (1994) applied the

SIMPLEC algorithm. In this dissertation, however, the PISO algorithm was found to be the most robust technique avoiding possible occurring numerical divergences.

3.3 Numerical techniques used in Fluent

Whereas Sections 3.1 and 3.2 already mentioned different numerical techniques available in Fluent, this section will shortly deal with the methods applied in this dissertation.

The Fluent software utilises the finite volume method to solve the governing integral equations for the conservation of mass and momentum, and (when appropriate) for scalars such as turbulence and solids concentration. In this dissertation, the so-called *segregated solver* was applied; its solution procedure is schematically given in Figure 3.10. Using this approach, the governing equations are solved sequentially, i.e. segregated from one another. Because the governing equations are non-linear (and coupled), several iterations of the solution loop must be performed before a converged solution is obtained.

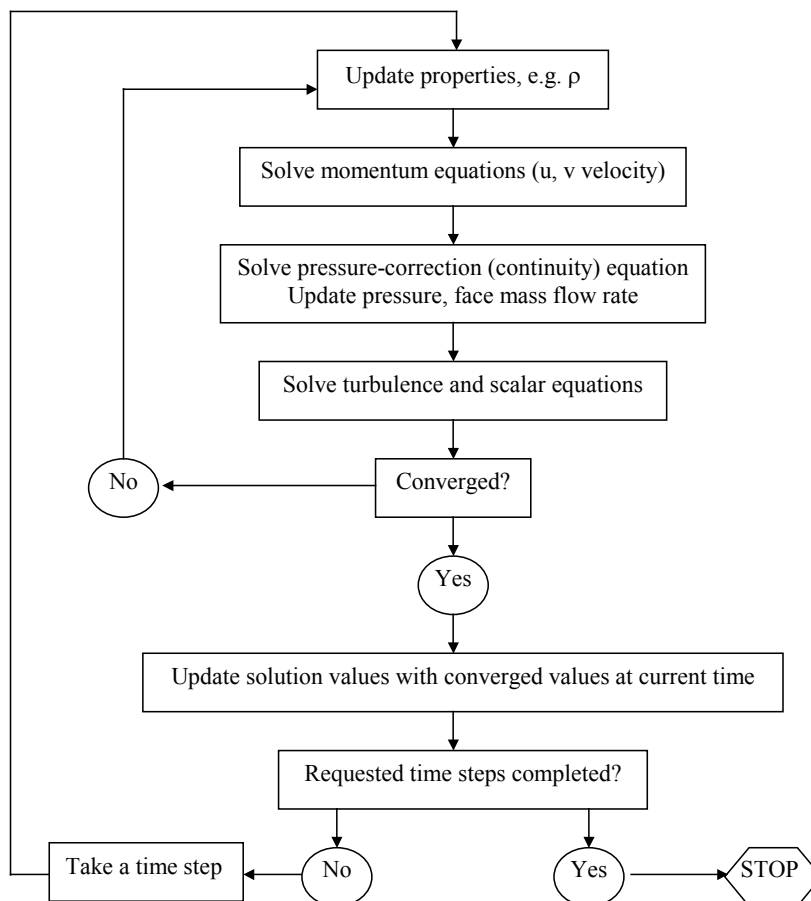


Figure 3.10 Solution procedure in Fluent

Concerning the spatial discretisation, this work applied the central difference and the QUICK scheme for the diffusion and advection terms respectively. Being a member of the new generation of QUICK schemes, it does not suffer from under- or overshoots when large

gradients of the considered variable occur. To further cope with large gradients, under-relaxation was applied as well. The QUICK scheme was shown to be the most robust when performing simulations of unsteady density-driven flows. To solve the pressure field, the PISO algorithm was found to avoid numerical divergences. Time-marching was always adopted to improve convergence. With respect to time discretisation, an implicit second-order backward scheme was used as it is the most accurate scheme implemented in Fluent. Finally, the resulting set of algebraic equations was solved with the point Gauss-Seidel method in conjunction with multi-grid techniques.

3.4 Conclusions

Many techniques exist to discretise the flow equations and subsequently solve the set of algebraic or ordinary differential equations. It is emphasised that this dissertation does not aim for the development of new numerical schemes to solve the flow equations. However, the commercial software used, Fluent (Fluent Inc. UK), gives the user the opportunity to choose from a number of numerical schemes. It was therefore opted to include a chapter providing a short overview of numerical techniques introducing the reader into this large and complicated field of computational fluid dynamics.

To solve time-dependent and time-independent flow problems, both the spatial domain and the governing equations need to be discretised. Space is discretised by setting up a mesh or grid, whereas the discretisation of the PDEs results in a system of algebraic equations. To perform the latter, three options are available to the modeller, i.e. finite difference, finite element and finite volume methods. In this respect, Fluent utilises the finite volume method, which is very effective on irregular meshes. Although the approaches of the three techniques are different, the discretisation schemes used are very similar. An overview was given in Section 3.1.2.

Concerning the spatial discretisation, this dissertation applied the central difference and the QUICK scheme for the diffusion and advection terms respectively. Although the QUICK scheme, when used appropriately, copes with large gradients, under-relaxation was applied as well. To solve the pressure field, the PISO algorithm was found to avoid numerical divergences. Because time-marching was adopted, the time derivative was discretised by an implicit second-order backward scheme. Finally, the resulting set of algebraic equations was solved with the point Gauss-Seidel method combined with multi-grid techniques as presented in Sections 3.2.2.1 and 3.2.2.4 respectively.

4 Experimental Techniques for Model Calibration and Validation

Computational fluid dynamics belong to the category of new tools being used by the engineer for analysis and design of systems. CFD simulations are widely used by academics, industry and government to help study and understand basic flow physics. An underlying concern of all CFD users is the issue of credibility of the results. These concerns arise because the accuracy of the numerical solution remains uncertain despite the large knowledge base. This results from inadequate calibration of the models and numerical techniques. Therefore, in order to establish credibility for the CFD code verification and validation must be performed. In performing verification and validation both the numerical accuracy and the physical modelling capabilities are scrutinised.

The numerical accuracy is addressed in the verification process. During verification, errors in the computational solutions are identified and quantified. They arise from the approximation of the solution of the governing phenomenological equations. One of the most important tasks to identify such errors consists in refining the mesh size and time steps used for solving. These reductions are performed until the computational solution no longer shows any dependence on the mesh or time step size. The issue of mesh size will be demonstrated in Chapter 5.

The validation process identifies and assesses error and uncertainty in the conceptual and computational models. This task involves the comparison of simulation results with actual measurements. Experimental fluid dynamics play a dominant role in this portion of code development and assessment. However, there is a major problem with the use of most experimental data for validation purposes; it is usually incomplete. Indeed, CFD use of data puts very stringent requirements on the experiments. These requirements include the need for a complete set of physical modelling data and a qualification/quantification of the uncertainty involved with the experimental measurements.

The process of developing (incl. calibration), verifying, and validating a CFD code requires the use of experimental, theoretical and computational sciences. This process is a closed loop as presented in Figure 4.1.

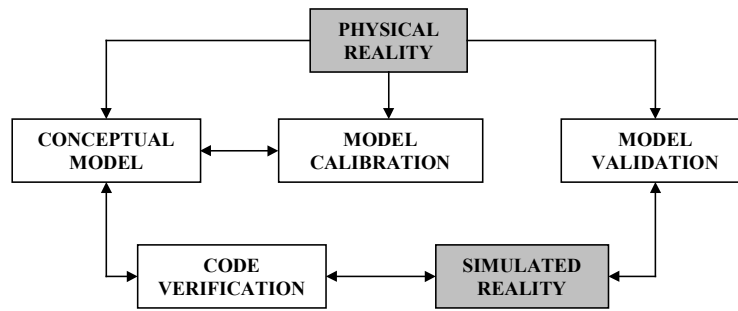


Figure 4.1 Process of developing CFD code

The above clearly indicates that good experimental data are indispensable for secondary settling tank model validation; their quality largely depends on the applied experimental technique. The remaining of this chapter will therefore discuss different experimental techniques with their advantages and disadvantages. The following topics are dealt with,

- settling velocity
- residence time distribution
- solids concentration
- velocity
- particle size distribution
- viscosity

Though the variables are discussed in the general context of wastewater treatment, their relevance for secondary settling tanks will be emphasised. Of most techniques examples are given.

Although concentrations of oxygen, nitrogen and phosphate compounds are crucial variables for calibration and validation of biological reaction models, they are not dealt with in this chapter. Temperature measurements are not discussed either. The reasons for omitting these are the relative simplicity of the measurement technique and data handling, and the fact that they have not been used in the CFD work in this dissertation.

4.1 Settling velocity

Before the settling models of Chapter 2 can be applied in a settling tank CFD model, they need to be calibrated. Experiments are therefore needed to determine the model parameters, and these should be consistent with the case under consideration. Indeed, the experimental conditions should be comparable to real-life. As a result, it is important to define the prevailing settling regime, i.e. discrete or hindered settling. The latter is crucial in order to determine the experimental technique largely depending on the settling regime itself.

In this section, different techniques will be discussed. Important to consider is the discrepancy observed when different experimental procedures are used to measure settling velocities (Lucas-Aiguier *et al.*, 1998). Some new techniques with future potential are mentioned at the end of this section.

4.1.1.1 Hindered settling

The hindered settling velocity is measured by a simple batch settling test. A suspension of sludge is brought into a settling column in which the solids are allowed to settle. Because the solids concentration of the hindered settling region remains constant during this stage and is equal to the initial concentration, the velocity corresponds to the initial solids concentration at which the test is commenced. APHA (1992) recommends that the column is at least 1 m tall and 0.1 m in diameter. In general, gentle stirring is required in small settling columns to destroy the bridging within the solids bed (Dick & Vesilind, 1969). By experience, the same sample should not be reused in subsequent repeat experiments due to a deteriorated solids interface (data not shown). Cho *et al.* (1993) came to a similar conclusion; settling velocities decreased with every iteration.

The hindered settling velocity of the sludge is obtained from the solids-liquid interface depth-time plot, and is given by the slope of the initial linear part. An example is given in Figure 4.2.

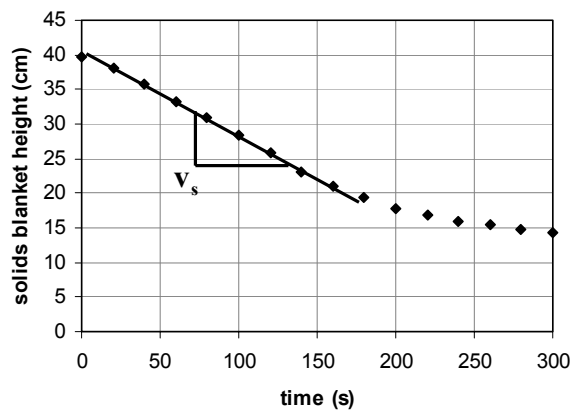


Figure 4.2 Example of solids-liquid interface height plotted against time (diamonds are measurement points)

The settling velocity decreases as the solids concentration increases. To obtain the settling velocity as function of solids concentration, the batch settling test should be conducted at least at 6 different concentrations (Ekama *et al.*, 1997). From these results the model parameters are estimated. In literature, another approach to calculate the model parameters is mentioned. Cacossa & Vaccari (1994), Vanrolleghem *et al.* (1996) and Vanderhasselt & Vanrolleghem (2000) estimate the parameters by taking into account a single and complete settling curves. Hence, the entire settling trajectory is modelled instead of only its linear part. Vanderhasselt & Vanrolleghem (2000) recognised, however, that the reliability of the subsequent settling flux predictions is insufficient. Compression phenomena and bottom boundary processes were assumed to be the major reasons. Therefore, Cacossa & Vaccari (1994) modelled and calibrated their model for the compression zone too.

One of the disadvantages of setting up batch settling curves is the tedious and time-consuming character of the test. Many researchers therefore tried to automate the test. In this respect, Reid & Nason (1993) constructed a settling column with stirrer and tracked the solids blanket level by means of a fixed vertical series of light-emitting diodes and

photodiodes. An infrared solids monitor measured the solids concentration. Comparable to this system is the so-called *Schlumosed* of Fuchs & Staudinger (1999). Here, only three photodiodes are utilised at different heights. Although no hindered settling velocities are measured, the time-evolution of the sludge transparency provides information on the clarification process. On the other hand, Vanrolleghem *et al.* (1996) described a sensor to the Reid & Nason (1993) apparatus but with a moving light detection system.

To determine the settling velocity, Rasmussen & Larsen (1997) used a non-batch technique. Sludge was continuously pumped through a column at a constant rate. With this approach, reality is mimicked in a better way since the secondary clarifier is a continuous system. From a solids concentration measurement at the inlet and the middle of the column the settling velocity can be calculated with the law of mass conservation. Oscillating grids at the middle of the column replace the gentle stirring but they were primarily mounted to study the effect of (homogeneous) turbulence on the settling velocity (Rasmussen & Larsen, 1996; Larsen, 2000).

4.1.1.2 Discrete settling

Proper settling of single particles is crucial for good settling tank performance because discrete settling occurs in the upper tank regions. Hence, knowledge about settling characteristics is needed and settling tests to determine the discrete settling velocity need to be performed. Again, settling columns are used. In 1976, Owen introduced the bottom-withdrawal tube for use in field conditions (van Rijn & Schaafsma, 1986). For this purpose, the tube was equipped with two valves on both ends. The instrument was lowered parallel with the flow and with open valves. After closing the valves, the tube was risen and a traditional batch settling test was performed. In time, many improvements have been made to this experimental set-up. For phenomenological settling models also particle characteristics need to be determined simultaneously with the velocity. With this in mind, Ganczarczyk (1994) applied a photographic technique, i.e. from consecutive photos (with known time interval) the settling velocity of a single particle could be calculated. From the pictures, the needed particle characteristics could be computed as well. A later, and improved, version used a stroboscope to illuminate the particles (Li & Ganczarczyk, 1987). A related but more advanced technique is the so-called *Digital Particle Image Velocimetry* (DPIV), which applies a CCD camera. The innovating aspect is to be found in the mathematical algorithm to compute the settling velocity, i.e. cross-correlation and fast Fourier transforms (Hoffmann *et al.*, 1999).

Instead of image processing other particle sizer techniques may be utilised. In this context, Xue *et al.* (1992) determined a mean settling velocity by fluidisation. Particles with larger or smaller settling velocities compared to the upflowing fluid settle or flush out of the system respectively. Laser diffraction was used to determine the particle size. Here, solids fractions should be kept low in order to remain in the discrete settling zone but also to avoid flocculation. This might alter the particle size and, hence the settling velocity. For that reason, devices that can be used *in situ* will give a more realistic measurement. *In situ* laser diffraction combined with batch settling in a single instrument has already been applied in oceanography (Agrawal & Pottsmith, 2000). Available commercial instruments are e.g. the

LISST-ST (Sequoia Scientific Inc., USA) and the INSSEV (developed at the Institute of Marine Studies, University of Plymouth, UK).

A technique with future potential is the acoustic Doppler velocimetry. The technique can determine particle velocities *in situ*. In view of its relevance, also in flow velocity measurement, the technique will be thoroughly discussed in Section 4.4.3.

4.2 Residence time distribution

In his work, Camp (1946) deduced a relation for the solids removal efficiency of a settling tank. It accounted for the effect of turbulence, which was included as an eddy diffusion term. Hence, it is crucial to have information about the state of mixing in the reactor. Next to velocity measurements, which will be described later, tracer studies are a popular way to gather mixing information. In practice, the test results are used to indicate short circuiting, determine existing mixing regimes, locate dead zones, evaluate baffle arrangements and identify predominant flow patterns within the unit process (CG&S & Hydromantis, 1996). The technique is applied in many systems, i.e. waste stabilisation ponds (Agunwamba *et al.*, 1992; Wood, 1997), gas-liquid columns (Humeau *et al.*, 2000), trickling filters (Riemer *et al.*, 1980; De Clercq *et al.*, 1998), flocculators (Ives & Hoyer, 1998), primary and secondary clarifiers (El-Baroudi & Fuller, 1973; Adams & Rodi, 1990; Lindeborg *et al.*, 1996), aeration basins (De Clercq *et al.*, 1998; Burrows *et al.*, 1999) and sequencing batch reactors (Keller & Yuan, 2002). The remainder of this chapter will deal with the selection of appropriate tracers, their preparation and application, and data analysis.

4.2.1 Tracer selection

Flow behaviour was first recorded by Leonardo da Vinci and he was also the first to propose the use of suspended particles to observe flow currents; a prerequisite is the complete entrainment of the particles. Hence, a tracer can be defined as a marker that consists of small particles. These particles follow the streamlines in the vessel under consideration; they can be molecules, particles or even microorganisms. Many tracers can be found in literature, e.g. rhodamine (Stevens *et al.*, 1986; Hinton & Stensel, 1991), radio-isotopes (Tariq, 1975; Riemer *et al.*, 1980), phenols (Battaglia *et al.*, 1993) and salts (Agunwamba *et al.*, 1992; van Sonsbeek *et al.*, 1992). Also BOD (NCASI, 1983) and inorganic nitrogen compounds (Stevens *et al.*, 1986) have been considered. To study trickling filter hydraulics, Hinton & Stensel (1991) even used cow's milk.

By means of the tracer, fluid parcels at the entrance of the vessel are marked. The system response is then measured in time at the exit of a vessel (so-called *dispersion test*, resulting in a Residence Time Distribution or RTD; e.g. Wood (1997)) or at specific locations inside the vessel (so-called *flow pattern test*, e.g. Samstag *et al.* (1992) and Lindeborg *et al.* (1996)). The so-called *Crosby dye test* combines both techniques (CG&S & Hydromantis, 1996). It should be stressed that tracers also can be used to investigate the solids flow in, for instance, settling tanks (Katz & Geinopolis, 1962; Murk, 1969; Lumley & Horkeby, 1989; Audic *et al.*, 1994).

In general, problems inherent to the tracer technique are due to the characteristics of the tracer and its detection. An overview of common tracers is given in Table 4.1. For a general discussion about the applicability of different tracers the reader is referred to Heijnen *et al.* (1984).

Table 4.1 Comparison of tracers (Heijnen *et al.*, 1984; Lübbert, 1991; Groen, 1994; Rozzi & Massone, 1995)

	fluorescent dyes	lithium salts	acid / base	salt	heat	In ^{113m} , Tc ^{99m}
stability	+ / -	+	+	+	+	+
toxicity	+	+	- / +	- / +	- / +	-
volume	+	+	-	-	-	+
simplicity	+	+	+	+	+	-
safety	+	+	+	+	+	-
density	+	-	-	-	- / +	+
background	+ / -	+	-	-	-	+
on-line	+	-	+	+	+	+
acceptation	+ / -	+	+	+	+	-

in order of quality: +, +/-, -/+, -

According to NCASI (1983) and Heijnen *et al.* (1984), four primary concerns characterise the selection of a tracer; (i) the tracer must be truly conservative in the system of interest, (ii) the tracer must be measurable by some accurate and sensitive means, (iii) the tracer must not be toxic, and (iv) the tracer must not be excessively costly.

To NCASI (1983), the two most common tracer types utilised in wastewater treatment systems are fluorescent dyes, measured by fluorometry, and lithium salts, measured by flame atomic absorption spectrophotometry. The advantages and disadvantages of the various tracer options are discussed next.

4.2.1.1 Characteristics of fluorescent tracers

An overview of fluorescent tracers is given by Groen (1994). This class of dyes mainly covers rhodamine WT and sulforhodamine B (NCASI, 1983). Rhodamine WT is probably the most cost effective dye, although it is not a completely conservative tracer. It is also the most popular because of its high detectability (CG&S & Hydromantis, 1996; Grijspeerdt, 1996). Relative to other dyes it has a low photochemical decay rate. A major disadvantage of rhodamine WT is its potential for adsorption onto suspended solids (NCASI, 1983; Hinton & Stensel, 1991; CG&S & Hydromantis, 1996). Stevens *et al.* (1986) mentioned that dye adsorption on activated sludge biomass resulted in <5% dye loss after 6h of contact time in batch tests. Also, they calculated the dye recovery to be 90-110% for fluidised bed experiments. Next to its solids adsorption capacity, rhodamine WT is very temperature sensitive and may be degraded by free chlorine and other strong oxidising agents in the water.

An alternative to rhodamine WT is sulforhodamine B; this fluorescent tracer is less adsorbed onto solids. But, just like rhodamine WT, it is highly temperature sensitive, slightly more photosensitive than rhodamine WT and more costly (approximately x2.5).

4.2.1.2 Characteristics of lithium salts

NCASI (1983) report a comparative study between lithium and rhodamine WT concerning the conservative nature of the tracer. The research showed that only 50% tracer recovery was achieved with rhodamine WT, whereas more than 85% recovery was observed for lithium. It is not reported that lithium adsorbs or photochemically decays in wastewater systems. In this respect, the reader is also referred to Section 4.2.2.2.

In general, the background level of lithium in wastewater treatment is below the detection limit of the analytical technique. The required amount of tracer is thus solely based on the sensitivity and detection limit.

4.2.2 Tracer preparation, introduction, sampling and analysis

When preparing a tracer test, three primary considerations must be made, i.e. (i) the tracer must be converted into a form suitable for introduction, (ii) the location for and mode of introduction must be selected, and (iii) the period of time over which the introduction will take place must be determined. Those three issues are discussed in NCASI (1983) and CG&S & Hydromantis (1996).

The period of time over which the tracer should be introduced carries two constraints. Firstly, the methods of data analysis assume that the tracer injection is a pulse or spike. The introduction should therefore take place on a time scale much smaller than the residence time of the basin. According to NCASI (1983) a time period less than 1% of the theoretical residence time should be sufficient to meet this criterion. Secondly, the rapid introduction of a large amount of tracer might not result in appropriate mixing in order to behave hydraulically like the basin contents. As a result, the introduction time should be taken as large as possible with the upper bound of 1% of the theoretical residence time. This is especially important when a large density difference exists between the tracer solution and the bulk.

The location of sampling is very important and depends on the goal of the study. When the vessel exit is sampled, care should be taken in order to sample from a well-mixed and representative location. Sampling should take place during at least twice the theoretical residence time. If the system is unclear or there are known dead spaces, it might be considered to prolong the measurement campaign to capture the complete hydraulic behaviour. To NCASI (1983) the minimum number of samples to be collected is 25 and more samples are to be gathered in the first 25% of the testing period. This experimental approach should enable to cover the fast hydraulic phenomena at the start of the tracer test (CG&S & Hydromantis, 1996). Figure 4.3 gives an example of fast sampling in an oxidation

ditch (De Clercq *et al.*, 1998). If the lithium concentration had not been measured frequently enough, the initial dynamics of water recirculation would not have been revealed.

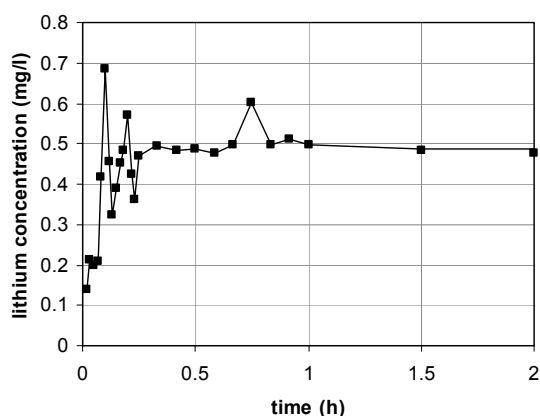


Figure 4.3 Concentration-time profile of lithium in an oxidation ditch

After prolonged storage, and particularly when in contact with glass, lithium may tend to adsorb onto container walls and solids in the sample. Acidification of the samples can reduce this problem though (NCASI, 1983).

Since only lithium is used as tracer in Chapter 5, the following text will only deal with analysis techniques applicable to lithium. Firstly, the applied technique of Atomic Absorption Spectroscopy (AAS) is shortly reviewed.

Atomic absorbance spectrometry requires a liquid sample to be aspirated, aerosolised, and mixed with combustible gases, such as acetylene and air or acetylene and nitrous oxide. The mixture is ignited in a flame whose temperature ranges from 2100 to 2800 °C. During combustion, atoms of the element of interest in the sample are converted to free, unexcited ground state atoms, which absorb light at characteristic wavelengths. For lithium, the characteristic wavelength is 670 nm. To provide element specific wavelengths, a light beam of a lamp whose cathode is made of the element to be determined is passed through the flame. A device such as a photomultiplier detects the amount of light intensity reduction due to absorption by the analyte, and this can be directly related to the amount of the element in the sample.

The necessary amount of lithium depends on the detection limit of AAS, but additional research about sample pre-concentration should be performed in order to reduce the cost on tracer amount. Pre-conditioning is very sample specific and, of course, a higher analytical cost is faced. To demonstrate the principles of pre-conditioning a case study is discussed below.

4.2.2.1 Sample pre-conditioning: case study

In this study a secondary settling tank (Oxley Creek WWTP, Brisbane, Australia) is considered at which a lithium tracer test was performed. Samples were taken from the effluent, RAS and at the water surface from the middle of the scraper bridge.

Preliminary experiments were conducted with effluent samples (April 20th 2001) spiked with lithium. The results of AAS are shown in Table 4.2; reliable measurements can only be made down to approximately 0.05 mg Li/l at which the background level of lithium is reached and measurement noise becomes important. For AAS noise becomes important around absorbances of 10^{-2} - 10^{-3} . From the calibration curve of AAS for lithium (Table 4.3) this corresponds to a concentration of approximately 0.1 mg Li/l. The experiments therefore conclude that 0.1 mg Li/l is the lowest concentration detectable in a reliable way.

Table 4.2 AAS of tap water, effluent and spiked deionised water

	lithium (mg/l)
tap water	0.03
effluent	0.03
spiked deionised water (10 mg Li/l)	9.7

Table 4.3 Calibration curve of AAS for Li

Li (mg/l)	absorbance (670 nm)
0	0.0001
1	0.3371
2	0.6257
3	0.8588
4	1.0361
5	1.1935

$$[\text{Li}] = 2.68 + 2.707 e^{-\text{absorbance}/1.147}$$

$$r^2 = 0.9997$$

Next, experiments were conducted to examine the possibility of pre-concentration in order to reduce the amount of lithium in the tracer experiment, i.e. to reduce the cost. As ion exchange resin, a Dowex 50X-8 100-200 mesh, acidified form, was used. The concentration procedure applied is described below:

- put slurry of freshly regenerated resin (with water and HCl) into a 10 ml Bio Rad Poly-Prep column
- filter sample through GF/A filter
- pump sample through column at 5-6 ml/min
- elute resin with 45 ml of 1 M HCl into a 50 ml volumetric flask. Add 2 ml of 50000 mg K/l (Na^+ -suppressor), and dilute to mark
- calibrate AAS using lithium standards 0, 1.0, 2.0, 3.0, 4.0 and 5.0 mg Li/l with 2000 mg K/l as ionisation suppressor
- use the 670 nm line

The concentration test for lithium was performed using 500 ml of effluent spiked with 500 μg Li. The amount of resin used in the experiment was 10 ml. The elution was done with 25 ml of 1 M HCl. The first 25 ml elution recovered 83% of the lithium and the second run another 7%. On the third 25 ml elution of the resin only approximately 1% of lithium came off the column. Hence, a single 50 ml elution recovered close to 90% of the lithium. This result was promising since recoveries of 95 - 105 % are extraordinary in chemical-analytical studies (Kerven, Analytical Services Laboratory, University of Queensland, personal communication). Nevertheless, this error of 10% seems considerable, but the (inherent) error of 5% on AAS measurements should be kept in mind as well.

To conclude, a concentration factor of approximately x10 seemed to be achievable. While it may be possible to increase the sampling volume to 1000 ml to increase the concentration factor to x20, it was likely that Ca^{2+} would saturate the resin and displace lithium. This is very plausible since the Ca^{2+} concentration in the effluent was 110 mg/l. In a preliminary experiment 2 ml of resin was used with 500 ml of spiked effluent, and recoveries were extremely low due to Ca^{2+} saturation. A concentration factor of x10 was therefore probably the best that could be achieved.

After elution, an unspiked effluent sample gave a lithium concentration of 0.05 mg/l. The latter concentration corresponded to a lithium concentration of 0.005 mg/l in the original sample (prior to pre-concentration). This offset was probably due to interferences at the same wavelength by Na^+ present in the concentrated sample. The already considerable concentration of this cation in the original sample (Table 4.4) only aggravates the interferences after concentration. Therefore, the lowest detectable lithium concentration distinguishable from the background concentration is generally accepted as being twice the background concentration, i.e. ± 0.01 mg Li/l.

Table 4.4 Chemical composition of effluent and tap water

	Ca^{2+} (mg/l)	K^+ (mg/l)	Mg^{2+} (mg/l)	Na^+ (mg/l)
tap water	0.24	2.48	1.33	1.92
effluent	110.23	75.12	64.44	96.71

According to the lithium recoveries and the background concentration, it seemed that pre-concentration helped but it made interferences a larger problem. From the previous experiments, it was concluded that the amount of lithium could be reduced with a factor x10. Of course, other wastewaters with less calcium might give better results.

4.2.2.2 Does lithium adsorb onto solids?

As mentioned before, many tracers have the disadvantage to adsorb onto the biomass. In order to get some insight in the relevance of this phenomenon for lithium, the adsorption capacity of solids was investigated. To perform the analyses 45 ml of sample was taken. The well-mixed samples were centrifuged at 2500 rpm for 5 minutes. The supernatant was removed and measured for lithium with AAS. After centrifugation approximately 3-4 ml of a wet plug of solids was left. This was reconstituted in 45 ml of 1 M HCl and then analysed for lithium. Hence, the amount of lithium in this acid solution could then be added to the one of the supernatant to obtain the total concentration. Only solids from the RAS line were considered due to their high solids content. It is assumed that the low solids concentration in the effluent has no influence on the total lithium concentration. Figure 4.4 shows the bulk lithium concentrations associated to both liquid and solid phases. Note that when expressing lithium concentration as function of the phase volume (and not the bulk volume), concentrations for both phases are comparable. From Figure 4.4, it is obvious that the mass of lithium related to solids is considerable, especially in the beginning of the experiment. Although the concentrations are close to the detection limit, the trend is clear; hence, the solids content should be accounted for when making the lithium mass balance of the system.

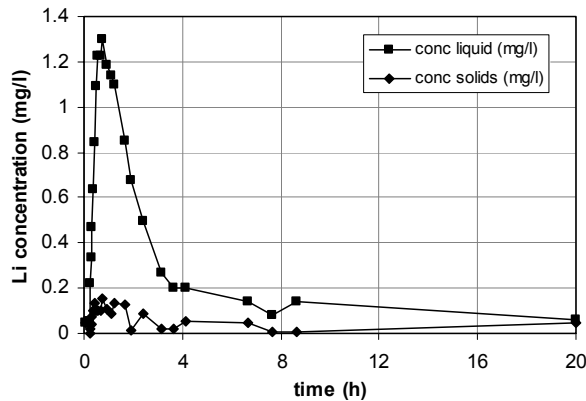


Figure 4.4 Bulk lithium concentration associated to liquid and solids phase of RAS

The question arises if this sink of lithium is due to adsorption phenomena or not. As mentioned previously, there was a considerable amount of Ca^{2+} in the effluent. Therefore, the solids acting as an ion exchange resin are presumably saturated with Ca^{2+} . It is thus proposed that the lithium is predominantly located in the entrained or interstitial water. This also corresponds with literature, i.e. many researchers claim that lithium does not adsorb onto the solids (see Section 4.2.1.2).

4.2.3 Mathematical analysis of RTDs

From the residence time distribution (e.g. Figure 4.3 and Figure 4.4), also called *flow-through curve*, flow behaviour can be deduced. In traditional sanitary engineering practice it was common to estimate the hydraulic efficiency of a basin by the central tendencies of the RTD, i.e. the mean, mode and the median of the distribution. From these, some basic understanding about flows can be obtained (see e.g. Camp, 1946; Rebhun & Argaman, 1965; NCASI, 1983), but for a full description of the flow characteristics an additional criterion, the dispersion or Morrill index, is utilised. This index is the ratio of the 90- and 10-percentiles of the flow curve and indicates the degree of mixing in the basin. The three central tendency values and the dispersion index have been used as criteria to estimate the hydraulic efficiency. However, using this conventional method, the degree of mixing and the extent of, for instance, dead spaces cannot be quantitatively determined.

Rebhun & Argaman (1965) partly overcame this problem by considering the entire RTD. Their formulation of the RTD is based on contributions of different flow types, such as plug flow, perfect mixing, and short circuiting (defined as that part of flow with infinite velocity or zero detention time). However, no information about the flow physics is included.

A more rigorous way to extract information from the RTD is to model the transport phenomena in the system. This approach leads to the so-called *axial dispersion model* (e.g. Burrows *et al.*, 1999) including both advective and dispersive (flow) transport. Fitting this model to the RTD results in the dispersion coefficient D_c and the Peclet number Pe (Levenspiel, 1972; NCASI, 1983; Froment & Bischoff, 1990). For the definition of the latter one refers to Section 3.1.2.

A different approach to model the RTD is the application of the tanks-in-series model (Levenspiel, 1972; Froment & Bischoff, 1990). This model originates from the field of

chemical engineering and different flow types from completely mixed to plug flow can be simulated by changing the number of linearly connected Completely Stirred Tank Reactors (CSTRs). Levenspiel (1972) noted that criticism to this approach is mainly due to the absence of physical parameters such as the dispersion coefficient. Except for the spread or variance of the RTD, the number of CSTRs can also be estimated based on the dimensions of the installation. An empirical relation was set up by Chambers (1992) but is only valid for rectangular diffused aeration basins and within a specific range of dimensions.

Nevertheless, the advantage and popularity of the tanks-in-series model is due to its simplicity allowing the model to extend to more complicated flow patterns. With the multi-zone models the vessel is split into two or more zones, each characterised by a specific flow field, e.g. stagnant or plug flow (Levenspiel, 1972). Subsequently, each zone is described by an appropriate tanks-in-series model or axial dispersion model. An example of such a multi-zone model is given in Figure 4.5 showing a continuously operated stirred reactor compartmentalised in a zone with intense shearing near the mixer blades. The remainder of the reactor volume is characterised by recirculation flows.

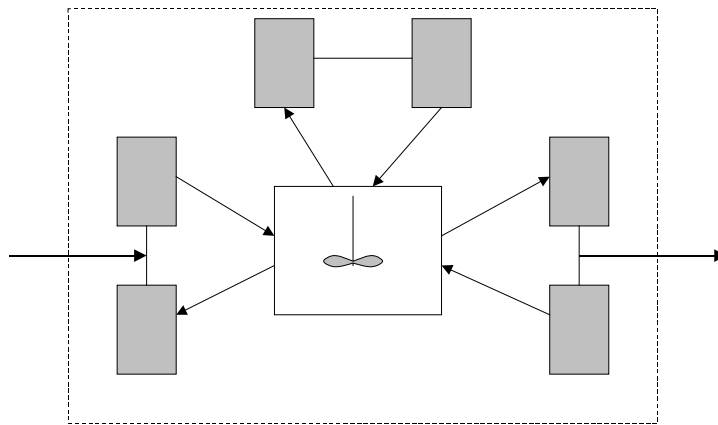


Figure 4.5 Example of a multi-zone model for a stirred reactor

The most sophisticated analysis of the RTDs is done by comparison with CFD models (e.g. Stamou *et al.*, 1989; Szalai *et al.*, 1994; Wood, 1997). It is even used to validate these models. It should be kept in mind, however, that different flow fields may result in identical RTDs. Despite this comment, the use of RTDs is widespread due to its experimental simplicity. More information about the internal flow field can be revealed by the flow pattern test (see Section 4.2.1).

4.3 Solids concentration

Since settling tanks have the task to gravitationally separate solids from water, it is obvious that solids concentration profiles inside the basin are very relevant for model validation. Solids concentrations are measured in view of other aspects of settling tank dynamics; e.g. calibrating models for settling velocity and rheology. In view of its importance, a review of different measurement techniques with a special emphasis on field applications is given below. In the following discussion, two groups of techniques can be considered, i.e. *ex situ* and *in situ* techniques.

4.3.1 *Ex situ* solids concentration measurements

Several techniques available on the market demand for *in situ* sampling of the solids-liquid suspension, prior to determining the solids concentration in the lab. It is obvious that any measurement bias from invasive sampling may determine the final accuracy of the measurement. Because of its importance, van Rijn & Schaafsma (1986) reviewed different sampling techniques such as mechanical traps, bottles and pumps. Though a trap sampler, i.e. a horizontal cylinder that can be suddenly closed by two valves at both ends, is used for the FSS/DSS settling tank test (e.g. Ekama *et al.*, 1997), attention is given here to the pump sampler. With this approach, the suspension is simply pumped from the location under investigation. Basically, the intake velocity should equal the local flow velocity in order to have a representative sample. However, it has been shown for river sediments that deviations from isokinetic sampling result in errors smaller than 20%, provided that the intake velocity is between $\times 0.8$ and $\times 2$ the local flow velocity (van Rijn & Schaafsma, 1986; Wren *et al.*, 2000). These conditions may be hard to satisfy in e.g. a settling tank; there, local flow velocities are very low and a considerable pump speed is needed to avoid solids settling in the tube out of the settling tank. Note, however, that sludge floc densities are much lower than those of inorganic sediment particles. Hence, sludge flocs follow more accurately streamlines. The technique further has a poor temporal resolution compared to *in situ* techniques (Wren *et al.*, 2000). According to Nasr-El-Din & Taggart (1996), measurement errors are also associated with the tube shape; especially for coarse particles of 1000 μm this seems to be important. Further, the same author reports sampling errors depending on the particle size and bulk concentration. In general, errors are due to particle inertia, flow structures ahead of the sampler and particle bouncing (Nasr-El-Din & Taggart, 1996).

After sampling, the solids concentration has to be determined. Again, several techniques are available, i.e. gravimetric methods (APHA, 1992), nuclear methods (Wren *et al.*, 2000) and image analysis (Grijspeerdt & Verstraete, 1996). Image analysis reveals information about particle properties, and a good calibration can be performed between solids concentration and the percentage area of an image covered with solids. But it remains a very tedious work making a widespread application doubtful. The nuclear technique utilises the attenuation or backscatter of radiation. The latter is generally emitted by an artificial source. Its major advantages are its continuous monitoring and use over a wide range of solids concentrations, i.e. 0.5-12 g TSS/l. The most important technique is the gravimetric determination of solids concentration; APHA (1992) is the internationally standardised method to determine solids concentration in wastewater treatment. The technique consists of evaporating the water from the sample and a subsequent determination of the solids weight. The temperature of drying depends on what fraction of solids to be determined, i.e. total suspended solids (drying of filter residue at 103-105 °C), total dissolved solids (drying of filtrate at 180 °C) or fixed and volatile solids (igniting the residue of former two cases at 550 °C). In practice this method is used to calibrate *in situ* solids concentration sensors too; these will be discussed next.

4.3.2 *In situ* solids concentration measurements

The previous section concludes that the accuracy of the solids concentration measurement largely depends on the introduced sampling bias. For that reason, *in situ* measurement techniques are gaining interest. Unfortunately, in many cases it concerns highly technological tools that are very expensive compared to the *ex situ* methods. Below, an overview of the *in situ* solids concentration techniques is given.

In the 80'ies, the impact sampler was developed in the field of oceanography (van Rijn & Schaafsma, 1986; Wren *et al.*, 2000). This device works according to the principle of momentum transfer. The impact rate of particles hitting the sensor is measured and depends on the particles' mass, velocity, and angle of incidence. Unfortunately, determining the solids concentration requires a separate flow meter.

Instead of the particle moment, other instruments rely on the relation between solids concentration, number of particles and their respective sizes. These particle sizers (see Section 4.5) clearly have the advantage that the solids concentration measurement inherently accounts for the particle size. Depending on the application, disadvantages are costs, applicable concentration range and particle properties (Wren *et al.*, 2000).

The next two paragraphs deal with optical and acoustic sensors. Their advantage over the previous techniques is the continuous measurement of solids concentrations. Although based on different physical phenomena, optical and acoustic sensors are very similar in a macroscopic sense. For both methods, the measuring principles can be classified in transmission and scattering approaches.

The optical sensors for solids concentration are common practice in wastewater treatment (Vanrolleghem & Lee, 2002). Infrared or visible light is directed into the suspension. A portion of the light will be scattered by the particles. Scattering is not homogeneous with the angle; forward scattering is more pronounced, while backscattering is the least effective (Vanrolleghem & Lee, 2002). A series of photodiodes positioned around the emitter detect the scattered signal. On the other hand, another portion of the light will be absorbed by the particles. The remaining part that is transmitted through the sample volume can be measured by means of photodiodes located opposite the light source.

Both types of sensors show a nearly linear signal response to varying solids concentrations (Wren *et al.*, 2000). At low solids concentrations, however, optical transmission instruments show a small signal to noise ratio (Vanrolleghem & Lee, 2002). At high concentrations the measurement is characterised by a non-linear behaviour, and the optical backscattering sensors are characterised by a saturation concentration (Wren *et al.*, 2000). Figure 4.6 demonstrates this non-linearity for backscatter-based sensors. Three calibration curves are shown for two wastewater treatment plants, i.e. Dresden WWTP (Germany) and Oxley Creek WWTP (Australia). The graphs clearly indicate that the devices should not be deployed above a certain threshold solids concentration to avoid wrong measurements.

The major disadvantage for using backscattering is the particle-size dependency of the signal (van Rijn & Schaafsma, 1986; Wren *et al.*, 2000). Wren *et al.* (2000) report that the measured solids concentration may increase up to x10 when compared to readings for the

same concentration but with a different particle size. In particular, optical backscattering sensors are more sensitive to small particle sizes; the backscatter gain is greatly affected for sizes smaller than 100 μm . On the other hand, the particle-size dependency is less severe for optical transmission instruments.

According to Vanrolleghem & Lee (2002), measurement errors are typically 5-10%, which is of the same order of magnitude as the gravimetric measurements.

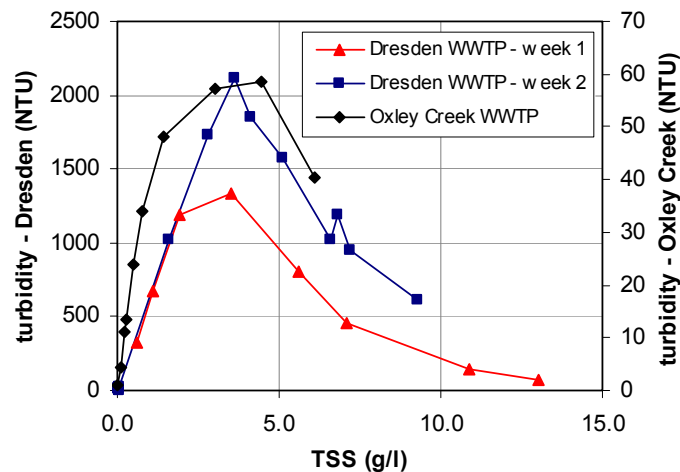


Figure 4.6 Non-linear relation between TSS and turbidity for optical backscatter instruments (Dresden data from Krebs, personal communication)

A truly non-invasive measurement system is based on acoustics (van Rijn & Schaafsma, 1986; Reichel & Nachtnebel, 1994; Wren *et al.*, 2000). High-frequency sound emitted from a transducer is directed toward the measurement volume. Again, particles in suspension will backscatter a portion back to the transducer. Based on the return echo, the water column can be investigated at different heights. When particles have a uniform size, the strength of the backscattered signal allows the calculation of solids concentration (Wren *et al.*, 2000). The main advantage is its high degree of temporal (~ 0.1 s) and spatial (~ 1 cm) resolution (Wren *et al.*, 2000). If particles of different sizes are present in the water column, multiple frequencies should be used. In practice, available acoustic Doppler current profilers just employ one acoustic frequency. Hence, the backscatter strength is dominated by one particle size D ; this size is proportional to λ/π , with λ being the wavelength of sound in water. For larger sizes the strength decreases linearly with D , for smaller sizes the backscattering decreases with D^3 (van Rijn & Schaafsma, 1986). Regardless the comments, Lee & Hanes (1995) were able to measure the concentration profile of suspended sediments. Their success was due to the underlying condition of an invariable particle size distribution along the sound path. Additionally, Thorne *et al.* (1993) obtained reasonable agreements between acoustic and pumped sample measurements for close to three orders of magnitude change in suspended sediment concentration. The highest solids concentration only measured 1-2 g/l though (Figure 4.7).

Besides interpreting the backscattering, the acoustic attenuation can be investigated as well (Reichel & Nachtnebel, 1994). By performing an acoustic spectroscopy of the transmitted signal the particle size distribution and the concentration within the water column can be determined. Estimates of the distribution of these parameters as a function of depth cannot

be drawn, however (Reichel & Nachtnebel, 1994). Also based on transmission of ultrasonic signals, Stolojanu & Prakash (1997) were able to measure the solids concentration in a slurry bubble column. They used the transmission time of the signal and related this to the solids concentration; the technique could only detect concentration changes of 1%.

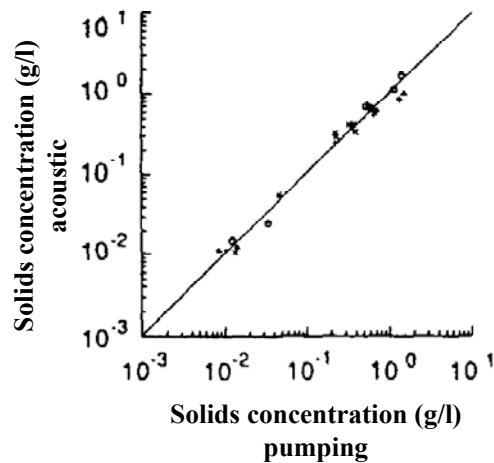


Figure 4.7 Comparison between solids concentrations measured by acoustic backscattering and pumped-gravimetric determination (Thorne *et al.*, 1993)

4.4 Liquid velocity

To validate a CFD model velocity measurements are very important. Although the residence time distribution describes the hydraulic behaviour of the reactor, it only allows indirect knowledge about the flow pattern. Hence, to validate the flow field velocity data are essential. In literature, however, not many references to lab-scale or full-scale velocity measurements can be found; most CFD modellers refer to the work of e.g. Larsen (1977), Bretscher *et al.* (1992) and Krebs *et al.* (1998).

Many possibilities exist to measure liquid velocities which vary between zero and 8 cm/s in secondary settling tanks (Anderson, 1945; Bretscher *et al.*, 1992; Ueberl & Hager, 1997; Kinnear, 2000). The application of each technique in practice depends on e.g. lab- or full-scale, *in situ* or *ex situ*, solids concentration and cost. The remainder of this chapter will therefore discuss different measurement techniques; they are subdivided in two main classes, i.e. lab-scale and full-scale measurement techniques. Finally, a more in-depth discussion of acoustic Doppler current profilers is given. Not only the technique is discussed but also the data analysis by spectral techniques is described.

4.4.1 Lab-scale velocity measurement techniques

Leonardo da Vinci was the first to propose the use of suspended particles to observe flow currents. The first scientific application of flow visualisation is credited to Reynolds in 1883. An overview of several flow visualisation techniques can be found in Quraishi & Fahidy (1986). It is clear that any external visualisation requires a reactor equipped with transparent walls

in order to observe the flow field. Scale models of settling tanks have therefore been frequently used in literature. To visualise the flow, dye clouds can be released from a manifold into the flow (Zhou *et al.*, 1992; McCorquodale & Zhou, 1993; Taebi-Harandy & Schroeder, 2000). The movement of these clouds is subsequently recorded using a video camera. By image analysis the fluid velocity is computed assuming complete entrainment of the dye particles. Instead, Adams & Rodi (1990) applied the so-called *hydrogen bubble-wire flow visualisation method*. With this technique, a cathode wire is placed in the flow and the direct current to the cathode is pulsed at a known frequency. This generates distinct time lines with hydrogen bubbles; because of their small size they accurately follow the flow pattern. By measuring the distance between the time lines, the streamwise velocity can be determined. Velocities agreed with laser Doppler velocimeter measurements to within 10% of the experimentally imposed flow velocity.

Laser Doppler Velocimetry (LDV) is a very popular technique to measure flows in reactors. The basic idea of LDV is that the velocity of a particle leads to a frequency change of scattered light due to the Doppler effect. Hence, the particle velocity can be deduced from this light frequency shift. According to van Beeck (1999), four possible optical set-ups are applied in practice. The main advantage of LDV is the non-intrusive character of the technique. It provides instantaneous and local velocities. Therefore, it also allows the measurement of turbulence (Lyn & Rodi, 1990). One of the major drawbacks of the technique is intrinsic to the measurement principle itself: the fluid velocity is assumed to equal the particle velocity. Particles are supposed to accurately follow the flow, which is very dependent on the particles' drag. Also the cost of the high quality components is a drawback. Its application is further limited to suspensions with solids concentrations below 4 g TSS/l (STOWa, 2002).

As mentioned before, LDV provides a velocity at only a few spatial locations. However, in many situations such as in settling tanks both temporal and spatial information is desired. With particle image velocimetry small particles are released in the flow similar to the bubble-wire technique. With recorders the particle flow is observed. Again, it is assumed that the particles are completely entrained by the fluid flow. Usually, data is analysed by spectral analysis (Lourenco, 1999).

As far as the full-scale techniques described below are not restricted by their size (relative to the reactor) they can be applied on lab-scale too. In order not to repeat the measurement principles, the reader is referred to the next section for more information.

4.4.2 Full-scale velocity measurement techniques

Anderson performed the first important full-scale velocity measurements in 1945. In his work, floats were used to follow the flow; Figure 4.8 shows a scheme of such a device utilised. The length of the line between the vanes and the cork is adjustable, and the area of the vanes is much larger than the area of the cork. Anderson therefore assumed that the travel of the cork at the surface approximately represents the liquid velocity at the elevation of the vanes. In 1992, Bretscher improved Anderson's method in terms of positioning the device in the basin. Also Lindeborg *et al.* (1996) and Ueberl & Hager (1997) applied this simple measurement technique to settling tanks. With the method velocities can be measured between 2 mm/s and 100 mm/s within ± 2 mm/s (Bretscher *et al.*, 1992; Ueberl &

Hager, 1997). The measurement of only horizontal flow components is clearly a major drawback. Although the method of Anderson is still in use, other measurement techniques are available. These alternative flow velocity devices can be subdivided in three groups, i.e. mechanical, electromagnetic and acoustic Doppler velocity meters. Whereas the former two techniques measure the true liquid velocity, the acoustic Doppler velocity meter measures the velocity of small particles suspended in the liquid.

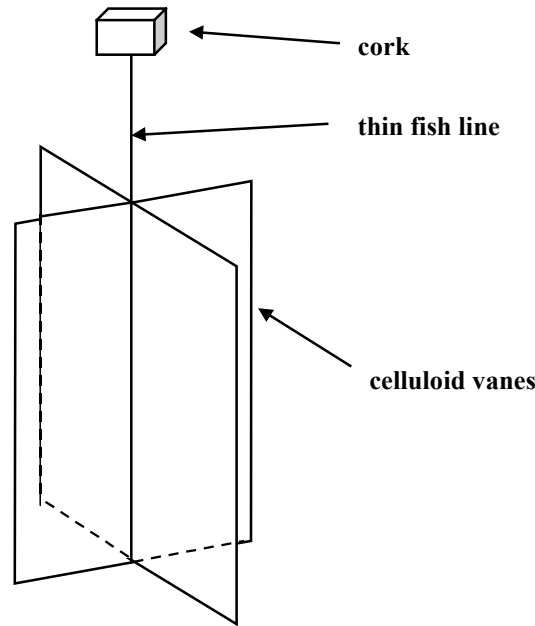


Figure 4.8 Float used by Anderson (1945) to observe currents in settling tanks

Mechanical velocity meters are only applicable to high velocities. The measurement techniques are manifold, e.g. flow turbines and pitot tubes (Lindeborg *et al.*, 1996; STOWa, 2002). Hence, they can only be used at inlet and outlet channels.

Fulford (1995) investigated thirteen mechanical velocity meters on their ability to accurately measure sinusoidally varying flow velocities. This ability largely depends on the inertia of the turbine blades and the efficiency of the device to translate linear flow velocities into angular turbine blade velocities. Errors increase with the ratio of the maximum velocity to the mean velocity of the pulsating flow. In the investigation of Fulford (1995) an electromagnetic meter was also considered. Compared to the mechanical meters, no sensitivity to changes in the mentioned ratio was observed.

Electromagnetic velocity meters work according to Faraday's law which describes that any change in magnetic environment will cause a voltage to be induced in the conductor. For velocity measurements the magnet is stationary and the liquid, being the conductor, moves... This movement causes a voltage, which is measured over electrodes, and is proportional to the liquid velocity. Krebs *et al.* (1998) calibrated the device against laser Doppler velocimetry in a lab-scale settling tank. For their experiments the absolute deviation from the laser Doppler velocimetry measurements was below ± 1.6 mm/s. It was shown that velocity values were reliable down to a velocity of about 1 cm/s. Dahl (1993) also applied an electromagnetic velocity meter to settling tanks. Although the sensors record velocities in one dimension,

they can be combined to measure two- or three-dimensional velocities. The measurement accuracy typically is about 1% of the measured velocity. The bias, i.e. the systematic deviation from the true value, of the device remains below 0.5 cm/s.

As the name already indicates, acoustic Doppler velocity meters work on the principle of the Doppler effect. These probes emit acoustic waves from a transmitter. After the signal transmission, part of the signal is reflected back to the transducers from particles, or other scatterers, in the water column. The difference in frequency between transmitted and reflected sound is proportional to the relative velocity between the acoustic velocity meter and the scatterers in the water. Due to its potentials and recent use in wastewater treatment this measurement technique is discussed more thoroughly below.

4.4.3 Acoustic Doppler velocity meters

Acoustic Doppler velocity meters are gaining interest in the field of wastewater treatment. In urban water systems, an array of transducers allows the measurement of flow fields in sewers (Hughes *et al.*, 1996). On the other hand, Wang *et al.* (2002) applied the technique to multi-phase flow reactors; velocities and solids concentrations could be measured up to 20 cm/s and 250 g/l respectively. Concerning settling tanks, Deininger *et al.* (1998) and Kinnear & Deines (2001) measured complete velocity profiles with a single measurement. Instead, Winkler *et al.* (1999) investigated the influence of the solids removal mechanism on the flow field by measuring at one location with an acoustic Doppler velocity meter.

An important consideration for this type of velocity meters is that, in contrast to electromagnetic velocity meters, the particles' velocity is measured and not the liquid velocity. This has major consequences for velocity measurements in settling tanks. Acoustic velocity measurements are normally used in estuaries and oceans where particle concentrations are low and particles are fairly small (e.g. Stacey *et al.*, 1999b). With inorganic particles, STOWa (2002) found that the technique is reliable up to a solids concentration of approximately 50 g/l. Secondary clarification never deals with such high concentrations, but the process implies large particles that may experience considerable drag; this results in particle velocities deviating from the liquid's velocity. This is clearly demonstrated in Figure 4.9 showing velocity measurements in a secondary settling tank (Kinnear & Deines, 2001). Only the measurements at the bottom part of the settling tank were accurate because fluid velocities are high at these locations and complete flow entrainment of the particles occurs. Near the surface, however, fluid velocities are too low to completely entrain the particles and, as a result, they settle. This explains the vertical velocities found in the upper part of the settling tank. In this region the probe's ability to measure the fluid velocity is definitely restricted, though particle velocities are of interest as well for settling tank analysis.

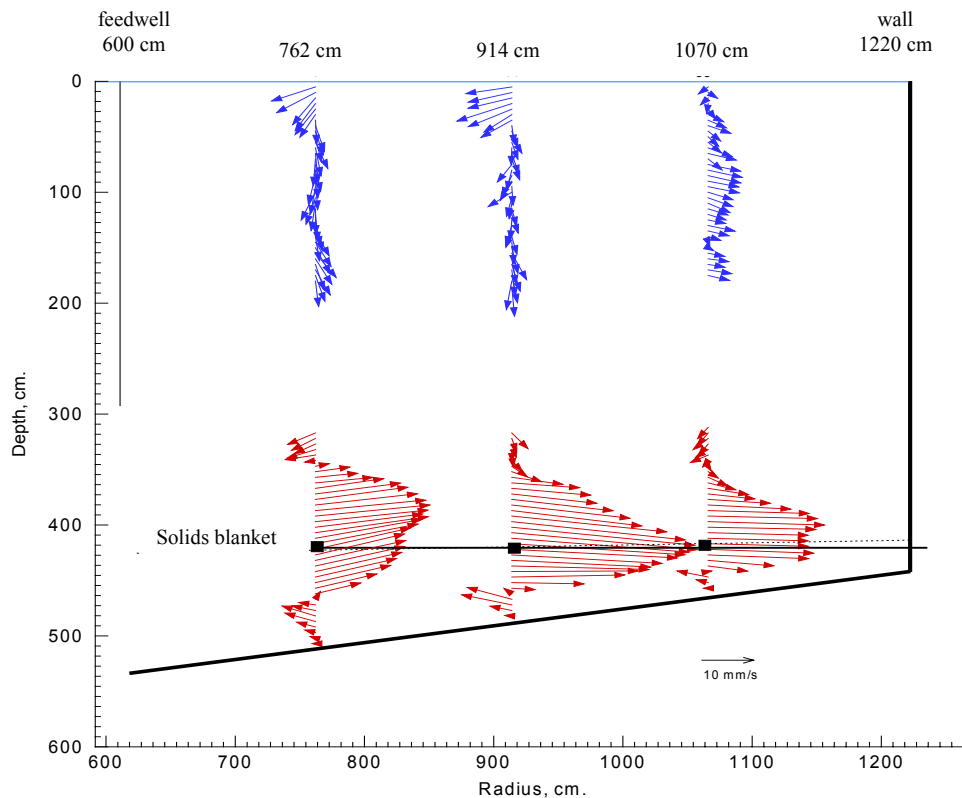


Figure 4.9 Measured velocity profiles with acoustic Doppler velocimetry (Kinneer & Deines, 2001)

The presence of particles of different sizes negatively impacts accurate velocity measurements. Indeed, the echoed signal is a function of solids concentration and size distribution, of their properties such as shape, density, compressibility and rigidity and of the particle size to wavelength ratio (Reichel & Nachtnebel, 1994). However, Reichel & Nachtnebel (1994) also admit that a certain particle size of the distribution dominates the backscatter signal; the question is only what particle size prevails. At a frequency of 1200 kHz the dominant scatterer size is about 0.2 mm, or about 1/6 of the wavelength applied (Gordon, 1989). Note, however, that this scatterer size was only found for compact and spherical particles.

Finally, the issue of signal shadowing of ensonified particles at high particle concentrations is to be mentioned. This signal shadowing is less restrictive for accurate measurements as it seems since the wavelength of the acoustic wave is roughly correlated to the dominant particle size. It is mainly an important feature for the current profilers and not for the point-velocity meters (see further). Besides the occurrence of signal shadowing, the concentration inside the solids blanket may be also too high for the acoustic waves to penetrate; apparently, this did not pose any problems to Kinneer & Deines (2001) though. The acoustic velocity meters can be subdivided in two major categories, i.e. the current profilers and the point-velocity meters. They are dealt with in the following two sections.

4.4.3.1 Acoustic Doppler Velocimeter (ADV)

In essence, the ADV measures the velocity by means of the Doppler frequency shift. To measure a 3D velocity one transmitter and three transducers, placed under a certain angle, are employed (Figure 4.10). Since the velocity is measured in a single point, one is able to validate the probe in a so-called *tow tank*. There, the ADV is mounted on a trolley that is towed with a fixed velocity along a water channel. Hence, the measured ADV velocity can be validated.

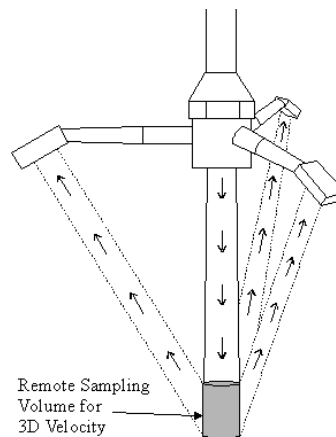


Figure 4.10 Layout and measurement principle of the ADV (Sontek/YSI Inc.)

ADVs typically measure velocities between -10 m/s and $+10$ m/s, and have an accuracy of about 0.5-1% of the measured velocity. The bias ranges between ± 1 mm/s and ± 2.5 mm/s. Drawbacks of ADVs are similar to those for current profilers. Therefore, the reader is referred to the discussion below.

4.4.3.2 Acoustic Doppler Current Profiler (ADCP)

This instrument transmits and receives signals via three or four transducers (if it concerns a 3D measurement). The transducers are positioned in a Janus configuration (see Figure 4.11), i.e. around a horizontal circle every 120 or 90 degrees respectively, and directed outwards at a certain angle to the vertical.

The larger the angle, the more sensitive the instrument is for horizontal velocities, but, at the same time, the down-looking instrument loses its ability to measure velocities close to the bottom of the tank. The device listens to and processes the echoes coming from successive elementary liquid volumes, also called *bins*, along the beams to determine the Doppler frequency shift. The bin length can be set by the user. The emitted signals show a fixed working frequency between 75 - 2400 kHz, depending on the transducer head.

Due to the size of the submerged transducer head, no measurements can be obtained in the first ± 0.5 m below the water surface. Also below the device itself there exists a distance over which measurements are impossible. This distance depends on the so-called *blanking period*, i.e. the time needed to convert the equipment head from transmitter to receiver. Within this time frame no measurements can be performed. Also at the bottom of the tank a loss of measurement capability occurs. When the acoustic signal is transmitted, the signal

produces unwanted *side-lobes*. Some of these side-lobes travel in a vertical direction, while the primary signal travels at a set angle to the vertical. The side-lobe signal will therefore reach the bottom before the primary signal. The reflected side-lobe signals thus return to the transducer from the bottom before the primary signals do. These unwanted signals are much stronger than those returning from solids particles, thus overshadowing particle return signals. The percentage of the depth that cannot be measured, D_p , is approximately equal to (Cobb, 1994):

$$D_p = 100(1 - \cos \alpha)$$

where α is the angle of the acoustic beam from the vertical. For an angle of 20 degrees, 6% of the depth cannot be measured. Also, the measurement uncertainty increases with decreasing depths, velocities and bin size (Cobb, 1994).

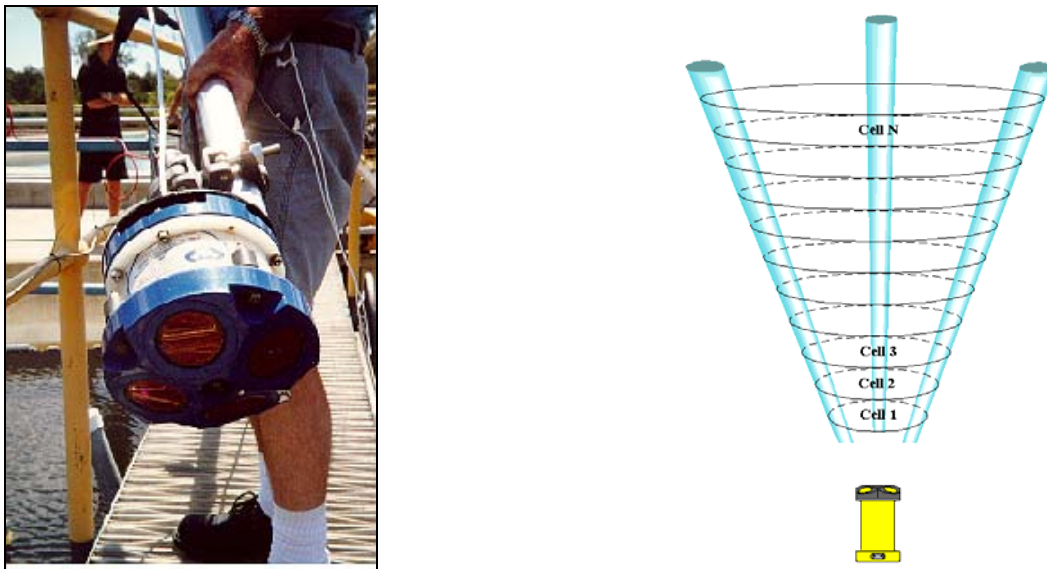


Figure 4.11 Example of an ADCP (left) and its working principle (right) (Sontek/YSI Inc.)

In practice, ADCPs have already been applied to secondary settling tanks; e.g. Deininger *et al.* (1998) and Kinnear & Deines (2001). Similar to the ADV, these sensors measure between -10 m/s and +10 m/s. Unfortunately, ADCPs perform less than ADVs in terms of accuracy; i.e. $\pm 1\%$ of the measured velocity and a bias of at most 5 mm/s. They measure however a complete velocity profile instead of performing a point measurement.

The following discussion will deal with the method of data analysis, i.e. spectral analysis. It will also demonstrate the limitations of the ADCP technique.

4.4.3.3 Example of spectral analysis of ADCP velocity data

To demonstrate the statistical data analysis of the velocity measurements with the ADCP, an example is discussed. The velocity data is investigated in the frequency domain to determine the necessary averaging period to obtain information about the mean and turbulent flows.

The entire data analysis procedure is implemented in the statistical software S-Plus (Insightful, UK). See Appendix B for the computer program. The results will also show some limitations of the ADCP technique.

Experimental set-up

The investigated system is the channel Coupure, located in Ghent (Belgium). The channel is approximately 25-30 m wide and 2 m deep (Figure 4.12). From the middle of a bridge the ADCP's transducer head was deployed with two ropes to a depth of 50 cm; beam 3 was directed according to the mean flow direction.



Figure 4.12 Deployment of ADCP in channel Coupure, located in Ghent (Belgium)

The current profiler was deployed in Mode 5, i.e. high-resolution water profiling mode. With this mode of operation two consecutive pulses (so-called *pings*) are processed to create the velocity estimate. The standard deviation for this mode is very low (<3 cm/s) compared to others because there is a relatively long lag between the two pulses (RD Instruments, 1999). However, fast ADCP equipment movements, high turbulence and shear are detrimental to a good measurement. But for velocities below 1 m/s no problems are expected. Due to the low energy pulses the return signal is rather weak. For that reason, Mode 5 is only applicable to shallow waters. Stacey *et al.* (1999a) used Mode 4 providing a data set in which the noise characteristics are independent of the velocities being measured. With these data characteristics, they were able to estimate the bias on the measurements and perform many turbulence calculations. Unfortunately, Mode 4 is only applicable for large depths, where large bins can be used. For shallow waters, this mode is not feasible.

Velocity data along the four beams were collected for 11.75 minutes at a frequency of 1 Hz. No ping averaging was performed for the 23 bins of 5 cm each. For this deployment, a blanking distance of 25 cm was applied. Within this distance from the transducer head no measurements were available. According to Gargett (1994), recording the raw ping data has two major advantages, i.e. (i) access to the raw data allows greater flexibility for noise reduction techniques, and (ii) averaging over more than one ping may lead to non-uniform statistical accuracies of the resulting data as data values in an average may be rejected by the device when data quality limits are exceeded.

Applied method for velocity calculation

From the ADCP only velocity data along the beam directions are obtained. Hence, beam velocities have to be converted into Cartesian coordinates. Gordon (1996) reviewed the principles of this conversion. The Janus configuration allows the calculation of the vertical and two horizontal velocities as follows

$$u = \frac{u_3 - u_4}{2 \sin \alpha}$$

$$v = \frac{u_1 - u_2}{2 \sin \alpha}$$

$$w_1 = \frac{u_1 - u_2}{2 \cos \alpha}$$

$$w_2 = \frac{u_3 - u_4}{2 \cos \alpha}$$

The velocity along the i -th beam is denoted as u_i ; u , v and w are the velocities in the main flow direction, horizontal and perpendicular to the main flow, and vertical and perpendicular to the main flow respectively. Note that only three beams are needed to compute the velocities making the fourth beam redundant (Cobb, 1994). However, with this extra beam an additional independent estimate of the vertical velocity can be obtained. Since each beam samples velocity from a different portion of the flow stream due to the ADCP geometry, the difference between the two vertical velocities provides an estimate of the spatial variability of the flow (Gordon, 1989).

Every (turbulent) flow field can be decomposed into mean and turbulent fields. When an inhomogeneous flow field prevails, it is obvious that both mean and turbulent fields will be different between the beams. In order to avoid a difference in error propagation for each beam velocity when converting to Cartesian velocity, averaging should be performed on the beam velocities themselves. With the obtained mean velocities, the Cartesian velocities are computed. Once the mean velocities are known the turbulent velocity field can be investigated as well.

Crucial to the entire analysis is the definition of the averaging period. As long as stationary flow is studied the complete set of data at the location under consideration can be considered for averaging. In that way, the variance on the mean will be smallest. The same holds for pseudo-stationary flow where the flow field can be assumed constant for the considered time frame. This approach was applied by several researchers, e.g. Stacey *et al.* (1999a) and Kinnear & Deines (2001). When stationary flow cannot be assumed *a priori*, it is necessary to systematically determine the period over which the turbulent properties are averaged. Turbulence is characterised by velocity fluctuations on a small temporal scale, whereas the mean flow only shows changes over longer time frames.

Piquet (1999) proposes to select the averaging period based on a spectral analysis of the recorded time series of velocity data. Here, this implies a Fourier analysis of each time series of each bin and beam (Lohrmann *et al.*, 1990). Because no flow homogeneity can be assumed in advance, the four beams are treated separately. Since both mean and turbulent flow are established on different scales, the Fourier transform of every time series differs

from zero only for small and high frequencies, while it vanishes for intermediate frequencies. However, due to non-linearities, both peaks in the Fourier spectra are rather smeared; hence, depending on the studied flow the mean of the turbulent flow may be difficult to separate in the spectra (Piquet, 1999).

Central in the spectral analysis is the representation of an arbitrary signal with a finite or infinite series of trigonometric functions, i.e. Fourier series (periodic signals) or Fourier integral (aperiodic signal). Lourenco (1999) reviews how any function $f_\lambda(x)$, with period λ , can be expressed by an infinite Fourier series, i.e.

$$f_\lambda(x) = a_0 + \sum_{m=1}^{\infty} a_m \cos(m\omega_0 x) + \sum_{m=1}^{\infty} b_m \sin(m\omega_0 x)$$

where $\omega_0 = 2\pi/\lambda$ is the fundamental wavenumber. Minimising the sum of squared errors between fitted and target function y , results in the following formulae to calculate the different Fourier components. The total number of these Fourier components equals $2M+1$. When the total number of samples is N , the Fourier components can be written as (for $N = 2M$)

$$a_0 = \frac{\sum_{n=0}^{N-1} y_n}{N}$$

$$a_m = \frac{2}{N} \sum_{n=0}^{N-1} y_n \cos\left(m \frac{2\pi}{N-1} n\right) \quad \text{with } m = 1, 2, \dots, M$$

$$b_m = \frac{2}{N} \sum_{n=0}^{N-1} y_n \sin\left(m \frac{2\pi}{N-1} n\right) \quad \text{with } m = 1, 2, \dots, M$$

From the spectral analysis the magnitude of the velocity fluctuations as function of their frequency is obtained. The magnitude A_m can be calculated as follows,

$$A_m = \sqrt{a_m^2 + b_m^2}$$

In this illustrative case study on the use of the ADCP it was decided not to investigate all bins and beams, but to select bins 1, 5, 10, 15, 20 and 23. From the spectra it was assumed that enough information could be collected about the turbulent properties of the flow. In Figure 4.13 the frequency spectra of the four beams are given for bin 5. A top view of the ADCP is given to orient the beam directions relative to the mean flow (indicated with an arrow). It is worth mentioning that frequencies only go up to 0.5 Hz, and not the sampling frequency of 1 Hz itself. This is due to the ability of calculating only M Fourier components with the available data. Therefore, frequency components of the signal can only be played back up to one-half the sampling frequency (cfr. Nyquist theorem).

From the figure two time scales can be detected, although both peaks in the spectra are faded due to interactions between flow structures. Firstly, a peak in magnitude can be observed at low frequencies corresponding to the total sampling period and indicates velocities changing at a very slow rate. Since the plane through beams 3 and 4 is parallel to the mean flow direction their frequency spectra show higher amplitudes compared to beams 1 and 2. The latter beams are perpendicular to the flow direction; hence, they show small peaks. Based on the large magnitude and sharpness of the peak at low frequency it is assumed that the flow is stationary over the measured period. A second, but smaller peak is seen at 0.3 Hz. These velocity fluctuations occur on a temporal scale of 3.3 s, and are believed to be related to small-scale flow structures.

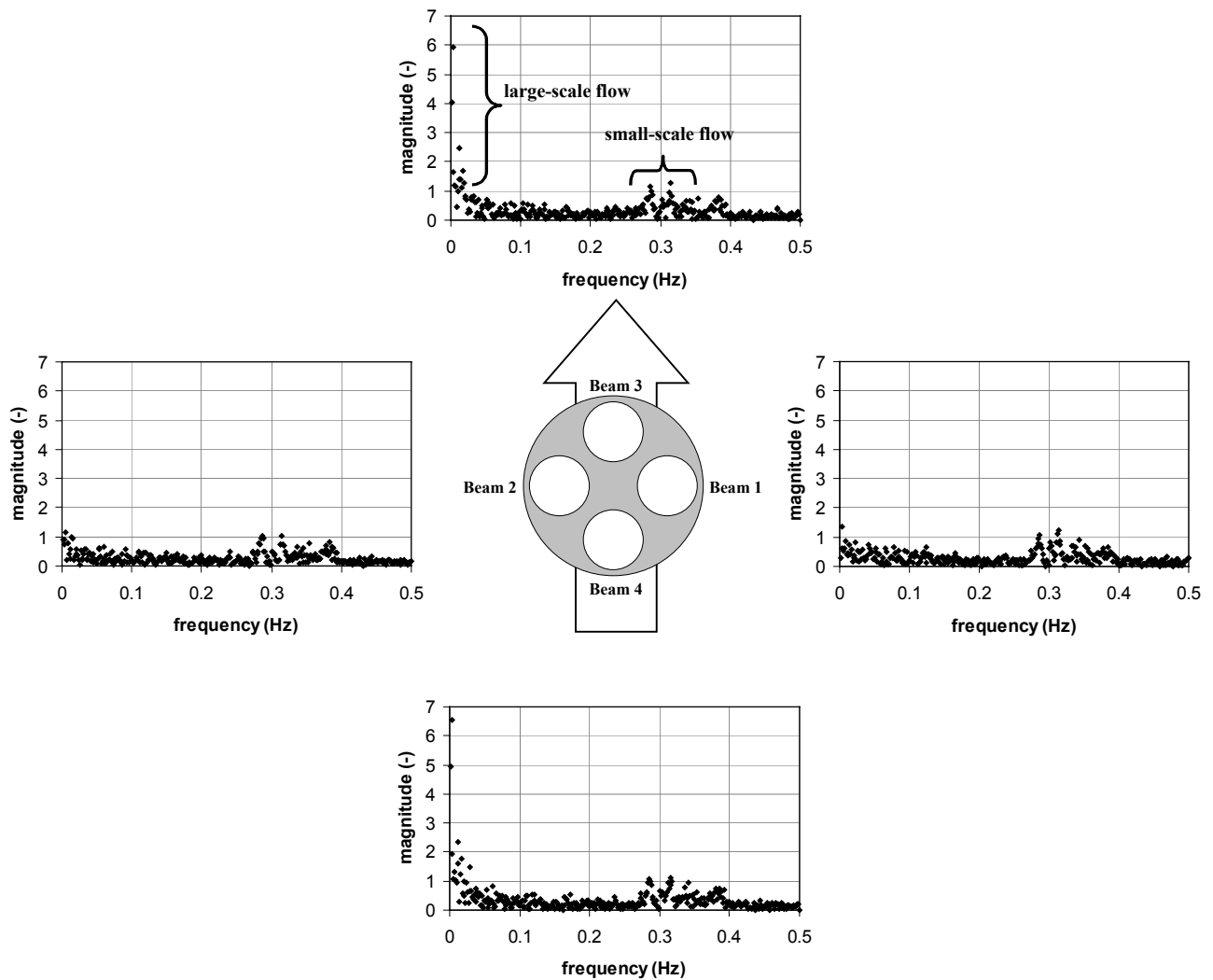


Figure 4.13 Frequency spectra of time series for every beam of bin 5; the arrow indicates the mean flow direction

The frequency spectra are subsequently used to determine the necessary averaging period in order to obtain information about the mean velocities and turbulent flow properties. When no flow homogeneity prevails or cannot be assumed in advance, a cutoff frequency has to be chosen for every spectrum (e.g. Figure 4.14); the inverse of this frequency determines the size of the (moving) time window over which the velocity is averaged. Clearly, turbulence is

filtered out when adopting a cutoff frequency smaller than 0.3 Hz. Here, the channel flow is assumed to be stationary such that the mean flow velocity is retained after averaging over the total sampling time. Other applications may result in different cutoff frequencies though.

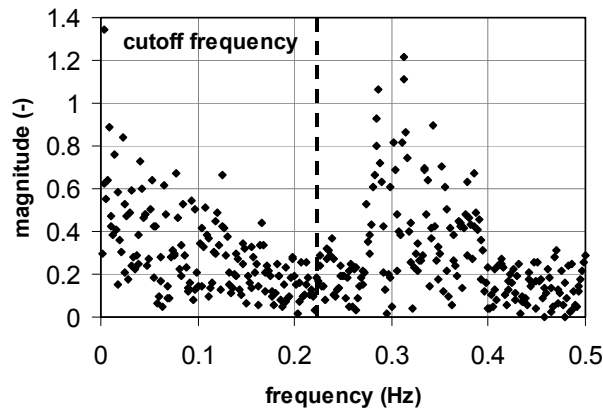


Figure 4.14 Choice of cutoff frequency for beam 1 of bin 5

Observed velocity profiles

Finally, the averaged beam velocities can be transformed into Cartesian coordinates (as mentioned before). The results are plotted in Figure 4.15. Supplementary, the error velocity is given in Figure 4.15 (bottom, right). The latter velocity is simply the difference between the two vertical estimates of vertical velocity. This error allows an evaluation of the assumption of horizontal homogeneity; any discrepancies from zero refer to non-homogeneous flow.

In Figure 4.15 (top, left), a bottom flow can be observed similar to density-driven flows in settling tanks. This seems unrealistic due to the fresh-water character of the channel. Further, Stacey *et al.* (1999a) mentioned that a logarithmic mean velocity profile should prevail in steady and unstratified flows in open channels. For narrow channels, secondary currents due to sidewall effects can result in maximum liquid velocities below the water surface (Gonzalez *et al.*, 1996). Although this is the case here, the channel cannot be classified as being narrow. Besides the main flow velocity, the other velocities do not show a specific profile either.

A closer look to all profiles reveals that the estimated velocity is only 2.6 mm/s at maximum. Although a nice velocity profile for the mean flow is obtained, such low values cannot be trusted. Indeed, the error velocities are in the order of 1 mm/s. Though the error is small, it is considerable compared to the magnitudes of the velocities. In general, standard deviations vary between 3.5 and 8.3 mm/s; this is the fourfold of the actually measured velocities. As a consequence, the applicability of the ADCP to velocity measurements in settling tanks may be questioned. Compared to current profilers from other companies, e.g. Nortek AS (Sandvika, Norway) and SonTek/YSI, Inc. (San Diego, USA), RD Instruments (San Diego, USA) delivers the profiler with the highest accuracy, i.e. $\pm 0.25\%$ of the measured value ± 2.5 mm/s. Also ADVs from the mentioned suppliers do not perform better than the ADCPs. Since velocities in settling tanks may go up to more than 6-8 cm/s (e.g. Tay & Heinke, 1983; Dahl, 1993;

STOWa, 2002), the accuracy of the ADCP should not restrict its application. Regarding average velocities in a settling tank, STOWa (2002) mentions values of 1 cm/s and less. Hence, mainly the density current is accurately measured. The more the settling tank is hydraulically overloaded, the better the velocity measurements will be.

The Reynolds stresses cannot be measured directly by the ADCP, but the streamwise and cross-streamwise correlations, i.e. $\overline{u'w'}$ and $\overline{v'w'}$ respectively, can be easily calculated as (Stacey *et al.*, 1999a,b)

$$\overline{u'w'} = \frac{\overline{u_3'^2} - \overline{u_4'^2}}{4 \sin \alpha \cos \alpha}$$

$$\overline{v'w'} = \frac{\overline{u_1'^2} - \overline{u_2'^2}}{4 \sin \alpha \cos \alpha}$$

The prime superscript indicates the fluctuating component of the velocity while the bar refers to the time-averaging operator. Due to the large errors on the velocities, stresses were completely scattered and did not show any profile (data not shown). Hence, any attempt to perform stress calculations when velocities are inaccurate is doomed to fail.

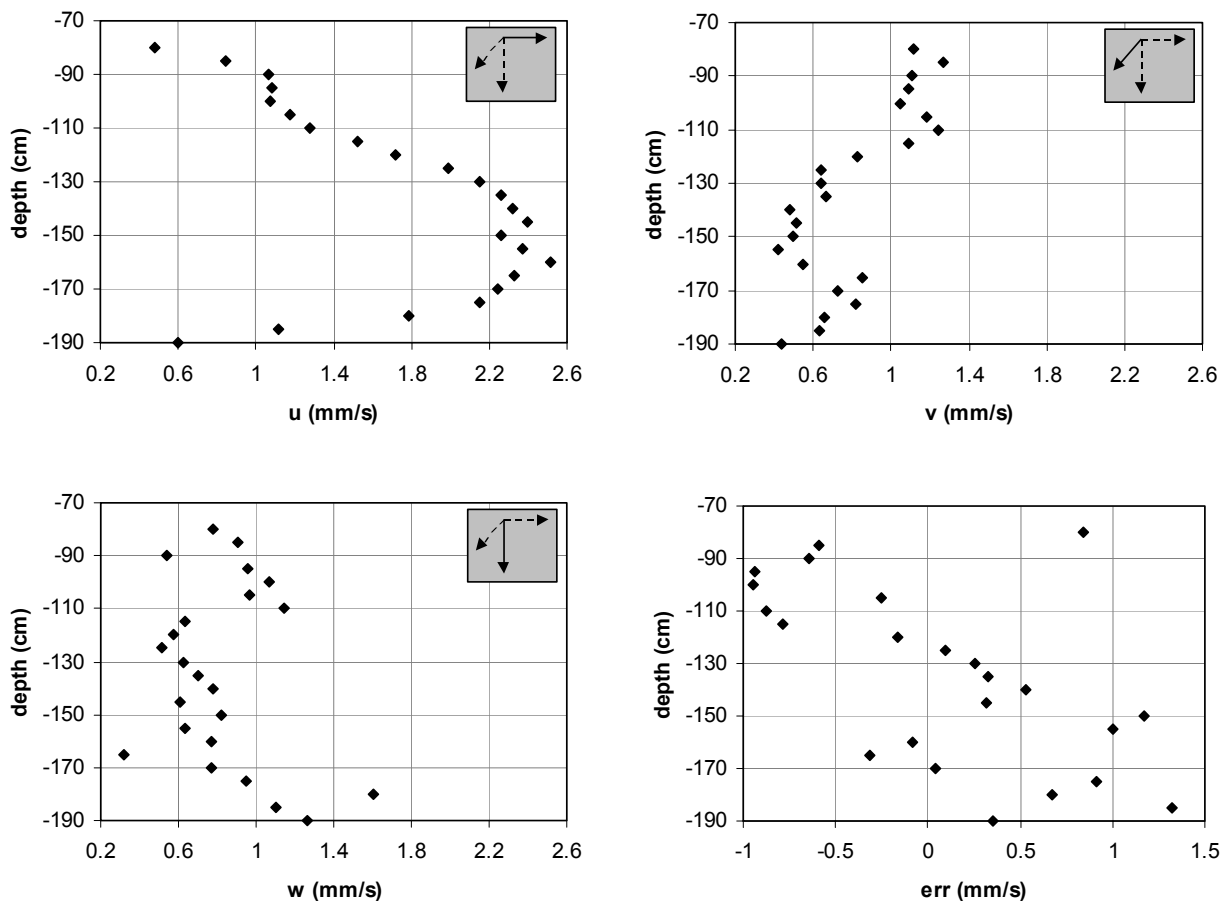


Figure 4.15 Measured velocity-depth profiles; in the main flow direction (top, left), horizontal and perpendicular to the main flow (top, right), and vertical and perpendicular to the main flow (bottom, left). The vertical velocity error is also plotted as function of depth (bottom, right)

4.5 Particle size distribution

The behaviour of particles is of major interest when studying settling tanks. In the hindered settling regime, particle settling is primarily dictated by the prevailing solids concentration. At low concentrations, however, discrete settling occurs. Here, the particle's behaviour is influenced by many factors; amongst them, particle size is the most commonly determined parameter. Particles are not critical solely to wastewater treatment but to many industries, and their economic impact is significant; a 1993 study estimated that particulate products annually contributed \$1 trillion to the US economy (Scott, 2002). Clearly, particle characterisation is crucial for process understanding and development.

In practice, many measuring techniques of Particle Size Distributions (PSD) exist, both *in situ* and *ex situ*. In this chapter different sizing techniques are discussed. A major characteristic of particle sizing technology is that every technique focuses on different particle characteristics and, therefore, results of the different methods will be different as well. Although some researchers combine techniques to cover a larger range of particle sizes (Pandya & Spielman, 1983; Li & Ganczarczyk, 1991), such practices should be avoided due to this incompatibility.

Due to different measurement principles particle sizers may be based on particle lengths, surface areas or volumes. Also the frequency of occurrence may be expressed differently; for instance, the particle numbers or volume fractions in specific size classes can be utilised. Knowledge on the particle shape is clearly necessary to enable any transformation between different size distributions; e.g. transforming a number-frequency to a volume-frequency size distribution. However, this particle shape information is generally absent and spherical shapes are adopted in the calculations.

In order to compare different PSDs statistical techniques are used. In this research, two statistical parameters were utilised, i.e. the number-weighted mean diameter $D[1,0]$ and the volume-weighted mean diameter $D[4,3]$, computed as

$$D[1,0] = \frac{\sum_{i=1}^N n_i M_i}{\sum_{i=1}^N n_i} \quad \text{for size classes } i = 1, 2, \dots, N$$

$$D[4,3] = \frac{\sum_{i=1}^N n_i M_i^4}{\sum_{i=1}^N n_i M_i^3} \quad \text{for size classes } i = 1, 2, \dots, N$$

with n_i and M_i the particle count and midpoint of size class i respectively. Whereas the $D[1,0]$ is the mean of a number frequency distribution, the $D[4,3]$ relates to the mean of the corresponding volume (or mass) frequency distribution.

4.5.1 Particle sizing techniques

Although many interesting sizing techniques are available on the market, it is beyond the scope of this work to cover them all. Therefore, traditional techniques such as sieving (e.g. Shillabeer *et al.*, 1992) and impactors (e.g. Schmidt-Ott, 2002) are not discussed; only (relatively) new techniques with potential toward biofloc characterisation are focused upon.

4.5.1.1 Electric resistance (electric sensing zone)

Sizing techniques based on electric resistance are also popularly called *Coulter Counter techniques*. They determine the sizes and number of particles suspended in a conductive fluid. Changes in the resistance between two electrodes immersed in the fluid are caused by particles passing through a small aperture located between the electrodes. Resistance changes are monitored as voltage pulses of short duration having a magnitude proportional to the particle volume.

According to Li & Ganczarczyk (1991), particle shape, surface roughness, and the nature of the material have little effect on the measurement. However, particles experience considerable squeezing forces when passing the aperture. Hence, particles with high porosity are not suited for this type of measurement; it is likely that errors occur due to particle breakage and compression. Andreadakis (1993) therefore applied a 200 μm aperture for size measurements in the range 2-75 μm . Instead, Li & Ganczarczyk (1991) used an aperture of 70 μm for particles smaller than 10 μm . Important is that usually high NaCl concentrations are utilised to increase the conductivity (Wilén, 1999), which may cause flocs to disintegrate (by destabilising the electric double layer) and cells to burst (by altering the osmotic pressure).

4.5.1.2 Image analysis

Originally, particle sizes were measured one by one on a microscope slide by means of an eyepiece micrometer (Barbusinski & Koscielniak, 1995). Although the method does not allow the measurement of all geometric parameters, e.g. cross-sectional area and perimeter, its main advantage is simplicity. Due to the tedious measurements, however, only 100 flocs could be determined for every PSD.

In order to obtain more representative distributions, i.e. more particles, images are taken by microscope and subsequently analysed. If colour images are obtained, they first need to be converted to monochrome images. Then, a user-defined threshold on the scale of varying tones of a specific colour, usually grey, distinguishes objects from the background. The image analysis software subsequently identifies an area of the image as a particle if the grey values of the contiguous pixels exceed the user-defined threshold. This threshold can be set manually (e.g. Li & Ganczarczyk, 1991) or automatically (e.g. Brewer & Ramsland, 1995). Because manual thresholding is tedious, only 500 particles or more are considered in a PSD (Spicer & Pratsinis, 1996), whereas the automatic technique easily can go up to 1000 particles and more (Brewer & Ramsland, 1995). The automatic thresholding, however, is doubtful in case of bioflocs; they have diffuse boundaries differing for every particle. Hence, to obtain representative PSDs every image should be treated individually and an appropriate threshold

should be set. Thanks to dark-field lighting, particles appear as white objects on a black background. As a result, black-and-white images are obtained, and the same threshold can be used for all images (Grijpspeerdt & Verstraete, 1996).

Image analysis as described is a well-known sizing tool applicable to suspensions characterised by low solids concentrations; Sievers *et al.* (2002) presented an advanced image analysis technique to obtain a PSD for highly concentrated suspensions though. The latter method could be applied online. Many other interesting studies exist, e.g. the study of discrete settling as function of particle size (Li & Ganczarczyk, 1987).

From the previous, optical microscopy is clearly less convenient for the analysis of floc size distributions, since it is very time-consuming to measure the large number of particles required for statistical relevance. Small flocs are further difficult to characterise correctly. In this respect, Vlaški *et al.* (1997) mention that the smaller the particle and the magnification, the larger the error on the size measurement. Nevertheless, image analysis is an evolving technique with great potential. Dez *et al.* (1997) used a microholographic technique applicable to high solids concentrations; the method can deal with number concentrations ranging from 10^4 to 10^5 particles per cm^3 . Another advantage is the visualisation of the total sample volume with a single holographic image by simply using the displacement of the optical system. Without sample contact, any squeeze of particles between microscope slide and plate is avoided.

4.5.1.3 Laser diffraction

Laser diffraction is a very popular sizing technique initially applied in the field of inorganic particles (e.g. Kyriakidis *et al.*, 1997; Serra & Casamitjana, 1998; Spicer *et al.*, 1998; Tang, 1999; Waite, 1999). The number of publications with applications to biological flocs is rapidly growing though (e.g. Wilén, 1999; Biggs, 2000; Govoreanu *et al.*, 2002; Nopens *et al.*, 2002). However, only dilute suspensions can be used for analysis. Therefore, Biggs (2000) had to dilute the activated sludge suspension considerably. To apply the technique correctly, knowledge of the underlying assumptions is also needed to interpret PSD measurements.

The principles of laser diffraction are based on the Generalised Lorentz-Mie Theory (GLMT), developed at the end of the 70ies (van de Hulst, 1981; Bohren & Huffman, 1983; Gréhan, 1999). The theory describes the interaction between *one* particle and an incident laser beam based on the solution of Maxwell's equations. Originally, it was only deduced for plane waves but later extensions made the theory also applicable to non-uniformly shaped laser beams; hence, the term "generalised". Gréhan (1999) further mentions that GLMT especially applies to spherical scatterers (some extensions of the theory exist for multi-layered spheres, circular and elliptical cylinders). Although the GLMT theory is strictly set up for spherical particles only, Bohren & Huffman (1983) indicate its use as a first-order description of the optical effects in non-spherical particles as well.

To obtain a PSD from light scattering patterns, an optical model is required to interpret the scattering pattern of particles. The technique actually consists of fitting the predicted to the measured scattering pattern. From this exercise the PSD is estimated; hence, the PSD is not measured directly as other methods do. Whereas the original LMT theory from 1908

exactly describes the light scattering and absorption of any spherical particle, several approximations are made to perform faster computations. In this respect, the Rayleigh approximation only incorporates absorption and scattering by small spheres that are smaller than the laser's wavelength; the following conditions have to be fulfilled,

$$D \ll \frac{\lambda}{2\pi}$$
$$|m| D \ll \frac{\lambda}{2\pi}$$

where D , λ and m are the particle diameter, wavelength and refractive index respectively. If particles are larger and they have an arbitrary shape, they behave according to the Rayleigh-Gans-Debye theory. Here, the scattering of the particle can be considered to be an integration of the scattering behaviour of each constituting primary particle. Again, some conditions have to be satisfied, i.e.

$$|m - 1| \ll 1$$
$$|m - 1| D \ll \frac{\lambda}{2\pi}$$

According to Selomulya *et al.* (2001), the Rayleigh-Gans-Debye theory can be extended beyond the range specified above. Less than 10% deviation in absorption and scattering can be obtained for primary particles with $|m-1|$ up to 1 or more and diameters D such that $\pi D/\lambda \leq 0.3$.

This approximation is also used a lot in practice to study the fractal dimension (see Section 2.2.3.1) of particles. Mainly inorganic particles have been investigated so far, e.g. Amal *et al.* (1998), Biggs *et al.* (1998), Guan *et al.* (1998) and Waite (1999). Attempts to determine the fractal dimensions for bacterial aggregates can be found in the works of Guan *et al.* (1998) and Biggs (2000). The main problem in these investigations is the unknown refractive index of bioflocs.

To deal with suspensions without known refractive index alternative scattering models have been developed. In this way, Fraunhofer diffraction is based on particle scattering only, and is applicable to suspensions with small particles that do not scatter much light. Because Fraunhofer diffraction observes the ensemble scattering of particles, it enables the PSD measurement of particle suspensions with relatively high number densities (Bachalo, 1999). For bioflocs, the major advantage of the theory is the absence of the refractive index in the model; in general this is not known for biological aggregates. To finalise this topic, Fraunhofer interpretation can only be applied for particles larger than 10 μm (Sparks & Dobbs, 1993). Above this threshold, the PSDs obtained by the Fraunhofer theory are similar to those measured with the GLMT model. For biological solids, this is demonstrated in Figure 4.16 for sludge from a lab-scale sequencing batch reactor.

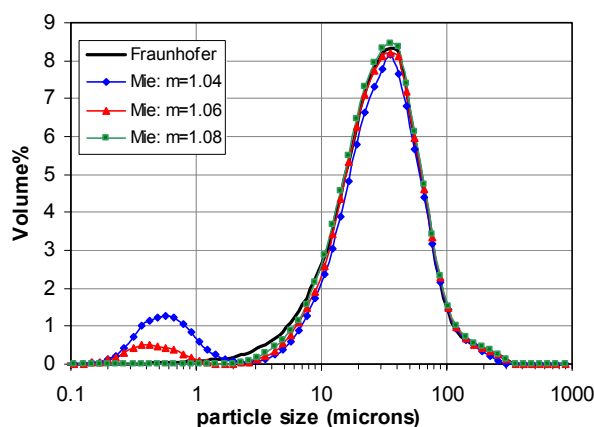


Figure 4.16 Comparison of the Fraunhofer and Mie interpretation for sludge from a sequencing batch reactor (m denotes the refractive index) (Govoreanu, personal communication)

Comparison with other sizing techniques is not possible since they are based on different physical properties. As a result, the PSDs will differ from each other. In this respect, Shillabeer *et al.* (1992) made a comparison between laser diffraction and dry sieving. They concluded that the similarity between samples analysed by the two techniques was 79%. Hence, the differences are large enough to mask possible changes in PSD. On the other hand, Brewer & Ramsland (1995) investigated laser diffraction and image analysis; they both resulted in bimodal PSDs. Further, it was observed that PSDs determined by laser diffraction fell between the size ranges of the microscopically determined area- and volume-weighted distributions.

4.5.1.4 Time of transition

The sizing technique presented here immediately returns a size distribution (e.g. Serra *et al.*, 1997; Serra & Casamitjana, 1998). Devices, such as delivered by Ankersmid N.V. (Edegem, Belgium), use a constantly rotating laser beam to scan the sample (Figure 4.17). Particles temporarily block the laser beam, and the time of interruption is measured by detectors opposite to the laser, i.e. the "time-of-transition". From the speed of rotation and the time-of-transition a so-called *chord length* is obtained; chord length ranges of 2-3600 μm may be covered. The last years many improvements to the technique have been obtained increasing the accuracy (Weiner *et al.*, 1998).

To obtain a statistically relevant PSD, enough particles are to be measured. Therefore, a stirrer should mix the samples or a continuous flow crossing the laser beam should be established. Depending on the strength of the particles, however, this measuring procedure may cause their breakup. Hence, the technique should only be applied to dilute suspensions with rather strong aggregates to minimise both floc growth and breakup. When these experimental conditions are fulfilled, the method compares well with laser diffraction methods (Serra *et al.*, 2001).

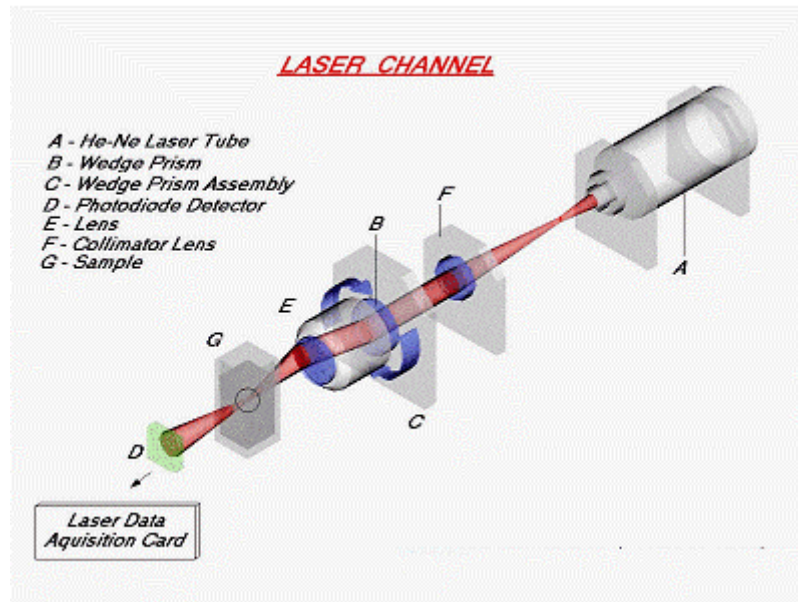


Figure 4.17 Measurement principle of time-of-transition technique (Galai, 2003)

4.5.1.5 Laser reflection

The laser reflection technique is also known as the Focused Beam Reflectance Method (FBRM) and is very similar to the time-of-transition method (see Section 4.5.1.4); instead of transmission of laser light, its reflectance is used. The major advantage of the FBRM technique is the operating range for solids concentrations, i.e. concentrations up to 50 g/l (Law *et al.*, 1997), or solids volume fractions up to 50% (Peng & Williams, 1994) can be applied. Further, to produce statistically acceptable PSDs, Michael *et al.* (2001) stated that 2000 particles or more need to be sampled per second. Of course, this number is highly dependent on the nature of the dispersion too. To retain this sampling frequency, mixing of the suspension is clearly very important; intense mixing increases the frequency of particle detection and decreases the measurement duration.

The FBRM probe used in this research was the Lasentec FBRM M500 (Lasentec, Redmond, Washington, USA). It consists of a laser that is focused in some focal plane outside the sapphire window (Figure 4.18, left). The laser rotates at a high fixed speed, i.e. 2 m/s, so that particle motion is insignificant to the measurement. As particles pass the focal plane, the focused beam intersects the edge of a particle and begins to backscatter the laser light. The backscatter continues until the focused beam reaches the particle's opposite edge. The backscatter is collected by the FBRM optics and converted into an electronic signal.

The FBRM uses a discrimination circuit to isolate the time period of backscatter from one edge of an individual particle to its opposite edge. This time period is multiplied by the scan speed and the result is a distance, i.e. the chord length as mentioned in Section 4.5.1.4 (Figure 4.18, right).

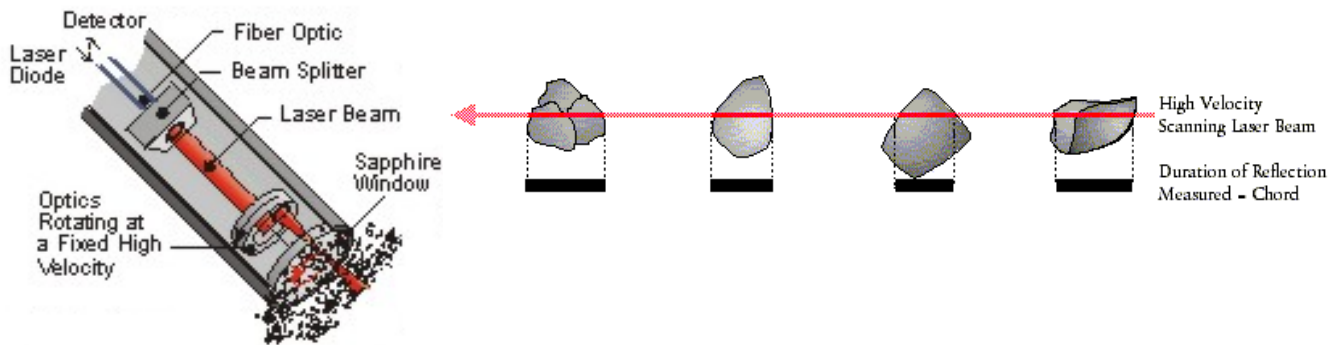


Figure 4.18 Principle of FBRM; probe layout (left) and definition of chord length (right) (Lasentec)

The FBRM hardware provides 1324 primary channels of data ranging between 0 and 1024 μm on a linear scale. This scale is split into two ranges, 0-100 μm and 100-1024 μm . The 400 channels in the 0-100 μm range provide finer, 0.25- μm resolution, whereas the upper 924 channels provide a coarser, 1- μm resolution, covering a wider micron range (100-1024 μm). The Lasentec software gives the user the ability to group the primary channels in a way that is optimal to the application.

Data processing of the detector responses interprets both the strength and the slope of the reflected light pulse. Current instrument data processing is adjustable through the use of either F-(fine) or C-(coarse) electronics modules, the main difference being the faster pre-amplification and greater edge definition of the former. The F-electronics are more sensitive to signal interruptions, hence small particles travelling closely together are more easily detected. Instead, the C-electronics allow the FBRM to track larger loosely packed flocs or large particles with extreme surface structures. The F-electronics are typically used for systems where the particles are primarily between 0.1 and 350 μm . The C-electronics are mainly used in applications where there are very rough surface features (larger than 20 μm). Compared to the F-electronics, the C-electronics are significantly less sensitive to changes below 20 μm (Neumann & Howes, 2002).

4.5.1.6 Acoustic and electroacoustic spectroscopy

A technique gaining popularity is acoustic spectroscopy (see also Section 4.3.2), which is based on the application of high-frequency sound waves to a suspension. Due to the sound wave, the ions in the double layer surrounding the particles move with the oscillating fluid. However, the particles' inertia resists the movement, translocating the double layer relative to the particle and, as a result, creating a small dipole. All the dipoles in the suspension are oriented identically and create an electric field, which is called the colloid vibration potential. Conversely, when an alternating electric field is applied to a suspension, a sound wave is generated similar to a piezoelectric crystal. The magnitude of this electroacoustic signal, and the phase lag between the applied signal and the suspension response are a result of the particle inertia, hence measurements of these two variables can be related to the mass-weighted mean particle size (Spicer, 1997; Scott, 2002).

Another approach is the measurement of the attenuation of the sound wave propagating through the suspension as function of the wave frequency (Spelt *et al.*, 1999). Besides the

attenuation, also the transit time of sound through the sample volume can be utilised (Coghill *et al.*, 2002). Both sizing approaches are based on an *ab initio* particle-wave interaction theory assuming spherical particles and including thermal, viscous and scattering effects (Spicer, 1997; Scott, 2002). These techniques enable the measurement of rather broad particle size ranges, i.e. 0.01-1000 μm (Coghill *et al.*, 2002).

Since the theory basically assumes single particle conditions, a multiple scattering correction has to be made at higher solids concentrations, i.e. >5-10% vol (Scott, 2002). New theoretical models enable particle sizing for solids concentration up to 250 g/l or 40-50% vol (Wang *et al.*, 2002).

4.5.2 *In situ* versus *ex situ* sizing techniques

Many of the previously described sizing techniques clearly cannot be applied *in situ*, though this is a very important issue because sampling, sample transport and preparation prior to analysis might influence the PSD considerably. In this respect, Phillips & Walling (1995a) investigated the influence of fluvial sediment particle settling during transport by laser reflection. One hour of settling, followed by resuspension, resulted in an increase of 14% for the volume-weighted mean size. The longer the sample was allowed to settle, the larger the increase in volume-weighted mean size. Because of sample transport, Daymo *et al.* (1999) even observed 25% changes for volume-weighted mean chord lengths. For microscopic sludge investigations, Parker (1970) noticed that flocs grow in size at the surface of the liquid drop, or underneath the microscope slide. To avoid this, floc impingement on Millipore filters was suggested. Pumping at a high flow rate influences the PSD as well. Biggs (2000) applied a peristaltic pump in order to pump sample to a laser diffraction instrument; floc fragmentation clearly occurred in the tubing. Similar effects were observed by Bale & Morris (1987) and Govoreanu *et al.* (2002). A study by Spicer *et al.* (1998) revealed that syringes have the same impact on the PSD as peristaltic pumps. Pipettes altered the PSD more dramatically and significantly smaller particles could be observed. Finally, Li & Ganczarczyk (1991) prepared their samples for image analysis by agar solidification. The function of agar was twofold; (i) sample dilution and (ii) floc stabilisation by stopping the nutrient and oxygen supply to the microorganisms. For the electric resistance technique (see Section 4.5.1.1), they used phenol to quickly kill the microorganisms in the flocs and, therefore, stop any further microbial activities that may lead to changes in floc structure.

From the previous, many errors are obviously introduced when investigating a sample *ex situ*. Researchers therefore try to apply the before-mentioned sizing techniques *in situ*.

Several waterproof laser diffraction instruments became available on the market after the work of Bale & Morris (1987). Bale *et al.* (1989), Agrawal & Pottsmith (2000) and Serra *et al.* (2001) applied the LISST-ST (Sequoia Scientific Inc., USA) to lakes and estuaries. Another commercial laser diffraction instrument, the INSSEV (developed at the Institute of Marine Studies, University of Plymouth, UK), has been used in estuaries too (Dyer & Manning, 1999). Despite their successful deployment in open waters, applications to settling tanks are doubtful. This scepticism is mainly due to the high prevailing solids concentrations in settling tanks, whereas these *in situ* laser diffraction instruments only operate at low concentrations.

Instead, instruments based on laser reflection can handle much higher solids concentrations, up to 50 g/l. Applications can be found in the fields of reactor technology (Peng & Williams, 1993), rivers (Phillips & Walling, 1995a,b) and radioactive slurry transport (Daymo *et al.*, 1999).

The flexibility of the acoustic techniques (see Section 4.5.1.6) opens a whole range of new applications. Commercial instruments, such as the Malvern Ultrasizer (Malvern Instruments Inc., UK), measure the acoustic velocity and attenuation of a suspension, compare the results with theory, and determine the best fit for the PSD. A very important advantage of this technology is its non-invasive character.

With an ADCP-like device (see Section 4.4.3.2), for instance, acoustic scattering from different depths can be obtained. In this respect, Reichel & Nachtnebel (1994) measured the solids concentration and the PSD at different depths in rivers, but could only obtain a coarse and very qualitative measurement of both variables with mono-frequency acoustic waves. Indeed, the received signal is an integrated system response. Multi-frequency acoustics should solve this problem though. Applications of acoustic spectroscopy can also be found in other fields, like metal industry (Coghill *et al.*, 2002) and food industry (Demetriades & McClements, 1999). Although the technique is still in its infancy, it has an important potential.

4.5.3 The focused beam reflectance method revisited

In Section 4.5.1.5 the reader was introduced to the FBRM technique. Here, the method will be discussed in more detail, as it will be an essential element in Chapter 6. There, a full-scale secondary settling tank is investigated with the Lasentec FBRM M500 (Lasentec, Redmond, Washington, USA).

Firstly, the issue of an optimal focal point for the laser beam is considered, since an improper choice may result in considerable differences in size distributions obtained. Secondly, in order to gain insight in the technique's response to inorganic particles and sludge, a comparative study with other sizing techniques is performed.

4.5.3.1 Optimisation of focal point position

Before starting FBRM measurements, it is essential to set the focal point of the FBRM probe (Sparks & Dobbs, 1993; Monnier *et al.*, 1996; Law *et al.*, 1997). When optimised, a calibrated probe is obtained allowing the user to measure a statistically acceptable PSD. Optimisation corresponds to finding the "maximal" reflectance response by changing the focal point position. Several researchers (Barrett & Glennon, 1999; Dowding *et al.*, 2001) retain the standard setting for the probe, i.e. 20 μm inside the sapphire window. According to the manufacturer, this generally results in a maximal signal-to-noise ratio. On the other hand, others focus the beam on the window itself (Williams *et al.*, 1992; Peng & Williams, 1993; Heath *et al.*, 2002). Instead, Phillips & Walling (1995a,b), Monnier *et al.* (1996), Law *et al.* (1997) and Richmond *et al.*, (1998) optimised the focal point position in order to have a maximum detection of counts per second. Recently, Worlitschek & Mazzotti (2001)

demonstrated for ceramic particles that the best focal point position to detect both large and small particles is at the probe window. Further away from the window a stronger attenuation of the reflectance signal may occur; this signal shadowing is mainly caused by the relatively high surface-to-volume ratio of small particles. Hence, small particles are not detected anymore and the large particles' size is underestimated (Figure 4.19). Large particles are still detected at more distant focal points though, due to their stronger reflectance signal.

Since biological flocs have highly irregular geometries as compared to ceramic particles as studied by Worlitschek & Mazzotti (2001), they might respond completely differently to the incident laser beam. Also, Worlitschek & Mazzotti (2001) worked with solids concentrations of only 40 mg/l. Such low concentrations are only encountered in secondary settling tanks near the effluent weirs. Hence, the reflectance response at high solids concentrations still needs to be evaluated. To this end, three different sludge samples were investigated that were thought to exhibit different laser reflectance responses due to their expected difference in PSD. Samples from the inlet, outlet and underflow of a secondary settling tank at Oxley Creek WWTP (Oxley, Australia) were considered. The outlet only showed a solids concentration of 7 mg/l, whereas the samples from the inlet and the underflow had a concentration of 2500 and 5140 mg/l respectively. In a gently stirred beaker, the focal plane of the laser was changed from the window to 3 mm into the suspension and one-minute measurements were performed.

In Figure 4.20 only the results for the underflow sludge and effluent are shown; the plot for the inlet sludge is comparable to the underflow case. From Figure 4.20 (left) it is clear that at high solids concentrations the signal is more shadowed with increasing focal distance, i.e. the number of counts per second decreases. On the other hand, the effluent is diluted to such extent that the reflectance signal is always detected by the FBRM optics with only a slight attenuation. This behaviour is also seen in Figure 4.20 (right) where the $D[1,0]$ is shown as function of the focal point distance. The corresponding $D[4,3]$ shows similar profiles. For the highly concentrated underflow small particles are not detected at all and the size of large particles is underestimated (Worlitschek & Mazzotti, 2001). As seen in Figure 4.20 (right) as well, this underestimation obviously becomes worse for larger focal point distances. This is in accordance to the fundamental study performed by Worlitschek & Mazzotti (2001). When performing this study, however, the work of Worlitschek & Mazzotti (2001) was not yet published. The optimal focal point position was therefore based on the maximal reflectance response as performed by Phillips & Walling (1995a,b), Monnier *et al.* (1996), Law *et al.* (1997) and Richmond *et al.* (1998). Hence from Figure 4.20 (left) different optimal focal point positions were found for underflow, inlet and effluent samples, i.e. 255, 305 and 55 μm . For practical reasons only two focal points were retained for *in situ* measurements in a full-scale secondary settling tank (see Chapter 6), i.e. one for measurements above the solids blanket (55 μm), and one for below the blanket (280 μm , being the average of the positions for the underflow and inlet). With these settings a maximum reflectance over the total measured chord length range was obtained.

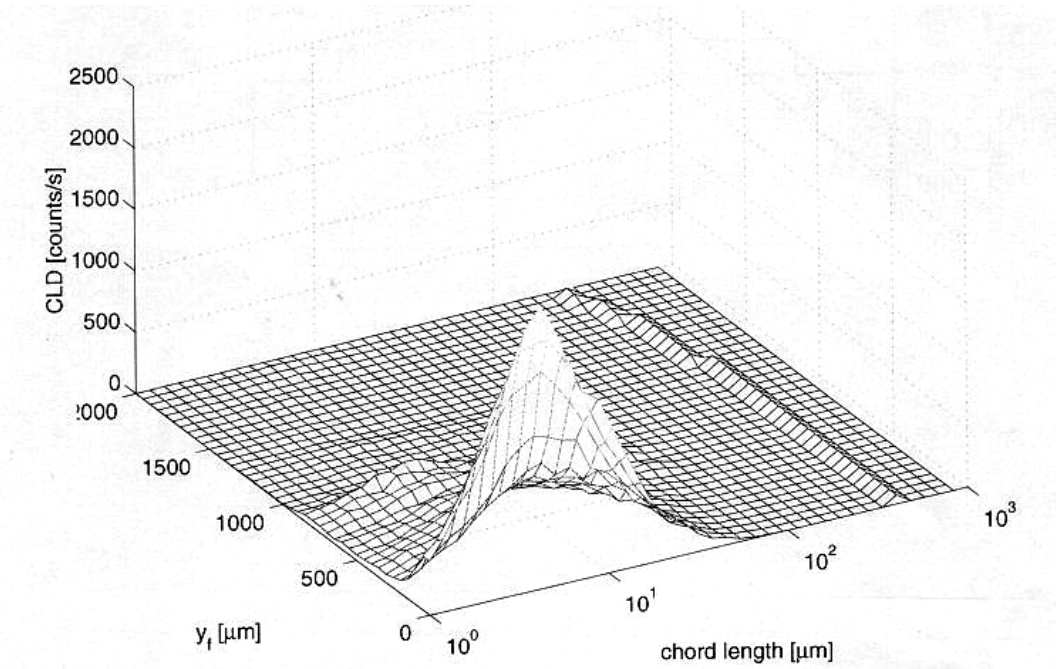
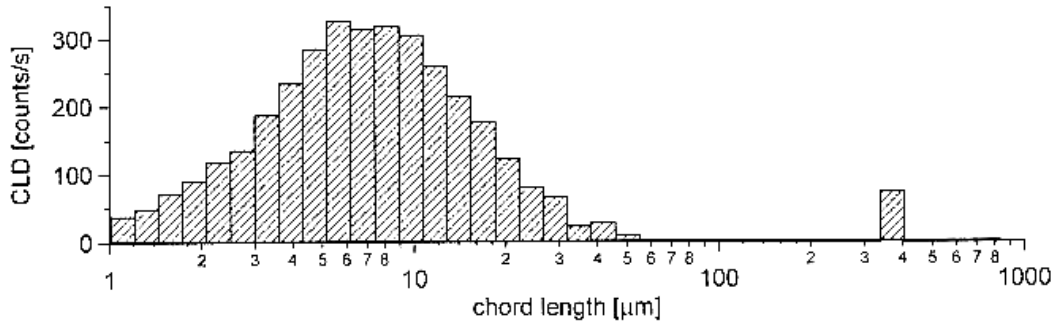


Figure 4.19 Measured PSD for different focal point distances from the window (y_f); real PSD (top), and observed PSD with FBRM (bottom) (Worlitschek & Mazzotti, 2001)

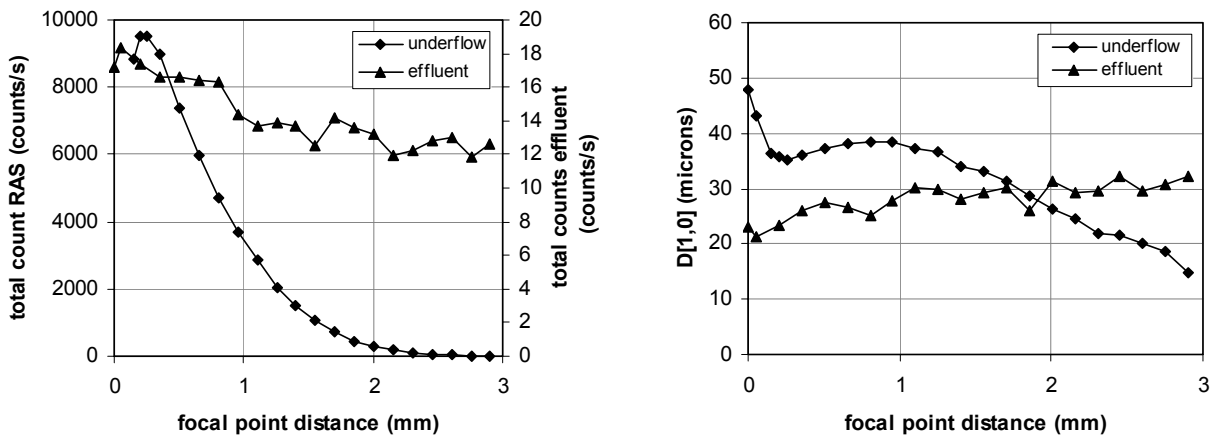


Figure 4.20 Influence of focal point position on the total number of counts per second (left) and the number-weighted mean chord length ($D[1,0]$) (right) for both underflow and effluent

The work of Worlitschek & Mazzotti (2001) clearly indicates that the robustness and accuracy of the FBRM technique largely depends on the focal point position. As solids concentrations vary within the secondary settling tank it seems essential to keep the focal point close to the window in order to measure all ranges of particle sizes. According to Figure 4.19, the previously set focal point positions in the settling tank will result in an underestimation of the small-particle frequency. Despite this underestimation, different PSDs, both in space and time, still can be compared with one another and reveal trends in PSD dynamics.

From experiments, it was observed that small particles may stick to the window and were as a result detected manifold. High count frequencies make the PSD spiky; hence, they are not a representation of the "real" PSD. This phenomenon was observed during *in situ* measurements in secondary settling tanks, where shear is very low (see Chapter 6). However, also at higher shears (up to 65 s^{-1}) Neumann & Howes (2002) noticed river sediment particles sticking at the sapphire window. To avoid any interference of sticking particles they placed the focal point outside the window, $480 \mu\text{m}$ into the suspension. Obviously, reconsidering Figure 4.19, this approach is questionable; the reflectance signal from small particles is considerably attenuated. Even more, in rivers and estuaries solids concentrations exceed 40 mg/l , especially during tide periods. These considerations further question the approach of Neumann & Howes (2002).

In this work, data filtering is used to account for the effect of particles that stick on the window. To investigate whether particles stick on the window, the number frequency is expressed as counts per second. Theoretically, immobile particles will be detected with the same frequency as the rotation frequency of the laser (75 Hz for Lasentec FBRM M500). However, perfect immobility does not occur and slight deviations from this 75 Hz are observed. Sticking particles typically result in very spiky PSDs instead of smooth distributions obtained from representative sampling. The peaks occur at one or a few data chord lengths. An example is given in Figure 4.21. Due to the easily identifiable peaks, filtering is proposed to remove the bad data; the latter are neglected from the PSD and replaced by interpolated values. In this way, statistical parameters of the PSD can be calculated more accurately. This approach is applied in Chapter 6 when performing PSD measurements in a secondary settling tank.

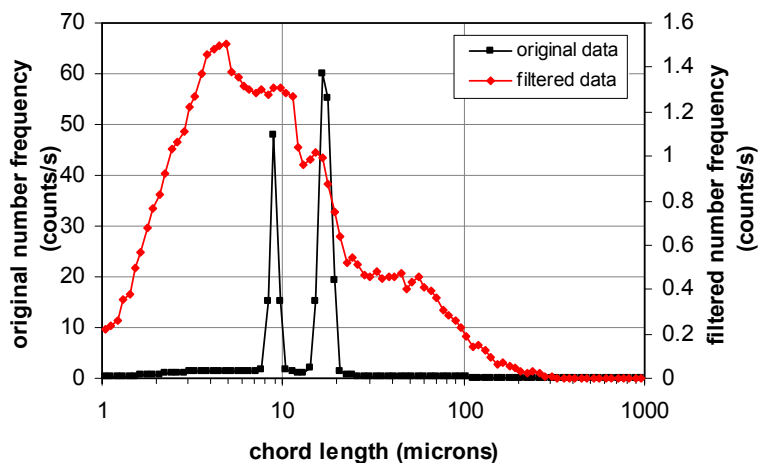


Figure 4.21 Filtering of PSD measured *in situ* in a secondary settling tank

4.5.3.2 Comparative study of FBRM, laser diffraction and image analysis

Many comparative studies with other sizing techniques can be found in literature. For different materials, Law *et al.* (1997) compared PSDs originating from laser reflection and other optical methods. It was observed that laser reflection oversized particles smaller than 150 μm , while undersizing particles above 500 μm . This seems to be valid for a wide range of particle compositions. Also Monnier *et al.* (1996) observed this under- and overestimation of particle sizes.

Due to its relative novelty, the FBRM technique will be compared to other sizing methods. The aim of the study was not the set-up of calibration rules between different techniques, but solely the understanding of the behaviour of the FBRM instrument. Hence, the discussed cases will only be approached in a qualitative manner. Here, two different particulate systems have been sampled in terms of their size distribution, i.e. inorganic and organic particles. As inorganic particles, glass beads and coric vinyl have been used. Because these particles have crisp boundaries the size distributions are relatively easy to interpret. Activated sludge flocs, however, do not have such crisp boundaries making data interpretation more difficult.

The comparative study will investigate three particle sizing techniques, i.e. laser diffraction, laser reflection and image analysis. Whereas all techniques were applied to inorganic particles, only the latter two were used for activated sludge.

Particle sizing by laser diffraction was performed with a Malvern Mastersizer/E which measures particle sizes between 1.2 and 600 μm . Because the size of a considerable fraction of flocs in activated sludge largely exceeds this size range, it was decided to exclude laser diffraction from the comparative study, but for sludge only. Laser reflection with FBRM measured sizes in 90 channels logarithmically distributed over the size range 1-1000 μm . The optical investigation of the PSD was done with a Nikon Microphot-FXA microscope (Figure 4.22). The objectives utilised in this study covered magnifications of 4x and 10x. Pictures of flocs were taken with the SPOT (SP100) camera, mounted on top of the microscope (Diagnostic Instruments Inc.). This digital Kodak KAF-1400 camera had a CCD resolution of 1315 x 1035 pixels. At a magnification of 4x and 10x, one millimetre corresponded to 424 and 1332 pixels respectively. Further, three images were taken, i.e. one each in red, green and blue (RGB). The software subsequently combined the images in one RGB colour image. For colours, one had the choice between 8-bit or 12-bit monochrome, and 24-bit or 36-bit RGB colour. To optimise the picture quality, the white balance (without flocs) was computed. Also the exposure time was optimised with the software and the shutter time was determined. For all pictures white light was used, together with a ND32-filter (part of the microscope system). Light from below the slides was minimised in order to have a black background. The flocs were mainly illuminated from above. It was concluded that this approach gave the best result for determining the particle boundaries; it is comparable to dark-field lighting as applied by Grijpspeerdt & Verstraete (1996).

Three slides with suspension were analysed in all cases. The slides measured 25.4 x 76.2 mm and had a thickness of 1 - 1.2 mm. Since a submersion lens was not available, cover slips of 22 x 64 mm were used. A couple of drops were applied by means of a syringe. From the slides, a total of 120-130 images were recorded.



Figure 4.22 Nikon microphot-FXA microscope

The images were analysed in ImageJ v1.24. This software package for image processing and analysis in Java is freeware and can be downloaded at <http://rsb.info.nih.gov/ij>.

The images were first converted from colour to an 8-bit grey scale. By means of a user-definable threshold set, the boundary of particles was defined. Whereas a common threshold was adopted for the case of inorganic particles, every image of activated sludge was individually manipulated by optimising the threshold. This was essential because the flocs did not show any crisp boundaries and the threshold might thus be different from one image to the other. The surface area was subsequently computed by means of a calibration ruler relating the number of pixels to a length scale. Obtained surfaces, and respective number frequencies, were converted to lengths and volumes with the assumption of a spherical floc geometry.

Inorganic particles

As inorganic particulate system, glass beads and coric vinyl particles were considered. They were investigated in terms of their PSDs; also a mixture of glass beads and coric vinyl particles was utilised. The PSDs were recorded with laser diffraction, image analysis and FBRM. All experiments were conducted in a 1.2 l baffled batch vessel (for the configuration, see Biggs (2000)). The liquor was stirred with a Heidolph RZR 2020 mixer at 500 rpm in all cases.

To detect enough scattering with the Malvern device and avoid multiple inter-particle scattering, the solids concentration should be kept low. Prior to any sizing experiment the concentration was set such that a specified obscuration threshold was not exceeded. Once fixed, this solids concentration was used for all experiments. In total 4000 sweeps (i.e. snapshots of PSDs) were recorded in one measurement. A Masterflex peristaltic pump with constant speed performed a continuous recycle of the suspension through the Malvern. The speed was chosen such that the particles did not settle in the tubes. This flow recycle was not needed when utilising the FBRM, i.e. the device was simply put in the suspension. A 20-seconds measurement period was maintained and no averaging was conducted. Measurements were taken over 90 channels logarithmically spread over the size range 1-1000 μm . Finally,

arbitrary samples were taken from the batch vessel and were investigated by image analysis. Between 150 and 190 particles were investigated.

Figure 4.23 shows the obtained volume-based PSDs from laser diffraction, image analysis and FBRM. The different distributions were very similar for coric vinyl. For glass beads laser diffraction and image analysis gave similar results, while the FBRM oversized the beads, which is in accordance to the work of Law *et al.* (1997). These researchers observed an oversizing by the FBRM for particles smaller than 150 μm . The coric vinyl particles had, according to laser diffraction, a $D[4,3]$ of 158.2 μm and did not show any discrepancy with the $D[4,3]$ of distributions obtained with other measurement techniques. Similar behaviour was seen in the distribution of the mixture of the latter two. The three distributions overlap each other at sizes corresponding to the coric vinyl particles. Instead, the FBRM oversized again the particles in the lower size range. In general, it can be noted that the distributions originating from image analysis were very similar to those from laser diffraction, although they measure surface-based and volume-based distributions respectively.

Activated sludge flocs

Whereas glass beads and coric vinyl particles have the advantage of crisp boundaries, biological sludge consists of bioflocs that are very irregular and have diffuse boundaries. As noted, laser diffraction will not be considered here because of the limited observable size range of the Malvern Mastersizer/E, i.e. 1.2 - 600 μm . In practice, this range is even smaller and the present floc sizes largely exceeded the upper boundary. Again, only qualitative information was aimed for; setting up a relation between the FBRM and image analysis was not the objective.

For the experiments, RAS was taken from the WWTP at Oxley Creek (Oxley, Australia). The sludge was examined on the day of sampling or, at the latest, two days after sampling. To study different PSDs the collected sludge was subjected to three treatments, i.e.

- diluted RAS
- diluted RAS with 50 g NaCl/l
- diluted and sonified RAS

Dilution was necessary in order to perform image analysis; otherwise particles cover one another and a wrong estimate of the size would be obtained. The last two cases focused on different influences on the size distribution, i.e. physico-chemistry (salt) and increased shear. It is well-known that high concentrations of monovalent cations may cause deflocculation; they exchange with specified adsorbed ions (Bruus *et al.*, 1992). Deflocculation is also obtained by applying high shears (Biggs, 2000; Govoreanu *et al.*, 2002).

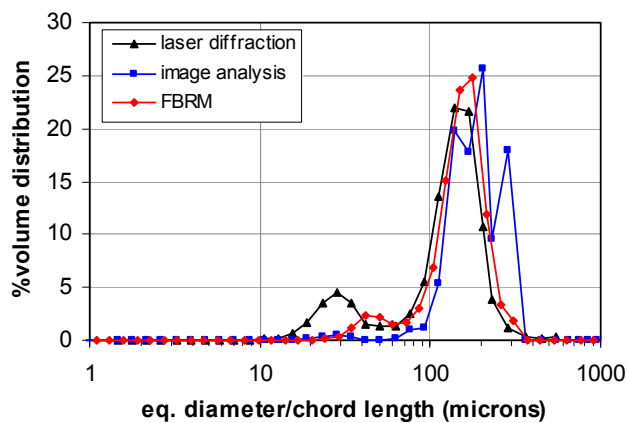
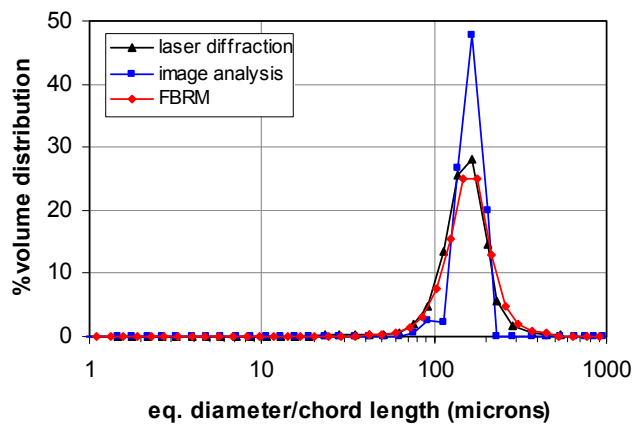
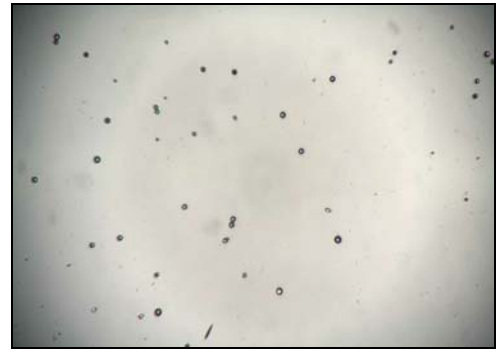
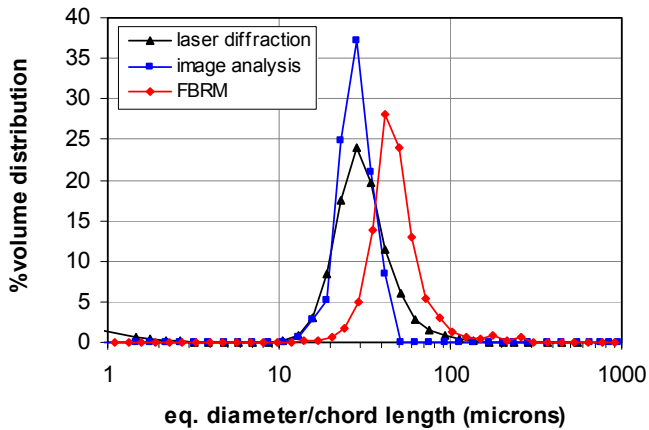


Figure 4.23 Volume distributions of three different systems measured with laser diffraction, FBRM and image analysis; glass beads (top), conic vinyl particles (middle), and a mixture (bottom)

For sonication, a Branson Sonifier Model 450 (Branson Ultrasonics Corporation, USA) was used. The device was equipped with a horn tip. Sonication of diluted RAS was applied for 2 minutes in continuous mode with a power of 65 W to a mixed liquor volume of 100 ml. Immediately after sonifying the suspension, a PSD was recorded with the FBRM with a 1-minute sampling time. Larger sampling times were not considered because of reflocculation. Notice that the sonication power was extremely high. In this respect, Biggs (2000) avoided a

power above 40 W in order to keep the cell structure intact. Here, the aim was to significantly alter the size distribution.

For all experiments, flocs were kept in suspension by a variable speed mixer (IKA LaborTechnik RW16 basic; "mixing grade" 1) placed 6 mm below the sapphire window of the FBRM probe. Steady-state conditions were reached before performing each experiment and was checked by means of the temporal stability of $D[4,3]$ and $D[1,0]$.

After examining the dispersion by FBRM, a sample was taken and brought to the microscope lab (wrapped in tin foil to protect against solar radiation). The microscopic work took on average 1-1.5 h. Hence, differential settling occurred and led to flocculation. Before taking sludge with the syringe, the sample cup was gently shaken for 30 seconds to resuspend the sludge.

Table 4.6 summarises the Total Suspended Solids concentration (TSS) and the total number of counts for every experimental case. Clearly, no straight relation existed between concentration and number of counts. Both image analysis and FBRM methods strongly depend on the nature of the dispersion, i.e. floc's irregularity and the frequency of small and large particles. However, to produce statistically acceptable PSDs with the FBRM, Michael *et al.* (2001) stated that 2000 or more particles need to be sampled per second; this sampling frequency is of course very dependent on the particulate system studied. Although this condition is not satisfied for sonified RAS the total number of counts is large enough to produce good statistics. For image analysis, Brewer & Ramsland (1995) used up to 1000 particles for computing the PSD. Here, many more particles were counted.

Table 4.6 Summary of experimental conditions

	TSS (mg/l)	Number of counts	
		<i>Image Analysis</i>	<i>FBRM</i>
Diluted RAS	580	4166	110000 (1 min)
Diluted RAS + NaCl	2120	3049	350000 (2 min)
Sonified diluted RAS	400	6192	65000 (1 min)

Firstly, the raw (length-weighted) number frequency distribution is discussed for the three situations, i.e. diluted RAS, diluted RAS with NaCl and sonified diluted RAS. The results are shown in Figure 4.24. Their respective statistical parameters are summarised in Table 4.7.

Starting with image analysis, it is clear that most flocs are smaller than 5 μm . This agrees with microscopic observations of Parker (1970), Li & Ganczarczyk (1991) and Jorand *et al.* (1995). Further, it is seen that the $D[1,0]$ decreases by addition of salt and by an applied shear stress. Apparently, sonication has a greater impact than salt addition; salt reduced $D[1,0]$ only with 39.5% of the value without any stress factors, whereas sonication resulted in a decrease of 61.1%. Although the frequencies change, the general shape of the distribution remains the same for the three investigated cases. They are all characterised by a positive skewness. From Table 4.7, $D[1,0]$ also decreases for the number distribution obtained with the FBRM, but sonication gives a more pronounced effect on $D[1,0]$ than image analysis, i.e. a reduction of 79.2% compared to 61.1% for image analysis. Further, it results in a strong positively skewed distribution. A negative skewness is observed in the other cases. Apparently, salt induces a strong peak around 40-60 μm in Figure 4.24 (top, right).

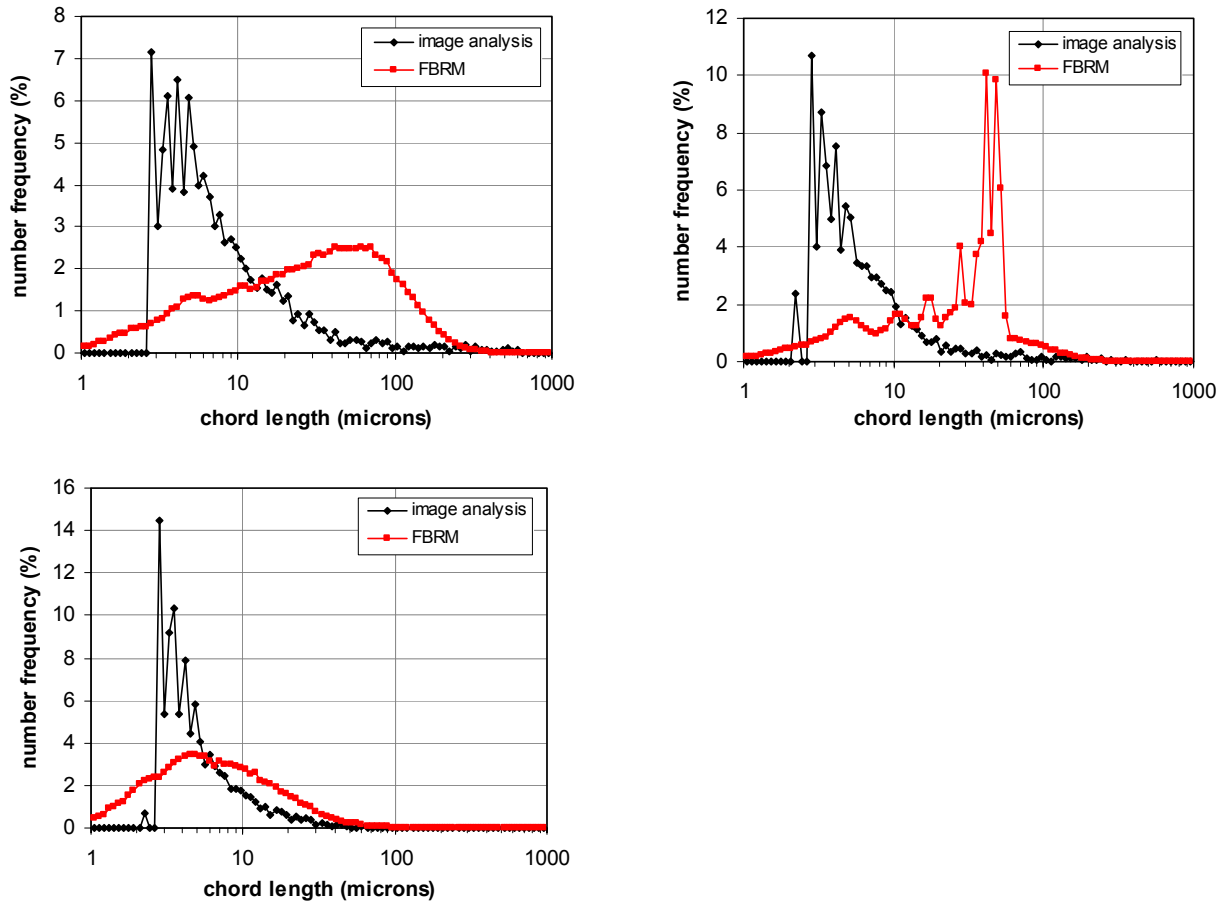


Figure 4.24 Length-weighted number frequency distributions for diluted RAS (top, left), diluted RAS with 50 g NaCl/l (top, right), and diluted RAS sonified at 65 W (bottom)

Table 4.7 Number-weighted and mass-weighted means for each investigated case

	Image Analysis		FBRM	
	$D[1, 0]$	$D[4, 3]$	$D[1, 0]$	$D[4, 3]$
Diluted RAS	16.3	445.4	44.8	204.3
Diluted RAS + NaCl	9.9	353.2	32.5	142.7
Sonified diluted RAS	6.3	76.8	9.3	88.2

By comparing both methods it can be concluded that a huge discrepancy exists between the number distributions; the peaks in Figure 4.24 are located completely differently. More specifically, the number-weighted means from image analysis are smaller compared to those from FBRM. This is caused by the irregularity of the floc shape. The chord length does not take into account any assumption about particle sphericity, i.e. the real dimensions of the floc are measured. Therefore, the largest and smallest dimensions of irregular flocs would be respectively larger and smaller than the equivalent spherical diameter as measured by image analysis. If, for instance, the largest dimension corresponds to the largest surface area, i.e. the largest count frequency, $D[1,0]$ would measure a higher value than the one based on equivalent spherical diameters.

Secondly, the volume-weighted number frequency distributions shown in Figure 4.25 are discussed. For image analysis, rather spiky and negatively skewed distributions are obtained, which is primarily due to the sporadically observed extremely large flocs. On the contrary, the FBRM distributions were more smooth. In general, as for the number frequency distributions, no direct resemblance exists between the two sizing techniques. Again, the sonified sludge showed the best correspondence.

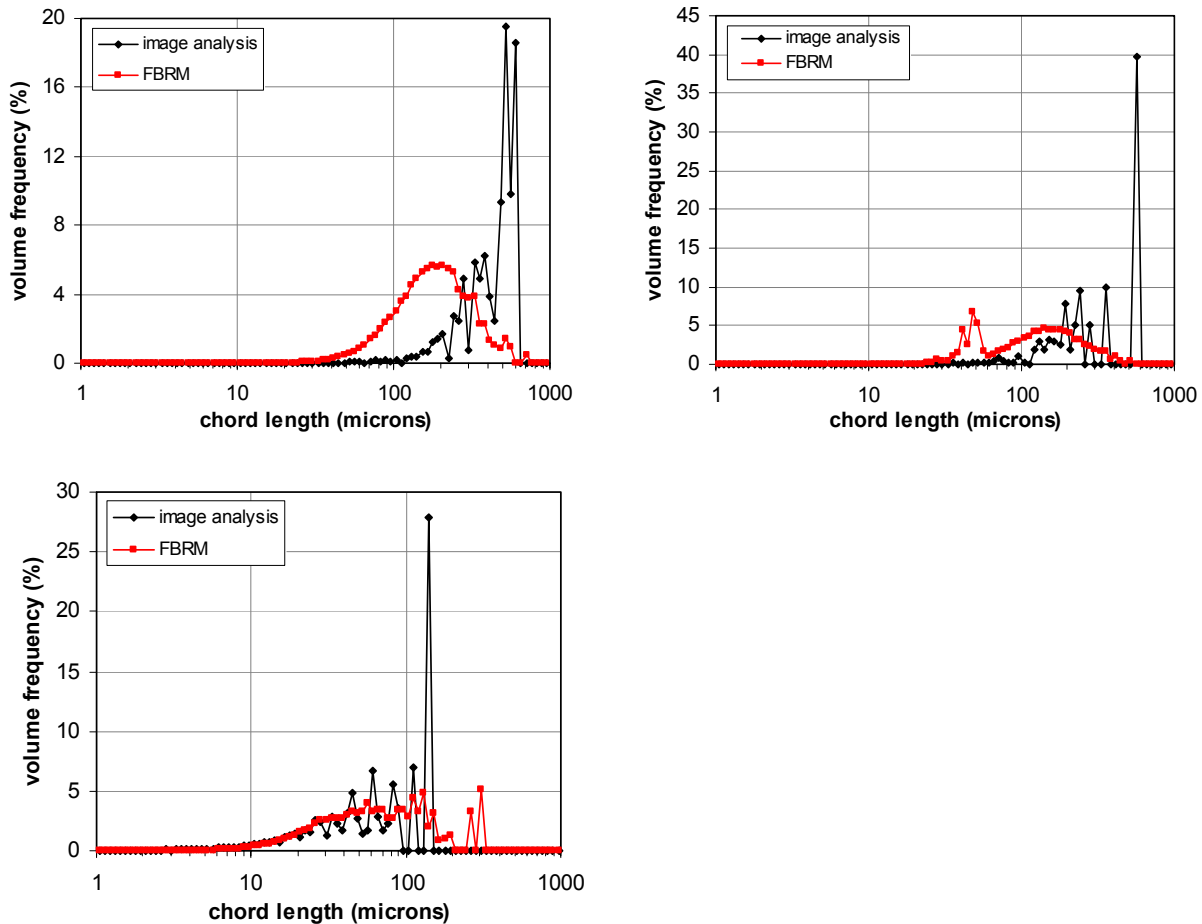


Figure 4.25 Volume-weighted number frequency distributions for diluted RAS (top, left), diluted RAS with 50 g NaCl/l (top, right), and diluted RAS sonified at 65 W (bottom)

As observed in Table 4.7, the volume-weighted mean for both sizing techniques decreased with the introduction of a stress factor. Apparently, sonication had a larger impact than salt addition. Comparison between the volume-weighted means for sonified sludge, reveals that the FBRM oversizes the particles when compared to image analysis. This agrees with the statements made in the beginning of this section. Instead, particles were undersized for the two other cases; the $D[4,3]$ was below 500 μm though. This proves that no universal calibration rules between different sizing techniques exist as Law *et al.* (1997) tried to set up for multiple materials. Here, it is concluded that a quantitative comparison between several techniques is impossible due to (i) the different measurement principles, and (ii) the natural variance inherent to biological sludges.

4.6 Rheology

The flow of thickened sludge in pipes or at the bottom of settling tanks largely depends on the flow characteristics of the material itself. In this respect, the shear stress defines the amount of momentum transport between parallel liquid layers, and is function of both the shear rate and the viscosity. The latter depends on the properties of the suspension. For more background information on sludge rheology, the reader is referred to Section 2.2.3.2.

Many techniques exist to determine viscosity; Steffe (1996) gives an in-depth discussion on available techniques. However, it is well-known that significant discrepancies exist for viscosity when different measurement methods are applied (Nir & Acrovis, 1974; Lotito *et al.*, 1997). In this respect, Forster (1982) noticed a 25% decrease in stress at any shear rate with a rotational rheometer, as compared to a tube rheometer. The trend of the shear-rate/shear-stress relation was similar though. Moreover, the design of the experimental apparatus as well as the shear conditions prevailing during the course of the experiments influence the final result. From a practical point of view this is an important issue because the empirical and semi-empirical models used to predict viscosities of concentrated suspensions need calibration. The considered parameters therefore cannot be uniquely determined but depend on the experimental conditions. The sequel describes the two main types of measurement instruments, i.e. the tube and rotational rheometers. The instruments, procedures and main difficulties of each rheometer are discussed.

4.6.1 Tube rheometers

This type of instruments may be placed into three basic categories: glass capillaries (often called *U-tube rheometers*), high-pressure capillaries, and pipe rheometers (see Figure 4.26). All establish a pressure difference to create flow. The major difference between a capillary and a pipe rheometer is the tube diameter. Although there is no clearly defined size at which a tube should be called a capillary or a pipe, some guidelines are given in Steffe (1996). U-tube rheometers are designed as gravity operated instruments. High-pressure capillaries, which are not U-shaped, are typically piston driven or gas operated. A pump or gas system can be used to create a driving force in pipe rheometers. Raw data from the tube rheometers consist of pressure drops and volumetric flow rates. From a force balance over the rheometer this data enables the calculation of viscosity.

Normally, laminar flow conditions are maintained in the tube, but if desired, turbulent flows can be realised too (Slatter, 1997). Another advantage of the method is its simplicity and the possibility to impose high shear rates. On the other hand, the sample is subjected to varying shear rates over the tube's cross-section. In addition, larger sample volumes are needed compared to rotational rheometers. Due to their small aperture, capillaries are not suitable for suspensions with large flocs such as biological sludges, and may result in floc rupture. The pipe rheometer circumvents this problem by applying larger apertures; they might go up to 32 mm (Steffe, 1996). Concerning the investigation of time-dependent flow behaviour of sludges, rotational rheometers are superior because the sample can be maintained in the cup during the experiment.

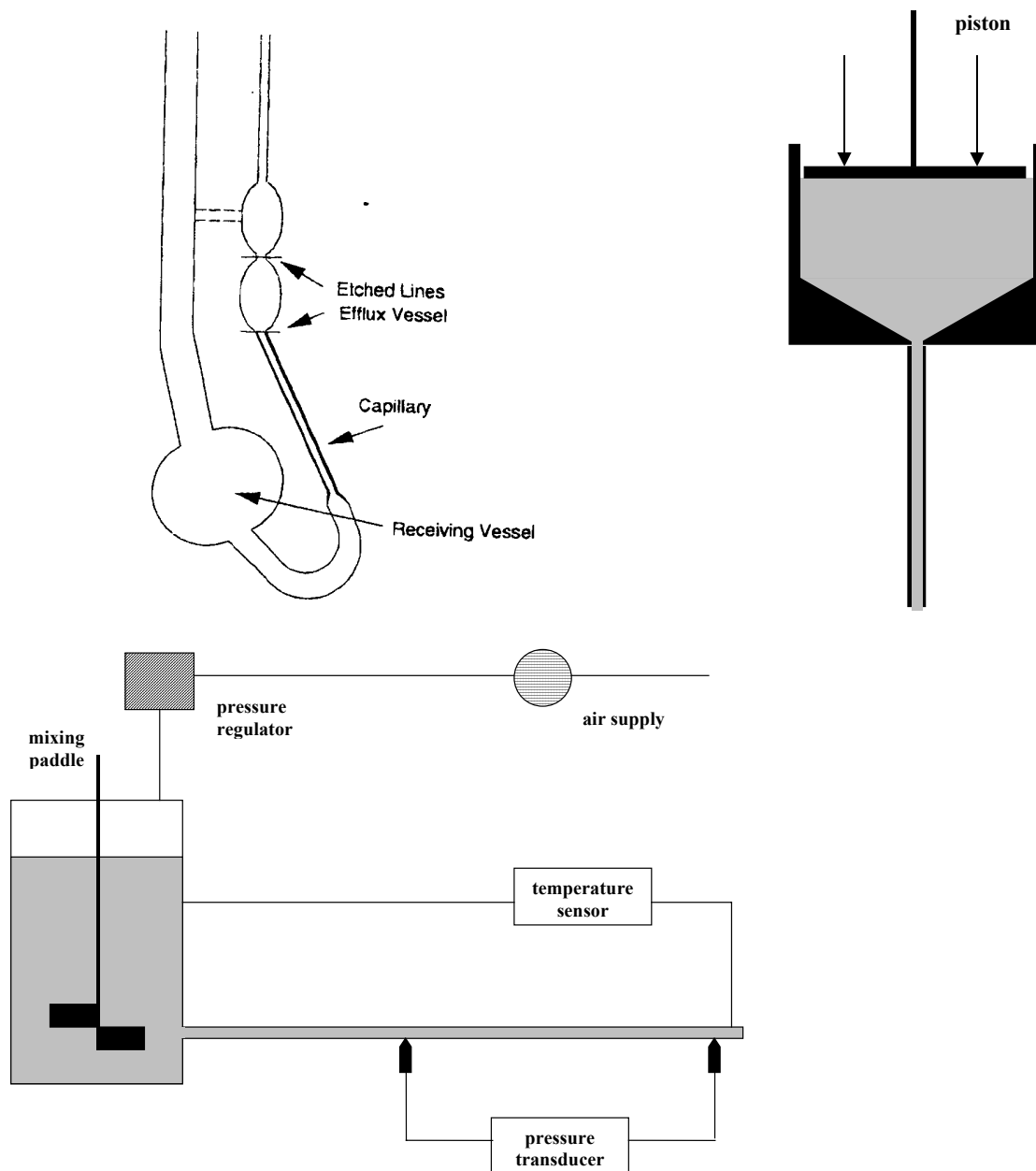


Figure 4.26 Examples of tube rheometer: U-tube rheometer (top, left), high-pressure capillary (top, right), and pipe rheometer (bottom)

4.6.2 Rotational rheometers

This type of rheometer is the mostly used class of rheometers to study sludge viscosity (e.g. Bokil, 1972; Battistoni, 1997; Sozanski *et al.*, 1997; Fitzpatrick *et al.*, 2002). The sample is placed in a cup in which a rotating element, the so-called *bob*, provides shear (Figure 4.27). With this system, the torque is measured and the shear rate is determined by the system geometry and the speed of rotation. The shear stress is subsequently obtained from the measured torque. For a proper application of the model behind the technique, it is essential to have steady and laminar flow, no slip at the walls, radial and axial velocities being zero, and

an incompressible fluid (Steffe, 1996). Turbulent flows are to be avoided; too high Reynolds numbers result in Taylor vortices that dramatically increase the viscosity (Monteiro, 1997).

To maintain the floc structure, the gap between cup and bob should be at least 10x larger than the largest floc size (Dentel, 1997). In practice, most applied gap spaces vary between 1.25 and 1.9 mm (e.g. Unno & Akehata, 1985; Monteiro, 1997; Sanin, 2002). Since bioflocs can be as large as 1 mm and more, the applicability of such small gaps can be questioned. To avoid flocs slipping at the wall and the associated floc rupture, some researchers (Battistoni, 1997; Lotito *et al.*, 1997) sieve the sample prior to the rheological experiment. To what extent the removal of large flocs from the suspension influences the results was not investigated though. However, care must be taken since Dabak & Yucel (1987) showed that there was a strong particle size influence on rheology for coal-oil suspensions. Bhattacharya *et al.* (1992) observed this for flour suspensions as well.

Finally, erroneous measurements may be obtained at high shear rates because the flocs may get separated from the liquid by centrifugal action (Lotito *et al.*, 1997; Slatter, 1997); a fictitious time-dependent thinning flow behaviour would be observed (see Section 2.2.3.2). A similar rheological effect is seen when particle sedimentation occurs.

As mentioned, this technique is widely applied in rheological research of wastewater treatment sludges. In Chapter 7 as well, a rotational rheometer is used to investigate viscosity and time-dependent thinning.

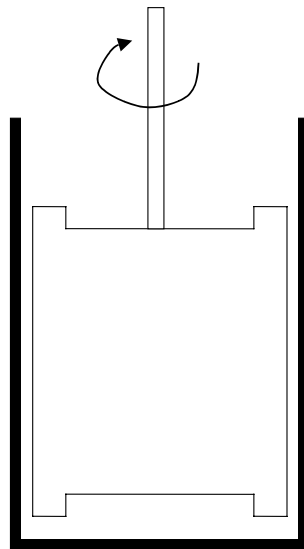


Figure 4.27 Typical rotational rheometer

4.7 Conclusions

In this chapter an extensive review of experimental techniques to calibrate and validate CFD models was given. Since settling tanks aim to gravitationally separate flocs from the liquid, it is clear that data about solids settling is crucial. Viscosity, which is important for momentum transport in the basin, is important as well. Next to this support for calibration, model validation has to be performed too in order to check the model's ability to predict the system's response to external disturbances. To this end, simulation results have to be

confronted with local measurements of solids concentrations, particle and/or liquid velocities and particle size distributions. Many methods are available and the pros and cons of each should be weighted in view of the applicability to the investigated system. In this respect, the reader is referred to the respective sections of this chapter that discuss the different measurement techniques. Advanced measurement techniques exist but are mostly restricted to use in lab-scale investigations. The reasons are manifold; absence of waterproof construction and the too large dimensions are returning causes for not applying the instruments *in situ*. A large size would indeed negatively influence the flow pattern close to the device and no relevant measurements could be obtained. The (relatively) innovating instruments reviewed here are costly as well, and hence, researchers stick to easy and known methods. For instance, tracer tests are frequently used to gain information on the flow pattern in a settling tank. Unless a flow pattern test is performed, however, tracers do not reveal the flow field.

To conclude, every application asks for a specific experimental approach. Many techniques are available on the market to choose from. Although it sometimes looks like finding a needle in a haystack, the final choice should be based on the pros and cons of the individual instruments.

5

Case Study Oxley Creek WWTP

This chapter presents a case study demonstrating the simulation and prediction power of CFD. The full-scale secondary settling tank at the municipal wastewater treatment plant of Oxley (Australia) was opted for. The WWTP is operated by Brisbane Water; this organisation is part of the Brisbane City Council.

Most settling tanks of Brisbane Water exhibit a horizontal bottom floor and suction lift scrapers. According to Brisbane Water's chief engineer, those scrapers did not work properly all the time and, therefore, could not be fully trusted. The Oxley Creek settling tanks made the exception; they were equipped with single-arm blade scrapers and a sloped floor. Hence, research was focused on this type of secondary settling tanks, although blade scrapers generally perform less than suction mechanisms (Parker *et al.*, 2001; Kinnear & Deines, 2001).

The sections below describe the plant layout and the modelling approach. At the same time, the settling tank physical characteristics will be highlighted. It is further attempted to validate the CFD model both in terms of hydrodynamics and solids transport.

5.1 Plant layout and settling tank description

The Oxley Creek WWTP was built to remove only carbon and no attention was given to the removal of nitrogen compounds; hence, anoxic and anaerobic zones are absent in the activated sludge part. Aeration is performed by means of fine bubble dome diffusers. The layout of the Oxley Creek plant can be summarised by the following stages,

- screening
- pre-aeration
- primary clarification (Figure 5.1)
- aeration system (Figure 5.1)
- secondary clarification (Figure 5.1)
- disinfection before discharging into Oxley Creek
- sludge thickening (sludge from secondary stage)
- sludge digestion (sludge from primary and secondary stages)
- centrifugal sludge dewatering

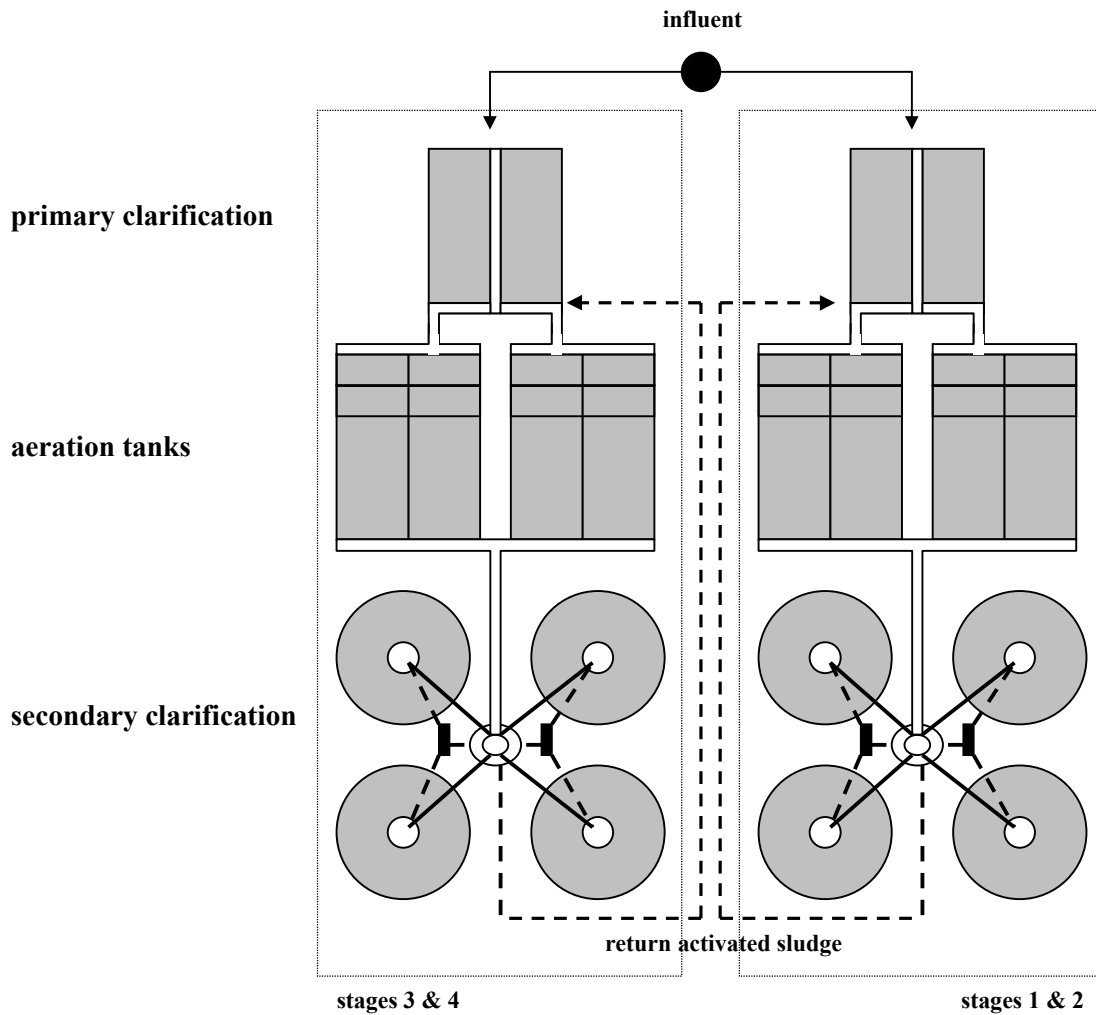


Figure 5.1 Layout of Oxley Creek WWTW

From Figure 5.1, the plant clearly consists of two parallel systems, each divided in two stages, i.e. stages 1 & 2 and stages 3 & 4 respectively. Stages 3 & 4 are the most recent and originate from 1979, whereas the others date from 1968. Annually averaged characteristics of the plant are given in the upper part of Table 5.1. Since it concerns a municipal wastewater treatment plant, the flow rate shows a diurnal flow pattern; typical patterns will be shown further in this chapter.

Each sludge system is provided with four secondary settling tanks (Figure 5.1). At a central pit mixed liquor from the aeration tanks is distributed over the four settling tanks. The Return Activated Sludge (RAS) is collected for every couple of settling tanks in a separate pit. From there, it is returned to the aeration tanks. The overflowing water is returned to a tank, built peripherally around the inlet distribution pit, from where it is discharged into the river.

The bottom part of Table 5.1 shows the settling tank design characteristics. Stages 3 & 4 were dimensioned for smaller solids and hydraulic loadings than stages 1 & 2. All settling tanks are circular with a centre feed and peripheral overflow weir with v-notch profile. The bottom floors have a steep slope of 20° and a blade scraper moves the sludge towards a

central conical sludge hopper. No scum removal facilities are installed. A special feature of the activated sludge system at the time of study was the continuous dosing of the zeolite ZELfloc (Zeolite Australia, Australia) at stages 3 & 4 to improve the settling properties and the nitrification capacity (Barr *et al.*, 1999). By enlarging the settling tank capacity and performance the solids residence time can be safely increased leading to an improved nitrification capacity. Since zeolite has no immediate effect on the settling properties (the microorganisms have to grow onto the zeolite particles), zeolite was dosed in the return line to the aeration tank.

Table 5.1 Summary of WWTP and settling tank characteristics

WWTP characterisation (annual averages)		
Biological capacity (<i>IE</i>)		185000
ADWF ^a (m^3/d)		42000
PDWF ^b / ADWF (-)		2.1
Q_{RAS} / ADWF (-)		0.8
PWWF ^c (m^3/d)		116000 (100-year storm)
BOD ₅ sewage (mg/l)		220
BOD ₅ removal after primary settling (%)		47
TSS _{AT} ^d (mg/l)		2500
Secondary settling tank characterisation		
	<i>stages 1 & 2</i>	<i>stages 3 & 4</i>
Volume (m^3)	1276	1132
Radius (m)	10.7	9.9
Area (m^2)	358	308
Average depth (m)	3.5	3.6
Side wall depth (m)	2.5	2.4
Q_{inlet} at ADWF (m^3/d)	6100	5800
Zeolite (ton/d)	-	1.7

^aADWF: Average Dry Weather Flow, ^bPDWF: Peak Dry Weather Flow

^cPWWF: Peak Wet Weather Flow, ^dAT: Aeration Tank

Due to ongoing works at the settling tanks of stages 1 & 2, it was decided to focus on a settling tank of stages 3 & 4. This implies the issue of zeolite in the experimental and computational efforts.

Before performing measurement campaigns it is necessary to check whether the settling tank is overloaded in order to design adequate experiments. Table 5.2 compares the loadings with some typical US EPA design values (Tchobanoglous & Burton, 1991; Ekama *et al.*, 1997). It is concluded that the settling tanks worked within their hydraulic design boundaries, whereas the system was underloaded in terms of solids.

Table 5.2 Comparison between operational and design parameters (Tchobanoglous & Burton, 1991)

	overflow rate ($m^3/m^2/h$)		solids loading ($kg/m^2/h$)	
	<i>on-site</i>	<i>design</i>	<i>on-site</i>	<i>design</i>
ADWF	0.8	0.7 - 1.4	3.2	5 - 7
PDWF	1.8	1.7 - 2	5.8	10

Since American settling tanks are typically deeper than European installations, the applicability of the former design values may be questioned. The use of e.g. Dutch (STOWa) design rules are therefore more appropriate. The procedure is based on the calculation of the Diluted Sludge Volume, DSV_{30} . This corresponds to the settled volume of sludge after 30 minutes of settling after the necessary dilutions to obtain $150 < DSV_{30} < 250$ ml/l. However, this information was not available; instead, the SV_{30} at 3.5 g TSS/l was used. This approximation is acceptable due to the low SV_{30} -value of 120 ml/l, which is close to the range specified above. Hence, the DSV_{30} at 3.5 g TSS/l can be assumed equal to this value. According to Ekama *et al.* (1997), the following STOWa design Surface Overflow Rate SOR is obtained:

$$\begin{aligned} SOR &= \frac{1}{3} + \frac{200}{DSV_{30}} \\ &= 2 \text{ m/h} \end{aligned}$$

The settling tank, however, operated at a surface overflow rate of 0.8 m/h. This is much lower than the calculated design value; the settling tank can therefore manage much higher loadings with the present well-settling solids.

In many cases, the performed measurement campaigns demanded for steady-state inflow. Pennstock valves at the entrance of the primary clarification split the influent flow over the two sludge systems, i.e. stages 1 & 2 and 3 & 4. Due to their manual operation, however, perfect flow equalisation could not be established. The experiments were therefore always subject to flow variations. The most stable flow rates occurred at night and in the afternoon (as will be shown later in this chapter). For obvious reasons, the last-mentioned periods were selected for the experimental runs. Unfortunately, on-line flow sensors were only present at the end of primary clarification and hydraulic buffering by the aeration system occurred. Although they are not equal to the inlet flows of the settling tanks, the measured flow rates are utilised as first approximation.

To conclude this section, a cross-section of the settling tank is given in Figure 5.2.

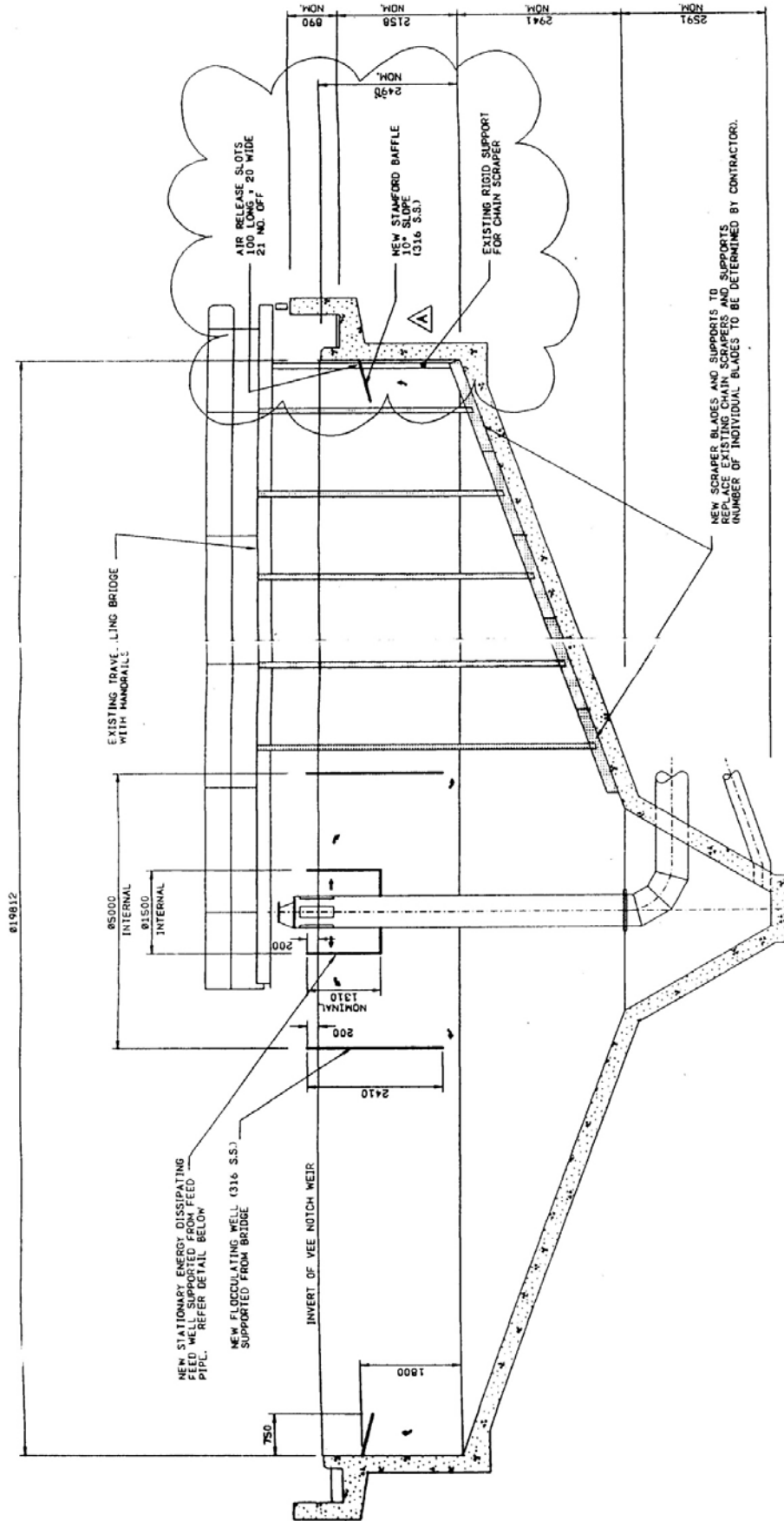


Figure 5.2 Cross-section of the Oxley Creek WWTP settling tank

5.2 Modelling the settling tank

This section deals with the set-up of the settling tank model. The fundamental equations are presented together with their boundary conditions. A real-life settling tank is a 3D system, hence an appropriate spatial simplification has to be realised in order to perform simulations (with 700 MHz Pentium III and 2 GHz Pentium IV processors, and 256 Mb RAM) within an acceptable time frame. The lowering of the model dimension to 2D has important ramifications for the modelling of the inlet structure and the scraper operation. Different approaches to model them in 2D are dealt with in this section. Because the solution largely depends on the spatial mesh resolution, several mesh sizes are investigated as well.

As known, the solids' ability to settle largely determines the solids removal efficiency of the settling tank. Some characterisation of the settling is thus crucial for a proper settling tank model. For that reason, the settling velocity was experimentally determined prior to the computational efforts. In this case study, zeolite was dosed to improve the settling properties; an estimate of the settling velocity based on literature therefore results in completely useless simulation efforts. Its experimental determination is covered in the next subsection.

5.2.1 Settling velocity of zeolite-composite sludge

At the time of the experiments, stages 3 & 4 of the WWTP were equipped with a zeolite-dosing system in the RAS line. Solids settling experiments were conducted with RAS before the zeolite was added. This choice was made for two reasons: (i) the sludge already had a high concentration which is useful to make a range of consecutive dilutions, and (ii) the sludge was essentially identical to the sludge in the aeration tanks, i.e. microorganisms had already grown onto the carrier material; there was no interest in investigating the separate settling of zeolite.

The collected sludge was allowed to settle for 45 minutes and the obtained thickened sludge was subsequently utilised for settling experiments with appropriate dilutions (by means of supernatant). Eight dilution ratios, defined as the ratio of the volume of thickened sludge to the total volume, were applied and the experiments were repeated once. The two experimental runs were performed on April 20th and April 26th 2001 respectively. The dilution ratios were based on an initial guess of the RAS and thickened RAS solids concentration, i.e. 4 and 20 g/l respectively. The applied dilutions were as follows: 1, 0.5, 0.375, 0.25, 0.2, 0.15, 0.1 and 0.05.

Thickened sludge and supernatant were mixed in a separate bucket. The mixture was subsequently introduced in a rectangular sedimentation column (Figure 5.3) with a scaled tape of 40 cm and mm-indication. Its width measured 10 cm. Four litres of diluted sludge were utilised in the column and after every test the sludge was drained. The sludge was not recycled for subsequent experiments since observations had shown a deteriorated solids blanket. Changes in settling properties by repetitive sample manipulations are also mentioned in literature (Cho *et al.*, 1993).



Figure 5.3 Rectangular sedimentation column

A stick was used to gently mix the liquor and, if necessary, to reduce the strength of major turbulent eddies by rotating the stick contra-directionally. Even with the absence of excess turbulence, a time lag occurs after which an almost constant settling rate can be observed. According to Fischerström *et al.* (1967), this time lag is characteristic for the settling material itself. The blanket height was measured in time for 30 minutes (with a stopwatch). Especially the first five minutes were critical since, in most cases, the solids settled very fast. At the end of every sedimentation test, the solids were allowed to compact further for another 15 minutes in order to determine the sludge volume index if necessary.

After each settling test, the content of the column was mixed in order to take a representative (70 ml) sample. Of the latter, the Total Suspended Solids concentration (TSS) was determined. To improve the statistical analysis of TSS (especially at low dilution ratios) three repetitions were performed. Samples were stored in a fridge (4 °C) for a maximum of 4 days. Determination of TSS was performed according Standard Methods (APHA, 1992). The non-settleable fraction was determined by measuring the TSS of the supernatant of the settled undiluted sludge (after 45 minutes); the average concentration of three samples measured 0.014 g/l.

Two typical settling curves are given in Figure 5.4 to demonstrate the impact of solids concentration on the settling behaviour.

For the calculation of the settling velocity the linear section of the settling curve was utilised, i.e. the initial shoulder and the tail of the curve were excluded from the calculation. Depending on the solids concentration, between 4 and 22 data points were retained for linear regression. The number of data points used was based on the minimisation of the standard deviation on the settling velocity.

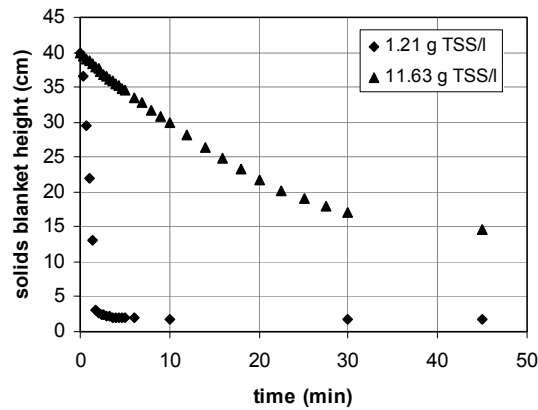


Figure 5.4 Two examples of representative settling curves (with a TSS of 1.21 and 11.63 g/l)

The calculated settling velocities were subsequently utilised to estimate the settling velocity parameters. As denoted in Chapter 2, the two most frequently used settling velocity functions are the single (Vesilind, 1968) and double (Takács *et al.*, 1991) exponential functions. They are recapitulated below.

$$v_s = v_0 e^{-r_h X} \quad (5.1)$$

$$v_s = v_0 \left[e^{-r_h (X - X_0)} - e^{-r_p (X - X_0)} \right] \quad (5.2)$$

where v_0 is the maximum settling velocity, r_h is the parameter characteristic for the hindered settling zone, r_p is a characteristic settling parameter at low solids concentrations, and X_0 is the concentration below which no settling occurs.

Figure 5.5 shows the fitted single exponential settling velocity function for the two data sets, i.e. 20/04/2001 and 26/04/2001. On the other hand, Table 5.3 resumes the estimated parameters. It is not surprising that they are significantly different. The discrepancy is due to the biological nature of the system inherently showing some natural variation. Comparable parameter values were obtained for 26/04/2001 when calibrating the single exponential settling velocity function with the complete set of batch settling curves (see Section 4.1.1.1). Figure 5.4 shows two of such curves.

Table 5.3 Estimated settling parameters for the single exponential settling velocity function

date	v_0 [m/h]	$sd(v_0)$ [m/h]	r_h [l/g]	$sd(r_h)$ [l/g]
20/04/2001	11.79	0.84	0.17	0.02
26/04/2001	19.88	0.61	0.26	0.01

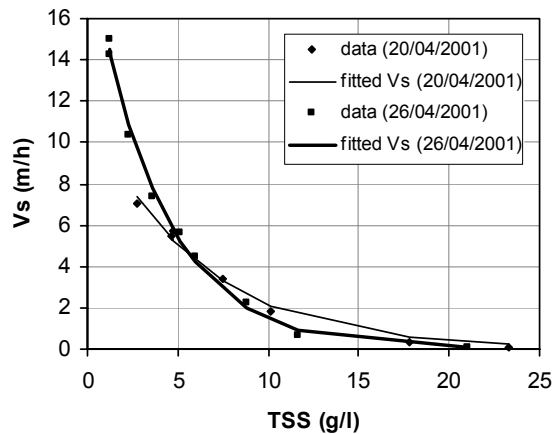


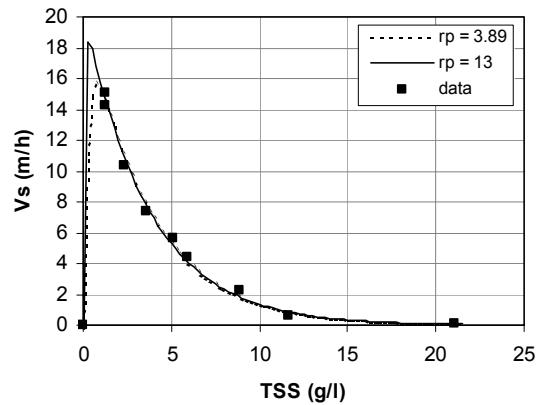
Figure 5.5 Experimental and modelled single exponential settling velocity

As mentioned in Chapter 2, the single exponential function is not very interesting for modelling purposes; at low solids concentration the function indeed returns unrealistically high settling velocities. To approximately include discrete settling into the settling relation a double exponential function should be used. This has only been applied to the data collected at 26/04/2001 due to its larger range of TSS. Parameter estimation is a problematic issue for this function. The first exponent of Equation 5.2 refers to zone settling, whereas the second exponent describes discrete settling. Due to the nature of the settling experiments the latter phenomenon is not measured; i.e. no data are available at low solids concentrations. Only the non-settleable fraction was determined and measured 14 mg TSS/l. Estimation of r_p was therefore difficult and no solution could be found, i.e. no minimum was found for the objective function. The optimisation algorithm returned any value dependent on the initial guess, without any sensible meaning. Figure 5.6 plots Equation 5.2 for two parameter values; r_p of 13 l/g is a randomly selected value to demonstrate the heart of the problem. Without any data in the lower concentration range, it is observed that the higher the overshoot, the smaller the residual error will be. However, it is not realistic to have an ever-increasing velocity. For that reason, the velocity is restricted to the maximum experimentally determined value. With the parameter values of Table 5.3, a value of 3.89 l/g was obtained as the most optimal one. This result is also plotted in Figure 5.6.

To conclude, a relation for the settling velocity has been experimentally determined in this subsection. Since the double exponential function describes the whole range of settling velocities, it is preferred over the single exponential function; the parameter r_p is determined in a rather heuristic way though. Equation 5.2 will be utilised in the remainder of this chapter; its parameters are summarised in Table 5.4.

Table 5.4 Settling parameters used in this work

Parameter	Value
v_0 [m/h]	19.88
r_h [l/g]	0.26
r_p [l/g]	3.89
X_0 [g/l]	0.014

Figure 5.6 Settling dependency on r_p

5.2.2 Mechanistic description of the settling tank: contributing mathematical equations

This section deals with the mathematical (model) equations necessary for simulation of the circular settling tank. For convenience, the Reynolds-averaged equations from Chapter 2 are recapitulated for 2D axisymmetric coordinates, i.e. the momentum and continuity equations are given. Scalar transport with the appropriate viscosity is focused as well. Turbulence features are dealt with in short.

Firstly, the continuity equation is as follows

$$\frac{\partial}{\partial t} \rho + \frac{\partial}{\partial x} \rho u + \frac{\partial}{\partial r} \rho v + \frac{\rho v}{r} = 0 \quad (5.3)$$

where x is the axial coordinate, r the radial coordinate, t time, ρ bulk density, u the axial velocity, and v the radial velocity.

Equation 5.3 is the general form of the mass conservation equation and is valid for incompressible as well as compressible flows. No mass source, such as (bio-)chemical reactions, is included.

Secondly, the axial and radial momentum conservation equations are written as

$$\begin{aligned} \frac{\partial}{\partial t} \rho u + \frac{1}{r} \frac{\partial}{\partial x} r \rho u u + \frac{1}{r} \frac{\partial}{\partial r} r \rho v u = & -\frac{\partial p}{\partial x} \\ & + \frac{1}{r} \frac{\partial}{\partial x} \left[r \rho v_{eff} \left(2 \frac{\partial u}{\partial x} - \frac{2}{3} \left(\frac{\partial u}{\partial x} + \frac{\partial v}{\partial r} + \frac{v}{r} \right) \right) \right] \\ & + \frac{1}{r} \frac{\partial}{\partial r} \left[r \rho v_{eff} \left(\frac{\partial u}{\partial r} + \frac{\partial v}{\partial x} \right) \right] - \rho g \end{aligned}$$

$$\begin{aligned}
\frac{\partial}{\partial t} \rho v + \frac{1}{r} \frac{\partial}{\partial x} r \rho u v + \frac{1}{r} \frac{\partial}{\partial r} r \rho v v = & -\frac{\partial p}{\partial r} \\
& + \frac{1}{r} \frac{\partial}{\partial x} \left[r \rho v_{eff} \left(\frac{\partial v}{\partial x} + \frac{\partial u}{\partial r} \right) \right] \\
& + \frac{1}{r} \frac{\partial}{\partial r} \left[r \rho v_{eff} \left(2 \frac{\partial v}{\partial r} - \frac{2}{3} \left(\frac{\partial u}{\partial x} + \frac{\partial v}{\partial r} + \frac{v}{r} \right) \right) \right] \\
& - 2 \rho v_{eff} \frac{v}{r^2} + \frac{2}{3} \frac{\rho v_{eff}}{r} \left(\frac{\partial u}{\partial x} + \frac{\partial v}{\partial r} + \frac{v}{r} \right)
\end{aligned}$$

In these equations, g and v_{eff} are the gravitational acceleration and the effective viscosity; the latter includes both the molecular ν and turbulent viscosity ν_t , i.e.

$$v_{eff} = \nu + \nu_t$$

The turbulent viscosity is computed by means of Equation 2.4 from Chapter 2; the necessary k - ε turbulence model in axisymmetric coordinates can be found in full version in Haas (1996). Restricted to locally isotropic and highly turbulent flows though, this model is generally applied to secondary settling tank modelling. Notwithstanding the low velocities, the Reynolds number is still large due to the large system dimensions and the fairly low viscosity of the suspension (Schamber & Larock, 1981; Lyn & Rodi, 1990; Zhou & McCorquodale, 1992b; Ekama *et al.*, 1997). Simonin *et al.* (1989) discussed to what extent the k - ε model including buoyancy correctly models stably stratified flows. It was assumed that the error in the turbulence model and the (in)accuracy of the numerical methods legitimate the omission of the density effect on turbulence. Also Zhou & McCorquodale (1992a,b) and McCorquodale & Zhou (1993) omitted the buoyancy correction terms in the k - ε model as a first approximation; their motivation was based on the conclusions of Devantier & Larock (1986). These researchers found that no solutions could be obtained for k and ε for any initially specified velocity, nor solids concentration field. The cause was the stable stratification in the settling tank, i.e. buoyancy was so large that it overwhelmed the shear production and drove k and ε towards negative values. The latter is of course impossible. Consequently, as a first approximation the correction terms were omitted from the turbulence model.

Below, the k - ε turbulence model in axisymmetric coordinates is recapitulated (Zhou & McCorquodale, 1992a).

$$\begin{aligned}
\frac{\partial}{\partial t} \rho k + \frac{1}{r} \frac{\partial}{\partial x} r \rho k u + \frac{1}{r} \frac{\partial}{\partial r} r \rho k v = & \frac{1}{r} \frac{\partial}{\partial r} \left[r \rho \left(v + \frac{v_t}{\sigma_k} \right) \frac{\partial k}{\partial r} \right] \\
& + \frac{1}{r} \frac{\partial}{\partial x} \left[r \rho \left(v + \frac{v_t}{\sigma_k} \right) \frac{\partial k}{\partial x} \right] + P_s - \rho \varepsilon
\end{aligned}$$

$$\begin{aligned} \frac{\partial}{\partial t} \rho \varepsilon + \frac{1}{r} \frac{\partial}{\partial x} r \rho \varepsilon u + \frac{1}{r} \frac{\partial}{\partial r} r \rho \varepsilon v = \frac{1}{r} \frac{\partial}{\partial r} \left[r \rho \left(v + \frac{v_t}{\sigma_\varepsilon} \right) \frac{\partial \varepsilon}{\partial r} \right] \\ + \frac{1}{r} \frac{\partial}{\partial x} \left[r \rho \left(v + \frac{v_t}{\sigma_\varepsilon} \right) \frac{\partial \varepsilon}{\partial x} \right] + c_{1\varepsilon} \frac{\varepsilon}{K} P_s - c_{2\varepsilon} \rho \frac{\varepsilon^2}{K} \end{aligned}$$

where

$$P_s = \mu_{eff} \left[2 \left(\frac{\partial u}{\partial r} \right)^2 + 2 \left(\frac{\partial v}{\partial x} \right)^2 + 2 \left(\frac{u}{r} \right)^2 + \left(\frac{\partial u}{\partial x} + \frac{\partial v}{\partial r} \right)^2 \right]$$

in which $c_{1\varepsilon} = 1.44$, $c_{2\varepsilon} = 1.92$, $\sigma_\varepsilon = 1.3$, and $\sigma_k = 1.0$ are given by e.g. Rodi (1984).

Sludge is considered as a non-Newtonian fluid. Whereas Slatter (1997), Sozanski *et al.* (1997) and others describe rheology with a Bingham plastic model, a modified Herschel-Bulkley model is adopted in this work (for its detailed development, see Section 7.2.2):

$$v = \frac{\tau_0}{\dot{\gamma}} (1 - e^{-m\dot{\gamma}}) + K \dot{\gamma}^{n-1} \quad (5.4)$$

with

$$\tau_0 = \beta_1 X^{\beta_2} \quad (5.5)$$

$$K = \mu_w + \beta_3 X^{\beta_2} \quad (5.6)$$

where μ_w is the dynamic viscosity of water; the magnitude of the strain rate $\dot{\gamma}$ is defined by

$$\dot{\gamma} = \sqrt{\frac{1}{2} \dot{\gamma}_{ij}^2}$$

The parameter values are given in Table 5.5 (see also Section 7.2.2). Despite the fact that sludge presumably exhibited a different rheological behaviour by dosing zeolite, the same parameter values were retained in this case study.

Since the settling tank's function is to separate solids from water, the solids transport equation is essential to the overall model. It is also concluded from Equations 5.5 and 5.6 that the local solids concentration is needed to calculate the viscosity. The solids transport equation as described below includes both advective and diffusive transport terms.

$$\frac{\partial}{\partial t} \rho \phi + \frac{1}{r} \frac{\partial}{\partial x} r \rho \phi (u - v_s) + \frac{1}{r} \frac{\partial}{\partial r} r \rho \phi v = \frac{1}{r} \frac{\partial}{\partial x} \left(r \frac{v_{eff}}{\sigma_s} \frac{\partial}{\partial x} \rho \phi \right) + \frac{1}{r} \frac{\partial}{\partial r} \left(r \frac{v_{eff}}{\sigma_s} \frac{\partial}{\partial r} \rho \phi \right)$$

where v_s is the settling velocity as calculated by Equation 5.2; ϕ is the solids mass fraction and σ_s is the Schmidt number. Traditionally, the last-mentioned is taken as 0.7 (e.g. Adams & Rodi, 1990; Szalai *et al.*, 1994; Krebs *et al.*, 1996; Lakehal *et al.*, 1999).

Table 5.5 Parameter values used by the rheological model

parameter	value
$\beta_1 (m^2/s^2)$	$9.04 e^{-3}$
$\beta_2 (-)$	1.12
$\beta_3 (m^2/s^{2-n})$	$2.48 e^{-4}$
$m (s)$	163.4
$n (-)$	0.777
$\mu_w (kg/m/s^{2-n})$	$1 e^{-3}$

For this case study, the model was implemented in Fluent (Fluent Inc., UK) performing all finite volume calculations in terms of solids fractions; hence, the solids concentration is simply the product of the solids fraction and the bulk density. The bulk density is computed as (see Appendix C)

$$\rho = \frac{\rho_l}{1 - \phi \left(1 - \frac{\rho_l}{\rho_s}\right)}$$

where ρ_l and ρ_s are the liquid and dry solids densities respectively. For the solids density three values can be found in literature, i.e. 1250 kg/m^3 (Li & Yuan, 2002), 1300 kg/m^3 (e.g. Zhou *et al.*, 1992; Mazzolani *et al.*, 1998) and 1450 kg/m^3 (e.g. Lyn *et al.*, 1992; Ekama *et al.*, 1997; Lakehal *et al.*, 1999; Stamou *et al.*, 2000). Further, Ekama *et al.* (1997) mentioned that the density may reach $1700 - 1800 \text{ kg/m}^3$ when chemical flocculants are dosed. Zeolite would increase the solids density by acting as a carrier, i.e. its own weight is included in the floc. An increased solids density results in an increase of the bulk density. Consequently, density has a more pronounced effect on the transport of momentum and all scalars, including turbulence. Solids blanket behaviour is presumably less influenced since the floc density is inherently incorporated in the settling velocity function.

Note that two dry solids densities were applied in this work. Firstly, a density of 1450 kg/m^3 for dry solids was utilised for investigations of mesh size, inlet structure and settling tank physics. This may be interpreted as if zeolite acts as if it was an addition of polymer (of organic composition as well) that primarily alters the settling velocity but not the bulk density. Secondly, to account for the effect of zeolite on the bulk density the dry solids density was calculated (see Appendix C) and measured 1750 kg/m^3 . Section 5.2.8 deals with this issue. For model validation, the correct bulk density and its influence on the flow field are essential. However, it is stressed again that till Section 5.2.8 a dry solids density of 1450 kg/m^3 is utilised.

With respect to the bulk density, it is noted that most researchers (e.g. Zhou & McCorquodale, 1992a; Lakehal *et al.*, 1999) apply the Boussinesq approximation, i.e. density is excluded from the momentum equations except for the buoyancy term, which dominates the inertial term for density-driven flows. In this work, the simplification is not carried through.

The above outlined a closed set of partial differential equations and related constitutive relations, but the prediction of a stratified flow in a settling tank is complete only when the relevant boundary conditions are specified. In order to accurately compute the velocity

distribution below the feed well baffle, the inlet region must be incorporated in the computational domain, rather than assuming a fixed inlet velocity below and perpendicular to the feed well.

The inlet and underflow structures were both characterised by a uniform velocity profile. The following uniform inlet profiles for v , ϕ , k and ε were used (Zhou & McCorquodale, 1992a,c; McCorquodale & Zhou, 1993; Ekama *et al.*, 1997; Celik *et al.*, 1999):

$$v = v_{inlet}; \quad k = \alpha v_{inlet}^2; \quad \varepsilon = c_{\mu}^{\frac{3}{4}} \frac{k^{\frac{3}{2}}}{l_m}; \quad \phi = \phi_{inlet}$$

where v_{inlet} is the inlet velocity; the constant $\alpha = 0.2$; and l_m , the mixing length, is defined as

$$l_m = 0.5c_{\mu} L_{inlet}$$

with L_{inlet} being the width of the inlet slot. The inlet solids concentration profile was also uniform, since the incoming flow is assumed fully turbulent. According to Adams & Rodi (1990), the correct value of turbulent properties is less crucial; exact values for k and ε are unimportant for the mean flow. Also Lyn & Rodi (1990) and Szalai *et al.* (1994) noted that turbulent transport is negligible beyond the inlet region. Hence, inlet turbulence is only important for the flow field inside the feed well and not for the main settling tank. Due to the 2D approximation of the real system, the effect of the inlet structure on the flow field in the feed well cannot be accurately simulated; only an approximation is obtained being important for proper simulation of the main settling tank flow behaviour however. Contrary to the inlet, a zero-gradient for turbulent properties and solids concentration was adopted at the underflow structure.

All variables at the outlet structure were extrapolated from near-outlet values; hence, they have no influence on the upstream flow. Note that gradients in the axial direction may exist at the outlet.

The water surface was modelled as a fixed surface; this plane of symmetry was characterised by zero normal gradients for all variables. Also, an axis of symmetry appeared because only half of the settling tank cross-section was modelled.

At the bottom floor, sump, outer walls, inlet pipe, Stamford baffle and feed well the logarithmic law of the wall was applied (see Equation 2.6). For the solids concentration, a zero gradient condition was used at the walls.

The partial differential equations and their boundary conditions have to be discretised in order to solve the resulting set of algebraic equations. Fluent gives the researcher the possibility to choose among different discretisation schemes, pressure-velocity coupling schemes and pressure interpolation schemes. For more information, the reader is also referred to Chapter 3.

Because of the non-linearity of the equation set, it is necessary to control the change of the variables. This is typically achieved by under-relaxation, which reduces the change of a particular variable during computational iterations. The relaxation factors were kept at

- 0.15-0.3 for pressure, density, body forces and velocities;
- 0.5 for turbulent kinetic energy and energy dissipation rate, and turbulent viscosity;
- 1 for the scalars applied.

Additionally, to avoid any divergence of the solution, the time step was kept as small as was necessary. Hence, time steps were small at the start of the simulation and were gradually increased. Because adaptive time-stepping in Fluent did not work properly, time steps were altered manually as the calculation proceeded. In the end, step sizes of 0.7 - 7 s could be applied when pseudo-steady state was obtained.

Table 5.6 Summary of the numerical schemes applied

	numerical scheme
pressure interpolation	body-force-weighted
pressure-velocity coupling	PISO
advection term	QUICK
diffusion term	central difference
time	second-order upwind
k	QUICK
ε	QUICK
solids fraction	QUICK

5.2.3 Some remarks on meshing...

Fluent solves the transport equations by means of the finite volume technique. For the work presented, the modelled domain was meshed with the software Gambit (Fluent Inc., UK) provided with Fluent. How meshing is performed, e.g. the selection of shape and size of the control volumes, has a pronounced effect on the numerical accuracy and convergence time (Bern & Plassmann, 1999). It is therefore essential to check the mesh quality. Here, the equiangle skew and the aspect ratio were investigated. The equiangle skew is a measure of how uniform the angle distribution of each control volume is; for triangular cells it indicates the deviation from 60 degrees. Therefore, the equiangle skew should be as low as possible; well-constructed control volumes are defined by values lower than 0.5.

Let us define the aspect ratio of an element to be the ratio of its maximum to its minimum width, where width refers to the distance between parallel supporting hyperplanes. In general, elements with large aspect ratios are not advisable since they worsen the speed and accuracy of the linear solver (Bern & Plassmann, 1999). Moreover, even assuming that the solver gives an exact answer, large aspect ratios may give unacceptable interpolation errors (Bern & Plassmann, 1999). However, sometimes elements with a large aspect ratio might be useful. If the solution of the partial differential equation is anisotropic, i.e. if its second derivative largely varies with direction, properly aligned high-aspect-ratio elements give a very efficient mesh. In this respect, Navier-Stokes simulations, that is including the effect of viscosity, are strongly anisotropic. Quadrilateral and hexahedral meshes have an advantage in accuracy over triangular meshes for control-volume formulations of boundary-layer problems, as they allow faces of elements to be either almost parallel or almost orthogonal to the surface. Away from the boundaries, however, the location of the high-aspect-ratio

elements cannot be predicted in advance. Adaptive meshing, i.e. solution-based remeshing, is one approach to deal with this issue and can be done more easily with triangles.

For the 2D modelling purposes in this work, a triangular mesh (see e.g. Figure 5.7) was used to ease the meshing of the "complex" computational domain, although it is only very rarely found in literature. Rectangular meshes are widely spread for settling tank modelling with both horizontal (e.g. Adams & Rodi, 1990; McCorquodale & Zhou, 1993) and sloped floors (e.g. Lainé *et al.*, 1999; Lakehal *et al.*, 1999; Stamou *et al.*, 2000). The major difference with the present settling tank configuration is the complexity; the presence of many non-parallel walls and baffles make the system hard to mesh. It becomes even more difficult when boundaries are to be meshed with certain distributions of vertices along the boundary. Notwithstanding the availability to do so within the Fluent software, it was decided not to use adaptive meshing. Instead, manual changes were preferred to keep track of the mesh adaptations.

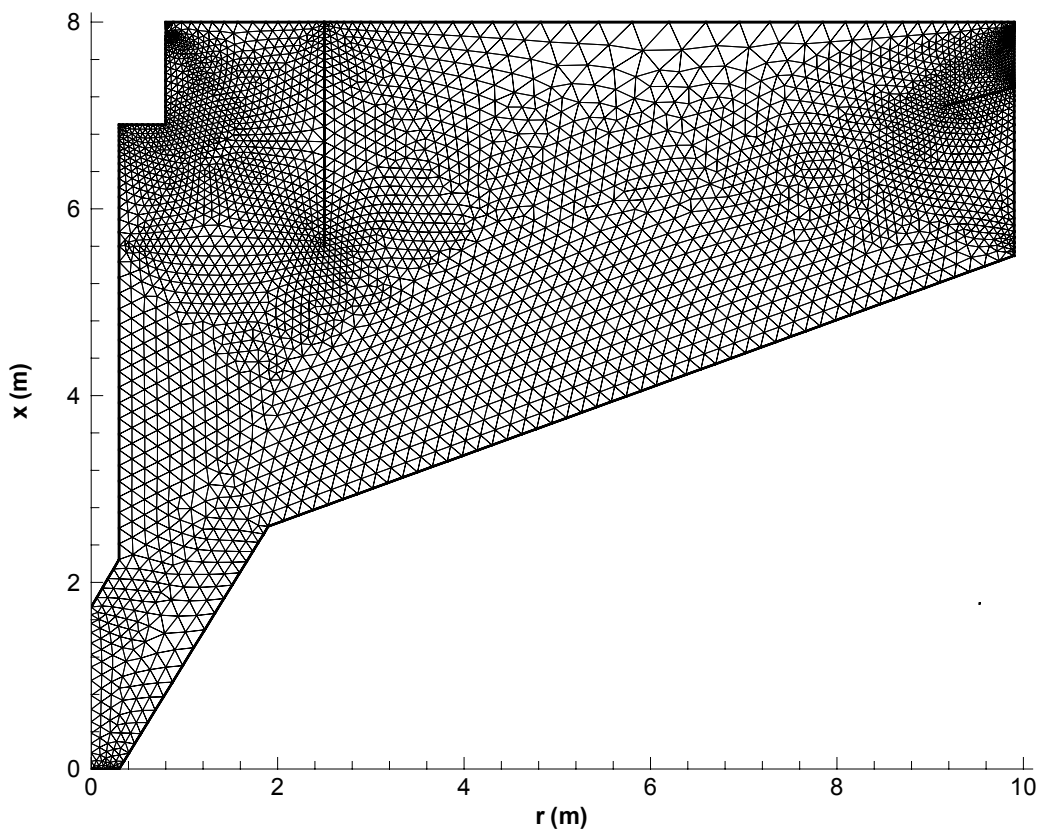


Figure 5.7 Example of triangular mesh for the investigated settling tank

For proper meshing, the aspect ratio and equiangle skewness were kept as low as possible. A rule of thumb is to keep the equiangle below 0.5; except when the boundary layer is modelled, the equiangles should be very low, such as 0.1. In this study, the equiangle skewness was below 0.5 for more than 99.5% of the elements. On the other hand, more than 99.7% of all elements in the mesh were characterised by an aspect ratio between 1 and 2. Nevertheless, it was noticed that these overall performance parameters were not satisfactory for all investigated cases; convergence issues occurred for a few cells with bad equiangle skewness

and/or aspect ratio. Mass or momentum mostly accumulated in these cells and resulted in a divergence of the residuals. Hence, mesh refinements were needed in the problematic zones.

5.2.4 Modelling the inlet structure

From a hydraulic point of view, a distinction has to be made between primary and secondary settling tanks in terms of density effects. Due to density currents along the bottom of a secondary settling tank a reverse flow at the surface is induced. The inlet structure and corresponding baffles are largely responsible for this highly non-uniform velocity field; hence, they will also affect the settling tank performance. Any good model should address this issue.

The first numerical models in literature accounting for turbulence did not consider the inlet region (e.g. Samstag *et al.*, 1992; McCorquodale & Zhou, 1993). It was assumed to be a completely mixed region due to the eddy behind the baffle (Imam *et al.*, 1983). Devantier & Larock (1986) neglected the inlet region as well, although they pointed out the need to calculate the flow pattern in the inlet zone rather than to prescribe conditions at the baffle section. They encountered, however, strong numerical instabilities near the submerged baffle lip, where the low-solids concentration surface return flow joins the high-solids concentration inlet flow.

Even when the baffle is included in the computational domain it is essential to consider the correct inlet structure. In this respect, potential-kinetic energy considerations in the inlet region have their influence on the global velocity pattern (Zhou & McCorquodale, 1992c; Szalai *et al.*, 1994; Krebs *et al.*, 1995). Some researchers (Lakehal *et al.*, 1999; Armbruster *et al.*, 2001) avoid the inlet structure modelling by evenly distributing the inlet flow at the free surface inside the feed well. This approach can be questioned since kinetic energy is not dissipated by the impingement of the inlet jet flow on the baffle as in reality.

Besides modelling the inlet region, Hervo *et al.* (2000) also included the inlet pipe in their computational domain.

For the investigated settling tank at Oxley Creek WWTP, inlet pipe, momentum diffuser and inlet region were initially modelled. It became clear that any coupling of these three structures were computationally too intensive (data not shown). Both inlet pipe and momentum diffuser were therefore excluded from the computational domain.

Subsequently, only the six inlet slots were modelled. These vertical slots with energy-dissipating deflector vanes definitely induce 3D flow patterns. Hence, to approximate this structure in a 2D environment the slots were placed horizontally and the deflectors were omitted. Of course, it is expected that less kinetic energy would dissipate with this approach. Indeed, the tangential introduction of sludge is crucial to the inlet energy dissipation and full utilisation of the feed well for flocculation (Ekama *et al.*, 1997). Figure 5.8 shows the predicted flow structure near the slots. Due to the strong interaction between the six jet flows, vortices arise between the jets themselves. Starting from a tank filled with only water, initial contact discontinuities in concentration develop near the inlet apertures because of the entering solids flow. This problem manifested itself as a need for small time-integration steps, which in turn demanded a large number of iterations to obtain a solution. For the inlet discussed, time steps of 10^{-3} - 10^{-4} s were needed in the first part of the

simulation. After 3 h of simulated time, steps of 0.1 s were still needed. Further, a fine mesh around the inlet structure was essential to resolve the flow field; this demands even more computational efforts. The flocculator was meshed with 4800 cells of which approximately 90% resides in the proximity of the inlet slots. For that reason, Krebs (1991a,b) did not model a porous wall inside the settling tank dissipating energy of the density current.

Due to the intensive computations with a 700 MHz Pentium III processor (at that time) and the necessary small integration time steps it was decided to further simplify the inlet structure. Moreover, since the real flow close to the inlet is strongly 3D, the present 2D model was incapable of simulating realistic flow features anyway. The inlet structure was therefore simplified to a plane jet with the same inlet mass and momentum flux as in reality. Lyn *et al.* (1992) adopted the same approach for a four square jets inlet of a rectangular settling tank. Again, by merging the separate slots less kinetic energy will be dissipated; this only enhances the density current. Although Figure 5.9 shows a well mixed inlet zone, in reality head losses result in low mixing, i.e. $G < 5 \text{ s}^{-1}$ (Ekama *et al.*, 1997). For that reason, the inlet zone is less accurately modelled compared to the main settling tank zone.

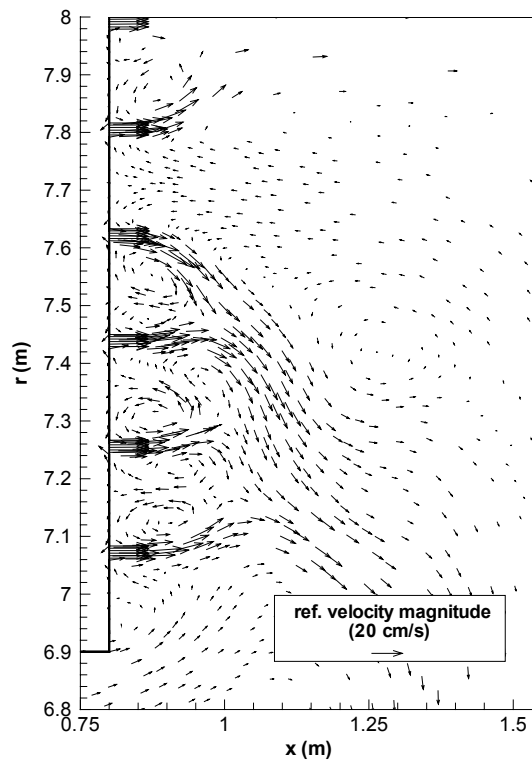


Figure 5.8 Flow field near the inlet structure with 6 slots

To find the optimal, simplified inlet structure description two cases were considered, i.e. a main slot located at the middle of the momentum diffuser (Figure 5.9, top) and a slot at the free water surface (Figure 5.9, bottom). Flow discrepancies clearly exist between the two cases and may be attributed to a difference in inlet densimetric Froude number Fr_{inlet} . This Froude number is the ratio of the kinetic to the potential energy of the flow. Hence,

$$Fr_{inlet} = \frac{u_{inlet}}{(g_{inlet}^c H_{inlet})^{\frac{1}{2}}}$$

Where u_{inlet} and H_{inlet} are the inlet velocity and the height of the inlet slot above the bottom floor respectively; g_{inlet}^c is the gravitational acceleration corrected for density differences, i.e.

$$g_{inlet}^c = g \frac{\rho - \rho_l}{\rho_l}$$

Despite the small difference in Froude number, only 3%, the inlet structures result in different flow patterns inside the feed well, i.e. the inlet flow remains parallel to the free surface for the top-slot and does not deviate as seen for the slot located in the middle of the diffuser. The discrepancy is due to the existence of eddies in the jet flow's proximity. When the slot is located mid-way the diffuser, two eddies are formed by the jet impingement on the wall; hence, the eddies are located laterally to the jet. The spatial development of the upper eddy forces the jet downwards. Instead, when the slot is located at the surface no upper eddy is formed; only one can be formed below the jet. This single eddy pushes the jet flow upwards explaining the location of the jet parallel to the water surface.

Although both slot configurations seem to be physically acceptable, the slot at the surface was preferred for further modelling. From the solids concentration profile observed in Figure 5.9 (top), it is concluded that solids settling already occurred above the jet flow for the submerged inlet slot. It was observed in practice, however, that no settling occurred in the inlet region due to intensive mixing. Hence, the top-slot configuration is preferred. Finally, note that the zone below the inlet jet is characterised by a lower solids concentration. Although it seems doubtful, it originates from flow entrainment underneath the momentum diffuser by the recirculation flow. Due to low velocities in the corner, solids have the possibility to settle. This clear liquid is then entrained towards the inlet jet.

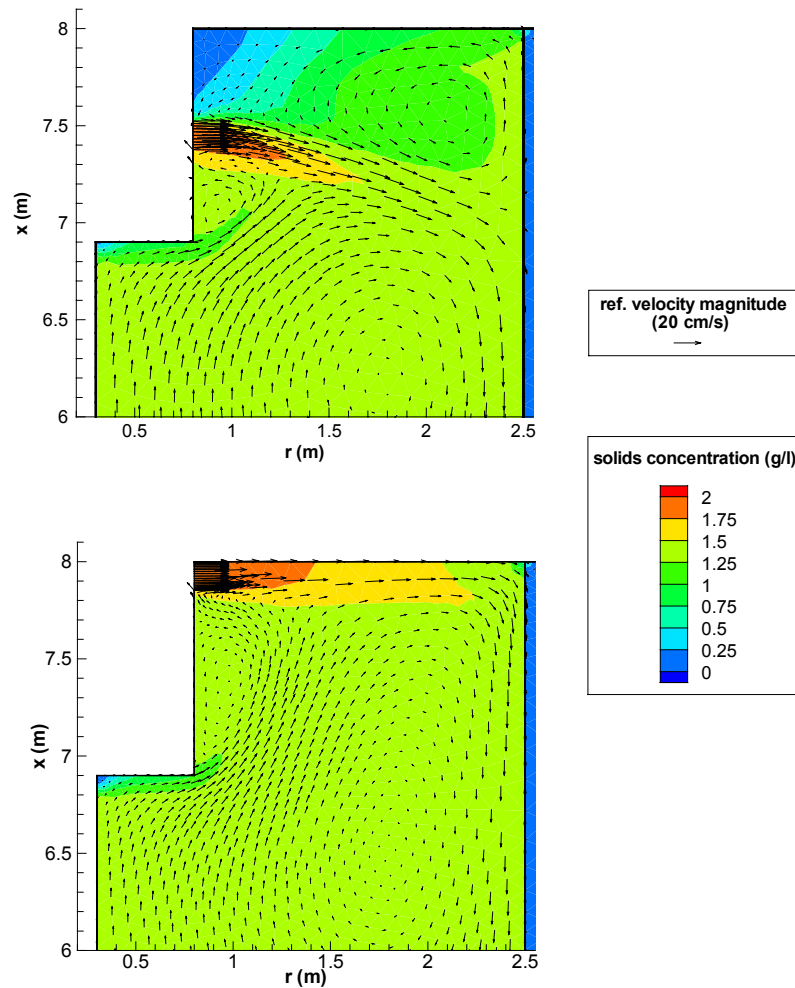


Figure 5.9 Solids concentration and flow field near the inlet located at the middle (top) and the top (bottom) of the momentum diffuser

5.2.5 Steady-state and dynamic simulations

In the previous section, the selection of the inlet structure description was based on steady-state simulations, although dynamic simulations can be utilised for comparison as well. In this section, both approaches are discussed.

In the past, many settling tank models assumed that hydrodynamics and solids transport are in steady-state (e.g. Devantier & Larock, 1986; Lyn *et al.*, 1992; Szalai *et al.*, 1994; Krebs *et al.*, 1995; Krebs *et al.*, 1996); hence, time variations were neglected. This implies an equilibrium between the influent solids loading and the combination of the bottom solids withdrawal and the effluent mass flux. However, an unsteady model (Zhou & McCorquodale, 1992a,b; McCorquodale & Zhou, 1993; Lakehal *et al.*, 1999) may be utilised not only to investigate the time-dependency of the system under investigation, but also to avoid convergence problems; time-marching is one of the existing techniques to overcome numerical instabilities for density-driven flows. With this technique the steady-state solution is

reached asymptotically. When time-marching is applied, the solution will be numerically more stable. Good initial values for the different variables speed up the calculations. In this respect, Zhou & McCorquodale (1992b) adopted zero initial velocities, and a uniform solids concentration equal to the non-settleable fraction. The same authors gave small initial values for k and ε to the entire computational domain. On the other hand, Devantier & Larock (1986) applied linearly varying profiles.

In this work, time-marching was applied as well. If no initial profiles were available from previous simulations, the computations started with an empty settling tank and the following conditions; atmospheric pressure was taken as initial value for the entire computational domain. Further, the solids concentration was assumed to be zero, whereas both radial and axial velocities were 1 cm/s. Finally, k and ε had as starting value 1 m²/s² and 1 m²/s³ respectively. Although this approach was needed for some cases, most simulation studies mentioned in this work were performed with previously obtained steady-state profiles as initial conditions.

The question always remains when and to what extent steady-state is reached. This is necessary to, for instance, reveal the quality of the solver used, i.e. mass/momentum loss or generation in the system cannot be tolerated. It is therefore essential to check the conservation of mass and momentum over the entire system. Unsteady simulations further reveal how fast the system dynamics are, i.e. how fast does the system respond on external disturbances and arrive at a new steady state.

In this respect, the dynamics of the Oxley Creek settling tank without scraper mechanism and the flow inlet at the top of the momentum diffuser will be demonstrated. Simulations were started with a settling tank initially filled with only water. Convergence based on residuals is hard since they depend on the time step. As first approximation, steady-state could then be evaluated based on the invariance of residuals with increasing time steps. It may be, however, more appropriate to investigate the temporal change of important variables. Snapshots were therefore taken during the simulation on a regular (simulated) time base and compared; time differences are investigated for concentrations (Figure 5.10), axial (Figure 5.11) and radial (Figure 5.12) velocities respectively. Note that absolute differences are shown in the graphs.

Firstly, the solids concentration profile clearly starts stabilising considerably after approximately 4 h. After 7 h the maximum discrepancy found is <0.05 g/l and primarily situates in the concentration ranges 0-2 and 4-6 g/l. Considerable variation also exists in the concentration range 2-4 g/l though. The continuing variation in time of solids concentration is attributed to unsteady gravity waves occurring at the solids blanket interface (see Section 5.2.7 for more information).

Secondly, axial and radial velocities are characterised by a similar time frame to reach pseudo-steady-state, i.e. 4 h. Again, velocities show continuing variation caused by the gravity waves. In general, variations are below 0.5 cm/s; largest variations occur at velocities smaller than 5 cm/s.

Finally, the mass balance for solids is investigated at all times. For this case study, an error below 1.5% of the theoretical inlet solids flux was retained. Its origin could be twofold: (i) no steady state is reached yet, or (ii) a mass loss from the system occurred due to numerics. As mentioned before, and will be discussed in Section 5.2.7, gravity waves prevail in the tank. These dynamics result in periodically changing underflow solids concentrations leading to

situations where even more mass may leave the system than it is entering. Hence, negative mass balances may occur as well and are intrinsically linked to the system dynamics. Average mass balances over the mentioned time periods approach zero.

Note that the previous exercise was only given as an example and the mentioned time thresholds for steady state will not be applied as such in other cases; the mass balance is checked at all times though.

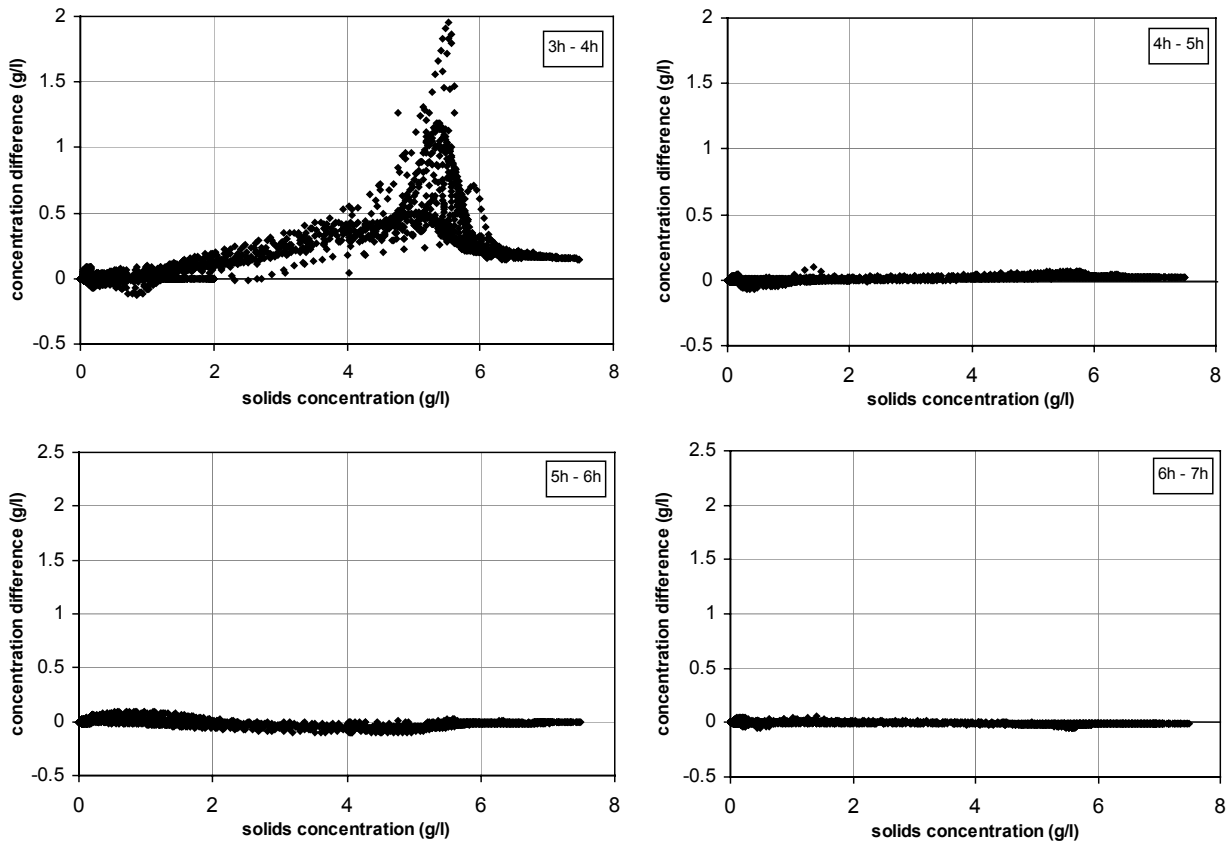


Figure 5.10 Investigation of the error dynamics for solids concentration

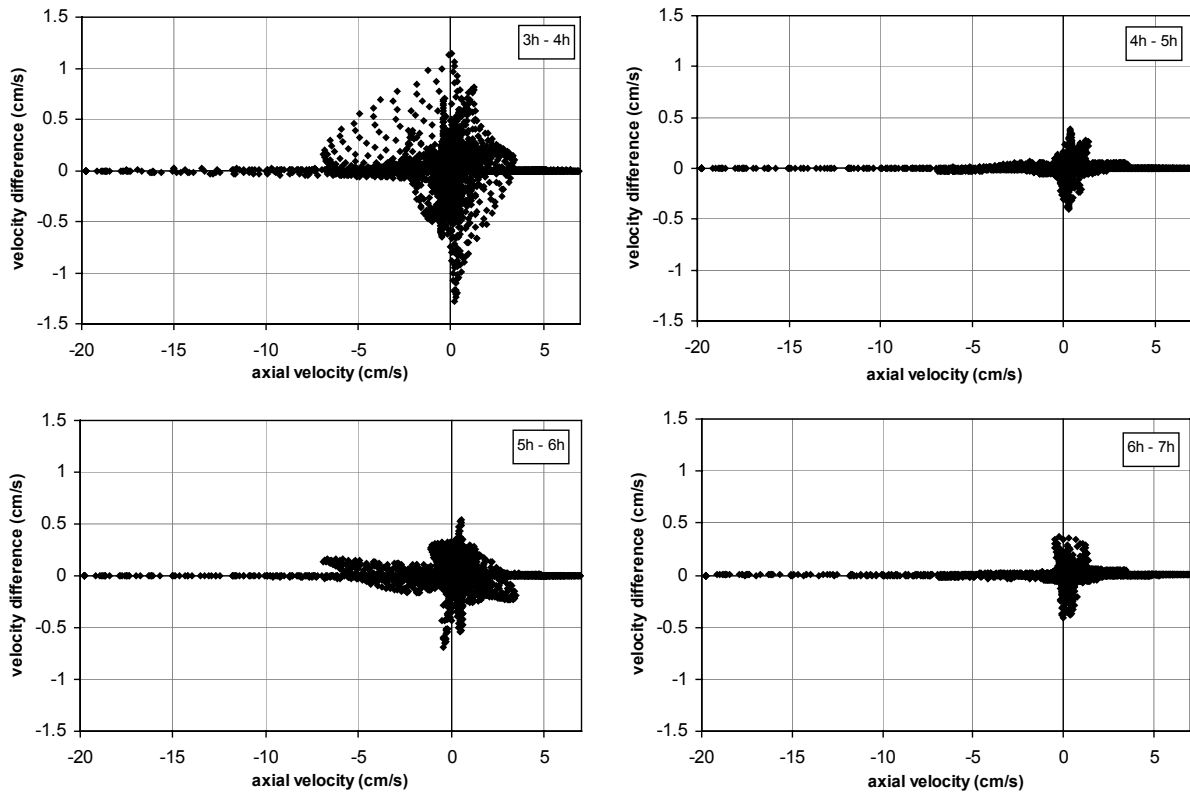


Figure 5.11 Investigation of the error dynamics for axial velocity

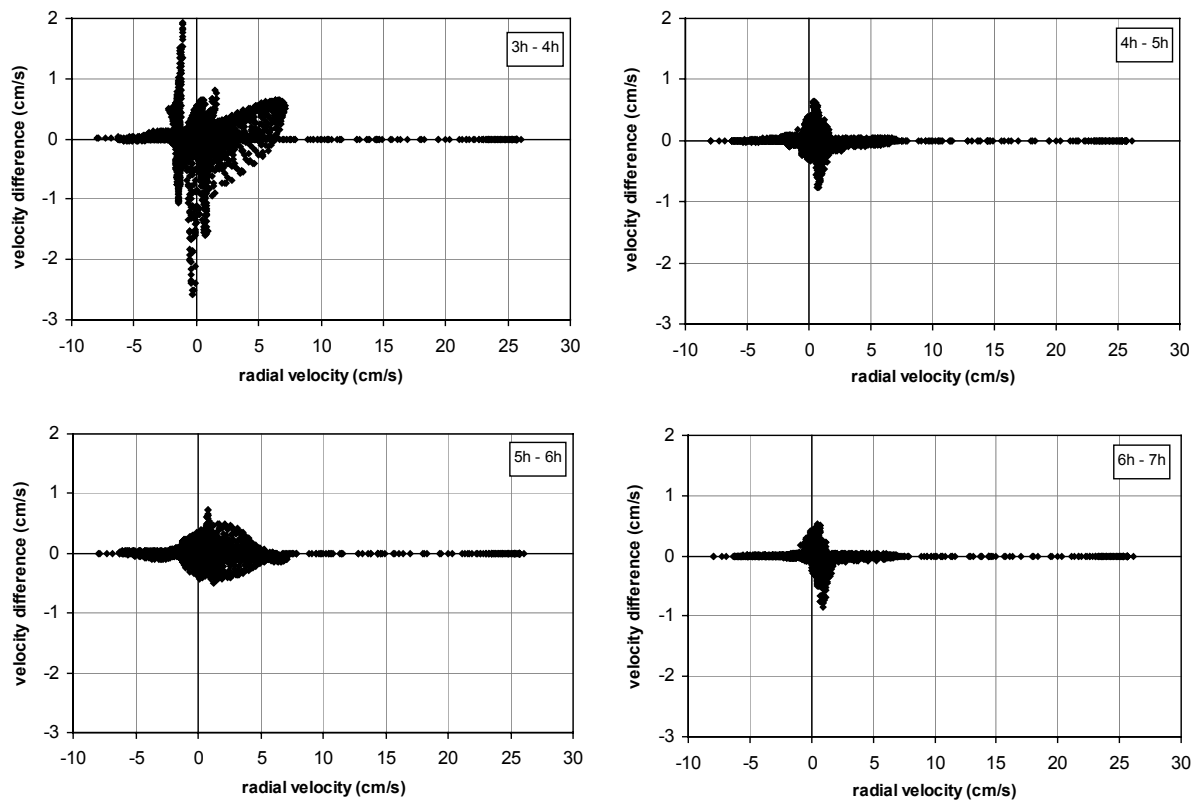


Figure 5.12 Investigation of the error dynamics for radial velocity

5.2.6 Mesh dependency of the flow field

Similar to the time dependency, the solution may depend on the mesh size. Every CFD study should therefore include a mesh test checking to what extent refining and/or coarsening the mesh alters the solution (e.g. McCorquodale & Zhou, 1993), i.e. a too coarse mesh can introduce numerical diffusion. The necessary mesh refinement resulting in invariable solution fields determines the final mesh size used in simulation studies. However, there is a trade-off with the necessary simulation time to obtain a converged solution. A cost-benefit analysis between both computation time and accuracy needs to be done.

In this work, the mesh size has been investigated for two cases. Firstly, the mesh of the feed well and the baffle region have been altered; most gradients are to be found here anyway. The necessary mesh resolution obtained is subsequently utilised to assess mesh refinements in the main part of the settling tank. Subdividing the mesh investigation in two parts allows tracking down the impact of specific mesh-refined regions on the flow field. Note, however, that re-meshing a specific zone alters the mesh of other zones as well.

In the investigation below, computed cell-centre values of concentration and velocity are used. Although interpolated values result in somewhat smoother profiles at the considered cross-sections, they do not allow the proper visualisation of discontinuities which will be smeared by averaging.

5.2.6.1 Mesh refinements of inlet and baffle region

Four different mesh sizes were applied to the feed well and baffle region; Table 5.7 summarises the investigated meshes.

Table 5.7 Mesh sizes investigated for flow field dependency study

	no. cells		
	<i>feed well</i>	<i>baffle region</i>	<i>total</i>
coarsest	300	14	2797
coarse	1159	126	5158
fine	1841	293	7584
finest	2732	454	10226

To analyse the mesh dependency of the solution, the solids concentration, axial and radial velocities were investigated at four different cross-sections (see Figure 5.13). Two locations were chosen inside the inlet region. For the baffle region, a single vertical cross-section was localised in front of the baffle. At last, in order to check any interdependency between inlet and baffle re-meshing, an extra vertical cross-section in the main settling tank region was selected.

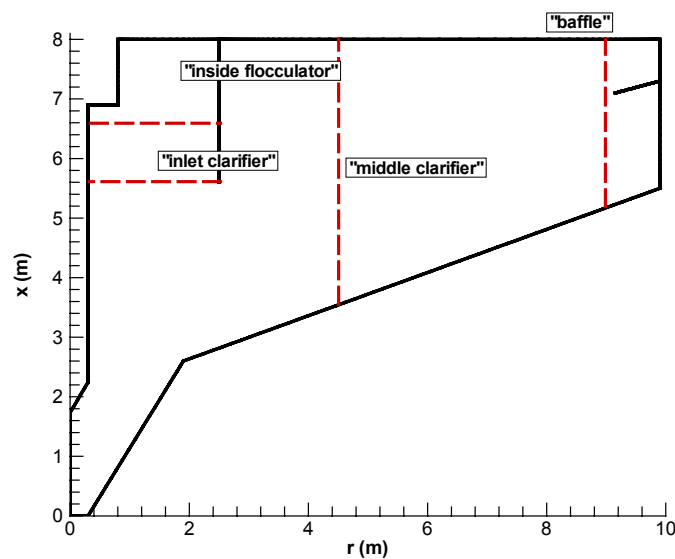


Figure 5.13 Cross-sections at which the mesh size effect is investigated

Firstly, the radial velocity component is discussed. In Figure 5.14 the profiles show obvious similarities; local discrepancies inside the feed well and the baffle region can be observed though. Further, the radial velocity profile inside the feed well does not show a smooth profile as compared to the other cases. From the figures, it seems that radial velocities decrease with mesh refinement at the end of the feed well. Moving to the velocity profile near the baffle reveals that the largest velocities are located near the bottom and the water surface. The sudden flow redirection at the bottom floor is obviously due to the flow impingement at the outer wall. At 7.1 m a local velocity maximum is clearly seen and attributed to the flow around the baffle. In general, it is concluded that the finer the mesh, the smaller the mentioned maximum radial velocities are. To check the mutual effect of mesh refinement at the inlet and baffle region, the flow pattern in the middle of the settling tank was investigated as well. The largest velocity deviations are observed for the density current at 4–4.5 m (axial) distance. Above this jet flow, no major discrepancies are worth mentioning. It is difficult to relate the mentioned velocity differences to (i) the (although limited) altered mesh outside the feed well and baffle region, (ii) the influence of the feed well, i.e. lower inlet velocities are translated to weaker density currents, and (iii) the dynamics of the gravity waves (see Section 5.2.7 for more information). The velocity profiles shown are snapshots in time; hence, the gravity waves are not exactly at the same location, which might explain the discrepancies. However, a trend can be observed, i.e. the finer the mesh at the inlet and baffle region, the more the profiles coincide. It is thus expected that the small effect of mesh refinement observed at the centre of the tank is due to the influence of the feed well.

Secondly, except the coarsest mesh, axial velocities in the feed well are similar for the different mesh sizes tested (Figure 5.15). Most variation is observed in the baffle region though, and is again located at the bottom floor and the baffle, where sudden flow redirections take place. Also some flow dependency between the inlet flow field and the main settling tank region is observed. Fortunately, for the fine and finest meshes these profiles coincide, i.e. no or little dependency between the flow fields exists.

Finally, the solids concentration profiles were investigated (Figure 5.16). Here, considerable impacts of mesh sizes are noticed. Inside the feed well it is seen that the finer the mesh, the higher the solids concentration becomes. Again, these higher concentrations are translated into higher concentrations at the middle of the settling tank. Presumably, the lower concentrations found for the coarse mesh are due to numerical diffusion. At the baffle no relevant differences are observed.

5.2.6.2 Mesh refinements of the settling tank's centre part

To study the impact of the mesh size of the main settling tank region on the solution, three cases were investigated. For the baffle and flocculator zones the "fine" mesh, as determined in the previous section and assumed to be optimal, was used. Supplementary, the number of nodes at the floor and the free surface were increased (Table 5.8).

To investigate the impact of mesh resolution, the flow and solids concentration fields at the floor were focused upon. Especially for the solids concentration, this region shows the largest gradients. Three differently located profiles were utilised for this purpose; they were taken at a (sloped) plane parallel with and at distances of 0.25 m, 0.5 m and 1 m above the floor. The profiles are shown as function of the radial distance from the tanks' centre.

Table 5.8 Mesh sizes investigated for flow field dependency in centre part of the tank

	no. cells
coarse	7584
medium	11516
fine	15840

Firstly, the radial velocity profile is discussed. As observed in Figure 5.17, more oscillations in the velocity profile occur when moving away from the floor. They are due to the existence of the density current and the associated gravity waves (see Section 5.2.7). This wavy density current periodically transects the sloped plane of observation, resulting in the mentioned oscillations. Not only are these waves more damped closer to the floor, mesh refinements here have the largest impact. Care should however be taken when interpreting the results. Any discrepancy in peak height and location of the oscillations may be due to the unsteady character of the gravity waves, which move away from the settling tank's centre. Notwithstanding, it is assumed that solutions obtained with the medium and fine meshes are independent of the mesh resolution.

Secondly, the axial velocity profiles in Figure 5.18 show a similar behaviour. Again, the largest discrepancies occur close to the floor. Finer meshes seem to result in higher axial velocities for distances less than 3 m, i.e. the region below the feed well. Note that here the floor stops and the profile is measured above the sump. Once more, the medium and fine mesh coincide at almost any place; only near the side wall discrepancies occur, similarly to the radial velocity profiles.

Lastly, the solids concentration profiles are shown in Figure 5.19. For all locations, good agreements between profiles for medium and fine meshes are obtained.

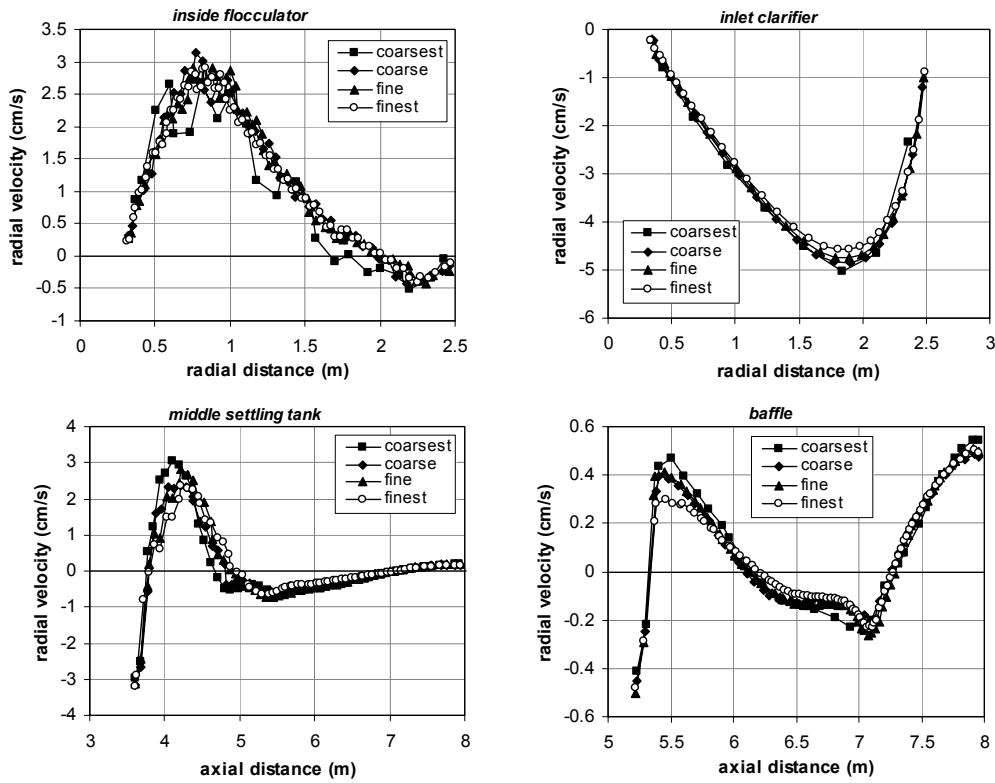


Figure 5.14 Influence of mesh size on the radial velocity profiles inside the feed well (top, left), the bottom of the feed well (top, right), the middle of the settling tank (bottom, left), and the baffle region (bottom, right)

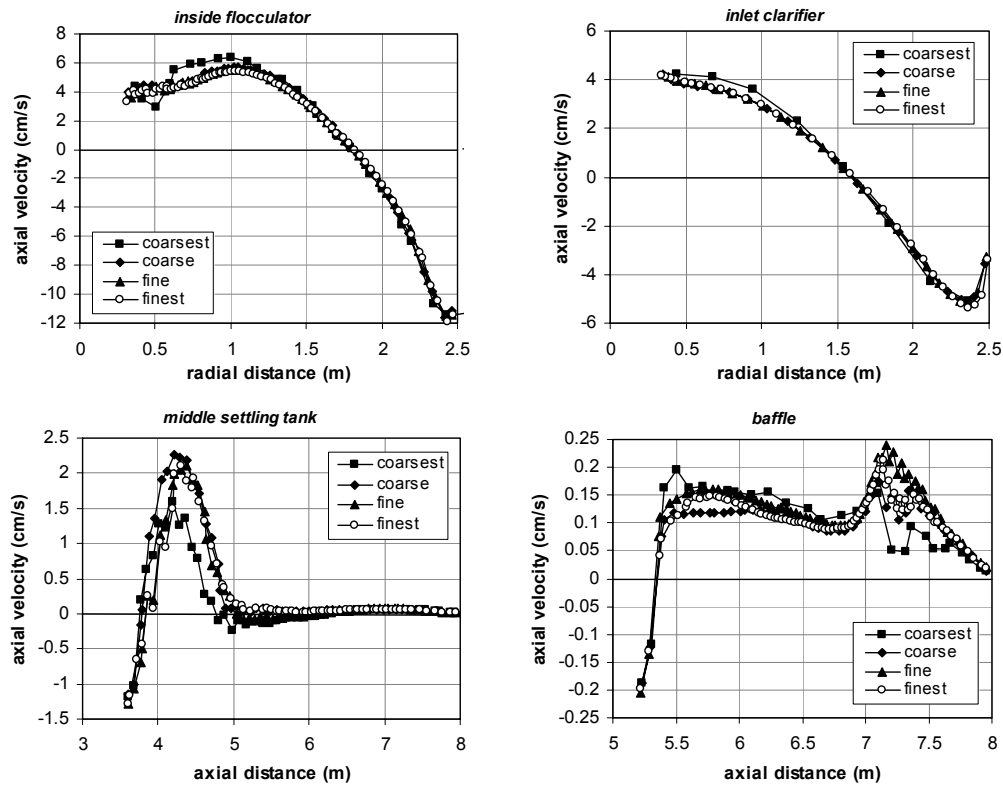


Figure 5.15 Influence of mesh size on the axial velocity profiles inside the feed well (top, left), the bottom of the feed well (top, right), the middle of the settling tank (bottom, left), and the baffle region (bottom, right)

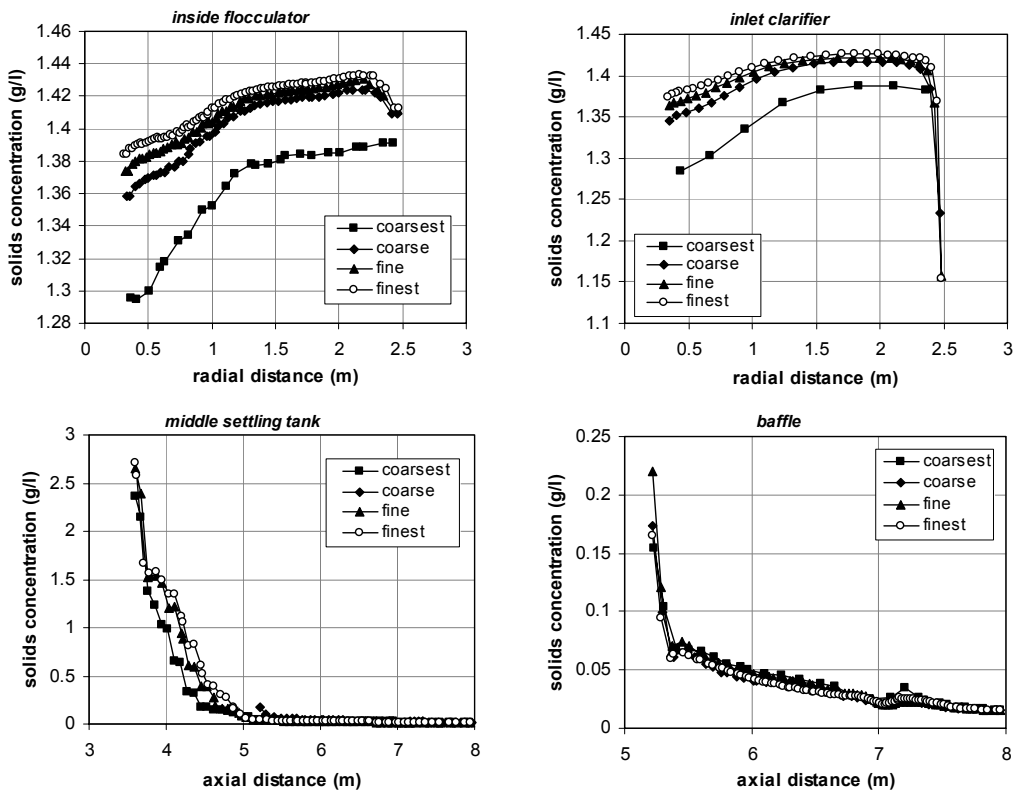


Figure 5.16 Influence of mesh size on the concentration profiles inside the feed well (top, left), the bottom of the feed well (top, right), the middle of the settling tank (bottom, left), and the baffle region (bottom, right)

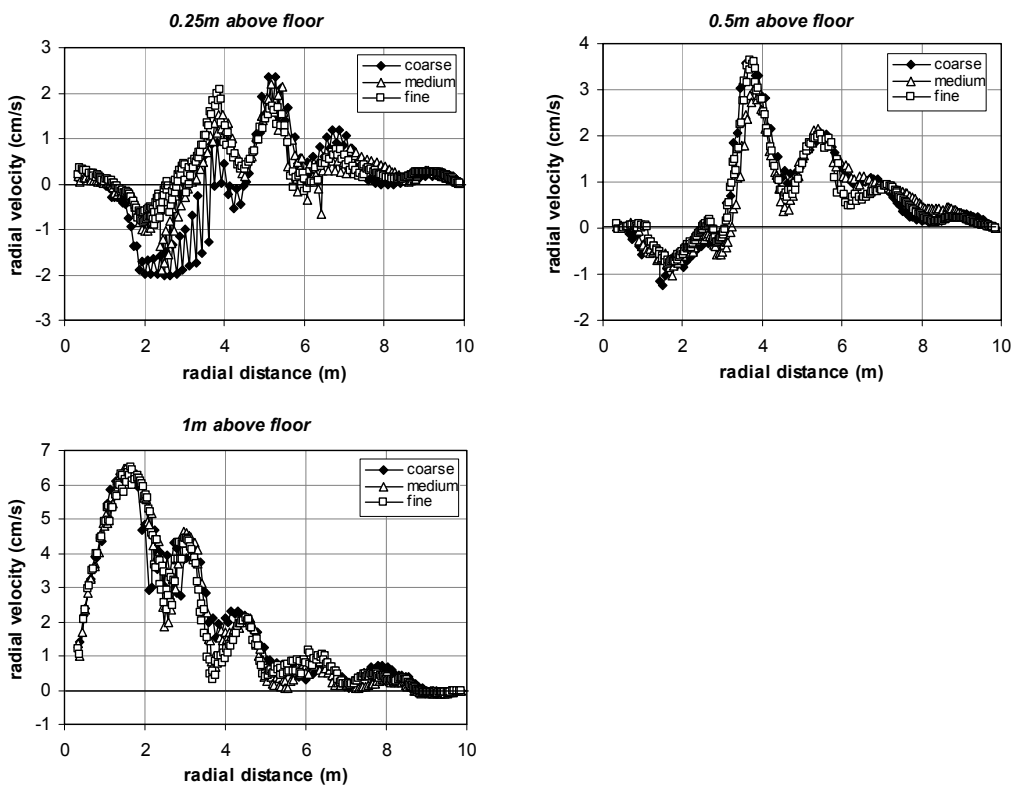


Figure 5.17 Influence of mesh size on the radial velocity at a plane parallel to the floor; 0.25 m (top, left), 0.5 m (top, right), and 1 m (bottom)

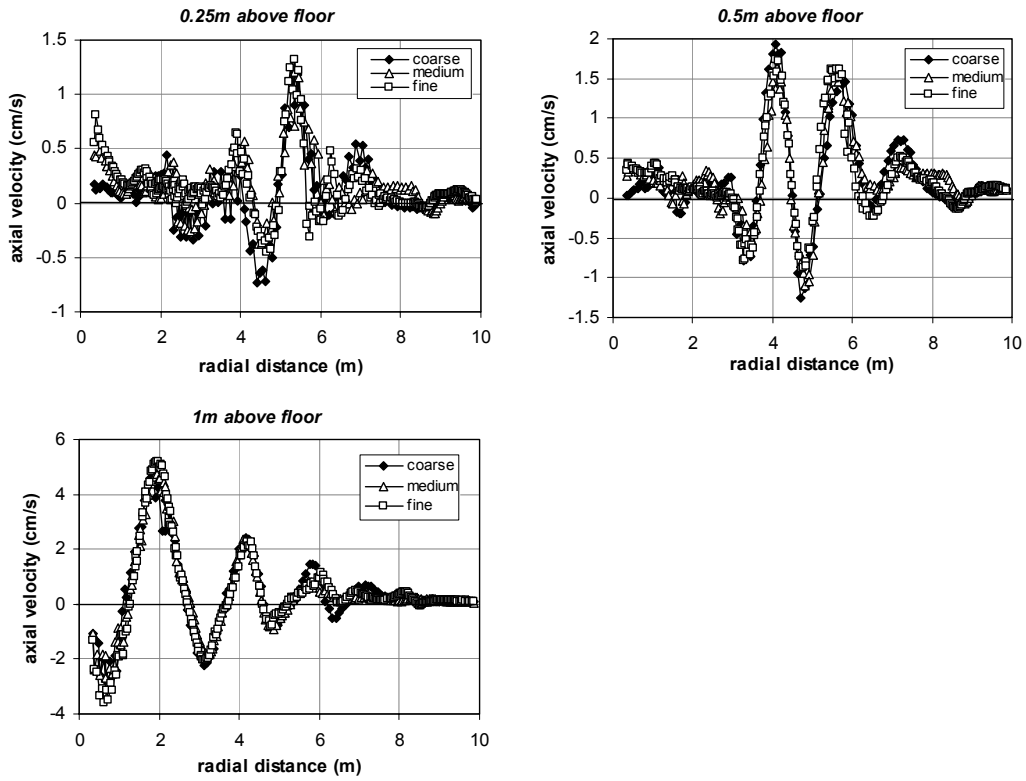


Figure 5.18 Influence of mesh size on the axial velocity at a plane parallel to the floor; 0.25 m (top, left), 0.5 m (top, right), and 1 m (bottom)

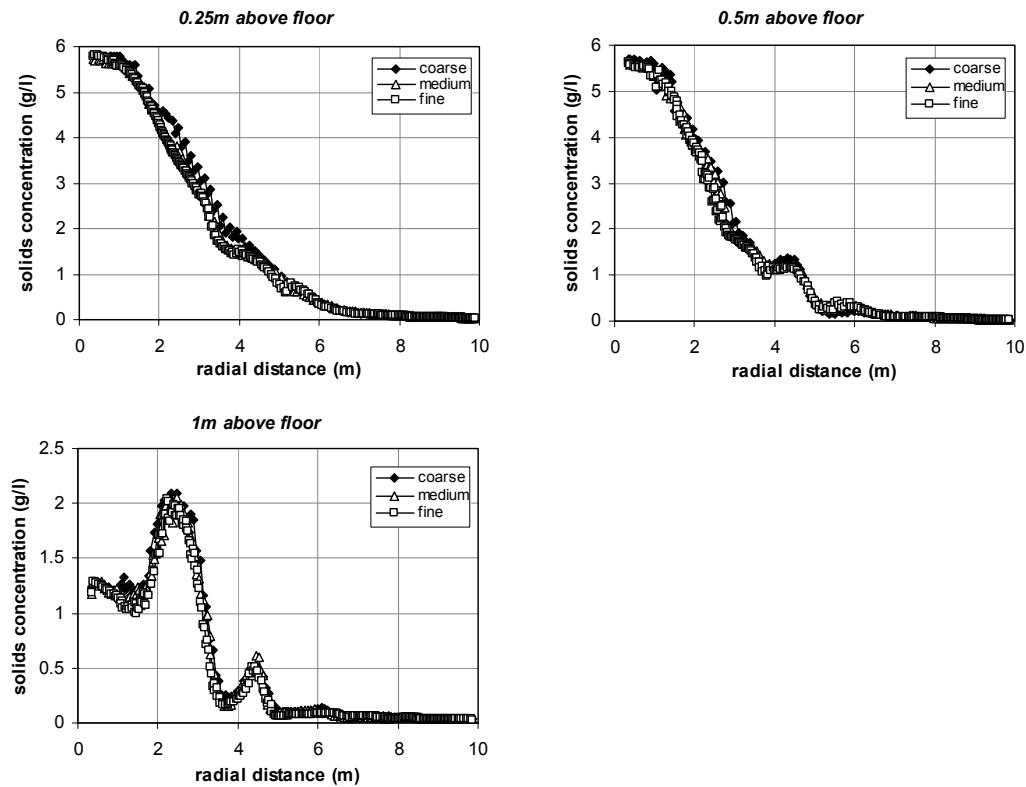


Figure 5.19 Influence of mesh size on the solids concentration profile at a plane parallel to the floor; 0.25 m (top, left), 0.5 m (top, right), and 1 m (bottom)

5.2.6.3 Conclusions

The final choice of mesh size is strongly based on (i) the solution independency and (ii) the needed computational time. A very fine mesh undoubtedly results in more correct solutions for the flow field. Unfortunately, against this stand long computational times making an acceptable mesh refinement dependent on the available computational power. In future investigations, the "fine" mesh is selected for the feed well and baffle region in view of the sufficient agreement with the "finest" mesh and accounting for the relative independency of feed well and baffle region results. On the other hand, the "medium" mesh is opted for the main settling tank region. As a result, the mesh consists of a total of 11516 cells. Notice that later mesh adaptations occurred due to numerical instabilities arising from locally improper meshing, and increased the mesh size to approximately 16000 cells.

5.2.7 Hydrodynamic phenomena in circular settling tanks

According to McCorquodale & Zhou (1993), two important hydrodynamic factors affecting the solids distribution in secondary settling tanks are the strength of the bottom density current and the upward current near the effluent weirs. The activated sludge entering the basin normally plunges as a density jet to the tank's bottom, thereby creating a secondary countercurrent at the surface. The density current inhibits the spreading of the inflow to the surface and, thus, promotes non-uniform velocity profiles (e.g. Bretscher *et al.*, 1992).

In literature (e.g. Krebs, 1991a,b; Zhou *et al.*, 1992; McCorquodale & Zhou, 1993; Krebs *et al.*, 1998), many investigations discuss the inlet densimetric Froude number. McCorquodale & Zhou (1993) noted that the smaller the inlet Froude number, the greater is the density current relative to the inflow. Krebs (1991b), Zhou *et al.* (1992) and Krebs *et al.* (1995) came to the same conclusion. One cause is the stronger downward velocity originating from the lower Froude number. Also, the inlet kinetic energy will be partly conserved and appears as a large kinetic energy in the bottom current.

In this work, the settling tank investigated had an inlet Froude number of one, meaning that shear flow is as important as gravity-driven flow. Although kinetic and potential energy are balanced, a strong inlet jet flow remains parallel to the water surface. After impingement at the wall, the jet is redirected towards the sump. Visual inspection of the inlet region did not show such a strong jet flow though. Instead, considerable mixing was observed. To resolve this problem, 3D modelling of the inlet structure seems necessary.

In this respect, the importance of the Froude number to specify the flow type is controversial as well, especially towards flow stability (Lyn & Rodi, 1990). This is due to the association of the Froude number with the importance of free-surface effects (e.g. damping of turbulence); numerical models typically neglect these effects by imposing a rigid-lid condition at the free surface. According to Celik & Rodi (1988), turbulence is indeed dampened by the free surface. Here, this issue might be of particular importance since the inlet jet is located at the surface. Although a symmetry plane, and no rigid-lid condition, is assumed in this work, energy dissipation at the free surface may be inaccurately modelled. Another reason for the strong jet flow is the absence of deflector vanes in the model. As a

result, mixing and energy dissipation in the feed well might be underestimated (Lyn & Rodi, 1990; Szalai *et al.*, 1994; Ekama *et al.*, 1997). According to Lyn & Rodi (1990), turbulent transport is indeed important in the proximity of the deflectors. Although no deflectors were modelled, most turbulence was seen near the inlet slot (data not shown). Ekama *et al.* (1997) stressed the importance of the tangential introduction of sludge in order to dissipate the inlet energy and induce some flocculation. Further, as seen in Figure 5.8, six slots formed the inlet structure; they led to many vortices also increasing the energy dissipation and, as a consequence, weakening the waterfall effect.

This waterfall effect is largely affected by the size of the feed well. According to Ekama *et al.* (1997), the feed well diameter of the investigated test case is within the recommended design rules. Zhou & McCorquodale (1992c) demonstrated that the feed well diameter should decrease with decreasing Froude numbers. The density waterfall due to a low Froude number enhances not only flow entrainment in the main settling tank part, it also may result in a short cut to the inlet, being detrimental to the process as well (Zhou *et al.*, 1992; Zhou & McCorquodale, 1992c; McCorquodale & Zhou, 1993; Ekama *et al.*, 1997; Parker *et al.*, 2001). This short cut indeed restricts the available space for the inlet flow in the feed well, and enhances the downward flow. Smaller feed wells should therefore be designed for low Froude numbers. Figure 5.20 (bottom) shows that no flow penetrates the feed well. Instead, the large eddy in the feed well entrains some liquid towards the centre of the settling tank; this leads to a flow constriction and a further increase of the downward velocity as well. This enhancement of density current was also investigated by Krebs *et al.* (1995).

Figure 5.20 (bottom) demonstrates a stable stratification near the sump; so-called *rat-holing* does not occur, i.e. no short cut between inlet and underflow is observed. Instead, the downward jet bounces off the solids blanket acting as a boundary, and is directed to the main part of the settling tank. Here, the current weakens as it approaches the outer wall (McCorquodale & Zhou, 1993; Krebs *et al.*, 1998). According to Fischerström *et al.* (1967), the effective depth of the density current is about 60 cm, irrespective of the real depth of the settling tank. However, a slight increase was observed in those cases in which the Froude number was high or the solids concentration was low. As mentioned before, the lower the Froude number, the stronger is the density current. This accounts for both settling tanks with (Krebs, 1991b; Zhou *et al.*, 1992; Zhou & McCorquodale, 1992c) and without feed wells (Zhou & McCorquodale, 1992c; McCorquodale & Zhou, 1993). The flow rate of the bottom current may even go up to triple the inlet flow rate. For the operating conditions investigated here, the Froude number is one indicating a rather weak density current. Note that bulk density was probably underestimated, i.e. accounting for zeolite into the bulk density would considerably increase the downward jet. This is investigated in Section 5.2.8. In the present context, the possible incorrect viscosity relation used needs to be mentioned as well; Formulae 5.4-5.6 are valid only for typical sludges without polymer and zeolite. There will be a difference indeed; for instance, Campbell & Crescuolo (1982) noticed a peak at low shear rates in the rheogram when polymers are dosed. Armbruster *et al.* (2001), however, showed that the maximal forward density current is hardly affected by the rheological properties. For a thorough discussion the reader is referred to Chapter 7 though.

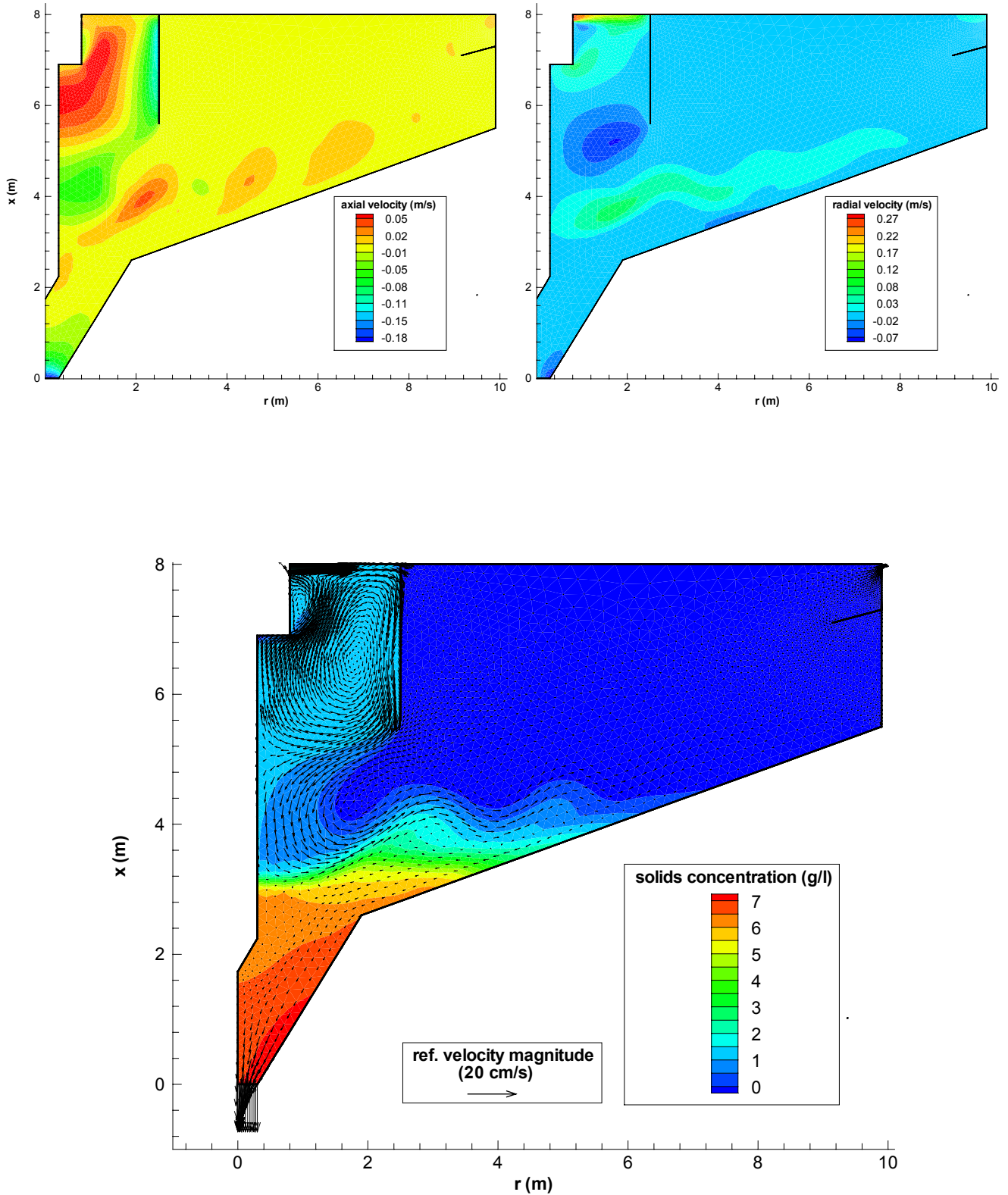


Figure 5.20 Computed solids concentration and flow fields (inlet solids concentration: 2 g/l; inlet flow rate: $0.191 \text{ m}^3/\text{s}$; underflow rate: $0.056 \text{ m}^3/\text{s}$): axial velocity (top, left), radial velocity (top, right), and solids concentration (bottom)

The extinction of the density current with radial distance is mentioned in literature as well (Krebs *et al.*, 1998). Because of this weakening a strong impingement at the outer wall is not observed. Consequently, the surface return flow is weak too and, to close the circle, it only contributes to a small extent to the flow entrainment below the feed well (Ueberl & Hager, 1997).

In the main part of the settling tank, the density current clearly has some oscillating behaviour. Simulations conducted by Armbruster *et al.* (2001) and STOWa (2002b) have shown a similar phenomenon. These so-called *internal gravity waves* are due to the intrusion of a jet into a stratified ambient fluid. Different types of gravity waves can be found in nature. Following the classification of Sutherland (2002), the density current in a settling tank is a so-called *even-mode internal wave*. To first order, these waves are characterised by momentum transport. Whether a gravity wave becomes unstable depends on the degree of stratification, which is usually given by the ratio of buoyancy and inertial forces, i.e. the Richardson number Ri or

$$Ri = \frac{g \frac{\partial \rho}{\partial x}}{\rho \left(\frac{\partial v}{\partial x} \right)^2}$$

When $Ri > 0.25$, stratification is stable and vertical mixing due to shear is reduced. In case of activated sludge, Krebs *et al.* (1998) expected stratification to be more pronounced since hindered settling generates a sharp solids blanket interface. Thus, vertical mixing is less intensive and the layers are more stable. Instead, small values of Ri (< 0.25) are associated with Kelvin-Helmholtz instabilities (Krebs, 1991a; Krebs *et al.*, 1998). These instabilities occur when a stably stratified layer between two fluids of different density is rolled up by shear across that layer, i.e. vortices are formed (Chapman & Browning, 1999). These Kelvin-Helmholtz billows overturn/break and generate turbulence. Some of the turbulent energy released by the instability propagates along the stratified layer as a gravitational wave (Moum & Smyth, 2000; Smyth & Moum, 2000a). In their research however, Smyth & Moum (2000b, 2002) concluded that any initial stratification, as weak as above the solids blanket, eventually prevails over the shear and damps the turbulence.

In Figure 5.20 two billows are clearly observed, which may be commented by calculating the local Ri . Figure 5.21 shows the regions where $Ri < 0.25$; shear obviously dominates in the feed well, at the outlet and, to a lower extent, also at the underflow. In the main part of the settling tank, several distinct zones parallel to the floor and unstably stratified are observed, i.e. shear is dominating buoyancy. To elucidate this, comparison between Figure 5.20 and Figure 5.21 is recommended. The unstable zones correspond to weak vortices on top of and inside the solids blanket; they are overturned billows with alternating rotational direction. Towards the end of the solids blanket the waves are weakened because of wave reflection from the bottom slope (Slinn & Riley, 2002). The wave breaks down and generates turbulence. Slinn & Riley (2002) suggested that wave reflection is a source of boundary-shear stress possibly causing solids resuspension.

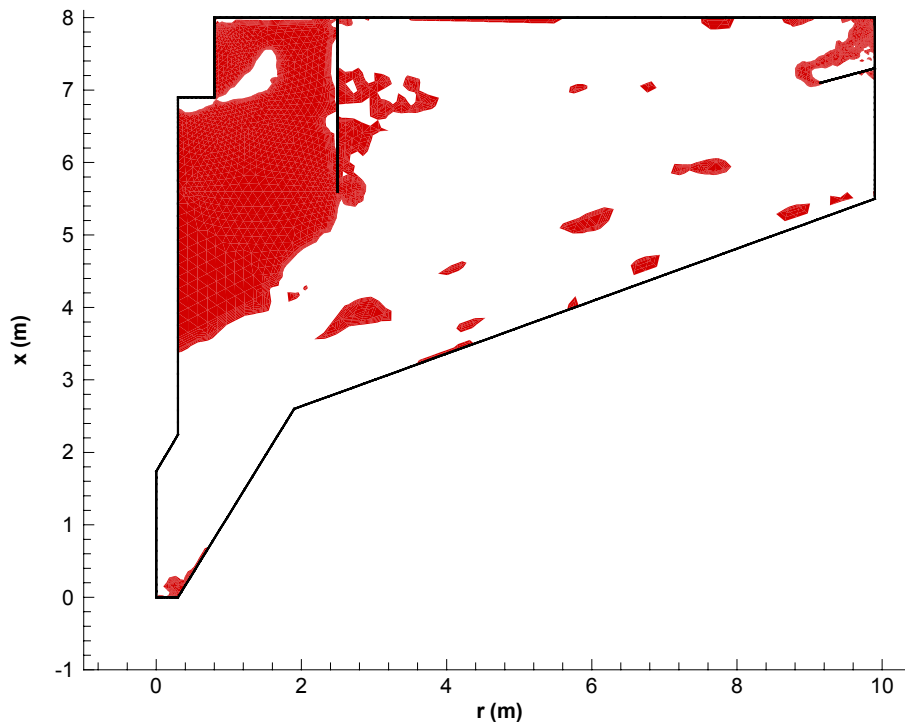


Figure 5.21 Computed shear-dominated zones; grey indicates zones with $Ri < 0.25$

5.2.8 Adjusting bulk density for zeolite

In previous sections, bulk density was calculated with a dry solids density of 1450 kg/m^3 , i.e. solids were assumed to consist of biomass and organic polymers with comparable density. However, in practice, zeolite is dosed which affects the dry solids density. According to Appendix C, the dry solids density of the zeolite-conditioned flocs now measures 1750 kg/m^3 . Note that the settling velocity is assumed to be similar for both cases. The effect on the solids concentration, axial and radial velocity fields is investigated by computing the difference between the respective fields originating from zeolite adjusted and unadjusted bulk densities (see Figure 5.20 for the flow fields with unadjusted bulk densities). The results are shown in Figure 5.22.

The general view of computed velocity and solids concentration fields are comparable to Figure 5.20; yet, there are some interesting discrepancies.

Since zeolite introduces an extra downward momentum, differences in axial velocity are clearly seen close to the wall at the inside of the feed well (Figure 5.22, top, left). An increase in downward momentum is also observed below the well. It seems that flow regions with strong downward flows are influenced mostly; these flows are strengthened and the waterfall effect is more pronounced. The latter still bounces off the stratified layers below but penetrates them further due to the increased momentum. The effect is a downward translocation of the internal gravity waves; this explains the differences in axial velocity

above the sloped floor as well. Contrary to the velocity of the density current, the axial bottom flow inside the sump has increased. Similar remarks on the radial velocities may be given (Figure 5.22, top, right).

Major differences in the solids concentration field are located at the top of the solids blanket (Figure 5.22, bottom). Adjusting the bulk density for zeolite lowers the entire blanket with about 20 cm. Due to the sharp solids concentration gradient at the top of the blanket, any blanket lowering results in large concentration differences between the two scenarios.

From the above observations, it is obvious that a proper calculation of bulk density is crucial for future validation studies. Hence, the adjusted dry solids density will be maintained in subsequent simulation studies.

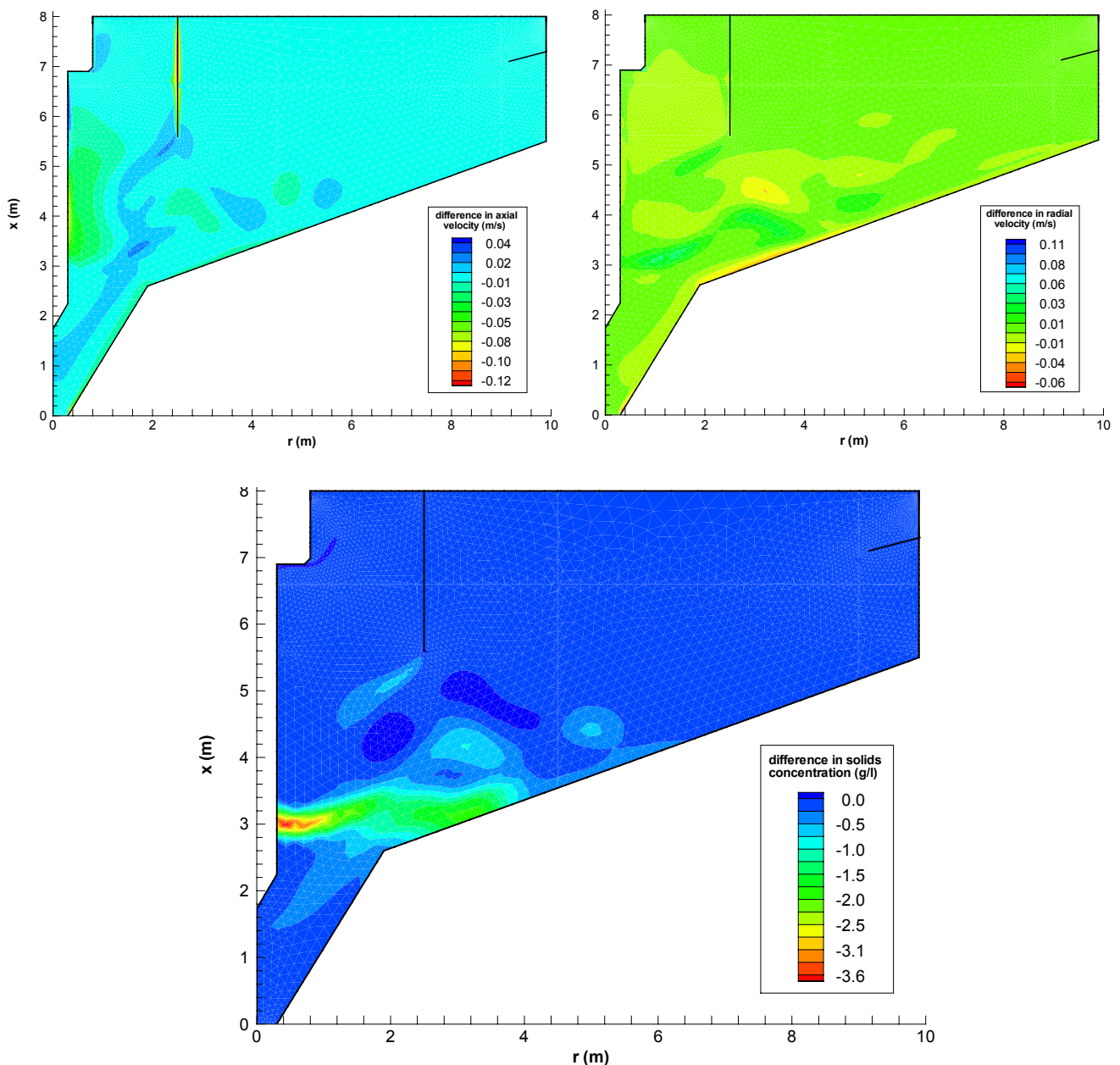


Figure 5.22 Differences in axial (top, left) and radial (top, right) velocities, and solids concentration (bottom) for bulk density adjusted and unadjusted for zeolite. The reference flow fields used are shown in Figure 5.20

5.2.9 Modelling the scraper mechanism

The solids removal mechanism is a major consideration during the design of a secondary settling tank (Boyle, 1980); Section 1.4.3. summarised the available techniques. The settling tank at Oxley Creek WWTP operates with a scraper. What the mechanism of the scraper's operation really is, is still under debate. Two theories are commonly accepted. Firstly, the scraper is considered from a mechanical perspective, i.e. it pushes the solids to the hopper (Warden, 1981; Günthert, 1984; Billmeier, 1988; Albertson, 1991; Albertson & Okey, 1992; Albertson, 1994; Narayanan *et al.*, 2000). Secondly, the scrapers are not truly conveying the solids, but are merely resuspending it (Murk, 1969; Boyle, 1980; Kinnear & Deines, 2001).

In this work, the scraper itself is not incorporated in the CFD meshing but the scraper velocity is computed and this velocity is imposed on the liquid parcel where the scraper resides at the time instant considered. Because the settling tank is modelled in 2D, only the radial velocity component of the scraper is computed. Appendix E supplies the calculation of this radial velocity as function of both radial distance and time. Every 51 minutes the rectilinear scraper passes the modelled transect in 2.9 minutes (see Figure 5.23); the more the scraper approaches the centre, the smaller the radial velocity becomes (Figure 5.24). Winkler (2001) performed 3D simulations of a circular settling tank of comparable geometry, and incorporated the scraper design in the meshing as a wall boundary. Importantly, in the neighbourhood of the scraper he obtained radial fluid velocities similar to the scraper velocity as calculated here. Full-scale measurements supported his work. At least for the radial velocity, the corresponding velocities indicate that the 2D scraper model approximates very well the effect of the scraper on the real 3D flow with possible swirl.

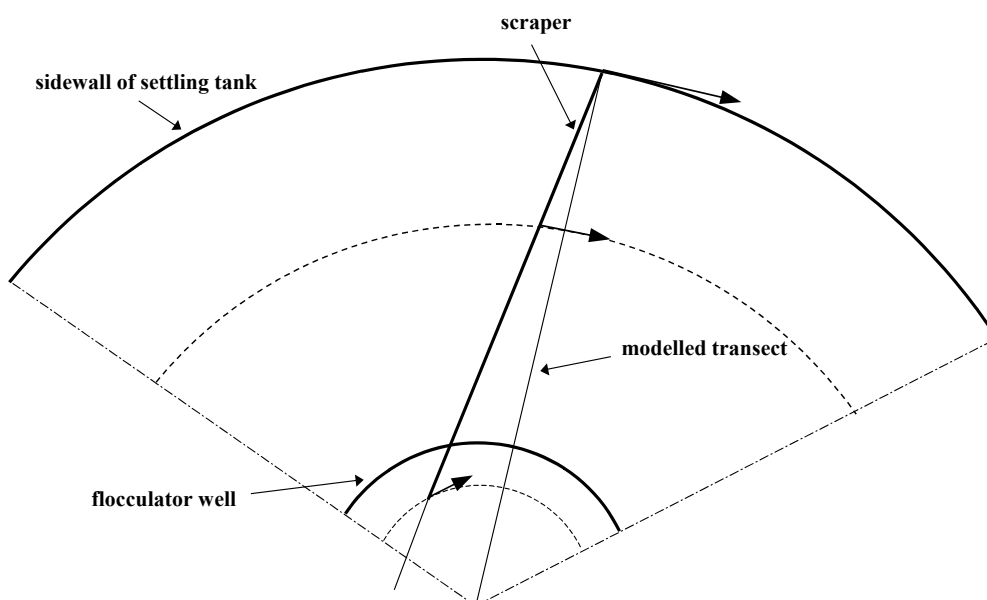


Figure 5.23 Scheme of circular settling tank with straight scraper blade

Fluent software makes it possible to force the solver to return the desired velocity in the computational cell corresponding to the present scraper location. This method, however, failed and led to numerical instabilities shortly after the start of the simulation; it is believed that the mesh was not fine enough to resolve the flow field between scraper and end-wall. A finer mesh was not adopted though because it would demand for more computational power. Alternatively, the extra momentum transferred by the scraper to the liquid is computed (see Appendix E). Note that this extra momentum may be positive or negative, and depends on whether the scraper moves (i) faster or slower than the local fluid respectively, and (ii) in the same direction as the fluid. When investigating the resolved flow field for this momentum-based approach, deviations to the desired scraper velocity occur. These deviations decrease with the scraper velocity magnitude. Notwithstanding, the modelling appears to approach the real behaviour of the scraper when comparing the simulated velocities near the scraper with the work of Winkler (2001). Hence, as a first approximation, it may be utilised to simulate the impact of the scraper on the solids blanket behaviour.

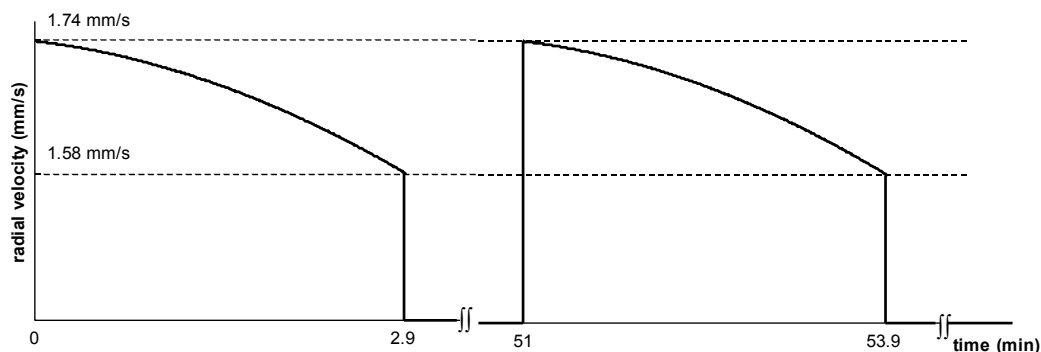


Figure 5.24 Temporal evolution of the radial scraper velocity component

To investigate the scraper effect on the solids distribution in the settling tank, two case studies were performed. Firstly, simulations were run with the rheological model as described by Equation 5.4, i.e. a modified Herschel-Bulkley model. Secondly, the viscosity of water was adopted. Steady-state profiles of solids concentration, radial and axial velocities just before each scraper passage are shown in Figure 5.25.

As clearly observed in Figure 5.25, the presence of a scraper deteriorates the settling tank performance when applying the modified Herschel-Bulkley model, i.e. the solids blanket resides near the free water surface. Although no true yield stress occurs, high viscosities at low shears are dictated by this rheological model; hence, the sludge almost acts as a Bingham fluid. Adopting the very low viscosity of water, the solids blanket stays near the bottom floor and no solids from the blanket escape the settling tank.

Whether solids accumulation occurs appears to depend on the flow field close to the bottom floor. When no scraper operates, a strong bottom floor flow current may be observed which strongly depends on gravity and the rheological nature of sludge. For more information on this topic, the reader is referred to Section 7.1.2.3. Further, Figure 5.24 learns that the scraper's radial velocity varies between 1.58 and 1.74 mm/s. Consequently, the gravitational (and laminar) flow along the bottom, which may go up to 25-30 mm/s near the sump, is

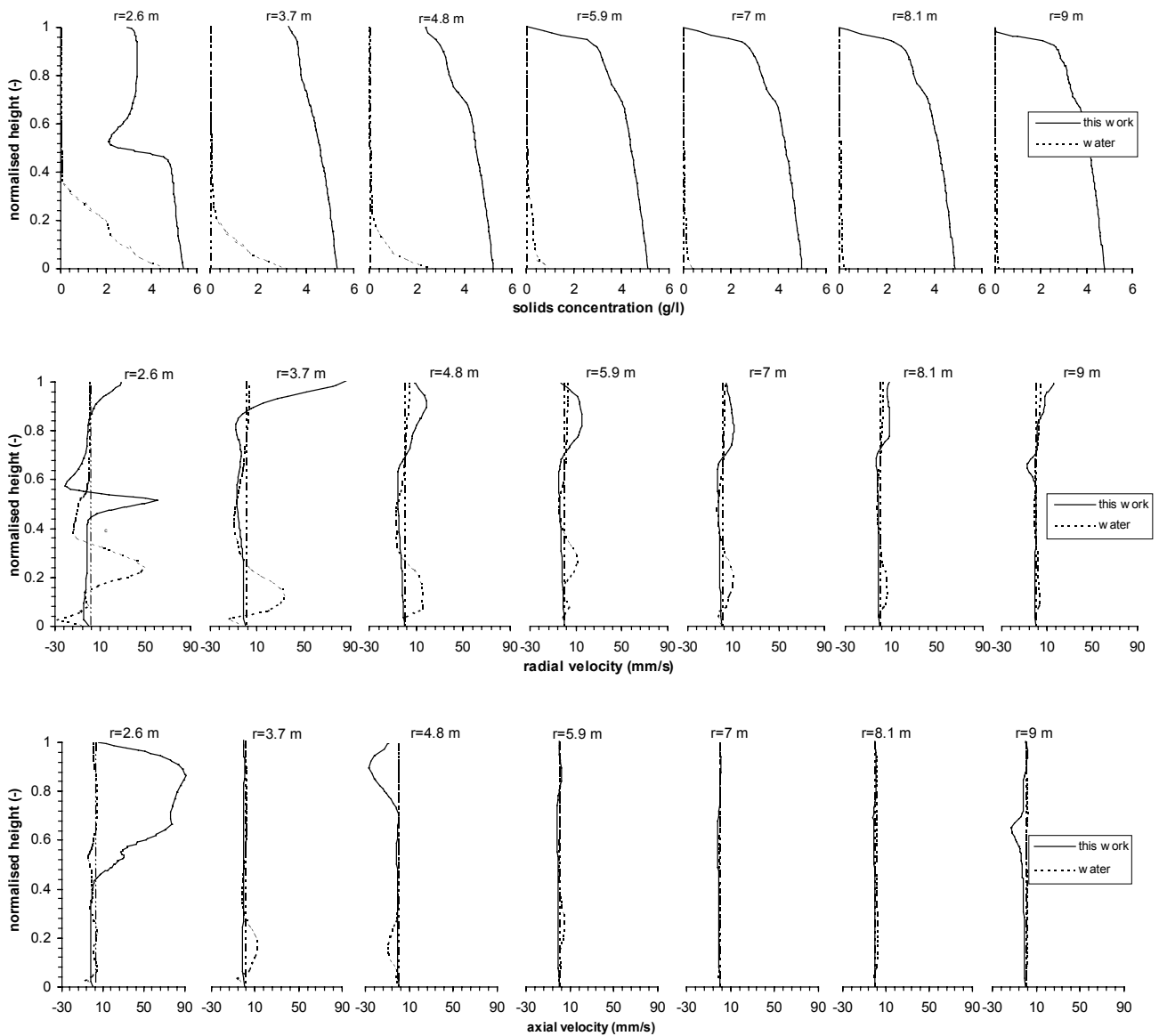


Figure 5.25 Scraper effect on solids concentration (top), radial velocity (middle) and axial velocity (bottom) profiles for the rheologies of water and the model as presented by Equation 5.4. The profiles are shown just before each scraper passage; no further changes are observed between consecutive passages (pseudo-steady-state). The profiles are shown at seven radial distances r measured from the centre. They all situate outside the flocculator well. The heights above the bottom floor are normalised with the local depth

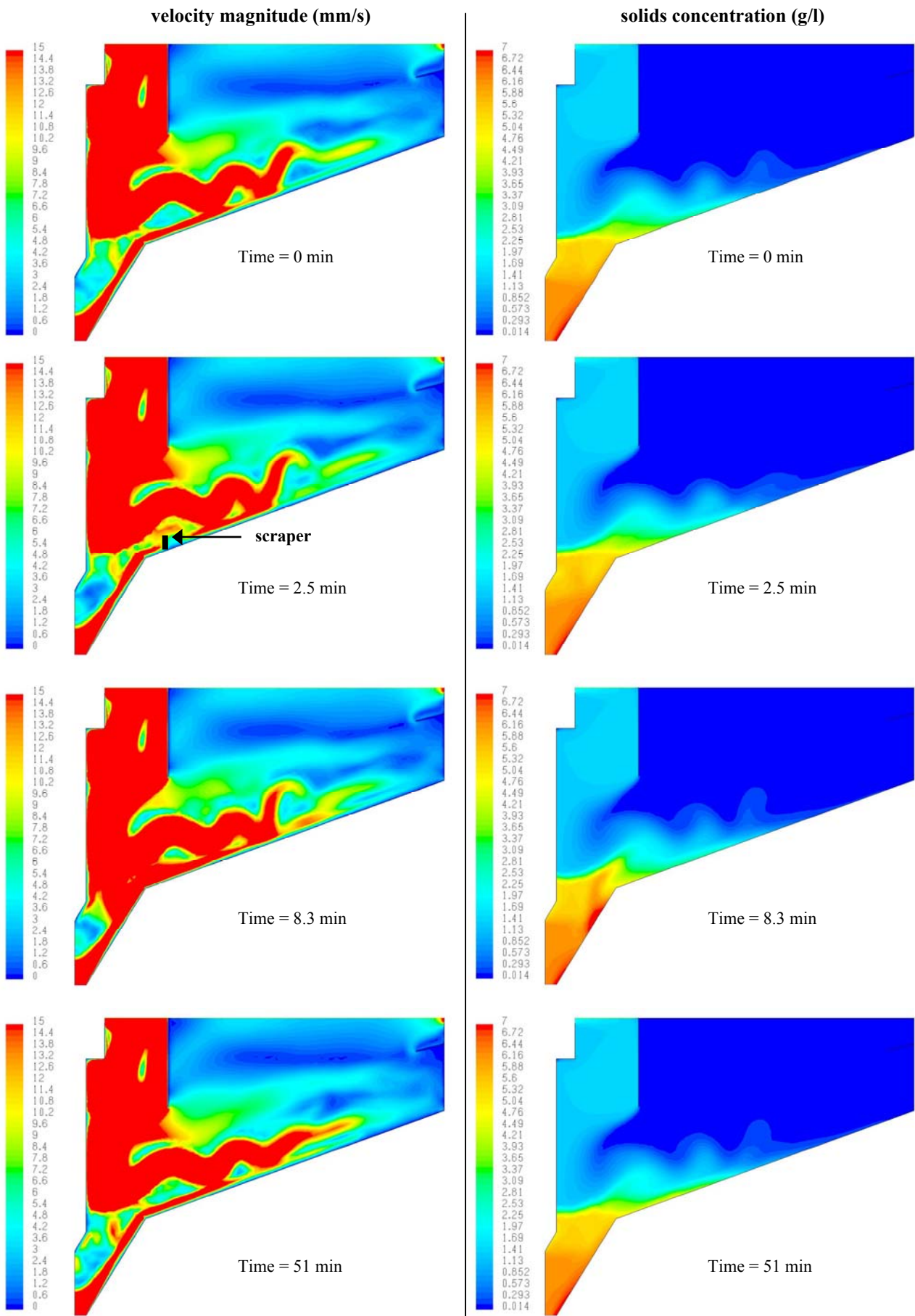


Figure 5.26 Effect of scraper on velocity magnitude (left) and solids concentration (right) profiles when applying the viscosity of water

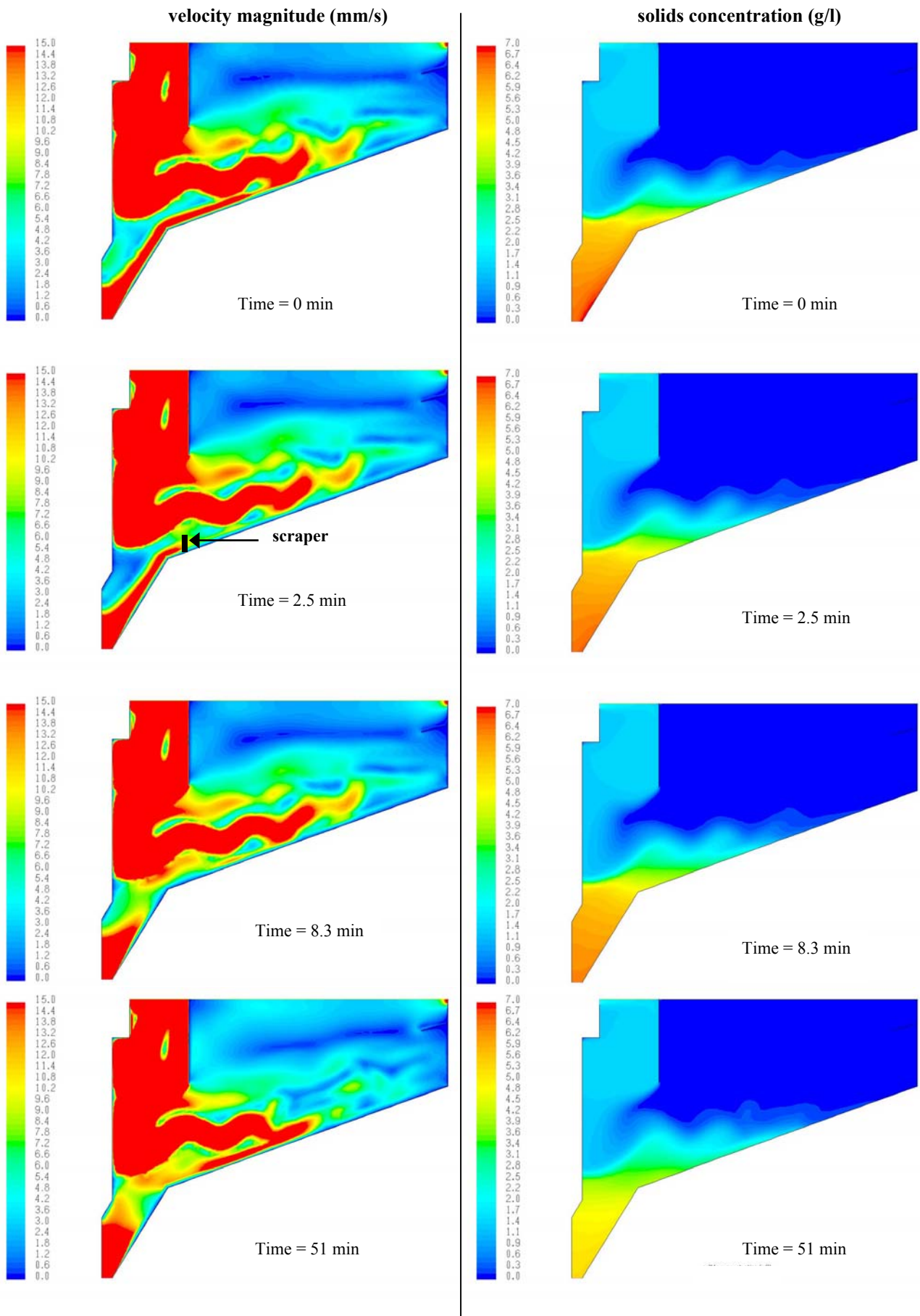


Figure 5.27 Effect of scraper on velocity magnitude (left) and solids concentration (right) profiles when applying the modified Herschel-Bulkley rheological model

blocked for 2.9 minutes of scraper passage. This is clearly seen in Figure 5.26 and Figure 5.27 for water and the modified Herschel-Bulkley rheological model respectively. The scraper blade thus constrains the bottom flow discharge by counteracting the gravitational force. Near the floor the radial velocity increases with height in the shear flow region, but is obviously limited by the scraper's velocity.

The sludge is obviously expected to gravitationally accelerate after the scraper has passed the modelled transect in the time period 0-2.9 minutes. The solids blanket height should therefore decrease again due to enhanced sludge removal. Two-dimensional simulations of the settling tank, however, show this is only the case for water viscosity (Figure 5.26). For the modified Herschel-Bulkley model the bottom flow does not recover and solids accumulate in the main settling tank volume. As clearly observed in Figure 5.27 (time = 51 minutes), the underflow flux is redistributed and consists of contributions from the entire cross-sectional area of the sump. This is shown schematically in Figure 5.28 (left). Instead, for water the strong bottom flow to the sump remains (Figure 5.28, right). A possible cause for this flow pattern discrepancy is brought forward by Huang & García (1997). They investigated the flow behaviour of Bingham-plastic mudflows and concluded that the higher the yield stress, the faster the flow decelerates on a slope. In accordance to these fundamental calculations, Figure 5.26 and Figure 5.27 allow to conclude that sludge described by the modified Herschel-Bulkley rheological model accelerates slower than sludge characterised by the viscosity of water. The flow system considered here is of course different, much more complicated than this mud system and, hence, demands for more fundamental research.

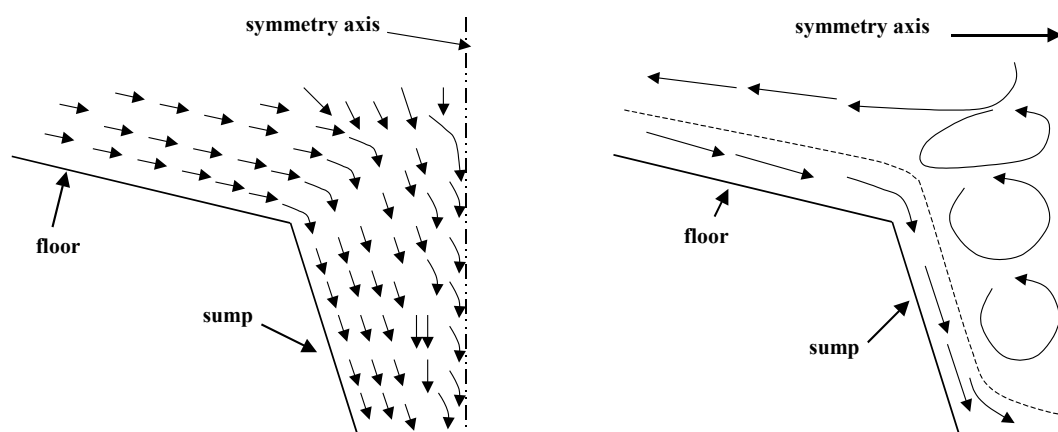


Figure 5.28 Scheme of velocity field near the sump for the modified Herschel-Bulkley rheological model (left) and water (right)

Based on the above statements, it takes more time for the modified Herschel-Bulkley sludge to recover from flow disturbances. For a circular settling tank with a scraper operating at a similar rotation speed as calculated here, Winkler (2001) observed that the scraper influences the velocity field for 12 minutes after it had passed by. Here, it took only 6 minutes for the sludge characterised by water viscosity; for the modified Herschel-Bulkley sludge the flow pattern never recovered though. Note however, that the present 2D simulations do not account for tangential velocities. In practice and shown by 3D simulations of Winkler (2001), the tangential velocity is much larger than the radial component; it might go up to 2-3 cm/s. This stirring creates large stresses avoiding the yield stress to express,

i.e. the sludge acts more as a low-viscous fluid. Clearly, only 3D modelling of settling tanks can incorporate this rheological behaviour. To support these theories, however, more fundamental research on the sludge rheology and scraper's nearby flow field is required.

Figure 5.25 clearly indicates that 2D simulations do not result in realistic solids blanket elevations. It is therefore concluded that 3D simulations and 2D simulations that account for swirl seem essential to correctly incorporate the scraper action in the CFD model. For that reason, the scraper model was not included in the validation study below.

5.3 Model validation

Up till now, the CFD model of the secondary settling tank under study has been developed and described. To investigate the accuracy of the CFD model, however, simulation results should be confronted with measurement data. Depending on which part of the model is to be validated different data sets may be used.

Firstly, the simulated solids concentrations should be validated with measured profiles. If unsteady simulations are performed, also some measurements in time should be conducted at e.g. inlet, outlet, underflow and some other measurement points located inside the settler. This will be discussed in Section 5.3.1.

Secondly, to validate velocity profiles several possibilities exist. In this respect, Section 4.4 gave an extended summary of available measurement techniques. They range from simple flow-through curves to complex *in situ* 3D velocity measurements. In this work, flow-through curves obtained from a LiCl tracer injection were utilised for validation. This is dealt with in Section 5.3.2.

5.3.1 Validation of solids concentration profiles

Because turbidity by optical backscattering (Minisonde, Hydrolab Co., Austin, USA) resulted in too large measurement errors, sludge samples were collected with a peristaltic pump (Chemaster dose pump CP-Z/100-P-DC, Dema Australia) and 6 mm ID PVC tubing. The tubing was mounted on a rigid PVC pole. Even with a maximum hydrostatic head of 6 m, the pump provided a flow rate of 300 ml/min. This enabled the 8 m-tubing to be flushed in 45 s. A 1 min-flushing prior to sampling therefore ensured correct solids concentration measurements. Preliminary experiments indicated that solids settling in the tubing did not occur. Samples of 70 ml were taken below the solids blanket and at the settling tank's inlet. Instead, 200 ml-volume samples were collected above the blanket. The latter allowed a more accurate determination of solids weight. The solids concentration was determined according Standard Methods (APHA, 1992). To quantify the measurement accuracy ten repetitions of three different concentrations have been examined on their 95% confidence interval. The samples covered the range of concentrations dealt with in practice. Hence, samples from the aeration tank, effluent and RAS flows were taken. Table 5.9 shows that the confidence interval was relatively large for low solids concentrations, i.e. above the solids blanket, probably due to the low sample volume of 150 ml. Measurements for aeration tank and RAS sludge only demanded a 10 ml sample.

Table 5.9 Error estimation on the gravimetric determination of solids concentration X

	\bar{X} (mg/l)	$sd(X)$ (mg/l)	95% confidence interval (mg/l)
effluent	13.87	1.15	[13.05 , 14.69]
aeration tank	1735	53	[1697 , 1773]
RAS	4131	132	[3044 , 4219]

Both dynamic and steady-state solids concentration profiles were investigated on Friday 19 October 2001 (see Figure 5.29). To study the dynamics, samples were taken hourly between 2 am and 1 pm at the following settling tank locations,

- inlet,
- effluent,
- RAS.

Due to the Pennstock valves at the entrance of the primary settling tanks that could only be adjusted manually, flow rates could not be maintained fixed. Therefore, "steady-state" solids concentration profiling was conducted between 1:30 pm and 7:30 pm when the most stable inlet flow rates occurred. Confrontation of measured profiles and data from the mounted acoustic solids blanket depth sensor (located at approximately 8 m from the tank's centre) revealed that the latter blanket depth corresponded to solids concentrations of between 25-65 mg/l (see Figure 5.32, left). At Oxley Creek WWTP the effluent solids concentration has to meet a one-year 80-percentile of 30 mg TSS/l. Hence, the threshold of the blanket sensor set by experience corresponds rather well with the prevailing effluent quality standard. Consequently, the solids blanket depth in time may be utilised for validation as well.

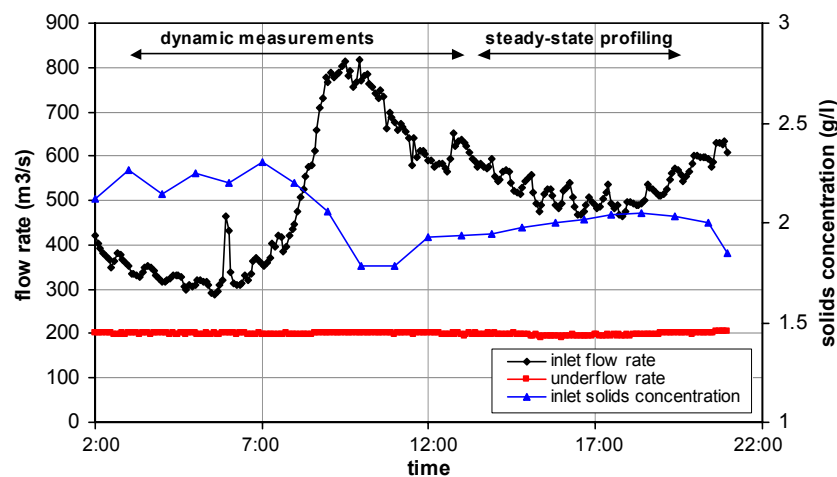


Figure 5.29 Flow rates and inlet solids concentration during dynamic and steady-state validation

The settling tank was modelled with the rheological model developed in this work (see Equation 5.4 and Table 5.5) and the Takács settling function calibrated using batch-settling tests (see Section 5.2.1). As discussed above, no scraper was incorporated in the exercise.

Simulations of a settling tank system with appropriate initial conditions were conducted. The initial state was obtained by subjecting the settling tank to a 2-day dynamic inlet solids concentration, inlet flow rate and underflow rate (see Figure 5.30). A supplementary 2-day simulation showed that identical system states were obtained after 2 and 4 days. For each validation exercise, solids concentration data were collected every 15 minutes from simulations.

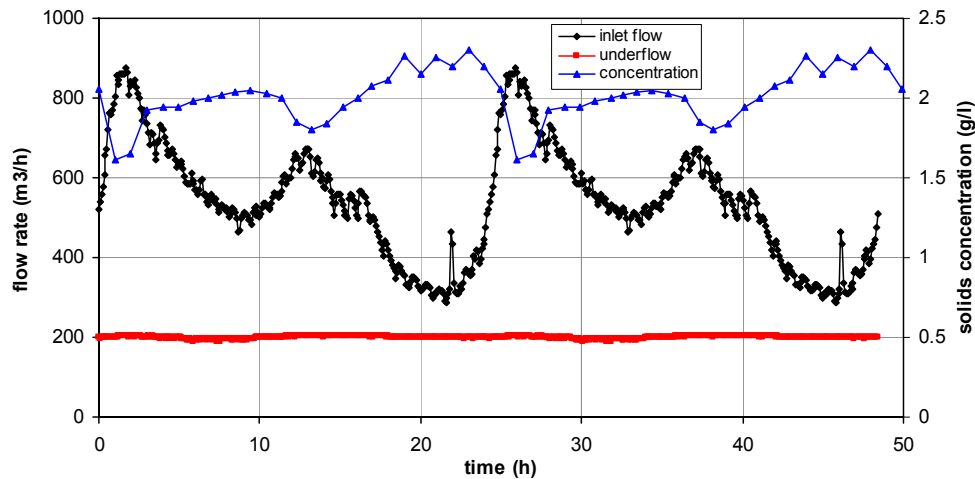


Figure 5.30 Input profiles for the 2-day pre-simulation to initialise the settling tank model

5.3.1.1 Steady-state solids concentrations

The first validation consisted of comparing simulations with pseudo-steady-state solids concentration profiles measured at 6 different radial distances, i.e. 2.6, 3, 4.7, 6.6, 8.2 and 8.9 m, all situated outside the feed well. The profiling was conducted at afternoon flow rates as depicted in Figure 5.29; these operating conditions were therefore adopted for the dynamic simulations. Simulated profiles were recorded every 15 minutes giving a range of profiles between which the measured solids concentrations should be found for successful validation. Results are shown in Figure 5.31.

Without any additional calibration, an excellent agreement is found between simulations and measurements. Only close to the bottom floor at a radial distance of 2.6 m, the simulated concentration largely deviates from the measured value. A possible cause may be a clump of solids stuck to the bottom, not being removed by the scraper, and sucked by the peristaltic pump. Badly modelled solids compression also leads to lower bottom floor concentrations. Good predictions of RAS concentration (see below), however, indicate the opposite. Figure 5.32 further shows a close-up of the profiles at 8.2 and 8.9 m. Although the simulated profile at the radial distance of 8.2 m is slightly shifted to higher concentrations, good agreement between measured and simulated solids concentrations profiles is observed.

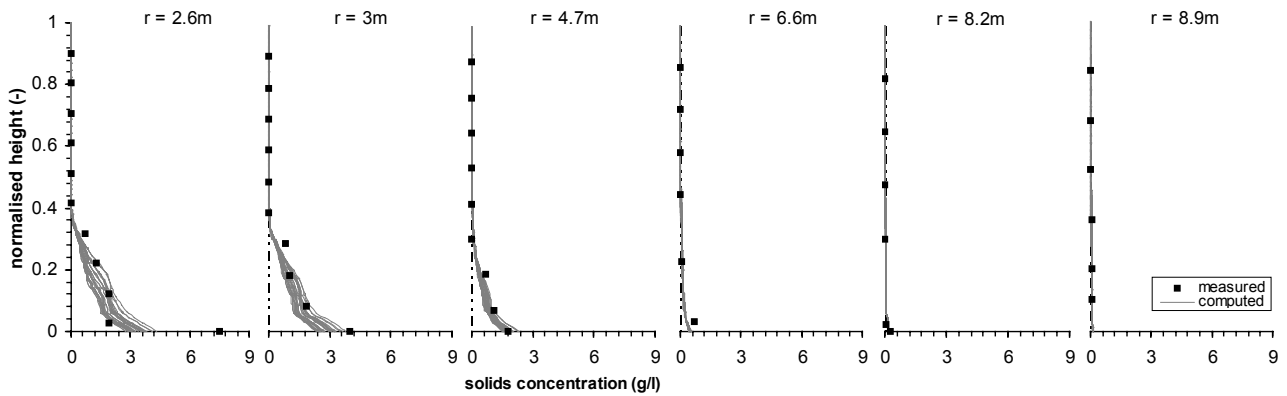


Figure 5.31 Comparison between simulated and measured solids concentration profiles. Simulated profiles were recorded every 15 minutes

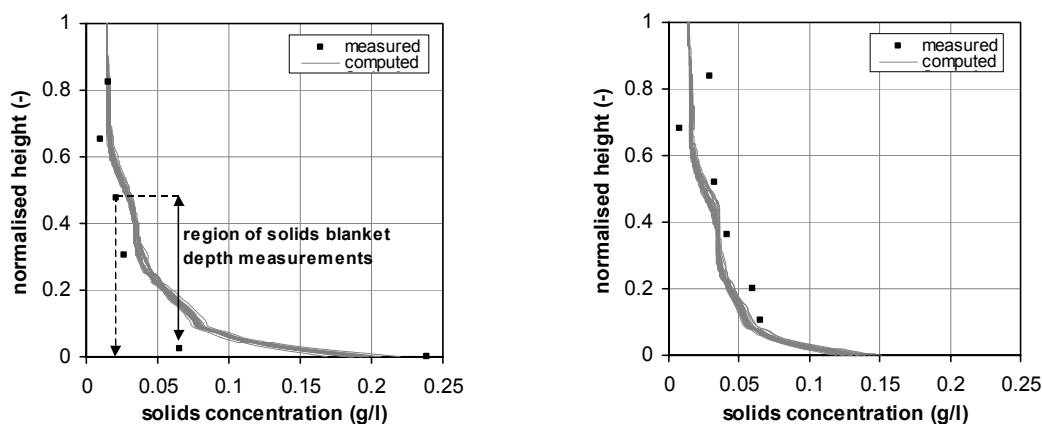


Figure 5.32 Detail of measured and simulated solids concentration profiles at 8.2 m (left) and 8.9 m (right)

5.3.1.2 Dynamic solids concentrations

The second validation focused on the solids flow dynamics by considering effluent and RAS solids concentration trajectories. The experiment basically consisted of a “step” change in inlet flow rate (see Figure 5.29). Figure 5.33 (left) shows the results. The measured underflow concentrations closely follow the simulated trend, which suggests that an additional solids compression model is not needed. Presumably, compression phenomena hardly exist because the zeolite dosed results in compact flocs. A large discrepancy is observed for the effluent solids concentration though. Till 9:00, solids concentration is constant and equals the non-settleable solids concentration of the Takács settling function X_0 , i.e. 14 mg TSS/l. This concentration was determined as the supernatant solids concentration of a batch-settling test as described in Section 5.2.1. Obviously, this solids concentration obtained corresponds to the Dispersed Suspended Solids (DSS) concentration (see Section 1.1). Whereas stagnant water characterises the batch-settling test, flows prevailing above the solids blanket may promote flocculation and, hence, discrete settling velocities would increase. As a result, the Flocculated Suspended Solids (FSS) concentration would be lower than the DSS concentration. However, the DSS/FSS test (see Section 1.1) should be performed to determine whether flocculation affects the effluent solids concentration in

the full-scale settling tank. Consequently, the non-settleable solids concentration might be much lower in the full-scale installation compared to the batch-settling test. Reducing this non-settleable concentration X_0 to 3 mg TSS/l clearly has a pronounced effect on the effluent solids concentration as shown in Figure 5.33 (right); concentrations decrease for the entire trajectory, and correspond well with the measurements. With respect to Figure 5.31, decreasing X_0 would only move the upper part of the concentration profiles to smaller solids concentrations. No change is observed for the RAS concentration since the enhanced settling at low solids concentrations only has a small impact on the entire mass balance; a negligible change in solids removal efficiency, but a major improvement in effluent suspended solids concentration, is obtained.

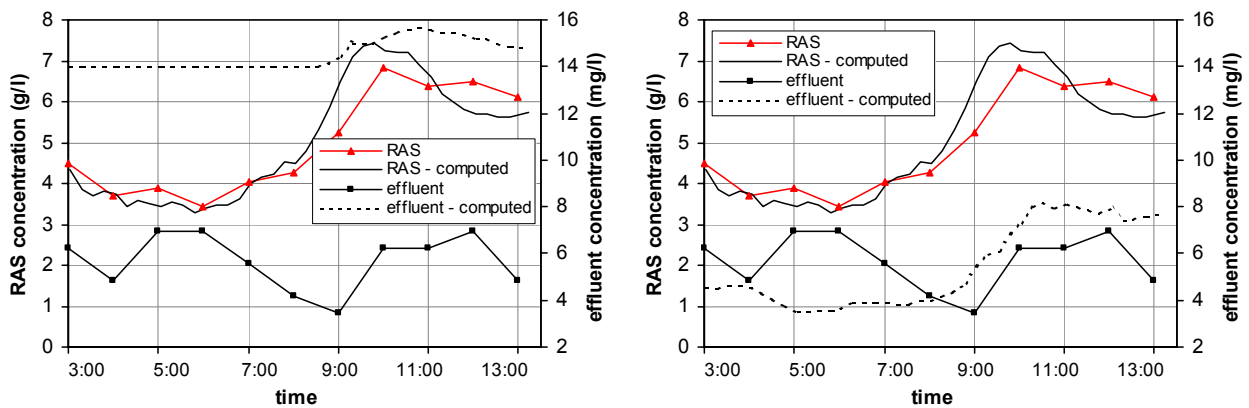


Figure 5.33 Validation of effluent and RAS solids concentration with temporally changing inlet flow rates and solids concentrations, and a non-settleable solids concentration X_0 of 14 mg/l (left) and 3 mg/l (right)

For validating solids transport, data from the solids blanket depth meter as shown in Figure 5.34 may be utilised as well. The non-settleable solids concentration of 3 mg TSS/l was adopted as it resulted in good effluent solids concentrations as demonstrated above. Whereas a blanket depth concentration threshold of 30 mg TSS/l results in too low blanket depths, the trend is well resolved. Instead, the blanket depth corresponds very well to the concentration threshold set at 70 mg TSS/l. Important is that oscillations in the solids blanket depth can be observed in the simulations as well; they correspond with oscillations in the inlet flow rate which, in turn, are caused by the operation of the pumping station located upstream. In conclusion, it can be assumed that in practise the threshold solids concentration of the blanket depth sensor was set at 70 mg TSS/l, which is close to the experimentally observed threshold of 25-65 mg TSS/l (see Figure 5.32, left).

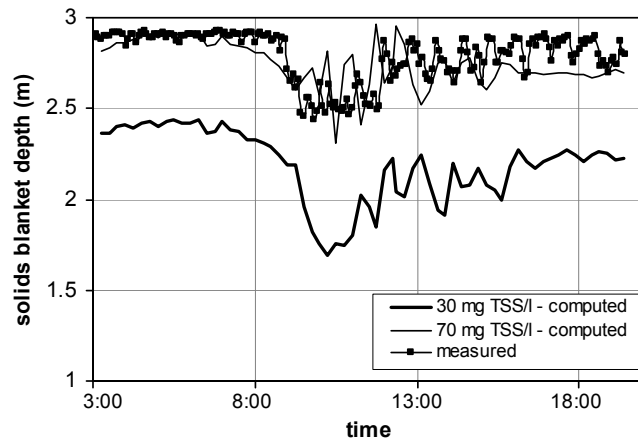


Figure 5.34 Validation of solids blanket depth data with simulated trends of concentrations of 30 and 70 mg TSS/l, and a non-settleable solids concentration of 3 mg/l

5.3.2 Validation of hydraulics

A flow-through curve or FTC (see Section 4.2) is an easy way to check the overall hydraulics of the settling tank (De Clercq *et al.*, 1998). The technique consists of introducing an inert material, i.e. a tracer, at the inlet. At different locations the tracer concentration is measured in time; in many cases, only the outlet and underflow of a settling tank are sampled. Theoretically, an infinite number of different flow fields may result in the observed FTCs. The CFD model, however, only returns a limited number of possible flow fields for specific operational conditions of the settling tank. The CFD therefore enables the differentiation between possibly correct and incorrect flow fields. Note that the more sampling positions are considered, the better the internal flow pattern will be validated and fewer proposed flow fields may lead to the observed system responses. In this respect, flows recirculating along the free water surface make it interesting to sample at the middle and near the surface of the settling tank in order to measure these flows.

Three sampling locations were adopted in the tracer test presented here. Samples were collected from the RAS, the effluent and at the surface 4 m from the centre of the settling tank (called location P(0,4)). Sampling the effluent launders was not recommended due to the time-composite character of the sample obtained. For that reason, sampling inside the settling tank, i.e. in front of the weirs, was preferred.

As tracer, lithium was dosed as the salt LiCl. All samples were stored at 4°C on-site; filtration of the samples was not performed on-site due to (i) the initial fast sampling, and (ii) lithium does not tend to adsorb onto solids. In total, 8.12 kg of LiCl was dissolved in two drums of 30 l effluent each; the exact mass added to the drums was back-calculated from lithium concentration measurements. The reason for this approach is due to the extremely hygroscopic nature of LiCl; hence, gravimetric measurement of the exact mass is difficult and inaccurate.

Similar to the experiments for solids concentration profiling, no steady inlet flow rates could be imposed. Therefore, to avoid the morning peak flow, it was decided to start the tracer

test in the early afternoon of 26 September 2001, at 12:35 am (Figure 5.35). The measurement campaign ended at 8:25 pm. This sampling period was estimated as 3-4x the theoretical residence time of 2.5 h (see Section 4.2.2 for more information). Although the evening flow peak disturbed the steadiness of flows, it impacts less than the larger morning flow peak. The underflow rate was kept rather constant at 201.6 m³/h.

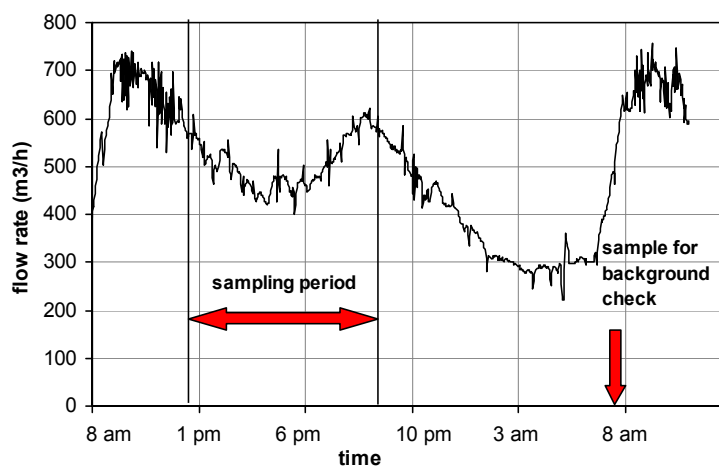


Figure 5.35 Inlet flow rate during the tracer test

Table 5.10 summarises the sampling protocols adopted for the RAS and effluent flows, and location P(0,4). The sampling frequency at P(0,4) was identical to the effluent, but with a one-minute delay. Note that not all samples were analysed for lithium; lithium analysis was performed parallel to the data analysis so that only interesting time instants were taken for lithium analysis. This allowed to save costs.

Noteworthy is that for the RAS the lithium concentration of both bulk and interstitial liquid was determined. Filtered solids were washed with acid and the lithium concentration of the filtrate was measured. The measurement protocol is given in Section 4.2.2.2. In the same section it was shown that the part of lithium associated to the filtered solids might be significant and should be considered in the data analysis as well. All samples and standards were analysed with 2000 ppm K⁺ as ionisation suppressant.

Table 5.10 Summary of sampling protocol

	Δt (min)	no. samples	elapsed time (h)
RAS	1	5	0.08
	2	10	0.42
	5	4	0.75
	10	4	1.42
	15	5	2.67
	30	12	8.67
Effluent & P(0,4)	5	20	1.67
	10	10	3.33
	15	6	4.83
	30	8	8.83

Figure 5.36 shows the results of the tracer test. The pulse responses are clearly shifted in time and the peak magnitudes also decrease as one moves from underflow to effluent to position P(0,4). The early peak for RAS indicates a short cut to the underflow and the late response at location P(0,4) is presumably due to a recirculating flow. A possible flow pattern resulting in these FTCs is given in Figure 5.37 (left); however, simulations done later in this section indicate flow patterns as depicted in Figure 5.37 (right).

Whereas the background concentration prior to the sampling measured 0.03 mg Li/l, 20 h after the tracer injection concentrations were still higher. Therefore, the sampling period may have been too short. This reasoning is also supported by the low flow rates at night (see Figure 5.35), i.e. lithium stays longer in the system due to the little dilution. Another reason for the high concentrations after 20 h may be the return of lithium-containing underflow sludge to the aeration tank and, subsequently, back to the settling tank. De Clercq *et al.* (1998) showed that, depending on the hydraulic residence time of the aeration tank, the combined system *aeration tank-secondary settling tank* may indeed lead to different FTCs as compared to the single-pass system. Whereas mixing of different flows at the entrance of both aeration tanks of stages 3 & 4 already decreases the lithium concentration with a factor 10x, the total volume of the aeration tanks ($2 \times 3850 \text{ m}^3$) further dilutes the lithium. Whether the obtained concentration is negligible should be investigated by modelling the coupled system. Finally, the lithium concentrations observed after 20 h may also originate from measurement inaccuracies. Whereas the lithium concentrations at the different sampling locations are expected to be equal at the start of the tracer test, concentration differences of almost 0.1 mg Li/l are observed. This confirms the inaccuracy of the measurements.

A successful tracer test should have a 100% lithium recovery. For this experiment, a recovery of 138% is obtained. This discrepancy in mass balance may be attributed to the different possible causes as mentioned above. Still, the trend and the time of occurrence are believed to be correct, and can be utilised for validation purposes.

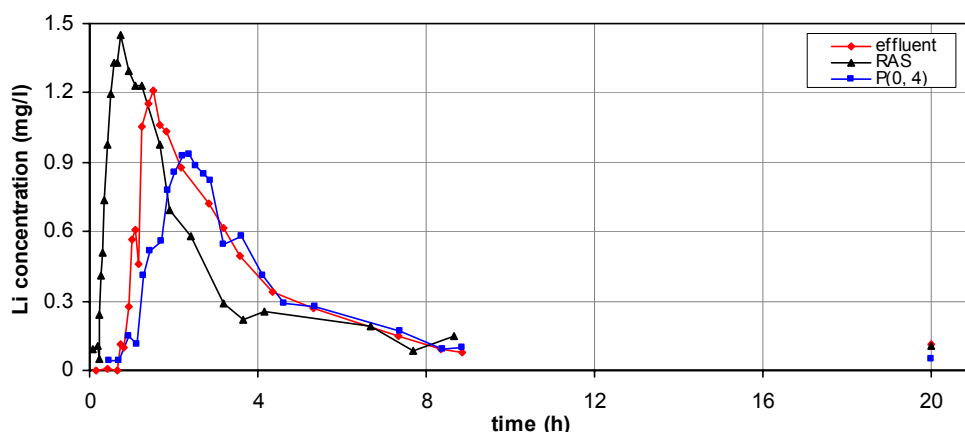


Figure 5.36 Lithium concentration measured in time for effluent, RAS and at P(0,4)

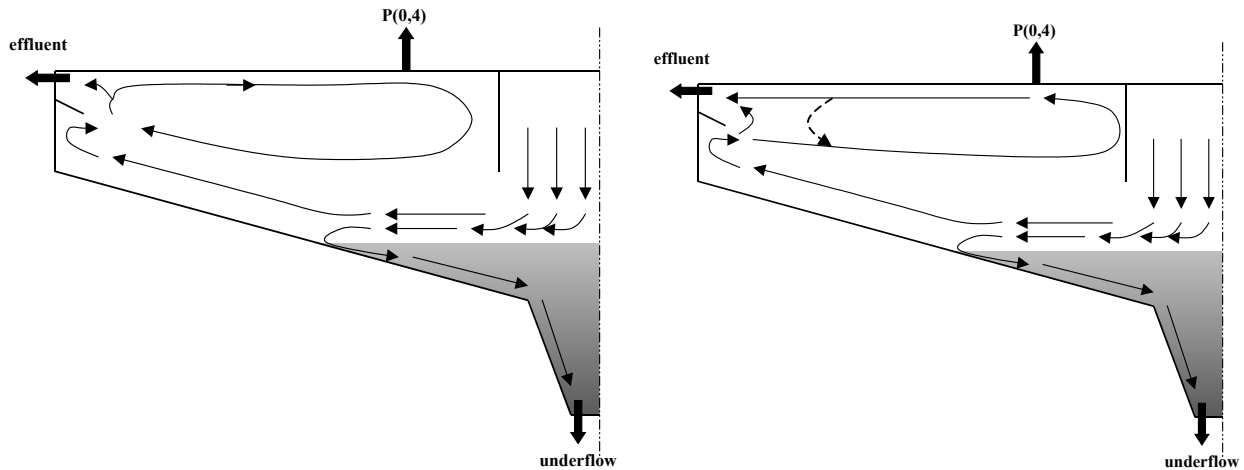


Figure 5.37 Flow pattern in the investigated settling tank: proposed from tracer test results (left) and obtained from CFD simulations (right)

In the simulation software Fluent, lithium was modelled as a scalar, and transported similarly to solids except that settling did not occur. Any introduction of tracer should also account for buoyancy effects due to temperature differences and salt concentration. Here, effluent was used at the same temperature as the influent. According to Misztal & Sangwal (1999), only negligible density changes are observed for the amount of LiCl added in the tracer test. With their data, a very conservative calculation for an inlet concentration of 4 g LiCl/l (obtained when introducing the tracer in the momentum diffuser, see further) and at 23 °C results in a bulk density increase of only 0.0026 kg/m³. Buoyancy effects from LiCl addition were therefore not included in the modelling efforts.

The tracer was introduced in the momentum diffuser in a time frame of approximately 15 s. Due to mixing in the diffuser volume, tracer dilution occurs. Because the momentum diffuser is not modelled, a correct introduction of tracer at the inlet slot should therefore consider this dilution effect. From a mass balance over the perfectly mixed momentum diffuser and a pulse as input, the system response may be analytically computed by Laplace transforms as

$$\begin{aligned}
 C_{Li} &= 2 \frac{\text{flux}(Li)}{Q} e^{-0.5 \frac{Qt}{V}} \sinh\left(0.5 \frac{Qt}{V}\right) & t < \Delta t \\
 C_{Li} &= \frac{\text{flux}(Li)}{Q} \left[-1 + e^{\frac{Q(-t+\Delta t)}{V}} + 2e^{-0.5 \frac{Qt}{V}} \sinh\left(0.5 \frac{Qt}{V}\right) \right] & t \geq \Delta t
 \end{aligned} \tag{5.7}$$

with C_{Li} , $\text{flux}(Li)$, Q , V , t , Δt being the inlet lithium concentration, the lithium mass flux, the inlet flow rate, the momentum diffuser volume, time and injection time period respectively.

Figure 5.38 shows the time evolution of the inlet tracer concentration when introducing the tracer (i) directly at the inlet slots and (ii) in the perfectly mixed momentum diffuser prior to entering the settling tank. Consideration of the diffuser volume clearly decreases the tracer concentration at the inlet. Although the injection time remains 15 s, a longer tracer release period prevails at the inlet slots; 95% of the tracer had entered the settling tank after 53 s.

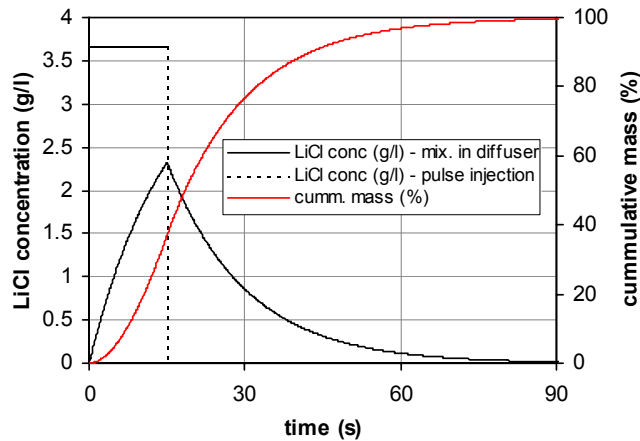


Figure 5.38 Pulse-wise injection of LiCl tracer at the inlet slot with and without consideration of momentum diffuser as mixing volume

After a pre-simulation of 2 days, the validation was preceded with a second pre-simulation period of 4.6 h; measured underflow and inlet flow rates for the validation period were considered. Because data on the inlet solids concentration were not available, it was decided to use the data from the dynamic solids concentration validation exercise (see Section 5.3.1.2). These data were accepted to be representative for the tracer test conditions because the same diurnal flow pattern occurs, and no operational changes were known. When performing the FTC simulations, the mass balance of lithium was checked and found to be conserved at all times.

Figure 5.39 (left) shows the comparison of simulated with measured FTCs at the underflow, effluent and location P(0,4). From the figure, a too fast simulated tracer response is observed at the underflow and P(0,4). Consequently, the simulated peak concentrations are too high as well. Higher concentrations are also observed for the effluent sampling location, but the peak of appearance is delayed. For both effluent and P(0,4) a small peak occurs after 1 h and can be attributed to a short cut to the sampling locations when the flow bounces off the side wall; the main flow returns to the settling tank's centre however. Although slightly present in the effluent FTC, the simulations are unable to recover this small peak.

Note that all lithium left the system after already 6-8 h depending on the sampling location. In reality, the tracer clearly stayed longer in the settling tank.

Before tackling the causes of discrepancies between measured and simulated FTCs, some remarks on the numerical methods are given. Whereas in literature (e.g. Imam *et al.*, 1988; Adams & Rodi, 1990; McCorquodale *et al.*, 1991; Samstag *et al.*, 1992; Szalai *et al.*, 1992) only steady inflow conditions are adopted, flow rates and inlet solids concentration changed during the validation exercise. Obviously, unsteady FTC validations are more difficult to be successful than steady validations (Imam *et al.*, 1983) because the (in)accuracy of the numerical time integration introduces an additional uncertainty. Further, concerning the too high peak concentrations in the simulated FTCs, Adams & Rodi (1990) encountered overshoots with the QUICK algorithm (see Section 3.2.1.5) used. The Fluent software, however, applies the new generation of QUICK schemes (Leonard & Mokhtari, 1990) that successfully

eliminate this overshooting. The mesh density may have an influence on the solutions as well. A too coarse mesh introduces numerical diffusion and leads to wider simulated peaks as measured (e.g. Szalai *et al.*, 1994). Therefore, in this study the mesh clearly does not pose problems.

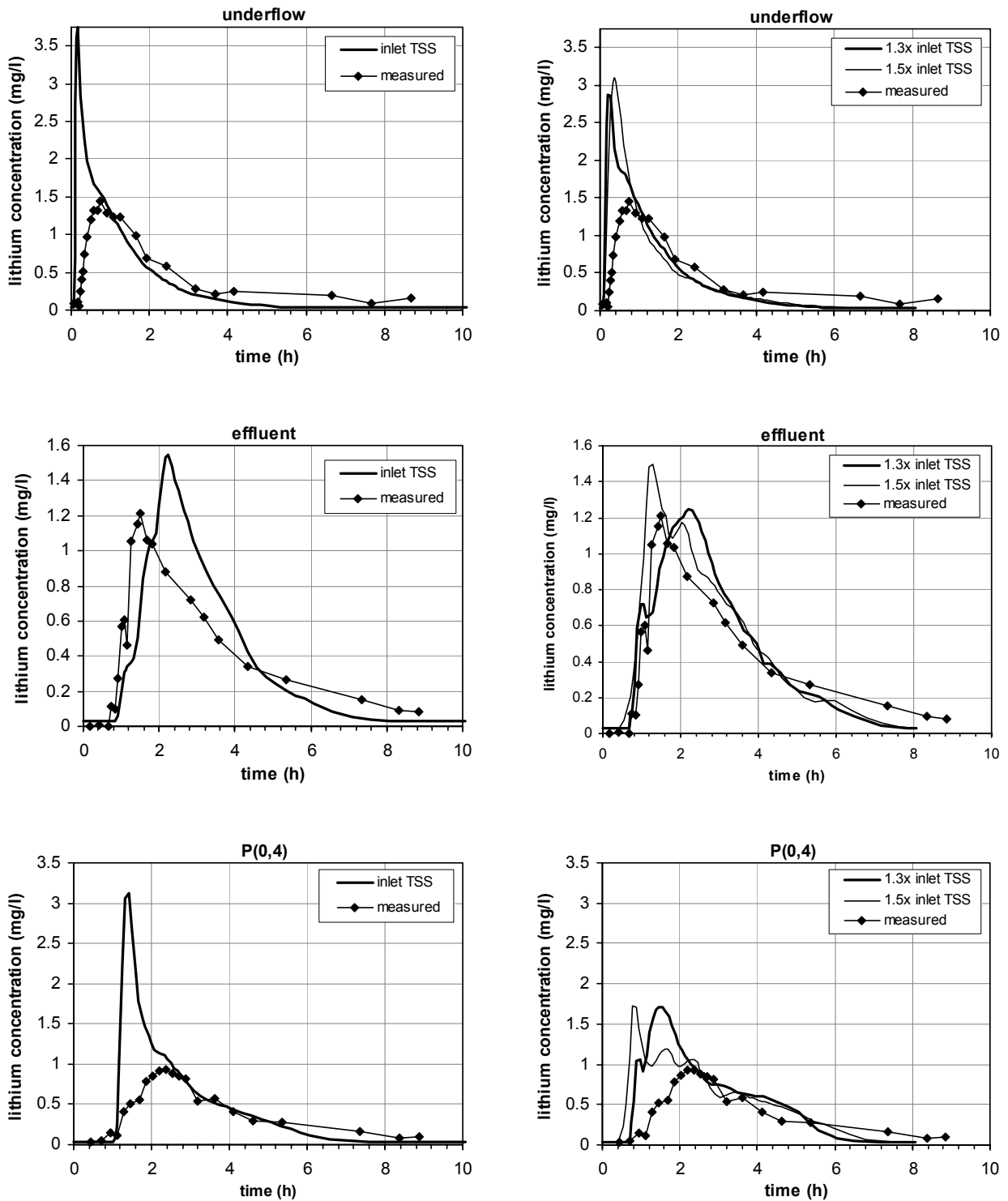


Figure 5.39 Validation of flow-through curves for underflow (top), effluent (middle) and P(0,4) (bottom). Flow-through curves for the original inlet solids concentration (left), 1.3x and 1.5x the inlet solids concentration (right) are shown

From the above, it seems more plausible that physical phenomena in the settling tank are not adequately modelled even though the solids profile validation had been successful. Two possible causes were considered, i.e.

- an improperly simulated solids blanket evolution due to incorrect boundary conditions imposed at the inlet,
- a too small diffusion is modelled.

Firstly, a flow field should prevail that enables a faster system response at the effluent than at location P(0,4). The flow patterns simulated and prevailing in reality were already shown in Figure 5.37. In this respect, a higher solids blanket might alter the flow field. A solids blanket height evolution different from the previous simulation case could be due to (i) an incorrect boundary condition for solids concentration at the inlet, or (ii) different settling parameters. The settling properties were not expected to have changed though; they were dominated by the zeolite and not by any biological effects. As mentioned before, inlet solids concentration data were not available and, hence, were taken from the dynamic solids concentration validation exercise (see Section 5.3.1.2). Although typical values for the WWTP, the solids concentration prevailing at the time of the tracer test might have been different. In that respect, two higher inlet solids concentrations were investigated in terms of their impact on the FTC. Identical flow rates were maintained, but the dynamic inlet concentrations were taken as 1.3x and 1.5x the original values. Figure 5.40 (left) obviously shows that the solids blanket height and the local solids concentration increase when more solids enter the tank. This increase in blanket height, however, does not lead to a weaker density current (see Figure 5.40, right) as would be expected from the reduced conversion of potential to kinetic energy when the inlet flow plunges down to the bottom. Instead, the opposite occurs. Note that the stronger the stratification of solids concentration at the blanket interface, the more the density current stays on top of it and the shallower it becomes. In this respect, the original inlet solids concentration leads to a blanket of comparable concentration and, thus, leads to a blanket-penetrating density current. This is not the case for higher inlet concentrations, i.e. strong density differences prevent the density current to penetrate the blanket and to spread over a large area. As a result, the velocity of the current remains high.

As seen in Figure 5.39 (right), the stronger density current with increasing inlet solids concentration results in faster tracer transport to the effluent weirs and P(0,4). Clearly, the stronger the density current, the more the peak after 1 h is pronounced, i.e. the short cut originating from the flow bouncing off the side wall becomes stronger (see Figure 5.37, right). Consequently, more tracer is observed in the effluent and P(0,4) samples. Figure 5.39 (right) also shows that simulations at the 1.3x inlet solids concentration correctly return this small initial FTC peak. Although delayed, the main peak (after 1 h 30 min) and its width are well predicted too. These good predictions cannot be found at location P(0,4). The oscillatory FTC at P(0,4) at high inlet concentrations is clearly due to a (partially) trapped recirculating flow (see dotted line in Figure 5.37 (right)) above the blanket, and originates from a strong density current and a reduced supernatant volume. Increasing the inlet solids concentration does not result in a later system response at P(0,4).

The delay of tracer at the underflow with increasing blanket heights is due to the smaller flow velocities along the bottom floor as indicated in Figure 5.40 (right). Apparently, the

lower velocities near the floor overcompensate the quicker tracer transport by the density current (see Figure 5.37). Obviously, increasing the inlet TSS does not improve the simulated FTCs considerably. Other causes for the discrepancies between measured and simulated FTCs should be looked for.

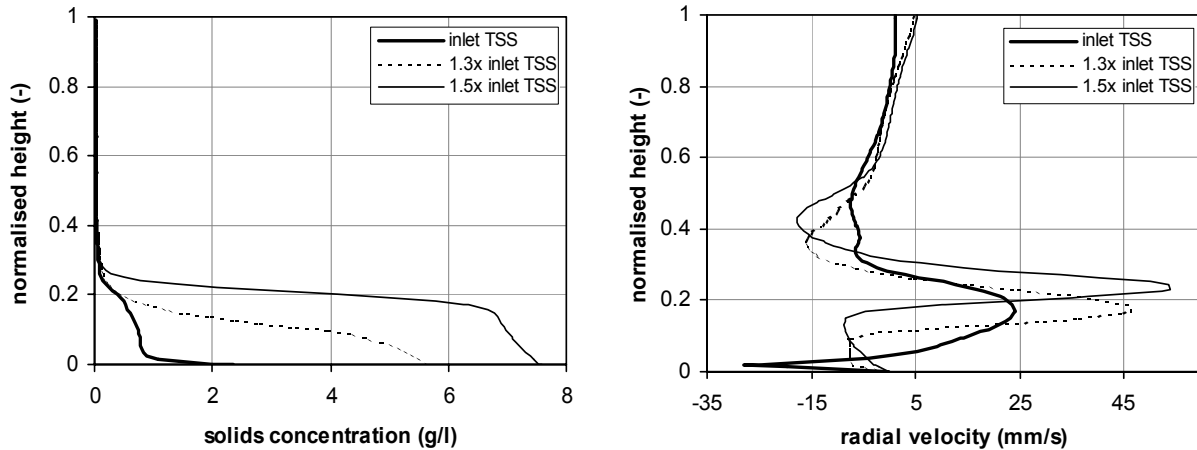


Figure 5.40 Solids concentration (left) and radial velocity (right) profiles at 4 m from the tank's centre after pre-simulation

Secondly, the too fast tracer response may be attributed to a too little simulated diffusion (see also Celik *et al.*, 1985). More viscous and turbulent diffusion obviously would decrease the strength of the density current. In this respect, Imam *et al.* (1983) pointed out that errors in diffusion rate may significantly alter the FTC. However, preliminary simulations with different Schmidt numbers did not reveal much improvement in predicted FTCs. In this respect, more research should be conducted on the proper choice of turbulence models for settling tanks (e.g. low-Reynolds $k-\varepsilon$ and Reynolds-stress models). Idealisation errors may further introduce discrepancies between simulated and measured FTCs (Imam *et al.*, 1983; Stamou *et al.*, 1989). According to Celik *et al.* (1985), uniform inlet velocity profiles do not represent very well the inflow jet characteristics and may influence the FTC. Further, geometric simplifications of the inlet structure with deflector vanes, e.g. a single horizontal inlet slot, can have consequences on the energy dissipation and, consequently, on the density current strength as well. In this respect, Szalai *et al.* (1994) considered tangential flows in their computations to account for swirls originating from deflector vanes at the inlet. Their simulations clearly showed that swirls both delay and decrease the tracer peak.

Therefore, future 2D simulations that account for swirl, 3D simulations and a proper turbulence model are believed to resolve the FTC validation problems. Additional measurements of solids concentrations and settling properties should eliminate the uncertainty on the solids blanket elevation.

5.4 Conclusions

This chapter dealt with the setup and evaluation of a CFD model in the commercial software Fluent (Fluent Inc., UK) for a secondary settling tank at Oxley Creek WWTP (Oxley, Australia). The transport of the slurry in the tank was modelled by means of the Navier-

Stokes equations, supplemented with the $k-\varepsilon$ turbulence model. To describe the important process of sedimentation, an experimentally determined solids settling velocity relation was incorporated in an additional solids transport equation. The model was further calibrated with a rheological submodel as set up in Chapter 7.

To limit computational power requirements, the circular settling tank was modelled in 2D. For similar reasons, the inlet pipe was omitted from the computational domain. A geometric simplification of the inlet structure further decreased the needed computation time. The domain finally obtained was meshed with triangular control cells. An improperly meshed domain is known to influence the solution field and, therefore, different mesh sizes were investigated. For the flow field considered, the selected size resulted in 11516 cells and was a trade-off between numerical accuracy and computation time. Other flows, however, demanded a mesh size of around 16000 cells to avoid numerical instabilities.

In practice, solids removal may largely depend on the removal mechanism. In this respect, the studied settling tank operated with a scraper mechanism, and it therefore seemed essential to properly model the scraper. However, solids mixing and/or conveyance by the scraper are by definition 3D phenomena making a 2D modelling approach hard to realise. To account for the scraper effect in the model, its force exerted on the solids was decomposed. Only the radial component was considered due to the 2D modelling approach. The temporally and spatially varying radial scraper's force obtained was implemented in Fluent as a momentum source. Although the analytically computed 2D scraper velocities corresponded well with 3D measurements and modelling results found in literature, the scraper modelled in this way was found to be detrimental for the tank's operation. Due to the flow obstruction near the bottom floor caused by the scraper's velocity being lower than the (local) free flow, the scraper made the blanket rise; this did not correspond to reality though. Note that such blanket rises were not observed for sludges with a rheology of Newtonian fluids. This had to do with the higher flow acceleration of a Newtonian fluid compared to a Herschel-Bulkley fluid, which made the passage of the scraper in the section only temporally affect the flow. In reality however, the yield stress will not be expressed because shear is a 3D phenomenon with a large tangential component, not considered in the 2D model. Although not applied in this research, 2D models that account for swirl exist and return also the tangential velocity. For the validation exercise, the scraper was therefore not taken into consideration.

Finally, the simulated solids concentration and velocity fields were confronted with measurements in order to evaluate the model's prediction power.

Pseudo-steady-state solids concentration profiles corresponded well with measurements. With varying inlet flow rates, the predictions of underflow and effluent concentrations were good as well. Only the non-settleable solids concentration in the Takács settling function had to be lowered to better predict effluent concentrations. Because the supernatant of a batch-settling test can be considered as a DSS sample, orthokinetic flocculation possibly occurring in the settling tank would result in a FSS concentration being lower than the DSS concentration. Consequently, when considering flocculation in the settling tank a decrease of the non-settleable solids concentration is acceptable. Also solids blanket depths could be well predicted with a blanket depth solids concentration threshold set at 70 mg TSS/l. In conclusion, geometric info, proper inlet conditions, settling characteristics from batch-

settling test, and sludge rheology obtained from dedicated tests may result in a CFD model able to predict the system almost exactly provided a proper non-settleable solids concentration measurement can be performed.

In this modelling exercise, flow-through curves under dynamic inflow conditions differentiated between possibly correct and incorrect flow fields and, consequently, allowed to validate the flow field. As tracer, LiCl was utilised and injected as a pulse at the surface of the momentum diffuser. Measurements were conducted at three locations, i.e. underflow, effluent and at the water surface midway the bridge (called location P(0,4)). Although simulated flow-through curves showed features similar to the measured ones, the system's response was too fast at both the underflow and P(0,4); consequently, lithium concentrations were too high as well. Due to some uncertainty on the inlet solids concentration, other concentrations were imposed at the inlet boundary, but they failed to simultaneously delay the tracer peak of occurrence at P(0,4), and fasten the response at the effluent location. For better validations though, simulations should be conducted with 2D models accounting for swirl or models including 3D geometries. Turbulence should require more attention as well.

Whereas the predictive power of the CFD model still can be improved with respect to the velocity field, the solids distribution in the settling tank seems to be well modelled. This contradiction may be attributed to the large solids settling flux, resulting from the zeolite dosing. In conclusion, future 2D simulations that account for swirl, 3D simulations and a proper turbulence model are believed to resolve the FTC validation problems. Due to the important interactions in settling tanks between solids concentration and flow field, one should not forget to perform additional measurements of solids concentrations.

6 Particle Sizing in Secondary Settling Tanks

Solids transport in settling tanks depends on both hydrodynamics and floc properties. At high solids concentrations it is believed that hindered settling rates are independent of the individual particle characteristics. Above the solids blanket, however, low concentrations prevail and discrete settling occurs. Hence, floc sizes are of crucial importance; indeed, the smaller the flocs, the slower they settle. Floc porosity complicates this situation if porous flocs permit internal flows resulting in reduced drag forces and, as a consequence, in higher settling rates.

To properly model solids transport in the settling tank it is clear that Particle Size Distributions (PSD) should be considered. By the variability of the PSD, both in space and time, the influence of structural changes to the settling tank on the solids removal efficiency can be investigated. Existing structures also may be investigated with respect to their efficiency; as an example, the flocculator well can be mentioned.

This chapter investigates the spatial and temporal evolution of PSDs in settling tanks. Size distributions were measured in full-scale by means of the optimised FBRM technique described in Section 4.5.3. From the experimental results, the function of the flocculator well is discussed. The necessity of PSD modelling is dealt with as well.

6.1 *Experimental layout*

This study focused on a settling tank at the Oxley (Australia) WWTP, discussed in Chapter 5. Since most variability in PSD is expected around the flocculator, research was focused here. The Lasentec FBRM M500 (Lasentec, Redmond, Washington, USA) was deployed from the rotating bridge. To protect the probe, it was lowered in a PVC tube with a seal at the bottom to make it waterproof (Figure 6.1). For the applied focal point positions, see Section 4.5.3.3. PSD measurements were conducted under both constant and dynamic inlet flow conditions.



Figure 6.1 Experimental layout for *in situ* particle sizing

6.2 Results and discussion

6.2.1 In situ steady-state PSD profiling

PSD profiling was performed by sampling at different locations around the flocculator. Measurements were performed at afternoon inlet flow rates ($0.147 \pm 0.012 \text{ m}^3/\text{s}$), which were the most stable that could be obtained. The flow dynamics of both underflow and inlet are shown in Figure 6.2. Solids blanket depth measurements confirmed that the blanket was stable in the afternoon. Both solids blanket depth and inlet flow rates were characterised by some oscillatory behaviour, caused by the pumping station located upstream.

Inside the flocculator five PSDs were recorded at increasing depths. Measurements outside the well and at different depths were performed as well. The necessary measurement duration was determined by the total number of chord counts in order to obtain a statistically representative PSD. Hence, all locations were sampled over a 10-minute interval, except for the four upper locations outside the flocculator. There, 30 minutes of sampling and a different focal point position were applied. These measurement periods were checked in preliminary experiments; the total number of counts satisfactorily ranged between 400000 and 4000000.

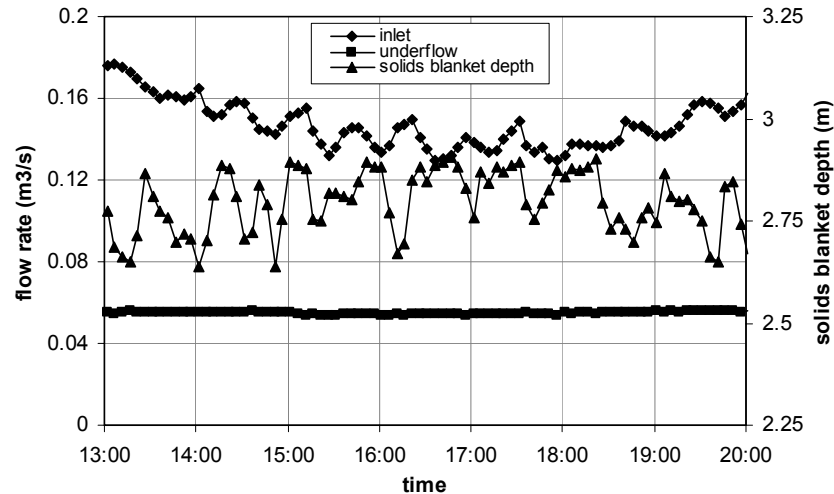


Figure 6.2 Flow rates and solids blanket depth during the steady-state profiling

Figure 6.3 shows the PSD measurements inside and outside the flocculator. All PSDs obtained at high solids concentration were very similar; hence they are grouped and represented by a single representative PSD in Figure 6.3. It is clear that the number distribution shows a slight tri-modal shape. Instead, the corresponding volume distribution looks Gaussian.

With the FBRM the raw data consists of the number distribution. From this the volume distribution was calculated. As long as no particles stick on the sapphire window smooth number distributions are obtained. However, those interferences are difficult to avoid. Neumann & Howes (2002) encountered similar problems in lab-scale experiments as well. Further, accidental measurements of large particle chords may lead to peaks in the volume distribution due to their corresponding large volume. For these reasons, the volume distributions look spikier than the number distributions. Even after filtering, peaks in the number distributions still occur leading to considerable gradients in frequency. If located in the higher chord length range, they may induce spiky behaviour of some volume distributions in Figure 6.3. It should be mentioned that the FBRM probe was employed with the F-electronics, i.e. the instrument is more sensitive to floc structure (see Section 4.5.3). Because flocs are highly irregularly shaped, spiky behaviour can be expected then.

Compared to the distributions collected at high concentrations it is clear that at low concentration both the number and volume distributions are shifted to the lower chord length range. For the most upper measurement location and next to the well this feature is most obvious (Figure 6.3). A strong peak exists at small chord lengths indicating that at these locations large flocs have been removed by gravity. Indeed, due to the low local shear/velocity large flocs are able to settle. Instead, small ones remain more in suspension due to local turbulence.

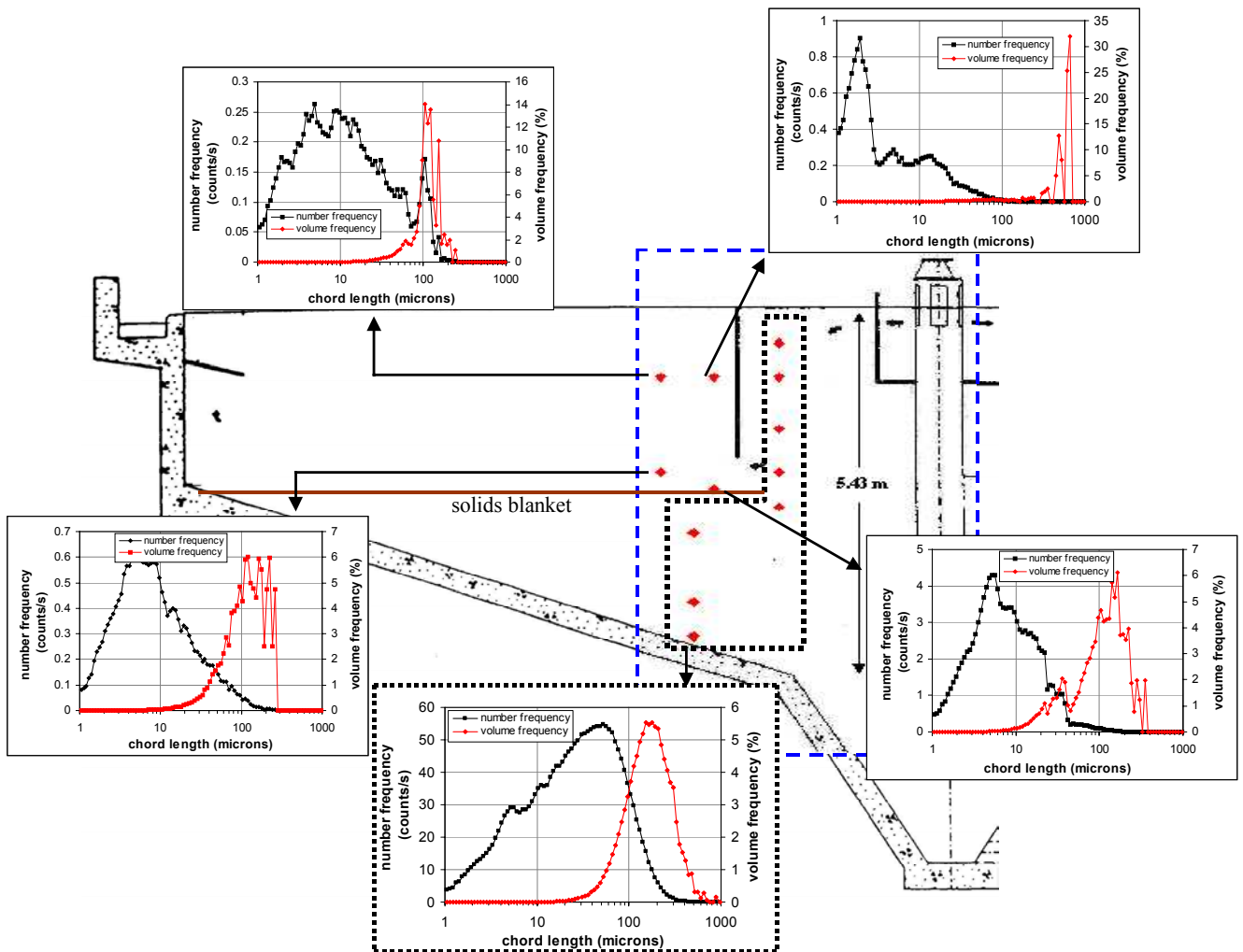


Figure 6.3 Measured PSDs at pseudo-constant inflow rates; both number and volume frequency distributions are given. The diamond symbols indicate the sampling locations in the settling tank. The dotted line delineates the region with identical PSDs.

The apparently invariable PSD inside the flocculator questions its role in terms of flocculation. However, conclusive comments on the flocculator's purpose demand for more samples near the momentum diffuser. For this case study, two parallel hypotheses can be put forward explaining the invariability of the PSD in the flocculator.

Firstly, zeolite on which microorganisms grow was dosed to improve the solids settling properties. It may therefore be hypothesised that strong flocs exist with a mineral core, which minimises floc breakup. Presumably, not much variation in PSD dynamics may thus be observed during the floc's transport from aeration basin to settling tank. Under this hypothesis, large biofouled zeolite particles do not tend to aggregate any more after arrival in the flocculator.

Secondly, it may be assumed that the majority of the flocs are not formed inside the well, but inside and close to the momentum diffuser. Of course, floc aggregation would prevail right outside the diffuser too. Wahlberg *et al.* (1994) determined that most aggregation occurs within 2 minutes, whereas 99% of the floc aggregation is completed after 10 minutes. These high rates are in accordance with the present observations. Since the residence time of the momentum diffuser is only 5.1 s, not much flocculation would be expected there.

However, deflector vanes enhance tangential fluid movement outside the diffuser. As a consequence, flocs travel a larger distance before reaching the sample location. It is therefore believed that most flocculation occurs close to the diffuser due to this prolonged trajectory. As will be thoroughly discussed in Chapter 7, fast floc aggregation also prevails because of the combination of both high solids concentration and moderate shear rates. According to Spicer & Pratsinis (1996) and simulations in Chapter 5, shear rates in flocculator wells vary between 10 and 40 s⁻¹. Whether aggregation occurs inside the inlet pipe depends on the flocculation state of sludge in the aeration basin. There, high shear rates and stresses prevail (see Figure 1.3) and, hence, lower stresses in the inlet pipe would favour aggregation. In this respect, Chapter 7 provides rheological experiments where sludge samples are subjected to shear stresses comparable to the wall stress in pipes. They indicated considerable destruction of the floc's structure. In this experiment however, the initial PSD obtained after settling is difficult to compare to the PSD observed in aeration tanks. This makes an extrapolation of experimental results to the situation of the inlet pipe difficult. More research is needed to clarify the issue whether flocculation in the inlet pipe occurs or not.

Although the floc aggregation capacity of the studied flocculator might be overestimated, the well is still important to cut short-circuit flows between inlet and outlet. If the well is properly designed, it also might serve to prevent damaging density currents (Parker *et al.*, 2001).

6.2.2 In situ dynamic PSD profiling

In this research the effect of time-varying inlet flow rates on the PSD has also been investigated. For this experiment the measurement location was situated just outside the flocculator well, approximately 20 cm above the solids blanket. It was assumed that shear dominated in this region and that a possible blanket rise could be observed in the PSD measurements. Figure 6.4 shows the temporal evolution of the PSDs with the varying flow rate. Every measurement covers 30 minutes of (particle) counting with the FBRM probe. Again, the raw data are the number distributions and the volume distributions deduced from them. In general, similar remarks as for steady-state profiling can be made. In Figure 6.4, note that at 4:30 am a large particle slowly crossed the window resulting in a smooth peak covering the size range 200-600 μm . The PSDs shown required filtering to eliminate peak counts with sharp gradients; particles sticking to the window occurred because of the low flow velocities at the measurement location. It also seems that the rotation of the bridge was not enough to generate sufficient flow around the probe to remove particles from the window. However, in the future such problem can be limited by choosing a proper probe position relative to the flow direction. Actually, the vertical position of the probe in this measurement campaign should be abandoned and a horizontal position preferred. Indeed, particles settle perpendicular to the laser beam. More particles will be scanned and the chance of particles sticking to the window will be reduced.

A shift in chord length with flow rate can be observed for both number and volume distributions. When the inlet flow rate increases in the morning, the mean of the volume distribution increases too. The same can be observed for the number distribution, where higher frequencies are observed for chord lengths larger than 100 μm . Moreover, the total

number frequency is related to the magnitude of the inlet flow rate. When the flow rate increases, more particles are scanned and the number frequencies increase. Due to the higher prevailing flow velocities, more particles are washed out of the solids blanket or are scoured from the blanket interface. However, the most plausible explanation of the increased number of particles scanned is a rise of the solids blanket. From Figure 6.4 the blanket interface clearly reaches the location of the FBRM around 9 pm. From this time on, the PSDs show higher frequencies for chord lengths larger than 100 μm ; obviously, this shift is related to the solids blanket rise. Comparison between Figure 6.3 and Figure 6.4 reveals that PSD measurements near the blanket interface closely correspond.

6.3 Implications to settling tank modelling

Particle size distributions have been measured *in situ* in a secondary settling tank. Significant particle size dynamics can be clearly observed. Hence, the question arises whether these dynamics should be included in a numerical settling tank model since the modelling of PSDs alone demands considerably computational power (Ramkrishna, 2000; Nopens & Vanrolleghem, 2003).

From the 2D numerical simulations in Chapter 5, the highest shear rates observed, up to 25 s^{-1} , occur near the inlet of the settling tank. Inside the blanket shears go down further. Of course, due to the 2D approximation of the flow problem, it may be expected that the magnitude of shear near the inlet structure is higher in practice. Inside the blanket, on the other hand, shears have been measured to go down well below 1 s^{-1} (Kinnear and Deines, 2001). Such low shears therefore lower the floc breakup rate and result in large flocs. Possible causes for the invariable PSDs observed in the solids blanket may be twofold: (i) a zeolite core strengthening the floc structure and, (ii) the high solids concentration. The higher the solids concentration, the higher the floc aggregation rate is. Floc breakup is therefore virtually non-existent, and both zeolite and solids concentration dominate the PSD dynamics.

Above the blanket, more dynamics could be observed. Whether those temporal changes were due to floc washout or blanket scouring could not be concluded. More research about transient behaviour of the top blanket layers therefore seems to be needed.

From a modelling point of view, PSDs appear only interesting to be modelled above the solids blanket where concentrations are low and dynamics are expected to be relevant. There, population balance modelling could improve the calculation of the discrete settling velocity as opposed to the very heuristic calibration of the parameter r_p in the Takács settling velocity function (see Section 5.2.1). In this respect, Lyn *et al.* (1992) included the aggregation dynamics in a settling tank in order to compute discrete settling velocities; floc breakup was neglected in their research however. At least for their conditions, the effects of orthokinetic aggregation were negligible. Even in the inlet region where the energy dissipation is high, differences between predicted solids concentrations including and excluding aggregation were at most 1%. Therefore, only small improvements in removal efficiency were observed. Lyn *et al.* (1992) attributed this to at least two major causes that reduce the effect of aggregation, i.e. (i) the small concentrations involved (80 mg TSS/l at the inlet), and (ii) the very restricted region where large values of energy dissipation prevail.

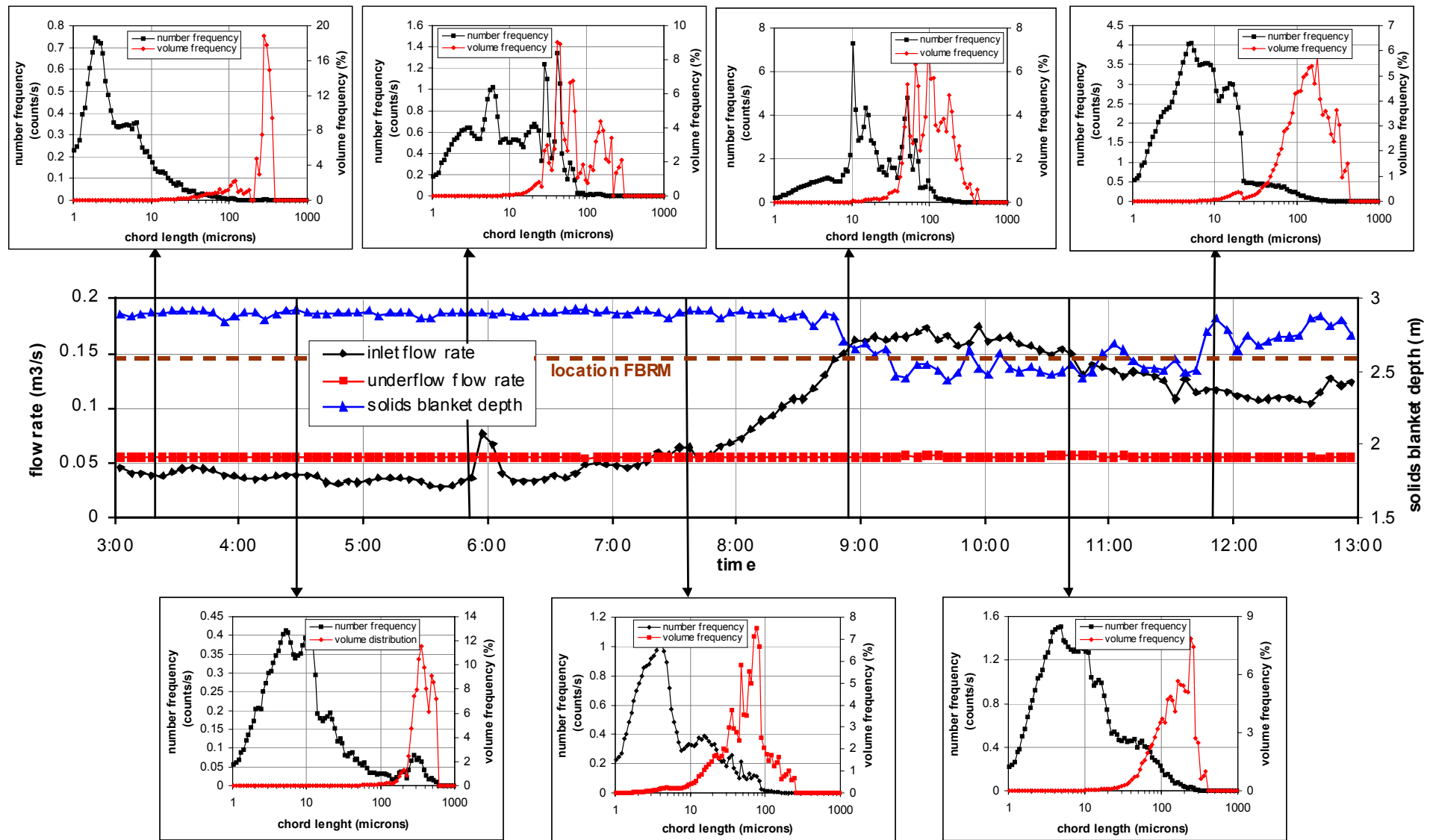


Figure 6.4 Measured PSDs at variable inflow rate (sampling at the outer wall of the flocculator, right above the solids blanket)

From their simulations, they concluded that orthokinetic floc aggregation only plays a minor role in settling tanks. Differential sedimentation was not included either, although this might play a more significant role. Although the secondary settling tank at Oxley Creek WWTP operates at much higher solids concentrations, a similar conclusion can be drawn, i.e. no significant dynamics were observed. However, for this system zeolite was dosed to improve the settling properties of the flocs. It could be that non-conditioned sludge behaves differently in terms of aggregation dynamics. In conclusion, more research is needed.

6.4 Conclusions

This chapter discussed the *in situ* measurement of particle sizes in secondary settling tanks. The sizing technique used was the FBRM technique. Although many improvements in experimental layout were identified, some interesting observations could be made.

Surprisingly, there were not many PSD dynamics in the settling tank. Also the flocculator did not show any variation in PSD, although it is built with the purpose of enhancing flocculation. Different hypotheses may be put forward to explain this:

- the zeolite dosed strengthens the floc structure making the zeolite-biomass composite flocs unsusceptible to breakup. Because of their already large size, the composite particles are believed not to aggregate anymore. As a result, identical PSDs are observed in the flocculator.
- the solids concentration plays an important role, i.e. the higher the concentration, the more flocculation is enhanced.
- the inlet tubing and momentum diffuser are believed to be crucial for floc aggregation. Whether floc aggregation prevails in the tubing depends on the flocculation state of sludge in the aeration basin.

Above the solids blanket, PSDs clearly consist of smaller particles due to sedimentation of large particles. More PSD dynamics could be observed as well, as floc washout or blanket scouring occurred at varying inlet flow rates. Here, modelling the floc aggregation and breakup could be interesting. The above conclusions, however, must be treated with care since zeolite was used to condition the sludge. Therefore, more research should be performed on typical wastewater treatment sludges in order to draw more general conclusions.

7 Sludge Rheology in Secondary Settling Tanks

This chapter deals with viscosity modelling. Viscous stresses are very important in the transport of momentum and, hence, they can alter the velocity field. As a result, solids transport will be affected as well. In this respect, Lakehal *et al.* (1999) showed the impact of different yield stress magnitudes on the solids blanket height and velocity field. Increased yield stresses prevented solids transport along the bottom floor.

Here, the state-of-the-art modelling of viscosity as performed in settling tanks is discussed and criticised. Firstly, experimental results will demonstrate that sludge rheology is very hard to measure and model. Although many simplifications have typically been made in practice, future model adaptations will have to reveal the true impact of the complex rheological sludge behaviour as discussed below. Secondly, the implementation of viscosity models with yield stress inherently results in numerical inconsistencies. As will be shown, solutions to this problem have been proposed in other research fields. Although the corrections are made for numerical reasons, their physical acceptance will be demonstrated by means of experimental work. Finally, a comparison between different rheological models is made indicating their intrinsic effects on the solution field of a 2D settling tank model. The selection of investigated models was based on a literature survey.

7.1 On the complexity of sludge rheology

7.1.1 Properties affecting experimental layout

In Chapter 2 it was discussed that many researchers investigated correlations between (viscosity) model parameters and sludge properties. Although essential for settling tank modelling, it is known that rheology depends on both the experimental procedure and the sample history (e.g. Koke *et al.*, 1999). One of the major problems when studying sludge rheology at moderate and low solids concentrations is sedimentation in the rheometer. In this study, a rotational stress-controlled Bohlin CVO rheometer with a gap of 1.25 mm was used. With this device different time delays, i.e. the time between subsequent stress-shear rate measurements, could be set; this time is sufficient to allow the rotor of the rheometer to rotate stationary. It was observed that low solids concentrations resulted in dilatant rheological behaviour, whereas higher solids concentrations revealed pseudoplastic

characteristics. Figure 7.1 gives an exemplary rheogram for a solids concentration of 1.24 g/l; the shear rate was measured by gradually increasing the shear stress every 15 s. Inspection of the cup after the experiment indicated a significant sedimentation of solids. As a result, the solids thickening at the bottom led to the increasing viscosity with time. Even for high shear rates the problem occurred; due to the prevailing laminar flow in the cup, no vertical velocities are present. Hence, the bob cannot stir up settled solids.

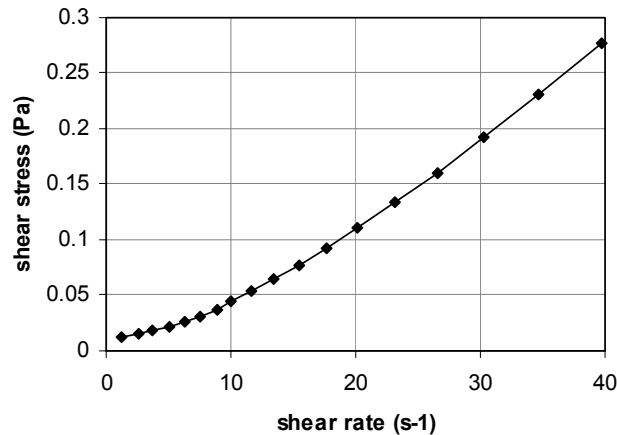


Figure 7.1 Typical rheogram when solids settling occurs (TSS = 1.24 g/l)

In order to minimise the influence of sedimentation, a lower bound for the solids concentration has to be set to obtain correct rheology readings. For this lower bound, information about settling velocities is needed; standard settling properties were taken from Takács *et al.* (1991), i.e.

$$v_s = 0.00824 e^{-0.426 X}$$

where v_s [m/s] and X [kg/m³] are the hindered settling velocity and solids concentration respectively. Because sedimentation never can be excluded, it was decided that settling over a distance less than 20% of the total cup height was acceptable. For a cup with a height of 5 cm and a typical experiment length of 5 minutes the lowest acceptable solids concentration is approximately 9.16 g/l. With slower settling sludge lower threshold concentrations can be allowed. Hence, the threshold solids concentration only serves as a guideline. As a result, correlations between rheological and sludge properties need to be extrapolated to lower concentrations. Different solids concentrations were prepared by setting up dilution series with thickened sludge (\pm 3-4 hours of settling) and effluent; the concentration was measured according Standard Methods (APHA, 1992).

To overcome the issue of solids settling in the cup, Dick & Buck (1985) constructed a rotational rheometer with a continuous upward flow to counteract sedimentation. In this research, however, such experimental layout was not available.

Besides the experimental procedure, also the suspension itself has a pronounced effect on rheology. Therefore, isothermal conditions of 20°C were imposed, and the sample was

withdrawn after every experiment. It is well-known that time- and shear-dependent behaviours have been observed for biological sludges (Campbell & Crescuolo, 1982; Bache *et al.*, 1997; Dentel, 1997). In such situations the macroscopic and microscopic structures of the suspension are altered during the rheological experiment. This time and shear dependency makes it difficult to investigate the rheology. According to Higgs & Norrington (1971), no less than 18 constants are required to fully quantitatively characterise a fluid with time-dependent thinning properties.

In general, time-dependent thinning is examined by measuring the time evolution of viscosity with constant shear rate (Steffe, 1996). From such experiments the time-scale of thinning can be estimated. Hence, if the time-scale at different shear rates largely exceeds the experiment time, the rheogram can be assumed to be time-independent. Unfortunately, several researchers observed considerable time-dependent thinning making assumptions as steady state impossible. Indeed, history effects do not allow any comparison between subsequent measurements. Forster (1982) therefore used the concept of equilibrium viscosity. For any sample a viscosity-time curve was obtained and the asymptotic value was taken as the apparent equilibrium viscosity throughout his research. Here, time-dependent phenomena were the aim of research; thus, an alternative procedure had to be used.

Before registering values of shear rate and shear stress, the suspension was pre-treated such that standardised conditions were obtained. To approximately mimic the settling tank process, the same stress as in the inlet pipe was applied. To calculate this stress, the friction at the pipe wall needs to be computed. Correlations for Bingham fluids can be used to calculate the friction factor f_r . In this work, the following implicit relation was retained (Steffe, 1996),

$$\frac{1}{\sqrt{f_r}} = 4.35 \log_{10}(1-c) + 4.53 \log_{10}(Re \sqrt{f_r}) - 2.3$$

For the Reynolds number Re and the parameter c the following formulae were utilised,

$$Re = \frac{d u \rho}{K}$$

$$c = \frac{\tau_0}{\tau_w} = \frac{2\tau_0}{f_r \rho u^2}$$

where d , u , ρ , τ_0 , τ_w , and K are the pipe diameter, velocity, bulk density, yield stress, wall stress and fluid consistency index respectively. Once the friction factor is iteratively calculated, the wall stress can be obtained as

$$\tau_w = f_r \frac{\rho}{2} u^2.$$

It is this wall stress that ultimately was applied to pre-condition the suspension. The time of application was arbitrarily chosen to be 10 s. To calculate the wall stress an average velocity of 0.8 m/s in the inlet pipe to the secondary settling tank was assumed. Further, preliminary estimates of yield stress and consistency index of thickened sludges (up to 16 g TSS/l) from the Lokeren and Ossemeersen WWTP (Belgium) were applied. The mean values for yield stress and consistency index were 0.13 Pa and 0.02 Pa.s respectively. Hence, the wall stress measured 2.18 Pa. Obviously, the values are not representative for the dilute sludge coming into the settling tank; the friction and the wall stress would typically be lower. The time the sludge is subjected to the wall stress is larger than 10 s as well. Further, bends and other flow restrictions that increase the friction are not incorporated in the calculation. Consequently, the result should only be used qualitatively.

Taking all above remarks into account, time-dependent thinning was investigated for sludge from the Ossemeersen WWTP (Belgium).

An easy test to study time-dependent thinning is to check whether hysteresis occurs for a sequence of increasing-decreasing shear stresses and/or *vice versa*. In this respect, Figure 7.2 (left) demonstrates the impact of an increasing, and subsequently followed by a decreasing, shear stress on the shear rate ("up-down" rheogram). Instead, the "down-up" rheogram results from the inverse shear stress sequence. The figure clearly indicates the existence of hysteresis. Care should be taken, however, as some fluids are known to behave in a time-dependent thinning sense without any hysteresis (Higgs & Norrington, 1971). According to Bache *et al.* (1997), the existence of hysteresis suggests that coagulation structures are present. Figure 7.2 (left) indicates a distinct discrepancy between the hystereses of a sequence of increasing-decreasing stresses and *vice versa*. The major differences are obviously seen at high stresses where the macrostructure of the suspension is destroyed. Because the down-up curve starts at a high shear stress, the structure is partially broken down and the viscosity decreases; the loss of structure makes the sludge act more as a liquid. As a result, the initial decrease of shear stress does not lead to a decreasing shear rate as expected. This also explains why the down-curve crosses the up-curve. Similar behaviour is not seen for the up-down rheogram.

The time delay between subsequent measurements has a significant influence; this is expected due to the time-dependent thinning nature of the biological sludge. Longer delay times will result in more breakdown of the macrostructure. For the down-up rheograms, it was therefore observed that shorter delays between measurements resulted in initial and final shear rates that were situated closer to each other. The dramatic impact of delay time was also clearly noticed in the up-down curves (Figure 7.2, right). These observations indicate that rheograms should be determined with rheological analysis of individual samples, i.e. the sample should be replaced after every imposed shear stress. Sample pre-conditioning should be avoided as well. Of course, many other problems arise. Firstly, every sample has its own history and results in a different rheological behaviour. Therefore, standardisation must be performed before any measurement. Secondly, the rotor of the rheometer needs time to accelerate and arrive to a stationary shear rate (corresponding to the imposed shear stress). Especially when high shear rates are set, necessary delay times of 40 s and more are not unusual. This issue will be further demonstrated below.

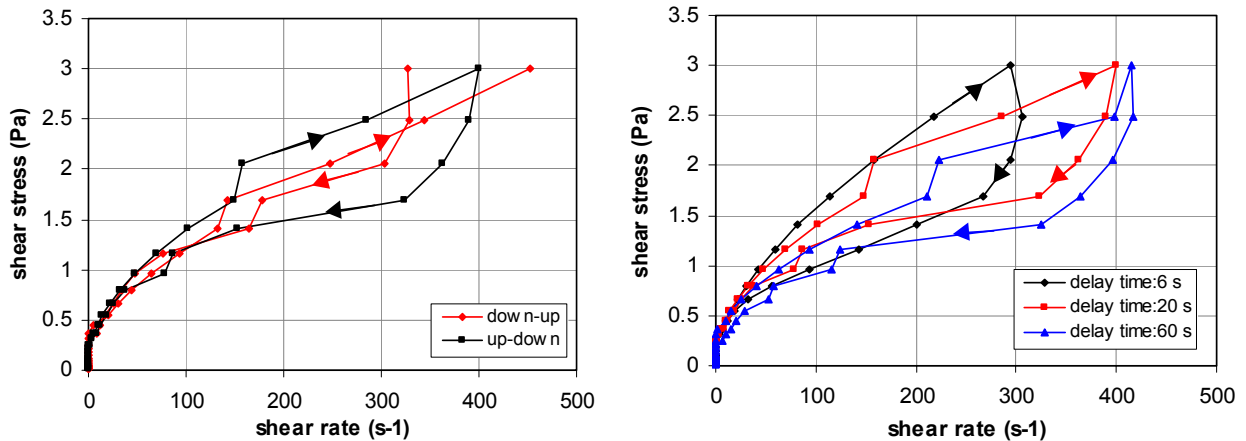


Figure 7.2 Hysteresis of rheological properties of sludge with a TSS of 15.8 g/l; up-down and down-up hysteresis (delay time of 20 s) (left), and for different delay times (right)

Because history effects have a severe impact on the rheogram, the use of fresh sludge for every observation was believed to reduce its influence. In this respect, Figure 7.3 illustrates the impact of partitioning the total measurement range on the rheogram, i.e. instead of measuring the total range of stresses (<1.7 Pa) in a single experiment, it is subdivided in five separate experiments. In every experiment, fresh sludge was utilised for only four observations; hence, history effects are expected to be reduced as compared to the full measurement range. The following five ranges for stress were retained: $1.23 \cdot 10^{-2}$ - $3.2 \cdot 10^{-2}$ Pa, $3.2 \cdot 10^{-2}$ - $6.8 \cdot 10^{-2}$ Pa, $6.8 \cdot 10^{-2}$ - 0.1 Pa, 0.1 - 0.5 Pa and 1 - 1.5 Pa. Since a delay time of 30 s was used, it is obvious that the observations of the partition experiments are found in between the complete rheograms measured with delay times of 20 and 60 s. It is seen in Figure 7.3 (left) that no major discrepancies exist between the trends of the different curves. In the partition experiments it was expected that time-dependent thinning would hardly occur and lower shear rates would be obtained. But again, this experiment proves that it is mainly the delay time being detrimental for rheological measurements; partitioning does not solve the problem. Moreover, Figure 7.3 (right) clearly shows that time-dependent thinning is less pronounced at low shear stresses; the macroscopic structure better resists the imposed stresses. In this respect, Figure 7.3 (left) indicates that the rheograms for different delay times converge, i.e. the relative difference in stress decreases. At very small stresses they even coincide completely (Figure 7.3, right). This clearly demonstrates that the macroscopic structure of the suspension is retained at low stresses and no structural breakdown occurs.

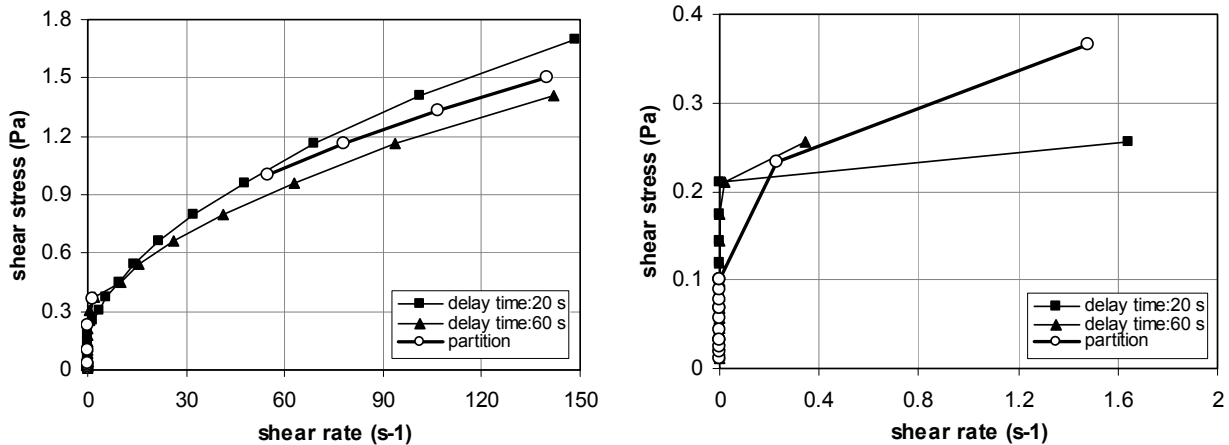


Figure 7.3 The influence of partitioning the measurement range compared to a complete rheogram with different delay times (left); zoom-in at lower shear rates (right). Sludge with a TSS of 15.8 g/l was used

7.1.2 Thixotropy or rheomalaxis?

Because of the rapid breakdown of the internal structure of the suspension, the question arises whether this phenomenon is reversible. According to Steffe (1996), the term *thixotropy* refers to the time-dependent decrease in viscosity, due to shearing, and the subsequent recovery of viscosity when shearing is removed. Irreversible thixotropy, called *rheomalaxis* or *rheodestruction*, is common in food products. Thixotropy is a result of sol-gel transition phenomena (Higgs & Norrington, 1971; Steffe, 1996). When shear rate increases, the three-dimensional network, i.e. gel state, collapses and the product exists in the sol state, i.e. in a suspension. In foods that show reversibility, the network is rebuilt and the gel state reobtained. Irreversible materials remain in the sol state.

Unno & Akehata (1985) performed experiments to evaluate the structural reversibility of biological sludges. They subjected the sludge to a constant shear rate and the decay in stress was measured. Subsequently, a variable rest period was included in order to partially or completely recover the original structure. From their observations they concluded that 90% recovery occurred after 18.3 minutes. The researchers linked this reversible thixotropy to the flocculated nature of sludge. They hypothesised that the highly irregular floc shapes and the electrochemical surface structure led to both reversible inter-solid interactions and interactions between solids and surrounding liquid. In this respect, Forster (1982) showed that surface polysaccharides and proteins are important factors in determining the viscosity of sludge. Also the amount of metals and water bound by these charged biopolymers are of considerable importance (Forster, 1983).

Here, a similar study has been performed for sludge sampled at the Ossemeersen WWTP (Belgium); the solids concentration measured 12.6 g/l. A constant stress of 2.18 Pa was applied for the first 17 minutes. Then, three different rest periods were evaluated, i.e. 5, 30 and 60 minutes during which restructuring could occur. Finally, the initial stress of 2.18 Pa was reapplied for 17 minutes. Shear rates were measured every 32 s. At the start of the experiment the shear rate measured between 11 and 23 s⁻¹; 70 s⁻¹ was observed at the end of

each experimental run. The time-dependent viscosities are shown in Figure 7.4. It is stressed that the rest period mentioned in this figure corresponds to different lengths, i.e. 5, 30 and 60 minutes. Obviously, no structural recovery occurs for the sludge. After stressing the sample again, the viscosity simply decays further. Whereas Unno & Akehata (1985) tied thixotropy to the reversible electrochemical nature of the colloidal suspension, it is believed that rheomalaxis as observed here can be linked to both the solids concentration and the flow conditions. During the rest period, electrochemical bounds are not built up again as observed by Unno & Akehata (1985), i.e. no orthokinetic aggregation occurs due to the stagnant flow conditions inside the cup. These authors used centrifugally thickened sludge (up to 40 g TSS/l and more), which enhances interparticle contact and the recovery of electrochemical bounds. For silica suspensions and using the FBRM technique, Peng & Williams (1993) observed mean particle diameters increasing with solids concentration; concentrations between 10 and 50 g TSS/l were used. Hence, at identical flow conditions particle aggregation is enhanced by solids concentration. Although bulk mixing was involved, it is believed that at high concentrations and zero flow, particles are close enough to spontaneously aggregate. In this study, however, much lower solids concentrations were used. Hence, interparticle distances are too large to allow particles to approach each other by Brownian motion. In other words, perikinetic aggregation does not occur. Because no flow is present, orthokinetic aggregation does not occur either. The high solids concentration further does not allow differential settling. The absence of any particle aggregation presumably explains the rheomalaxis as observed.

In Figure 7.4, the viscosity is found to be higher for the experiment in which a 60-minute rest period was evaluated. These initial discrepancies between the rheograms with different rest periods may be explained by a difference in particle size distributions at the start of the experiment. All samples were taken from the same sludge reservoir that was once filled with Ossemeersen sludge. Before each test the sludge was first resuspended. This short mixing period may have led to increasing aggregation. As a result, due to the larger particles, higher initial viscosities can be expected for the subsequent experiments with rest periods of 5, 30 and 60 minutes respectively. Note that all rheograms ultimately converge though. Viscosities increasing with particle size were also observed by Bhattacharya *et al.* (1992) when investigating flour suspensions. In their research, however, no complete structural breakdown was seen as probably occurs with biological sludges.

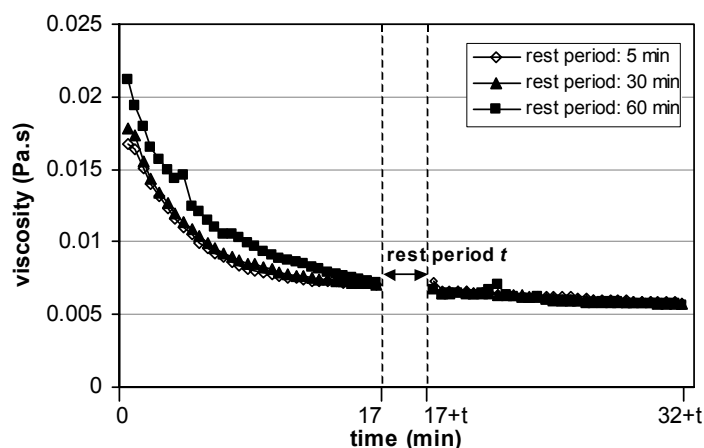


Figure 7.4 Rheomalaxis of sludge (12.6 g TSS/l) observed from viscosity decay curves

7.1.3 Modelling of rheomalaxis

In literature, numerous rheological models describing time-dependent behaviour and their application can be found (Higgs & Norrington, 1971; Paredes *et al.*, 1988; Adeyemi *et al.*, 1991; Bhattacharya *et al.*, 1992; Holdsworth, 1993; Steffe, 1996; Bhattacharya, 1999). However, so far, these models were only applied to food products. To the author's knowledge, no quantitative modelling of thixotropy or rheomalaxis has already been done for biological sludges. Battistoni *et al.* (1993) investigated the impact of solids concentration, whereas Unno & Akehata (1985) performed a very systematic study on thixotropy. Unfortunately, no quantification of the structural decay in time was studied.

According to Cheng (1973), structural models provide more insight into the physical basis of thixotropy and rheomalaxis. The information these models return on the rheograms and the rates of structural buildup and breakdown are the most suitable for correlating with the molecular and microscopic fluid properties and processes that go on in the suspension. Many structural models exist in literature. Here, the model as described and applied by Tiu & Boger (1974), Ford & Steffe (1986) and Steffe (1996) will be used to describe rheomalaxis; to account for breakdown a structural property is added to the Herschel-Bulkley model:

$$\tau = f(\lambda, \dot{\gamma}) = \lambda(\tau_0 + K\dot{\gamma}^n) \quad (7.1)$$

where λ , the structural property, is a function of time. It equals one before the onset of shearing and equals an equilibrium value (λ_e) obtained after complete breakdown from shearing. On the other hand, Koke *et al.* (1999) believed that the structural parameter λ can go as low as zero. In order to prevent the viscosity from dropping to zero, the authors added a pure liquid viscosity, i.e. a constant, to Equation 7.1.

According to Tiu & Boger (1974), Ford & Steffe (1986) and Steffe (1996), the decay of the structural parameter with time can be assumed to obey second-order kinetics:

$$\frac{d\lambda}{dt} = -r(\lambda - \lambda_e)^2 \quad \text{for } \lambda > \lambda_e \quad (7.2)$$

where r is a decay rate constant that is function of shear stress. The entire model is then completely determined by five parameters: τ_0 , K , n , $r(\tau)$, and λ_e . τ_0 , K , and n are determined under the initial shearing conditions when $\lambda = 1$ and $t = 0$. In other words, they are determined from the initial shear rate in the material, observed at the beginning of a series of tests, each imposing a fixed stress.

To find r , λ and λ_e are expressed as function of both shear stress and the time-dependent shear rate. Equation 7.1 can thus be rewritten as

$$\lambda = \frac{\tau}{\tau_0 + K\dot{\gamma}^n}.$$

This equation is valid for all values of λ including λ_e at $\dot{\gamma}_e$, being the equilibrium value for shear rate. Differentiating λ with respect to time, at a constant shear stress, gives

$$\frac{d\lambda}{dt} = -\frac{\tau n K \dot{\gamma}^{n-1}}{(\tau_0 + K \dot{\gamma}^n)^2} \frac{d\dot{\gamma}}{dt}$$

Using Equation 7.2 and applying simple algebra finally results in

$$r = \frac{nK}{\tau(t_e - t_{init})} \int_{\dot{\gamma}_{init}}^{\dot{\gamma}_e} \frac{\dot{\gamma}^{n-1}}{\left(1 - \frac{\tau_0 + K\dot{\gamma}^n}{\tau_0 + K\dot{\gamma}_e^n}\right)} d\dot{\gamma}$$

where t_{init} and t_e are the start and final time of the experiment respectively; $\dot{\gamma}_{init}$ is the initial shear rate. At a particular stress, r is computed by numerical integration. This is done for numerous shear stresses and the resulting information is used to determine the relation between r and τ . This is the final information required to completely specify the mathematical model.

Case study

Sludge samples from the Ossemeersen WWTP (Belgium) were exposed to different shear stresses, i.e. 0.32, 0.375, 0.5, 0.75, 1 and 2 Pa. Low settling velocities allowed concentrations as low as 6.1 g TSS/l to be measured without significant sedimentation in the cup. Measurement noise made any analysis impossible at applied stresses lower than 0.32 Pa. On the other hand, a stress of 2 Pa did not show much temporal variation in shear rate. Because most structural breakdown already occurred before the first measurement of shear rate, the shear stress of 2 Pa was excluded from the experiments. Figure 7.5 shows the results of this temporal breakdown at different stresses.

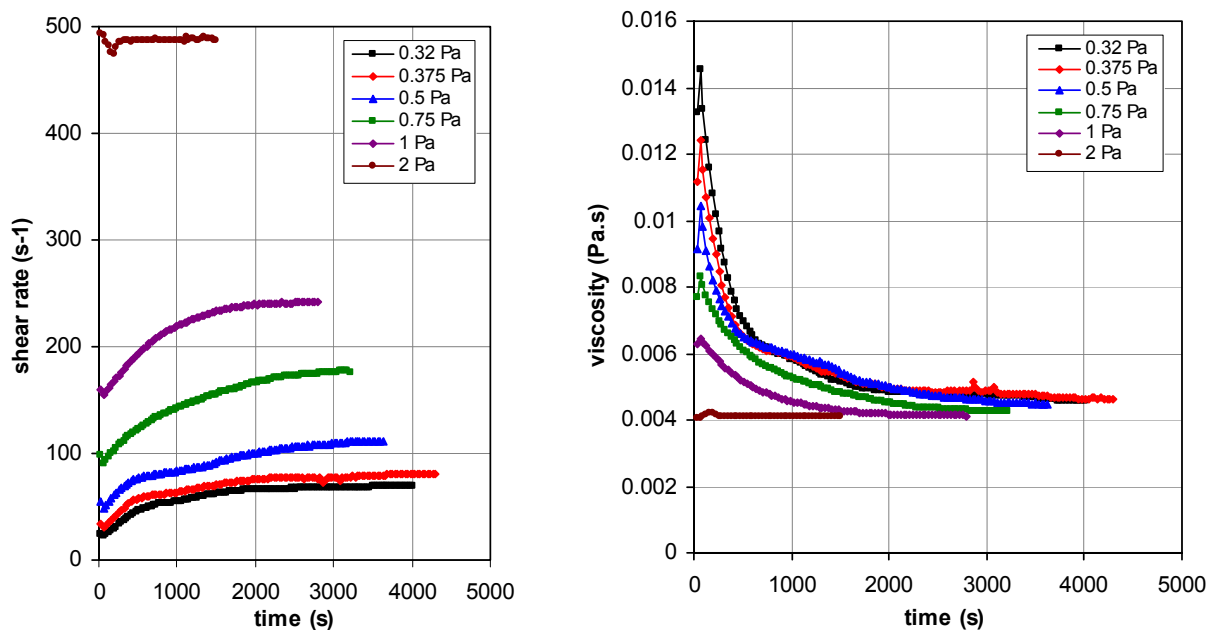


Figure 7.5 Evolution in time of shear rate (left) and viscosity (right) at different imposed stresses

Firstly, in Figure 7.5 (left) it is observed that the shear rate initially declines and then increases to evolve to a steady state. This initial decrease is due to an overshoot in the rotor speed response to the imposed shear stress. Secondly, for stresses below 0.5 Pa a region can be identified (± 500 - 1500 s) where the shear rate increases less with time. The identical gradient observed for the different stresses may indicate some floc structure resistance to the imposed shear stresses. At 0.5 Pa this structure is broken down at ± 1500 s, i.e. a "sudden" increase in shear rate is seen. Above this threshold stress the phenomenon is not observed any more; hence, the mentioned floc structure is destroyed before the first measurement. These observations demonstrate the existence of different structures in the suspension, i.e. the floc structures present. It is indeed well accepted that biological flocs are characterised by several structural levels with different fractal dimensions (Wahlberg *et al.*, 1992; Jorand *et al.*, 1995), i.e. with different resistance to shear.

On the other hand, Figure 7.5 (right) shows the evolution of the apparent viscosity. Obviously, the lower the imposed stress, the higher the initial viscosity. Due to a loss of structure during the 32 s prior to the first data point, viscosities at high stresses do not correspond to those at low shear stresses. Again, this emphasises the inability of the rheometer to capture (very essential) rheological behaviour at the start of an experiment. Further, Figure 7.5 (right) also indicates that every stress ultimately leads to approximately the same viscosity. This shows that a complete structural loss of the suspension is obtained under all conditions.

The data of Figure 7.5 (left) was subsequently utilised to determine the structural decay parameter r . After exclusion of the first data point of each time series (to avoid the use of the initial decrease in shear rate), the second data points are used to determine the Herschel-Bulkley parameters. From least-squares error minimisation, Table 7.1 gives the estimated parameters obtained with a coefficient of determination of 0.9997. Next, the decay parameter r was determined as function of shear stress. The result is shown in Figure 7.6.

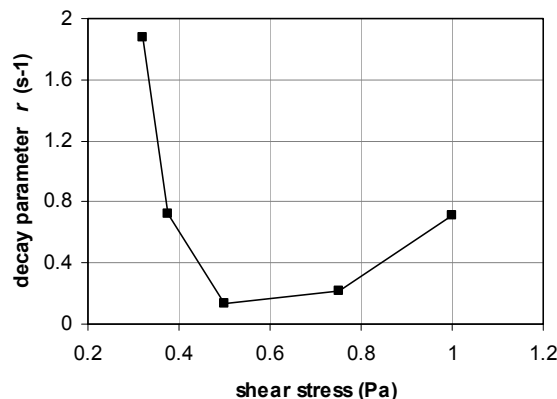


Figure 7.6 Shear stress dependency of the structural decay parameter r

Table 7.1 Estimated Herschel-Bulkley parameters

Parameter	Value
τ_0 (Pa)	0.0373
K (Pa.s ^{0.6667})	0.0330
n (-)	0.6667

Although it was expected that r would increase with shear stress, the curve as presented in Figure 7.6 is clearly different. This behaviour can, however, be explained by means of Figure 7.5 (left). From the figure, it became clear that at least two floc structures exist, which are broken down at increasing shear stresses. These structural levels obviously may be related to the dependency of the structural decay parameter r on the shear stress applied. At low stresses, many structural levels are degraded over the period of experiment and, therefore, r will be large. Note that at low shear stresses the initial structure is not maintained either. Due to the preliminary stress of 2.18 Pa the structure is already partially destroyed before the first measurement is taken. Increasing stresses, however, destroy the floc structures more prior to the initial measurement of shear rate. Hence, the decay parameter decreases with increasing stresses since the floc structures are not altered during the entire measurement as much as at low stresses. Figure 7.6 further indicates that the decay parameter increases again when the shear stress becomes larger than 0.5 Pa. This observed increase of r is due to the smaller time constant of the (remaining) structural breakdown process at high stresses, i.e. the viscosity reaches its equilibrium quicker (Figure 7.5, right).

From the previous it is clear that the inability to measure the initial shear rates results in a (structural decay) model not representing reality. Because of the applied delay times, and the related structural breakdown, the estimated parameters of the standard Herschel-Bulkley model are not linked with the original structure of the suspension, i.e. $\lambda \neq 1$. As a result, the relation of r versus shear stress is not only increasing as observed in Figure 7.6. It is obvious that this does not represent any real rheological behaviour. If the structure of this relation would be known *a priori*, all rheograms (measured at constant shear stress) could be used to estimate the structural parameter λ and the Herschel-Bulkley parameters *together*. Unfortunately, due to the lack of this knowledge, it is experimentally impossible to measure the decay parameter.

Hence, history effects could only be accounted for in a model if the measurement technique avoids delay times and preliminary stresses. In view of this, the sludge standardisation can be questioned; the question arises whether the different experiments still can be related to each other. Only at very low shear stresses the structure of the suspension may be investigated. Indeed, from Figure 7.3 (right) it was concluded that low stresses do not destroy the structure, or at least it occurs very slowly. This gives the opportunity to investigate rheomalaxis as it occurs in the secondary settling tank. For more details, the reader is referred to Section 7.3. Finally, in this respect, it is important to note that the rheometer should be sensitive enough to perform such measurements.

7.2 Considerations about yield stress

In this section, a rheological model is set up that accounts for low-shear rheology. Model parameters are estimated by using sludges from three different WWTPs. Finally, simulations are shown to demonstrate the discrepancies in flow and solids concentration fields resulting from different rheological models. The different models evaluated are often used in practice.

7.2.1 Theoretical background

A major goal of this study is to select a sludge rheological model to be implemented in CFD code. Due to the 2D or 3D characteristics of the investigated problem, the standard rheological notations valid for 1D flows (see Chapter 2) should be altered. In the following, only rheological isotropy is considered, i.e. the parameters do not change with direction. Typically, the apparent viscosity $\tau_{ij} / \dot{\gamma}_{ij}$ is implemented in CFD code. For Bingham-type fluids the rheological model is rewritten as,

$$\tau_{ij} = \left(\frac{\tau_0}{\dot{\gamma}} + K \right) \dot{\gamma}_{ij} \quad \text{for } \tau \geq \tau_0 \quad (7.3a)$$

$$\dot{\gamma}_{ij} = 0 \quad \text{for } \tau < \tau_0 \quad (7.3b)$$

where τ_{ij} and $\dot{\gamma}_{ij}$ are the tensors for stress and strain rate respectively. It is noticed that the shear rate is the component of the strain tensor describing velocity gradients perpendicular to the velocity direction. The magnitude of the strain rate is denoted as $\dot{\gamma}$ and writes

$$\dot{\gamma} = \sqrt{\frac{1}{2} \dot{\gamma}_{ij}^2}.$$

Similarly, the Herschel-Bulkley model can be modified as

$$\tau_{ij} = \left(\frac{\tau_0}{\dot{\gamma}} + K \dot{\gamma}^{n-1} \right) \dot{\gamma}_{ij} \quad \text{for } \tau \geq \tau_0 \quad (7.4a)$$

$$\dot{\gamma}_{ij} = 0 \quad \text{for } \tau < \tau_0 \quad (7.4b)$$

Models with a yield stress inherently show a basic inconsistency in the flow fields (Balmforth & Craster, 1999). The cause is the infinite apparent viscosity when the magnitude of the strain rate evolves to zero. To surmount this inconsistency problem, three solutions have been proposed in literature.

Firstly, the use of bi-viscous fluids avoids the Bingham model (Balmforth & Craster, 1999 and 2002) and its numerical inconsistency. The bi-viscous model is given below as

$$\begin{aligned}\tau_{ij} &= \tau_0 + K\dot{\gamma}_{ij} && \text{for } \tau \geq \tau_0 \\ \tau_{ij} &= K_\tau\dot{\gamma}_{ij} && \text{for } \tau < \tau_0\end{aligned}$$

where K and K_τ are the two fluid consistency indices. For most materials, the ratio K/K_τ is usually small, typically 10^{-2} or less (Phan-Thien *et al.*, 2000).

Secondly, an arbitrarily small perturbation ε of the Bingham model leads to a consistent theory (Frigaard & Scherzer, 1998; Balmforth & Craster, 1999). This solution can also be applied to solve the inconsistency of the Herschel-Bulkley model. Hence, for Bingham behaviour the model becomes (van de Fliert & van den Berg, 1999)

$$\tau_{ij} = \left(\frac{\tau_0}{\dot{\gamma} + \varepsilon} + K \right) \dot{\gamma}_{ij}$$

where ε is a fixed small parameter. This regularisation improves numerical convergence; at low strain rates ε makes sure that a finite viscosity is retained.

Thirdly, Papanastasiou (1987) proposed a modification in the rheological relation by introducing a material parameter m , which controls the growth of stress as the strain rate increases. This way the equation is valid for both yielded and unyielded areas, i.e. stresses below and above the yield stress. Papanastasiou's modification when applied to the Bingham model becomes

$$\tau_{ij} = \left[\frac{\tau_0}{\dot{\gamma}} (1 - e^{-m\dot{\gamma}}) + K \right] \dot{\gamma}_{ij}$$

where m is the stress growth exponent. Blackery & Mitsoulis (1997) showed that the equation mimics the ideal Bingham model for $m \geq 100$ s. From the number of publications (e.g. Papanastasiou, 1985; Blackery & Mitsoulis, 1997; Alexandrou *et al.*, 2002), this exponential model has clearly gained popularity in the field of numerical modelling. The inclusion of this exponential term in the Herschel-Bulkley model is applicable as well and only stresses its flexibility. Beaulne & Mitsoulis (1997) demonstrated that for $m \geq 1000$ s the Herschel-Bulkley model fits data well.

To illustrate the different models as presented above, Figure 7.7 shows their behaviour at low shear rates. This region may become very important because shear rates go well below 1 s^{-1} in the solids blanket of a settling tank. Comparisons should only be based on general rheogram features and not on absolute values of shear rates and shear stresses because of the arbitrarily chosen parameter values.

All model adaptations are carried out on the standard Bingham model. Clearly, the bi-viscous model shows similarities with the Bingham model modified with the perturbation factor. Because this factor is extremely small, it results in very large viscosities as reflected by the steep slope in Figure 7.7. Depending on the value of K_τ the bi-viscous model approaches this perturbation-modified Bingham model; the former model however shows a discontinuity in the rheogram. A completely different rheogram is obtained with the modification as proposed by Papanastasiou. Here, the rheogram is smoother and no discontinuity is observed. Depending

on its parameters a large variety of rheograms may be obtained. This flexibility makes the model so useful.

As mentioned at the start of this section, rheological models *with* yield stress must be adapted in order to perform correct numerical simulations. The experience gained in this research shows that numerical inconsistencies do not occur, however, because the strain rate in the settling tank never becomes zero. Nevertheless, viscosities are inconsistent in a physical manner, i.e. their numerical value is unrealistically high. The proposed model adaptations should therefore be adopted. Before applying such rheological model in CFD, however, it needs to be calibrated for biological sludges. This issue is dealt with in the following section.

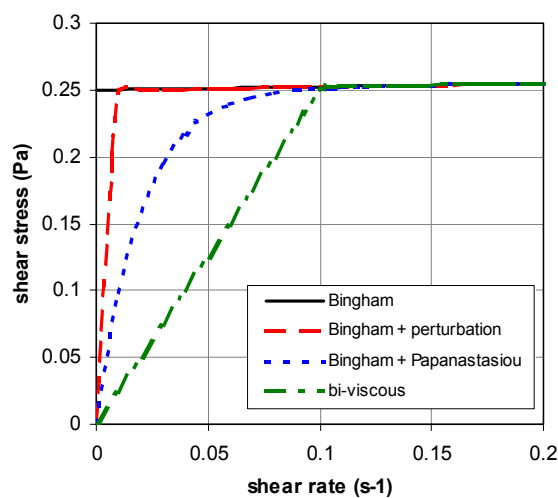


Figure 7.7 Comparison of different models accounting for the yield stress

7.2.2 Calibration of the rheological model

As mentioned above, in literature, many rheological models for sludge typically take into account a yield stress (e.g. Equations 7.3a,b and 7.4a,b). To calculate the yield stress, the data are mostly extrapolated to a zero shear rate. In this respect, Dick & Buck (1985) demonstrated the existence of a yield stress by a self-fabricated rheometer of which the inner and outer cylinder can rotate independently. When the outer cylinder was slowly rotated, equivalent rotation of the inner cylinder occurred. If the rotation was stopped before the shear stress on the inner cylinder reached the yield stress, the inner cylinder would be held in place by the suspension. Rasmussen (1997) produced similar results. He calculated the yield stress from the angle at which a pendulum is in equilibrium state, i.e. the location at which the gravitational force is compensated by the yield stress. Due to the yield stress of the sludge, the pendulum ball is held at an angle different from the vertical.

Barnes & Walters (1985), on the other hand, described how yield stress only results from the insensitivity of the rheometer applied. Experiments for biological sludge, conducted with a sensitive rheometer for this research, indicate that a real yield stress indeed does not exist; the rheogram in Figure 7.8 demonstrates this. However, at a certain shear rate an abrupt

change in viscosity is observed; decreases of 100-1000x are typical. These extremely high viscosities at low shear rates also explain the observations of "yield stress" by Dick & Buck (1985) and Rasmussen (1997). For the former, a velocity discrepancy between inner and outer cylinder existed, but was so low that it was not observable. They could only measure shear rates above approximately 35 s^{-1} . The same holds for Rasmussen (1997); it is believed that the very high viscosity still allowed some movement of the pendulum but to an unobservable small extent. This assumption is further supported by the fact that Rasmussen's yield stresses are of the same order of magnitude as the stresses corresponding to the point of abrupt viscosity change as seen in this study.

The existence of finite viscosities makes the rheological models presented in Section 7.2.1 more acceptable; for instance, modifications as applied by Papanastasiou (1987) get a physical interpretation. Moreover, the exponential term of Papanastasiou correctly determines the transient between high and low viscosities; a characteristic that is not shown by the other model modifications. The adaptation of Papanastasiou will therefore be utilised to incorporate the rheological behaviour at low shear rates or stresses.

Whether the absence of a true yield stress has a significant influence on solids transport in the settling tank is unknown. However, 2D simulations have shown that shear rates in the settling tank are below 25 s^{-1} . Even more, these values are only found near the inlet structure; inside the blanket shear rates go down to well below 1 s^{-1} ; the deeper one goes into the blanket, the lower the shear rate becomes. This can be concluded from velocity profiles experimentally obtained by Kinnear & Deines (2001) as well. A good solids transport model therefore requires a rheological model accurate at low shear rates.

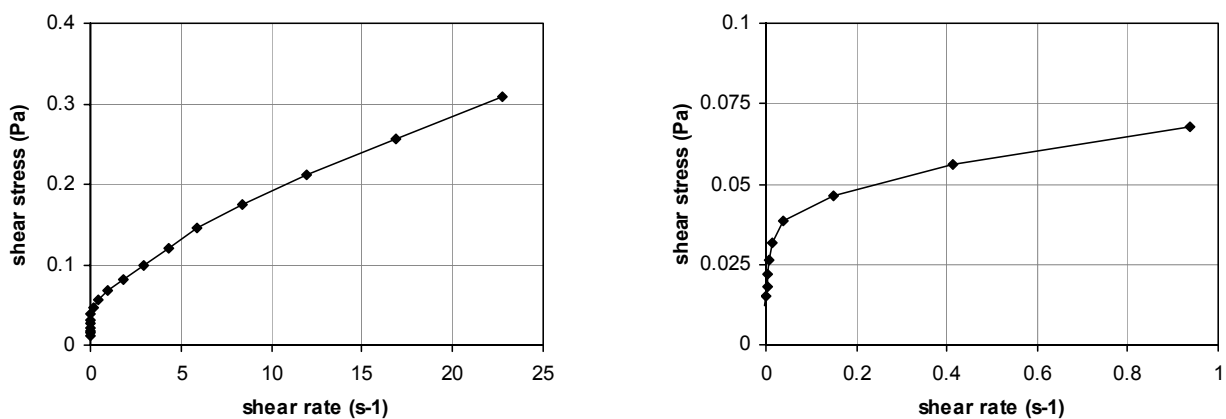


Figure 7.8 Typical rheogram for sludge (left), and zoom-in (right), demonstrating the non-existence of yield stress

To investigate the impact of this rheological behaviour on the flow field and the solids transport, a comparison between different models from literature was conducted. To make such comparison, a model structure and corresponding parameters representative for typical municipal wastewater treatment sludge are needed. Three sludges from different WWTPs were therefore investigated in terms of their rheology. The following Belgian WWTPs were considered: Ossemeersen (Ghent), Lokeren and Destelbergen. Samples were taken from the RAS and the effluent.

To evaluate the dependency of rheology on the solids concentration, a dilution series was set up for every WWTP; RAS sludge thickened for 4-5 h was diluted with effluent to the appropriate concentrations. The solids concentration was subsequently determined according Standard Methods (APHA, 1992). As mentioned in Section 7.1 only solids concentrations above 9.16 g/l were taken into account, except for poorly settling sludges. In the latter case, solids settling in the rheometer cup is of less importance for a proper measurement. As in Section 7.1 every sludge sample was exposed to a pre-stress of 2.18 Pa for 10 s. After 10 s of equilibration, 30 shear rate-stress measurements were performed at increasing shear stresses. The applied stresses covered the range 0.012 - 3 Pa. For every measurement a delay time and timeout of 8 and 2 s respectively were used throughout the experiment. One experiment took in total 5 minutes.

To describe the rheograms the Herschel-Bulkley model with Papanastasiou's adaptation was utilised. Although a yield stress is present, it does not act as such; the viscosity at stresses below the yield stress is finite, and shear rates different from zero occur (see Figure 7.7). The yield stress as used here indicates the stress at which the viscosity strongly varies. The model is written as

$$\tau_{ij} = \left[\frac{\tau_0}{\dot{\gamma}} (1 - e^{-m\dot{\gamma}}) + K\dot{\gamma}^{n-1} \right] \dot{\gamma}_{ij}$$

where τ_0 is the yield stress, m is the stress growth exponent, K is the fluid consistency index, and n is the flow behaviour index. For every sludge and solids concentration the parameters were estimated by means of least-squares error minimisation. The estimation results, together with their standard deviations, are shown in Figure 7.9. As can be observed in Figure 7.9 (top, left&right), the sludges from the three WWTPs exhibit the same trend for the yield stress and the fluid consistency index; only the highest solids concentration for the Destelbergen WWTP deviates from this behaviour and is believed to be an outlier. This particular data point is therefore not considered in modelling efforts any further. On the other hand, no trend exists for the stress growth exponent m and the flow behaviour index n . As a result, a constant value is retained in the rheological model.

Chapter 2 describes that the yield stress and the consistency index may depend on the solids concentration by both an exponential and a power model. In the field of CFD settling tank modelling, the relations proposed by Dahl (1993) are frequently used to calculate the yield stress and consistency index as function of solids concentration. For instance, Lakehal *et al.* (1999) and Armbruster *et al.* (2001) applied this model, which writes

$$\tau_0 = \beta_1 e^{\beta_2 X} \quad (7.5a)$$

$$K = \mu_w + \beta_3 X^2. \quad (7.5b)$$

Concerning the yield stress, Dahl (1993) related the parameter values to different experimental conditions to obtain accurate velocity profiles in the settling tank. In this respect, he made the yield stress dependent on the inlet solids concentration. Only two inlet concentrations were considered in his work, i.e. 2 and 4 g TSS/l. Lakehal *et al.* (1999) used

the data of Dahl for their simulations. However, they applied the rheological parameters valid for an inlet concentration of 4 g TSS/l whereas their inlet solids concentration measured 3.2 g/l. No interpolation was conducted. Table 7.2 shows the parameter values as used by Lakehal *et al.* (1999). As will be shown later in this section the yield stress experimentally determined in this research agrees to the data of Dahl (1993) only for solids concentrations below 6 g/l.

According to Ekama *et al.* (1997), another frequently used rheological model in CFD is the one of Bokil (1972); here, the apparent viscosity exponentially depends on the solids concentration. Bokil suggested the following equation:

$$\frac{\tau}{\dot{\gamma}} = 0.00327 10^{0.132 X} \quad (7.6)$$

It is noted that the parameters are only valid for solids concentrations above 0.7 g/l. In this respect, in their comparative study of rheological models, Lakehal *et al.* (1999) linearly extrapolated this equation to the viscosity of water at zero solids concentration. The relation as proposed by Bokil is also intensively applied by McCorquodale and his co-workers (personal communication).

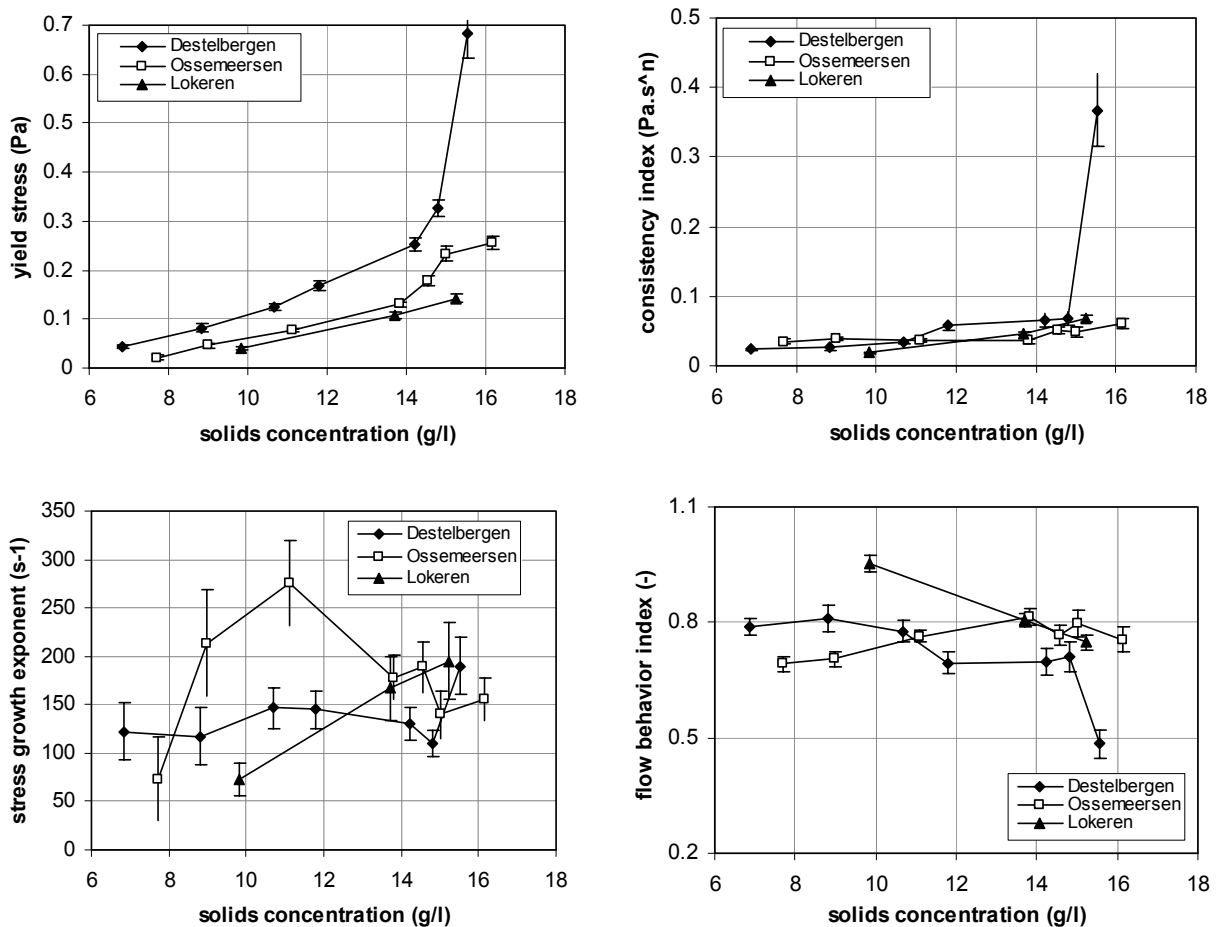


Figure 7.9 Fitted model parameters for 3 different WWTPs, i.e. Destelbergen, Ossemeersen (Ghent) and Lokeren: yield stress (top, left), fluid consistency index (top, right), stress growth exponent (bottom, left), and flow behaviour index (bottom, right)

Table 7.2 Parameter values used for the calculation of yield stress and Bingham viscosity (Lakehal *et al.*, 1999)

Parameter	Value
β_1 (kg/m/s ²)	$1.1 e^{-4}$
β_2 (m ³ /kg)	0.98
β_3 (m ⁵ /kg/s ²)	$2.473 e^{-4}$
μ_w (kg/m/s)	$1 e^{-3}$

Both models are compared with the present measurements in Figure 7.10. When comparing different shear rate-stress models, care has to be taken when interpreting the results. To complete the picture, the experimental data of Dick & Buck (1985) are plotted as well. They investigated the sludge rheology of two full-scale WWTPs; one of them received significant industrial discharges (plant I), whereas the other treated municipal wastewater (plant II).

Figure 7.10 (top) obviously indicates a strong similarity between measurements of the consistency index in this research and the model of Dahl (1993). The consistency indices as measured by Dick & Buck (1985) are consistently lower, however. Instead, the relation of Bokil (1972) shows a considerable discrepancy. The same structure as the relation used by Dahl, i.e. a second-order polynomial (see Equation 7.5b), will therefore be applied to describe the dependency of the fluid consistency index on the solids concentration; its parameters are estimated together with those of the yield-stress model.

From Figure 7.10 (bottom) it is observed that only the sludge of plant II (Dick & Buck) corresponds well with the yield stresses obtained in this research. The sludge of plant II deviates from this trend probably because it is a different sludge type, i.e. it originates from an industrial WWTP. Nevertheless, the data set of Dick & Buck (1985) gives some confidence in the measurements performed in this study. The yield stresses obtained by Dahl (1993), on the other hand, clearly do not show any correspondence with the present results. Although a yield stress is obtained for the Herschel-Bulkley model with Papanastasiou's modification, its magnitude equals the yield stress as calculated when omitting Papanastasiou's adaptation. However, the range of values for the proposed model and for the one of Dahl is completely different. Because Dahl's model quickly goes to extremely large values, it is believed to be physically unrealistic and incorrect.

Due to the inconsistencies discussed above, in this research a new model for the yield stress dependency on the solids concentration was developed. Three different model structures were investigated, i.e. a quadratic, a power and an exponential model. The parameters were estimated by means of all observed rheograms, i.e. 380 shear rate-stress measurements, and considering the previously determined second-order equation as model structure for the fluid consistency index (Equation 7.5b). The fitted parameters for the different models are shown in Table 7.3. It is clear that the quadratic model is a special case of the power model. Accounting for the Residual Standard Error (RSE) in Table 7.3, however, it is concluded that the power model as obtained here is better than the quadratic one.

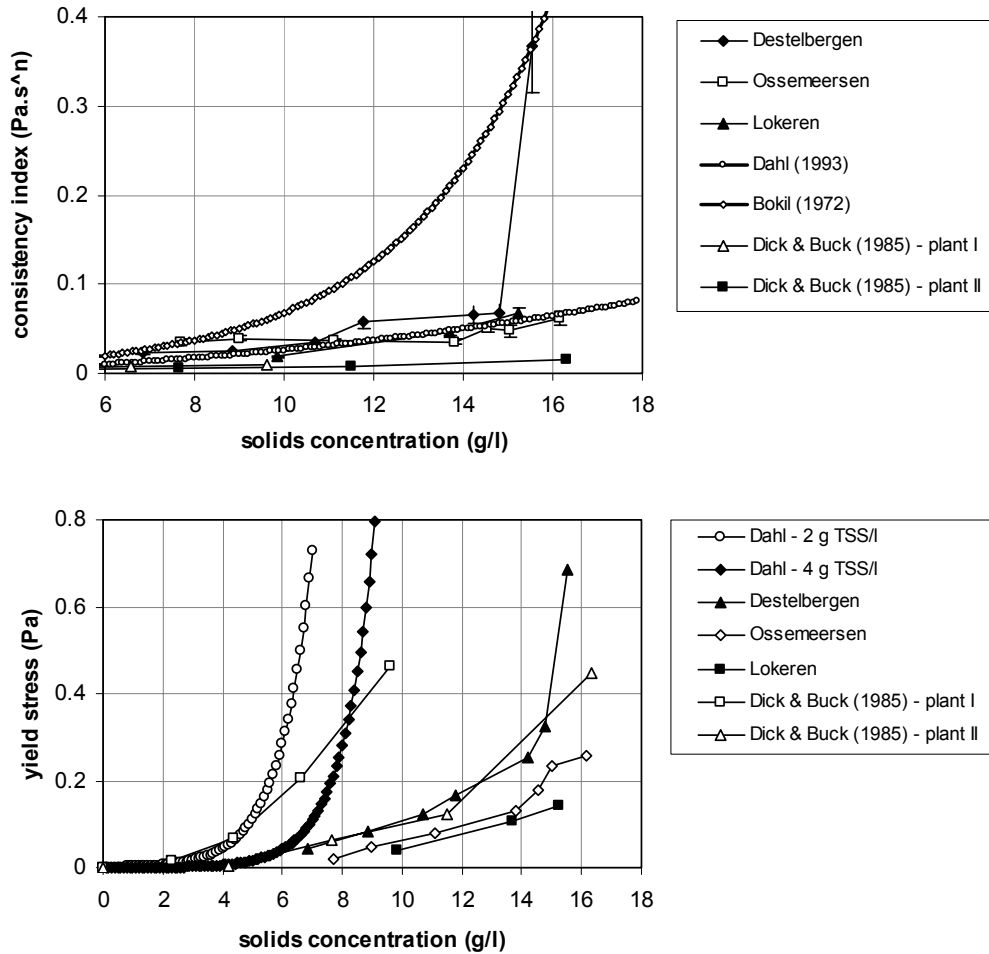


Figure 7.10 Comparison between measurements and models from literature; fluid consistency index (top), and yield stress (bottom)

Table 7.3 Parameter estimation for different yield stress models

parameter	investigated yield stress models					
	$\tau_0 = \beta_1 X^2$		$\tau_0 = \beta_1 X^{\beta_2}$		$\tau_0 = \beta_1 e^{\beta_2 X}$	
	value	standard error	value	standard error	value	standard error
β_1	$9.04 e^{-4}$	$0.53 e^{-4}$	$9.04 e^{-3}$	$2.68 e^{-3}$	$4.38 e^{-2}$	$0.57 e^{-2}$
β_2	-	-	1.12	0.12	$9.77 e^{-2}$	$1.01 e^{-2}$
β_3	$2.49 e^{-4}$	$2.86 e^{-5}$	$2.48 e^{-4}$	$2.69 e^{-5}$	$2.47 e^{-4}$	$2.67 e^{-5}$
m	169.5	28.0	163.4	25.6	162.6	25.3
n	0.775	0.029	0.777	0.027	0.778	0.027
RSE	0.0584		0.0553		0.0551	
R-squared	0.976		0.979		0.979	

RSE: Residual Standard Error

From the coefficients of determination clearly no significant difference exists between the different proposed models for yield stress. Based on these findings, all models are evenly predictive. However, the coefficient of determination is a relative measure to test lack-of-fit; it may result in the same value even though large discrepancies exist between the considered models. It is therefore better to apply other statistical techniques; one of the

easiest methods is an investigation of the plot of measured versus predicted values. Here, the stress is considered as output of the rheological model. For the three models the results are shown in Figure 7.11; again, no large differences are observed though.

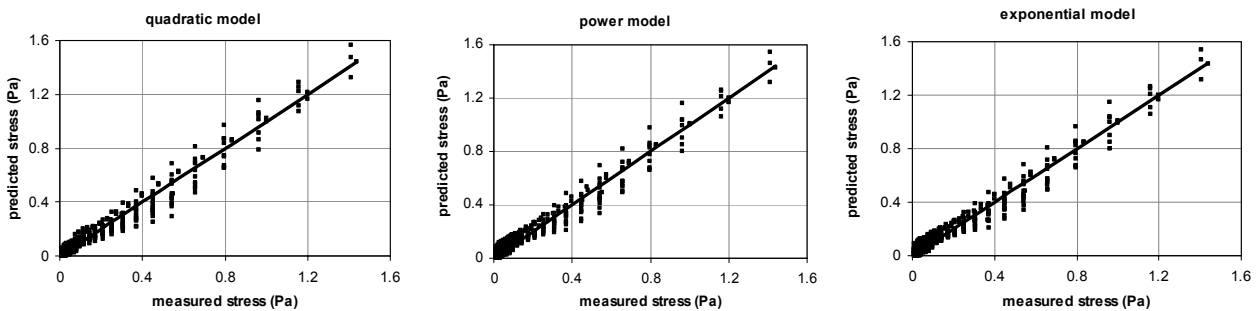


Figure 7.11 Comparison between measured and predicted stresses for the quadratic (left), the power (middle), and the exponential (right) model

To identify the most predictive and least complex model, different selection criteria may be used from literature. As presented here, they are all based on the Sum of Squared Errors SSE and account for the model complexity by the number of parameters p . The investigated criteria may be written as (Dochain & Vanrolleghem, 2001):

$$N \ln \left(\frac{SSE}{N} \right) + \alpha(N, p)$$

Here, N is the total number of data points. Different complexity penalty functions α may be used (Lindsey, 1996; Dochain & Vanrolleghem, 2001), for instance,

Akaike's Information Criterion (AIC):	$\alpha(N, p) = 2p$
Bayesian Information Criterion (BIC):	$\alpha(N, p) = p \ln(N)$
LILC:	$\alpha(N, p) = p \ln(\ln(N))$

In the end, the model structure with the smallest criterion value is selected. For the three investigated model structures the values of the criterion are given in Table 7.4. Although the relative differences between the values are small, the absolute values of the criterion need to be interpreted. Hence, the exponential model shows a slightly better performance than the other two. Although the quadratic model has a parameter less to estimate, its lower complexity does not compensate for its lack-of-fit. The exponential and power models have almost equal model selection criterion values. The exponential model, however, does not predict a zero yield stress at zero solids concentration. Therefore, the power model and not the exponential model is selected.

Table 7.4 Values of selection criteria for model discrimination

	$\tau_0 = \beta_1 X^2$	$\tau_0 = \beta_1 X^{\beta_2}$	$\tau_0 = \beta_1 e^{\beta_2 X}$
<i>AIC</i>	-2155	-2195	-2198
<i>BIC</i>	-2140	-2176	-2178
<i>LILC</i>	-2156	-2196	-2199

Hence, to summarise, the overall rheological model as implemented in Fluent is

$$\tau_{ij} = \left[\frac{\tau_0}{\dot{\gamma}} (1 - e^{-m\dot{\gamma}}) + K\dot{\gamma}^{n-1} \right] \dot{\gamma}_{ij} \quad (7.7)$$

with the following constitutive relations for yield stress and consistency index (and corresponding parameter values from Table 7.3):

$$\begin{aligned} \tau_0 &= \beta_1 X^{\beta_2} \\ K &= \mu_w + \beta_3 X^2 \end{aligned}$$

7.2.3 Effect of rheology on settling tank performance

To identify the effects of different rheological models on settling tank performance, CFD simulations were conducted. The settling tank investigated in Chapter 5 was utilised, and operated at an inlet solids concentration of 2 g/l. Zeolite improved the solids settling properties; although zeolite may affect rheology as well, this influence is not considered here. Four rheological models were compared by steady-state solids concentration, axial and radial velocity profiles. Firstly, the Bingham model (Equation 7.5) as used by Lakehal *et al.* (1999) was applied. Whereas they utilised the model parameters at an inlet solids concentration of 3.2 g/l, the parameters applicable to inlet concentrations of 2 g TSS/l were taken from Dahl (1993). Secondly, the effect of the absence of yield stress was investigated by using the model of Bokil (Equation 7.6). A constant water viscosity was also considered in the comparison to study the impact of the fluid consistency index as compared to the model of Bokil. Finally, the model proposed in this dissertation (Equation 7.7) is confronted with the others to reveal any flow discrepancies.

Similar to Chapter 5, simulations incorporated the k - ε turbulence model, and applied time-marching to reach steady state. A mass balance checked the fulfilment of the steady-state condition over the entire settling tank. Due to slow solids compression phenomena simulations were interrupted prior to (full) steady state. The error retained was below 2.5% of the theoretical inlet solids flux. Note that the error varied between +3% and -3% for cases where the solids blanket resided near the free water surface; periodic solids washouts by gravity waves made a stationary state impossible.

The outcome of the simulation study is shown in Figure 7.12. From Figure 7.12 (top) a Bingham fluid with the rheological parameters of Dahl (1993) clearly results in deviating blanket elevations. This behaviour is obviously linked to the artificially high yield stress as demonstrated in Figure 7.10 (bottom). The proposed model also employs a yield stress but it differs from the Bingham model of Dahl in two aspects; (i) the yield stress is much lower, and (ii) the model structure enables a very high, but finite, viscosity at low shears whereas the Bingham model of Dahl shows an infinite viscosity at zero shear (see e.g. Figure 7.7). Hence, the lower yield stress applied results in a low blanket elevation. Lastly, the Bokil model and

the constant water viscosity, both without any yield stress, lead to low blanket elevations as well.

The elevation of the solids blanket significantly impacts the location of the density current. Except the first transect where the density current may penetrate the solids blanket, the current always resides near the top of the blanket (Figure 7.12, middle). A flow along the bottom floor and towards the sump is clearly present as well. The radial velocity profiles are further characterised by a four-layer structure, i.e. the velocity changes direction four times.

Considering Figure 7.12 (bottom) a strong upward flow near the feed well ($r=2.6$ m) is observed for a Bingham fluid as described by Dahl. Due to the elevated solids blanket, the density current is forced by buoyancy to flow parallel and close to the feed well wall. Instead, when the blanket is positioned lower, the density current spreads out and reduced velocities are observed. Because of gravity waves, see Section 5.2.7, the axial velocity component of the density current (at a normalised height of ~ 0.2) changes direction when moving away from the tank's centre as seen in Figure 7.12 (bottom).

The solids blanket level depends both on rheology and gravitational forces. To explain this, consider a fluid stationary flowing in a laminar way on a sloped floor and with a free discharge at its down-end. In this respect, Figure 7.13 shows the flow situation for a Bingham fluid. Only gravitational and viscous forces are considered; normal and shear stresses vanish at the solids blanket-supernatant interface (Hunt, 1994). As shown in Appendix F the steady momentum balance equation over a sludge parcel may be written as

$$\tau = \Delta\rho g \sin \beta x \quad (7.8)$$

where β and x are the floor slope and the depth measured from the interface respectively. The density difference may be calculated by the solids concentration present and the formulae from Appendix C. Equation 7.8 can subsequently be utilised to compute the velocity profiles for both Newtonian (Figure 7.14, left) and Bingham (Figure 7.14, right) fluids. The mathematical derivations can be found in Appendix F as well. Whereas the velocity increases with the height above the floor for a Newtonian fluid, the velocity stabilises at a plug flow velocity for Bingham fluids (Liu & Mei, 1989; Piau, 1996; Huang & Garcíá, 1997). Here, the viscous stress is below the yield stress and no velocity gradients exist. The depth of this plug flow region measured from the solids blanket-supernatant interface is computed by means of Equation 7.8 (see Appendix F) and clearly depends on the solids concentration, the floor slope and the yield stress. In practice however, this yield depth is very small, i.e. ~ 8 mm for the sludge investigated in this research. Hence, the yield depth does not pose any stringent restriction on the fluid velocity increase with height. Due to the high fluid consistency index, however, a Bingham fluid flows considerably slower than water. As demonstrated in Figure 7.14, increasing solids concentrations enhance both gravitational and viscous forces, but the latter increases more than proportional compared to the gravitational force. Hence, the flow velocity reduces for the Bingham fluid. In case of water, higher solids concentrations only enlarge the density difference since the fluid consistency index is fixed. Consequently, the velocity increases.

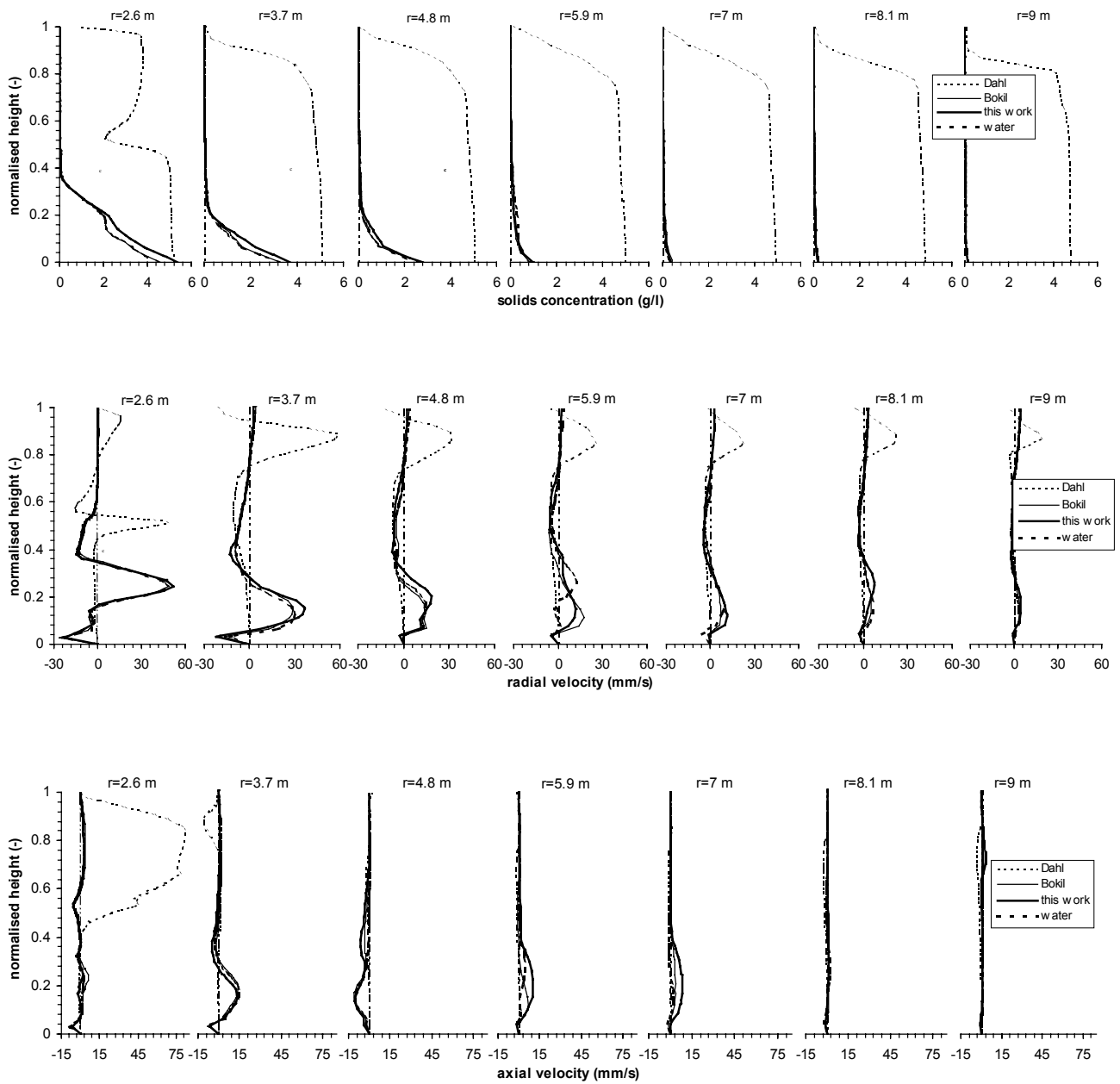


Figure 7.12 Comparison of four rheological models, i.e. Bingham, Bokil, water and the model proposed in this work, for zeolite-treated sludge by means of solids concentration (top), radial velocity (middle) and axial velocity (bottom) profiles. The profiles are shown at seven radial distances r measured from the centre. They all situate outside the feed well. The height above the bottom floor is normalised by the local depth

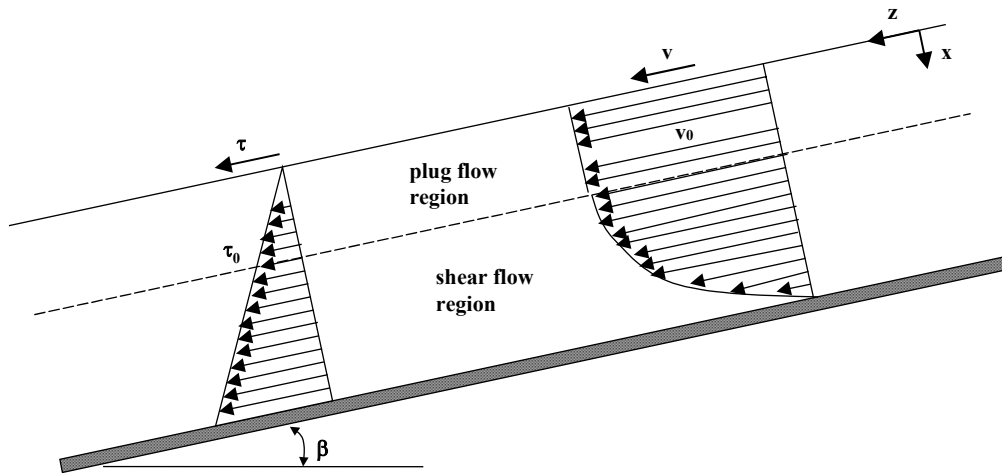


Figure 7.13 Viscous (Bingham) flow on top of a sloped floor

In Figure 7.14 (left), water velocities increase to unrealistically high values for observed solids blanket depths of, for instance, one meter. Indeed, velocity measurements in secondary settling tanks show a laminar and weak flow in the solids blanket and near the bottom floor (Kinnear & Deines, 2001). Simulations as shown in Figure 7.12 further confirm the presence of low velocities in the blanket. The latter may be attributed to two causes. Firstly, the density current near the surface of the solids blanket has the opposite direction of the bottom flow. Hence, they counteract each other, and the density current thus restricts the development of the bottom flow velocity profile. Because the mathematical derivation in Appendix F assumes no momentum transfer at the blanket-supernatant interface, the effect of the density current is unaccounted for. Secondly, in practice, no free discharge of sludge occurs in the secondary settling tank. Because of the fixed underflow rate, the discharge is constrained which imposes a force opposite to the gravitational flow direction. This leads to reduced flow velocities and the occurrence of laminar flow.

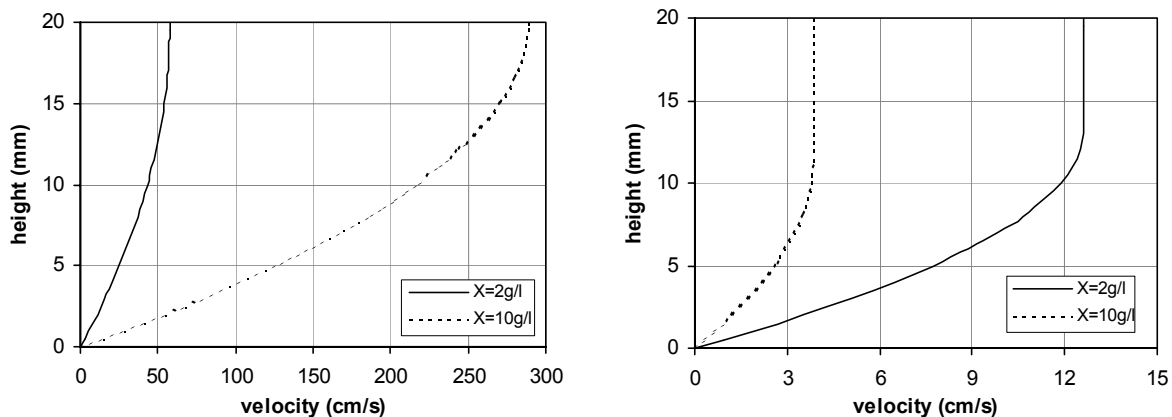


Figure 7.14 Velocity profiles for Newtonian (left) and Bingham (right) fluids on a sloped floor and as function of solids concentration X . As Newtonian fluid water is utilised; the Bingham parameters used are taken from Table 6.2

From the above, the flow along the bottom floor is thus clearly maintained at a low velocity by boundary conditions, i.e. boundary-related forces counteract the gravitational force. In this respect, the yield depth becomes more important as the resulting force reduces (Figure 7.15). Although the actual force cannot be computed from the prevailing velocities, it is hypothesised that this increase in yield depth (besides the high fluid consistency index) is at the origin of the low pseudo-plug flow velocities in the solids blanket (see e.g. the radial velocity profiles for Dahl rheology in Figure 7.12 (middle)). As a result, the shallow shear flow region only leads to a small velocity at the yield depth; it is this velocity that is maintained throughout the rest of the solids blanket. Since the yield depth depends on the yield stress it is clear that the artificially large yield stress as applied by Dahl results in an elevated solids blanket. The proposed model considers a more moderate yield stress resulting in lowered solids blankets; they are still higher than the corresponding simulations with the viscosities of Bokil and water though.

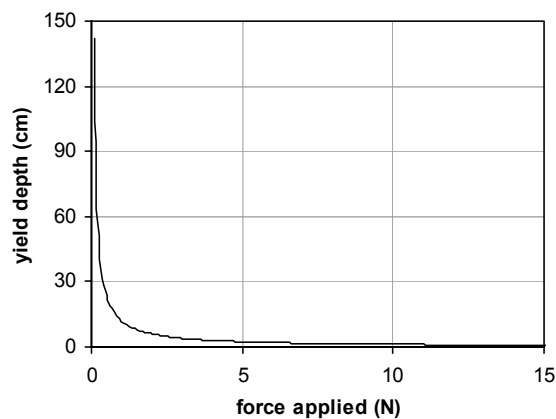


Figure 7.15 Yield depth as function of force applied

Summarised, a Bingham fluid leads to reduced solids discharges to the sump resulting in a piling up of solids in the main settling tank volume. For the Newtonian fluids discussed, this bulk (gravitationally induced) advective transport is much larger. As long as no clarification failure occurs, the same solids concentration range is covered for all simulations independent of the rheological model used. Whereas Bingham rheology results in an underflow concentration of ± 5.5 g TSS/l and a blanket rise, the other models lead to solids concentrations of ± 6.5 g/l without a blanket rise. The question thus arises why the solids compression in the entire settling tank is not equal for the different rheological models. Indeed, the settling function identical for all cases also tries to empirically model solids compression. In a 2D model however, besides the settling flux, also advective bulk transport occurs. Whereas the settling fluxes equal for all simulations, the advective bottom transport flux differentiates the simulation cases; rheology indeed influences the gravity (advective) flow along the floor as discussed above. When no yield stress is considered, the solids flow along the bottom and are discharged as a *waterfall* into the sump (Figure 7.16, left). While gravitationally flowing to/into the sump, the solids concentration increases by the solids settling influx. The concentration is therefore higher near the wall than at the inner section of the sump. The higher bulk density consequently induces the waterfall effect that primarily contributes to the underflow solids mass flux. For "strong" Bingham sludges with an

observed solids overflow, this bottom flow is weak and the underflow flux consists of contributions from the entire cross-sectional area of the sump (Figure 7.16, right). Starting with a tank filled with only water a bottom flow is observed independent of the rheological model utilised. Increasing solids concentrations on the floor (by settling), however, increase the yield stress of Bingham fluids. The bottom flow velocity reduces and, hence, the underflow flux originates from less viscous regions. As a result, more less thickened sludge is discharged from close to the tank's centre line. In this respect, Figure 7.12 (middle) clearly shows that the bottom flow velocities are $\pm 25\times$ larger for Newtonian fluids as compared to the Bingham fluid.

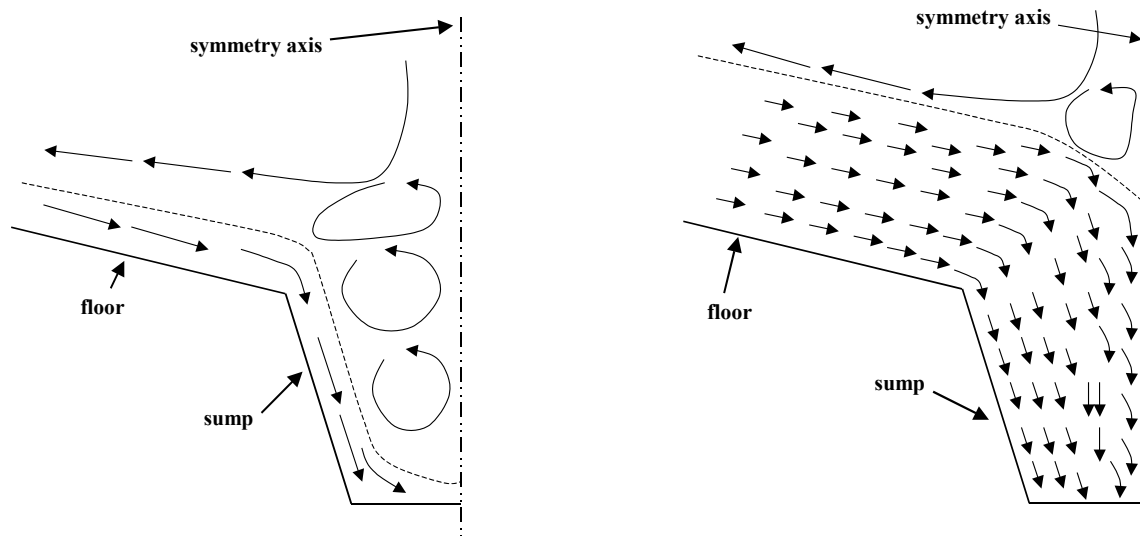


Figure 7.16 Scheme of velocity field near sump for rheologies without (left) and with (right) yield stress. Only half a cross-section of the sump is shown

The underflow solids concentration is therefore assumed to originate from the advective bottom flux. Hence, the local solids concentration is directly related to the rheological model since the latter largely determines this advective transport.

According to Equation 7.8 and the deduced velocity profiles, the solids density co-determines both the bottom flux and the yield depth. From the analysis, discrepancies should therefore be observed when comparing zeolite-treated sludge with untreated sludge by their density difference. Steady-state simulations for untreated sludge are shown in Figure 7.17.

In this situation, both the Dahl and proposed rheological models result in elevated solids blankets. They even reach the effluent weirs and solids from the blanket are discharged directly into the effluent stream. Apparently, the reduced buoyancy cannot compensate the viscous forces; even the reduced yield stress in the proposed model cannot avoid the blanket to rise. Again, the density current leaves the feed well and bounces off the stratified solids blanket towards the free surface (Figure 7.17, bottom). Instead, rheological models without yield stress lead to shallow solids blankets. From the simulations it seems that the fluid consistency index hardly has any influence on the observed profiles; even the increased consistency index of Bokil does not impact the profiles. Instead, a small yield stress already seems sufficient to result in a blanket rise. Whether rheology is indeed the cause of elevated solids blankets may be further demonstrated by a 1D 20-layer settling tank model

(see Section 2.1 for the model assumptions). Here, only the settling flux, and no rheology, is accounted for. Operational conditions identical to the CFD model are maintained. However, the tank geometry is not considered; only an average settling tank depth is applied. As observed in Figure 7.18 the blanket stays close to the bottom floor, which is in accordance to the rheology cases of Bokil and water in Figure 7.17. The 1D model does not return the same blanket heights as the 2D simulations because of (i) geometric simplifications, and (ii) the absence of rheology in the model whereas the 2D models incorporate (low) viscosities. The results stress again the impact of rheology on the solids blanket elevation.

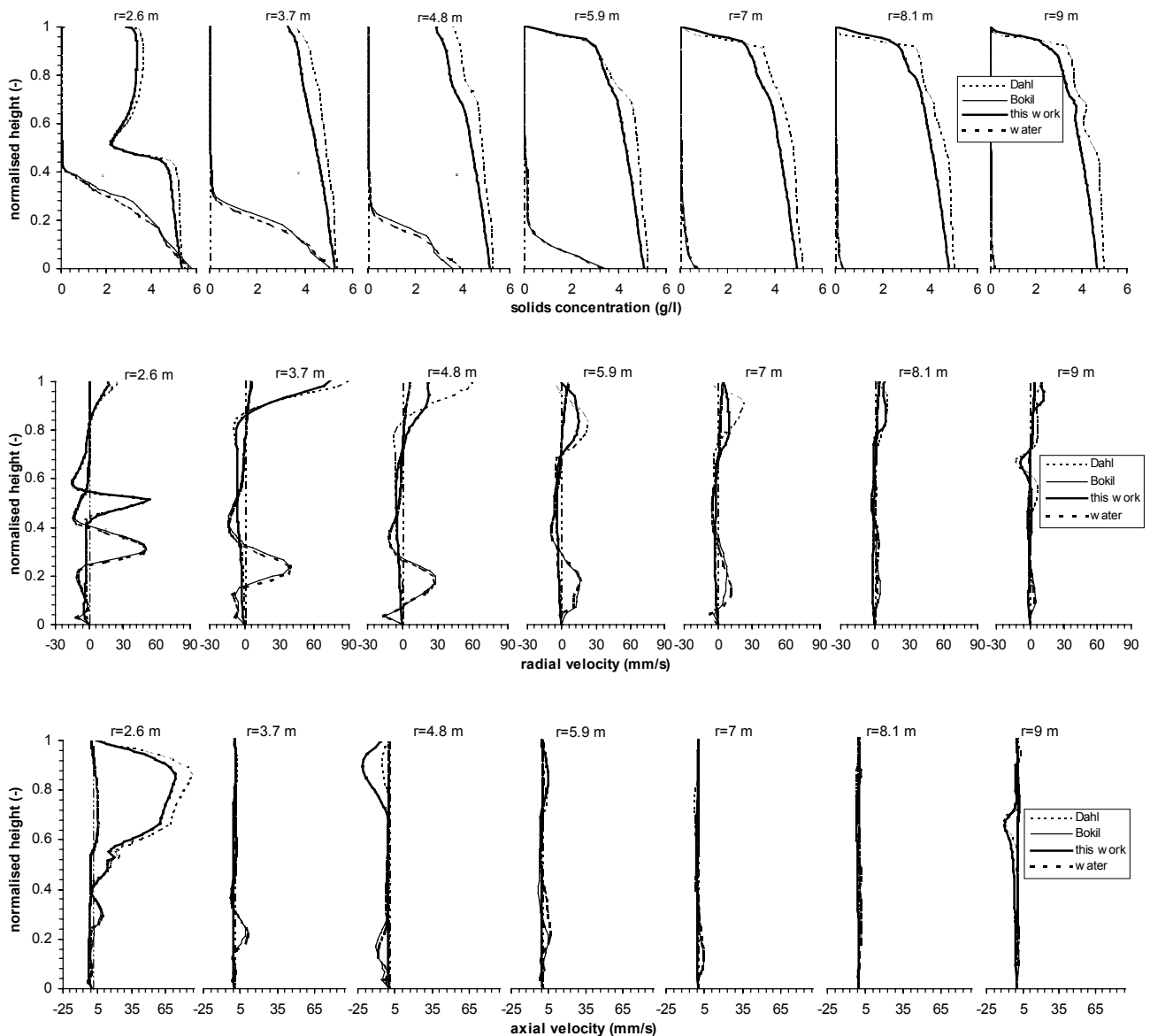


Figure 7.17 Comparison of four rheological models, i.e. Bingham, Bokil, water and the model proposed in this work, for sludge not treated with zeolite by means of solids concentration (top), radial velocity (middle) and axial velocity (bottom) profiles. The profiles are shown at seven radial distances r measured from the centre. They all situate outside the feed well. The height above the bottom floor is normalised by the local depth

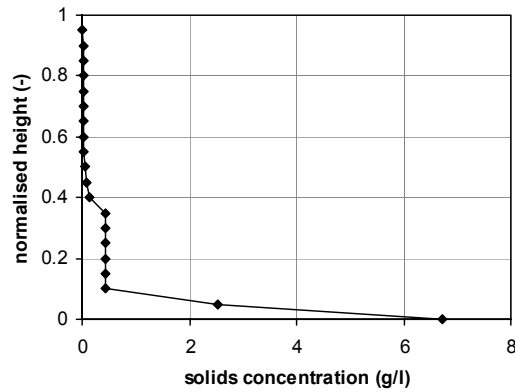


Figure 7.18 Solids concentration profile as obtained with a 1D 20-layer settling tank model (the feed is introduced at a normalised height of 0.35)

From Figure 7.17, one concludes that Newtonian fluids clearly enable an easy solids removal from the settling tank. Only the fluid consistency index may lead to more elevated solids blankets. The lower the consistency index, the higher the solids loading rates that can be handled by the tank without solids washout. To demonstrate this, Figure 7.19 shows the solids concentration profiles for two different inlet concentrations; the Bokil rheology relation and the viscosity of water are adopted as well. The increased solids concentrations stress the settling tank more, but, apparently, solids are discharged and compressed to such concentrations that an overload does not occur. The large fluid consistency index from the Bokil relation (see Figure 7.10, top) only leads to a slight increase of blanket elevation. A rheological model with yield stress would definitely result in solids washout. Consistency indices therefore only have a secondary effect on the solids blanket elevation.

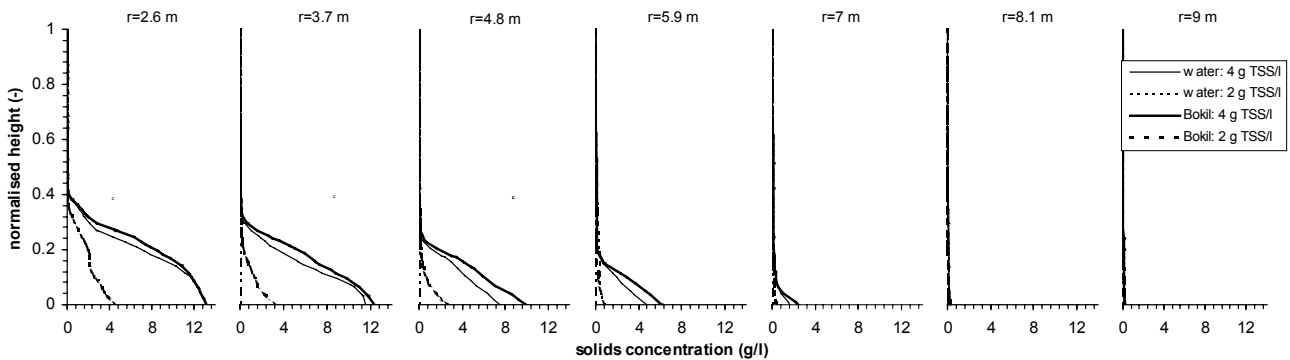


Figure 7.19 Comparison of solids concentration profiles for an inlet concentration of 2 g TSS/l and 4 g TSS/l. The Bokil viscosity relation and the viscosity of water are applied. The profiles are shown at seven radial distances r measured from the centre. They all situate outside the feed well. The height above the bottom floor is normalised by the local depth

7.3 Implications to settling tank modelling

Solids transport in a settling tank depends on two major parameters, i.e. hydrodynamics and floc characteristics. The latter incorporates both the structure and the colloidal properties

of the biological flocs. Inside the settling tank flocs are subjected to shear forces that result in floc aggregation and breakup. From a rheological point of view, the particle size distribution is important in the sense that it greatly influences the viscosity (Frankel & Acrivos, 1967; Brenner, 1974; Campbell & Crescuolo, 1982; Dabak & Yucel, 1987). In this respect, it is concluded from Section 7.1 that the magnitude and duration of the locally applied shear can have important consequences on the PSD and, hence, the viscosity as well. The presence of time-dependent thinning (thixotropy or rheomalaxis) may thus be important to consider in settling tank modelling.

From structural decay testing (Section 7.1.3) it is believed that floc breakup is (partly) responsible for the time-dependent thinning behaviour. To recover the original floc structure at low solids concentrations though, shear is needed to promote aggregation, i.e. orthokinetic aggregation. Instead, at very high concentrations, the negligible interparticle distances allow flocs to aggregate and orthokinetic aggregation is not essential. As a result, time-dependent thinning depends on the rates of the processes of aggregation and floc breakup. When this dynamic interaction is in equilibrium, no time-dependent thinning effects are to be expected. Consideration of this time-dependent thinning in settling tank modelling depends on the local shear magnitude and its corresponding time of exposure. Typically, low shears exist in the solids blanket (from 2D numerical simulations performed in this work, and based on *in situ* measurements by Kinnear & Deines (2001)) that lead to time-dependent thinning characterised by large time constants. On the other hand, high solids concentrations result in fast aggregation dynamics (Peng & Williams, 1993). In Chapter 6 the PSDs in a settling tank were discussed and observed to be invariable at high solids concentrations. For the settling tank investigated, two possible causes for the invariable PSDs in the solids blanket were hypothesised: (i) the high solids concentration and not the shear determines the particle aggregation, and (ii) zeolite dosed makes flocs unsusceptible to breakup (by strengthening the floc structure) and to aggregation (because flocs already have a large size). The invariable PSD thus results in a constant viscosity (at constant solids concentration) and time-dependent thinning would not be observed. Experiments conducted at similar blanket concentrations, but without zeolite dosing, revealed that structural recovery did not occur. In the recovery period of the experiment, however, no flow was present while local small shears do occur in the solids blanket, which intensify aggregation and result in fast PSD dynamics. This phenomenon and the use of zeolite lead to invariable PSDs that, presumably, avoid any consideration of time-dependent thinning to occur in the solids blanket.

Summarising, at least for the settling tank investigated, it is believed that time-dependent thinning should *not* be considered for rheological modelling of the solids blanket of settling tanks. Near and above the blanket, solids concentrations are considerably lower than below such that the apparent viscosity approaches the viscosity of water. However, the problem is the proper determination of viscosity at such low concentrations. Further, at these concentrations PSDs, shear history and solids settling greatly influence the rheological results and definitely needs further research.

Low-shear stress measurements revealed that a true yield stress does not exist, i.e. zero shear rates for stresses below the yield stress do not occur. The yield stress as defined

here, and described in literature, is the stress at which an abrupt change in viscosity occurs; high viscosities prevail at low shears. To account for this rheological behaviour in settling tank modelling a modified and calibrated Herschel-Bulkley model (Equation 7.7) was adopted. The dependency of yield stress and consistency index on the solids concentration was described by a power and quadratic model respectively. Section 7.2.3 discussed how rheology affects solids transport. The Oxley case study indicates that rheologies described by water viscosity, Bokil's model and the model proposed in this dissertation result in the observed solids blanket behaviour, although they do not include any possible additional effects of zeolite on rheology. However, as soon as the gravity force reduces by excluding the effect of zeolite, a blanket rise is observed for the modified Herschel-Bulkley model. This is clearly caused by the very high apparent viscosity at low shears given by the proposed rheological model. The fluid almost acts as if a yield stress is present. Because this *pseudo* yield stress is very small, it is therefore reasoned that the occurrence of blanket rise is very sensitive to viscosity variations at low shear. Hence, accurate shear stress and shear rate measurements to calibrate the rheological model are crucial. More research is definitely needed to scrutinise the necessity of a (pseudo) yield stress (since Bokil's model and the viscosity of water keep the blanket low, in accordance to 1D multi-layer settling tank models frequently used in practice for solids blanket dynamics), although experiments reveal the existence of such high viscosities at low shears.

7.4 Conclusions

This chapter was dedicated to the rheological modelling of sludge. Research has been performed to more accurately and more representatively measure viscosities. In this respect, the consideration of time-dependent thinning becomes important when measuring rheograms at high shear rates; increased shear rates indeed result in structural destruction of both flocs and suspension. Experiments to investigate rheomalaxis indicated that at least two structural levels exist for biological flocs. Depending on the flocs' history, i.e. their flocculation state, locally prevailing shear stresses in the settling tank destroy these floc structures to a large or small extent, and consequently, influence the sludge viscosity as well. Attempts to measure associated rates of destruction have been conducted but failed due to experimental and technical constraints. However, both here and in Chapter 6, it was hypothesised that invariable PSDs at high solids concentrations result from (i) zeolite dosing and/or (ii) the combination of high solids concentrations and low shears. The resulting conservation of floc structure and PSD thus makes modelling of time-dependent thinning in the solids blanket unnecessary.

Low-shear measurements further demonstrated that a true yield stress does not exist. A modified Herschel-Bulkley model has therefore been proposed and calibrated for three municipal wastewater treatment sludges. The dependency of yield stress and consistency index on the solids concentration was described by a power and quadratic model respectively. The proposed model especially focuses on the low-shear region, which is important in settling tanks, but is applicable to higher shears as well. Indeed, CFD simulations have shown that shear rates go well below 1 s^{-1} in the solids blanket. Calculations of shear based on the work of Kinnear & Deines (2001) confirm this.

The question only remains whether this adopted model performs better than other rheological models and returns better predictions of solids concentration and velocity fields. Comparison with frequently applied models in literature, i.e. Dahl (1993), Bokil (1972) and water, reveals that increased viscosities at very low shear rates may be detrimental. In this respect, models applying a yield stress are to be mentioned; the higher the yield stress becomes, the more pronounced the solids blanket rises. Although the rheological model proposed in this work does not contain a true yield stress (which makes it numerically easier to use), it inherently incorporates high viscosities at low shears. When gravitational forces become too small, e.g. in the absence of zeolite, this model leads to elevated blankets too. In such situations solids slowly move along the bottom floor and, hence, accumulation occurs in the main settling tank part. From the simulations performed it seems that Newtonian fluids, even with increased consistency indices, still result in lower blankets. For the case study of Chapter 5, with zeolite dosage, Newtonian fluids (water and Bokil) and the model proposed in this research predicted the solids blanket correctly. However, deciding which rheological model performs better depends on different variables of which the particulate properties are very important. As observed in this research, several models may result in similar flow fields. The results presented indicate the importance of rheology, its complexity and the fact that more fundamental research is needed to correctly model momentum transport in the solids blanket. To adequately measure viscosities rheometers appropriate for (settling) sludge should be developed.

8

Conclusions and Perspectives

The introduction of this PhD dissertation made clear that many factors influence the performance and capacity of settling tanks. They may be categorised as biological, physico-chemical and hydraulic influences. To account for them in terms of process operation and design, mathematical models may be utilised. In this respect, Computational Fluid Dynamics (CFD) enables the investigation of internal processes, such as local velocities and solids concentrations, to identify process inefficiencies and resolve them. Although these complex models demand for considerable computational power, they may become an option for the study of process operation and control as computer speed increases. Nowadays, they mostly find applications in the world of settling tank design.

In this dissertation, a 2D CFD model for a secondary settling tank was set up. This 2D modelling approach has been frequently applied to settling tanks in literature. Here, attention was focused on submodels related to the solids transport to increase our process understanding and arrive at correctly predicting effluent solids concentrations. In this respect, the necessity to model Particle Size Distributions (PSD) and rheology was discussed by both experimental and CFD work. However, setting up a CFD model does not only incorporate particulate properties, but also the system's geometry and operational mode deserve attention; research was conducted on these aspects as well. Settled solids at the bottom of the settling tank can be transported to the sump both hydraulically and mechanically. To correctly model the fate of solids in the tank, consideration of the solids removal mechanism is needed. A 2D implementation complicates the modelling effort though. Obviously, any model should be confronted with reality to demonstrate its reliability. The validation exercise in this work included full-scale data such as solids concentration profiles. Whereas they validate the simulated solids concentration field, a tracer test revealed information about the flow pattern.

The next sections will discuss the main conclusions of the research conducted. Simultaneously, gaps in our understanding of certain physical processes are identified, and research perspectives are presented.

8.1 Particle size distributions (PSD)

Solids flow in the settling tank depends on many factors of which particulate properties, such as porosity and PSDs, are very important. At high solids concentrations, it is believed that hindered settling rates are independent of individual particle characteristics. Above the solids blanket, however, low concentrations prevail and discrete settling occurs. Here, floc sizes are very important as the smaller the floc becomes, the larger the drag is it experiences, and the slower the floc settles. Process optimisation may therefore consist of stimulating particle aggregation. Evaluation of any design modification improving flocculation is experimentally difficult to perform *in situ*. In this respect, so-called Population Balance Modelling (PBM) may be useful to investigate the effect of different operational conditions on the PSD dynamics. Calibration and validation of the model demand again for *in situ* experiments though. However, particle sizers able to measure *in situ* are rare.

In this respect, the Focused Beam Reflectance Method (FBRM) enables the *in situ* measurement of PSDs using laser light reflection by particles. The major advantage of the FBRM is the large operating range of solids concentration, i.e. up to 50 g/l. Due to its measurement principle, PSDs of both inorganic and sludge suspensions differ from those obtained by laser diffraction and image analysis. From preliminary experiments, it was concluded that the focal point position of the laser largely influences the obtained PSD; the focal point should be taken near the optical window. Obtained PSDs further required low-pass filtering to eliminate peak counts with sharp gradients, i.e. particles sticking to the window occurred due to the low flow velocities at the measurement location. Future probe locations should limit this problem though. The vertical probe positioning should therefore be abandoned and a horizontal position preferred. Because particles settle perpendicular to the laser beam, more particles are scanned and the chance of particle sticking is reduced. Also a small mixer in front of the optical window could be useful; however, care should be taken not to disturb the local flocculation dynamics.

Applying the FBRM to a secondary settling tank at Oxley Creek (Australia) WWTP revealed an invariable PSD inside the feed well. This obviously questions the role of the feed well as a flocculator. Although concluding measurements are necessary, two parallel hypotheses may be put forward to explain this, i.e.

- the dosed zeolite strengthens the floc structure making the zeolite-biomass composite flocs unsusceptible to breakup in the aeration tank and the transport piping. Because of their already large size, the composite particles are believed not to aggregate anymore in the settling tank. As a result, identical PSDs are observed in the feed well;
- the inlet piping and momentum diffuser are sufficient for floc aggregation. Whether floc aggregation prevails in the piping depends on the flocculation state of sludge in the aeration basin.

Note that the feed well still may be important to cut short-circuit flows between the settling tank's inlet and outlet, and prevent any penetration of recirculating flows into the well.

Inside the solids blanket, the same PSD prevailed as in the feed well. Again, possible causes for the invariable PSDs observed in the solids blanket may be twofold: (i) a zeolite core strengthening the floc structure eliminating the need for aggregation and, (ii) the high solids concentration. The higher the solids concentration, the higher the floc aggregation rate is. Moreover, due to the prevailing low shears, i.e. they go down well below 1 s^{-1} (from 2D numerical simulations performed in this work, and based on *in situ* velocity measurements of Kinnear & Deines (2001)), the floc breakup rate is restricted resulting in large flocs. Floc breakup is therefore virtually non-existent, and both zeolite and solids concentration dominate the PSD dynamics.

Above the solids blanket, PSDs clearly consisted of smaller particles due to selective sedimentation of large particles. More PSD dynamics could be observed as well, as floc washout, blanket rise or blanket scouring occurred when the inlet flow rates varied. Here, modelling the floc aggregation and breakup by means of PBM could be interesting.

Lyn *et al.* (1992) included particle aggregation dynamics in a primary settling tank CFD model to compute discrete settling velocities; floc breakup was neglected in their research however. For their operating conditions at least, only small effects of orthokinetic aggregation on solids removal efficiency were observed. The secondary settling tank investigated in this work operated at much higher solids concentrations, hence, small changes in solids removal efficiencies may result in large improvements/deteriorations of effluent quality. The observed PSD dynamics above the solids blanket can thus have a significant impact on effluent solids concentration and should therefore be modelled.

The above conclusions, however, must be treated with care since zeolite was used to condition the sludge. Therefore, more research should be performed on typical wastewater treatment sludges in order to draw more general conclusions. Such studies are currently ongoing at the department and focus on both the modelling (Nopens *et al.*, 2002; Nopens & Vanrolleghem, 2003) and the experimental investigation (Govoreanu *et al.*, 2002) of how environmental conditions affect the PSD.

8.2 Sludge rheology

Particulate properties not only affect discrete settling, but they also determine the rheological behaviour of the suspension. Viscous stresses are very important for the transport of momentum and, hence, they can alter the velocity field. As a result, solids transport will be affected as well.

Because existing rheological models significantly differ in their structure and parameter values giving rise to completely different rheological behaviour, research was conducted on three municipal WWTP sludges. For this exercise, a rotational stress-controlled Bohlin CVO rheometer allowed low-shear viscosity measurements. It was found that the experimental layout largely influenced the rheograms. In this respect, solids settling in the rheometer should be avoided by adopting high solids concentrations. To overcome this issue, Dick & Buck (1985) constructed a rheometer with a continuous upward flow to counteract sedimentation. In this research, however, such device was not available.

Phenomena such as time-dependent thinning become important when measuring rheograms at high shear rates; increased shear indeed results in structural destruction of flocs and suspension. For rheological modelling it is important to know whether this destruction is reversible and the original floc structure can be obtained again. Experiments on irreversible time-dependent thinning (rheomalaxis) indicated that at least two structural levels exist for biological flocs. This is in accordance to Wahlberg *et al.* (1992) and Jorand *et al.* (1995) stating that flocs show a structured build-up with several levels and different resistances to shear. Depending on the floc's history, i.e. its flocculation state, locally prevailing shear stresses in the settling tank destroy the floc structure to a large or small extent and, consequently, influence the sludge viscosity as well. Attempts to measure the associated rate of destruction have been conducted but failed partly due to experimental and technical constraints. Models of time-dependent thinning in settling tanks should include a dependency on the local shear magnitude and its corresponding time of exposure. Typically, low shears exist in the solids blanket leading to time-dependent thinning characterised by large time constants. On the other hand, high solids concentrations result in fast aggregation dynamics (Peng & Williams, 1993). In this respect, it is noteworthy that the PSDs in the Oxley Creek settling tank were observed to be invariable at high solids concentrations. For the settling tank investigated, two possible causes for the invariable PSDs in the solids blanket were hypothesised: (i) the high solids concentration and not the shear determined the particle aggregation, and (ii) zeolite dosed made flocs unsusceptible to breakup (by strengthening the floc structure) and to aggregation (because flocs already have a large size). The invariable PSD thus results in a constant viscosity (at constant solids concentration) and time-dependent thinning would not be observed. Experiments conducted at similar blanket concentrations, but without zeolite dosing, revealed that structural recovery did not occur after floc breakup though. In the recovery period of the experiment, however, no flow was present while in the solids blanket local small shears do occur, which intensify aggregation and result in faster PSD dynamics. This phenomenon and the use of zeolite led to invariable PSDs that, at least for this case study, avoid any consideration of time-dependent thinning to occur in the solids blanket. Near and above the blanket, solids concentrations are considerably lower than below such that the apparent viscosity approaches the viscosity of water. Here, the proper determination of viscosity becomes problematic. At these low concentrations PSDs, shear history and solids settling largely influence the rheological results and definitely need further research.

In literature, different rheological models are utilised for CFD purposes, and consider the sludge as Newtonian or non-Newtonian fluids (with yield stress). Whereas Dahl (1993) obtained model parameters from fitting simulated to observed velocity profiles in a settling tank, Bokil (1972) and Dick & Buck (1985) extracted their parameters from rheograms. Large differences in the reported yield stresses and fluid consistency indices, however, question the general applicability. Rheological experiments therefore aimed at finding a good model structure and appropriate parameters.

Barnes & Walters (1985) described how yield stress only results from the insensitivity of the rheometer applied. For that reason, low-shear stress measurements have been conducted and revealed that a true yield stress indeed does not exist, i.e. zero shear rates for stresses below the yield stress do not occur (Figure 8.1). Consequently, yield stress was defined as the stress at which an abrupt change in viscosity occurs, i.e. viscosities of 100-1000x larger than

those prevailing at stresses beyond the yield stress. The applicability for sludge rheological modelling of the widely used Bingham and Herschel-Bulkley models may thus be questioned because (i) they contain a yield stress, and (ii) very low shears prevail in the solids blanket. Rheological measurements on three different municipal WWTP sludges resulted in a modified Herschel-Bulkley model:

$$\tau_{ij} = \left[\frac{\tau_0}{\dot{\gamma}} (1 - e^{-m\dot{\gamma}}) + K\dot{\gamma}^{n-1} \right] \dot{\gamma}_{ij}$$

where τ_{ij} and $\dot{\gamma}_{ij}$ are the tensors for stress and strain rate respectively. Note that shear rate is the component of the strain tensor describing velocity gradients perpendicular to the velocity direction. The magnitude of the strain rate is denoted as $\dot{\gamma}$. Further, τ_0 is the yield stress, m the stress growth exponent, K the fluid consistency index, and n the flow behaviour index. Although it still contains a yield stress, the growth of stress as shear rate increases is controlled by an exponential correction term. Papanastasiou (1987) originally introduced this adaptation to deal with numerical inconsistencies when going from one-dimensional to multi-dimensional flows; here, its physical relevance has been justified.

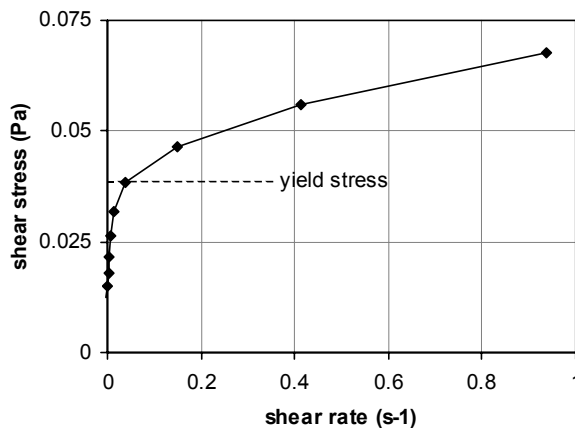


Figure 8.1 Rheogram demonstrating the non-existence of yield stress

The question thus remains whether this proposed model performs better than other rheological models and returns better predictions of solids concentration and velocity fields. Comparison with frequently applied models in literature, i.e. Dahl (1993), Bokil (1972) and water, revealed that increased viscosities at low shear rates might be detrimental for settling tank performance. In this respect, models applying a true yield stress are important; the higher the yield stress, the more pronounced the solids blanket rises. Although the rheological model proposed in this work does not contain a true yield stress (which makes it numerically easier to use), it predicts high viscosities at low shears. When vertical (downward) forces on flocs become too small, e.g. in the absence of zeolite, this model leads to elevated blankets as well. In such situations solids slowly move along the bottom floor and, hence, accumulation occurs in the main settling tank part. Simulations showed that Newtonian fluids, even with increased consistency indices, result in low blankets. Consequently, it is concluded that the fluid consistency index only exerts a secondary effect on the solids transport. On the other hand, yield stresses or very high viscosities (100-1000x larger than

for stresses beyond the yield stress) at low shears largely determine the solids blanket behaviour.

For the case study of Chapter 5, with zeolite dosage, Newtonian fluids (water and Bokil) and the model proposed in this research correctly predicted the solids blanket. However, deciding which rheological model performs better depends on different variables of which the particulate properties are very important. As observed in this research, several models may result in similar flow fields. The results, however, indicate the importance of rheology, its complexity and the fact that more fundamental research is needed to correctly model momentum transport in the solids blanket. To adequately measure viscosities rheometers appropriate for sludge should be developed as well.

8.3 Development of a CFD model

The development of a secondary settling tank CFD model was conducted by means of a case study. It concerned a medium-size circular tank at Oxley Creek (Australia) WWTP with a steep bottom floor and a scraper as solids removal mechanism. The commercial software utilised was Fluent (Fluent Inc., UK).

The transport of the slurry in the tank was modelled by means of the Navier-Stokes equations, supplemented with the k - ε turbulence model. To describe the important process of sedimentation, the experimentally calibrated Takács solids settling velocity relation was incorporated in an additional solids transport equation. The model was completed with the modified Herschel-Bulkley rheological submodel as mentioned in Section 8.2.

To restrict the computational demands, the circular settling tank was modelled in only two dimensions. For similar reasons, the inlet pipe was omitted from the computational domain. A geometric simplification of the inlet structure further decreased the computational mesh size. The domain finally obtained was meshed with triangular cells. An improperly meshed domain is known to influence the solution field and, therefore, different mesh sizes were investigated. For the flow field considered, the selected size resulted in 11516 cells and was a trade-off between numerical accuracy and computation time.

8.3.1 Modelling of the scraper

Modelling the scraper mechanism in 2D inherently poses some problems since its action is by definition 3D. To resolve this dimensionality problem, only radial influences were modelled. From geometric considerations and decomposition of the force exerted by the scraper on the fluid, it was possible to implement a submodel for the scraper's action. Because the scraper rotates, the latter was time and space dependent. Every 51 minutes the rectilinear scraper passed the modelled transect in 2.9 minutes; the more the scraper approached the centre, the smaller the radial velocity became. For a settling tank with similar geometry, Winkler (2001) performed 3D simulations and measurements of liquid velocities close to the scraper blade. His results showed good agreement with the computed scraper's radial velocity. Hence,

imposing this velocity at the location the scraper resides at the time instant considered seemed to be a good 2D approximation of the 3D flow with swirl, at least for the radial velocity component. Initially, the scraper's movement was implemented in Fluent as an imposed velocity, which temporally and spatially changed according to the scraper location. However, this approach led to numerical instabilities probably due to a too coarse mesh. The scraper was therefore implemented as a momentum source introducing a positive/negative momentum depending on whether the scraper moved (i) faster/slower than the (local) free flow, and (ii) in the same direction as the local liquid. Although small deviations to the imposed scraper velocity occurred, this implementation technique could be used as a first approximation to investigate the effect of the scraper on both solids transport and flow field.

In this respect, scenario analyses with the modified Herschel-Bulkley rheology and the rheology of water were conducted. Simulations clearly demonstrated that the scraper had a negative impact on the settling tank performance when applying the modified Herschel-Bulkley model, i.e. the solids blanket rose close to the free water surface and solids from the blanket escaped the settling tank. When adopting the very low viscosity of water, however, the solids blanket stayed near the bottom floor.

Whether the solids blanket rises depends on the flow field close to the bottom floor. When no scraper operated, a strong bottom floor flow current was observed which strongly depended on gravity and the sludge rheology. The scraper passage, however, blocked this bottom flow for 2.9 minutes; it constrained the bottom flow discharge by counteracting the gravitational force. After the scraper had left the modelled transect, the sludge was expected to gravitationally re-accelerate and the solids blanket height should therefore decrease again. Two-dimensional simulations of the settling tank, however, showed this was only the case for water viscosity. For the modified Herschel-Bulkley model the bottom flow did not recover prior to the next scraper passage and, consequently, solids accumulated in the main settling tank volume. A possible cause for this rheologically induced flow pattern discrepancy was brought forward by Huang & García (1997). They investigated the flow behaviour of Bingham-plastic mudflows and concluded that the higher the yield stress, the faster the flow decelerates on a slope. In accordance to these fundamental calculations, sludge described by the modified Herschel-Bulkley rheological model accelerates slower than sludge characterised by the viscosity of water. Sludge flows in settling tanks are of course more complicated than the simple mudflow and, hence, demands for more fundamental research. Based on the above statements, it takes more time for the modified Herschel-Bulkley sludge to recover from flow disturbances. In this respect, measurements conducted by Winkler (2001) revealed that the scraper influences the velocity field for 12 minutes after it had passed by; a scraper operating at a similar circulation speed as investigated here was utilised. For the system studied in this dissertation, it took only 6 minutes for the sludge to re-accelerate when characterised by water viscosity; for the modified Herschel-Bulkley sludge the flow pattern even did not recover after 50 minutes.

However, in practice and shown by 3D simulations of Winkler (2001), the tangential velocity of the scraper is much larger than the radial component and may go up to 2-3 cm/s. This stirring creates large stresses avoiding the yield stress to express, i.e. the sludge acts more as a low-viscous fluid. To support these theories, however, more fundamental research on the

sludge rheology and the scraper's nearby flow field is required. Consequently, the 2D scraper modelling is not optimal and only 3D simulations or 2D models accounting for swirl may correctly incorporate the scraper action in CFD models. The scraper was therefore not included in the validation study conducted for the Oxley Creek plant.

8.3.2 Model validation

Finally, the simulated solids concentration and velocity fields were confronted with measurements in order to evaluate the model's prediction power.

Most validation studies in literature use boundary conditions being constant in time. Obviously, by omitting system dynamics, validation becomes much easier as compared to unsteady validation exercises (Imam *et al.*, 1983). Importantly, in this study a diurnally changing flow rate was dealt with during all validation studies. Of course, the inlet solids concentration changed accordingly.

Firstly, the solids transport model was validated. Pseudo-steady state solids concentration profiles were therefore measured at afternoon flow rates, which were the most stable that could be obtained. Simulations conducted with the prevailing flow rates returned a range of profiles between which the measured solids concentrations should be found for successful validation. For both high and low concentrations good agreement was found without any additional calibration. To validate the solids flow dynamics in the settling tank, effluent and underflow solids concentrations under dynamic inflow conditions were utilised. Both were well predicted and only the non-settleable solids concentration X_0 of the Takács settling velocity function had to be lowered for good effluent predictions. As X_0 was determined from batch-settling tests, it corresponded to the Dispersed Suspended Solids (DSS) concentration. Obviously, shear-induced flocculation possibly occurring in the settling tank increases the discrete settling velocity and, hence, decreases the non-settleable solids fraction. The obtained Flocculated Suspended Solids (FSS) concentration is thus expected to be lower than X_0 as determined from batch-settling tests. Consequently, a decrease of the non-settleable solids concentration seems plausible. In conclusion, the CFD model set up predicts the system almost exactly with respect to solids concentration provided a proper non-settleable concentration measurement can be performed.

The hydrodynamics of the settling tank were validated by Flow-Through Curves (FTC). Again, the validation was performed under dynamic inflow conditions. As tracer, LiCl was used and injected as a pulse at the surface of the momentum diffuser. Measurements were conducted at the underflow, effluent and at the water surface midway the bridge. Although the simulated FTCs showed features similar to the measured ones, a too fast system's response was observed for both underflow and bridge. Instead, the system responded too slowly at the effluent. Additionally, lithium peak concentrations were too high irrespective the sampling location. Discrepancies between measured and simulated FTCs were believed to be attributed to (i) an improperly simulated solids blanket evolution due to uncertain boundary conditions imposed at the inlet, and/or (ii) a too little simulated diffusion.

In this respect, other inlet solids concentrations have been adopted but they all failed to correctly simulate the observed FTCs. Varying the inlet solids concentration could not delay

the tracer peak of occurrence at the bridge location. An inlet concentration of 1.3x the concentration used in the other simulations led to a relatively good agreement between the simulated and observed FTC for the effluent location.

For better validations though, simulations should be conducted with models including 3D geometries. In this respect, Szalai *et al.* (1994) observed both a delay and decrease of tracer peaks when considering the 3D flow close to an inlet structure with deflector vanes. Turbulence should require more attention as well.

Whereas the predictive power of the CFD model still could be improved with respect to the velocity field, the solids distribution in the settling tank seemed to be well modelled. To conclude, future 2D simulations that account for swirl, 3D simulations and a proper turbulence model are believed to resolve the flow-through curve validation problems.

8.4 General conclusions

This dissertation is situated within the SediFloc project currently ongoing at the department. The ultimate goal of the project is to adequately model flocculation and deflocculation in the secondary settling tank, and accounting for all its hydraulic and physico-chemical influences. As a result, better predictions of effluent quality should be possible.

The conducted research focused on the modelling aspects of the project and aimed at the correct prediction of the flow and solids concentration fields in the settling tank by means of CFD. Whereas the Navier-Stokes equations described the flow behaviour of the slurry, submodels were needed to account for specific physical phenomena occurring in the settling tank. Four process characteristics influencing the solids removal were investigated, i.e.

- *Solids settling velocity*

Solids settling was modelled with the widely used Takács settling function. Laboratory batch-settling tests allowed its adequate calibration as was shown by the validation results of the case study. However, a proper measurement of the non-settleable solids concentration seemed essential to correctly simulate the effluent solids concentration. In this respect, the DSS/FSS test allows to study the impact of flocculation on this non-settleable solids fraction.

- *Particle size distributions*

Particle size distributions have been experimentally determined *in situ* and can be considered to be the first attempt ever in activated sludge systems. The plant investigated, however, did not show much PSD dynamics and an invariable PSD was found at high solids concentrations. More dynamics could be observed at low concentrations though, i.e. above the solids blanket. Here, modelling the PSD dynamics by means of PBM could be interesting. Important is that zeolite was dosed to improve the settling properties, and that non-conditioned sludge may behave differently. More research is therefore needed.

- *Rheology*

Sludge from different WWTPs has been experimentally investigated on its time-dependent rheological behaviour (time-dependent thinning) and indicated the existence of multi-levelled structures for sludge flocs. A new rheological model has been proposed as well. It is especially applicable at the low shears that prevail in the solids blanket. CFD simulations revealed that different, widely used rheological models result in different flow patterns and solids concentration distributions. Therefore, more research should be conducted on the proper model structure and its parameters. For this purpose, rheometers appropriate for (settling) sludge should be developed.

- *Scraper mechanism*

Due to its mixing and/or conveyance capacity of solids toward the sump, a 2D model of the scraper has been proposed. However, it had to be excluded from the overall settling tank model of the case study because its inclusion resulted in unrealistic solids blanket elevations. Although computed velocities compared well with literature, the observed blanket failure originated from unaccounted 3D effects, in particular tangential flows. Noteworthy was that the failure largely depended on the rheological model as well.

To investigate the predictive power of the CFD model, validation studies have been set up. Solids concentrations and flow-through curves obtained at unsteady inlet boundary conditions led to a more powerful model validation.

Whereas in general the solids concentration field was well predicted, the simulated flow-through curves differed considerably from the measured curves. It is believed that diffusion is a key factor in obtaining a correct validation. The use of 2D models with swirl, the 3D inlet geometry and an appropriate turbulence model should be listed on future research efforts.

The research conducted focused on different aspects of the settling tank. As a result, much process knowledge has been gained. CFD submodels have been set up for solids settling, rheology and the scraper mechanism. Although acceptable model predictions for the solids distribution in the settling tank were obtained, more questions arose than were answered. The previous sections indeed clarified that sludge transport modelling in the tank is ambitious. Continuing research is therefore needed.

A

Appendix A

Introduction to Tensor Notation

Tensor notation is used in some chapters of this dissertation. It is a useful tool to write equations in a considerably more compact way compared to the conventional notation. The summary as presented here is based on Rodi (1984).

In Cartesian tensor notation, an index is attached to the symbol of the considered vector quantity; the index denotes the different elements of the vector. For instance, the space and velocity vectors can be written as respectively

$$x_i \equiv \{x_1, x_2, x_3\}$$
$$u_i \equiv \{u_1, u_2, u_3\}.$$

With this notation, the three components of the vector in a Cartesian coordinate system can be obtained by setting the index i to 1, 2, and 3 respectively.

Extrapolating this notation to a quantity with two indices, a *tensor*, results in

$$a_{ij} \equiv \begin{Bmatrix} a_{11} & a_{12} & a_{13} \\ a_{21} & a_{22} & a_{23} \\ a_{31} & a_{32} & a_{33} \end{Bmatrix}$$

The stresses σ_{ij} appearing in the Reynolds-averaged Navier-Stokes equations are an example of such a tensor. In this case, the first index denotes the surface, perpendicular to x_i , on which the stress acts and the second index denotes the direction of the stress. The product of two velocity vectors yields a tensor, i.e.

$$u_i u_j \equiv \begin{Bmatrix} u_1 u_1 & u_1 u_2 & u_1 u_3 \\ u_2 u_1 & u_2 u_2 & u_2 u_3 \\ u_3 u_1 & u_3 u_2 & u_3 u_3 \end{Bmatrix}$$

Similarly, the Reynolds stress tensor can be introduced. A particular tensor is the Kronecker-delta δ_{ij} which has the following components

$$\delta_{ij} \equiv \begin{Bmatrix} 1 & 0 & 0 \\ 0 & 1 & 0 \\ 0 & 0 & 1 \end{Bmatrix}$$

Hence, $\delta_{ij} = 1$ for $i = j$, and $\delta_{ij} = 0$ for $i \neq j$.

An important issue to mention about tensor notation is the Einstein summation convention, i.e. the sum over all 3 directions whenever the same index is repeated in the same term, e.g.

$$u_j \frac{\partial u_i}{\partial x_j} = u_1 \frac{\partial u_i}{\partial x_1} + u_2 \frac{\partial u_i}{\partial x_2} + u_3 \frac{\partial u_i}{\partial x_3}.$$

Finally, note that the divergence of a tensor results in a vector; e.g. the divergence of the stress tensor σ_{ij} is given as

$$\frac{\partial \sigma_{ij}}{\partial x_j} = \left(\frac{\partial \sigma_{11}}{\partial x_1} + \frac{\partial \sigma_{12}}{\partial x_2} + \frac{\partial \sigma_{13}}{\partial x_3}, \right. \\ \left. \frac{\partial \sigma_{21}}{\partial x_1} + \frac{\partial \sigma_{22}}{\partial x_2} + \frac{\partial \sigma_{23}}{\partial x_3}, \right. \\ \left. \frac{\partial \sigma_{31}}{\partial x_1} + \frac{\partial \sigma_{32}}{\partial x_2} + \frac{\partial \sigma_{33}}{\partial x_3} \right)$$

B

Appendix B Spectral Analysis of ADCP Data

B.1 Introduction

Velocity data from the Acoustic Doppler Current Profiler (ADCP) has to be converted from beam to Cartesian coordinates. Prior to this mathematical conversion, data needs to be checked for its quality; i.e. bad data is skipped from the analysis. Next, a spectral analysis is performed for each time series of every beam, and bin. From these results a cutoff frequency is chosen, which is subsequently utilised for time averaging. After moving-window averaging, the mean velocity and statistical variance are computed for every bin. Finally, with the pre-treated data the velocities and Reynolds stresses (in a Cartesian coordinate system) can be calculated.

The mathematical treatment of the data is performed in the statistical software package S-Plus, v6 (Insightful, UK). The necessary subroutines are given below.

B.2 Program in S-Plus

```
# STEP I ##### GENERAL SUBROUTINES #####

#GIVE NUMBERS OF BINS:
tot.bin <- 23

#IMPORT DATA AND PARAMETERS
depth.ADCP <- 50
dist.first.bin <- 30
attach(DataCoupure)
all.beam.velocities <- as.matrix(DataCoupure)
rows <- dim(all.beam.velocities)[1]
col <- dim(all.beam.velocities)[2]
n <- rows/tot.bin
Magn.all.beams <- matrix(0,col,n%/2)

#CHECK FOR BAD BINS (ADAPTATION OF N)
number.good.meas <- function(bin.nr=1, beam.nr=1)
{
  num <- {0}
  for (i in 1:n)
  {
    if(all.beam.velocities[bin.nr+(i-1)*tot.bin,beam.nr] != 99999) num <- num+1
  }
}
```

```

return(num)
}

#STORAGE OF LOCAL BEAM VELOCITY
beam.velocity <- function(bin.nr=1, beam.nr=1)
{
  x <- NULL
  p <- {0}
  for (i in 1:n)
  {
    if(all.beam.velocities[bin.nr+(i-1)*tot.bin,beam.nr] != 99999) {p <- p+1; x[p] <- all.beam.velocities[bin.nr+(i-1)*tot.bin,beam.nr]}
  }
  return(x)
}

##### SPECTRAL ANALYSIS OF BEAM DATA #####

par(mfrow=c(2,2))

# LOOP OVER 4 BEAMS TO CALCULATE FOURIER SPECTRUM OF EACH BEAM/BIN
for (beam.count in 1:col)
{
  vel.meas <- beam.velocity(bin.nr=23, beam.nr=beam.count)           #choose bin number
  n <- number.good.meas(bin.nr=23, beam.nr=beam.count)             #choose bin number
  tot.meas.time <- n                                               #sampling frequency: 1Hz

  # CALCULATION OF FOURIER PARAMETERS (FFT)
  a <- NULL
  alfa <- NULL
  beta <- NULL
  for (i in 1:n)
  {
    a[beam.count] <- a[beam.count] + vel.meas[i]
  }
  a[beam.count] <- a[beam.count]/n
  for (j in 1:(n%/2))
  {
    interm.alfa <- {0}
    interm.beta <- {0}
    for (i in 1:n)
    {
      interm.alfa <- interm.alfa + vel.meas[i]*cos(j*(2*pi/n)*(i-1))
      interm.beta <- interm.beta + vel.meas[i]*sin(j*(2*pi/n)*(i-1))
    }
    alfa[j] <- 2/n*interm.alfa
    beta[j] <- 2/n*interm.beta
  }

  #CALCULATION OF MAGNITUDES AND FREQUENCIES
  Magn.beam <- NULL
  Freq.beam <- NULL
  for (i in 1:(n%/2))
  {
    Magn.beam[i] <- sqrt(alfa[i]^2 + beta[i]^2)
    Freq.beam[i] <- i/tot.meas.time
  }
  for (i in 1:(n%/2))
  {
    Magn.all.beams[beam.count,i] <- Magn.beam[i]
  }
}

```

```

#PLOTING OF FOURIER SPECTRA
plot(Freq.beam, Magn.beam)
}

# STEP II ##### CALCULATION OF MEAN BEAM VELOCITY AND VARIANCE #####

cutoff.freq <- tot.bin/rows
av.period <- 1/cutoff.freq
mean.vel <- array(0, dim=c(tot.bin, col, rows/tot.bin-av.period+1))
variance.vel <- array(0, dim=c(tot.bin, col, rows/tot.bin-av.period+1))

for (bin.count in 1:tot.bin)
{
  for (beam.count in 1:col)
  {
    for (j in 1:(rows/tot.bin-av.period+1))
    {
      num <- {0}
      for (i in j:(j+av.period-1))
      {
        if(all.beam.velocities[bin.count+(i-1)*tot.bin,beam.count] != 99999)
        {
          mean.vel[bin.count, beam.count, j] <- mean.vel[bin.count, beam.count, j] + all.beam.velocities[bin.count+(i-1)*
            tot.bin,beam.count]
          num <- num+1
        }
      }
      mean.vel[bin.count, beam.count, j] <- mean.vel[bin.count, beam.count, j]/num
      for (i in j:(j+av.period-1))
      {
        if(all.beam.velocities[bin.count+(i-1)*tot.bin,beam.count] != 99999)
        {
          variance.vel[bin.count, beam.count, j] <- variance.vel[bin.count, beam.count, j] + (all.beam.velocities[bin.count+(i-1)*
            tot.bin,beam.count]-mean.vel[bin.count, beam.count, j])^2/num
        }
      }
    }
  }
}

##### CALCULATION OF CARTESIAN VELOCITIES AND STRESSES #####

u <- NULL
v <- NULL
w <- NULL
uw <- NULL
vw <- NULL
err <- NULL
depth <- NULL
for (j in 1:(rows/tot.bin-av.period+1))
{
  for (bin.count in 1:tot.bin)
  {
    u[bin.count] <- (mean.vel[bin.count, 4, j]-mean.vel[bin.count, 3, j]) / (2*cos(0.34906585))
    v[bin.count] <- (mean.vel[bin.count, 2, j]-mean.vel[bin.count, 1, j]) / (2*cos(0.34906585))
    w[bin.count] <- -(mean.vel[bin.count, 1, j]+mean.vel[bin.count, 2, j]+mean.vel[bin.count, 3, j]+mean.vel[bin.count, 4, j]) /
      (4*sin(0.34906585))
    err[bin.count] <- (-mean.vel[bin.count, 1, j]-mean.vel[bin.count, 2, j]+mean.vel[bin.count, 3, j]+mean.vel[bin.count, 4, j]) /
      (2*sin(0.34906585))

    uw[bin.count] <- -(variance.vel[bin.count, 4, j]-variance.vel[bin.count, 3, j]) / (2*sin(2*0.34906585))
    vw[bin.count] <- -(variance.vel[bin.count, 2, j]-variance.vel[bin.count, 1, j]) / (2*sin(2*0.34906585))
  }
}

```

```
    depth[bin.count] <- -(depth.ADCP + dist.first.bin + 5*(bin.count-1))
  }
}

par(mfrow=c(2,2))

plot(u, depth)
plot(v, depth)
plot(w, depth)
plot(err, depth)

par(mfrow=c(2,1))

plot(uw, depth)
plot(vw, depth)
```

C

Appendix C

Calculation of Bulk and Solids Density

C.1 Governing formula

This section shows the calculation of the bulk density as applied in the Fluent model. Bulk density is crucial for the fluid flow since gravitational force is a dominating term in the momentum equations. The developed formula was also used in another application, i.e. for the computation of dry solids density. This will be demonstrated at the end of the appendix.

Assume a sludge parcel composed of two phases, i.e. the liquid (denoted with "l") and solids (denoted with "s") phases. The total, or bulk, parcel is denoted with "b". For the calculation of bulk density the total mass M and total volume V are to be used.

$$M_b = M_l + M_s \quad (C.1)$$

$$V_b = V_l + V_s \quad (C.2)$$

In order to perform the calculations, density definitions for bulk, liquid and solids are needed,

$$\text{bulk density : } \rho_b = \frac{M_b}{V_b}$$

$$\text{liquid density : } \rho_l = \frac{M_l}{V_l} \quad (C.3)$$

$$\text{solids density : } \rho_s = \frac{M_s}{V_s} \quad (C.4)$$

Substituting Equations C.3 and C.4 in Equation C.1 results in

$$M_b = \rho_l V_l + \rho_s V_s$$

Next, Equation C.2 is used to eliminate the liquid volume:

$$\begin{aligned} M_b &= \rho_l (V_b - V_s) + \rho_s V_s \\ M_b &= \rho_l V_b + (\rho_s - \rho_l) V_s \end{aligned} \quad (C.5)$$

Further, the bulk density is substituted in Equation C.5 together with the solids fraction ϕ_m , given as

$$\phi_m = \frac{M_s}{M_b} = \frac{\rho_s V_s}{\rho_b V_b}$$

After some calculations the bulk density finally can be written as

$$\rho_b = \frac{\rho_l}{1 - \phi_m \left(1 - \frac{\rho_l}{\rho_s} \right)} \quad (\text{C.6})$$

C.2 Calculation of dry solids density

As mentioned before, the latter formula was used in Fluent to describe the bulk density under varying solids concentrations. Besides this application, it was also partially utilised for the calculation of the solids dry fraction of zeolite-composite solids. Here, the biomass and zeolite fractions correspond to the "liquid" and "solids" phase respectively; hence, Equation C.6 can be applied directly.

Before calculating the solids dry density it is stressed that, besides zeolite and biomass, the floc consists of liquid to a large extent. This fraction is inherently considered in the bulk (solids-liquid) density calculation. On the other hand, the zeolite used in this research is characterised by porosities that even go up to 38% (values range between 24 and 38%); this should be accounted for when calculating the dry solids density. Stages 3 & 4 of Oxley Creek WWTP received 1.7 ton zeolite/d in the RAS flow.

In order to compute the dry solids density the mass fraction, and hence the concentration, of zeolite is needed. This can be calculated from the Waste Activated Sludge (WAS) rate. It is assumed that all the zeolite is incorporated in the flocs and that no zeolite exits the system via the effluent. In order to retain steady state, all zeolite therefore has to be removed with the WAS flow. With an annual average of 604 m³/d and 6.95 g/l for WAS flow rate and solids concentration respectively, a zeolite fraction of 40% is calculated from the mass balance. The zeolite ZELfloc (Zeolite Australia, Australia) is primordially composed of the mineral clinoptilolite, clearly having a serious effect on the dry solids density.

In literature (Lyn *et al.*, 1992; Zhou *et al.*, 1992; Ekama *et al.*, 1997; Mazzolani *et al.*, 1998; Lakehal *et al.*, 1999; Stamou *et al.*, 2000), the biomass density is reported to be between 1250 and 1450 kg/m³. Here, 1450 kg/m³ was used. On the other hand, ZELfloc has a density of approximately 2200 kg/m³. In this respect, the void fraction of zeolite has to be considered as well. Indeed, the ZELfloc density is expressed with air in the pores; in practice this will be water. This parameter therefore has to be corrected. For the calculation, Equation C.5 is recapitulated in terms of air (subscript *air*) and zeolite (subscript *z*), i.e.

$$M_{z-a} = \rho_z V_{z-a} + (\rho_{air} - \rho_z) V_{air}$$

The subscript *z-a* refers to the composite. In this equation, the volume fraction ϕ_v will be substituted

$$\rho_{z-a} = \rho_z + \phi_v(\rho_{air} - \rho_z) \quad (C.7)$$

with

$$\phi_v = \frac{V_{air}}{V_{z-a}}$$

Finally, a relationship for the zeolite's density is to be found, i.e.

$$\rho_z = \frac{\rho_{z-a} - \phi_v \rho_{air}}{1 - \phi_v}$$

A mean porosity of 30%, a zeolite-air composite density of 2200 kg/m³ and an air density of 1.29 kg/m³ result in a zeolite density of approximately 3140 kg/m³. As mentioned before, the total voidance is filled with water. Hence, Equation C.7 can be used to calculate the zeolite-water composite density, resulting in approximately 2500 kg/m³.

Substituting the densities of air-saturated zeolite and biomass, and the biomass-zeolite mass fraction into Equation C6 results in the biomass-zeolite dry solids density of around 1750 kg/m³.

C.3 Bulk density affected by multiple components

Above, only one component, i.e. dispersed solids, affected the bulk density. In practice however, more components dispersed in the liquid may be present. A similar mathematical derivation as in Section C.1, but for multiple components *N*, leads to an alternative formula for the bulk density ρ_b

$$\rho_b = \frac{\rho_l}{1 - \sum_{i=1}^N \phi_{m,i} \left(1 - \frac{\rho_l}{\rho_i}\right)} \quad \text{for } i = 1, 2, \dots, N \quad (C.8)$$

where $\phi_{m,i}$ and ρ_i are the mass fraction and density of component *i* respectively dispersed in the liquid. However, Equation C.8 does not apply to the density calculation for solutions. Solutes indeed only contribute to the total mass but not to the volume. Therefore, new formulae for the local bulk density need to be developed. Equation C.8 can be rewritten as

$$\rho_b = \frac{\rho_l}{1 - \sum_{i=1}^N \phi_{m,i} \left(1 - \frac{\rho_l}{\rho_i}\right) - \sum_{j=1}^M \phi_{m,j}} \quad \text{for } i = 1, 2, \dots, N; j = 1, 2, \dots, M \quad (C.9)$$

where the indices i and j denote the N dispersed solids and M dissolved compounds respectively.

D

Appendix D

User-Defined Functions used in Fluent

This appendix describes the User-Defined Functions (UDFs) as used in this dissertation. Information about each UDF, i.e. its purpose, is to be found in the local comments; theoretical background is given in the respective Chapters 5 and 7. Finally, all parameters utilised are expressed in SI units.

D.1 Solids transport in settling tanks

```
#include "udf.h"
#include "sg.h"

static real sigma_t = 0.7;          /* Schmidt number */
static real g = -9.81;             /* gravitational acceleration */
static real rho_water = 998.2;     /* density of water */
static real rho_solid_polymer = 1450.0; /* density of polymer-treated sludge */
static real rho_solid_zeolite = 1750.0; /* density of zeolite-treated sludge */

/* The UDS represents the solids fraction, and not the solids concentration!*/

/* -----
   UDS Flux [kg/s]
   This routine provides the flux function for the advective part of the solids transport equation
   NO ZEOLITE IS DOSED!
   ----- */
DEFINE_UDS_FLUX(UDS_FLUX_no_zeolite, f, t, i)
{
    real flux, sed_vel;
    real psi[3], A[3];
    real scalar, conc_solids, rho;
    F_AREA(A, f, t);
    F_FLUX(f, t);
    if (BOUNDARY_FACE_THREAD_P(t))
    {
        scalar = 0.;
    }
    else
    {
        rho = ((C_R(F_CO(f,t),F_CO_THREAD(f,t))+C_R(F_C1(f,t),F_C1_THREAD(f,t))) / 2.);
        conc_solids = rho * ((C_UDSI(F_CO(f,t),F_CO_THREAD(f,t),0)+C_UDSI(F_C1(f,t),F_C1_THREAD(f,t),0)) / 2.);
        if (conc_solids >= 30.)
        {
            sed_vel = 0.;
        }
    }
}
```

```

    else if (conc_solids < 0.00456)
    {
        sed_vel = 0.;
    }
    else
    {
        sed_vel = -0.0054861 * (exp(-0.576*(conc_solids-0.00456))-exp(-2.86*(conc_solids-0.00456)));
        if (sed_vel < -0.0028935)
        {
            sed_vel = -0.0028935;
        }
    }
    NV_D(psi, =, sed_vel, 0., 0.);
    NV_S(psi, *=, rho);
    scalar = NV_DOT(psi, A);
}
flux = F_FLUX(f,t) + scalar;
return flux;
}

/* -----
UDS Flux [kg/s]
This routine provides the flux function for the advective part of the solids transport equation
ZEOLITE IS DOSED!
----- */
DEFINE_UDS_FLUX(UDS_FLUX_zeolite, f, t, i)
{
    real flux, sed_vel;
    real psi[3], A[3];
    real scalar, conc_solids, rho;
    F_AREA(A, f, t);
    F_FLUX(f, t);
    if (BOUNDARY_FACE_THREAD_P(t))
    {
        scalar = 0.;
    }
    else
    {
        rho = ((C_R(F_CO(f,t),F_CO_THREAD(f,t))+C_R(F_C1(f,t),F_C1_THREAD(f,t))) / 2.);
        conc_solids = rho * ((C_UDSI(F_CO(f,t),F_CO_THREAD(f,t),0)+C_UDSI(F_C1(f,t),F_C1_THREAD(f,t),0)) / 2.);
        if (conc_solids >= 30.)
        {
            sed_vel = 0.;
        }
        else if (conc_solids < 0.014)
        {
            sed_vel = 0.;
        }
        else
        {
            sed_vel = -0.0057111 * (exp(-0.2725*(conc_solids-0.014))-exp(-3.8902*(conc_solids-0.014)));
        }
        NV_D(psi, =, sed_vel, 0., 0.);
        NV_S(psi, *=, rho);
        scalar = NV_DOT(psi, A);
    }
    flux = F_FLUX(f,t) + scalar;
    return flux;
}

```

```

/* -----
UDS Density - polymer [kg/m3]
This routine returns the overall density of sludge treated with polymer.
----- */
DEFINE_PROPERTY(density_polymer, c, t)
{
    real rho, frac_solids;
    frac_solids = C_UDSI(c,t,0);
    rho = rho_water / (1-frac_solids*(1 - (rho_water/rho_solid_polymer)));
    return rho;
}

/* -----
UDS Density - zeolite [kg/m3]
This routine returns the overall density of solids treated with zeolite.
----- */
DEFINE_PROPERTY(density_zeolite, c, t)
{
    real rho;
    real frac_solids;
    frac_solids = C_UDSI(c,t,0);
    rho = rho_water / (1-frac_solids*(1 - (rho_water/rho_solid_zeolite)));
    return rho;
}

/* -----
UDS Diffusivity [m2/s]
This routine returns the turbulent diffusivity.
----- */
DEFINE_DIFFUSIVITY(turb_mass_diffusivity, c, t, i)
{
    return C_MU_EFF(c,t) / sigma_t;
}

/* -----
UDS Bingham viscosity
This routine returns the Bingham viscosity for an inlet solids concentration of 3.2 g/l:
it is added to the turbulent viscosity. [ref. Dahl, 1993; Lakehal et al., 1999]
----- */
DEFINE_PROPERTY(Bingham_visc_conc_3_2, c, t)
{
    real beta1 = 1.1e-4;           /* kg/m/s2 */
    real beta2 = 0.98;           /* m3/kg */
    real Cpl = 2.473e-4;        /* m5/kg/s2 */
    real Muw = 0.001;          /* kg/m/s */
    real conc_solids;           /* sludge concentration */
    real Tau0;                  /* yield stress */
    real viscosity, Mu;
    real density = C_R(c,t);
    conc_solids = C_UDSI(c,t,0) * density;
    Tau0 = beta1 * exp(beta2 * conc_solids);
    Mu = Muw + Cpl * pow(conc_solids, 2);
    viscosity = Mu + (Tau0 / Strainrate_Mag(c,t));
    return viscosity;
}

```

```

/* -----
UDS Bingham viscosity
This routine returns the Bingham viscosity for an inlet solids concentration of 2 g/l:
it is added to the turbulent viscosity. [ref. Dahl, 1993; Lakehal et al., 1999]
----- */
DEFINE_PROPERTY(Bingham_visc_conc_2, c, t)
{
  real beta1 = 9.71e-4;          /* kg/m/s2 */
  real beta2 = 0.98;           /* m3/kg */
  real Cpl = 2.473e-4;        /* m5/kg/s2 */
  real Muw = 0.001;          /* kg/m/s */
  real conc_solids;          /* sludge concentration */
  real Tau0;                 /* yield stress */
  real viscosity, Mu;
  real density = C_R(c,t);
  conc_solids = C_UDSI(c,t,0) * density;
  Tau0 = beta1 * exp(beta2 * conc_solids);
  Mu = Muw + Cpl * pow(conc_solids, 2);
  viscosity = Mu + (Tau0 / Strainrate_Mag(c,t));
  return viscosity;
}

/* -----
UDS Bokil viscosity
This routine returns the Bokil viscosity; it is added to the turbulent
viscosity. Viscosity is linearly extrapolated to concentrations below 0.7 g TSS/l
----- */
DEFINE_PROPERTY(Bokil_visc, c, t)
{
  real beta1 = 0.00327;       /* kg/m/s2 */
  real beta2 = 0.132;        /* m3/kg */
  real conc_solids;          /* sludge concentration */
  real viscosity;
  real density = C_R(c,t);
  conc_solids = C_UDSI(c,t,0) * density;
  if (conc_solids < 0.7)
  {
    viscosity = 0.001 + (0.003045/0.7)*conc_solids;
  }
  else
  {
    viscosity = beta1 * pow(10, beta2*conc_solids);
  }
  return viscosity;
}

/* -----
UDS viscosity model proposed
This routine returns the viscosity; it is added to the turbulent viscosity.
----- */
DEFINE_PROPERTY(De_Clercq_visc, c, t)
{
  real a = 9.0364e-4;
  real b = 2.49338e-4;
  real d = 1.12;
  real m = 169.47;
  real p = 0.7748;
  real conc_solids, viscosity, Tau0, n;
  real density = C_R(c,t);
  conc_solids = C_UDSI(c,t,0) * density;
  Tau0 = a*pow(conc_solids, d);

```

```

n = 0.001+b*pow(conc_solids, 2);
viscosity = (Tau0*(1-exp(-m*Strainrate_Mag(c,t)))/Strainrate_Mag(c,t))+n*pow(Strainrate_Mag(c,t), p-1);
return viscosity;
}

/* -----
UDS Richardson number [-]
This routine returns the local Richardson number. A value of 1 is returned when Ri>0.25; for Ri<0.25 zero is
returned.
----- */
DEFINE_ON_DEMAND(Richardson)
{
  Domain *d;
  Thread *t;
  cell_t c;
  real Ri;
  d = Get_Domain(1);          /* Get the domain using Fluent utility */

  /* Loop over all cell threads in the domain */
  thread_loop_c(t,d)
  {
    if (FLUID_THREAD_P(t))
    {
      begin_c_loop(c,t)
      {
        if (C_DVDX(c,t) == 0.)
        {
          Ri = 100.;
        }
        else
        {
          Ri = (g * C_D_DENSITY(c,t)[0]) / (C_R(c,t) * pow(C_DVDX(c,t),2));
        }
        if (Ri > 0.25)
        {
          C_UDMI(c,t,0) = 1;
        }
        else
        {
          C_UDMI(c,t,0) = 0;
        }
      }
      end_c_loop_all(c,t)
    }
    else
    {
      begin_c_loop_all(c,t)
      {
        Ri = 0.;
      }
      end_c_loop_all(c,t)
      if (Ri > 0.25)
      {
        C_UDMI(c,t,0) = 1;
      }
      else
      {
        C_UDMI(c,t,0) = 0;
      }
    }
  }
}

```

```

/* -----
UDS saving of variables [-]
This routine stores solids concentration, axial and radial velocity in 3 UDM's that are subsequently used for
comparison with other data (this data is interpolated data)
----- */
DEFINE_ON_DEMAND(save_UDM)
{
  Domain *d;
  Thread *t;
  cell_t c;
  d = Get_Domain(1);          /* Get the domain using Fluent utility */

  /* Loop over all cell threads in the domain */
  thread_loop_c(t,d)
  {
    begin_c_loop(c,t)
    {
      C_UDMI(c,t,0)=C_UDSI(c,t,0)*C_R(c,t);
      C_UDMI(c,t,1)=C_U(c,t);
      C_UDMI(c,t,2)=C_V(c,t);
    }
    end_c_loop_all(c,t)
  }
}

/* -----
UDS inlet velocity [m/s]
This routine sets the temporal varying normal inlet velocity component.
----- */
DEFINE_PROFILE(inlet_velocity, t, i)
{
  real time;
  face_t f;
  int k, j = 0;
  real surface = 0.7;

  /* No.elements = number of data points; the vectors are filled with experimental data */
  float dat_time[No.elements] = {...};      /* definition of the time vector */
  float dat_flow[No.elements] = {...};     /* definition of the flow rate vector */
  time = RP_Get_Real("flow-time");
  for (j=0; j<= No.elements-1; ++j)
  {
    if (time > dat_time[j]) k=j;
  }
  begin_f_loop(f, t)
  {
    if (time >= dat_time[No.elements-1])
      F_PROFILE(f,t,i) = dat_flow[No.elements-1]/surface;
    else if (time == dat_time[0])
      F_PROFILE(f, t, i) = dat_flow[0]/surface;
    else
      F_PROFILE(f,t,i) = (((dat_flow[k+1] - dat_flow[k]) / (dat_time[k+1] - dat_time[k])) * (time - dat_time[k]) +
                          dat_flow[k])/surface;
  }
  end_f_loop(f, t)
}

```

```

/* -----
UDS underflow velocity [m/s]
This routine sets the temporal varying normal underflow velocity component.
----- */
DEFINE_PROFILE(underflow_velocity, t, i)
{
    real time;
    face_t f;
    int k, j = 0;
    real surface = 0.2827;

    /* No.elements = number of data points; the vectors are filled with experimental data */
    float dat_time[No.elements] = {...}; /* definition of time vector */
    float dat_flow[No.elements] = {...}; /* definition of underflow velocity vector */
    time = RP_Get_Real("flow-time");
    for (j=0; j<= No.elements-1; ++j)
    {
        if (time > dat_time[j]) k=j;
    }
    begin_f_loop(f, t)
    {
        if (time >= dat_time[No.elements-1])
            F_PROFILE(f,t,i) = -dat_flow[No.elements-1]/surface;
        else if (time == dat_time[0])
            F_PROFILE(f, t, i) = -dat_flow[0]/surface;
        else
            F_PROFILE(f,t,i) = -(((dat_flow[k+1] - dat_flow[k]) / (dat_time[k+1] - dat_time[k])) * (time - dat_time[k]) +
                                dat_flow[k])/surface;
    }
    end_f_loop(f, t)
}

/* -----
UDS solids concentration [g/l]
This routine sets the temporal varying inlet solids fraction.
----- */
DEFINE_PROFILE(inlet_concentration, t, i)
{
    real time;
    face_t f;
    int k, j = 0;

    /* No.elements = number of data points; the vectors are filled with experimental data */
    float dat_time[No.elements] = {...}; /* definition of time vector */
    float dat_frac[No.elements] = {...}; /* definition of solids fraction vector */
    time = RP_Get_Real("flow-time");
    for (j=0; j<= No.elements-1; ++j)
    {
        if (time > dat_time[j]) k=j;
    }
    begin_f_loop(f, t)
    {
        if (time >= dat_time[No.elements-1])
            F_PROFILE(f,t,i) = dat_frac[No.elements-1];
        else if (time == dat_time[0])
            F_PROFILE(f, t, i) = dat_frac[0];
        else
            F_PROFILE(f,t,i) = ((dat_frac[k+1] - dat_frac[k]) / (dat_time[k+1] - dat_time[k])) * (time - dat_time[k]) +
                                dat_frac[k];
    }
    end_f_loop(f, t)
}

```

```

/* -----
UDS Scraper y-momentum [kg.m/s2]
This routine returns the variable scraper y-momentum along the bottom floor.
The momentum source is discontinuous in time.
----- */
DEFINE_SOURCE(scraper_variable_momentum, c, t, dS, eqn)
{
    real deltat_cycle = 174.676;          /* time period in which scraper passes the considered radial section */
    double deltat_rot = 3110.;           /* time period for 1 complete rotation of scraper */
    real v_wall = 0.02;                  /* tangential velocity at outer wall, i.e. 9.9m */
    real alfa1 = 0.0873;                 /* angle between scraper and cross-section at first crossing [rad] */
    real R1 = 9.9;                       /* radius of clarifier */
    real R2 = 0.863;                     /* distance centre - fictitious prolongation of scraper */
    real omega = 0.00202032;             /* angular velocity of bridge [rad/s] */
    double t_rot, time, x_pos, y_pos;
    real source, gamma, alfa;
    real delta_t;
    real r;                               /* radial distance from centre to bridge */
    real v_s;                             /* tangential velocity of bridge at distance r from centre */
    real v_s_perp;                        /* radial velocity towards centre */
    real x[ND_ND];
    real height_floor;

    C_CENTROID(x, c, t);
    delta_t = RP_Get_Real("physical-time-step");
    time = RP_Get_Real("flow-time");
    t_rot = floor(time / deltat_rot)*deltat_rot;
    if ((time >= t_rot) && (time <= (t_rot + deltat_cycle)))
    {
        gamma = omega*(time - t_rot);
        alfa = gamma + alfa1;
        r = R2/(sin(alfa));
        height_floor = 0.3625*r + 1.91125;
        v_s = v_wall*r/R1;
        v_s_perp = 0.5*sin(2*alfa)*v_s;
        if ((x[0] <= (height_floor+0.3)) && (x[1] <= (r+0.06)) && (x[1] >= (r-0.06)) && (x[1] <= 9.6))
        {
            source = C_R(c,t)*(v_s_perp - C_V(c,t)) / delta_t;
            dS[eqn] = -C_R(c,t) / delta_t;
            return source;
        }
    }
    else
    {
        source = 0.;
        dS[eqn] = 0.;
        return source;
    }
}
}

```

D.2 Solids and tracer transport in settling tanks

```

#include "udf.h"
#include "sg.h"

/* defines for user-defined scalars */
#define UDS_SOLID 0
#define UDS_TRACER 1
#define C_UDS_SOLID(c,t) C_UDSI(c,t,UDS_SOLID)
#define C_UDS_TRACER(c,t) C_UDSI(c,t,UDS_TRACER)

/* solids transport properties */
static real sigma_t = 0.7;          /* Schmidt Number */
static real g = -9.81;             /* gravitational acceleration */
static real rho_water = 998.2;     /* density of water */
static real rho_solid = 1750.0;    /* density of zeolite treated sludge */

/*-----
UDS Flux [kg/s]
This routine provides the flux function for the advective part of the solids and tracer transport equation
ZEOLITE IS DOSED!
-----*/
DEFINE_UDS_FLUX(UDS_FLUX_tracertest, f, t, i)
{
    real flux, sed_vel;
    real psi[3], A[3];
    real scalar, conc_solids, rho;
    F_AREA(A, f, t);
    F_FLUX(f, t);
    if (BOUNDARY_FACE_THREAD_P(t))
    {
        scalar = 0.;
    }
    else
    {
        rho = ((C_R(F_CO(f,t),F_CO_THREAD(f,t))+C_R(F_C1(f,t),F_C1_THREAD(f,t))) / 2.);
        conc_solids = rho * ((C_UDS_SOLID(F_CO(f,t),F_CO_THREAD(f,t))+C_UDS_SOLID(F_C1(f,t),F_C1_THREAD(f,t))) /
            2.);
        if (conc_solids >= 30.)
        {
            sed_vel = 0.;
        }
        else if (conc_solids < 0.014)
        {
            sed_vel = 0.;
        }
        else
        {
            sed_vel = -0.0057111 * (exp(-0.2725*(conc_solids-0.014))-exp(-3.8902*(conc_solids-0.014)));
        }
        NV_D(psi, =, sed_vel, 0., 0.);
        NV_S(psi,*=,rho);
        scalar = NV_DOT(psi, A);
    }
    flux = F_FLUX(f,t) + scalar;
    if (i == UDS_SOLID)
        return flux;
    else
        return F_FLUX(f,t);
}

```

```

/* -----
UDS Density - zeolite [kg/m3]
This routine returns the overall density of solids treated with zeolite and tracer added.
----- */
DEFINE_PROPERTY(density_tracertest, c, t)
{
    real rho;
    real frac_solids;
    frac_solids = C_UDS_SOLID(c,t);
    rho = rho_water / (1-frac_solids*(1 - (rho_water/rho_solid_zeolite)));
    return rho;
}

/* -----
UDS Diffusivity [m2/s]
This routine returns the turbulent diffusivity.
----- */
DEFINE_DIFFUSIVITY(diffusivity_tracertest, c, t, i)
{
    if (i == UDS_SOLID)
        return C_MU_EFF(c,t) / sigma_t;
    else
        return C_MU_EFF(c,t);
}

/* -----
UDS viscosity model proposed
This routine returns the viscosity; it is added to the turbulent viscosity.
----- */
DEFINE_PROPERTY(viscosity_tracertest, c, t)
{
    real a = 9.0364e-4;
    real b = 2.49338e-4;
    real m = 169.47;
    real p = 0.7748;
    real conc_solids;
    real viscosity;
    real Tau0,n;
    real density = C_R(c,t);
    conc_solids = C_UDS_SOLID(c,t) * density;
    Tau0 = a*pow(conc_solids, 2);
    n = 0.001+b*pow(conc_solids, 2);
    viscosity = (Tau0*(1-exp(-m*Strainrate_Mag(c,t)))/Strainrate_Mag(c,t))+n*pow(Strainrate_Mag(c,t), p-1);
    return viscosity;
}

/* -----
UDS inlet velocity [m/s]
This routine returns the temporal varying normal inlet velocity.
----- */
DEFINE_PROFILE(inlet_vel_tracertest, t, i)
{
    real time;
    face_t f;
    int k, j = 0;
    real surface = 0.745;

    /*No. elements = number of data points; the vectors are filled with experimental data */
    float dat_time[No.elements] = {...}; /* definition of the time vector */
    float dat_flow[No.elements] = {...}; /* definition of the flow rate vector */
}

```

```

time = RP_Get_Real("flow-time");
for (j=0; j<= No.elements-1; ++j)
{
    if (time > dat_time[j])
        k=j;
}
begin_f_loop(f, t)
{
    if (time >= dat_time[No.elements-1])
        F_PROFILE(f,t,i) = dat_flow[No.elements-1]/surface;
    else
        F_PROFILE(f, t, i) = dat_flow[k]/surface;
}
end_f_loop(f, t)
}

/* -----
UDS underflow velocity [m/s]
This routine sets the temporal varying normal underflow velocity component.
----- */
DEFINE_PROFILE(underflow_vel_tracertest, t, i)
{
    real time;
    face_t f;
    int k, j = 0;
    real surface = 0.2827;

    /*No. elements = number of data points; the vectors are filled with experimental data */
    float dat_time[No.elements] = {...};      /* definition of the time vector */
    float dat_flow[No.elements] = {...};      /* definition of the flow rate vector */
    time = RP_Get_Real("flow-time");
    for (j=0; j<= No.elements-1; ++j)
    {
        if (time > dat_time[j])
            k=j;
    }
    begin_f_loop(f, t)
    {
        if (time >= dat_time[No.elements-1])
            F_PROFILE(f,t,i) = -dat_flow[No.elements-1]/surface;
        else if (time == dat_time[0])
            F_PROFILE(f, t, i) = -dat_flow[0]/surface;
        else
            F_PROFILE(f,t,i) = -(((dat_flow[k+1] - dat_flow[k]) / (dat_time[k+1] - dat_time[k])) * (time - dat_time[k]) +
                                dat_flow[k])/surface;
    }
    end_f_loop(f, t)
}

/* -----
UDS solids concentration [g/l]
This routine returns the temporal varying inlet solids concentration.
----- */
DEFINE_PROFILE(inlet_solids_tracertest, t, i)
{
    real time;
    face_t f;
    int k, j = 0;

    /*No. elements = number of data points; the vectors are filled with experimental data */
    float dat_time[No.elements] = {...};      /* definition of time vector */

```

```

float dat_frac[No.elements] = {...};          /* definition of solids fraction vector */
time = RP_Get_Real("flow-time");
for (j=0; j<= No.elements-1; ++j)
{
    if (time > dat_time[j]) k=j;
}
begin_f_loop(f, t)
{
    if (time >= dat_time[No.elements-1])
        F_PROFILE(f,t,i) = dat_frac[No.elements-1];
    else if (time == dat_time[0])
        F_PROFILE(f, t, i) = dat_frac[0];
    else
        F_PROFILE(f,t,i) = ((dat_frac[k+1] - dat_frac[k]) / (dat_time[k+1] - dat_time[k])) * (time - dat_time[k]) +
                            dat_frac[k];
}
end_f_loop(f, t)
}

/* -----
UDS solids concentration [g/l]
This routine returns the temporal varying inlet solids concentration.
Compared to the previous UDS, this returns a double solids load
----- */
DEFINE_PROFILE(inlet_solids_double_load, t, i)
{
    real time;
    face_t f;
    int k, j = 0;

    /*No. elements = number of data points; the vectors are filled with experimental data */
    float dat_time[No.elements] = {...};      /* definition of time vector */
    float dat_frac[No.elements] = {...};      /* definition of solids fraction vector */
    time = RP_Get_Real("flow-time");
    for (j=0; j<= No.elements-1; ++j)
    {
        if (time > dat_time[j]) k=j;
    }
    begin_f_loop(f, t)
    {
        if (time >= dat_time[No.elements-1])
            F_PROFILE(f,t,i) = 2*dat_frac[No.elements-1];
        else if (time == dat_time[0])
            F_PROFILE(f, t, i) = 2*dat_frac[0];
        else
            F_PROFILE(f,t,i) = 2*(((dat_frac[k+1] - dat_frac[k]) / (dat_time[k+1] - dat_time[k])) * (time - dat_time[k]) +
                                dat_frac[k]);
    }
    end_f_loop(f, t)
}

/* -----
UDS LiCl concentration [g/l]
This routine returns the temporal varying inlet LiCl concentration.
(inflow rate: 0.158105 m3/s; start tracer test: t=16488 s)
----- */
DEFINE_PROFILE(inlet_LiCl_tracertest, t, i)
{
    real time;
    face_t f;
    real flux;

```

```

real vol = 2.21;
real delta_t = 15;
real Q = 0.1471375;
time = RP_Get_Real("flow-time");
flux = 8.121/delta_t;
begin_f_loop(f, t)
{
  if ((time >= 16488) && (time <= (16488+delta_t)))
    F_PROFILE(f,t,i) = flux/Q*2*exp(-0.5*Q*(time-16488)/vol)*sinh(0.5*Q*(time-16488)/vol) /
      C_R(F_CO(f,t),F_CO_THREAD(f,t));
  else
    F_PROFILE(f,t,i) = flux/Q*(-1+exp(Q/vol*(-(time-16488)+delta_t))+2*exp(-0.5*Q*(time-16488)/vol)*sinh(0.5*Q*
      (time -16488)/vol)) / C_R(F_CO(f,t),F_CO_THREAD(f,t));
}
end_f_loop(f, t)
}

/* -----
UDS initialisation LiCl concentration [g/l]
This routine returns the initial background LiCl concentration.
----- */
DEFINE_ON_DEMAND(background_LiCl_conc)
{
  Domain *d;
  cell_t c;
  Thread *t;
  d = Get_Domain(1);
  thread_loop_c(t,d)
  {
    begin_c_loop_all(c,t)
    {
      C_UDSI(c,t,UDS_TRACER) = 183.2e-6 / C_R(c, t);
    }
    end_c_loop_all(c,t)
  }
}

```


E

Appendix E

Calculation of the Scraper's Force

This appendix describes how the scraper action is implemented in Fluent. Because only 2D simulations are considered in this dissertation, some simplifications of the 3D scraper configuration have to be made. The implementation in Fluent will thus only consider the radial momentum component of the scraper. Since the scraper itself is not modelled, the approach consists of giving an additional momentum source to the fluid parcel corresponding to the present location of the scraper. This source of momentum equals the extra momentum that the scraper transfers to the fluid; i.e. if the scraper moves faster than the liquid the momentum source will be positive. *Vice versa*, a slow scraper will decelerate the liquid. The analysis as presented here is inspired by the work of Warden (1981) and Albertson (1992). These researchers described scrapers as devices that push the solids towards the hopper. To analyse and quantify the mechanism they consider the force balance on the scraper.

Before broaching the subject, a quick look at a similar system is presented. Consider a mass m sliding on a slope θ by gravity (Figure E.1, left). Obviously, the mass will not move as long as the component of the gravity force tangential to the slope is compensated by the friction force. Only when the slope exceeds a critical value the gravitational force will be large enough to let the mass slide. If the reference coordinate system is fixed to the ground, the mass will have a certain velocity relative to the ground. Conversely, for a coordinate system linked to the mass, the ground will move relatively to the mass, but in the opposite direction as before. The scraper in Figure E.1 (right) can be treated in a similar way. Here, a force F_s is exerted by the scraper on the mass, i.e. the sludge. The difference with the previous system is that here the scraper is moving and the mass is stationary. Again, this force can be decomposed into components perpendicular F_{\perp} and tangential F_{\parallel} to the scraper. If the frictional force between scraper blade and sludge compensates for F_{\parallel} , the sludge will only move in a direction perpendicular to the blade. If, on the other hand, the angle θ between F_s and F_{\perp} increases, the frictional force may reach its critical value and the sludge will move along the blade as well. Again, with a reference coordinate system linked to the blade, the sludge will move the opposite of the tangential force.

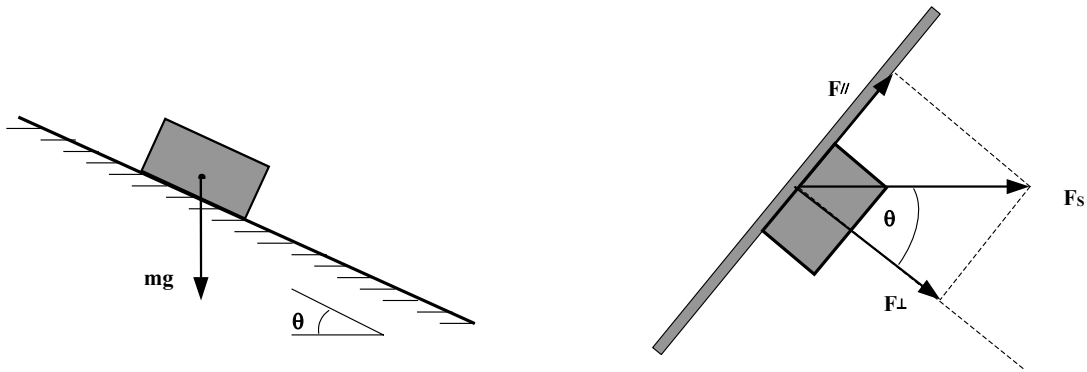


Figure E.1 Force balance similarity between a mass moving on a slope (left) and a scraper (right)

In the next stage, these preliminary concepts are used to model the complete system of settling tank and moving scraper. Only a straight scraper blade is considered here (as it applies to the settling tanks at the Oxley Creek (Australia) WWTP. It is important to note that the calculation of the forces in the radial direction, i.e. along the radius of the tank, are only possible when the angle the scraper makes with the tangent at the side wall is different from ninety degrees. If it is perpendicular to this tangent, the force exerted by the blade is normal to the modelled cross-section and no radial component exists.

The force exerted by the blade onto the sludge parcel may be calculated as the time-derivative of the blade's momentum. It is this momentum that is ultimately transferred to the sludge.

$$F_s = \frac{\partial \rho v_s}{\partial t} \quad (\text{E.1})$$

with v_s the scraper's local velocity. In a complex system as the settling tank it is very likely that the sludge already has a velocity v_{sludge} . It is clear that no momentum from the blade is transferred if the sludge has the same velocity. Hence, Equation E.1 needs to be rewritten as

$$F_s = \frac{\rho(v_s - v_{sludge})}{\Delta t} \quad (\text{E.2})$$

In this way, the problem is reformulated as the determination of the scraper velocity both in time and space.

E.1 Needed information about the scraper

Before starting the mathematical development some information about the settling tank and the scraper is needed. From mechanical drawings of the settling tank, the following parameters may be extracted (see also Figure E.2):

- the angle between blade and considered cross-section at first transect, i.e. α_1
- the radius of the settling tank, i.e. R_1
- the length of the blade, i.e. L

The scraper velocity (tangent) at the side wall v_{wall} can be easily measured on-site. From this and the perimeter of the tank, the angular velocity ω is calculated as

$$\omega = \frac{2\pi R_1}{v_{wall}}.$$

Once the scraper transects the (CFD) modelled cross-section of the tank (see Figure E.2), its force needs to be computed that changes in both time and space (Equation E.2). For the simulations it is essential to know during which period the force is applied, i.e. the time needed by the scraper to completely pass the considered cross-section. This transfer time $t_{transfer}$ may be computed as follows (see Figure E.2)

$$t_{transfer} = \frac{\theta}{\omega}.$$

The angle θ between the outer ends of the scraper is calculated as

$$\theta = \tan^{-1}\left(\frac{L \sin \alpha_1}{R_1 - L \cos \alpha_1}\right)$$

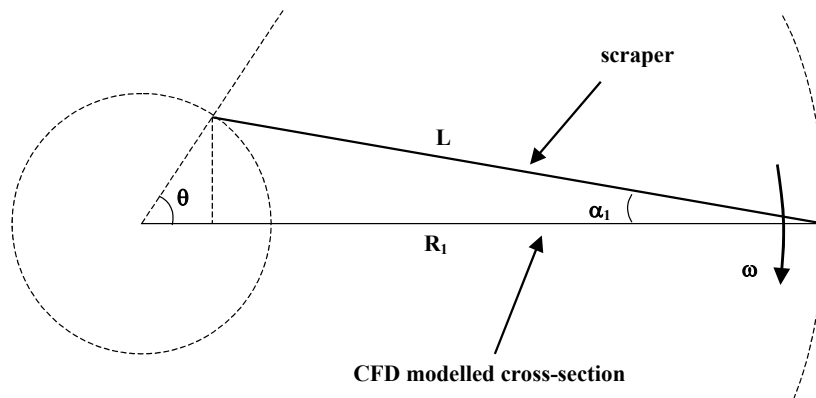


Figure E.2 Scheme used for the calculation of transfer time

E.2 Calculation of the scraper's radial velocity

With the above information it is possible to compute the radial velocity component of the scraper blade. Consider first a sketch of the circular settling tank section as presented in Figure E.3; this allows an understanding of what is exactly considered. The radial velocity component clearly decreases the more the blade passes the considered cross-section. Indeed, the tangential velocity decreases towards the centre of the settling tank. From the measured velocity at the side wall, the tangential velocity v_r at a distance r from the centre equals

$$v_r = v_{wall} \frac{r}{R_1}. \quad (E.3)$$

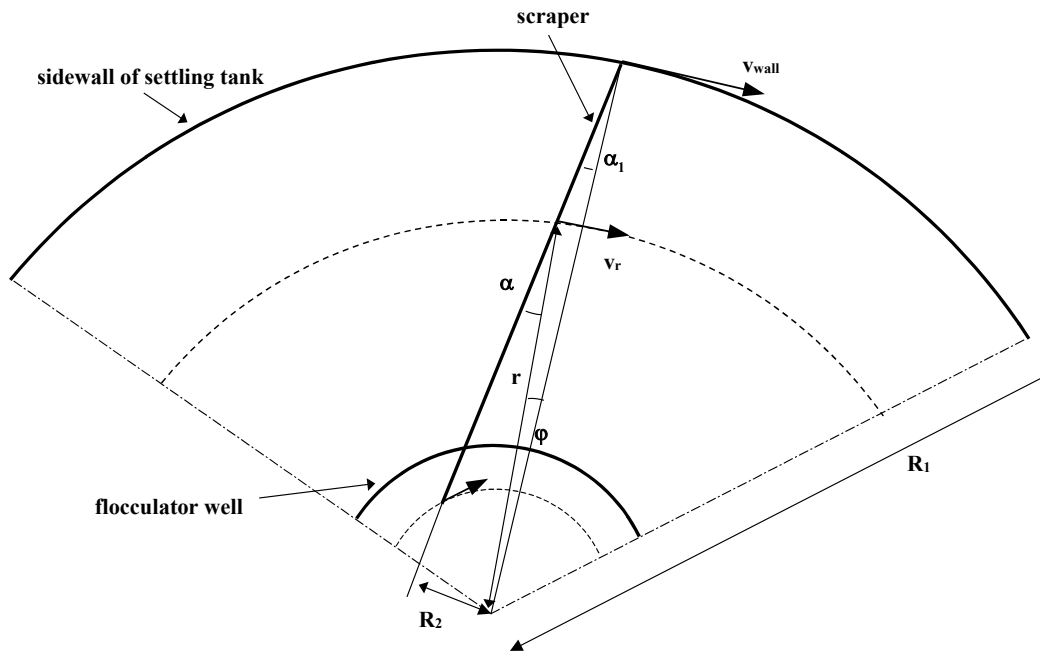


Figure E.3 Scheme of circular settling tank with straight scraper blade

To derive expressions for the radial velocity components, the velocity v_r is decomposed in components perpendicular and tangential to the blade. This is presented in close-up in Figure E.4 for both velocity components.

Firstly, the perpendicular velocity component is discussed (Figure E.4, left). Obviously, this velocity equals $v_r \cos \alpha$ and is responsible for the sludge movement towards the hopper. To compute this velocity radial to the hopper, $v_{r,in}$ may be written as

$$\begin{aligned}
 v_{r,in} &= v_r \cos \alpha \cos \left(\frac{\pi}{2} - \alpha \right) \\
 &= v_r \cos \alpha \sin \alpha \\
 &= \frac{1}{2} v_r \sin 2\alpha
 \end{aligned} \tag{E.4}$$

Substitution by Equation E.3 results in the radial velocity component that moves the sludge to the hopper.

Secondly, the tangential component of v_r , equal to $v_r \sin \alpha$, also results in a radial velocity component $v_{r,out}$ as depicted in Figure E.4 (right). It is this radial velocity that reduces the inward velocity to the hopper from Equation E.4. However, this outward radial velocity only exists when friction prevails between scraper and sludge. Without any friction, no tangential momentum is transferred and the blade moves (only tangentially) independently of the sludge flocs. Whether a frictional force is effectively exerted onto the sludge parcel depends on the roughness of the blade. In this respect, Albertson (1992) included a transport efficiency factor to account for the reduced inward velocity by friction. Warden (1981), however, mentioned a virtual zero friction; due to the large portion of water in the floc structure a lubrication film between solids particles and blade exists reducing the angle of friction to zero. Hence, it will not be considered any further in this mathematical derivation.

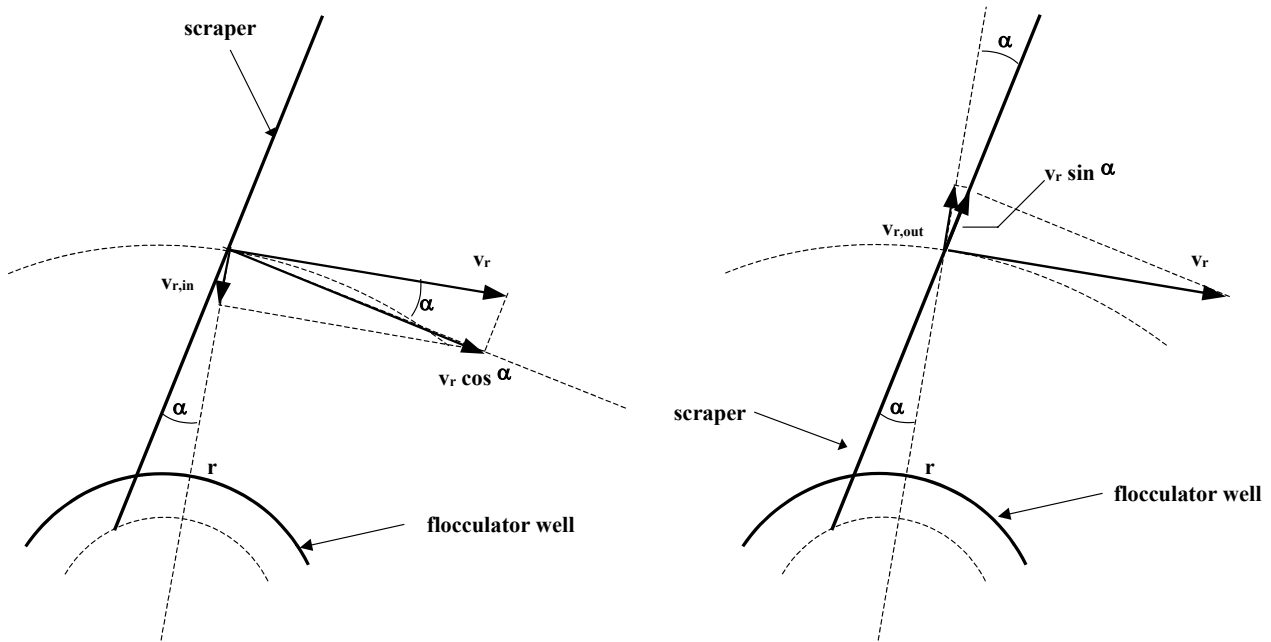


Figure E.4 Decomposition of the tangential velocity vector into components perpendicular (left) and tangential (right) to the blade

At this point, the angle α is still unknown and needs to be resolved in order to compute the radial velocity with Equation E.4. Figure E.3 clearly indicates that its value changes in time as the scraper moves across the modelled cross-section. At time t_0 the scraper transects this cross-section at the side wall at an angle α_1 . The distance between this transect and the centre of the settling tank changes from R_1 to minimally R_2 . The latter may only be obtained for α equalling $\pi/2$ at the end of the scraper's passage. Identically to the moving scraper, the cross-section may be assumed to rotate at an angular velocity ω while the scraper is taken stationary (Figure E.5). This situation is simply obtained by changing the reference coordinate system from the cross-section to the scraper. To compute the angle α , the angle φ (at time t) from Figure E.5 first needs to be resolved. This is easily calculated from

$$\varphi = \omega(t - t_0). \quad (\text{E.5})$$

Hence, α is computed by

$$\alpha = \varphi + \alpha_1. \quad (\text{E.6})$$

When this angle is known, the distance r may finally be computed as

$$r = \frac{R_2}{\sin \alpha}. \quad (\text{E.7})$$

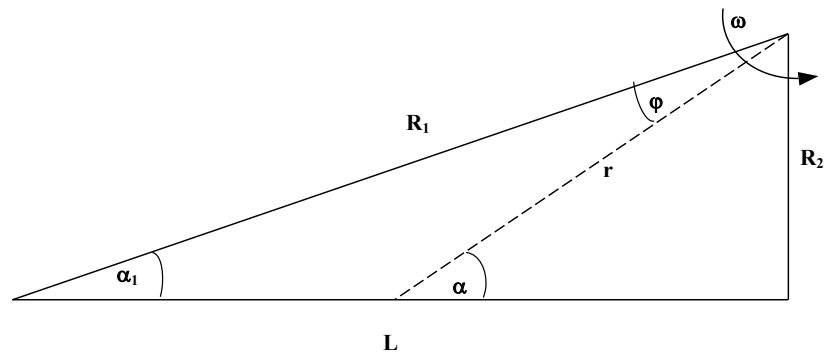


Figure E.5 Scheme of scraper movement

To conclude, the radial velocity momentum is computed by the following sequence of calculations, i.e.

1. the angle φ at time t (Equation E.5)
2. the angle α (Equation E.6)
3. the radial distance r between scraper transect and the centre of the tank (Equation E.7)
4. the tangential velocity v_r at distance r (Equation E.3)
5. the radial velocity $v_{r,in}$ at distance r (Equation E.4)
6. the momentum source F_S (Equation E.2)

It is stressed that the computed force is only directed horizontally because the blade is assumed vertical.

E.3 Application: Scraper at Oxley WWTP

As an example, the previous calculations are applied to the rectilinear scraper at the Oxley Creek (Australia) WWTP. The resulting radial (and horizontal) velocities are used for simulations in Chapter 5.

From mechanical drawings and on-site observations, the operational data in Table E.1 are obtained.

Table E.1 Characterisation of Oxley WWTP scraper

parameter	value
R_1 (m)	9.9
R_2 (m)	0.863
L (m)	8.03
v_{wall} (m/s)	0.02
α_1 (rad)	0.0813

With these data the radial velocity may be computed in both time and space. The location in time of the scraper's transect with the cross-section for the Oxley Creek WWTP settling tank is given in Figure E.6. Due to its rotational movement, the scraper passes the cross-

section slower at small radii. As a result, the radial velocity component will decrease too (Figure E.7). Relatively, the radial velocity does not change as much as the tangential velocity; however, its magnitude is a factor 3-11x lower than the tangential velocity (Figure E.8).

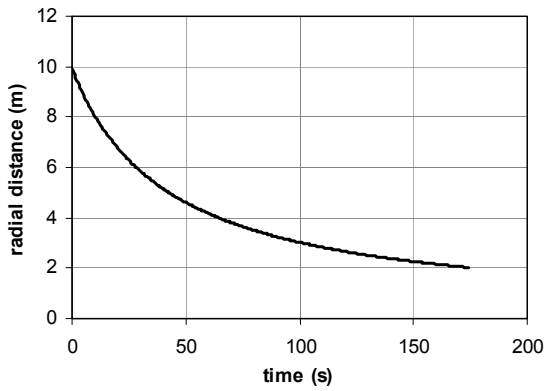


Figure E.6 Temporal evolution of the scraper's transect position

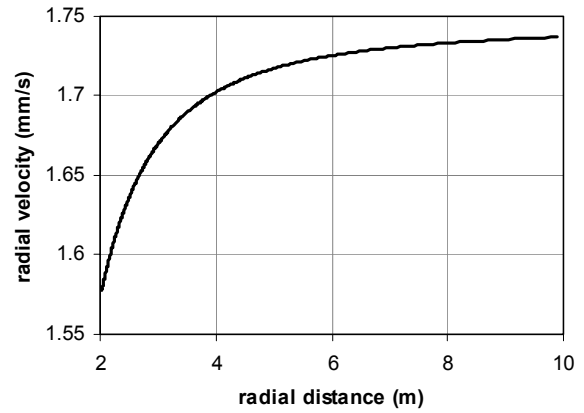


Figure E.7 Evolution of radial scraper velocity as function of radial distance

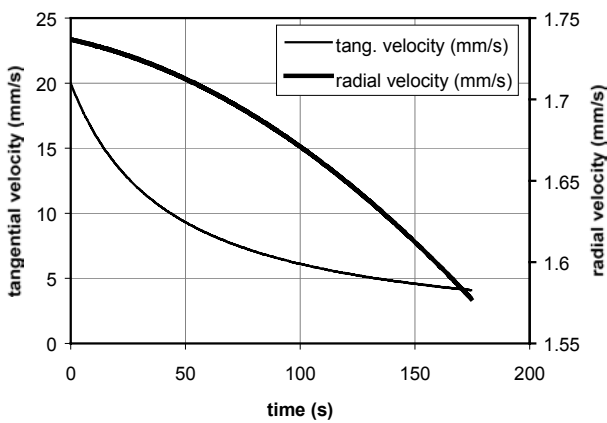


Figure E.8 Temporal evolution of both tangential and radial velocity of the scraper

F

Appendix F

Sludge Flow on Sloped Flat Floors

Solids transport in the secondary settling tank largely depends on the force balance acting on a sludge parcel. The two major influences are gravity and viscous forces. It is therefore hypothesised that different solids densities and rheology determine whether the solids are properly transported along the bottom floor of a settling tank or not. To calculate this solids transport, the velocity profiles are computed and investigated for both Newtonian and Bingham flows. This is subsequently utilised in Chapter 7 to describe discrepancies in flow behaviour as a consequence of rheology and zeolite dosing.

F.1 Momentum balance of the flow system

In a settling tank solids reside on the sloped floor and are transported to the sump by both gravitational forces and advection. For simplicity one only considers gravitational flow; however, also buoyancy is included in the governing equations. At the solids blanket-supernatant interface it is further assumed that no momentum is exchanged (Hunt, 1994) and no solids concentration gradients exist in the blanket. Accounting for laminar flow in the system, the momentum balance on a control volume (Figure F.1) is found to reduce to

$$\tau = \Delta\rho g \sin \beta x \quad (\text{F.1})$$

with $\Delta\rho$, g , β and x being the density difference between sludge and the surrounding water, the gravitational acceleration, the bottom slope and the depth from the interface respectively. A similar mathematical derivation can be found in Bird *et al.* (1960) and Hunt (1994). Whereas they only consider the fluid density, Jiang & LeBlond (1992, 1993) made notice of the density difference to account for buoyancy.

To further calculate the velocity profile information about rheology is needed. Two flow situations will be discussed, i.e. a Newtonian and a Bingham flow.

F.2 Computed velocity profiles

Newtonian flow

From Table 2.4 the stress-shear rate relation for Newtonian fluids is substituted in Equation F.1:

$$-\mu \frac{dv}{dx} = \Delta\rho g \sin \beta x$$

Integration, and accounting for the no-slip boundary condition at the floor, $x = D$, gives

$$\int_0^v dv = -\frac{\Delta\rho g \sin \beta}{\mu} \int_D^x x dx$$

Finally, the velocity profiles reads

$$v = \frac{\Delta\rho g \sin \beta}{2\mu} (D^2 - x^2)$$

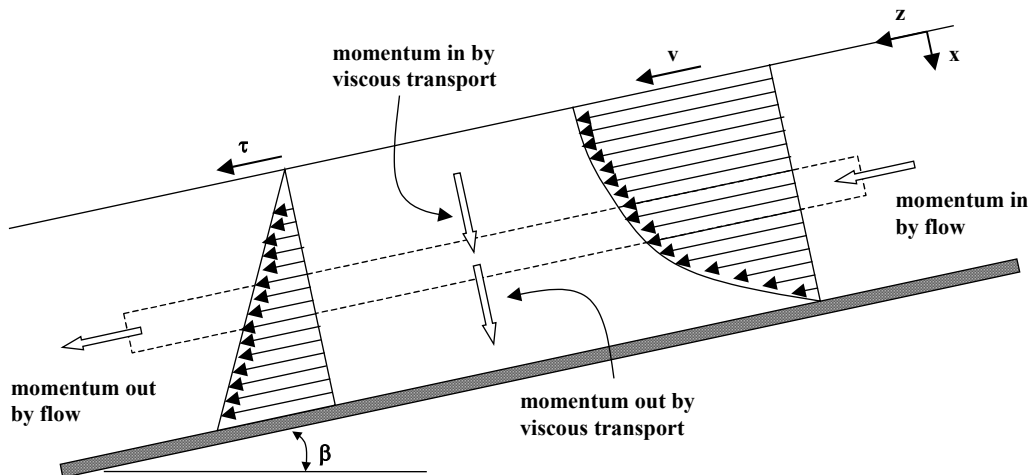


Figure F.1 Viscous flow on top of a sloped floor

Bingham flow

For Bingham fluids no velocity gradient is observed when the stress is below a certain threshold, the so-called *yield stress*. When a sludge layer is built up by a sedimentation influx clearly no flow will exist as long as the stress (by gravitation) does not exceed this yield stress. Knowing the yield stress of sludge, which is a fluid property, the yield depth x_0 is calculated by Equation F.1 as (see also Huang & Garcíá (1997))

$$x_0 = \frac{\tau_0}{\Delta\rho g \sin \beta}$$

If the sludge layer is deeper than this yield depth the sludge starts flowing and two velocity profiles will establish, (i) a plug flow near the interface and extending over the yield depth, and (ii) a shear flow between the yield depth and the bottom floor where the no-slip boundary condition exists (Figure F.2). The latter expresses itself as a parabolic velocity profile. Following Figure F.2 the velocity of the plug v_0 is determined by the total layer depth D . Below the yield depth, the velocity profile can be computed utilising Table 2.4 as

$$\tau_0 - K \frac{dv}{dx} = \Delta\rho g \sin \beta x$$

Integration between depths x_0 and x with their respective velocities v_0 and v results in

$$\int_{v_0}^v dv = -\frac{\Delta\rho g \sin \beta}{K} \int_{x_0}^x x dx + \frac{\tau_0}{K} \int_{x_0}^x dx$$

$$v = v_0 + \frac{\Delta\rho g \sin \beta}{2K} (x_0^2 - x^2) - \frac{\tau_0}{K} (x_0 - x)$$

Clearly, the flow velocity reduces to the plug velocity v_0 for $x = x_0$. A similar result was obtained by Sozanski *et al.* (1997). They did not account for buoyancy however.

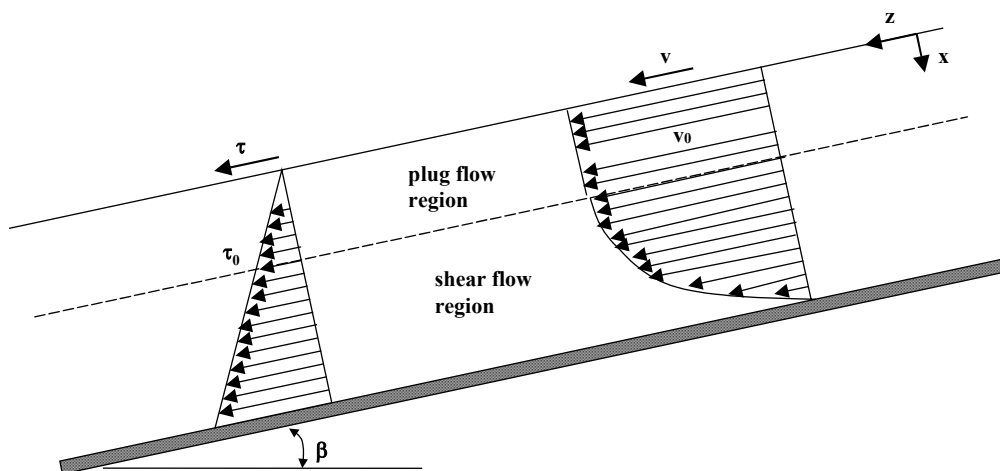


Figure F.2 Velocity and stress profiles of a Bingham flow on top of a sloped floor

References

- Adams E.W. and Rodi W. (1990). Modeling flow and mixing in sedimentation tanks. *J. Hydr. Engrg.*, **116**(7), pp. 895-913.
- Adeyemi I.A., Akanbi C.T. and Fasoro O.G. (1991). Effect of soy fractions on some functional and rheological properties of maize-banana mixtures. *J. Food Process. Preserv.*, **15**, pp. 31-43.
- Agrawal Y.C. and Pottsmith H.C. (2000). Instruments for particle size and settling velocity observations in sediment transport. *Mar. Geol.*, **168**, pp. 89-114.
- Agunwamba J.C., Egbuniwe N. and Ademiluyi J.O. (1992). Prediction of the dispersion number in waste stabilization ponds. *Wat. Res.*, **26**(1), pp. 85-89.
- Albertson O.E. (1991). Improving the rapid sludge removal collector. *Proc. 64th Annual WEF Conference and Exposition on Water Quality and Wastewater Treatment*, October, Toronto, Canada.
- Albertson O.E. (1994). Sludge hopper design for activated sludge clarifiers. *Proc. 1994 Nat. Conf. On Envir. Engrg.*, ASCE, 11-13 July, Boulder, CO, USA.
- Albertson O.E. and Okey R.W. (1992). Evaluating scraper designs. *Wat. Environ. & Technol.*, **4**(1), pp. 52-58.
- Alex J., Kolish G. and Krause K. (2002). Model structure identification for wastewater treatment simulation based on computational fluid dynamics. *Wat. Sci. Tech.*, **45**(4-5), pp. 325-334.
- Alex J., Tschepetzki R., Jumar U., Obenaus F. and Rosenwinkel K.-H. (1999). Analysis and design of suitable model structures for activated sludge tanks with circulating flow. *Wat. Sci. Tech.*, **39**(4), pp. 55-60.
- Alexandrou A.N., Pan Y., Apelian D. and Georgiou G. (2002). Semisolid material characterization using computational rheology. *Proc. 7th S2P 2002, Int. Conf. on Semi-Solid Processing of Alloys and Composites*, 24-28 September, Tsukuba, Japan.
- Amal R., Bushell G.C., Lembong P. and Raper J.A. (1998). Fractal aggregates of hematite ellipsoids. *Proc. 26th Austr. Chem. Eng. Conf (Chemeca '98)*, 28-30 September, Port Douglas, Queensland, Australia.
- Anderson J.D., Grundmann R., Dick E. and Degrez G. (2003). *Introduction to computational fluid dynamics*. Annual Lecture Series von Karman Institute, St. Genesius-Rode, Belgium (ISSN 0377-8312)
- Anderson N.E. (1945). Design of final settling tanks for activated sludge. *Sewage Works Journal*, **17**(1), pp. 50-65.
- Andreadakis A.D. (1993). Physical and chemical properties of activated sludge floc. *Wat. Res.*, **27**(12), pp. 1707-1714.
- Andrews J.F., Stenstrom M.K. and Buhr H.O. (1976). Control systems for the reduction of effluent variability from the activated sludge process. *Progr. Wat. Tech.*, **8**(1), pp. 41-68.
- APHA (1992). *Standard methods for the examination of water and wastewater*. Eds. Clesceri L.S, Greenberg A.E. and Eaton A.D., 2nd Ed. APHA, Washington DC, USA.
- Armbruster M., Krebs P. and Rodi W. (2001). Numerical modelling of dynamic sludge blanket behaviour in secondary clarifiers. *Wat. Sci. Tech.*, **42**(11), pp. 173-180.

- Audic J.M., Fayoux Ch., Lesty Y. and Brisset P. (1994). Sludge retention times distribution in clarifier: a key point for population dynamic and nutrients removal control. *Wat. Sci. Tech.*, **29**(7), pp. 57-60.
- Bachalo W.D. (1999). Particle sizing by diffraction, interference, and imaging techniques. In: *Optical diagnostics of particles & droplets*, Lecture Series 1999-01, von Karman Institute for Fluid Dynamics, 25-29 January.
- Bache D.H., Johnson C., McGilligan J.F. and Rasool E. (1997). A conceptual view of floc structure in the sweep floc domain. *Wat. Sci. Tech.*, **36**(4), pp. 49-56.
- Bale A.J. and Morris A.W. (1987). In situ measurement of particle size in estuarine waters. *Estuarine, Coastal and Shelf Science*, **24**, pp. 253-263.
- Bale A.J., Barrett C.D., West J.R. and Oduyemi K.O.K. (1989). Use of in-situ laser diffraction particle sizing for particle transport studies in estuaries. In: *Developments in Estuarine and Coastal Study Techniques*. Eds. McManus J. and Elliott M. International Symposium Series, Olsen & Olsen, Fredensborg, Denmark.
- Balmforth N.J. and Craster R.V. (1999). A consistent thin-layer theory for Bingham plastics. *J. Non-Newtonian Fluid Mech.*, **84**, pp. 65-81.
- Balmforth N.J. and Craster R.V. (2002). Geophysical aspects of non-Newtonian fluid mechanics. In: *Geomorphological fluid mechanics*. Eds. Balmforth N.J. and Provenzale A., Springer-Verlag, Germany.
- Barbusinski K. and Koscielniak H. (1995). Influence of substrate loading intensity on floc size in activated sludge process. *Wat. Res.*, **29**(7), pp. 1703-1710.
- Barnes H.A. and Walters K. (1985). The yield stress myth? *Rheol. Acta*, **24**, pp. 323-326.
- Barr K.G., Bathes C.A. and Cooksey P.A. (1999). A low capital cost option for improved nitrogen removal - ZELflocc process. AWWA 18th Federal Convention, Adelaide, Australia.
- Barrett P. and Glennon B. (1999). In-line FBRM monitoring of particle size in dilute agitated suspensions. *Part. Part. Syst. Charact.*, **16**, pp. 207-211.
- Barthés-Biesel D. and Acrivos A. (1973). The rheology of suspensions and its relation to phenomenological theories for non-Newtonian fluids. *Int. J. Multiphase Flows*, **1**, pp. 1-24.
- Batchelor G.K. (1972). Sedimentation in a dilute dispersion of spheres. *J. Fluid Mech.*, **52**(2), pp. 245-268.
- Battaglia A., Fox P. and Pohland F.G. (1993). Calculation of residence time distribution from tracer recycle experiments. *Wat. Res.*, **27**(2), pp. 337-341.
- Battistoni P. (1997). Pre-treatment, measurement execution procedure and waste characteristics in the rheology of sewage sludges and the digested organic fraction of municipal solid wastes. *Wat. Sci. Tech.*, **36**(11), pp. 33-41.
- Battistoni P., Fava G., Stanzini C., Cecchi F. and Bassetti A. (1993). Feed characteristics and digester operative conditions as parameters affecting the rheology of digested municipal solid wastes. *Wat. Sci. Tech.*, **27**(2), pp. 37-45.
- Baud O. and Hager W.H. (2000). Tornado vortices in settling tanks. *J. Environ. Eng.*, **126**(2), pp. 189-191.
- Baumer P., Volkart P. and Krebs P. (1996). Dynamic loading tests for final settling tanks. *Wat. Sci. Tech.*, **34**(3-4), pp. 267-274.
- Beaulne M. and Mitsoulis E. (1997). Creeping motion of a sphere in tubes filled with Herschel-Bulkley fluids. *J. Non-Newtonian Fluid Mech.*, **72**, pp. 55-71.
- Behn V.C. (1960). Flow equations for sewage sludges. *J. WPCF*, **32**(7), pp. 728-740.

- Bern M. and Plassmann P. (1999). Mesh generation. In: *Handbook of computational geometry*, Eds. Sack J.-R. and Urratia J., Elsevier Science.
- Beun J.J., Hendriks A., van Loosdrecht M.C.M., Morgenroth E., Wilderer P.A. and Heijnen J.J. (1999). Aerobic granulation in a sequencing batch reactor. *Wat. Res.*, **33**(10), pp. 2283-2290.
- Bhattacharya S. (1999). Yield stress and time-dependent rheological properties of mango pulp. *J. Food Sci.*, **64**(6), pp. 1029-1033.
- Bhattacharya S., Bhat K.K. and Raghuvver K.G. (1992). Rheology of Bengal gram (*Cicer arietinum*) flour suspensions. *J. Food Engineering*, **17**, pp. 83-96.
- Bidault A., Clauss F., Helaine D. and Balavoine C. (1997). Floc agglomeration and structuration by a specific talc mineral composition. *Wat. Sci. Tech.*, **36**(4), pp. 57-68.
- Biggs C.A. (2000). *Activated sludge flocculation: investigating the effect of shear rate and cation concentration on flocculation dynamics*. PhD dissertation, Advanced Wastewater Management Centre, Dep. Chem. Eng., The University of Queensland, Queensland, Australia.
- Biggs S., Habgood M., Jameson G.J. and Yan Y.-d. (1998). The fractal analysis of aggregates formed via a bridging flocculation mechanism. *Proc. 26th Austr. Chem. Eng. Conf (Chemeca '98)*, 28-30 September, Port Douglas, Queensland, Australia.
- Billmeier E. (1988). The influence of blade height on the removal of sludge from activated sludge settling tanks. *Wat. Sci. Tech.*, **20**(4-5), pp. 165-175.
- Bird R.B., Stewart W.E. and Lightfoot E.N. (1960). *Transport Phenomena*. John Wiley & Sons, New York, USA, 780 pp.
- Bird R.B. (1976). Useful non-Newtonian models. *Ann. Rev. Fluid Mech.*, **8**, pp. 13-34.
- Blackery J. and Mitsoulis E. (1997). Creeping motion of a sphere in tubes filled with a Bingham plastic material. *J. Non-Newtonian Fluid Mech.*, **70**, pp. 59-77.
- Bohren C.F. and Huffman D.R. (1983). *Absorption and scattering of light by small particles*. John Wiley & Sons, 530 pp.
- Bokil S.D. (1972). *Effect of mechanical blending on the aerobic digestion of waste activated sludge*. PhD dissertation, Department of Civil Engineering, University of Windsor, Ontario, Canada.
- Botsch B. (1990). Runde Absetzbecken mit Schlammräumen. *Korrespondenz Abwasser*, **37**(7), pp. 770-777.
- Bott C.B., Abrajano J. and Love N.G. (2000). A physiological mechanism for activated sludge deflocculation caused by shock loads of toxic chemicals. *Proc. 73rd Annual WEF Conference and Exposition on Water Quality and Wastewater Treatment*, 14-18 October, Anaheim, California, USA.
- Boyle W.H. (1980). Ranking sludge removal methods. *Water & Sewage Works*, June, pp. 70-72.
- Bradshaw P. (1978). *Turbulence*. Springer-Verlag, Heidelberg, Germany.
- Brenner H. (1974). Rheology of a dilute suspension of axisymmetric Brownian particles. *Int. J. Multiphase Flow*, **1**, pp. 195-341.
- Bretscher U., Krebs P. and Hager W.H. (1992). Improvement of flow in final settling tanks. *J. Environ. Engrg.*, **118**(3), pp. 307-321.
- Brewer E. and Ramsland A. (1995). Particle size determination by automated microscopical imaging analysis with comparison to laser diffraction. *J. Pharma. Sci.*, **84**(4), pp. 499-501.
- Brouckaert C.J. and Buckley C.A. (1999). The use of computational fluid dynamics for improving the design and operation of water and wastewater treatment plants. *Wat. Sci. Tech.*, **40**(4-5), pp. 81-89.

- Bruus J.H., Nielsen P.H. and Keiding K. (1992). On the stability of activated sludge flocs with implications to dewatering. *Wat. Res.*, **26**(12), pp. 1597-1604.
- Bürger R., Concha F., Fjelde K.-K. and Karlsen K.H. (2000). Numerical simulation of the settling of polydisperse suspensions of spheres. *Powder Technol.*, **113**, pp. 30-54.
- Burrows L.J., Stokes A.J., West J.R., Forster C.F. and Martin A.D. (1999). Evaluation of different analytical methods for tracer studies in aeration lanes of activated sludge plants. *Wat. Res.*, **33**(2), pp. 367-374.
- Buscall R., McGowan I.J., Mills P.D.A., Stewart R.F., Sutton D., White T.R. and Yates G.E. (1987). The rheology of strongly-flocculated suspensions. *J. Non-Newtonian Fluid Mech.*, **24**, pp. 183-202.
- Bye C.M. and Dold P.L. (1998). Sludge volume index settleability measures: effect of solids characteristics and test parameters. *Wat. Environ. Res.*, **70**(1), pp. 87-93.
- Cacossa K.F. and Vaccari D.A. (1994). Calibration of a compressive gravity thickening model from a single batch settling curve. *Wat. Sci. Tech.*, **30**(8), pp. 107-116.
- Camp T.R. (1946). Sedimentation and the design of settling tanks. *Trans. ASCE*, **111**, pp. 895-958.
- Camp T.R. (1952). Studies of sedimentation basin design. *Sewage Works*, **25**(1), pp. 1-14.
- Camp T.R. and Stein P.C. (1943). Velocity gradients and internal work in fluid motion. *J. Boston Soc. Civil Eng.*, **30**, pp. 219-237.
- Campbell H.W. and Crescuolo P.J. (1982). The use of rheology for sludge characterization. *Wat. Sci. Tech.*, **14**, pp. 475-489.
- Celik I. and Rodi W. (1988). Modeling suspended sediment transport in nonequilibrium situations. *J. Hydr. Engrg.*, **114**(10), pp. 1157-1188.
- Celik I., Rodi W. and Stamou A.I. (1985). Prediction of hydrodynamic characteristics of rectangular settling tanks. *Proc. Int. Symp. Refined Flow Modelling and Turbulence Measurements*, Iowa City, Iowa, USA.
- Celik I.B., Umbel M.R. and Wilson W.M. (1999). Computations of turbulent mixing at the interface of a density stratified, shear layer. *Proc. 3rd ASME/JSME Joint Fluids Engineering Conf.*, 18-23 July, San Fransisco, California, USA.
- CG&S and Hydromantis Inc. (1996). *Guidance manual for sewage treatment plant process audits*. Report prepared for Ministry of Environment and Energy (Ontario), Water Environment Association of Ontario, Great Lakes 2000 Cleanup Fund.
- Chambers B. (1992). Design methodology for optimisation of aeration efficiency in activated sludge plants. *Med. Fac. Landbouww. Univ. Gent*, **57**(4a), pp. 1631-1642.
- Chapman D. and Browning K.A. (1999). Release of potential shearing instability in warm frontal zones. *Q. J. R. Meteorol. Soc.*, **124**, pp. 1-26.
- Cheng D.C.-H. (1973). A differential form of constitutive relation for thixotropy. *Rheol. Acta*, **12**, pp. 228-233.
- Cho S.H., Colin F., Sardin M. and Prost C. (1993). Settling velocity model of activated sludge. *Wat. Res.*, **27**(70), pp. 1237-1242.
- Chudoba J., Grau P. and Ottova V. (1973). Control of activated sludge filamentous bulking - II. Selection of microorganisms by means of a selector. *Wat. Res.*, **7**, pp. 1389-1406.
- Clark M.M. (1985). Critique of Camp and Stein's RMS velocity gradient. *J. Environ. Eng.*, **111**(6), pp. 741-754.

- Clauss F., Helaine D., Balavoine C. and Bidault (1998). Improving activated sludge floc structure and aggregation for enhanced settling and thickening performances. *Wat. Sci. Tech.*, **38**(8-9), pp. 35-44.
- Cleasby J.L. (1984). Is velocity gradient a valid turbulent flocculation parameter? *J. Environ. Engrg.*, **110**(5), pp. 875-897.
- Cobb E.D. (1994). Broad-band acoustic Doppler current profiler. *Flow Measurement and Instrumentation*, **5**(3), pp. 35-37.
- Coe H.S. and Clevenger G.H. (1916). Methods for determining the capacities of slime-settling tanks. *Trans. Amer. Inst. Min. Engrs.*, **60**, pp. 356-384.
- Coghill P.J., Cunningham K.D., Millen M.J., Rainey S., Sowerby B.D. and Stevens R.J. (2002). On-line slurry particle size analysis. *Proc. 4th World Congress on Particle Technology (WCPT4)*, 21-25 July, Sydney, Australia.
- Colella P. and Puckett E.G. (1994). *Modern numerical methods for fluid flow*. Lecture notes University of California, 152 pp.
(http://www.amath.unc.edu/Faculty/minion/class/puckett/C_P_Noted.pdf)
- Coussot P., Proust S. and Ancey C. (1996). Rheological interpretation of deposits of yield stress fluids. *J. Non-Newtonian Fluid Mech.*, **66**, pp. 55-70.
- Crochet M.J. and Walters K. (1983). Numerical methods in non-Newtonian fluid mechanics. *Ann. Rev. Fluid Mech.*, **15**, pp. 241-260.
- Dabak T. and Yucel O. (1987). Modeling of the concentration and particle size distribution effects on the rheology of highly concentrated suspensions. *Powder Tech.*, **52**, pp. 193-206.
- Dahl C. (1993). *Numerical modelling of flow and settling in secondary settling tanks*. PhD dissertation, Dep. Civil Eng., Aalborg University, Denmark.
- Daigger G.T. and Roper R.E. (1985). The relationship between SVI and activated sludge settling characteristics. *J. WPCF*, **57**(8), pp. 859-866.
- Das D., Keinath T.M., Parker D.S. and Wahlberg E.J. (1993). Floc breakup in activated sludge plants. *Wat. Environ. Res.*, **65**(2), pp. 138-145.
- Davies W.J., Le M.S. and Heath C.R. (1998). Intensified activated sludge process with submerged membrane microfiltration. *Wat. Sci. Tech.*, **38**(4-5), pp. 421-428.
- Daymo E.A., Hylton T.D. and May T.H. (1999). Acceptance testing of the Lasentec focused beam reflectance measurement (FBRM) monitor for slurry transfer applications at Hanford and Oak Ridge. *Proc. SPIE, Nuclear Waste Instrumentation Engineering*, pp. 82-92.
- De Clercq B., Coen F., Vanderhaegen B. and Vanrolleghem P. (1998). Calibrating simple models for mixing and flow propagation in waste water treatment plants. *Wat. Sci. Tech.*, **39**(4), pp. 61-69.
- De Cock W., Blom P., Vaes G. and Berlamont J. (1999). The feasibility of flocculation in a storage sedimentation basin. *Wat. Sci. Tech.*, **39**(2), pp. 75-83.
- Deininger A., Holthausen E. and Wilderer P.A. (1998). Velocity and solids distribution in circular secondary clarifiers: full scale measurements and numerical modelling. *Wat. Res.*, **32**(10), pp. 2951-2958.
- Demetriades K. and McClements D.J. (1999). Ultrasonic attenuation spectroscopy study of flocculation in protein stabilized emulsions. *Colloids and Surfaces A*, **150**, pp. 45-54.
- Dentel S.K. (1997). Evaluation and role of rheological properties in sludge management. *Wat. Sci. Tech.*, **36**(11), pp. 1-8.
- Devantier B.A. and Larock B.E. (1986). Modelling a recirculating density-driven turbulent flow. *Int. J. Num. Meth. Fluids*, **6**, pp. 241-253.

- Dez H., Bert J. and Dupuy-Philon J. (1997). Colloid stability and population density studied by means of a microholographic technique. *J. Colloid Interface Sci.*, **185**, pp. 190-196.
- Dick R.I. and Buck J.H. (1985). Measurement of activated sludge rheology. *Proc. Environmental Engineering Division Specialty Conference, ASCE*, **111**, pp. 539-545.
- Dick R.I. and Vesilind P.A. (1969). The sludge volume index - what is it? *J. WPCF*, **41**(7), pp. 1285-1291.
- Dixon D.C. (1985). Capacity and control of clarifiers and thickeners. *J. WPCF*, **57**(1), pp. 46-52.
- Dochain D. and Vanrolleghem P.A. (2001). *Dynamical modelling and estimation in wastewater treatment processes*. IWA Publishing, London, UK. 342 pp.
- Dowding P.J., Goodwin J.W. and Vincent B. (2001). Factors governing emulsion droplet and solid particle size measurements performed using the focused beam reflectance technique. *Colloids and Surfaces A*, **192**, pp. 5-13.
- DuCoste J.J. and Clark M.M. (1998). The influence of tank size and impeller geometry on turbulent flocculation: I. Experimental. *Environ. Engrg. Sci.*, **15**(3), pp. 215-224.
- Dyer K.R. and Manning A.J. (1999). Observation of the size, settling velocity and effective density of flocs, and their fractal dimensions. *J. Sea Res.*, **41**, pp. 87-95.
- Dymaczewski Z., Kempa E.S. and Sozanski M.M. (1997). Coagulation as a structure-forming separation process in water and wastewater treatment. *Wat. Sci. Tech.*, **36**(4), pp. 25-32.
- Echeverría E., Seco A. and Ferrer J. (1992). Study of the factors affecting activated sludge settling in domestic wastewater treatment plants. *Wat. Sci. Tech.*, **25**(4-5), pp. 272-279.
- Edzwald J.K. (1995). Principles and applications of dissolved air flotation. *Wat. Sci. Tech.*, **31**(3-4), pp. 1-23.
- Ekama G.A. and Marais G.v.R. (1986). Sludge settleability. Secondary settling tank design procedures. *Water Pollut. Control*, **85**(1), pp. 101-113.
- Ekama G.A., Barnard J.L., Günthert F.W., Krebs P., McCorquodale J.A., Parker D.S. and Wahlberg E.J. (1997). *Secondary settling tanks: theory, modelling and operation*. IAWQ Scientific and Technical Report No. 6.
- El-Baroudi H. and Fuller D.R. (1973). Tracer dispersion of high rate settling tanks. *J. Environ. Engrg.*, **99**(EE3), pp. 347-368.
- Engelhardt N., Firk W. and Warnken W. (1998). Integration of membrane filtration into the activated sludge process in municipal wastewater treatment. *Wat. Sci. Tech.*, **38**(4-5), pp. 429-436.
- EPA (1987). *The causes and control of activated sludge bulking and foaming*. Summary Report, U.S. Environmental Protection Agency, Centre for Environmental Research Information, Cincinnati, USA.
- Fischerström C.N.H., Isgård E. and Larsen I. (1967). Settling of activated sludge in horizontal tanks. *J. Sanitary Eng. Div.*, **93**(SA3), pp. 73-83.
- Fitch B. (1979). Sedimentation of flocculent suspensions: state of the art. *AIChE Journal*, **25**(6), pp. 913-930.
- Fitch B. (1983). Kynch theory and compression zones. *AIChE Journal*, **29**(6), pp. 940-947.
- Fitch B. (1993). Thickening theories - an analysis. *AIChE Journal*, **39**(1), pp. 27-36.
- Fitzpatrick J.J., Weber M., Schober C., Weidendorfer K. and Teunou E. (2002). Effect of viscosity and vortex formation on the mixing of powders in water to form high concentration solutions in stirred-tanks. *Proc. 4th World Congress on Particle Technology (WCPT4)*, 21-25 July, Sydney, Australia.

- Font R. (1988). Compression zone effect in batch sedimentation. *AIChE Journal*, **34**(2), pp. 229-238.
- Ford E.W. and Steffe J.F. (1986). Quantifying thixotropy in starch-thickened, strained apricots using mixer viscometry techniques. *J. Texture Studies*, **17**, pp. 75-85.
- Forster C.F. (1982). Sludge surfaces and their relation to the rheology of sewage sludge suspensions. *J. Chem. Tech. Biotechnol.*, **32**, pp. 799-807.
- Forster C.F. (1983). Bound water in sewage sludges and its relationship to sludge surfaces and sludge viscosities. *J. Chem. Tech. Biotechnol.*, **33B**, pp. 76-84.
- Frankel N.A. and Acrivos A. (1967). On the viscosity of a concentrated suspension of solid spheres. *Chem. Eng. Sci.*, **22**, pp. 847-853.
- Frigaard I.A. and Scherzer O. (1998). Uniaxial exchange flows of two Bingham fluids in a cylindrical duct. *IMA J. Appl. Math.*, **61**, pp. 237-266.
- Frisch U. (1998). *Turbulence: the legacy of A.N. Kolmogorov*. Cambridge University Press, Cambridge, UK, 296 pp.
- Froment G.F. and Bischoff K.B. (1990). *Chemical reactor analysis and design*. 2nd ed., Wiley, New York, USA.
- Fuchs A. and Staudinger G. (1999). Characterising the clarification of the supernatant of activated sludges. *Wat. Res.*, **33**(11), pp. 2527-2534.
- Fulford J.M. (1995). Effects of pulsating flow on current meter performance. *Proc. 1st Int. Conf. on Water Resources Eng*, ASCE.
- Galai (2003). <http://www.galai.co.il>
- Galil N.I., Schwartz-Mittelman A. and Saroussi-Zohar O. (1998). Biomass deflocculation and process disturbances exerted by phenol induced transient load conditions. *Wat. Sci. Tech.*, **38**(8-9), pp. 105-112.
- Ganczarczyk J.J. (1994). Microbial aggregates in wastewater treatment. *Wat. Sci. Tech.*, **30**(8), pp. 87-95.
- Gargett A.E. (1994). Observing turbulence with a modified acoustic Doppler current profiler. *J. Atmos. Oceanic Technol.*, **11**, pp. 1592-1610.
- Gonzalez J.A., Melching C.S. and Oberg K.A. (1996). Analysis of open-channel velocity measurements collected with an acoustic Doppler current profiler. *Proc. of the 1st Int. Conf. on New/Emerging Concepts for Rivers*, 22-26 September, Chicago, USA.
- Goodwin J.A.S. and Forster C.F. (1985). A further examination into the composition of activated sludge surfaces in relation to their settlement characteristics. *Wat. Res.*, **19**(4), pp. 527-533.
- Gordon R.L. (1989). Acoustic measurement of river discharge. *J. Hydr. Engrg.*, **115**(7), pp. 925-936.
- Gordon R.L. (1996). *Acoustic Doppler current profilers Principles of operation: a practical primer*. 2nd Ed., RD Instruments.
- Govoreanu R., Seghers D., Nopens I., De Clercq B., Saveyn H., Capalozza C., Van der Meeren P., Verstraete W., Top E. and Vanrolleghem P.A. (2002). Linking floc structure and settling properties to activated sludge population dynamics in an SBR. *Wat. Sci. Tech.* (accepted)
- Gréhan G. (1999). Theory on laser light scattering by particles and droplets: GLMT approach. In: *Optical diagnostics of particles & droplets*, Lecture Series 1999-01, von Karman Institute for Fluid Dynamics, 25-29 January.
- Grijspeerdt K. (1996). Development of an on-line sensor for the sedimentation process in activated sludge plants. PhD dissertation, Ghent University, Ghent, Belgium.

- Grijspeerdt K. and Verstraete W. (1996). A sensor for the secondary clarifier based on image analysis. *Wat. Sci. Tech.*, **33**(1), pp. 61-70.
- Grijspeerdt K., Vanrolleghem P. and Verstraete W. (1995). Selection of one-dimensional sedimentation: models for on-line use. *Wat. Sci. Tech.*, **31**(2), pp. 193-204.
- Groen D.J. (1994). *Macromixing in bioreactors*. PhD dissertation, Technical University Delft, Delft, The Netherlands.
- Guan J., Waite T.D. and Amal R. (1998). Rapid structure characterization of bacterial aggregates. *Environ. Sci. Technol.*, **32**, pp. 3735-3742.
- Guan J., Waite T.D., Amal R., Bustamante H. and Wukasch R. (1998). Rapid determination of fractal structure of bacterial assemblages in wastewater treatment: implications to process optimisation. *Wat. Sci. Tech.*, **38**(2), pp. 9-15.
- Gujer W., Henze M., Mino T., Matsuo T., Wentzel M. and Marais G.V.R. (1995). Activated sludge model No. 2: biological phosphorus removal. *Wat. Sci. Tech.*, **31**(2), pp. 1-11.
- Günder B. and Krauth K. (1998). Replacement of secondary clarification by membrane separation - results with plate and hollow fibre modules. *Wat. Sci. Tech.*, **38**(4-5), pp. 383-393.
- Günthert F.W. (1984). Thickening zone and sludge removal in circular final settling tanks. *Wat. Sci. Tech.*, **16**, pp. 303-316.
- Haas S. (1996). Turbulent transport equations in cylindrical and spherical coordinate systems. In: *Achsensymmetrische Quell- und Senkenströmungen*, PhD dissertation, Technical University Vienna, Austria.
- Han M. and Lawler D.F. (1992). The (relative) insignificance of G in flocculation. *J. Am. Water Works Assoc.*, **84**, pp. 79-91.
- Hazen A. (1904). On sedimentation. *Trans. ASCE*, **53**, pp. 45-71.
- Head R., Hart J. and Graham N. (1997). Simulating the effect of blanket characteristics on the floc blanket clarification process. *Wat. Sci. Tech.*, **36**(4), pp. 77-84.
- Heath A.R., Fawell P.D., Bahri P.A. and Swift J.D. (2002). Estimating average particle size by focused beam reflectance measurement. *Part. Part. Syst. Charact.*, **19**(2), pp. 84-95.
- Henze M., Dupont R., Grau P. and de la Sota A. (1993). Rising sludge in secondary settlers due to denitrification. *Wat. Res.*, **27**(2), pp. 231-236.
- Henze M., Grady Jr. C.P.L., Gujer W., Marais G.v.R. and Matsuo T. (1987). *Activated sludge model No. 1. IAWQ Scientific and Technical Reports No. 3*, IAWQ, London, England.
- Herath G., Yamamoto K. and Urase T. (1998). Mechanism of bacterial and viral transport through microfiltration membranes. *Wat. Sci. Tech.*, **38**(4-5), pp. 489-496.
- Hervo O., Lainé S., Phan L. and Lesavre J. (2000). Optimisation du fonctionnement hydraulique des clarificateurs avec le logiciel de simulation hydraulique "Fluent". *Proc. Of Journées thématiques "Automatique et Environnement"*, 9-10 March, Centre de Recherche en Automatique de Nancy, Nancy, France.
- Heynen J.J., Kossen N.W.F. and van 't Riet K. (1984). *Bioprocess Technology*. Course notes, Dep. Chem. Tech., Technical University Delft, Delft, The Netherlands.
- Higgs S.J. and Norrington R.J. (1971). Rheological properties of selected foodstuffs. *Process Biochemistry*, **6**(5), pp. 52-54.
- Hinton S.W. and Stensel H.D. (1991). Experimental observation of trickling filter hydraulics. *Wat. Res.*, **25**(11), pp. 1389-1398.
- Hirsch C. (1997). *Numerical computation of internal and external flows. Vol. 1, Fundamentals of numerical discretization*. John Wiley & Sons, West Sussex, UK, 515 pp.

- Hirsch C. (1998). *Numerical computation of internal and external flows. Vol. 2, Computational methods for inviscid and viscous flows*. John Wiley & Sons, West Sussex, UK, 691 pp.
- Hoffmann K., Reuter C. and Köngeter J. (1999). Direct settling velocity detection of activated sludge flocs using DPIV. *Proc. 8th Int. Conf. On Laser Anemometry - Advances and Applications*, 6-9 September, Rome, Italy.
- Höfler K., Schwarzer S. and Wachmann B. (1999). Simulation of hindered settling in bidisperse suspensions of rigid spheres. *Comp. Phys. Comm.*, **121-122**, pp. 268-269.
- Holdsworth S.D. (1993). Rheological models used for the prediction of the flow properties of food products: a literature review. *Trans. I. Chem. E.*, **71**(part C), pp. 139-179.
- Huang X. and García M.H. (1997). A perturbation solution for Bingham-plastic mudflows. *J. Hydr. Engrg.*, **123**(11), pp. 986-994.
- Hughes A.W., Longair I.M., Ashley R.M. and Kirby K. (1996). Using an array of ultrasonic velocity transducers to improve the accuracy of large sewer mean velocity measurements. *Wat. Sci. Tech.*, **33**(1), pp. 1-12.
- Humeau P., Baléo J.-N., Raynaud F., Bourcier J. and Le Cloirec P. (2000). Flow characterization in a gas-liquid column: application to a bioscrubber for the deodorization of waste gases. *Wat. Sci. Tech.*, **41**(12), pp. 191-198.
- Hunt B. (1994). Newtonian fluid mechanics treatment of debris flows and avalanches. *J. Hydr. Engrg.*, **120**(12), pp. 1350-1363.
- Imam E., McCorquodale J.A. and Bewtra J.K. (1983). Numerical modeling of sedimentation tanks. *J. Hydr. Engrg.*, **109**(12), pp. 1740-1754.
- Issa R.I. (1986). Solution of the implicit discretized fluid flow equation by operator splitting. *J. Comput. Phys.*, **62**, pp. 40-65.
- Ives K.J. and Hoyer O. (1998). Tracer studies of the hydraulics of tapered flocculation. *Wat. Sci. Tech.*, **37**(10), pp. 69-77.
- Jackson R. (1997). Locally averaged equations of motion for a mixture of identical spherical particles and a Newtonian fluid. *Chem. Eng. Sci.*, **52**(15), pp. 2457-2469.
- Jeffrey D.J. and Acrivos A. (1976). The rheological properties of suspensions of rigid particles. *AIChE Journal*, **22**(3), pp. 417-432.
- Ji Z., McCorquodale J.A., Zhou S. and Vitasovic Z. (1996). A dynamic solids inventory model for activated sludge systems. *Wat. Environ. Res.*, **68**(3), pp. 329-337.
- Jiang L. and LeBlond P.H. (1992). The coupling of a submarine slide and the surface waves which it generates. *J. Geophys. Res.*, **97**(8), pp. 12731-12744.
- Jiang L. and LeBlond P.H. (1993). Numerical modeling of an underwater Bingham plastic mudslide and the waves which it generates. *J. Geophys. Res.*, **98**(6), pp. 10303-10317.
- Jones R.M., Harvey A.D. and Acharya S. (1999). Two-equation turbulence modeling for impeller stirred tanks. *Proc. 3th ASME/JSME Joint Fluids Engineering Conf.*, 18-23 July, San Francisco, California.
- Jorand F., Zartarian F., Thomas F., Block J.C., Bottero J.Y., Villemin G., Urbain V. and Manem J. (1995). Chemical and structural (2D) linkage between bacteria within activated sludge flocs. *Wat. Res.*, **29**(7), pp. 1639-1647.
- Kalbskopf K.H. (1970). European practices in sedimentation. In: *Water quality improvement by physical and chemical processes (Water Resources Symposium 3)*, Eds. Gloyna E.F. and Eckenfelder W.W., University of Texas Press, Austin, Texas, USA.

- Katz W.J. and Geinopolos A. (1962). A study of the solids retention characteristics of a final clarifier in the activated sludge process. *Proc. 1st Int. Water Pollution Conference*, 6 September, London, UK.
- Kawamura S. and Lang J. (1986). Re-evaluation of launders in rectangular sedimentation basins. *J. WPCF*, **58**(12), pp. 1124-1128.
- Keinath T.M. and Laquidara V.D. (1982). Clarification failure control strategies. *J. Environ. Eng. Div.*, **108**(EE6), pp. 1121-1127.
- Keinath T.M., Ryckman M.D., Dana C.H. and Hofer D.A. (1977). Activated sludge-unified system design and operation. *J. Environ. Eng. Div.*, **103**(EE5), pp. 829-849.
- Keller J. and Yuan Z. (2002). Combined hydraulic and biological modelling and full-scale validation of SBR process. *Wat. Sci. Tech.*, **45**(6), pp. 219-228.
- Kim M.H., Al-Ghusain I.A., Hao O.J. and Lim B.S. (1994). Modeling of nitrate disappearance and sludge rising in a settling column system. *Wat. Res.*, **28**(9), pp. 1861-1872.
- Kinnear D.J. (2000). Evaluating secondary clarifier performance and capacity. *Florida Water Resources Conference*, 16-19 April, Tampa, Florida, USA.
- Kinnear D.J. (2002). *Biological solids sedimentation: a model incorporating fundamental settling parameters*. PhD dissertation, Dep. Civil Environ. Engrg., University of Utah, USA.
- Kinnear D.J. and Deines K. (2001). Acoustic Doppler current profiler: clarifier velocity measurement. *Proc. 74th Annual WEF Conference and Exposition on Water Quality and Wastewater Treatment*, 13-17 October, Atlanta, USA.
- Kinnear D.J., Williams R, Olson C., Johnson H., Pollack E. and Vitasovic C. (1998). Theoretical and field comparison of clarifier feedwell sizing. *Proc. 71th Annual WEF Conference and Exposition on Water Quality and Wastewater Treatment*, Orlando, Florida, USA.
- Kiuru H.J. (2001). Development of dissolved air flotation technology from the first generation to the newest (third) one (DAF in turbulent flow conditions). *Wat. Sci. Tech.*, **43**(8), pp. 1-7.
- Koch G., Pianta R., Krebs P. and Siegrist H. (1999). Potential of denitrification and solids removal in the rectangular clarifier. *Wat. Res.*, **33**(2), pp. 309-318.
- Koke J., Modigell M. and Petera J. (1999). Rheological investigations and two-phase modeling on semi-solid metal suspensions. *Appl. Mech. Engrg.*, **4**, pp. 345-350.
- Konicek Z. and Burdych J. (1988). Effects of activated sludge processes on secondary settling tank efficiencies. *Wat. Sci. Tech.*, **20**(4-5), pp. 153-163.
- Kos P. (1978). *Gravity thickening of sludges*. PhD dissertation, University of Massachusetts, USA.
- Krebs P. (1991a). *Modellierung und Verbesserung der Strömung in Nachklärbecken*. PhD dissertation, ETH, Swiss.
- Krebs P. (1991b). The hydraulics of final settling tanks. *Wat. Sci. Tech.*, **23**(4-6), pp. 1037-1046.
- Krebs P. (1995). Success and shortcomings of clarifier modelling. *Wat. Sci. Tech.*, **31**(2), pp. 181-191.
- Krebs P. (1999). Gestaltung und Betrieb von Nachklärbecken. *Dresdner Berichte*, **14**, pp. 95-119.
- Krebs P., Armbruster M. and Rodi W. (1998). Laboratory experiments of buoyancy-influenced flow in clarifiers. *J. Hydr. Res.*, **36**(5), pp. 831-851.
- Krebs P., Armbruster M. and Rodi W. (2000). Numerische Nachklärbecken-Modelle. *KA-Wasserwirtschaft, Abwasser, Abfall*, **47**(7), pp. 985-999.

- Krebs P., Stamou A.I., García-Heras J.L. and Rodi W. (1996). Influence of inlet and outlet configuration on the flow in secondary clarifiers. *Wat. Sci. Tech.*, **34**(5-6), pp. 1-9.
- Krebs P., Vischer D. and Gujer W. (1992). Improvement of secondary clarifiers efficiency by porous walls. *Wat. Sci. Tech.*, **26**(5-6), pp. 1147-1156.
- Krebs P., Vischer D. and Gujer W. (1995). Inlet-structure design for final clarifiers. *J. Environ. Engrg.*, **121**(8), pp. 558-564.
- Kusters K.A. (1991). *The influence of turbulence on aggregation of small particles in agitated vessels*. PhD dissertation, TU Eindhoven, The Netherlands, 203 pp.
- Kynch G.J. (1952). A theory of sedimentation. *Trans. Faraday Soc.*, **48**, pp. 166-176.
- Kyriakidis A.S., Yiantsios S.G. and Karabelas A.J. (1997). A study of colloidal particle Brownian aggregation by light scattering techniques. *J. Colloid Interface Sci.*, **195**, pp. 299-306.
- Lainé S., Phan L., Pellarin P. and Robert P. (1999). Operating diagnostics on a flocculator-settling tank using Fluent CFD software. *Wat. Sci. Tech.*, **39**(4), pp. 155-162.
- Lakehal D., Krebs P., Krijgsman J. and Rodi W. (1999). Computing shear flow and sludge blanket in secondary clarifiers. *J. Hydr. Engrg.*, **125**(3), pp. 253-262.
- Larock B.E., Chun W.K.C. and Schamber D.R. (1983). Computation of sedimentation basin behavior. *Wat. Res.*, **17**(8), pp. 861-867.
- Larsen P. (1977). *On the hydraulics of rectangular settling basins*. Report No. 1001, Dept. of Wat. Res. Engrg., Lund Institute of Technology, Lund, Sweden.
- Larsen T. (2000). Measuring the variations of the apparent settling velocity for fine particles. *Wat. Res.*, **34**(4), pp. 1417-1418.
- Lasentec (2001). *Data processing in the FBRM CI software*, 22 pp.
- Lauder B.E. and Spalding D.B. (1974). The numerical computation of turbulent flows. *Computer Methods in Applied Mechanics and Engineering*, **3**, pp. 269-289.
- Lavelle J.W. and Thacker W.C. (1978). Effects of hindered settling on sediment concentration profiles. *J. Hydr. Res.*, **16**(4), pp. 347-355.
- Law D.J., Bale A.J. and Jones S.E. (1997). Adaptation of focused beam reflectance measurement to in-situ particle sizing in estuaries and coastal waters. *Mar. Geol.*, **140**, pp. 47-59.
- Lee D.G., Bonner J.S., Garton L.S., Ernest N.S. and Autenrith R.L. (2000). Modeling coagulation kinetics incorporating fractal theories: a fractal rectilinear approach. *Wat. Res.*, **34**(7), pp. 1987-2000.
- Lee D.S. and Vanrolleghem P.A. (2003). Monitoring of a sequencing batch reactor using adaptive multiblock principal component analysis. *Biotechnol. Bioeng.* (in press)
- Lee S.-E., Koopman B., Bode H. and Jenkins D. (1983). Evaluation of alternative sludge settleability indices. *Wat. Res.*, **17**(10), pp. 1421-1426.
- Lee T.H. and Hanes D.M. (1995). Direct inversion method to measure the concentration profile of suspended particles using backscattered sound. *J. Geophys. Res.*, **100**(C2), pp. 2649-2657.
- Leonard B.P. (1979). A stable and accurate convective modelling procedure based on quadratic upstream interpolation. *Comp. Meths. Appl. Mech. Eng.*, **19**, pp. 59-98.
- Leonard B.P. and Mokhtari S. (1990). Beyond first-order upwinding: the ultra-sharp alternative for non-oscillatory steady-state simulation of convection. *Int. J. Num. Methods Eng.*, **30**, pp. 729-766.
- Levenspiel O. (1972). *Chemical reaction engineering*. 2nd ed., Wiley, New York, USA.

- Levy T. and Sanchez-Palencia E. (1983). Suspension of solid particles in a Newtonian fluid. *J. Non-Newtonian Fluid Mech.*, **13**, pp. 63-78.
- Li D. and Ganczarczyk J. (1991). Size distribution of activated sludge flocs. *Res. J. WPCF*, **63**(5), pp. 806-814.
- Li D.-H. and Ganczarczyk J.J. (1987). Stroboscopic determination of settling velocity, size and porosity of activated sludge flocs. *Wat. Res.*, **21**(3), pp. 257-262.
- Li D.-H. and Ganczarczyk J.J. (1990). Structure of activated sludge flocs. *Biotechnol. Bioeng.*, **35**, pp. 57-65.
- Li X.-Y and Yuan Y. (2002). Settling velocities and permeabilities of microbial aggregates. *Wat. Res.*, **36**, pp. 3110-3120.
- Lindeborg C., Wiberg N. and Seyf A. (1996). Studies of the dynamic behaviour of a primary sedimentation tank. *Wat. Sci. Tech.*, **34**(3-4), pp. 213-222.
- Lindsey J.K. (1996). *Parametric statistical inference*. Oxford University Press, New York, USA, 490 pp.
- Liu K.F. and Mei C.C. (1989). Slow spreading of a sheet of Bingham fluid on an inclined plane. *J. Fluid Mech.*, **207**, pp. 505-529.
- Logan B.E. and Hunt J.R. (1988). Bioflocculation as a microbial response to substrate limitations. *Biotechnol. Bioeng.*, **31**, pp. 91-101.
- Logan B.E. and Kilps J.R. (1995). Fractal dimensions of aggregates formed in different fluid mechanical environments. *Wat. Res.*, **29**(2), pp. 443-453.
- Logan B.E. and Wilkinson D.B. (1991). Fractal dimensions and porosities of *Zoogloea ramigera* and *Saccharomyces cerevisiae* aggregates. *Biotechnol. Bioeng.*, **38**(4), pp. 389-396.
- Lohrmann A., Hackett B. and Roed L.P. (1990). High resolution measurements of turbulence, velocity and stress using a pulse-to-pulse coherent sonar. *J. Atmos. Oceanic Technol.*, **7**, pp. 19-37.
- Lomax H., Pulliam T.H. and Zingg D.W. (2001). *Fundamentals of computational fluid dynamics*. Springer-Verlag, 251 pp.
- Londong J., Kolish G., Alex J. and Holthausen E. (1998). Ein neuer Ansatz zur Ableitung von Modellstrukturen für die dynamische Simulation kommunaler Kläranlagen. *Korrespondenz Abwasser*, **45**(4), pp. 717-723.
- Lotito V., Spinosa L., Mininni G. and Antonacci R. (1997). The rheology of sewage sludge at different steps of treatment. *Wat. Sci. Tech.*, **36**(11), pp. 79-85.
- Lourenco L.M. (1999). Particle image velocimetry. In: *Optical diagnostics of particles & droplets*, Lecture Series 1999-01, von Karman Institute for Fluid Dynamics, 25-29 January.
- Lübbert A. (1991). Biotechnology. In: *Measuring, modelling and control*, Vol. 4, VCH, Weinheim.
- Lucas-Aiguier E., Chebbo G., Bertrand-Krajewski J.-L., Gagné B. and Hedges P. (1998). Analysis of the methods for determining the settling characteristics of sewage and stormwater solids. *Wat. Sci. Tech.*, **37**(1), pp. 53-60.
- Lumley D.J. and Horkeby G. (1989). Detention time distribution of sludge in rectangular secondary settlers. *Wat. Sci. Tech.*, **21**, pp. 1763-1766.
- Lyn D.A. and Rodi W. (1990). Turbulence measurement in model settling tank. *J. Hydr. Engrg.*, **116**(1), pp. 3-21.
- Lyn D.A., Stamou A.I. and Rodi W. (1992). Density currents and shear-induced flocculation in sedimentation tanks. *J. Hydr. Engrg.*, **118**(6), pp. 849-867.
- Malcherek A. (1994). Numerical modeling of cohesive settling velocities. *Int. J. Sed. Res.*, **9**, pp. 97-106.

- Manning W.T., Garrett M.T. and Malina J.F. (1999). Sludge blanket response to storm surge in an activated-sludge clarifier. *Wat. Environ. Res.*, **71**(4), pp. 432-442.
- Manoliadis O. and Bishop P.L. (1984). Temperature effect on rheology of sludges. *J. Environ. Engrg.*, **110**(1), pp. 286-290.
- Martin J., Rakotomalala N. and Salin D. (1995). Hydrodynamic dispersion of noncolloidal suspensions: measurement from Einstein's argument. *Phys. Rev. Lett.*, **74**(8), pp. 1347-1350.
- Matsui Y., Fukushi K. and Tambo N. (1998). Modeling, simulation and operational parameters of dissolved air flotation. *J. Water SRT-Aqua*, **47**(1), pp. 9-20.
- Mazzolani G., Pirozzi F. and d'Antoni G. (1998). A generalized settling approach in the numerical modelling of sedimentation tanks. *Wat. Sci. Tech.*, **38**(3), pp. 95-102.
- McCorquodale J.A. and Zhou S. (1993). Effects of hydraulic and solids loading on clarifier performance. *J. Hydr. Res.*, **31**(4), pp. 461-477.
- McCorquodale J.A., Yuen E.M., Vitasovic Z. and Samstag R. (1991). Numerical simulation of unsteady conditions in clarifiers. *Water Poll. Res. J. Canada*, **26**(2), pp. 201-222.
- Merrill M.S., Tetreault M., Parker D.S., Vitasovic Z. and McCorquodale J.A. (1992). Mathematical simulation of secondary clarifiers coupled with activated sludge reactors. *Proc. 65th Annual WEF Conference and Exposition on Water Quality and Wastewater Treatment*, 20-24 September, New Orleans, Louisiana, USA.
- Michael Y., Snowden M.J., Chowdhry B.Z., Ashurst I.C., Davies-Cutting C.J. and Riley T. (2001). Characterisation of the aggregation behaviour in a salmeterol and fluticasone propionate inhalation aerosol system. *Int. J. Pharmaceutics*, **221**, pp. 165-174.
- Misztal R. and Sangwal K. (1999). Analysis of the concentration and temperature dependence of densities of aqueous alkali halide solutions: a new power-law approach. *Cryst. Res. Technol.*, **34**(5-6), pp. 769-775.
- Mohammadi B. and Pironneau O. (1994). *Analysis of the k-epsilon turbulence model*. John Wiley & Sons, John Wiley & Sons, West Sussex, UK, 196 pp.
- Monnier O., Klein J.-P., Hoff C. and Ratsimba B. (1996). Particle size determination by laser reflection: methodology and problems. *Part. Part. Syst. Charact.*, **13**, pp. 10-17.
- Monteiro P.S. (1997). The influence of the anaerobic digestion process on the sewage sludges rheological behaviour. *Wat. Sci. Tech.*, **36**(11), pp. 61-67.
- Moum J.N. and Smyth W.D. (2000). Upper ocean mixing. In: *Encyclopedia of Ocean Sciences*, Academic Press.
- Murk J.S. (1969). *Factors affecting sludge movement in final sedimentation tanks*. Report County Sanitation Districts of Los Angeles County, September, California, USA.
- Narayanan B., Buhr H.O., Leveque E.G., Lee M.C. and Dielmann D. (2000). Could your secondary clarifier sludge removal mechanism be a process bottleneck? *Proc. 73th Annual WEF Conference and Exposition on Water Quality and Wastewater Treatment*, 14-18 October, Anaheim, California, USA.
- Narayanan B., Demir J., Chan R., Sheehan G., Gray R. and Jones S. (2001). Hydrodynamic modeling helps improve secondary clarifier performance. *Proc. 74th Annual WEF Conference and Exposition on Water Quality and Wastewater Treatment*, 13-17 October, Atlanta, USA.
- Narkis N. and Rebhun M. (1997). Flocculation in presence of organic macromolecules of natural water and secondary effluents. *Wat. Sci. Tech.*, **36**(4), pp. 85-91.
- Nasr-El-Din H.A. and Taggart R.S.M. (1996). Local solids concentration measurement in a slurry mixing tank. *Chem. Eng. Sci.*, **51**(8), pp. 1209-1220.

- NCASI (1983). *A review of procedures for conducting conservative tracer studies in the hydraulic characterization of effluent treatment basins*. Technical Bulletin No. 408, National Council of the Paper Industry for Air and Stream Improvement (NCASA Inc.), New York, USA.
- Neumann L.E. and Howes T. (2002). On-line monitoring of estuarine sediment flocculation using laser reflection. Submitted to *J. Coastal Res.*
- Nir A. and Acrovis A. (1974). Experiments on the effective viscosity of concentrated suspensions of solid spheres. *Int. J. Multiphase Flow*, **1**, pp. 373-381.
- Nopens I., Biggs C.A., De Clercq B., Govoreanu R., Wilén B.-M., Lant P. and Vanrolleghem P.A. (2002). Modelling the activated sludge flocculation process combining laser light diffraction particle sizing and population balance modelling (PBM). *Wat. Sci. Tech.*, **45**(6), pp. 41-49.
- Nopens I. and Vanrolleghem P.A. (2003). Comparison of discretisation methods to solve a population balance model of activated sludge flocculation including aggregation and breakage. *Proc. IMACS 4th MATHMOD Conference*, 5-7 February, Vienna, Austria.
- Pandya J.D. and Spielman L.A. (1983). Floc breakage in agitated suspensions: effect of agitation rate. *Chem. Eng. Sci.*, **38**(12), pp. 1983-1992.
- Papanastasiou T.C. (1987). Flows of materials with yield. *J. Rheol.*, **31**(5), pp. 385-404.
- Paredes M.D.C., Rao M.A. and Bourne M.C. (1988). Rheological characterization of salad dressings. 1. Steady shear, thixotropy and effect of temperature. *J. Texture Studies*, **19**, pp. 247-258.
- Parker D. and Stenquist R. (1986). Flocculator-clarifier performance. *J. WPCF*, **58**(3), pp. 214-219.
- Parker D.S., Butler R., Finger R., Fisher R., Fox W., Kido W., Merrill S., Newman G., Pope R., Slapper J. and Wahlberg E. (1996). Design and operations experience with flocculator-clarifiers in large plants. *Wat. Sci. Tech.*, **33**(12), pp. 163-170.
- Parker D.S., Kaufman W.J. and Jenkins D. (1970). *Characteristics of biological flocs in turbulent flows*. SERL Report No. 70-5, University of California, Berkeley, USA.
- Parker D.S., Kaufman W.J. and Jenkins D. (1971). Physical conditioning of activated sludge. *J. WPCF*, **43**, pp. 1817-1833.
- Parker D.S., Kaufman W.J. and Jenkins D. (1972). Floc breakup in turbulent flocculation processes. *J. Sanitary Eng. Div.*, **98**(SA1), pp. 79-99.
- Parker D.S., Kinnear D.J. and Wahlberg E.J. (2001). Review of folklore in design and operation of secondary clarifiers. *J. Environ. Engrg.*, **127**(6), pp. 476-484.
- Parker D.S., Kinnear D.J., Gerges H.Z. and Wahlberg E.J. (1999). Approach for diagnosing secondary clarifier performance problems and prescribing improvements. *WEF Plant Operations Specialty Conference*, 6-9 June, Milwaukee, Wisconsin, USA.
- Parker D.S., Merrill M.S. and Tetreault M.J. (1992). Wastewater treatment process theory and practice: the emerging convergence. *Wat. Sci. Tech.*, **25**(6), pp. 301-315.
- Patankar S.V. (1980). *Numerical heat transfer and fluid flow*. Hemisphere Publishing Co./McGraw-Hill Co., Washington DC.
- Patankar S.V. and Spalding D.B. (1972). A calculation procedure for heat, mass and momentum transfer in three-dimensional parabolic flows. *Int. J. Heat Mass Transfer*, **15**, pp. 1787-1806.
- Pattijn S. (1999). *Non-linear, low-Reynolds, two-equation turbulence models*. PhD dissertation, Dep. Flow Mechanics, Heat and Incineration, Ghent University, 525 pp.

- Pedras M.H.J. and de Lemos M.J.S. (1999). On volume and time averaging of transport equations for turbulent flow in porous media. *Proc. 3rd ASME/JSME Joint Fluids Engineering Conf.*, 18-23 July, San Francisco, California, USA.
- Peng S.J. and Williams R.A. (1993). Control and optimisation of mineral flocculation and transport processes using on-line particle size analysis. *Minerals Engineering*, **6**(2), pp. 133-153.
- Peng S.J. and Williams R.A. (1994). Direct measurement of floc breakage in flowing suspensions. *J. Colloid Interface Sci.*, **166**, pp. 321-332.
- Phan-Thien N., Nasserri S. and Bilston L.E. (2000). Oscillatory squeezing flow of a biological material. *Rheol. Acta*, **39**, pp. 409-417.
- Phillips J.M. and Walling D.E. (1995a). An assessment of the effects of sample collection, storage and resuspension on the representativeness of measurements of the effective particle size distribution of fluvial suspended sediment. *Wat. Res.*, **29**(11), pp. 2498-2508.
- Phillips J.M. and Walling D.E. (1995b). Measurement in situ of the effective particle-size characteristics of fluvial suspended sediment by means of a field-portable laser backscatter probe: some preliminary results. *Mar. Freshwater Res.*, **46**, pp. 349-357.
- Piau J.M. (1996). Flow of a yield stress fluid in a long domain. Application to flow on an inclined plane. *J. Rheol.*, **40**(4), pp. 711-723.
- Piirtola L., Hultman B., Andersson C. and Lundeberg Y. (1999). Activated sludge ballasting in batch tests. *Wat. Res.*, **33**(8), pp. 1799-1804.
- Piquet J. (1999). *Turbulent flows: models and physics*. Springer-Verlag, Berlin, Heidelberg, New York.
- Quraishi M.S. and Fahidy T.Z. (1986). Techniques for flow pattern studies. In: *Encyclopedia of Fluid Mechanics*, Vol. 3 (Gas-Liquid Flows). Ed. Cheremisinoff N.P., Gulf Publishing Company, Houston, Texas, USA.
- Ramkrishna D. (2000). *Population balances: theory and applications to particulate systems in engineering*. Academic Press, San Diego, USA, 355 pp.
- Rasmussen M.R. (1997). *Solids dynamics in secondary settling tanks*. PhD dissertation, Dep. Civil Eng., Aalborg University, Denmark (in preparation).
- Rasmussen M.R. and Larsen T. (1996). A method for measuring sludge settling characteristics in turbulent flows. *Wat. Res.*, **30**(10), pp. 2363-2370.
- Rasmussen M.R. and Larsen T. (1997). On-line measurements of settling characteristics in activated sludge. *Wat. Sci. Tech.*, **36**(4), pp. 307-312.
- Rasmussen M.R., Larsen T. and Clauss F. (1996). Improving settling dynamics of activated sludge by adding fine talc powder. *Wat. Sci. Tech.*, **34**(5-6), pp. 11-18.
- RD Instruments (1999). *High resolution water-profiling: addendum*. Report, RD Instruments, San Diego, California, USA.
- Rebhun M. and Argaman Y. (1965). Evaluation of hydraulic efficiency of sedimentation basins. *J. Sanitary Engrg. Div.*, **91**(SA5), pp. 37-45.
- Reichel G. and Nachtnebel H.P. (1994). Suspended sediment monitoring in a fluvial environment: advantages and limitations applying an acoustic Doppler current profiler. *Wat. Res.*, **28**(4), pp. 751-761.
- Reid J.M. and Nason R.B. (1993). Automatic monitoring of activated sludge settling characteristics and plant control applications. *J. Inst. Water and Environmental Management*, **7**, pp. 636-645.

- Richardson J., Bailey W. Schulte R., Stallings B., Wilson T. and Albertson O. (2000). Optimization of final clarifier design. *Proc. 73rd Annual WEF Conference and Exposition on Water Quality and Wastewater Treatment*, 14-18 October, Anaheim, California, USA.
- Richardson J.F. and Zaki W.N. (1954). Sedimentation and fluidisation: part I. *Trans. Instn. Chem. Engrs.*, **32**, pp. 35-53.
- Richmond W.R., Jones R.L. and Fawell P.D. (1998). The relationship between particle aggregation and rheology in mixed silica-titania suspensions. *Chem. Eng. Sci.*, **71**(1), pp. 67-75.
- Riemer M., Kristensen G.H. and Harremoës P. (1980). Residence time distribution in submerged biofilters. *Wat. Res.*, **14**, pp. 949-958.
- Rodi W. (1984). *Turbulence models and their application in hydraulics - a state of the art review*. Int. Assoc. Hydraulic Research, The Netherlands.
- Rodi W. and Spalding D.B. (1970). A two-parameter model of turbulence, and its application to free jets. In: *Wärme- und Stoffübertragung*, Springer-Verlag, B3, pp. 85-95.
- Rozzi A. & Massone A. (1995). Residence time distribution analysis on biofilm reactors: an overview. *Med. Fac. Landbouww. Univ. Gent*, **60**(4b), pp. 2143-2153.
- Samstag R.W., Dittmar D.F., Vitasovic Z. and McCorquodale J.A. (1992). Underflow geometry in secondary sedimentation. *Wat. Environ. Res.*, **64**(3), pp. 204-212.
- Sanin F.D. (2002). Effect of solution physical chemistry on the rheological properties of activated sludge. *Water SA*, **28**(2), pp. 207-211.
- Schamber D.R. and Larock B.E. (1981). Numerical analysis of flow in sedimentation basins. *J. Hydr. Div.*, **107**(HY5), pp. 575-591.
- Schmidt-Ott A. (2002). On-line particle characterization: techniques and applications. *Proc. 4th World Congress on Particle Technology (WCPT4)*, 21-25 July, Sydney, Australia.
- Schofield T. (2001). Dissolved air flotation in drinking water production. *Wat. Sci. Tech.*, **43**(8), pp. 9-18.
- Schuler A.J., Jenkins D. and Ronen P. (2001). Microbial storage products, biomass density, and settling properties of enhanced biological phosphorus removal activated sludge. *Wat. Sci. Tech.*, **43**(1), pp. 173-180.
- Schultz M.P. (2000). Turbulent boundary layers on surfaces covered with filamentous algae. *J. Fluids Eng.*, **122**, pp. 357-363.
- Scott D.M. (2002). Characterizing particle characterization. *Proc. 4th World Congress on Particle Technology (WCPT4)*, 21-25 July, Sydney, Australia.
- Seddon J.A. (1889). Clearing water by settlement - observations and theory. *Association of Engineering Societies*, **8**(10), pp. 477-494.
- Selomulya C., Amal R., Bushell G. and Waite T.D. (2001). Evidence of shear rate dependence on restructuring and breakup of latex aggregates. *J. Colloid Interface Sci.*, **236**, pp. 67-77.
- Serra T. and Casamitjana X. (1998). Modelling the aggregation and break-up of fractal aggregates in a shear flow. *Appl. Sci. Res.*, **59**, pp. 255-268.
- Serra T. and Casamitjana X. (1998). Structure of the aggregates during the process of aggregation and breakup under a shear flow. *J. Colloid Interface Sci.*, **206**, pp. 505-511.
- Serra T., Colomer J. and Casamitjana X. (1997). Aggregation and breakup of particles in a shear flow. *J. Colloid Interface Sci.*, **187**, pp. 466-473.
- Serra T., Colomer J., Cristina X.P., Vila X., Arellano J.B. and Casamitjana X. (2001). Evaluation of laser in situ scattering instrument for measuring concentration of phytoplacton, purple

- sulfur bacteria, and suspended inorganic sediments in lakes. *J. Environ. Engrg.*, **127**(11), pp. 1023-1030.
- Sezgin M., Jenkins D. and Parker D.S. (1978). A unified theory of filamentous activated sludge bulking. *J. WPCF*, **50**, pp. 362-381.
- Shillabeer N., Hart B. and Riddle A.M. (1992). The use of a mathematical model to compare particle size data derived by dry-sieving and laser analysis. *Estuarine, Coastal and Shelf Science*, **35**, pp. 105-111.
- Siegrist H. and Gujer W. (1994). Nitrogen removal in activated sludge systems including denitrification in secondary clarifiers. *Wat. Sci. Tech.*, **30**(6), pp. 101-111.
- Siegrist H., Krebs P., Bühler R., Purtschert I., Röck C. and Rufer R. (1995). Denitrification in secondary clarifiers. *Wat. Sci. Tech.*, **31**(2), pp. 205-214.
- Sievers M., Schroeder C., Bormann H., Onyeche T.I., Schlaefer O. and Schaefer S. (2002). *Proc. Int. IWA Conf. on Automation in Water Quality Monitoring (AutMoNet2002)*, 21-22 May, Vienna, Austria.
- Simonin O., Uittenogaard R.E., Baron F. and Viollet P. (1989). Possibilities and limitations of the k-epsilon model to simulate turbulent fluxes of mass and momentum, measured in a steady, stratified layer. *Proc. 23rd Cong. of the IAHR*, Ottawa, Canada.
- Slatter P.T. (1997). The rheological characterisation of sludges. *Wat. Sci. Tech.*, **36**(11), pp. 9-18.
- Slinn D.N. and Riley J.J. (2002). Internal wave reflection from sloping boundaries. *J. Fluid Mech.* (in press).
- Smith T.N. (1998). A model of settling velocity. *Chem. Eng. Sci.*, **53**(2), pp. 315-323.
- Smyth W.D. and Moum J.N. (2000a). Anisotropy of turbulence in stably stratified mixing layers. *Phys. Fluids*, **12**, pp. 1343-1362.
- Smyth W.D. and Moum J.N. (2000b). Length scales of turbulence in stably stratified mixing layers. *Phys. Fluids*, **12**, pp. 1327-1342.
- Smyth W.D. and Moum J.N. (2002). Shear instability and gravity wave saturation in an asymmetrically stratified jet. *Dyn. Atm. Oceans* (in press).
- Soo S.L. (1990). *Multiphase fluid dynamics*. Science Press, Beijing, China, 691 pp.
- Sorour T., Olsson G. and Somlyody L. (1994). Potential use of step feed control using the biomass in the settler. *Wat. Sci. Tech.*, **28**(11-12), pp. 356-366.
- Sozanski M.M., Kempa E.S., Grocholski K. and Bien J. (1997). The rheological experiment in sludge properties research. *Wat. Sci. Res.*, **36**(11), pp. 69-78.
- Spalding D.B. (1972). A novel finite difference formulation for differential expressions involving both first and second derivatives. *Int. J. Num. Meth. Engrg.*, **4**, pp. 551-559.
- Sparks R.G. and Dobbs C.L. (1993). The use of laser backscatter instrumentation for the on-line measurement of the particle size distribution of emulsions. *Part. Part. Syst. Charact.*, **10**, pp. 279-289.
- Spelt P.D.M., Norato M.A., Sangani A.S. and Tavlarides L.L. (1999). Determination of particle size distributions from acoustic wave propagation measurements. *Phys. Fluids*, **11**(5), pp. 1065-1080.
- Spicer P.T. (1997). *Shear-induced aggregation-fragmentation: mixing and aggregate morphology effects*. PhD dissertation, Dep. Chem. Eng., University of Cincinnati, USA.
- Spicer P.T. and Pratsinis S.E. (1996). Shear-induced flocculation: the evolution of floc structure and the shape of the size distribution at steady state. *Wat. Res.*, **30**(5), pp. 1049-1056.

- Spicer P.T., Pratsinis S.E., Raper J., Amal R., Bushell G. and Meesters G. (1998). Effect of shear schedule on particle size, density, and structure during flocculation in stirred tanks. *Powder Technol.*, **97**, pp. 26-34.
- Stacey M.T., Monismith S.G. and Burau J.R. (1999a). Measurements of Reynolds stress profiles in tidal flows. *J. Geophys. Res.*, **104**, pp. 10933-10949.
- Stacey M.T., Monismith S.G. and Burau J.R. (1999b). Observations of turbulence in a partially stratified estuary. *J. Phys. Oceanogr.*, **29**, pp. 1950-1970.
- Stamou A.I., Adams E.W. and Rodi W. (1989). Numerical modeling of flow and settling in primary rectangular clarifiers. *J. Hydr. Res.*, **27**(5), pp. 665-682.
- Stamou A.I., Latsa M. and Assimacopoulos D. (2000). Design of two-storey final settling tanks using mathematical models. *J. Hydroinformatics*, **2**(4), pp. 235-245.
- Starkey J.E. and Karr P.R. (1984). Effect of low dissolved oxygen concentration on effluent turbidity. *J. WPCF*, **56**(7), pp. 837-843.
- Steffe J.F. (1996). *Rheological methods in food process engineering*. Freeman Press, East Lansing, USA. 418 p.
- Steindl R.J., Fitzmaurice A.L. and Alman C.W. (1998). Recent developments in clarifier design. *Proc. Aust. Soc. Sugar Cane Technol.*, **20**, pp. 477-483.
- Stevens D.K., Berthouex P.M. and Chapman T.W. (1986). The effect of tracer diffusion in biofilm on residence time distributions. *Wat. Res.*, **20**(3), pp. 369-375.
- Stolojanu V. and Prakash A. (1997). Hydrodynamic measurements in a slurry bubble column using ultrasonic techniques. *Chem. Eng. Sci.*, **52**(21-22), pp. 4225-4230.
- STOWa (2002a). *Optimalisatie van ronde nabezinktanks: modelproeven*. Report physical secondary settling tank model, Stichting Toegepast Onderzoek Waterbeheer (STOWA), Utrecht, Netherlands.
- STOWa (2002b). *Optimalisatie van ronde nabezinktanks: Ontwikkeling nabezinktankmodel en evaluatie STORA-ontwerprichtlijn*. Report physical secondary settling tank model, Stichting Toegepast Onderzoek Waterbeheer (STOWA), Utrecht, Netherlands.
- Stukenberg J.R., Rodman L.C. and Touslee J.E. (1983). Activated sludge clarifier design improvement. *J. WPCF*, **55**(4), pp. 341-348.
- Sutherland B.R. (2002). Interfacial gravity currents. I. Mixing and entrainment. *Phys. Fluids*, **14**(7), pp. 2244-2254.
- Szalai L., Krebs P. and Rodi W. (1994). Simulation of flow in circular clarifiers with and without swirl. *J. Hydr. Engrg.*, **120**(1), pp. 4-21.
- Taebi-Harandy A. and Schroeder E.D. (2000). Formation of density currents in secondary clarifier. *Wat. Res.*, **34**(4), pp. 1225-1232.
- Takács I., Patry G.G. and Nolasco D. (1991). A dynamic model of the clarification-thickening process. *Wat. Res.*, **25**(10), pp. 1263-1271.
- Takamatsu T., Naito M., Shiba S. and Ueda Y. (1974). Effects of deposit resuspension on settling basin. *J. Environ. Engrg. Div.*, **100**(EE4), pp. 883-903.
- Tang S. (1999). Prediction of fractal properties of polystyrene aggregates. *Colloids and Surfaces A*, **157**, pp. 185-192.
- Tariq M.N. (1975). Retention time in trickling filters. *Prog. Wat. Tech.*, **7**(2), pp. 225-234.
- Tay A.J.-H. and Heinke G.W. (1983). Velocity and suspended solids distribution in settling tanks. *J. WPCF*, **55**(3), pp. 261-269.
- Tchobanoglous G. and Burton F.L. (1991). *Wastewater Engineering: Treatment, Disposal and Reuse*. 3rd Ed., Metcalf & Eddy Inc.

- Tekippe R.J. (2002). Secondary settling tank inlet design: full scale test results lead to optimization. *Proc. 75th Annual WEF Conference and Exposition on Water Quality and Wastewater Treatment*, 28 Sept - 2 October, Chicago, Illinois, USA.
- Tennekes H. and Lumley J.L. (1972). *A first course in turbulence*. MIT Press, Massachusetts, USA.
- Thill A., Veerapaneni S., Simon B., Wiesner M., Bottero J.Y. and Snidaro D. (1998). Determination of structure of aggregates by confocal scanning laser microscopy. *J. Colloid Interface Sci.*, **204**, pp. 357-362.
- Thomas D.N., Judd S.J. and Fawcett N. (1999). Flocculation modelling: a review. *Wat. Res.*, **33**(7), pp. 1579-1592.
- Thompson D., Chapman D.T. and Murphy K.L. (1989). Step feed control to minimize solids loss during storm flows. *Res. J. WPCF*, **61**(11-12), pp. 1658-1665.
- Thorne P.D., Hardcastle P.J. and Soulsby R.L. (1993). Analysis of acoustic measurements of suspended sediments. *J. Geophys. Res.*, **98**(C1), pp. 899-910.
- Tiehm A., Herwig V. and Neis U. (1999). Particle size analysis for improved sedimentation and filtration in waste water treatment. *Wat. Sci. Tech.*, **39**(8), pp. 99-106.
- Tiller F.M. (1981). Revision of Kynch sedimentation theory. *AIChE Journal*, **27**(5), pp. 823-829.
- Tiu C. and Boger D.V. (1974). Complete rheological characterization of time-dependent food products. *J. Texture Studies*, **5**, pp. 329-338.
- Tomlinson E.J. (1976). *Bulking - a survey of activated-sludge plants*. Technical Report TR35, Water Research Centre, UK.
- Ueberl J. and Hager W.H. (1997). Improved design of final settling tanks. *J. Environ. Engrg.*, **123**(3), pp. 259-268.
- Unno H. and Akehata T. (1985). Some rheological features of concentrated excess activated sludge of thixotropic nature. *J. Chem. Eng. Japan*, **18**(6), pp. 533-540.
- Vallom J.K. and McLoughlin A.J. (1984). Lysis as a factor in sludge flocculation. *Wat. Res.*, **18**(12), pp. 1523-1528.
- van Beeck J.P.A.J. (1999). Optical diagnostics of particles & droplets: introduction. In: *Optical diagnostics of particles & droplets*, Lecture Series 1999-01, von Karman Institute for Fluid Dynamics, 25-29 January.
- van de Fliert B.W. and van den Berg J.B. (1999). Displacement of a viscoplastic fluid in an inclined slot. *Proc. SWI (Studiegroep Wiskunde met de Industrie)*, Eindhoven, Netherlands.
- van de Hulst H.C. (1981). *Light scattering by small particles*. Dover Publications Inc., 470 pp.
- van den Akker H.E.A. (1986). Momentum equations in dispersed two-phase flows. In: *Encyclopedia of Fluid Dynamics*, Vol. 3 (Gas-liquid flows), Ed. Cheremisinoff N.P., Gulf Publishing Company, Houston, Texas, USA.
- Van Doormaal J.P. and Raithby G.D. (1984). Enhancements of the SIMPLE method for predicting incompressible fluid flows. *Numer. Heat Transfer*, **7**, pp. 147-163.
- van Marle C. and Kranenburg C. (1994). Effects of gravity currents in circular secondary clarifiers. *J. Environ. Eng.*, **120**(4), pp. 943-960.
- van Rijn L.C. and Schaafsma A.S. (1986). Evaluation of measuring instruments for suspended sediment. *Proc. Int. Conf. Measuring Techniques of Hydraulics Phenomena in Offshore, Coastal & Inland Waters*, 9-11 April, London, UK.
- van Sonsbeek H.M., van der Tuin S.P. and Tramper J. (1992). Mixing in liquid-impelled loop reactors. *Biotechnol. Bioeng.*, **39**, pp. 707-716.

- Vanderhasselt A. and Vanrolleghem P.A. (2000). Estimation of sludge sedimentation parameters from single batch settling curves. *Wat. Res.*, **34**(2), pp. 395-406.
- Vanderhasselt A., De Clercq B., Vanderhaegen B., Verstraete W. and Vanrolleghem P.A. (1999a). On-line control of polymer addition to prevent massive sludge wash-out. *J. Environ. Engrg.*, **125**, 1014-1021.
- Vanderhasselt A., Fuchs A., Vanrolleghem P., Staudinger G. and Verstraete W. (1999b). Monitoring of the effects of additives on sludge separation properties by using sensors. *Wat. Environ. Res.*, **71**, pp. 355-362.
- Vanrolleghem P., Van der Schueren D., Krikilion G., Grijspeerdt K., Willems P. and Verstraete W. (1996). On-line quantification of settling properties with in-sensor-experiments in an automated settlometer. *Wat. Sci. Tech.*, **33**(1), pp. 37-51.
- Vanrolleghem P.A. and Lee D.-S. (2002). On-line monitoring equipment for wastewater treatment processes: state of the art. *Proc. Int. IWA Conf. on Automation in Water Quality Monitoring (AutMoNet)*, 21-22 May, Vienna, Austria.
- Veerapaneni S. and Wiesner M.R. (1996). Hydrodynamics of fractal aggregates with radially varying permeability. *J. Colloid Interface Sci.*, **177**, pp. 45-57.
- Versteeg H.K. and Malalasekera W. (1995). *An introduction to computational fluid dynamics: the finite volume method*. Addison-Wesley Pub. Co., 272 pp.
- Vesilind P.A. (1968). Theoretical considerations: design of prototype thickeners from batch settling tests. *Water & Sewage Works*, pp. 115-302.
- Vitasovic Z.C., Zhou S., McCorquodale J.A. and Lingren K. (1997). Secondary clarifier analysis using data from the Clarifier Research Technical Committee protocol. *Wat. Environ. Res.*, **69**(5), pp. 999-1007.
- Vlaški A., van Breemen A.N. and Alaerts G.J. (1997). The role of particle size and density in dissolved air flotation and sedimentation. *Wat. Sci. Tech.*, **36**(4), pp. 177-189.
- von Smoluchowski M. (1917). *Z. Physical Chem.*, **92**, pp. 129
- Wahlberg E.J. (1997). Activated sludge solids inventory control using state point concept. *Proc. Process Optimization Workshops (Brown and Caldwell)*, 18 March, Portland, Oregon, USA.
- Wahlberg E.J., Keinath T.M. and Parker D.S. (1992). Relationship between activated sludge flocculation characteristics and cell-surface polysaccharide concentration. *Wat. Sci. Tech.*, **26**(9-11), pp. 2527-2530.
- Wahlberg E.J., Augustus M., Chapman D.T., Chen C.-L., Esler J.K., Keinath T.M., Parker D.S., Tekippe R.J. and Wilson T.E. (1994). Evaluating activated sludge secondary clarifier performance using the CRTC protocol: four case studies. In: *Proc. 67th Annual WEF Conf. And Exp.*, Chicago, USA, **1**, pp. 1-12.
- Wahlberg E.J., Keinath T.M. and Parker D.S. (1994). Influence of activated sludge flocculation time on secondary clarification. *Wat. Environ. Res.*, **66**(6), pp. 779-786.
- Wahlberg E.J., Merrill D.T. and Parker D.S. (1995). Troubleshooting activated sludge secondary clarifier performance using simple diagnostic tests. *Proc. 68th Annual WEF Conference and Exposition on Water Quality and Wastewater Treatment*, 23 October, Miami, Florida, USA.
- Waite T.D. (1999). Measurement and implications of floc structure in water and wastewater treatment. *Colloids and Surfaces A*, **151**, pp. 27-41.
- Wallis G.B. (1969). *One-dimensional two-phase flow*. McGraw-Hill Co. New York.

- Wang H. and Falconer R.A. (1998). Numerical modeling of flow in chlorine disinfection tanks. *J. Hydr. Engrg.*, **124**(9), pp. 918-931.
- Wang T., Wang J. and Jin Y. (2002). Application of the Doppler ultrasound velocimetry in liquid-solid and gas-liquid systems. *Proc. 4th World Congress on Particle Technology (WCPT4)*, 21-25 July, Sydney, Australia.
- Wanner J. (1994). *Activated sludge bulking and foaming control*. Technomic Publishing, Basel, 327 pp.
- Warden J.H. (1981). The design of rakes for continuous thickeners: especially for waterworks coagulant sludges. *Filtration & Separation*, March/April, pp. 113-116.
- Watts R.W., Svoronos S.A. and Koopman B. (1996). One-dimensional modeling of secondary clarifiers using a concentration and feed velocity-dependent dispersion coefficient. *Wat. Res.*, **30**(9), pp. 2112-2124.
- Weber S.W. and Rowe D.S. (1986). Modeling techniques for dispersed multiphase flows. In: *Encyclopedia of Fluid Dynamics*, Vol. 3 (Gas-liquid flows), Ed. Cheremisinoff N.P., Gulf Publishing Company, Houston, Texas, USA.
- Weiner B.B., Tscharnuter W.W. and Karasikov N. (1998). Improvements in accuracy and speed using the time-of-transition method and dynamic image analysis for particle sizing. In: *Symposium Series 693, Particle Size Distribution III*. Ed. Provder T., American Chemical Society.
- Wells S.A. and LaLiberte D.M. (1998). Winter temperature gradients in circular clarifiers. *Wat. Environ. Res.*, **70**(7), pp. 1274-1279.
- White F.M. (1991). *Viscous fluid flow*. McGraw-Hill, Singapore, 614 pp.
- Wilén B.-M. (1999). *Properties of activated sludge flocs*. PhD dissertation, Dep. Sanitary Eng., Chalmers University of Technology, Göteborg, Sweden.
- Wilén B.-M. and Balmér P. (1999). The effect of dissolved oxygen concentration on the structure, size and size distribution of activated sludge flocs. *Wat. Res.*, **33**(2), pp. 391-400.
- Wilén B.-M., Keiding K. and Nielsen P.H. (2000). Anaerobic deflocculation and aerobic reflocculation of activated sludge. *Wat. Res.*, **34**(16), pp. 3933-3942.
- Williams R.A., Peng S.J. and Naylor A. (1992). In situ measurement of particle aggregation and breakage kinetics in a concentrated suspension. *Powder Technol.*, **73**, pp. 75-83.
- Winkler K. (2001). Räumung in Nachklärbecken von Abwassereinigungsanlagen: Numerische und experimentelle Untersuchungen zu verschiedenen Räumertypen. *Mitteilungen VAW* (Zürich), **170**, 268 pp.
- Winkler K., Hermann F. and Baumer P. (1999). Strömungsberechnung für ein rundes Nachklärbecken mit Schildräumer. *GWA*, **2**, pp. 137-147.
- Wood M.G. (1997). *Development of computational fluid dynamic models for the design of waste stabilisation ponds*. PhD dissertation, Dep. Chem. Eng., The University of Queensland, Australia.
- Worlitschek J. and Mazzotti M. (2001). Choice of the focal point position using Lasentec FBRM. Submitted to *Part. Part. Syst. Charact.*
- Wren D.G., Barkdoll B.D., Kuhnle R.A. and Derrow R.W. (2000). Field techniques for suspended-sediment measurement. *J. Hydr. Engrg.*, **126**(2), pp. 97-103.
- Xue J.-Z., Herbolzheimer E., Rutgers M.A., Russel W.B. and Chaikin P.M. (1992). Diffusion, dispersion, and settling of hard spheres. *Phys. Rev. Lett.*, **69**(11), pp. 1715-1718.

- Yuen W.A. (2002). Empirical equations for the limiting solids flux of final clarifiers. *Wat. Environ. Res.*, **74**(2), pp. 200-209.
- Yuki Y. (1991). Multi-story treatment in Osaka, Japan. *Wat. Environ. & Technol.*, July, pp. 72-76.
- Zheng Y. and Bagley D.M. (1998). Dynamic model for zone settling and compression in gravity thickeners. *J. Environ. Engrg.*, **124**(10), pp.953-958.
- Zheng Y. and Bagley D.M. (1999). Numerical simulation of batch settling process. *J. Environ. Engrg.*, **125**(11), pp. 1007-1013.
- Zhou S. and McCorquodale J.A. (1992a). Mathematical modelling of a circular clarifier. *Can. J. Civ. Eng.*, **19**, pp. 365-374.
- Zhou S. and McCorquodale J.A. (1992b). Modeling of rectangular settling tanks. *J. Hydr. Engrg.*, **118**(10), pp. 1391-1405.
- Zhou S. and McCorquodale J.A. (1992c). Influence of skirt radius on performance of circular clarifier with density stratification. *Int. J. Num. Meth. Fluids*, **14**, pp. 919-934.
- Zhou S., McCorquodale J.A. and Vitasovic Z. (1992). Influences of density on circular clarifiers with baffles. *J. Environ. Engrg.*, **118**(6), pp. 829-847.
- Zhou S., McCorquodale J.A. and Zhong J. (1993). Semi-implicit skew upwind method for problems in environmental hydraulics. *Int. J. Num. Meth. Fluids*, **17**, pp. 803-823.
- Zhu J. (1991). A low-diffusive and oscillation-free convection scheme. *Communications in Appl. Numer. Methods*, **7**, pp. 225-232.

List of Abbreviations and Symbols

Abbreviations

1D, 2D, 3D	one-, two- and three-dimensional	
AAS	Atomic Absorption Spectrometry	
ADCP	Acoustic Doppler Current Profiler	
ADI	Alternating Direction Implicit	
ADV	Acoustic Doppler Velocimetry	
ADWF	Average Dry Weather Flow	$[L^3T^{-1}]$
AIC	Akaike's Information Criterion	
ASM	Activated Sludge Modelling	
AT	Aeration Tank	
BIC	Bayesian Information Criterion	
BOD	Biological Oxygen Demand	$[ML^{-3}]$
CFD	Computational Fluid Dynamics	
COD	Chemical Oxygen Demand	$[ML^{-3}]$
CSTR	Continuously Stirred Tank Reactor	
DAF	Dissolved Air Flotation	
DNS	Direct Numerical Simulation	
DPIV	Digital Particle Image Velocimetry	
DSS	Dispersed Suspended Solids	$[ML^{-3}]$
DSVI	Diluted Sludge Volume Index	$[L^3L^{-3}]$
EPS	Extracellular Polymeric Substances	
ESS	Effluent Suspended Solids	$[ML^{-3}]$
FBRM	Focused Beam Reflectance Method	
FDM	Finite Difference Method	
FEM	Finite Element Method	
FSS	Flocculated Suspended Solids	$[ML^{-3}]$
FVM	Finite Volume Method	
GLMT	Generalised Lorentz-Mie Theory	
HLEPA	Hybrid Linear/Parabolic Approximation	
LDV	Laser Doppler Velocimetry	
PBM	Population Balance Modelling	
PDWF	Peak Dry Weather Flow	$[L^3T^{-1}]$
PISO	Pressure Implicit with Splitting of Operators	
PSD	Particle Size Distribution	
PWWF	Peak Wet Weather Flow	$[L^3T^{-1}]$
QUICK	Quadratic Upstream Interpolation for Convective Kinetics	
RANS	Reynolds-Averaged Navier-Stokes	
RAS	Return Activated Sludge	
RGB	Red-Green-Blue	
RSE	Residual Standard Error	
RTD	Residence Time Distribution	
SBR	Sequencing Batch Reactor	
SDA	Structured Diagnostic Approach	
SIMPLE	Semi-Implicit Method for Pressure-Linked Equations	
SIMPLEC	SIMPLE-Consistent	

SIMPLER	SIMPLE-Revised	
SLR	Sludge Loading Rate	$[ML^{-2}T^{-1}]$
SOR	Surface Overflow Rate	$[L^3L^{-2}T^{-1}]$
SS	Suspended Solids (concentration)	$[ML^{-3}]$
SSE	Sum of Squared Errors	
SVI	Sludge Volume Index	$[L^3L^{-3}]$
TSS	Total Suspended Solids (concentration)	$[ML^{-3}]$
WWTP	WasteWater Treatment Plant	

English symbols

A	surface area	$[L^2]$
A_m	signal magnitude in frequency domain	$[-]$
B(...)	basis function utilised in finite element method (Chapter 3)	
$C_u, C_m, C_{1\varepsilon}, C_{2\varepsilon}, C_{3\varepsilon}$	empirical constants in turbulence transport equations	$[-]$
C	chord length (Chapter 4)	$[L]$
	concentration (Chapter 5)	$[ML^{-3}]$
d	pipe diameter	$[L]$
D	particle diameter (Chapters 2, 4)	$[L]$
	thickness of solids blanket (Appendix F)	$[L]$
D_c	dispersion coefficient	$[L^2T^{-1}]$
D_f	fractal dimension	$[-]$
D_p	percentage of total water depth unmeasurable by ADCP	$[\%]$
$D[1,0]$	number-weighted mean particle diameter	$[L]$
$D[4,3]$	mass-weighted mean particle diameter	$[L]$
E	empirical roughness parameter	$[-]$
f	variable	
f_r	friction factor	$[-]$
F	force	$[MLT^{-2}]$
Fr	Froude number	$[-]$
g	gravitational acceleration (Chapters 2, 5)	$[LT^{-2}]$
	Dirichlet boundary condition (Chapter 3)	
G	volume-averaged root-mean square velocity gradient	$[T^{-1}]$
H	water depth	$[L]$
H(...)	discretised spatial operator (Chapter 3)	
H_{inlet}	height of settling tank's inlet slot	$[L]$
i	index	
j	index	
k	kinetic energy	$[L^2T^{-2}]$
k_r	flow resistivity	$[ML^{-3}T^{-1}]$
K, K_c	fluid consistency index	$[ML^{-1}T^{n-2}]$
l	length scale	$[L]$
l_o	length scale of reactor	$[L]$
l_m	mixing length	$[L]$
l_u	turbulent length scale	$[L]$
L	particle longest dimension (Chapter 2)	$[L]$
	length of scraper blade (Appendix E)	$[L]$
L(...)	differential operator (Chapter 3)	
L_{inlet}	width of the inlet slot	$[L]$
L_p	particle longest dimension perpendicular to settling direction	$[L]$

m	material parameter	
	order of accuracy (Chapter 3)	
	refractive index (Chapter 4)	[-]
M	mass	[M]
n	flow behaviour index	[-]
N	number of data points	
n_i	number of particle counts in size class i	[-]
$O(\dots)$	truncation error (Chapter 3)	
p	pressure	[ML ⁻¹ T ⁻²]
P_b	production/dissipation of kinetic energy by buoyancy	[ML ⁻¹ T ⁻³]
Pe	Peclet number	[-]
P_s	production of kinetic energy by shear	[ML ⁻¹ T ⁻³]
Q	volumetric source (Chapter 3)	
	flow rate (Chapters 2, 5, 6)	[L ³ T ⁻¹]
r	radial coordinate (Chapter 5)	
	structural decay parameter (Chapter 7)	[T ⁻¹]
r_h, r_p	settling parameters of model of Takács <i>et al.</i> (1991)	[L ³ M ⁻¹]
R	radial distance	[L]
$R(\dots)$	residual (Chapter 3)	
R^2	coefficient of determination	
Re	Reynolds number	[-]
Ri	Richardson number	[-]
S	convergence matrix	
	surface	
sd	standard deviation	
t	time	[T]
T	time period	[T]
T_u	turbulent intensity	[-]
u	velocity along x-coordinate	[LT ⁻¹]
u_e	free-stream fluid velocity	[LT ⁻¹]
u_s	solids settling velocity	[LT ⁻¹]
u_τ	wall-friction velocity	[LT ⁻¹]
v	velocity along y-coordinate	[LT ⁻¹]
v_0	maximum hindered settling velocity	[LT ⁻¹]
v_s	hindered settling velocity	[LT ⁻¹]
v_S	scraper velocity	[LT ⁻¹]
$v_{s,d}$	discrete settling velocity	[LT ⁻¹]
v_{wall}	scraper velocity at side wall	[LT ⁻¹]
V	volume	[L ³]
w	velocity along z-coordinate	[LT ⁻¹]
w_i	weighting factor for particle size class	[-]
$W(\dots)$	weighting function (Chapter 3)	
x	axial coordinate	
	yield depth	[L]
X	solids concentration	[ML ⁻³]
X_0	solids concentration below which no settling occurs	[ML ⁻³]
y	vertical coordinate	

Greek symbols

α	parameter rheological model (Chapter 7) beam angle of ADCP (Chapter 4)	[°]
β	empirical parameter defining the inlet boundary (Chapter 4) parameter rheological model (Chapter 7) empirical constant in k - ε turbulence model (Chapter 4) bottom floor slope (Appendix F)	[-] [rad]
δ_{ij}	Kronecker-delta	
$\Delta x, \Delta y$	mesh size	[L]
Δt	time interval	[T]
ε	rate of energy dissipation (Chapters 2, 4) small number (Chapter 7)	[L ² T ⁻³]
ϕ	mass fraction	[-]
$\dot{\gamma}$	strain rate tensor	[T ⁻¹]
Γ	turbulent mass diffusivity	[L ² T ⁻¹]
η	Kolmogorov length scale	[L]
φ	over-relaxation factor	
κ	von Kármán constant	[-]
λ	structural property (Chapter 7) wavelength (Chapter 4)	[-] [L]
μ	dynamic viscosity	[ML ⁻¹ T ⁻¹]
μ_w	dynamic viscosity of water	[ML ⁻¹ T ⁻¹]
ν	kinematic viscosity	[L ² T ⁻¹]
ν_{eff}	effective viscosity	[L ² T ⁻¹]
ν_t	turbulent viscosity	[L ² T ⁻¹]
θ	parameter of implicit numerical scheme angle	[rad]
ρ	bulk density	[ML ⁻³]
ρ_l	liquid density	[ML ⁻³]
ρ_s	solids density	[ML ⁻³]
σ	total stress tensor (Chapters 2, 5) Courant number (Chapter 3)	[ML ⁻¹ T ⁻²] [-]
σ_k	parameter expressing turbulent diffusion of kinetic energy	[-]
σ_s	Schmidt number	[-]
σ_ε	parameter expressing turbulent diffusion of energy dissipation	[-]
τ	viscous stress tensor	[ML ⁻¹ T ⁻²]
τ_0	yield stress	[ML ⁻¹ T ⁻²]
τ_w	wall shear stress	[ML ⁻¹ T ⁻²]
ω	angular velocity	[radT ⁻¹]
ω_0	fundamental wavenumber (Chapter 4)	[L ⁻¹]
ω_i	weighting factor for particle size class i	[-]
Ω	computational domain	
ξ	particle shape factor	[-]
ζ	parameter of implicit numerical scheme	
ς	time step in pre-conditioning technique	[T]

Superscripts

'	fluctuating component
–	mean/averaged component
+	dimensionless variable
~	first guess/approximation of variable
≈	second guess/approximation of variable
n	iteration number/time step
c	correction of variable
T	transpose of matrix

Subscripts

b	bulk
l	liquid
nb	neighbouring nodes
S	scraper
t	turbulent
V	volume
z	zeolite
z-a	zeolite-air composite
⊥	perpendicular to
//	tangential to

Summary

During the last decades, most research focused on the biological treatment of wastewater. Settling tanks having the task to remove particulates by sedimentation only had a second priority. However, cleaned water leaving the wastewater treatment plant still contains particulates considerably contributing to the amount of waste, phosphorous and nitrogen compounds discharged into the receiving river. In this respect, a specialised European COST meeting on settling tanks (COST Action 624, 14-15 November 2002, Prague) acknowledged that there is still a considerable lack of process knowledge on settling tanks.

To fill these gaps in knowledge, the SediFloc project was started in 2000. It is a joint project of BIOMATH (Department of Applied Mathematics, Biometrics and Process Control) and PAINT (Particle and Interfacial Technology Group) at the Faculty of Agricultural and Applied Biological Sciences (Ghent University). SediFloc is an acronym merging "SEDImentation" and "FLOCculation". The ultimate goal of the project is to adequately model flocculation and deflocculation in the final settling tank, and accounting for hydraulic and physico-chemical influences. These modelling efforts increase our process understanding and better predictions of effluent quality should be possible.

As part of the project, this dissertation focused on the hydraulic and mechanical transport of solids in the settling tank. It aimed at implementing submodels for important physical phenomena into the Computational Fluid Dynamics (CFD) software Fluent (Fluent Inc., UK). CFD allows the computation of the velocity and solids distribution in the settling tank. In this respect, the solids removal mechanism was modelled and compared to literature. The development of submodels for solids sedimentation and rheology was conducted parallel to lab-scale experiments. Full-scale measurement campaigns, however, were essential to validate the model's predictions for local solids concentrations and flow field. Additionally, both lab-scale and full-scale investigations of sludge floc size distributions were performed.

Solids flow in the settling tank depends on many factors of which particulate properties, such as porosity and floc size, are very important. Above the solids blanket, discrete settling prevails; hence, the smaller the floc, the larger the drag it experiences, and the slower the floc settles. Process optimisation therefore consists of stimulating particle aggregation. Evaluation of any design modification improving flocculation is experimentally difficult because most particle sizers are unable to measure *in situ*. The Focused Beam Reflectance Method (FBRM) makes an exception though, and enables the *in situ* measurement using laser light reflection by particles. Preliminary experiments indicated that the focal point position of the laser largely influenced the size distributions obtained. For both inorganic and sludge particles, comparisons between FBRM, laser diffraction and image analysis revealed considerable discrepancies in size distribution attributed to the different measurement principles. The full-scale application of the FBRM to a secondary settling tank can be seen as the first attempt ever. At least for the case study conducted, the observation of invariable size distributions at high solids concentrations questioned the purpose of the feed well as flocculator. Possible hypotheses put forward are related to the zeolite dosage, high

concentrations and low shears prevailing in the settling tank. Dynamics could only be seen above the blanket where population balance modelling of the floc aggregation and breakup appears to be a promising application for the settling tank investigated.

Particulate properties not only affect discrete settling, but they also determine the rheological behaviour of the suspension. Viscous stresses are very important for the transport of momentum and, hence, they alter the velocity field and affect the solids distribution as well.

Because existing rheological models significantly differ in their model structure and associated parameters, research was conducted on three different full-scale treatment plant sludges. Appropriately measuring sludge rheology was found difficult due to solids settling and time-dependent thinning. This time-dependent thinning was shown to be important at high shear rates and resulted from a structural destruction of flocs. Experiments indicated that at least a two-level floc structure existed with different resistances to shear. Modelling time-dependent thinning in the solids blanket should not be considered as long as the particle size distribution observed remains invariant.

A new rheological model has been proposed that especially accounts for the sludge's behaviour at low shears. Comparison with widely used rheological models demonstrated that the solids blanket elevation is sensitive to viscosities at shears well below 1 s^{-1} . The results indicate the importance of rheology, its complexity and the fact that more research is needed to correctly model momentum transport in the solids blanket.

The proposed rheological model and the Takács solids settling velocity function calibrated by laboratory settling tests were implemented in a CFD model for a full-scale circular secondary settling tank. A 2D modelling approach was chosen to restrict the necessary computation time. Modelling the scraper mechanism in 2D inherently posed problems because its action is by definition 3D. Based on geometric considerations and the decomposition of the force exerted by the scraper on the fluid, a submodel for the scraper influencing the flow field was implemented in Fluent. The 2D modelling approach only allowed the consideration of the scraper's radial momentum. Comparison with both 3D simulations and measurements from literature confirmed the computed scraper velocities. Although small discrepancies between simulated and real scraper velocity occurred due to the way of implementation in Fluent, the submodel was believed to approximate the real 2D scraper behaviour. Simulations showed that the system's response on the scraper action very much depended on the rheology formulation applied. In this respect, the solids blanket elevation deteriorated when a yield stress occurred or high viscosities prevailed at low shears. Sludge acting as a Newtonian fluid did not pose problems though. This again stresses the importance of rheology on the solids transport efficiency in the settling tank.

Validation of the CFD model was conducted without applying this scraper submodel and with unsteady inlet boundary conditions. The latter allows a more powerful model validation. Simulated pseudo-steady-state solids concentration profiles corresponded well with measurements without any additional calibration. With strongly varying inlet flow rates, the predictions of underflow and effluent concentrations were good as well and only demanded for a lowering of the non-settleable solids concentration in the Takács settling velocity relation. The implementation of a flocculation submodel should resolve this issue though. The trend of solids blanket depth was also well resolved. On the other hand, hydrodynamics were

confronted with flow-through curves measured under dynamic inflow conditions. Although simulated and measured flow-through curves showed similar features, the system's response did not correspond to the observed time of peak occurrence. Simulated tracer concentrations were too high as well. Discrepancies were believed to originate from a too small diffusion assumed. Future 3D simulations, or 2D simulations that account for swirl, and a proper turbulence model are believed to resolve the flow-through curve validation problems. Due to its large influence on the flow-through curve, the uncertainty on the solids distribution in the settling tank should be reduced by additional solids concentration measurements.

In conclusion, this dissertation focused on different aspects of the settling tank. As a result, much process knowledge has been gained, and CFD submodels were set up for solids settling, rheology and the scraper mechanism. Considerations about particle size distribution modelling have been made as well. The research conducted also demonstrated that CFD modelling in 2D enables the accurate prediction of solids distribution, whereas the hydrodynamics probably demand 3D modelling or 2D models that account for swirl effects.

Samenvatting

De laatste decennia richtte onderzoek zich voornamelijk op de biologische aspecten van de waterzuivering, meer bepaald op de microbiologische verwijdering van opgeloste vuilcomponenten. De afscheiding van slibvlokken van het gezuiverde water door middel van sedimentatie was slechts van secundair belang. Een niet-optimale afscheidingsefficiëntie resulteert echter in de lozing van slib, welke gepaard gaat met een vuilvracht en aanzienlijke hoeveelheden aan fosfor en stikstof. Tijdens een Europese COST-vergadering betreffende nabezinktanks (COST actie, 14-15 november 2002, Praag) werd het gebrek aan proceskennis als één van de belangrijkste redenen voor deze inefficiëntie naar voor geschoven.

Om de leemten in kennis aan te vullen werd het SediFloc-project opgestart in 2000. Het project loopt binnen drie onderzoekseenheden van de Universiteit Gent: BIOMATH (Vakgroep Toegepaste Wiskunde, Biometrie en Procesregeling), PAINT (Vakgroep Toegepaste Analytische en Fysische Chemie) en de Vakgroep Chemische Proceskunde en Technische Chemie. SediFloc is een acroniem dat staat voor "SEDImentatie" en "FLOcculatie". Het ultieme doel van het project is het adequaat modelleren van flocculatie en deflocculatie in een bezinktank in al zijn aspecten, m.a.w. hydrodynamische en fysisch-chemische invloeden worden in rekening gebracht. Het finaal model verleent ons proceskennis en laat betere predicties toe van de effluentkwaliteit.

Dit proefschrift maakte deel uit van het SediFloc-project en concentreerde zich op het hydrodynamisch en mechanisch slibtransport in de bezinktank. Hierbij werd gebruik gemaakt van het *Computational Fluid Dynamics* (CFD) softwarepakket Fluent (Fluent Inc., VK) dat toelaat locale vloeistofsnelheden en slibconcentraties te berekenen. De implementatie in Fluent van submodellen voor belangrijke fysische processen in bezinktanks vormde het hoofddoel van dit onderzoek. Zo werd het slibverwijderingsmechanisme gemodelleerd en vergeleken met literatuurgegevens. Verder werden submodellen voor slibbezinking en reologie parallel met laboratoriumexperimenten ontwikkeld. Volle-schaal meetcampagnes waren evenwel noodzakelijk om de modelpredicties van locale slibconcentraties en snelheden te toetsen. Ook werden labo- en volle-schaal metingen van slibvlokgroottedistributies uitgevoerd.

Slibtransport in bezinktanks hangt af van vele factoren; onder meer vlokeigenschappen zoals porositeit en vloggrootte zijn zeer belangrijk. Deze vlokeigenschappen zijn voornamelijk van belang boven het slibdeken waar discrete bezinking domineert. In deze zone geldt: hoe kleiner een vlok, des te groter de wrijving en des te trager een vlok bezinkt. Procesoptimalisaties bestaan daarom onder meer uit het stimuleren van vlokaggregatie. Evaluatie van een ontwerpmodificatie welke flocculatie bevordert, is experimenteel echter zeer moeilijk omdat het merendeel van de partikelgrootte-meettechnieken ongeschikt is om *in situ* te meten. De *Focused Beam Reflectance Methode* (FBRM) is een uitzondering hieromtrent, en laat een *in situ* meting toe op basis van de laserlichtreflectie door partikels. Voorafgaande experimenten toonden aan dat de locatie van de laser's focus in zeer sterke mate de opgemeten deeltjesgroottedistributies beïnvloedt. Ook werden er belangrijke

afwijkingen geconstateerd in deeltjesgroottedistributies die bekomen werden met FBRM, laserdiffractie en beeldanalyse. Deze golden voor zowel anorganische partikels als slibpartikels. De toepassing van de FBRM op een volle-schaal nabezinktank kan gezien worden als één van de eerste pogingen om deeltjesgroottedistributies *in situ* te meten op een waterzuiveringsinstallatie. De identieke deeltjesgroottedistributies waargenomen bij hoge slibconcentraties stelden de functie van de inlaatstructuur als flocculator in vraag, alhoewel meer onderzoek noodzakelijk is om een sluitende conclusie te trekken. Mogelijke hypothesen voor de identieke distributies zijn gerelateerd aan de zeolietdosering, hoge slibconcentraties en geringe snelheidsgradiënten in de nabezinktank. Enige dynamica kon wel gezien worden boven het slibdeken zodat populatiebalansmodellering van zowel de vlokaggregatie als de -opbreking hier een interessante toepassing kan zijn om de systeemefficiëntie te analyseren en te optimaliseren.

De partikeleigenschappen van het slib beïnvloeden niet enkel de discrete bezinking, maar ze bepalen eveneens het reologisch gedrag van de suspensie. Viskeuze afschuifspanningen zijn van groot belang voor momentumtransport en, zodoende, bepalen ze mede het snelheidsveld en de slibdistributie in de bezinktank.

Bestaande reologische modellen verschillen sterk in hun modelstructuur en bijhorende parameters. Daarom werd hieromtrent onderzoek gedaan op slib afkomstig van drie verschillende waterzuiveringsinstallaties. Het onderzoek wees uit dat slibbezinking en tijdsafhankelijke *thinning* een accurate meting met de reometer bemoeilijken. Deze *thinning* bleek verder voornamelijk van belang te zijn bij hoge snelheidsgradiënten en resulteerde in een structurele vlokdestructie. Gerelateerd hiermee werd aangetoond dat vlokken opgebouwd zijn uit tenminste twee structurele niveaus, waarbij elk een verschillende weerstand biedt aan afschuifspanningen. De modellering van tijdsafhankelijke *thinning* in het slibdeken dient echter niet beschouwd te worden zolang de waargenomen partikelgroottedistributie niet verandert.

Ook werd een reologisch model voorgesteld dat zich speciaal richt op het reologisch gedrag van slib bij lage snelheidsgradiënten. Een vergelijking met populaire reologische modellen demonstreerde dat de hoogte van het slibdeken sterk gevoelig is aan de viscositeit bij snelheidsgradiënten kleiner dan 1 s^{-1} . Al deze resultaten wijzen duidelijk op het belang van reologie, zijn complexiteit en het feit dat meer onderzoek noodzakelijk is om het momentumtransport in het slibdeken correct te modelleren.

Het voorgestelde reologisch model en de Takács slibbezinkingsfunctie, beiden gekalibreerd met behulp van labo-schaal experimenten, werden geïmplementeerd in een CFD model van een volle-schaal, ronde nabezinktank. Om de nodige rekentijd te limiteren werd voor een 2-dimensionale (2D) benadering geopteerd. De modellering van het slibverwijderingsmechanisme, een zogenaamde schraper, stelde echter wel enige problemen omdat zijn impact op het snelheidsveld per definitie 3D is. Het ontwikkelde submodel, dat geïmplementeerd werd in Fluent, is gebaseerd op geometrische beschouwingen en de kracht door de schraper uitgeoefend op de suspensie. De 2D benadering liet enkel toe de radiale momentumcomponent te beschouwen. Ondanks de ruimtelijke vereenvoudiging bevestigden 3D simulaties en metingen uit de literatuur de berekende (radiale) schrapersnelheden. Hoewel kleine discrepanties tussen gesimuleerde en waargenomen snelheden optraden wegens de manier van implementatie in Fluent, kon het submodel beschouwd worden als een eerste aanvaardbare

benadering van het 2D schrapergedrag. Simulaties toonden aan dat de invloed van de schraper op de werking van de bezinktank sterk afhangt van de reologische formulering. In dit opzicht trad er een slibdekenverhoging op wanneer een zwichtspanning voorkwam of hoge viscositeiten heersten bij lage snelheidsgradiënten. Slib dat zich daarentegen als een Newtoniaanse vloeistof gedroeg, resulteerde niet in een slechtere proceswerking. Dit benadrukt opnieuw de impact van reologie op de slibtransportefficiëntie in de bezinktank.

Validatie van het CFD model werd bewerkstelligd zonder het schraper-submodel en met beschouwing van tijdsveranderlijke condities opgelegd aan de ingang van de bezinktank. De laatste laat een krachtige validatie toe. Zonder enige bijkomende kalibratie kwamen gesimuleerde slibconcentratieprofielen bij pseudo-stationaire systeemcondities goed overeen met metingen. Ook wanneer sterk variërende ingangsdebieten optraden, werden goede predicties van onderstroom- en effluentslibconcentraties bekomen. Enkel de niet-bezinkbare slibconcentratie in de Takács bezinkingsfunctie diende verlaagd te worden, wat mogelijks kan verholpen worden door de implementatie van een flocculatie-submodel. De hydrodynamica werd geconfronteerd met verblijftijdsdistributies, eveneens opgemeten bij tijdsvariabele ingangscondities. Als merker werd LiCl benut. Alhoewel de gesimuleerde en waargenomen distributies gelijkaardige kenmerken vertoonden, kwam het tijdstip van piekconcentratie niet overeen met de waargenomen waarde. De gesimuleerde merkerconcentraties waren eveneens te hoog. Een te kleine gemodelleerde diffusie in het systeem wordt aangenomen als de reden van beide discrepanties. Toekomstige 3D simulaties of 2D simulaties met een in achtname van de tangentiële snelheidscomponent (zonder snelheidsgradiënt), en een goede keuze van het turbulentiemodel worden geacht deze problemen op te lossen. Ook additionele metingen van slibconcentraties in de bezinktank worden aangeraden wegens de grote impact van de slibdistributie op het snelheidsprofiel. De extra metingen verlagen de onzekerheid op de slibdistributie in de bezinktank.

Ter conclusie, dit proefwerk richtte zich op verschillende aspecten van de bezinktank. Hierdoor werd veel proceskennis vergaard ter ontwikkeling van CFD submodellen voor slibbezinking, reologie en slibverwijderingsmechanisme. Partikelgroottedistributies werden eveneens beschouwd. Het verrichte onderzoek toonde ook aan dat een 2D modellering met CFD een accurate predictie van de slibdistributie toelaat, maar dat een correcte voorspelling van de hydrodynamica wellicht een 3D aanpak vergt of een 2D model dat de tangentiële snelheid in rekening brengt.

Curriculum Vitae

Personalia

Bob De Clercq
Kapellen, 24/02/1974
Belg
Ongehuwd

adres:
Riddershoevelaan 32
2940 Stabroek
03/568.60.76
bob.declercq@biomath.rug.ac.be

Opleiding

- Secundair onderwijs, Wiskunde 8u, Sint-Lambertus Instituut Ekeren 1986 - 1992
- Bio-ingenieur in de milieutechnologie (grote onderscheiding) 1992 - 1997
Universiteit Gent
Scriptie: Studie van mengkarakteristieken in bioreactoren en hun invloed op bioprocessen

Bijkomende opleiding

In het kader van de doctoraatsopleiding werden de volgende cursussen gevolgd:

- R&D management 2003
- Easy pc logging & instrument control with LabView 2002
- Atmospheric dispersion modelling 2002
- Experimental design for bio-process engineering 2002

Werkervaring

- EPAS (samenwerking met Universiteit Gent) 1997 - 1998
Functie: project-ingenieur
Optimalisatie en simulatie van een industriële waterzuiveringsinstallatie (Janssen Pharmaceutica) met behulp van WEST++
- Universiteit Gent (Fac. Landb. Toeg. Biol. Wet.) 1998 - 2003
Functie: doctoraatstudent (NFWO)
Numerieke stromingsmechanica van bezinktanks: ontwikkeling van experimenten en submodellen voor reologie, slibbezinking en slibverwijdering

Verblijven in het buitenland

- Februari - November 2001: Advanced Wastewater Management Centre, University of Queensland, Brisbane, Australië

Publicaties

Tijdschriften

- De Clercq B., Coen F., Vanderhaegen B. and Vanrolleghem P. (1998). Calibrating simple models for mixing and flow propagation in waste water treatment plants. *Wat. Sci. Tech*, **39**(4), 61-69.
- Vanderhasselt A., De Clercq B., Vanrolleghem P., Vanderhaegen B. and Verstraete W. (1999). On-line control of polymer addition to prevent massive sludge wash-out from the settler. *J. Environ. Eng.*, **125**(11), 1014-1022.
- De Clercq B., Meirlaen J., Verdonck F. and Vanrolleghem P.A. (2001). An overview of the posters presented at Watermatex 2000. I. New models / Integrated urban water management / time series analysis. *Wat. Sci. Tech.*, **43**(7), 377-380.
- Nopens I., Biggs C.A., De Clercq B., Govoreanu R., Wilén B.-M., Lant P. and Vanrolleghem P.A. (2002). Modelling the activated sludge flocculation process combining laser diffraction particle sizing and population balance modelling (PBM). *Wat.Sci.Tech.*, **45**(6), 41-49.
- De Clercq B. and Vanrolleghem P.A. (2002). Computational fluid dynamics in wastewater treatment. *Med. Fac. Landb. Toegep. Biol. Wet.*, **67**(4), 15-19.

Proceedings met ISBN

- De Clercq B., Kinnear D.J. and Vanrolleghem P.A. (2002). Hydraulic characterization of a wastewater treatment clarifier by an acoustic Doppler current profiler. In: *Advances in Fluid Mechanics IV*. Eds. Rahman M., Verhoeven R. and Brebbia C.A., WIT Press, UK, 736 pp. (ISBN 1-85312-910-0)
- De Clercq B., Brannock M., Lant P. and Vanrolleghem P.A. (2002). In situ particle size characterization on a circular clarifier of a wastewater treatment plant. In: *Proceedings 4th World congress on Particle Technology*. 21-25 July, Sydney, Australia (ISBN 085-825-7947)

Proceedings en Cursussen

- Vanrolleghem P., De Clercq B. en Vanhooren H. (1997). RWZI Modellen, basisprincipes. PAO-cursus "Regelen en Besturen van Actief-slibinstallaties", Stichting Postacademisch Onderwijs, Delft, Nederland.
- Vanrolleghem P., De Clercq B., Devisscher M., Meirlaen J. and Vanhooren H. (1998). Bioprocessregeling. Cursus Faculteit Landbouwkundige en Toegepaste Biologische Wetenschappen, Universiteit Gent.
- Vanrolleghem P.A., De Clercq B. en Coen F. (1997). *Hydraulica: Startpunt voor calibratie van waterzuiveringsmodellen*. In: *Proceedings STOWA SIMBA Gebruikersplatform*, 27 maart, Amersfoort, The Netherlands, 27 pag.
- De Clercq B., Coen F., Vanderhaegen B. and Vanrolleghem P. (1998). Calibrating simple models for mixing and flow propagation in waste water treatment plants. In: *Proceedings of Conference on Application of Models in Water Management (Aquatech '98)*, 24-25 September, Amsterdam, The Netherlands.
- Vanrolleghem P., Gernay K., Petersen B., De Clercq B., Coen F. and Ottoy J.-P (1998). Limitations of Short-term Experiments Designed for Identification of Activated Sludge Biodegradation Models by Fast Dynamic Phenomena. In: *Proceedings 7th IFAC Conference on Computer Applications in Biotechnology (CAB7)*, 31 May - 4 June, Osaka, Japan.
- De Clercq B., Vanderhaegen B., Harmand J. and Vanrolleghem P. (1998). Evaluation of a rule-based control strategy for an industrial equalization facility with technical/physical constraints. In: *Proceedings European Control Conference*, 31 August - 3 September, Karlsruhe, Germany.
- Harmand J., Steyer J.P., Devisscher M., De Clercq B., Vanderhaegen B. and Vanrolleghem P.A. (1998). Advanced Control of an Industrial Equalization System. In: *Proceedings European Control Conference*, 31 August - 3 September, Karlsruhe, Germany.

- Gillot S., De Clercq B., Defour D., Simoens F., Gernaey K. and Vanrolleghem P.A. (1999). Optimization of wastewater treatment plant design and operation using simulation and cost analysis. In: Proceedings 72nd annual conference WEFTEC 1999. 9-13 October, New Orleans, USA.
- De Clercq B., Vanderhasselt A., Vanderhaegen B., Hopkins L.N., Vanrolleghem P.A. (1999). A model-based evaluation of control strategies for a clarifier at an industrial wastewater treatment plant. In: Proceedings 8th IAWQ Conference on Design, Operation and Economics of Large Wastewater Treatment Plants, 6-9 September, Budapest, Romania.
- De Clercq B., Debusscher D. en Vanrolleghem P. (2000). Bezinking: maken van adequate keuzes. PAO-cursus "Modelleren Afvalwaterzuiveringsprocessen", Stichting Postacademisch Onderwijs, Delft, Nederland.
- De Clercq B., Meirlaen J., Verdonck F. and Vanrolleghem P.A. (2001). An overview of the posters presented at Watermatex 2000. I. New models / Integrated urban water management / time series analysis. In: Proceedings of Watermatex 2000 Conference.
- Nopens I., Biggs C.A., De Clercq B., Govoreanu R., Wilén B.-M., Lant P. and Vanrolleghem P.A. (2001). Modelling the activated sludge flocculation process combining laser diffraction particle sizing and population balance modelling (PBM). In: Proceedings 5th IWA Seminar on Modelling of Activated Sludge Processes in Theory and Practise, 10-12 September, Kollokollo, Denmark.
- Govoreanu R., Nopens I., De Clercq B., Saveyn H., Van der Meeren P. and Vanrolleghem P.A. (2001). Influence of experimental parameters for on-line determination of floc size distribution. In: Proceedings 12th Romanian International Conference on Chemistry and Chemical Engineering, 13-15 September, Bucharest, Romania.
- De Clercq B., Lant P.A. and Vanrolleghem P.A. (2002). On-line particle size measurements in secondary clarifiers. In: Proceedings International IWA Conference on Automation in Water Quality Monitoring (AutMoNet 2002). 21-22 May, Vienna, Austria.
- De Clercq B., Kinnear D.J. and Vanrolleghem P.A. (2002) On-line dynamic fluid velocity profiling in secondary clarifiers. In: Proceedings International IWA Conference on Automation in Water Quality Monitoring (AutMoNet2002), 21-22 May 21-22, Vienna, Austria.
- Govoreanu R., Seghers D., Nopens I., De Clercq B., Saveyn H., Capalozza C., Van der Meeren P., Verstraete W., Top E. and Vanrolleghem P.A. (2002). Linking floc structure and settling properties to activated sludge population dynamics in an SBR. In: Proceedings 3th World Water Congress, 7-12 April, Melbourne, Australia.
- Brannock M., Howes T., Johns M., De Clercq B. and Keller J. (2002). CFD modelling of particle transport and biological reactions in a mixed wastewater treatment vessel. In: Proceedings International Conference on Scientific & Engineering Computation (IC-SEC2002), 3-5 December, Singapore.

Presentaties op conferenties

- De Clercq B., Coen F., Vanderhaegen B. and Vanrolleghem P. (1998). Calibrating simple models for mixing and flow propagation in waste water treatment plants. Conference on Application of Models in Water Management (Aquatech '98), 24-25 September, Amsterdam, The Netherlands.
- De Clercq B., Vanderhasselt A., Vanderhaegen B. and Vanrolleghem P. (1999). Control of polymer addition to maintain good clarifier performance. 18th Benelux Meeting on Systems and Control, 3-5 March, Houthalen-Helchteren, Belgium.
- De Clercq B., Vanderhaegen B., Harmand J. and Vanrolleghem P. (1998). Evaluation of a rule-based control strategy for an industrial equalization facility with technical/physical constraints. European Control Conference ECC'99, 31 August - 3 September, Karlsruhe, Germany.
- De Clercq B., Kinnear D.J. and Vanrolleghem P.A. (2002). Hydraulic characterization of a wastewater treatment clarifier by an acoustic Doppler current profiler. 4th International Conference on Advances in Fluid Mechanics (AFM 2002), 15-17 May, Ghent, Belgium.

- De Clercq B., Lant P.A. and Vanrolleghem P.A. (2002). On-line particle size measurements in secondary clarifiers. International IWA Conference on Automation in Water Quality Monitoring (AutMoNet 2002). 21-22 May, Vienna, Austria.
- De Clercq B., Brannock M., Lant P. and Vanrolleghem P.A. (2002). In situ particle size characterization on a circular clarifier of a wastewater treatment plant. 4th World Congress on Particle Technology. 21-25 July, Sydney, Australia.
- De Clercq B. and Vanrolleghem P.A. (2002). Computational fluid dynamics in wastewater treatment. PhD Symposium, 9 October, Ghent, Belgium.
- De Clercq B. and Vanrolleghem P.A. (2002). Secondary clarifier monitoring: some new tools. Working Group 4 Workshop on Secondary Clarifiers (COST 624). 14-16 November, Prague, Czech Republic.

Poster Presentaties

- Vanrolleghem P., Gernay K., Petersen B., De Clercq B., Coen F. and Ottoy J.-P (1998). Limitations of Short-term Experiments Designed for Identification of Activated Sludge Biodegradation Models by Fast Dynamic Phenomena. 7th IFAC Conference on Computer Applications in Biotechnology (CAB7), 31 May - 4 June, Osaka, Japan.
- De Clercq B., Vanderhasselt A., Vanderhaegen B., Hopkins L.N., Vanrolleghem P.A. (1999). A model-based evaluation of control strategies for a clarifier at an industrial wastewater treatment plant. 8th IAWQ Conference on Design, Operation and Economics of Large Wastewater Treatment Plants, 6-9 September, Budapest, Roemenia.

Reviews

- Spanjers H., Vanrolleghem P.A., Olsson G. and Dold P.L. (1998). Respirometry in control of the activated sludge process: principles. IAWQ Scientific and Technical Report No.7, IAWQ, London, England.